



HAL
open science

Construction of stimuli-responsive architectures through coordination-driven self-assembly

Maksym Dekhtiarenko

► **To cite this version:**

Maksym Dekhtiarenko. Construction of stimuli-responsive architectures through coordination-driven self-assembly. Organic chemistry. Université d'Angers; Kiiivs kij nacional nij univèrsitet imeni Tarasa Ševčenko (Kiiiv), 2021. English. NNT : 2021ANGE0034 . tel-04003624

HAL Id: tel-04003624

<https://theses.hal.science/tel-04003624v1>

Submitted on 24 Feb 2023

HAL is a multi-disciplinary open access archive for the deposit and dissemination of scientific research documents, whether they are published or not. The documents may come from teaching and research institutions in France or abroad, or from public or private research centers.

L'archive ouverte pluridisciplinaire **HAL**, est destinée au dépôt et à la diffusion de documents scientifiques de niveau recherche, publiés ou non, émanant des établissements d'enseignement et de recherche français ou étrangers, des laboratoires publics ou privés.

DOCTORAT / MATIERE
BRETAGNE / MOLECULES
LOIRE / ET MATERIAUX



THESE DE DOCTORAT DE

L'UNIVERSITE D'ANGERS

ECOLE DOCTORALE N° 596
Matière, Molécules, Matériaux
Spécialité : *Chimie Organique*

Par

Maksym DEKHTIARENKO
**Construction of stimuli-responsive architectures through
Coordination-driven self-assembly**

Thèse présentée et soutenue à Kiev (Ukraine), le 22 Décembre 2020
Unité de recherche : Laboratoire MOLTECH-Anjou, UMR CNRS 6200
Thèse N° :

Rapporteurs avant soutenance :

Dr. Jean-Francois NIERENGARTEN
Prof. Oleksandr ROSHAL

Directeur de Recherche CNRS, Université de Strasbourg
Professeur, Université nationale de Kharkiv

Composition du Jury :

Président
Prénom Nom

Fonction et établissement d'exercice (9) (à préciser après la soutenance)

Examineur
Dr. Oleksandr GRYGORENKO

Maître de conférences, Université nationale Taras-Chevtchenko de Kiev

Directeur de thèse
Dr. Sébastien GOEB

Chargé de Recherche CNRS, Université d'Angers

Co-directeurs de thèse
Pr. Marc SALLÉ
Pr. Zoia VOITENKO

Professeur, Université d'Angers
Professeur, Université nationale Taras-Chevtchenko de Kiev

Acknowledgements

At the end of those fruitful four years of my thesis, it is due to make conclusions of this important period of life of any young researcher. Years of Ph.D. are giving shape to a young person, teaching him to organize the mind, to effectively communicate and present thoughts.

The last two years of the world pandemic have never been harder for our society. The counter epidemic measures have introduced complications into a lot of professions and, in particular, to my thesis work. Luckily, modern communication technologies are keeping us in touch and allow us to work on the same thing and communicate from miles away. And we should all be grateful to modern society that embraces scientific research which allows us to have for granted various things that our fathers and grandfathers could only dream of.

I would first and foremost like to thank my supervisors Sebastien Goeb, Marc Sallé (University of Angers, France, laboratory MOLTECH-Anjou), and Zoia Voitenko (Taras Shevchenko National University of Kyiv, Ukraine) for allowing me to work within their research groups during this collaboration between two universities, as well as dealing with all the difficulties and specifics of such a joint project.

I am grateful to Jean-Francois Nierengarten and Oleksandr Roshal for accepting an offer to review my thesis, as well as Jean-Francois Nierengarten and Philippe Leriche for being members of my CSI committee.

I'm especially thankful to Sebastien Goeb, for everyday mentorship and for showing a personal example of how to be a great modern scientist, you are a perfect role model for young scientists.

I thank all the people without whom this thesis could not succeed: Frédéric Aubriet and Vincent Carré of the University of Lorraine (Metz) for the ESI-FTICR mass spectrometry analyzes; Ingrid Freuze for mass spectrometry analyzes in the laboratory; Valérie Bonnin and Cécile Mézière for making everything smooth in the lab; Benjamin Siegler for NMR analyzes; Éric Levillain and Olivier Alévêque for cyclic voltammetry tips; Iwona Nierengarten for NMR titration experiments in Strasbourg; Simon Pascal, Mourad Elhabiri and Olivier Siri for UV-vis experiments and collaboration in a perfect collab project. Finally, special gratitude to Magali Allain, for her time spent solving X-ray structures, which were never too easy.

I'm thankful to the members of SOMaF team for their welcome and advice, as well as useful discussions. Thanks to Dr. Pablo Simon and Dr. Fanny Peigneguy for tolerating me in the office for the whole three years. Thanks to Dr. Jose-Maria Andres, Dr. Amina Benchohra, Dr. Clemence Nicolas, Dr. Youssef Aidibi, Simon Sejourne, Marie Voltz, and all the Ph.D. students and post-docs for the perfect atmosphere in Moltech-Anjou of friendship and support. Thank you, Dr. Oleh Stetsiuk, Dr. Serhii Krykun, Dr. Natalya Plyuta, Dr. Viacheslav Shkirskiy, and all the Ukrainian master students these years, who helped me not to get homesick too much. And special thanks to Yohan Cheret for all those discussions and help, you have become a really good friend, man.

Thank you all!

ACKNOWLEDGEMENTS	3
CHAPTER 1	9
STATE OF THE ART	9
1. Self-assembly	11
1.1. General concepts.....	11
1.2. Example of self-assembled discrete structures.....	11
1.3. Coordination-driven self-assembly.....	13
1.4. Molecular recognition.....	16
1.4.1. Ion recognition.....	16
1.4.2. Neutral molecule recognition.....	18
1.5. Interlocked molecular rings.....	20
2. Guest release and stimuli-responsive self-assembly	23
2.1. Action on the guest.....	23
2.2. Action on the host.....	25
2.2.1. pH-active self-assemblies.....	25
2.2.2. Photo-active self-assemblies.....	26
3. Redox-active self-assemblies	27
3.1. Electron-rich self-assembled metalla-structures obtained in Angers.....	29
3.1.1. BPTTF-based assemblies.....	30
3.1.2. TTF-based assemblies.....	31
3.1.3. DTF-based assemblies.....	32
3.1.4. Extended TTF-based systems.....	33
4. Objectives of my thesis	37
CHAPTER 2	39
LIGANDS AND SELF-ASSEMBLIES INCORPORATING THE "EXTTF" SCAFFOLD	39
1. Tetrapyridyl-extTF ligands: a comparative study between two regioisomer ligands	41
2. Self-assemblies from the new ligands A1Me and A1TEG	44
2.1. Self-assemblies with cis-blocked transition metal complexes.....	44
2.2. Self-assemblies involving extTF-based ligands and bis(Ruthenium) complexes.....	50
3. Self-assemblies of 2,6 difunctionalized extended TTF ligand	65
3.1. Toward redox-active Banana-shaped cages.....	65
3.2. Toward redox-active tetrahedral cages.....	67
4. A pillar[5]arene scaffold modified with electroactive moieties	68
CHAPTER 3	77
SELF-ASSEMBLIES INCORPORATING THE "DTF" SCAFFOLD	77
1. Dithiafulvene-based self-assembled tweezers	79
2. Interlocking of DTF-based molecular clips	88
CHAPTER 4. CATENANE-TYPE INTERLOCKING OF BENZOBISIMIDAZOLE / BIS(RUTHENIUM) MOLECULAR RECTANGLE. EFFECTS OF PH, GUESTS AND CONCENTRATION	97
1. Concept of the project	99
2. Synthesis of the ligand BBI	100
3. Synthesis of metalla-structures Oxa₂BBI₂ and Naph₂BBI₂	100
4. Characterization of metalla-structures Oxa₂BBI₂ and Naph₂BBI₂	101
4.1. Interlocking properties of metalla-rectangle Naph ₂ BBI ₂	104
4.2. Complexation properties of Naph ₂ BBI ₂ and (Naph ₂ BBI ₂) ₂ dissociation.....	105
4.3. Optical properties of ligand BBI, metalla-structures Oxa ₂ BBI ₂ and Naph ₂ BBI ₂	108
4.4. Acid-base properties of the BBI ligand and the Naph ₂ BBI ₂ metalla-rectangle.....	111
4.4.1. BBI ligand.....	111
4.4.2. Naph ₂ BBI ₂ metalla-rectangle.....	114
4.5. pH-controlled dissociation of catenane (Naph ₂ BBI ₂) ₂	116
4.6. Complexation properties of Naph ₂ BBI ₂ H ₄	119
5. Conclusion	120

GENERAL CONCLUSION	121
EXPERIMENTAL PART	127
1. Instrumentation	129
2. Chemicals	129
3. Procedures	129
4. Supporting materials.....	152
4.1. Additional analyses related to Chapter 2	152
4.2. Additional analyses related to Chapter 3	180
4.3. Additional analyses related to Chapter 4	190
REFERENCES	205

Abbreviations

2D	two-dimensional
3D	three-dimensional
BBI	benzobisimidazole
CV	cyclic voltammetry
D	diffusion coefficient
DCTNF	9-dicyanomethylen-2,4,7-trinitrofluoren
DFT	density functional theory
DMF	dimethylformamide
DMSO	dimethyl sulfoxide
DOSY	diffusion-ordered spectroscopy
dppf	[1,1'-bis(diphenylphosphino)ferrocene]
DTF	dithiafulvalene
Equiv.	equivalent
ESI	electrospray ionization
exTTF	π -extended tetrathiafulvalene
GC	glassy carbon
HRMS	high resolution mass spectrometry
HWE	Horner-Wadsworth-Emmons reaction
IR	infrared
M	mol.l ⁻¹
MALDI	matrix-assisted laser desorption/ionization
MS	mass spectrometry
NMR	nuclear magnetic resonance
Pd(dppf)	[1,1'-bis(diphenylphosphino)ferrocenepaladium(II)]
Ph	phenyl
Ppm	parts per million
Py	pyridine
r_H	hydrodynamic radius
rt	room temperature
RuOxa	bis(triflate (p-cymene)ruthenium(ii)) oxalato-1,4-bis(olate)
RuBenzo	bis(triflate(p-cymene)ruthenium(ii)) 5,8-dioxo-5,8-dihydrobenzene-1,4-bis(olate)
RuNaph	bis(triflate(p-cymene)ruthenium(ii)) 5,8-dioxo-5,8-dihydronaphthalene-1,4-bis(olate)
RuTetra	bis(triflate(p-cymene)ruthenium(ii))6,11-dihydroxy-6,11-dihydrotetracene-5,12-bis(olate)
TDAE	tetrakis(dimethylamino)ethylene
OTf	triflate
PTZ	N-methylphenothiazinium tetrafluoroborate
TFA	trifluoroacetic acid
THF	tetrahydrofuran
TLC	thin layer chromatography
TLCV	thin layer cyclic voltammetry
TTF	tetrathiafulvalene
UV	ultraviolet
XRD	x-ray diffraction
δ	chemical shift, ppm

Chapter 1.
State of the art

1. Self-assembly

1.1. General concepts

Unlike molecular chemistry which involves non dynamic covalent bonds, supramolecular chemistry is based on the assembly of molecules through weak dynamic bonds. Several weak intermolecular interactions can be considered in the context of supramolecular chemistry and are depicted in Table 1. They constitute a complete toolbox that allows for the construction of complex supramolecular structures, allowing the implementation of two founding concepts of supramolecular chemistry, namely "host-guest chemistry (molecular receptors)" and "self-assembly".

Interaction	Energy (kJ × mol ⁻¹)	Example
Ion-ion	100-350	Sodium chloride
Ion-dipole	50-200	Crown ether – Na ⁺
Coordination bond	50-200	Transition metal complexes
Hydrogen bond	4-120	DNA
Cation-π	5-80	K ⁺ in benzene
Anion-π	20-50	Cl ⁻ with trifluoro-1,3,5-triazine
Dipole-dipole	5-50	Acetone
π-π	0-50	Benzene and graphite
Van der Waals	<5	Long alkyl chains
Hydrophobic interactions	Depends on the solvent	Inclusion compounds with cyclodextrins

Table 1: Typical supramolecular interactions

Beyond preorganization, lies the design of systems undergoing self-organization, that are, systems capable of spontaneously generating a well-defined (functional) supramolecular architecture by self-assembly from their components under a well-defined set of conditions.¹ To achieve such transformation, the system must be able to dynamically organize and disorganize in a reversible manner. This reversibility allows the system to correct itself and only the most thermodynamically stable product is obtained at the end. In this process, entropy favors formation of the discrete systems with a minimum number of components. These factors allow obtaining metallocycles with high yields in just one step.

1.2. Example of self-assembled discrete structures

One interaction that has been widely utilized for the construction of self-assembled structures is the hydrogen bond. A well-established natural example is the DNA double-helix where the geometric and electronic complementarity of the nucleotides allows a precise pairing by a combination of hydrogen bonding and π-π interactions between components of both strands.²

The reversible nature of the hydrogen bonds was also explored for the construction of synthetic molecular receptors. Representative examples are provided in Figure 1. For example, Reinhoudt *et al.* reported the self-assembly of melamine-modified calix[4]arene with barbiturate or cyanurate (molecules **1.1**) that can encapsulate planar aromatics by π -stacking.³ Mendoza *et al.* reported the self-complementary dimer cage **1.2** based on the modified cyclotrimeratrylene scaffold.⁴ Another interesting example was reported by Therrien *et al.* with the self-assembly formed by the combination of metal coordination and hydrogen bonding **1.3**.⁵

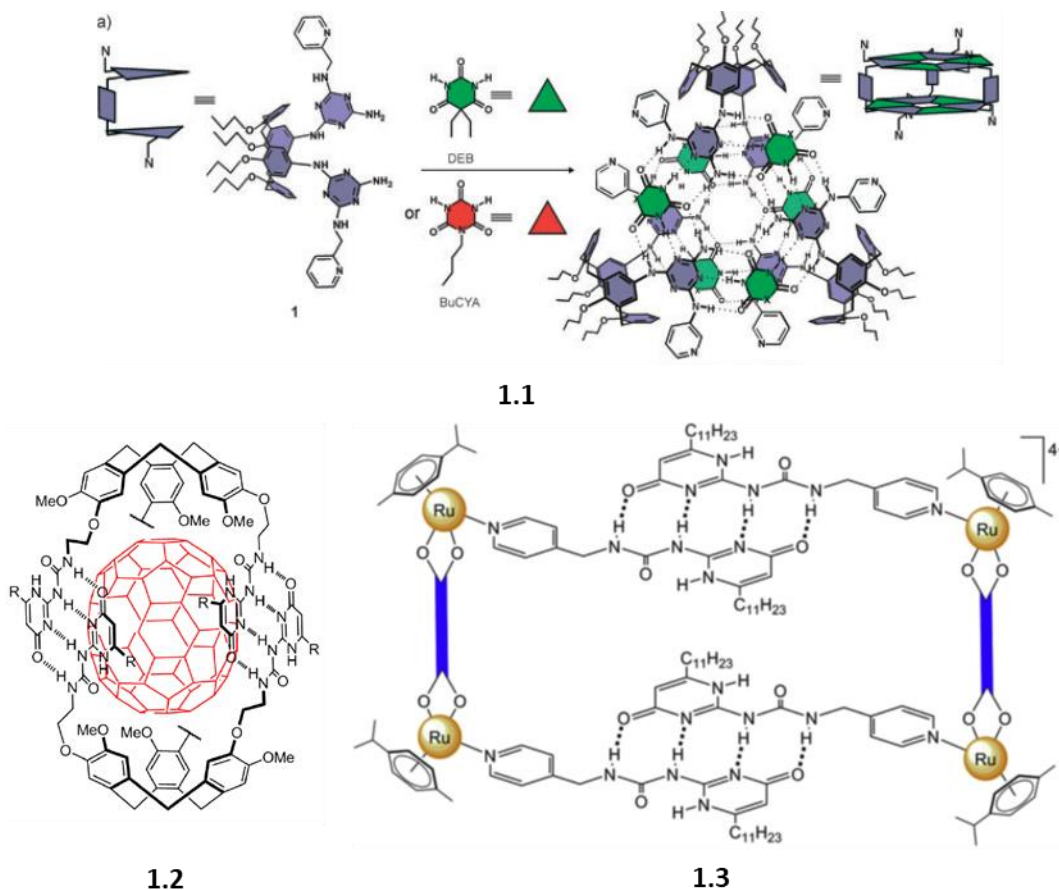
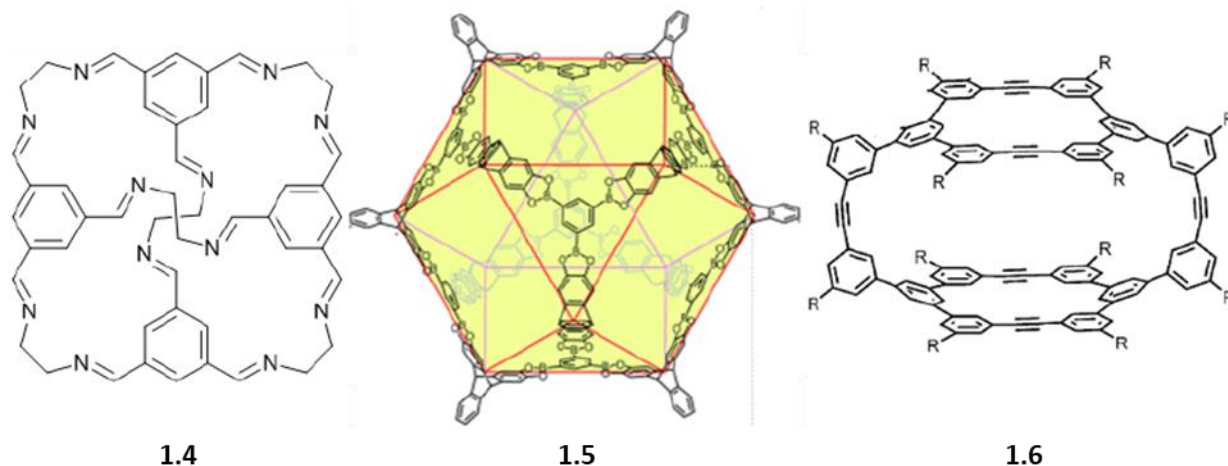


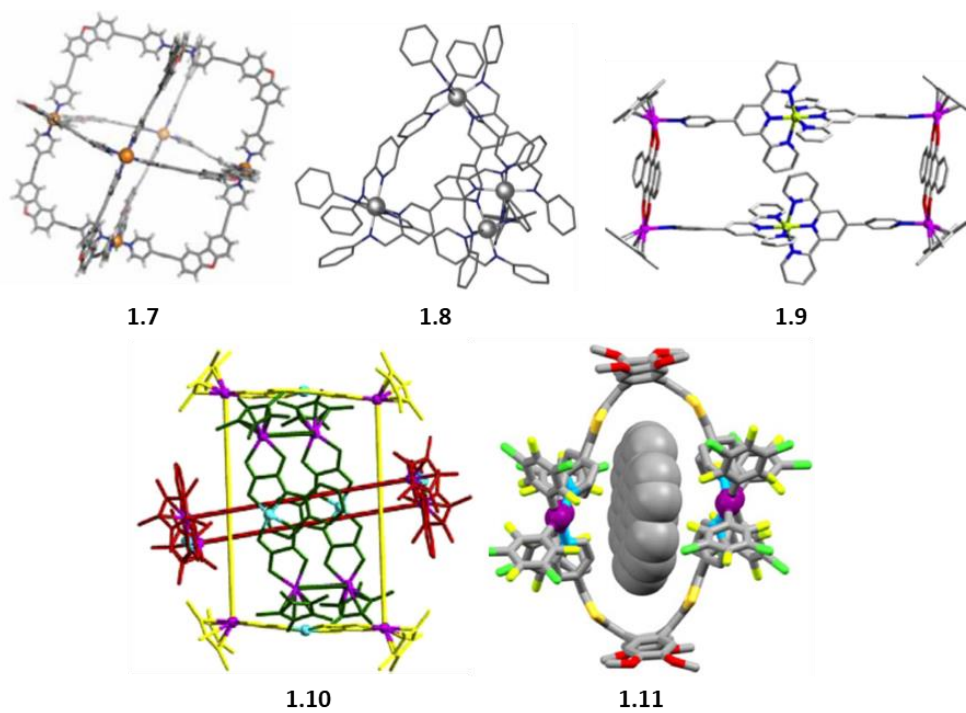
Figure 1. Self-assemblies provided by hydrogen bonds.³⁻⁵

A second kind of interaction that is widely exploited is the dynamic covalent bond. In general case, covalent bonds are too strong to assemble-disassemble under normal conditions. Yet, there is a multitude of bond-forming chemical reactions in the organic chemistry that are reversible at room temperature and can be applied to create complex moieties. Illustrative examples of those dynamic reactions are imine condensation (**1.4**), boronic ester formation (**1.5**), metathesis reactions (**1.6**), etc. (Figure 2).⁶

Figure 2. Self-assembled structures based on dynamic covalent bonds.⁶

1.3. Coordination-driven self-assembly

One other interaction which occupies a predominant place in the supramolecular chemistry is the coordination bond. It happens between a Lewis acid (electron acceptor, the metal) and a Lewis base (electron donor, L or X, the ligand) and has reasonably high bond energy ($50\text{-}200\text{ kJ}\times\text{mol}^{-1}$). The variety of intrinsic geometries of metal coordination and kinetic reversibility of coordination bonds allows to create great variety of edifices. The first example of a discrete metal-driven self-assembled receptor was reported by Fujita *et al.* in 1990.⁷ A molecular square was obtained by self-assembly of 4,4'-bipyridine and *cis*-blocked palladium (II) complex in aqueous conditions. Following this result, a wide variety of new examples with different geometries has been reported, be they bidimensional or three dimensional.

Figure 3. Some examples of coordination-driven discrete self-assemblies: monometallic **1.7**, **1.8**, Polymetallic **1.9**, Interlocked **1.10**, Stimuli responsive **1.11**.⁸⁻¹⁴

The metal driven self-assembly relies in general, on the interaction between two major components, a metal center and a polydentate ligand. The metal center is composed of the transition metal complex that is coordinated to one or several non-dynamic ligands and labile ligands, the latter acting as "free sites" and ensuring the correct geometry of the self-assemblies.

A huge variety of metals can be employed in the self-assembly development, mainly the transition metals that form stable complex compounds. Among them the Ti(IV), Ga(III), Ru(II) (hexagonal geometry), Fe(II), Cd(II), Zn(II) (tetragonal geometry) and Pd(II), Pt(II), Co(II), Ni(II) (square planar geometry) metal centers. For the choice of metal, one must consider the desired geometry, symmetry, and the ligand group. For example, *cis*-protected metal centers show a convergent coordination geometry. That means that those metal centers, while connected by straight ligands, converge into discrete units without the formation of oligomeric or infinite products.

In order to get an efficient self-assembly process, a self-correction must be processed, meaning that the ligand must be labile enough to exchange in solution. Therefore, thiol, phosphine or amine moieties are rarely used. Among the suitable ligand linking groups are pyridyl, pyridyl imine, pyridyl pyrazolo, terpyridine, catechol, etc. Those linking groups can be coupled to a backbone (functional or not) which determines the geometry of the ligand and whose design has a crucial role in the final self-assembly structure.

A multitude of approaches can be followed when designing the ligand backbone.¹⁵ The first one is a directional approach that has been extensively followed by Fujita and Stang groups for example.^{7, 16} For this approach the ligand requires to be rigid with well-predetermined bite angles, and an exact stoichiometric ratio of the precursors must be used. As shown in Figure 4, the bite angles and the symmetry of the precursors are vital in the design of the self-assembly. By tuning the bite angles of the ligands a wide library of structures can be achieved.

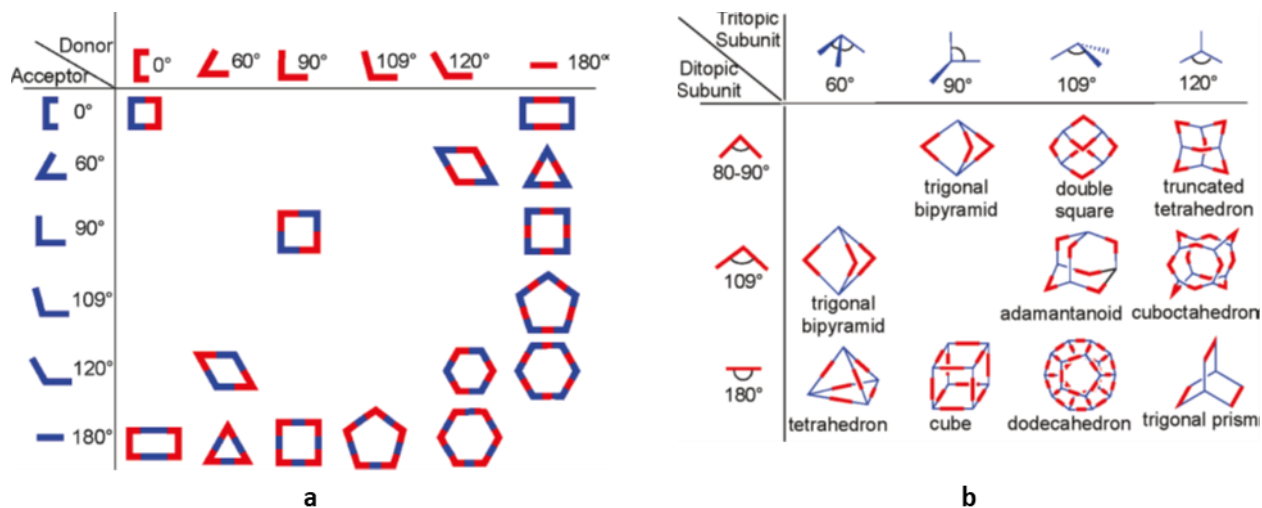
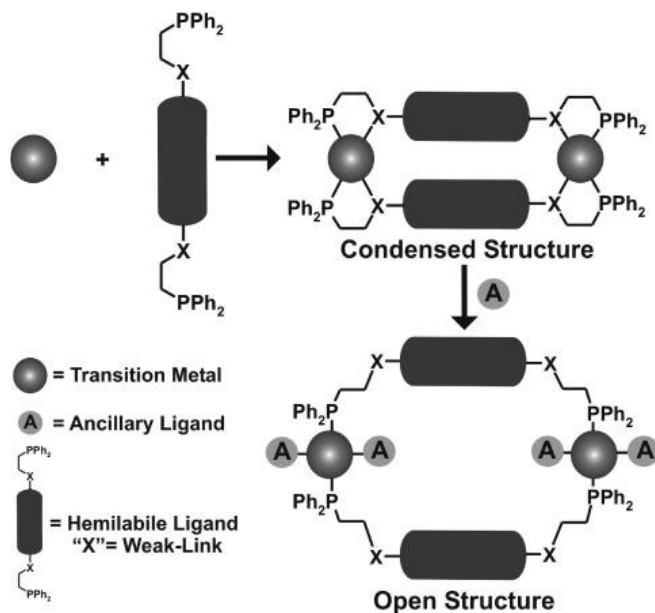


Figure 4. Combination of structural blocks for 2D (a) and 3D (b) architectures.¹⁵

The second is the symmetry interaction approach followed by Raymond.^{17, 18} This approach takes advantage of the strong binding affinity and coordination mode of chelating ligands, along with the inherent symmetry of the coordination sites available on the naked metal center. In general, multibranching chelating ligands with rigid backbones are used in conjunction with transition metals or main group metals. A coordinate vector

labile linker positions. As a result, a self-assembly with flexible cavity is formed, that is not achievable with the previous approaches that require rigid ligands.



Those different approaches present enough opportunities for an efficient and targeted design of self-assembled discrete structures of desired geometries and complexity, which would be otherwise challenging to reach through classical synthetic covalent chemistry.

The state of the art has stepped forward from the challenge to establish those synthesis concepts to new discrete structures, towards the preparation of new materials endowed with specific properties.

1.4. Molecular recognition

One of the main features of these self-assembled discrete systems is the presence of an intrinsic cavity. The latter has been extensively employed for molecular recognition. In 1977 Donald J. Cram proposed a definition for a host-guest complex: "A highly structured molecular complex is composed of at least one host and one guest component. A host-guest relationship involves a complementary stereo-electronic arrangement of binding sites in host and guest. The host component is defined as an organic molecule or ion whose binding sites converge in the complex. The guest component is defined as any molecule or ion whose binding sites diverge in the complex".²⁵ In other words, there is a need of geometric and electronic complementarity to form a host-guest complex.

1.4.1. Ion recognition

Anion encapsulation is the most obvious approach of application as the self-assemblies of coordination cages are usually positively charged, even though many examples of neutral cages have been described.²⁶ This charge may increase the binding constants due to electrostatic interaction. Also, the counter anion may play the role of a template during the molecular cage formation.

Some tetrahedral M_4L_6 self-assemblies obtained from different ligands have shown their ability to bind anions in their cavity. One of the early examples, **1.12**, was reported by Huttner *et al.*²⁷ During the synthesis this

self-assembly encapsulates one BF_4^- anion that is held inside the internal cavity. In contrast to other BF_4^- counter anions that can be exchanged with another anions, the internal tetrafluoroborate is never changed and resides within the molecule. The studies by Ward *et al.*²⁸ on similar structures **1.13** and **1.14**, have shown a selectivity in anion encapsulation favoring tetrahedral BF_4^- and ClO_4^- anions before octahedral and bigger SiF_6^- . This suggests that not only electrostatic forces take part in the host-guest interaction but the geometric considerations have also to be taken into account.

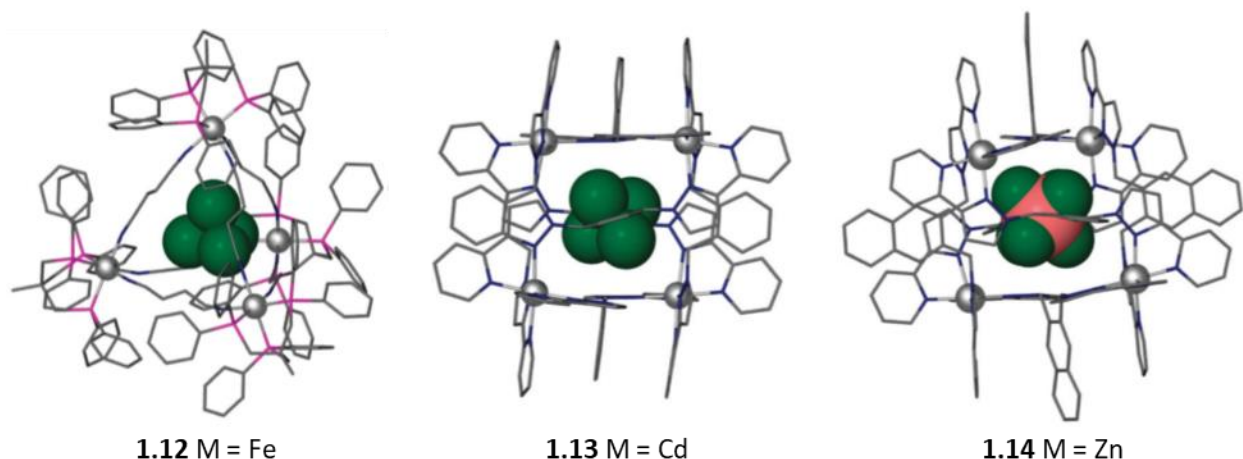


Figure 8. Anion-encapsulating M_4L_6 self-assemblies.^{27, 28}

Selective encapsulation has also been observed for cage **1.15**, reported by Stang *et al.*,²⁹ that complexes NO_3^- anion even in presence of PF_6^- . A banana-shaped type self-assembly³⁰ with C_4 symmetry was reported by McMorran and Steel (**1.16**).³¹ The particularity in this case is that the electrostatic binding is augmented by the weak coordination $\text{F}\cdots\text{Pd}$ bonds. In fact, the coordination and hydrogen bonds may be beneficial in the guest encapsulation. A similar effect has been observed by Amouri *et al.* that demonstrated BF_4^- encapsulation by the cage **1.17**.³² As in the previous example, the anion was weakly coordinated to the two metal centers via $\text{F}\cdots\text{Co}$ interactions.

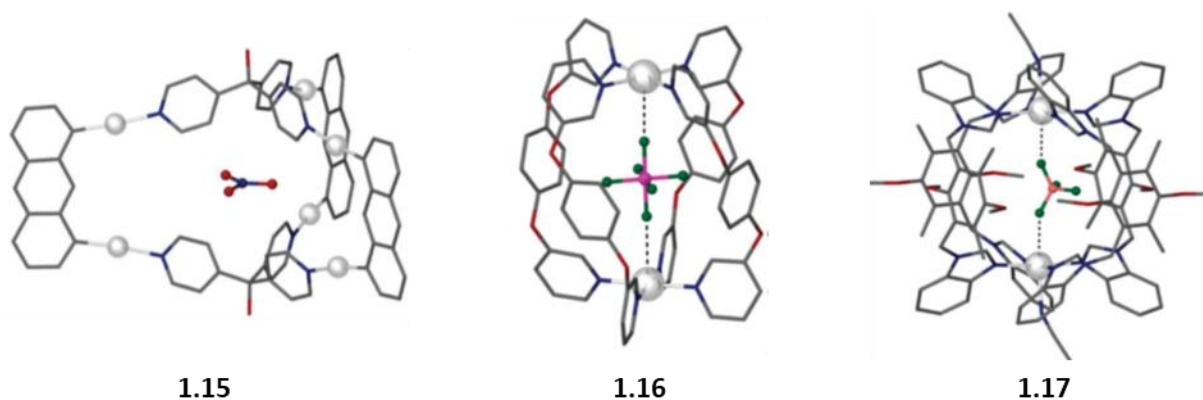


Figure 9. Anion-encapsulating self-assemblies with C_3 symmetry.^{29, 31, 32}

The molecular cages tend to encapsulate hydrophobic weakly charged anions that are poorly solvated. In contrast, the incorporation of hydrophilic molecules that have a strong affinity to the solvent is not thermodynamically favorable. Hay *et al.* have reported the M_4L_6 tetrahedral self-assembly **1.18** bearing urea functions in the ligand to overcome this limitation.³³ The geometry of the complex is complementary to the

highly charged PO_4^{3-} and SO_4^{2-} anions (Figure 10b) that otherwise are not incorporated from the outside media. Another example reported by Williams *et al.*³⁴ corresponds to metalla-structure **1.19** that allows the incorporation of hydrophilic Cl^- via the combination of complementary $\text{Ni}\cdots\text{Cl}$ bonding and $\text{NH}\cdots\text{Cl}$ hydrogen bonds (Figure 10c,d).

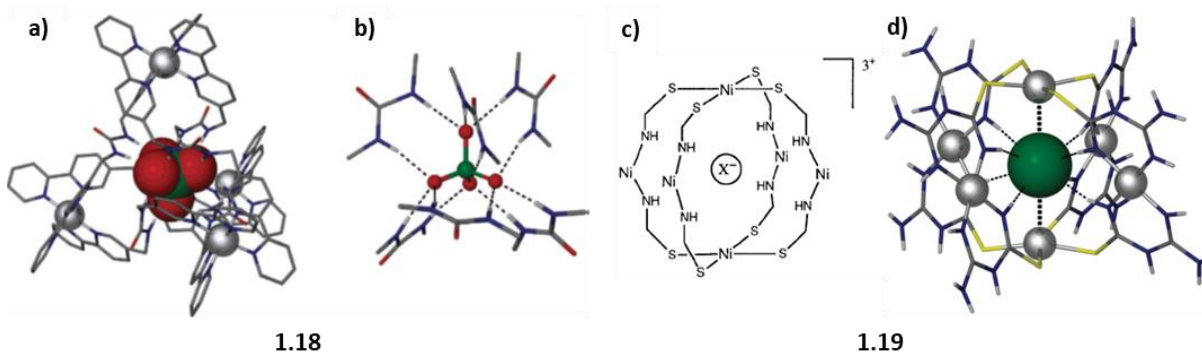


Figure 10. Encapsulation of the hydrophobic PO_4^{3-} and Cl^- .³⁴

On the other hand, the predominantly cationic nature of self-assemblies leaves a few examples of cation encapsulation. Raymond *et al.* have designed the tetrahedral M_4L_6 self-assembly **1.20** that hosts tetraalkylammonium cations.^{18, 35} This self-assembly has even shown a huge degree of selectivity to NEt_4^+ and the said cations quantitatively displaces longer and shorter NMe_4^+ and NPr_4^+ from inside the cavity.³⁵

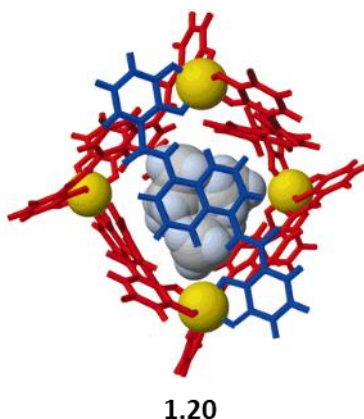


Figure 11. Cation-encapsulation.³⁵

1.4.2. Neutral molecule recognition

Given the lack of strong electrostatic intermolecular interactions, the complexation of neutral guests appears more challenging to address. Host-guest interactions are in this case more diffuse and require the design of pre-organized receptors having large interactions area. The hexagonal cage **1.21** reported by M. Fujita *et al.* has demonstrated being able to bind the water-insoluble *o*-carborane and adamantane with concomitant phase-transfer to the aqueous phase.³⁶ Further investigations have revealed that this cage offers different types and stoichiometries of molecular complexation depending on the size and symmetry of the guest molecule under consideration.³⁷ An important point is that no intermediate host-guest complexes have been detected. This is a direct indicator that the complementarity of host and guest must be maintained. On the other hand, the slight modification of volume or geometry of the cavity might lead to alteration of the compatible guest.

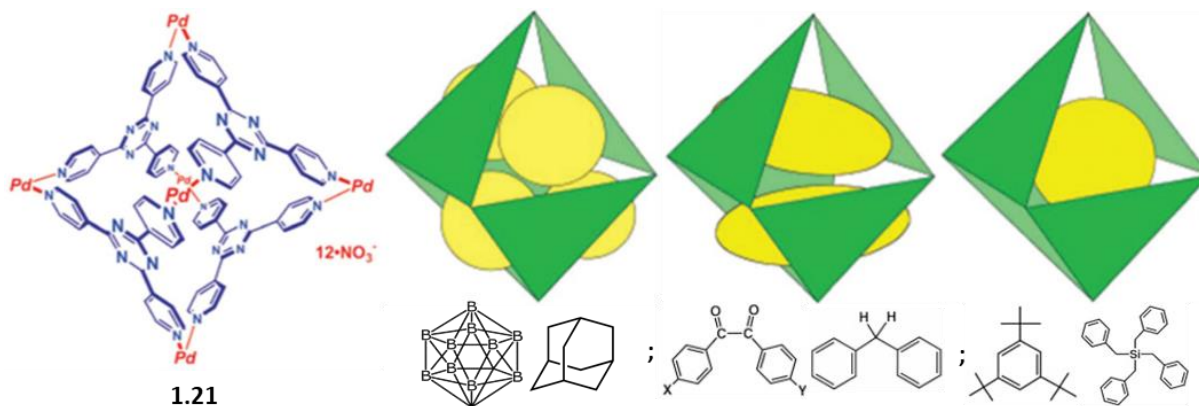


Figure 12. Encapsulation of different molecules by the M_6L_4 cage described by M. Fujita.³⁶

The group of Yoshizawa has designed the cage **1.22** bearing anthracene-based sidewalls ligands. It is suitable for incorporation of neutral polyaromatics but an adamantane derivative could also be incorporated. Interestingly, depending on the guest size, 1:1 or 1:2 host:guest complexes could be obtained (Figure 13). The main intermolecular interaction relies on π -stacking,³⁸ allowing a preference for neutral aromatic guests in front of counter anions.

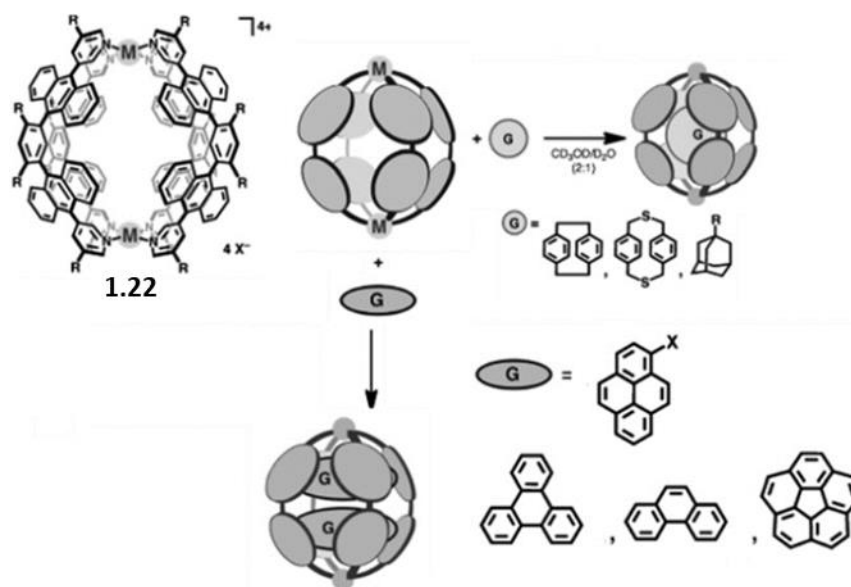


Figure 13. Incorporation of planar and non-planar aromatics into the M_2L_4 cage.³⁸

Buckminsterfullerenes are a class of nanosized molecules with application in a wide range of domains such as material science, molecular electronics or even pharmacy.³⁹ However, the very low solubility of non-functionalized fullerene in most common solvents introduces a limitation for their processing into microelectronic devices, and this is one of the reasons many efforts have been dedicated to the sequestration. For example and among many others, Yoshizawa *et al.* have employed the symmetrical M_2L_4 cage **1.23** for this purpose.⁴⁰ It has a C_4 symmetry, and the slight modification of the ligand leads to the cage **1.24** that shows a cavity elongated only in one direction. Interestingly, the incorporation of C_{60} fullerene to the mixture of **1.23** and **1.24** leads to rearrangement to an individual self-assembly due to the template effect of the guest. This leads to a heteroleptic entity that is unfavorable in the normal conditions.⁴¹

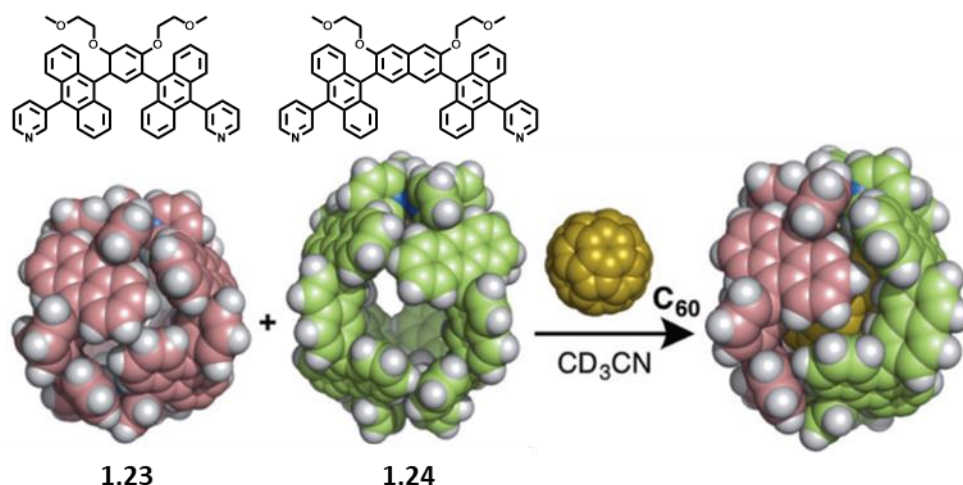


Figure 14. Reorganization of the cage mixture (M = Pd) in presence of C₆₀.⁴¹

1.5. Interlocked molecular rings

Along with host-guest interactions, one of the important aspects of the self-assembled structures lies on their ability to interact with one another. Indeed, while a ligand involved in the construction of a metalla-host might be designed to promote the complexation of a given guest molecule, it might also play the role of a guest for another host molecule, giving rise to an interlocked system. This expected dimerization must involve a sufficient force of interaction to overcome the entropic cost due to the decrease of the number of particles.

The first interlocked self-assembly **1.25** involving metals was synthesized by Fujita's group (Figure 15).⁴² It consist in two catenated hexagones and could even be characterized by X-ray crystallography.

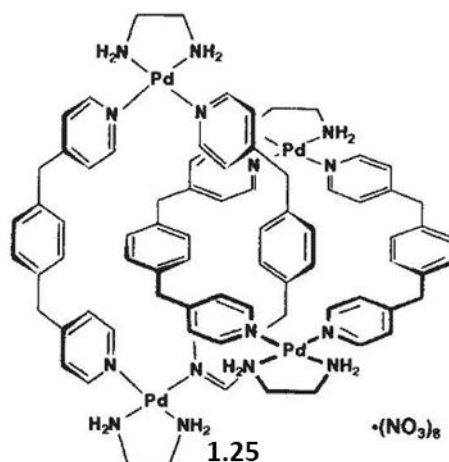


Figure 15. The first interlocked coordination driven self-assembly.⁴²

Since then, a multitude of varied interlocked self-assemblies such as catenanes dimers⁴³⁻⁴⁹ and trimers,^{50, 51} ring-in-ring complexes,^{52, 53} Solomon links,⁵⁴⁻⁵⁹ Trefoil Knots^{55, 60-63} or Borromean rings⁶⁴⁻⁷⁰ to cite a few have been described. The group of Ki-Whan Chi described catenane **1.26** (Figure 17a).⁴⁶ It is constructed from a linear ligand bearing a bis-functionalized anthracene and a bis(Ruthenium) complex. The latter exhibits two available parallel coordination sites and belongs to a family of complexes that are widely used for the preparation of molecular rectangles or sandwich-type metalla-cages (Figure 16).^{44-46, 53, 64-71} They are of particular interest since they provide an easy tuning of the Ru-Ru distance, and consequently a fine tuning of

the intramolecular ligand distance in the final sandwich-type structure, by simply changing the nature of the bridging ligand.

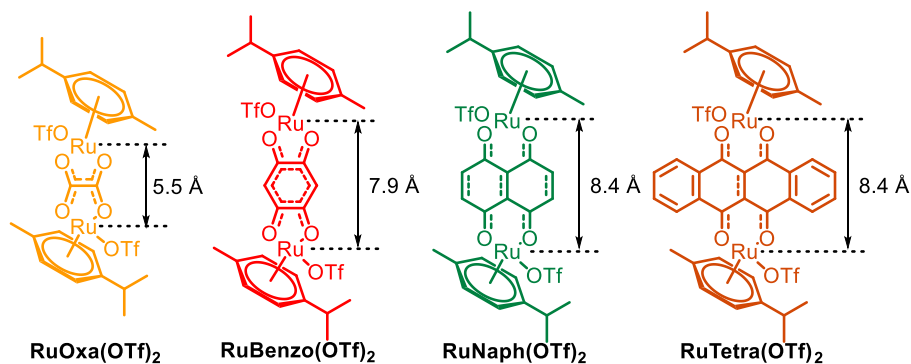


Figure 16. Bis(Ruthenium) complexes and their intermetallic distances.

The authors state that the major contribution in the catenane formation is the strong π - π stacking forces between anthracenyl moieties. Although the impact of those forces cannot be denied, another important factor is the size ratio of the rectangle that makes ring-in-ring structure unfavorable. The obtained interlocked structure is sensitive to the solvent media and the presence of competitive planar aromatics like pyrene. The same group also obtained the catenated structure **1.27** using a different approach. They prepared a metalla-ring from the same bis(Ruthenium) complex and a clip-like ligand. The metalla-ring spontaneously dimerizes in MeOH above $C = 0.5$ mM (Figure 17b).⁴⁵ In contrast, when synthesized from **RuNaph(OTf)₂** complex, even though it has comparable Ru-Ru distance and comprises polyaromatic linker, the metalla-ring did not result in the dimer formation at any observed concentrations, indicating the necessity of the strong π -interactions between tetracene moiety and aromatic rings of the ligand. A regioisomer of this bent ligand afforded the triply interlocked [3]catenane structure **1.28** with **RuNaph(OTf)₂** (Figure 17c).⁴⁴

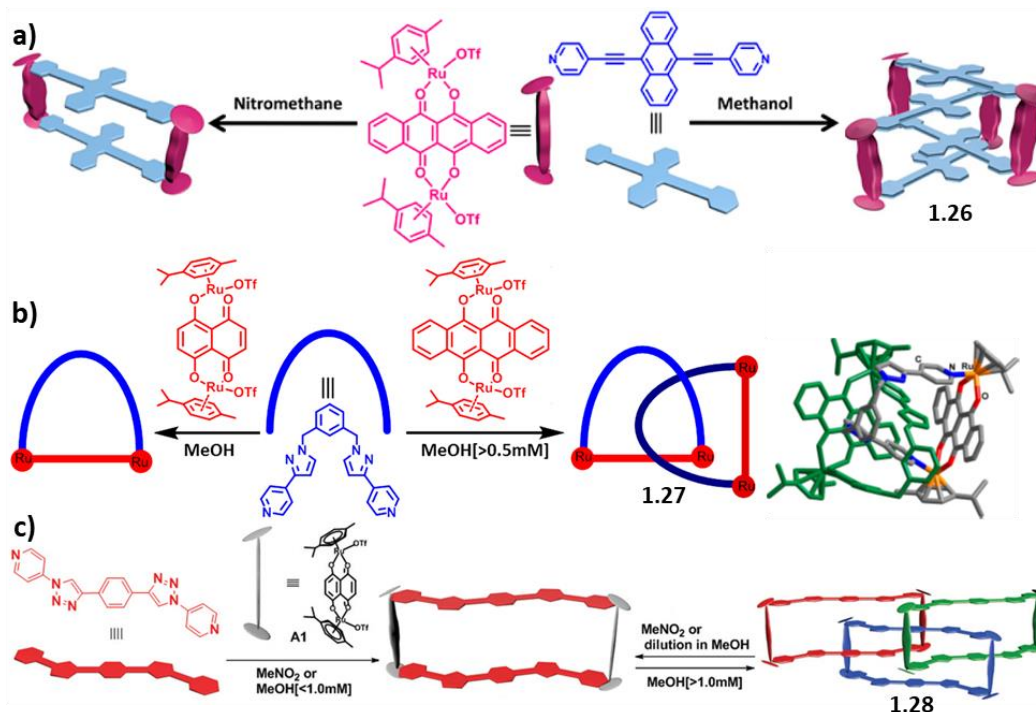


Figure 17. Catenane self-assembled structures of Chi group.⁴⁴⁻⁴⁶

Along with catenane-like structures, other modes of interlocking have also been observed. In 2011, Chi *et al.* reported the unexpected interlocked ring-in-ring dimer **1.29** from a linear acetylenic ligand and the bis(Ruthenium) complex **RuTetra(OTf)₂** (Figure 18a).⁵³ Back then, the DOSY⁷² technique was not yet widespread. Therefore, initially the researchers attributed the complexity of the NMR spectrum to an uncompleted reaction. Further HRMS experiments proved the formation of a dimeric ring-in-ring species whose structure was verified by X-Ray crystallography. The attempts to disassemble the dimer using pyrene, a small aromatic guest molecule, were unsuccessful. Interestingly, the latter could however act as a template to form the M₂L₂ rectangle.

Another interesting example of ring-in-ring complex comes from the group of Quintela *et al.* They could shift the equilibrium between the monomeric rectangle and the interlocked complex **1.30** through controlling the solvent, the concentration, and the temperature. While the molecular rectangle dimerized in water, its monomeric structure is retained in organic media (Figure 18b).⁷¹ The authors hypothesized that in addition to the π - π stacking, the hydrophobic interactions may further direct the dimerization as the highly hydrophobic aromatic moieties are shielded from the outer solvent in the dimer structure.

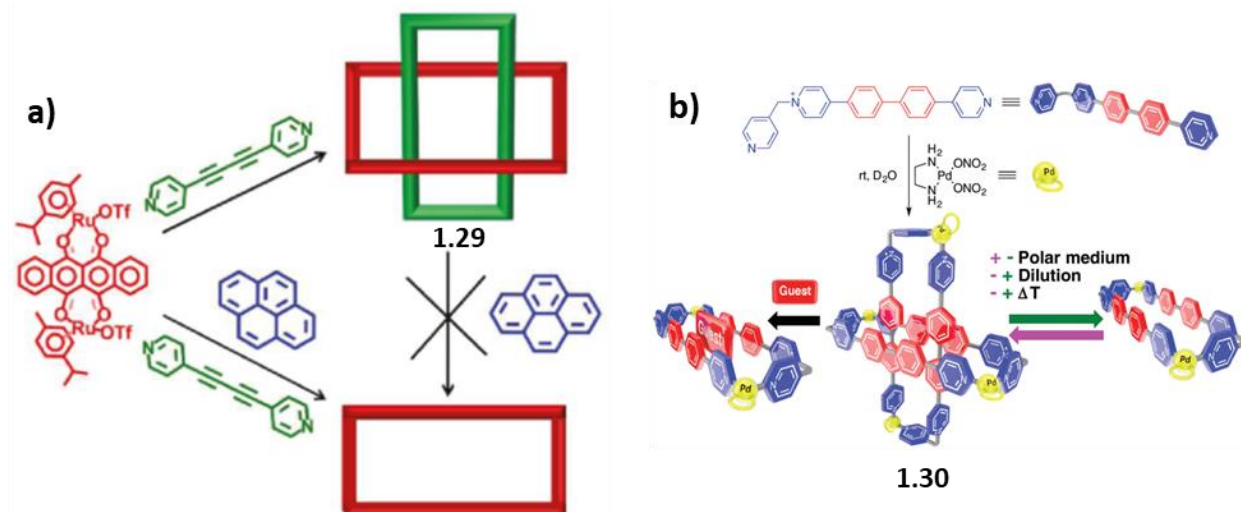


Figure 18. "Ring-in-ring" molecular rectangle dimers.⁵³

Another family of interlocked structures has been recently deeply investigated by the group of Guo-Xin Jin and corresponds to Borromean rings.⁶⁵ These interlocked trimers are generally obtained at high concentrations in polar solvents. The only procedure of Borromean ring preparation known before their work, was a template effect coordination-assisted interlocked complex formation (Figure 19a).⁷³ Since then, an extensive amount of research has been performed.⁶⁴⁻⁷⁰ It was discovered that a multitude of factors can facilitate the interlocked trimer formation. The obtained experimental data has resulted in a set of empirical rules: 1) the shorter ligand needs to be long enough to allow the longer ligand to pass through, 2) the longer ligand needs to be long enough to accommodate the entire shorter ligand and 3) the length difference between the longer and the shorter ligands should be close to the double length of π - π interaction (7 Å). However, the longer ligand can be curved inward or outward that leaves some room for error on that matter (Figure 19b). The obtained self-assembled trimers had different stability in solution. Highly polar solvents like water and methanol tend to

shift the equilibrium to the formation of a trimer while less polar solvents shift it to the monomer (Figure 19c). This equilibrium can also be altered by changing the concentration.

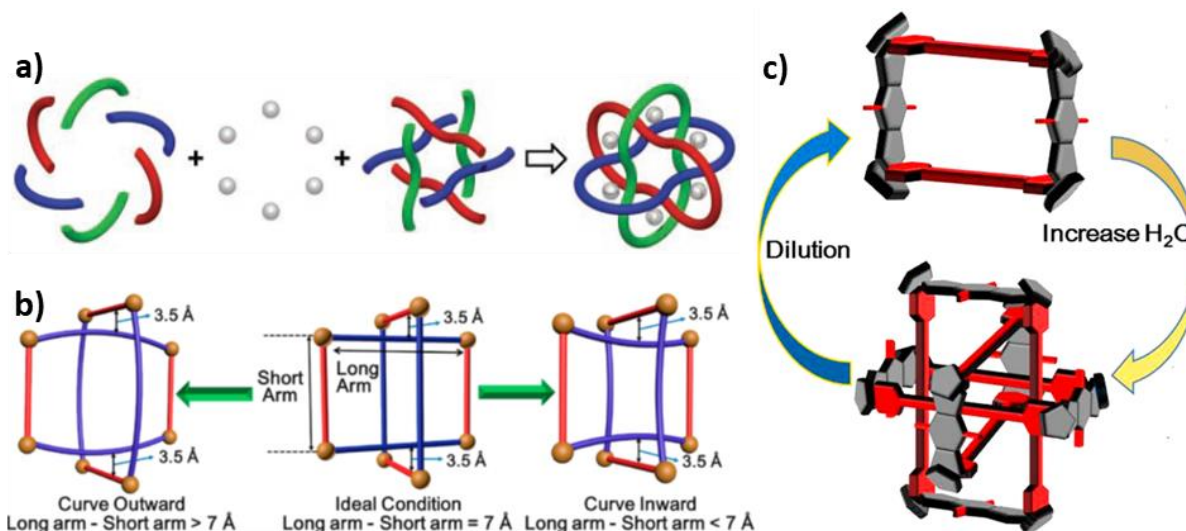


Figure 19. a) Template Borromean ring synthesis scheme, b) Ligand arms aspect ratio effects, c) Long arm length stability effects, d) The media stability effect in Borromean rings.⁶⁴⁻⁷⁰

The important aspect of the Borromean rings lies on their high symmetry. As a result, the NMR spectra of these systems have the same number of signals as the NMR spectra of the monomer rectangles.

2. Guest release and stimuli-responsive self-assembly

Beyond the incorporation of a guest, one important challenge which still needs to be addressed, is the controlled release of already encapsulated molecules.⁹ Such process offers wide perspectives, not only in terms of fundamental aspects, but also to target applications such as encapsulation of reactive species and pollutants, drug delivery, deposition of insoluble species on a surface and catalysis in confined space.⁷⁴ This control over encapsulation can be envisaged by several mechanisms, e.g.: stimulation of the guest, stimulation of the host, addition of a chemical to disassemble the host, releasing the guest through a competitive effect.

2.1. Action on the guest

The guest release can result from a stimulation applied to the guest. For example, Ward *et al.* shows the reversible encapsulation of pH-responsive guest molecules in the cage **1.31**. A variation of pH converts the neutral guests (GH or G) into a charged species (negatively (G⁻) or positively (GH⁺) charged) resulting in the release from the cage, thus modifying the host-guest properties without cage disassembly.⁷⁵

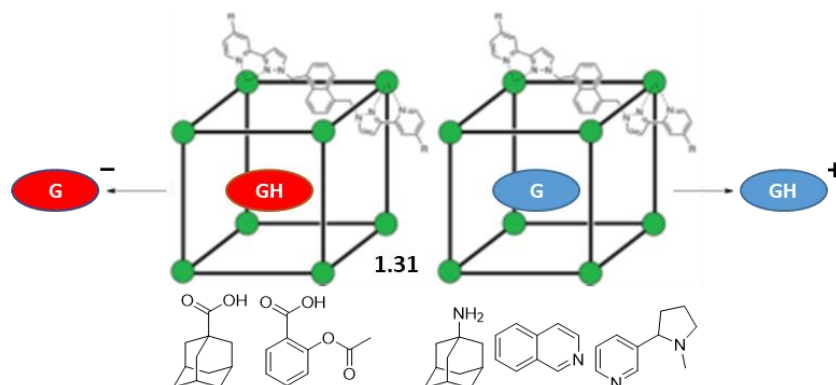


Figure 20. pH modulated guest encapsulation by guest protonation/deprotonation.⁷⁵

The group of Clever *et al.* investigated the idea of a guest release by modification of azobenzene light-responsive guest molecules bound in the cage **1.32**.⁷⁶ The *cis*-azobenzene is compact enough to fit in the cage **1.32**, but upon irradiation the molecule is switched to its *trans*-form which is too large for the cavity and is expelled (Figure 21).

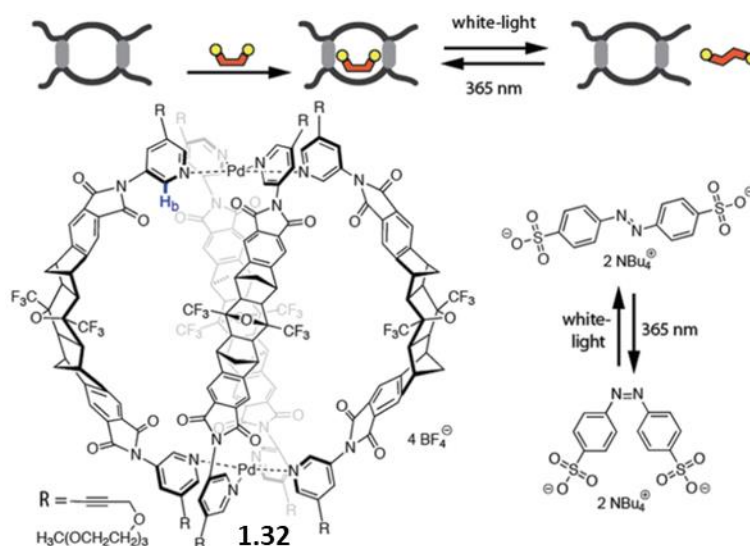


Figure 21. Controlled release of the guest molecule by light irradiation.⁷⁶

A very similar method of encapsulation control by guest modification has been reported by Fujita.⁷⁷ They have observed the release of ferrocene from the cage **1.21** by electrochemical oxidation. The oxidized ferrocene is a cation which is expelled from the cage due to electrostatic repulsion. The cage **1.21** has also been cleverly used for targeted release of *cis*-platin (a chemotherapy drug).⁷⁸ In this case, the Pt(IV) complex which is encapsulated in the cage by the specifically designed ligand is reduced by ascorbic acid to cleave the said ligand, affording the Pt(II) *cis*-platin which does not clathrate into the cage and thus is expelled from the cage (Figure 22).

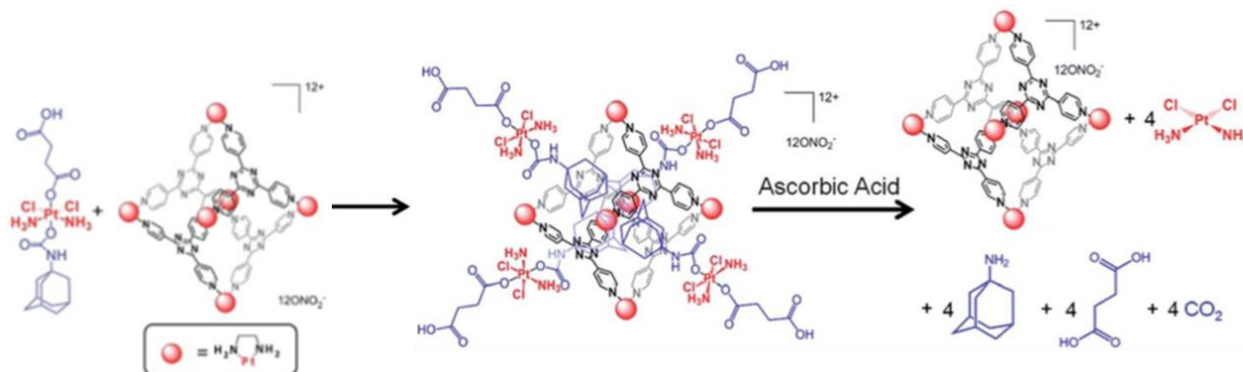


Figure 22. Controlled release of the guest molecule (Pt(II) cis-platin) (by chemical reduction).⁷⁸

An obvious method of guest release consists in introducing a competitive species into the solution. The group of J. Nitschke has encapsulated the white phosphorus P_4 molecule into the water-soluble cage **1.33**. Not only it is a remarkable example of reactive species protection by encapsulation in a self-assembled cage, but the P_4 guest molecule can also be released by addition of benzene, thus reacquiring its reactive properties (Figure 23).⁷⁹

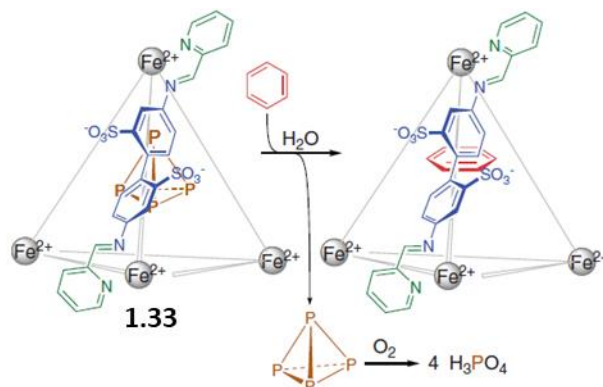


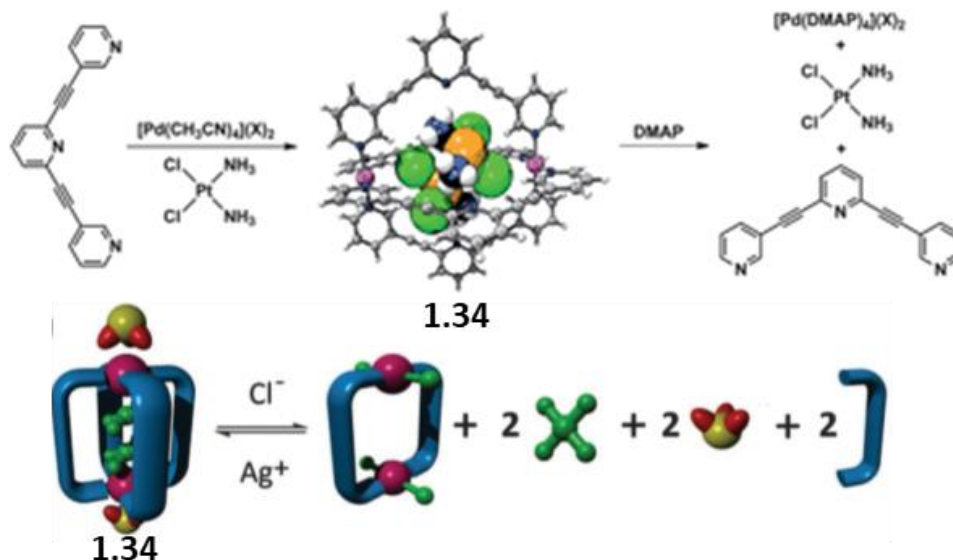
Figure 23. Controlled encapsulation of P_4 .⁷⁹

2.2. Action on the host

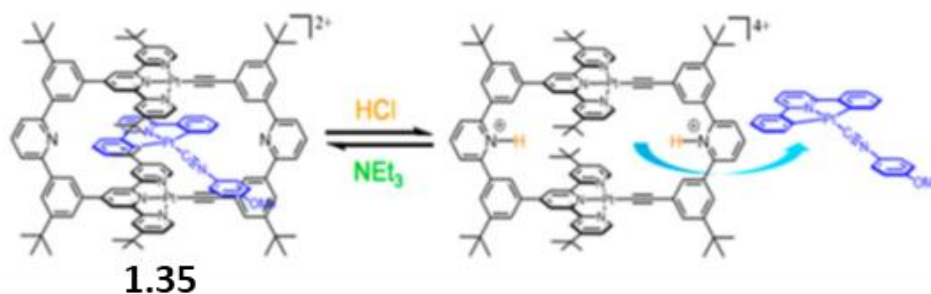
Alternatively, the stimulus promoting host-guest dissociation can be led on the host partner. This has been described through several mechanisms that are depicted below.

2.2.1. pH-active self-assemblies

The first obvious method of a guest release is the cage decomposition by addition of competitive agent.⁵⁵ For example, the cage **1.34** reported by Crowley *et al.* has been shown to release the chemotherapy drug *cis*-platin into the solution upon addition of DMAP that acts as a competitive Lewis base.⁸⁰ Crowley *et al.* have further developed the controlled release of *cis*-platin by the cage **1.34** by only partial disassembly. This was achieved by the addition of 4 equivalents of competitive Cl^- anion, a process which is reversible upon addition of a silver salt.⁸¹

Figure 24. pH modulated guest encapsulation by cage disassembly.^{80, 81}

An example of pH-modulated guest release without cage decomposition is proposed with cage **1.35** reported by Yam *et al.*⁸² This cage can encapsulate square-planar platinum(II), palladium(II), gold (III), and the related gold(I) complexes, and release them upon a pH change which was followed by NMR and UV-vis. The free pyridine groups pointing inside the cavity can be protonated selectively upon addition of acid without any cage decomposition. As a consequence, the charge of the cavity gets altered and the guest is released. The process is reversible with the addition of a base. No additional information is given regarding the release mechanism, but one can assume a competitive guest binding with Cl⁻ anions.

Figure 25. Controlled guest release of the pH-responsive cage **1.35**.⁸²

2.2.2. Photo-active self-assemblies

The promising concept of modifying the shape of the cage to modulate the guest complexation was proposed by the group of Clever *et al.*⁸³ The cage **1.36** incorporates a DTE photo-switchable moiety that isomerizes upon irradiation. This step leads to the alteration of the internal cavity size, and hence, promotes a different association constant for the guest molecule (Figure 26a). Another example of molecular cage able to breath upon application of a stimulation, constructed this time through covalent organic chemistry, was depicted by the group of V. Heitz and consists in a bis-porphyrin cage linked by four triazolyl based chains that are able to bind silver, a process with reduces the size of the cavity.⁸⁴

The DTE photoswitch moiety allows vast opportunities for cage geometry modulation. An interesting photoswitchable cage **1.37** was reported by Andreasson *et al.*⁸⁵ The length of the photoswitch in its closed form is too small to coordinate both porphyrine rings, and leaves the second one for Lewis base coordination. When the compound is irradiated, the resulting open form is flexible enough to coordinate both Zn-porphyrine centers with high constant, leading to the releasing of the coordinated Lewis base (Figure 26b).

Finally, another promising use of photoactive cages is a “molecular flask” that might effectively catalyze photoinduced reactions while insuring the release of the final compound. Su *et al.* have utilized the bimetallic cage **1.38** for enantioselective dimerization of a naphthalene derivative (Figure 26c).⁸⁶

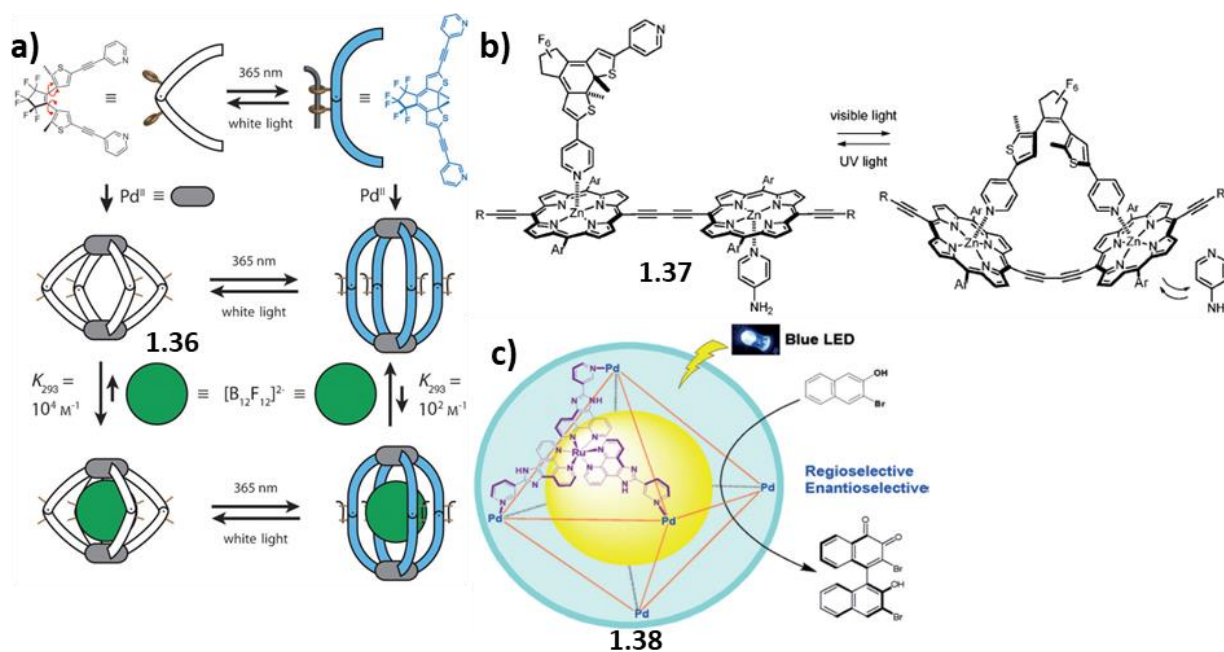


Figure 26. Examples of photoswitchable cages.^{83, 85, 86}

3. Redox-active self-assemblies

As mentioned earlier in this chapter, there is a growing interest in producing stimuli-responsive coordination-driven self-assembled architectures. On these ground, the number of electro-active metalla-structures has been increasing drastically in the very recent years.⁸⁷ The use of redox-active precursors in the self-assembly process can in principle produce discrete metalla-supramolecular assemblies which are themselves redox active, allowing for a fine tuning of the cavity charge through a redox stimulation. Various situations can be encountered, with the electroactivity located either on the organic ligand part, the metal or the co-ligand.

The cage **1.21**, for instance, is formed by an electron-poor triazine-based ligand (Figure 27a). The electrochemical properties of this cage were studied while investigating the photoinduced electron transfer between the cage and a guest molecule.⁸⁸ This cage can form a host-guest complex with four molecules of adamantane which, after irradiation, leads to a colored solution attributed to a radical derivative. The suggested mechanism involves the formation of the cage radical and the adamantane radical cation by electron transfer from the guest to one of the triazine panels. This was confirmed by a cyclic voltammetry experiment that reveals 2 redox systems: the first corresponds to the reversible reduction of only one triazine ligand and

the second to the other three triazines (Figure 27b). As can be seen, the self-assembly process may alter the electrochemical properties of otherwise equivalent ligand panels.

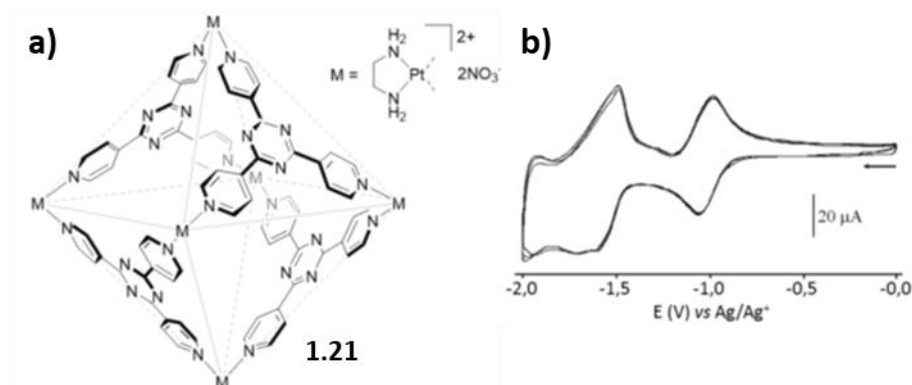


Figure 27. Redox-active cage **1.21** and its cyclic voltammogram: C = 0.5 mM, MeCN ($n\text{-Bu}_4\text{PF}_6$ (50 mM)), scan rate $100 \text{ mV}\cdot\text{s}^{-1}$.⁸⁸

Another example of an electron-poor moiety that has been introduced into a metalla-structure is the perylene diimide (PDI). The cage **1.39**, synthesized by Wurthner *et al.*, is assembled from a Fe(II) complex and a PDI-based ligand bearing two bipyridine moieties.⁸⁹ A cyclic voltammetry experiment (Figure 28) revealed a multitude of electrochemical processes centered on bipyridine, PDI and Fe fragments, all of them being reversible. This allows for a total exchange of 34 electrons and several oxidation states (from **1.39**¹⁶⁻ to **1.39**¹⁸⁺).

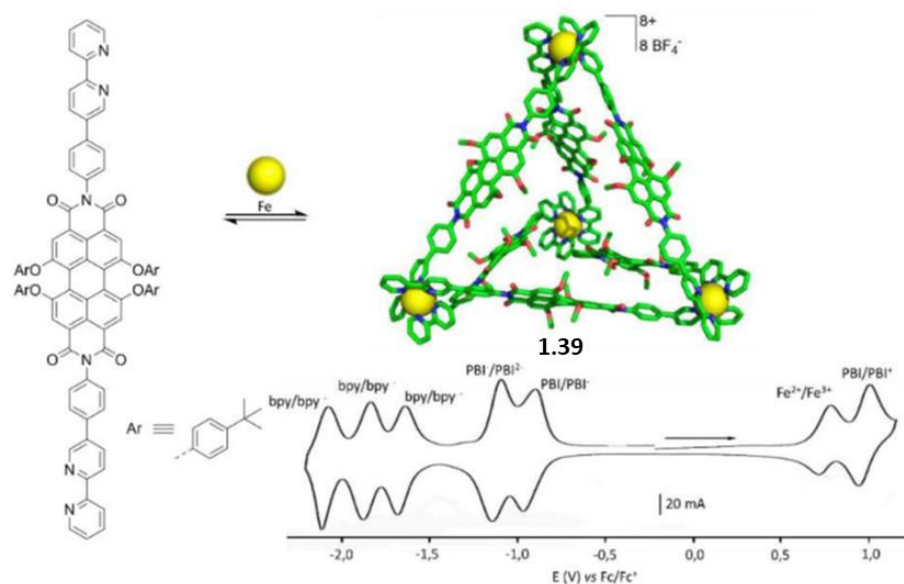


Figure 28. Redox-active cage **1.39** and its cyclic voltammogram: C = 0.1 mM, MeCN ($n\text{-Bu}_4\text{PF}_6$ (0.1 M)), scan rate $200 \text{ mV}\cdot\text{s}^{-1}$.⁸⁹

Clever *et al.* have incorporated the phenothiazine moiety in the interlocked cages **1.40** (Figure 29) and studied its chemical oxidation.⁹⁰ The results have shown that when incorporated as a cage constituent the phenothiazine-based ligands can be oxidized to their oxo and dioxo derivatives at conditions that are insufficient in case of a free phenothiazine. The authors suggest that the geometry of the cage with sulfur atoms situated inside the cavity allows the exchange of oxygen atoms among the active centers and

intramolecular disproportionation of two S=O groups to one SO₂ and one S group, which is followed by oxidation of the newly formed free sulfur atom.

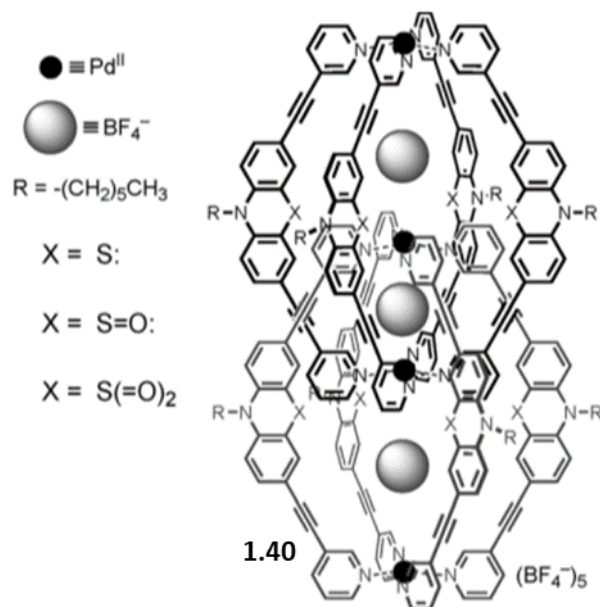
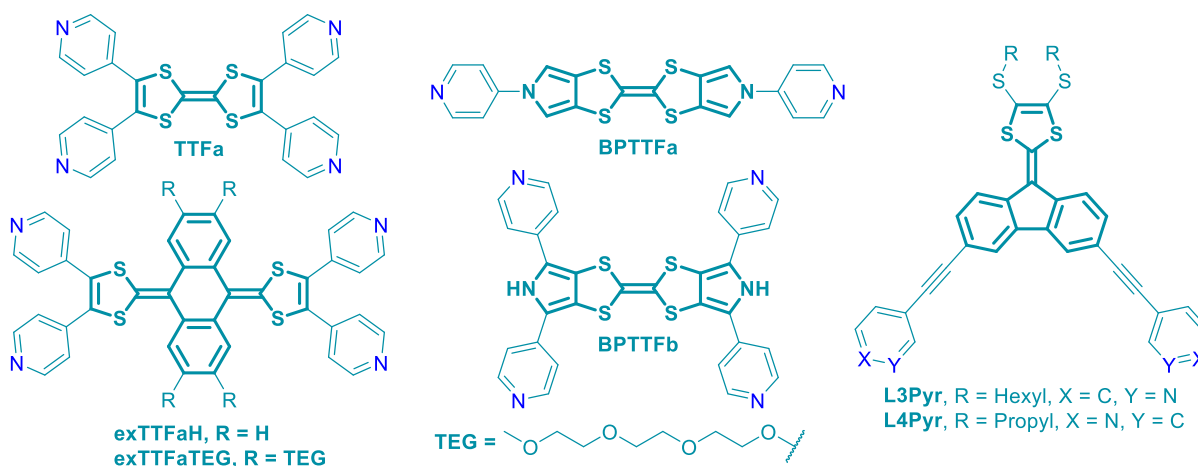


Figure 29. Redox-active cage **1.40** (X = S) and its oxidized states.⁹⁰

3.1. Electron-rich self-assembled metalla-structures obtained in Angers

The electron-rich electroactive self-assemblies that are the object of research in our group are based on the tetrathiafulvalene (TTF) moiety and some of its derivatives (Scheme 1).⁷⁴ The unique electrochemical properties characterized by two stable and easily accessible oxidized states (i.e., TTF^{•+} and TTF²⁺), and geometries of TTF derivatives⁹¹⁻⁹³ offer a clear opportunity for the design of functional electron-rich self-assemblies.

Construction of metalla-rings and cages requires the prior synthesis of di- or polytopic ligands, and some ligands used previously in the team are depicted in Scheme 1.



Scheme 1. Examples of ligands developed in our group.

3.1.1. BPTTF-based assemblies

The first family of ligands developed in our group was based on 5H,5'H-2,2'-bi[1,3]dithiolo[4,5-c]pyrrolylidene or bis-pyrroloTTF (BPTTF). This structural modification compared to TTF is convenient as it eliminates the cis-trans asymmetry that is observed when preparing bis-functionalized TTF derivatives. It allowed therefore for the preparation of a linear ligand (**BPTTFa**) that was targeted to provide a bi-dimensional self-assembled structure.

The reaction of ligand **BPTTFa** with $\text{Pt}(\text{dppp})(\text{OTf})_2$ ($\text{dppp} = 1,1'$ -bis(diphenylphosphino)propane) in dichloromethane afforded a mixture of the triangle **1.41** and the square **1.42** (Figure 30a). These two species could be separated by a simple precipitation since **1.42** is insoluble in dichloromethane.^{94, 95} Cyclic voltammetry experiments have demonstrated that the ligand retains its electrochemical behavior in the self-assembly, with two reversible oxidation waves corresponding to $\text{BPTTF}/\text{BPTTF}^{+\bullet}$ and $\text{BPTTF}^{+\bullet}/\text{BPTTF}^{2+}$ processes. After the determination of the number of transferred electrons by comparison with the known concentration of an internal reference (Figure 30b), it was confirmed that all the TTF moieties (3 and 4 respectively) are oxidized simultaneously and independently and that there is no electronic communication between the ligands. Also, the complexation properties of **1.41** and **1.42** with the electron-poor fullerenes were investigated by UV-vis spectrometry. These studies revealed a good affinity of **1.41** with C_{60} and C_{70} leading to 1:1 complex. In contrast, no binding with **1.42** was observed. This difference is assigned to the size and shape of the respective internal cavities of **1.41** and **1.42**, as the square has a cavity that is too large to accommodate a fullerene molecule.

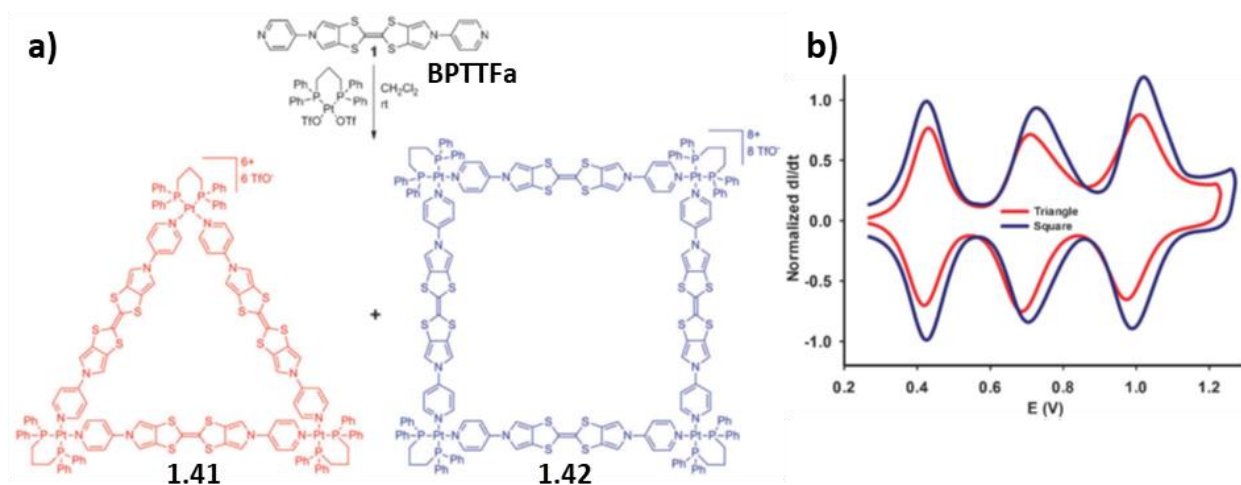


Figure 30. a) self-assemblies obtained from linear BPTTF ligand **BPTTFa**, b) deconvoluted cyclic voltammograms of triangle **1.41** (0.5 mM) and square **1.42** (0.5 mM) in presence of ferrocene (3 equiv. and 4 equiv., respectively) $\text{CH}_2\text{Cl}_2/\text{CH}_3\text{CN}$ (1/1 v/v) (Bu_4NPF_6 0.1 M), vs Ag/AgCl .^{94, 95}

The tetradentate BPTTF ligand **BPTTFb** was synthesized in order to target three-dimensional self-assemblies.^{96, 97} The reaction with *cis*-blocked $\text{Pt}(\text{PEt}_3)_2(\text{OTf})_2$ afforded the prism-like cage **1.43** (Figure 31a). A cyclic voltammetry experiment showed the presence of two irreversible oxidation waves (Figure 31b). The irreversibility might be attributed to the rigidity of the prism that alters the kinetics of electron transfer. All metalla-structures assembled from ligands **BPTTFa** and **BPTTFb** show oxidation potentials shifted to higher

values in comparison to the uncoordinated ligands, due to the electron withdrawing character of the metal acceptors that decrease the n-donating character of the electro-active ligands.

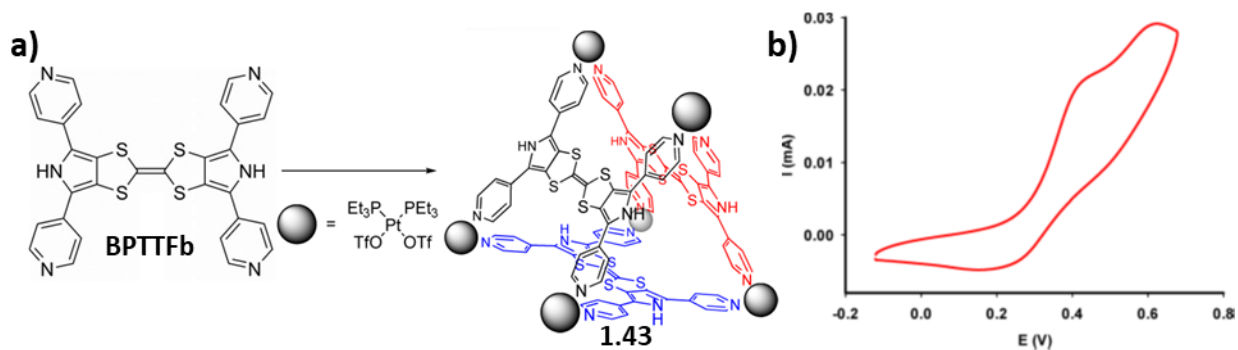


Figure 31. a) self-assembly with tetradentate ligand **BPTTFb** b) cyclic voltammogram of cage **1.43** $C = 0.6$ mM in acetonitrile 0.1 M NBu_4PF_6 , scan rate $50 \text{ mV}\cdot\text{s}^{-1}$, vs Fc/Fc^+ .^{96, 97}

3.1.2. TTF-based assemblies

The tetradentate TTF-based ligand **TTFa** was also used for self-assembly preparation. In combination with *cis*-blocked $\text{Pd}(\text{dppf})(\text{OTf})_2$ or $\text{Pt}(\text{dppf})(\text{OTf})_2$, it forms a large M_8L_4 square **1.44** (Figure 32a).⁹⁸ The cyclic voltammetry exhibits two reversible oxidation waves typical of TTF derivatives, but shifted to high potentials, due to the presence of metal acceptors (Figure 32b).

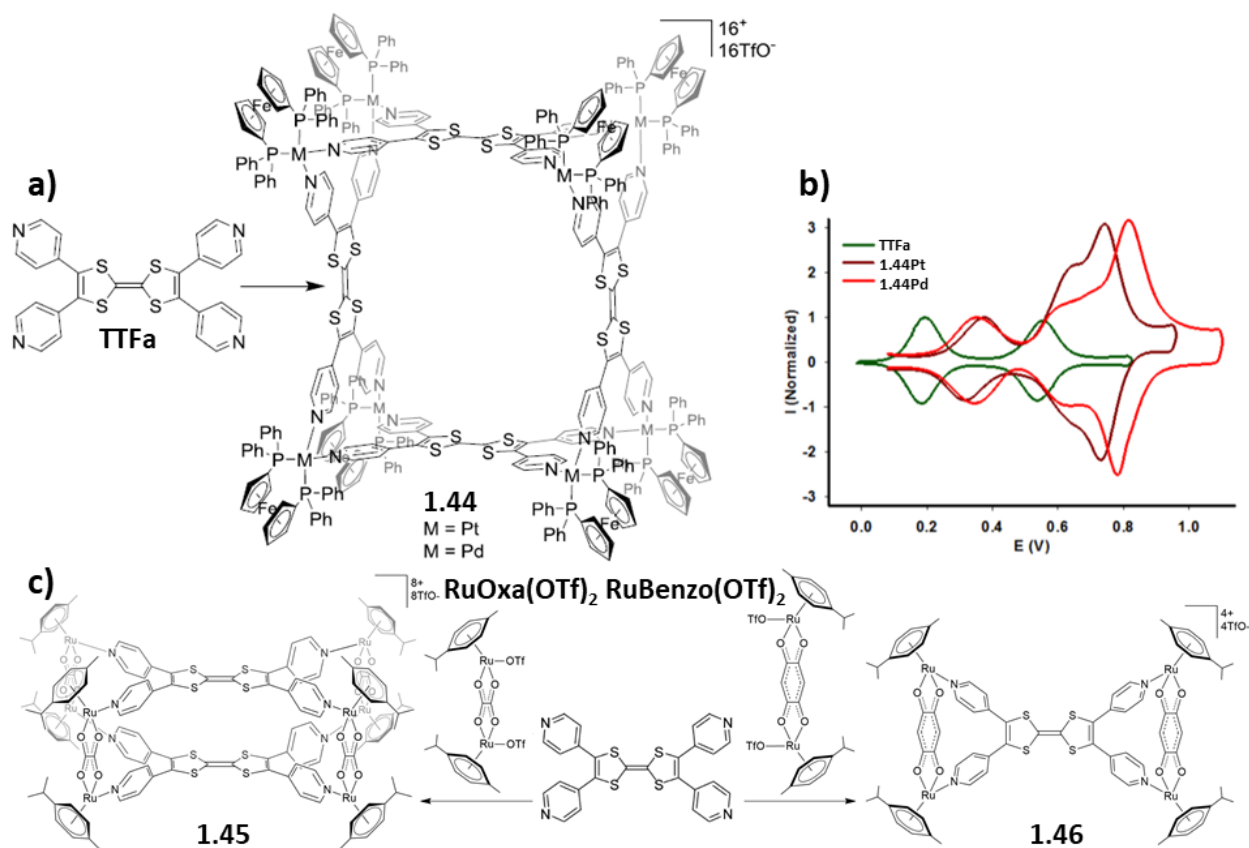


Figure 32. Self-assemblies obtained with TTF ligand **TTFa** a) molecular square **1.44**, b) deconvoluted cyclic voltammogram observed for **1.44** ($C = 10^{-3}$ M, $\text{CH}_3\text{CN}/\text{CH}_2\text{Cl}_2$, 0.1 M nBu_4NPF_6 , $20 \text{ mV}\cdot\text{s}^{-1}$, Cgr) and of squares **1.44Pt** and **1.44Pd** ($C = 0.5$ mM, CH_3CN , 0.1 M nBu_4PF_6 , $20 \text{ mV}\cdot\text{s}^{-1}$, Cgr) vs Fc/Fc^+ and c) sandwich cage **1.45** and molecular panel **1.46**.^{98, 99}

When reacted with bis(Ruthenium) complexes **RuOxa(OTf)₂** or **RuBenzo(OTf)₂** the ligand **TTFa** leads to two completely different geometries, the Ru₈L₂ sandwich-type self-assembly **1.45** and the Ru₄L panel **1.46** (Figure 32c).⁹⁹ Interestingly, the panel **1.46** exhibits two oxidation waves like the native TTF while the cage **1.45** has only one reversible oxidation wave at 0.44 V vs Fc/Fc⁺. This might be attributed to the rigid geometry that does not allow conformational changes. The distance between two neighboring pyridine nitrogen atoms in **TTFa** is very close to the Ru-Ru distances in complexes **RuBenzo(OTf)₂**, **RuNaph(OTf)₂** and **RuTetra(OTf)₂**, leading to a panel-type geometry in the corresponding self-assemblies.

To avoid the formation of panel type structures and to obtain larger sandwich structures with higher distance between TTF ligand planes, the ligand **TTFb** was designed. Its reaction with **RuNaph(OTf)₂** afforded the target sandwich structure **1.47** (Figure 33a). The electrochemical studies revealed the splitting of the TTF/TTF²⁺ oxidation wave (Figure 33b). This is attributed to the short distance of only 3.48 Å between the TTF moieties (Figure 33c) that allows the formation of mixed valence species (TTF)₂^{•+} and the corresponding n-dimer (TTF^{•+})₂, both species being characterized by spectroelectrochemical measurements.¹⁰⁰

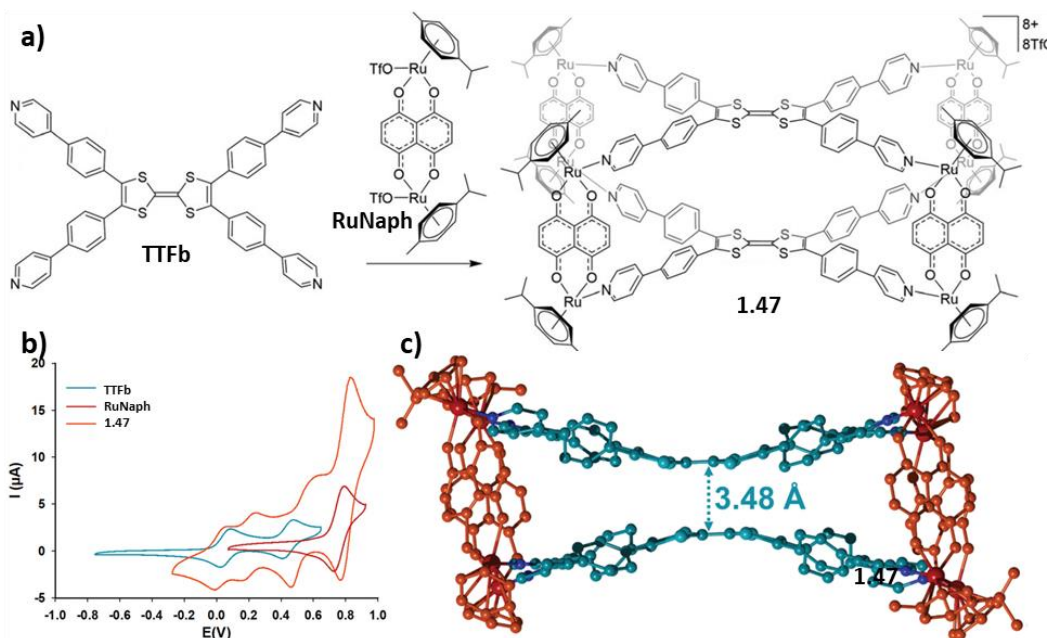


Figure 33. self-assembly with TTF ligand **TTFb** a) molecular sandwich **1.47**, b) cyclic voltammogram of **TTFb** (C = 1 mM, CH₂Cl₂, 0.1 M nBu₄NPF₆, 100 mV.s⁻¹, GCE), **RuNaph(OTf)₂** (C = 1 mM, CH₃CN/CH₂Cl₂, 0.1 M nBu₄NPF₆, 100 mV.s⁻¹, GCE) and **1.47** (C = 1 mM, CH₃CN/CH₂Cl₂, 0.1 M nBu₄PF₆, 100 mV.s⁻¹, Cgr) vs Fc/Fc⁺ and c) X-ray crystal structure of cage **1.47**.¹⁰⁰

3.1.3. DTF-based assemblies

Another approach to create a redox-active cavity lies on the combination of a naked metal acceptor and “banana-shaped” ligand. A multitude of M₂L₄ self-assembled structures has been reported, including “banana-shaped” ligands and metal acceptors for which all coordination sites are available.³⁰ The planar 9-(1,3-dithiol-2-ylidene)-fluorene (DTF) moiety (Figure 34) is known to undergo a reversible one-electron oxidation at low potential, to generate a radical-cation species.¹⁰¹ The ligand **L3Pyr** (X = N, Y = CH) was designed and was reacted with Pd(CH₃CN)₄(BF₄)₂ to afford the cage **1.48** (Figure 34a).¹⁰² The corresponding monocystals have

been analyzed by X-Ray crystallography, and a cavity of 600 \AA^3 was determined. However, no guest binding was detected in solution. The electrochemical properties of cage **1.48** were studied by cyclic voltammetry. The oxidation of DTF moiety in **1.48** was detected at the potential $E_{\text{ox}} = 0.62 \text{ V}$, which is slightly higher than the one observed for ligand **L3Pyr**. This difference is expected from coordination to the metal acceptor (Figure 34c). The existence of only one oxidation wave indicates that all DTF moieties are oxidized independently, and no electronic interaction occurs between the neighboring electro-active DTF moieties, mainly because of the rigidity of the self-assembly.

An isomer of ligand **L3Pyr** was also prepared, namely **L4Pyr** ($X = \text{CH}$, $Y = \text{N}$).¹⁰³ The reaction of **L4Pyr** with $\text{Pd}(\text{dppf})\text{OTf}_2$ afforded the self-assembly **1.49** (Figure 34b). The X-ray crystallography structure of **1.49** corresponds to a molecular clip formed by two ligand moieties linked together through two metal centers (Figure 34b). The electrochemical properties, studied by cyclic voltammetry, reveal an oxidation value of $E_{\text{ox}} = 0.59 \text{ V}$ and the expected shift to higher potential in comparison with the free ligand.

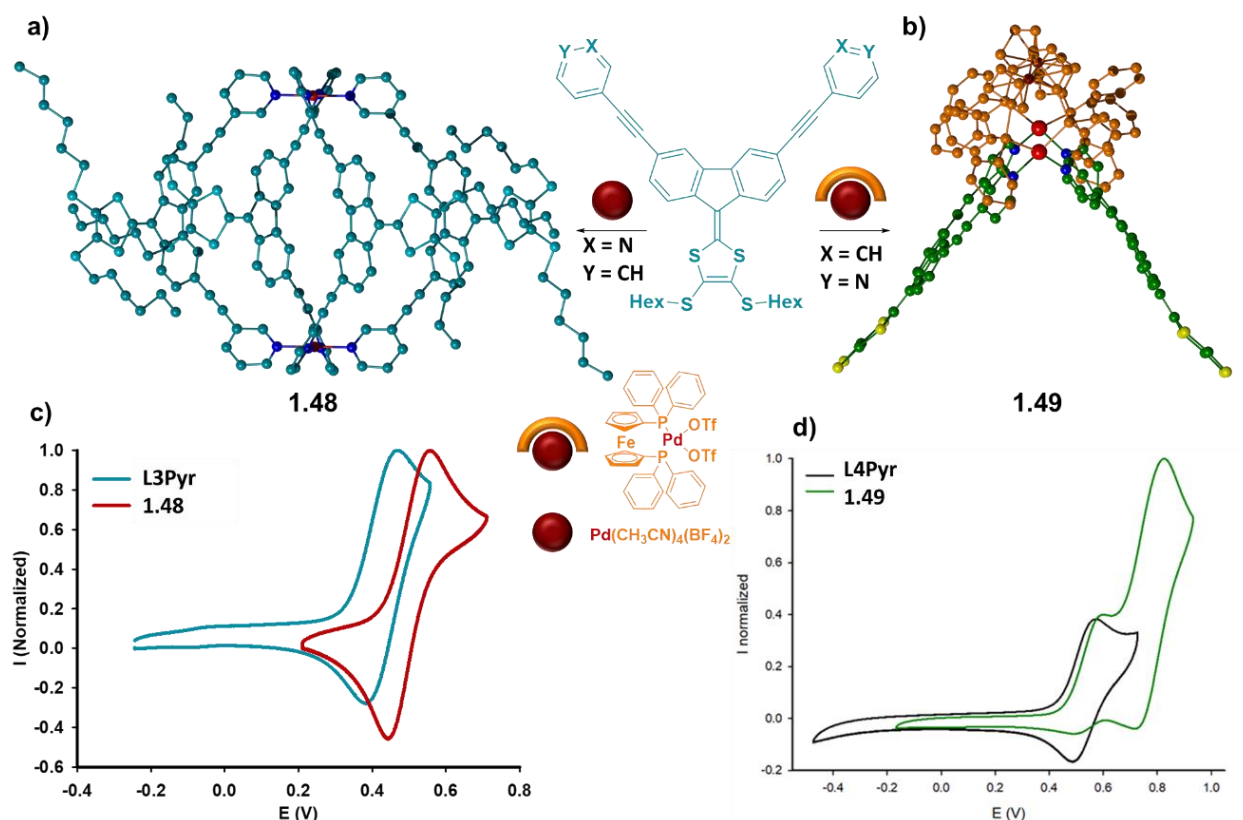


Figure 34. Discrete self-assemblies incorporating the DTF ligand a) cage b) molecular clip c) normalized cyclic voltammograms of ligand **L3Pyr** ($C = 10^{-3} \text{ M}$, $\text{CH}_3\text{CN}/\text{CH}_2\text{Cl}_2$, $0.1 \text{ M nBu}_4\text{NPF}_6$, $50 \text{ mV}\cdot\text{s}^{-1}$, Pt) and cage **1.48** ($C = 5 \times 10^{-4} \text{ M}$, CH_2Cl_2 , 0.05 M NaBARf , $50 \text{ mV}\cdot\text{s}^{-1}$, Pt), V vs Fc/Fc^+ d) normalized cyclic voltammograms of ligand **L4Pyr** and clip **1.49** ($C = 10^{-3} \text{ M}$, $\text{CH}_3\text{CN}/\text{CH}_2\text{Cl}_2$, $0.1 \text{ M nBu}_4\text{NPF}_6$, $100 \text{ mV}\cdot\text{s}^{-1}$, Pt) V vs Fc/Fc^+ .^{102, 103}

3.1.4. Extended TTF-based systems

A peculiar derivative of TTF moiety is the molecule called "n-extended TTF" (exTTF; 9,10-di(1,3-dithiol-2-ylidene)-9,10-dihydroanthracene) (Figure 35a). This molecule includes two dithiole units attached to the

dihydroanthracene moiety, thus forming an electron-rich system with singular geometric and electronic properties.¹⁰⁴⁻¹⁰⁶ Due to steric repulsions between the sulphur atoms and the periplanar dihydroanthracene hydrogens, the exTTF has a concave geometry. In contrast to TTF, the exTTF unit shows only one quasi-reversible oxidation process that involves 2 electrons (Figure 35b). Importantly, this process is accompanied by a drastic geometry change, from a butterfly shape (neutral state) to an aromatic anthracene derivative (dicationic state) (Figure 35c).¹⁰⁴

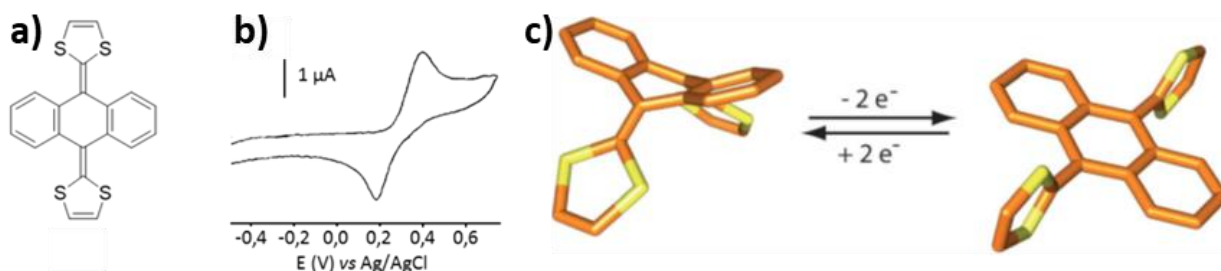


Figure 35. Quasi-reversible oxidation wave of exTTF and the related geometry change from neutral to dicationic states.¹⁰⁴

The exTTF derivatives are widely investigated as electron-rich moieties that can interact with electron deficient molecules such as C_{60} due to their complementary geometry (concave/convex) and electronic properties (donating/accepting). For all these reasons, the group was interested in constructing exTTF-based electro-active self-assembled metalla-structures that could i) bind electro-deficient guests and ii) change their structure upon oxidation with concomitant guest release.

Our group has developed the exTTF ligand **exTTFaH** and used it in preparation of metal-directed self-assembled cages with *cis*-blocked Pd complexes. A reaction of **exTTFaH** with **Pd(dppf)(OTf)₂** or **Pt(dppf)(OTf)₂** in nitromethane led to original self-assembled containers **1.50Pd** and **1.50Pt** with M_4L_2 stoichiometry (Figure 36a).¹⁰⁷ The ligand **exTTFaH** possesses the electrochemical properties of exTTF with the quasi-reversible oxidation wave ($E_{ox} = 0.40$ V; $E_{red} = -0.23$ V vs Fc/Fc⁺, Figure 36b). The oxidation potential is shifted to higher potential in the corresponding coordination cages due to the electron withdrawing effect of metal acceptors. The second oxidation process in case of **1.50Pd** and **1.50Pt** is located on Ferrocene based coligands.

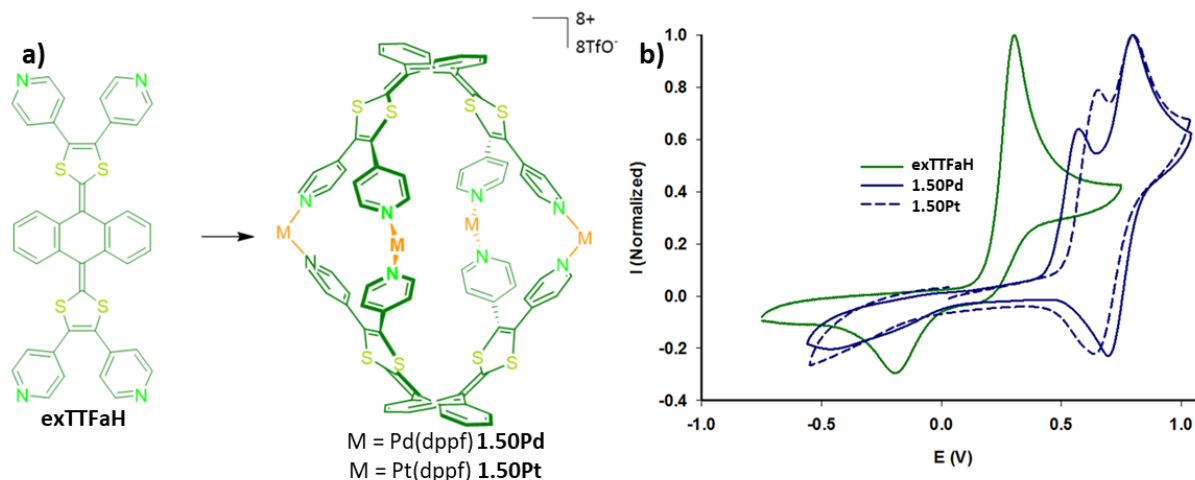


Figure 36. a) exTTF based cages **1.50Pd** and **1.50Pt**, b) cyclic voltammogram of ligand **exTTFaH** ($C = 1$ mM, $\text{CH}_3\text{CN}/\text{CH}_2\text{Cl}_2$, 0.1 M nBu_4NPF_6 , 100 $\text{mV}\cdot\text{s}^{-1}$, Pt) and of cages **1.50Pd** and **1.50Pt** ($C = 1$ mM, CH_3CN , 0.1 M nBu_4PF_6 , 100 $\text{mV}\cdot\text{s}^{-1}$, Cgr) vs Fc/Fc^+

Even though the self-assembled cages **1.50Pd** and **1.50Pt** have low solubility in usual organic solvents, the containers were able to bind one molecule of perylene with a K_a value of 3.9×10^3 in nitromethane. To improve the solubility, a modified version of the exTTF ligand **exTTFaTEG** carrying four triethylene glycol (TEG) chains was synthesized. This allowed to obtain not only cationic cage **1.51Pd**, but also neutral cages **1.52Pd** and **1.52Pt** (Figure 37).¹⁰⁸ The cages were investigated for the complexation of neutral and anionic molecules and it was discovered that the neutral cage **1.52Pd** has binding constants for neutral polyaromatic guest encapsulation 2-3 orders of magnitude higher than the charged analogue **1.51Pd**.¹⁰⁸⁻¹¹⁰ A X-ray structure of coronene \subset **1.52Pt** could even be characterized (Figure 37b). These lower association constants in the case of **1.51Pd** are due to the competition between the neutral guest molecule and counter anions that occupy the positively charged internal cavity of the cationic cage. Along with neutral guests, the cage **1.51Pd** has shown the ability to encapsulate anionic molecules such as $\text{B}_{12}\text{F}_{12}^{2-}$ (Figure 37c).¹⁰⁹ Importantly, both cages were able to release reversibly their guest through a redox stimulation. Oxidation of **1.51Pd** leads to the disassembly of the cage thanks to a combination of electronic and geometric parameters with concomitant release of both $\text{B}_{12}\text{F}_{12}^{2-}$ anions.¹⁰⁹ Since the Pt-N bond is much more energetic than the homologous Pd-N bond, oxidation of coronene \subset **1.52Pt** did not provide disassembly of the cage but release of the coronene thanks to a guest exchange with counter anions necessary to balance the charges of the oxidized species.¹⁰⁸

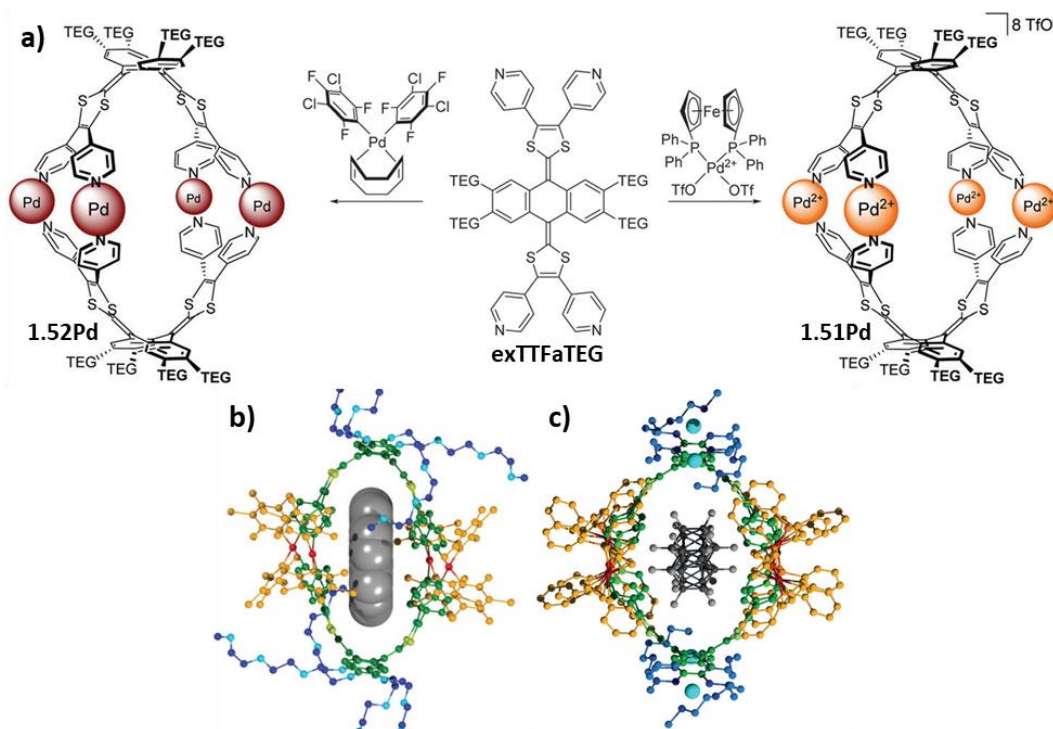


Figure 37. a) self-assemblies **1.51Pd** and **1.52Pd** (TEG: -OCH₂CH₂OCH₂CH₂OCH₂CH₂OCH₃), b) host-guest complex of **1.52Pt** with coronene and c) host-guest complex of **1.51Pd** with B₁₂F₁₂²⁻

The ligand **exTTFaTEG** was also reacted with linear metal acceptors such as AgBF₄ and PdCl₂(CH₃CN)₂.¹¹¹ The resulting M₁₂L₆ self-assemblies **1.53Ag** and **1.53Pd** get large cavities (Figure 38a). The electrochemical studies revealed different behavior for both cages (Figure 38b). While the Pd based cage **1.53Pd** has a reversible oxidation wave that corresponds to preservation of its structure upon oxidation, **1.53Ag** shows the typical electrochemical behavior observed upon disassembling of the cage. This was confirmed by addition of an excess of Ag⁺ as chemical oxidant that leads to the formation of a coordination polymer with Ag⁺ cations chelated by TEG chains on one side and to the pyridine on the other side (Figure 38c). This example corresponds to the first redox triggered supramolecular transformation of a discrete cage to a coordination polymer.

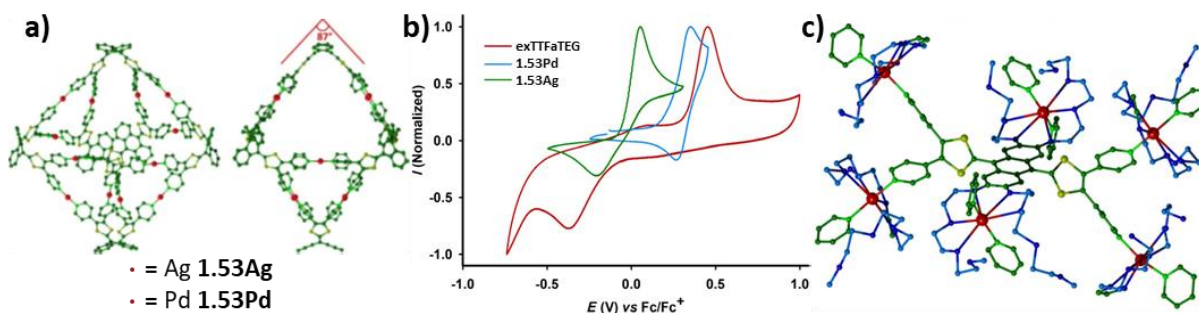


Figure 38. a) M₁₂L₆ self-assemblies **1.53Ag** and **1.53Pd**, b) cyclic voltammogram of ligand **exTTFaTEG** (C = 1 mM, CH₃CN) and of cages **1.53Pd** (C = 0.5 mM, CH₃CN/CH₂Cl₂ (1/1)) and **1.53Ag** (C = 0.5 mM, CH₃NO₂/CH₂Cl₂ (1/1)), 0.1 M nBu₄NPF₆, 100 mV.s⁻¹, GC, vs Fc/Fc⁺, c) X-Ray structure of oxidized coordination polymer obtained from **1.53Ag**.

4. Objectives of my thesis

Based on the recent results obtained in the team, my PhD thesis focuses on the development of new functional and stimuli sensitive discrete metalla-structures prepared by coordination-driven self-assembly. A part of the project targets stimuli-responsive self-assemblies involving electron-rich and S-enriched exTTF, DTF, as well as N-containing pH sensitive benzobisimidazole (BBI) moieties. Therefore, the manuscript is constructed around the following main items:

- The development of a new family of electron-rich ligands and assemblies constructed from an original regioisomer species of **exTTFa**. The objective is here to evaluate how changing the coordinating functions localization on the exTTF framework may offer new opportunities to produce original self-assembled structures (Chapter 2).

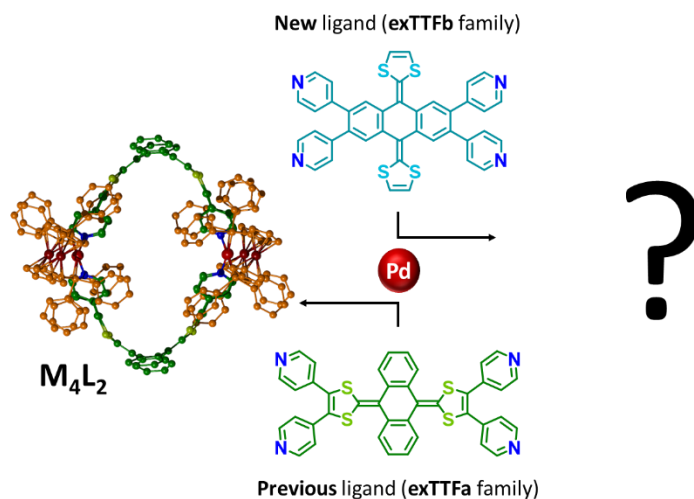


Figure 39. General concept of the work developed from a new family of exTTF ligands.

- The synthesis of pillar arene scaffolds bearing appended exTTF units. The goal of this study is to evaluate the effect of the accumulation of neighboring electron-rich units onto a given platform, notably in terms of its capacity to bind electron-poor guests (Chapter 2).

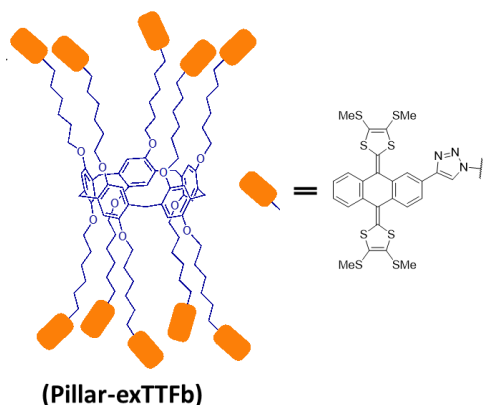


Figure 40. Targeted pillar arene scaffolds bearing appended exTTF units.

- The study of redox-driven supramolecular transformation from DTF-based coordination tweezers (Chapter 3) constructed either from square planar Palladium complexes or bi(Ruthenium) complexes (Figure 41).

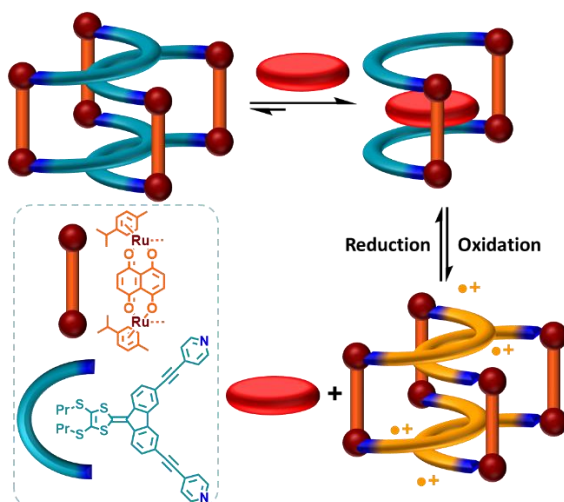


Figure 41. Redox driven supramolecular transformation occurring from a DTF based molecular tweezer

- The synthesis of pH-active self-assemblies featuring the pH sensitive BBI moiety and characterization of their supramolecular properties through pH change stimulation (Chapter 4).

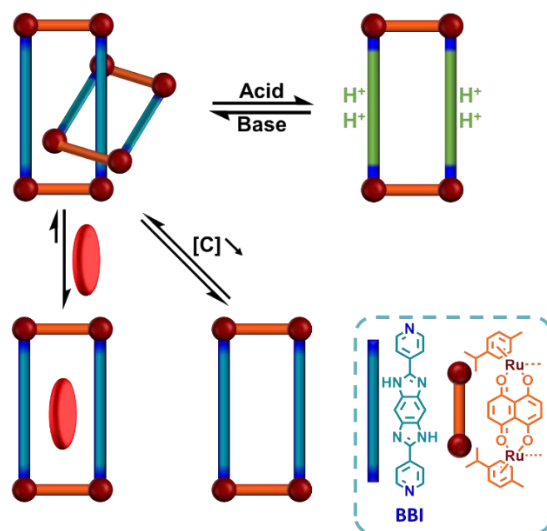


Figure 42. pH controlled supramolecular transformation from a BBI based metalla-rectangle.

Chapter 2.

Ligands and self-assemblies incorporating the "exTTF" scaffold

As mentioned above, the exTTF scaffold (Figure 43a) has unique electronic and geometrical properties that have been exploited in the laboratory for the preparation of metal-assembled cages. In particular, the geometry change occurring upon oxidation (see § 3 Chapter 1) offers the potential for an original control of the cavity size, shape and charge in the corresponding self-assembled receptors, and may introduce a steric factor for a guest release. Those are the reasons why we have been interested in investigating new electron-rich structures constructed from new exTTF ligands in a context of host-guest chemistry and guest release.

1. Tetrapyridyl-exTTF ligands: a comparative study between two regioisomer ligands

This study has been mainly developed in reference “Comparing the self-assembly processes of two redox-active exTTF-based regioisomer ligands” (New J. Chem. 2021).¹¹² Some additional data are provided below.

While the fully aromatic oxidized dicationic species of exTTF is characterized by a planar anthracene moiety bearing two nearly perpendicular 1,3-dithiolium rings,¹¹¹ neutral exTTF exhibits a highly bent butterfly shape with two non-identical faces (Figure 43a). The less curved dihydroanthracenyl one has successfully proven to interact with fullerene derivatives in macrocyclic covalent hosts.¹¹³⁻¹¹⁸ On the other hand, the cavity of our previously described M_4L_2 containers^{107, 109, 110} (Figure 37) rather explores the more bent face which incorporates both S-rich 1,3-dithiol rings (Figure 43b). On this basis, we were naturally interested in designing a novel class of tetrapyridil exTTF-based ligands (Figure 43c) bearing the coordinating units on the dihydroanthracenyl moiety instead of the dithiol rings.

With this idea in mind, we designed the structural “isomer B”, in order to reach new types of cavities and to compare the host-guest properties with those obtained from isomer A derivatives. One should note that isomers A and B are not strictly regioisomers but will be considered as so in this study, since the main difference concerns the relative positions of the pyridyl groups surrounding the exTTF framework.

As the coordination angles in isomer B are different than for isomer A, we can expect the development of new self-assembled architectures. In particular, cavities resulting from isomer B will be made from the bent dihydroanthracene fragments (instead of S-rich heterocycles in the case of isomer A). The corresponding interactions that could be reached within the cavity with an encapsulated guest, as well as the cavity size which is expected to be larger than with isomers A, could provide a better affinity for fullerene molecules.¹¹⁴ One should note that receptors made from isomer A derivatives, present a good affinity for planar guests.¹⁰⁷⁻

109

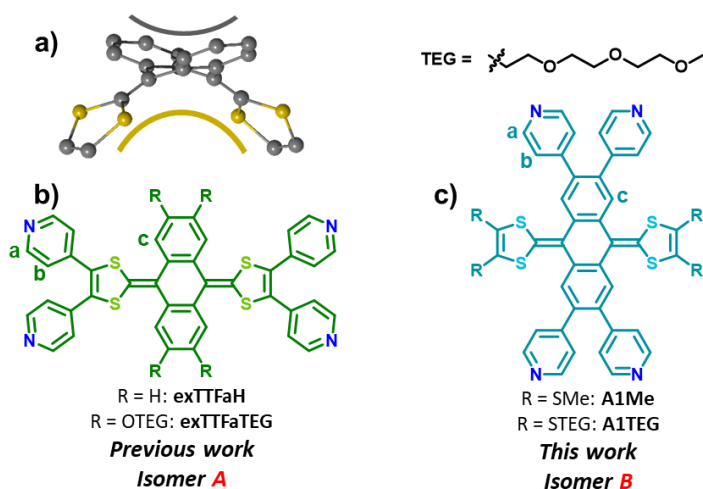
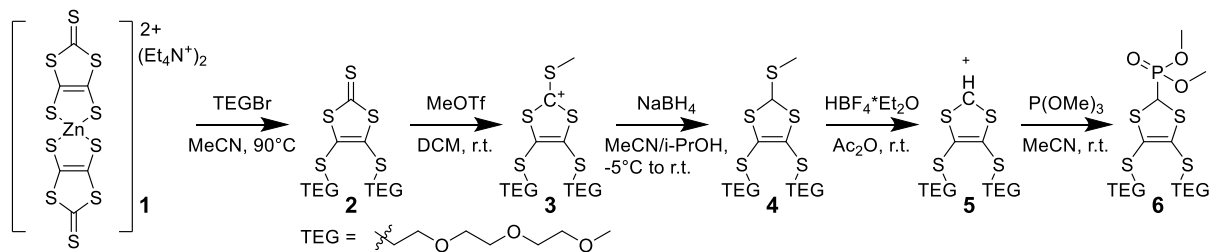


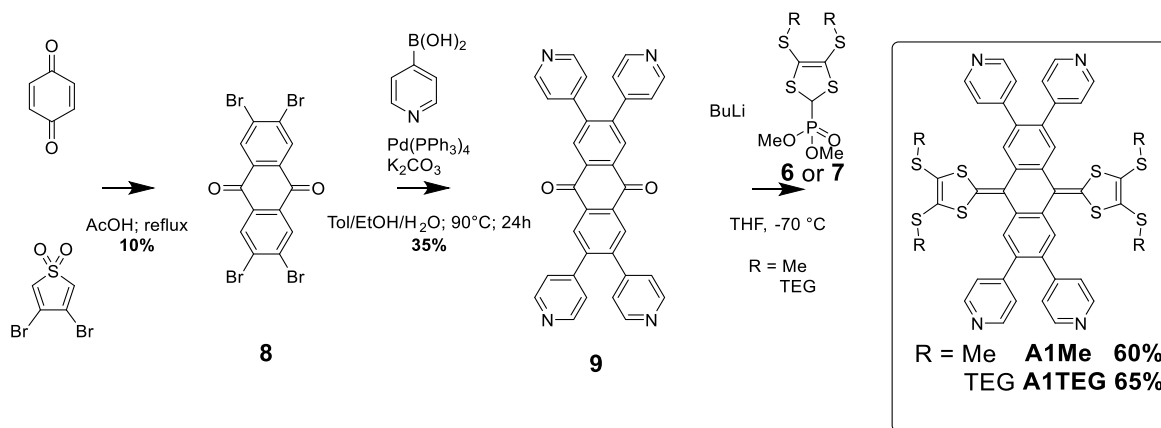
Figure 43. MM+ simulation of exTTF showing the difference in curvature between both faces (a) (yellow: most curved face, grey: less curved face). Structural exTTF-based ligands isomers where pyridine units are grafted on the dithiol rings (b, **exTTFaH** and **exTTFaTEG**) or the dihydroanthracenyl skeleton (c, **A1Me** and **A1TEG**)

The synthesis of exTTF ligands involves the preliminary preparation of phosphonate esters. By adaptation of a well-established methodology,¹⁰⁹ phosphonate **6** (R = TEG, CH₂CH₂OCH₂CH₂OCH₂CH₂OCH₃) was synthesized starting from the zincate complex **1** by alkylation of the dithiolate salt, alkylation-reduction of the thione followed by elimination of SMe group, and finally Arbuzov reaction (Scheme 2). Compound **6** is a new compound that has been targeted to insure the solubility of the final structures. It has been characterized by ¹H, ¹³C, ³¹P NMR and mass spectrometry.

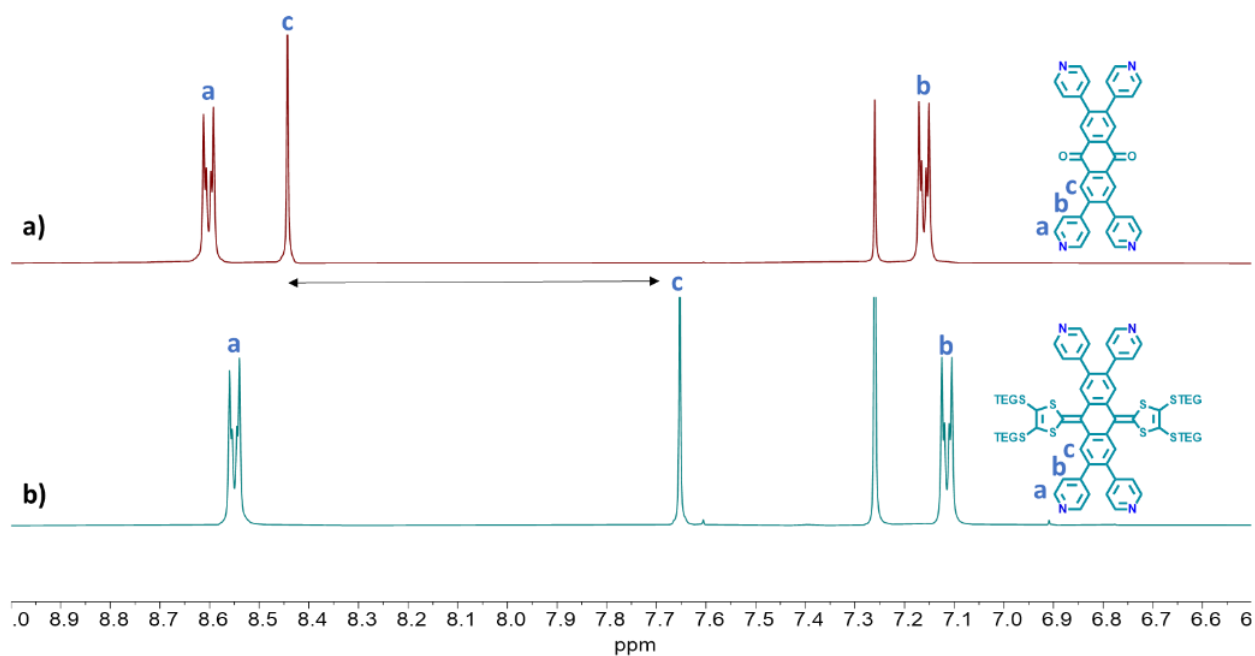


Scheme 2. Synthesis of phosphonate **6** (TEG : CH₂CH₂OCH₂CH₂OCH₂CH₂OCH₃)

The synthesis of ligands **A1TEG** and **A1Me** (Scheme 3) was considered in two steps from tetrabromo anthraquinone **8**¹¹⁹ through a Palladium catalyzed Suzuki coupling reaction, followed by a HWE reaction carried out at -78°C with the appropriate phosphonate anion (generated from the corresponding phosphonate esters **6** or **7** respectively, the latter being already available in the laboratory and prepared following the same procedure.

Scheme 3. Synthesis of ligands **A1Me** and **A1TEG**.

Both ligands **A1Me** and **A1TEG** (Scheme 3) were designed with different substituents in order to tune their solubility. They were both characterized by ^1H , ^{13}C NMR and mass spectrometry. Interestingly, the chemical shift of the dihydroanthracene/anthracene proton is significantly shifted upon the HWE functionalization.

Figure 44. ^1H NMR spectra of a) **9** and b) **A1TEG** in CDCl_3 .

Single crystals of **A1Me** were obtained by slow evaporation of a solution of **A1Me** in dichloromethane/n-hexane and analyzed by X-Ray diffraction. As expected from the exTTF scaffold geometry, the dihedral angle measured between the coordination planes is much higher than the one observed for the structural isomer **exTTFaH** (Figure 45a), with respective values of 145° and 84° . The length of the exocyclic double-bonds is similar in both ligands (1.36 \AA) and very close to the one observed in other analogous systems.¹⁰² While the dithiol rings are slightly folded with a deviation around the $\text{S}\cdots\text{S}$ vector of ca. 14° when they bear the pyridine units (case of ligand **exTTFaH**), they are nearly planar in **A1Me** (6.7°). Finally, the rectangle defined by the four nitrogen atoms (N_{pyr}) is slightly larger in the case of **A1Me** ($6.4 \times 13.7 \text{ \AA}$) in comparison with ligand

exTTFaH ($6.8 \times 13.3 \text{ \AA}$). No single crystal could be grown from **A1TEG** (viscous solid at room temperature), but its basic framework is assumed to be identical to the one of **A1Me**.

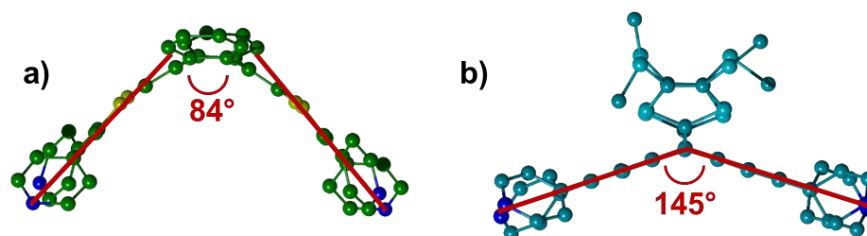


Figure 45. Structural comparison of isomer ligands a) **exTTFaH**¹⁰⁷ and b) **A1Me**.

2. Self-assemblies from the new ligands **A1Me** and **A1TEG**

2.1. Self-assemblies with cis-blocked transition metal complexes

To compare the self-assembly properties of ligands **A1Me** and **A1TEG** with the previously reported ligand **exTTFaTEG**, we investigated their behavior upon reaction with the square planar complex **Pd(dppf)OTf₂**. The reactions were performed at room temperature in nitromethane-*d*₃ and followed by ¹H NMR. While solubility issues with **A1Me** precluded the formation of self-assembled molecular structures, the reaction of **A1TEG** was compared with the same reaction carried out from **exTTFaTEG** (Figure 46).

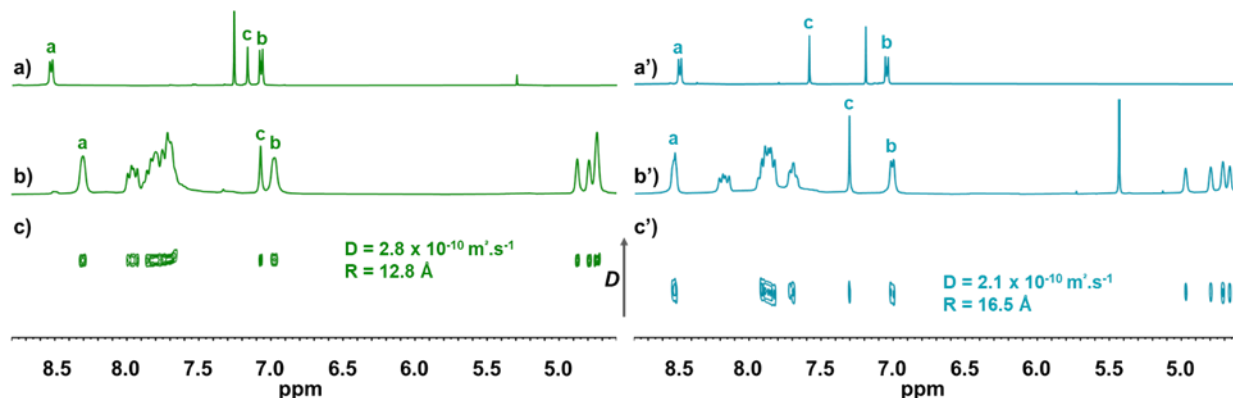


Figure 46. ¹H NMR recorded at $C = 2 \times 10^{-3} \text{ M}$, downfield region: (a) **exTTFaTEG** (CDCl_3), (b) **1.51Pd** (CD_3NO_2), (c) DOSY ¹H NMR of **1.51Pd** (CD_3NO_2), (a') **A1TEG** (CDCl_3), (b') **Pt(dppf)A1TEG** (CD_3NO_2) and (c') DOSY ¹H NMR of **Pt(dppf)A1TEG** (CD_3NO_2). See Figure 43 for assignments of a, b and c signals.

As for **exTTFaTEG**, the formation of a discrete self-assembled structure was detected after 5 minutes. It is characterized by a well resolved and symmetric ¹H NMR spectrum. As expected after coordination to the metal, the alpha (a) and beta (b) protons from pyridine rings are shifted when compared to the uncomplexed ligand **A1TEG** (Figure 46a'). A single diffusion coefficient of $D = 2.1 \times 10^{-10} \text{ m}^2 \cdot \text{s}^{-1}$ is extracted from a ¹H DOSY NMR (Figure 46c') and confirms the formation of a unique species. This value is smaller than the one observed after reaction of **exTTFaTEG** with **Pd(dppf)OTf₂** under similar conditions ($D = 2.8 \times 10^{-10} \text{ m}^2 \cdot \text{s}^{-1}$) which indicates that the self-assembled species recovered from **A1TEG** is larger than the homologous **1.51Pd** container. This is confirmed by the comparison of the respective hydrodynamic radii calculated from the Stokes-Einstein

equation (Equation 1),⁷² with values of 12.8 Å and 16.5 Å respectively, the latter being compatible with the formation of a M_6L_3 species (Scheme 2b).

$$D = \frac{kT}{6\pi\eta r}$$

Equation 1. Stokes-Einstein equation (η – viscosity of the medium, r – hydrodynamic radius of a molecule).

This stoichiometry was unambiguously confirmed by an ESI-FTICR-HRMS spectrometry measurement (Figure 47) carried out at $C = 10^{-3}$ M in CH_3NO_2 that shows characteristic signals at 1842.754 and 2340.672 (main contributions) corresponding respectively to $[Pd(dppf)A1TEG - 7TfO^-]^{5+}$ and $[Pt(dppf)A1TEG - 8TfO^-]^{4+}$. The formation of a larger species in the case of **A1TEG** as compared to **exTTFaTEG** was expected from the NMR study, and is consistent with the less pronounced curvature offered by the less bent conformation of this regioisomer. Unfortunately, any attempts to precipitate the product from the solution failed, leading to broadening the 1H NMR signals and probably indicating the formation of oligomeric species or degradation products. It should be noted that no other solvent allowed observation of a symmetrical 1H NMR spectrum.

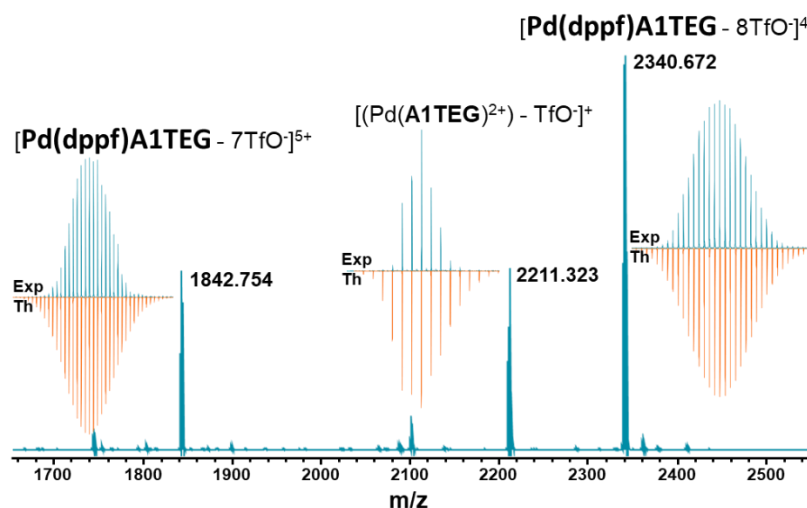


Figure 47. FTICR mass spectrum of **Pd(dppf)A1TEG** in CH_3NO_2 ($C = 10^{-3}$ M).

To deal with this issue we performed the same reaction with the homologous Platinum acceptor analogue, as the stronger bond between the platinum and pyridine moieties could lead to higher potential barrier of rearrangement in suboptimal solvent conditions during precipitation. The reaction with **Pt(dppf)OTf₂** was conducted at elevated temperature (50 °C) overnight as it took more time to reach the thermodynamic equilibrium.

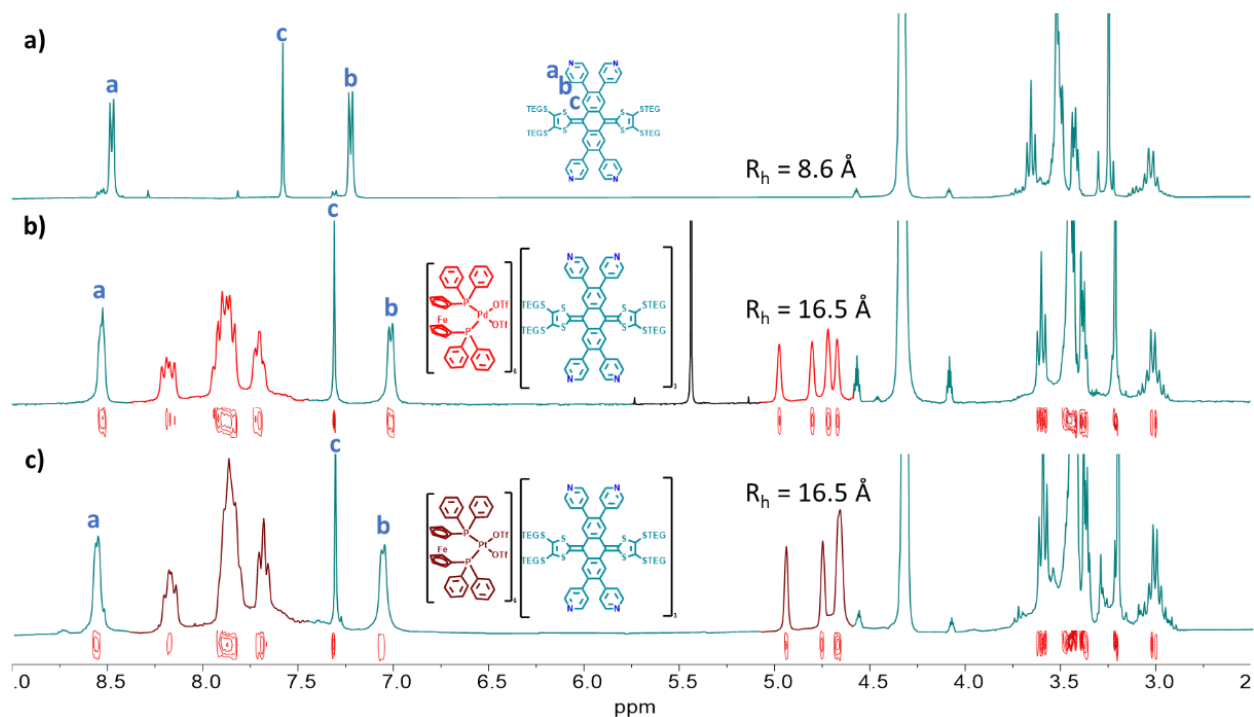
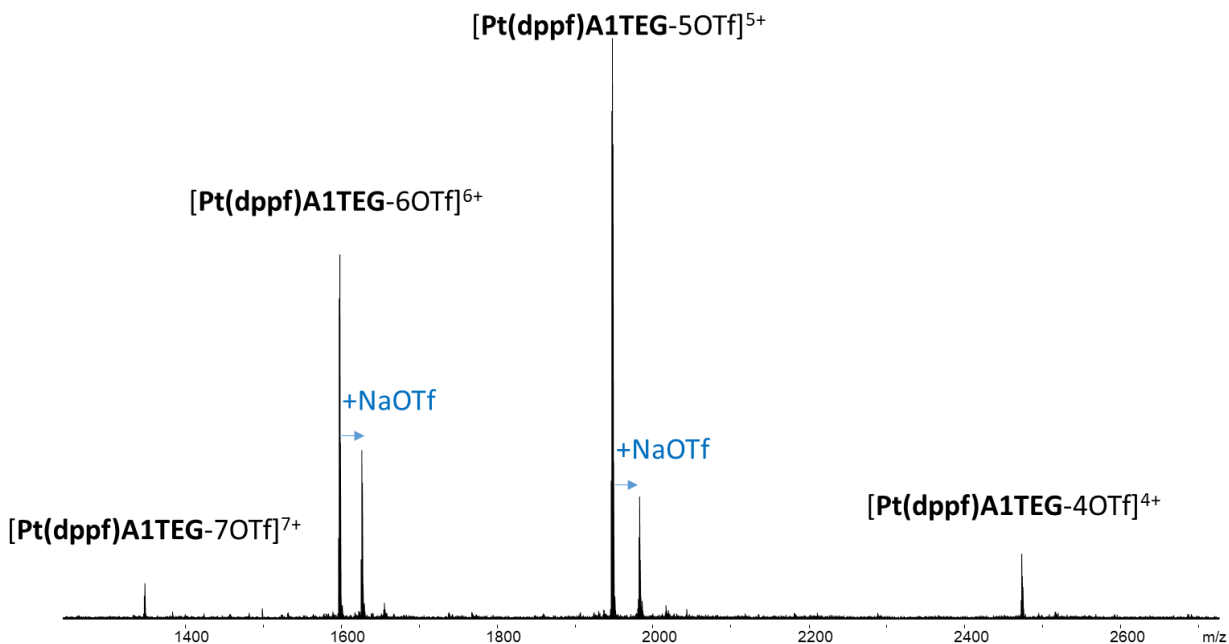


Figure 48. ^1H NMR spectrum comparison of a) ligand **A1TEG** and self-assemblies b) **Pd(dppf)A1TEG**, c) **Pt(dppf)A1TEG** in CD_3NO_2 .

The resulting discrete assembly **Pt(dppf)A1TEG** was stable enough for precipitation and was also characterized by mass spectrometry. HRMS spectrometry revealed a M_6L_3 stoichiometry with a signal at 1949.0258 corresponding to $[\text{Pt}(\text{dppf})\text{A1TEG} - 5\text{TfO}]^{5+}$ and additional fragmentation products at $m/z = 1349.7465$ (7+), 1599.3629 (6+) and 2473.5205 (4+) corresponding to $[\text{Pt}(\text{dppf})\text{A1TEG} - 7\text{TfO}]^{7+}$, $[\text{Pt}(\text{dppf})\text{A1TEG} - 6\text{TfO}]^{6+}$ and $[\text{Pt}(\text{dppf})\text{A1TEG} - 4\text{TfO}]^{4+}$, respectively. As can be seen from the spectrum, the platinum self-assembly is more stable as fewer fragmentation peaks are observed (Figure 49). However, attempts to redissolve the precipitate in any compatible solvent except nitromethane have resulted in a chemical evolution to a mixture of species with non-symmetrical ^1H NMR spectrum.

Figure 49. FTICR mass spectrum of **Pt(dppf)A1TEG**.

Unfortunately, all attempts to grow crystals from **Pt(dppf)A1TEG** were unsuccessful and led to films. We performed molecular modelling by using the molecular mechanics force field MM+ method from the HyperChem Professional 8.0.3 program (Hypercube, Inc., Waterloo, ON, Canada,) configured *in vacuo*, with an RMS of 10^{-5} kcal/mole, a number of maximum cycles of 32500, and a Polak-Ribiere algorithm. The MM+ modeled molecular structure that corresponds to this M_6L_3 stoichiometry is depicted on Figure 50. This M_6L_3 structure forms a tridimensional hexagon characterized by diagonals of 17.0 Å, side lengths of 8.7 Å and a depth of 19.5 Å (average values). The resulting circular cavity, that, at the difference of the parent M_2L_4 structure, is defined by the dihydroanthracenyl part of the exTTF units, exhibits a diameter of ca. 16 Å, a value which is much larger than the one of **1.51Pd** (11.4 Å × 15.6 Å). As for **1.51Pd** in which the exTTF skeleton is subjected to a severe bending in order to satisfy the geometry of the final ovoid cavity, the **A1TEG** part in the **Pd(dppf)A1TEG** complex undergoes a curvature increasing from 145° to 112° when compared to the isolated ligand. Nevertheless, these bending constraints appear less important in the case of the hexagonal assembly, as expected from a larger number of constitutive units. Such a geometry has been successfully used for designing macrocyclic covalent hosts for interacting with fullerene derivatives,¹⁰⁴ taking advantage of the convex-concave geometric complementarity of both constituents.

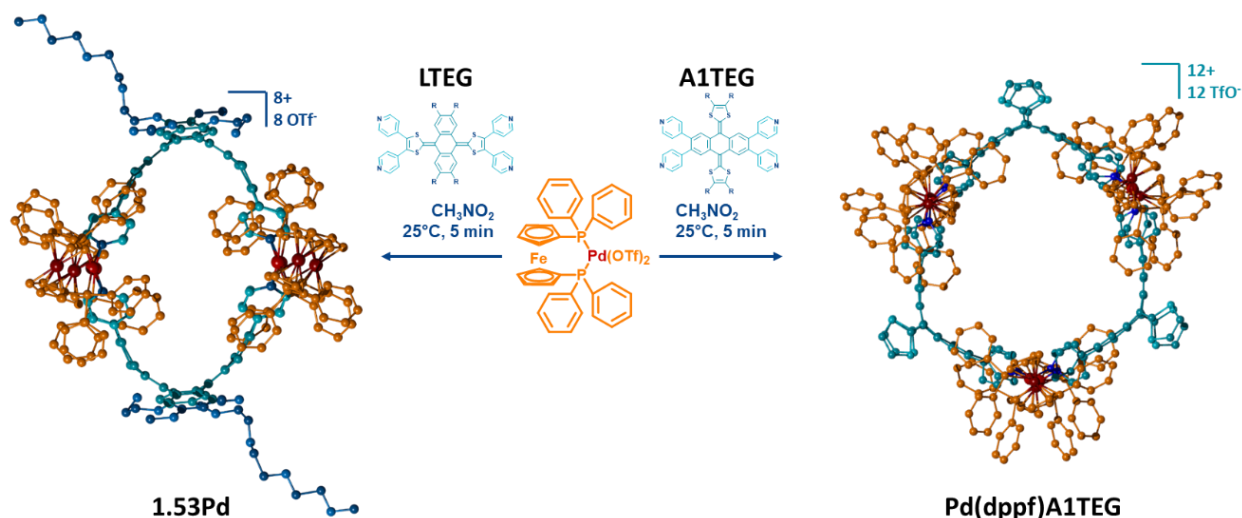


Figure 50. Two different discrete self-assemblies from two regio-isomer ligands **exTTFaTEG** and **A1TEG**.

Hence, the self-assembly **Pd(dppf)A1TEG** was characterized by cyclic voltammetry in nitromethane whereas the study was led in acetonitrile in the case of **1.53Pd**. Cyclic voltammetry of both ligands revealed that the oxidation wave of **A1TEG** is 0.25 V higher than the one of **exTTFaTEG** mainly because of the presence of the electron-donating mesomeric effect of the four OTEG chains in the latter. The cage **Pd(dppf)A1TEG** also shows the quasi-reversible wave of extended TTF, shifted to the higher potential in case of the self-assembly due to coordination to the metal.¹⁰⁷ This observed shift of 0.1 V is smaller than the difference between the ligand **exTTFaTEG** and its corresponding M_4L_2 self-assembly, which is 0.45 V (Figure 51). This can be attributed to the higher distance between the metal and the dithiole rings. The process observed at $E^{\text{ox}} = 0.7$ V is attributed to the ferrocenyl co-ligands.

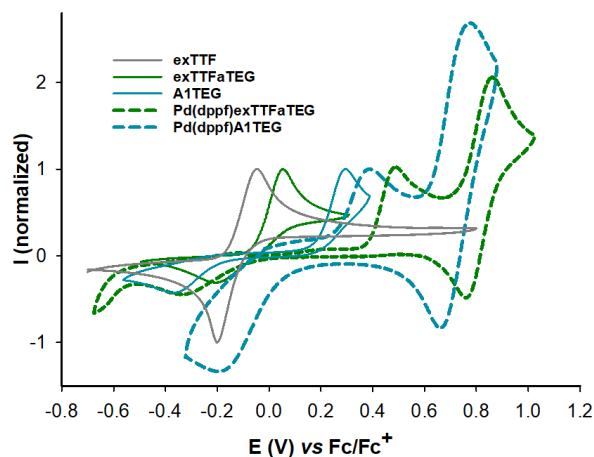


Figure 51. Cyclic voltammograms of **exTTF** ($C = 1$ mM, $\text{CH}_2\text{Cl}_2/\text{CH}_3\text{CN}$, Cgr), **exTTFaTEG** ($C = 1$ mM, CH_3CN , Cgr), **A1TEG** ($C = 1$ mM, CH_3CN , Pt), **Pd(dppf)exTTFaTEG** ($C = 0.5$ mM, CH_3CN , Cgr), **Pd(dppf)A1TEG** ($C = 0.3$ mM, CH_3NO_2 , Pt) ($n\text{-Bu}_4\text{NPF}_6$ (0.1 M), 100 $\text{mV}\cdot\text{s}^{-1}$, E vs Fc/Fc^+).

One objective of this study relies on the capacity of a given discrete receptor to bind and to deliver on-demand a given guest. Considering the redox-active character of the new receptors derived from **A1TEG**, an important issue concerns their behavior when exposed to an oxidizing agent.

The study was led with N-methylphenothiazinium tetrafluoroborate (**PTZ**) as an oxidant. The latter was chosen because i) it can be easily synthesized, ii) it shows a redox potential that is sufficient to oxidize exTTF derivatives and iii) it should not interfere with the coordination of pyridines. The study was first carried out on the starting ligand **A1TEG**. The oxidation reaction was performed in nitromethane with 2 equivalents of **PTZ**. The product was precipitated with diethyl ether and isolated as a solid in 65 % yield and characterized by ^1H and DOSY NMR (Figure 52). The ^1H NMR spectrum of the oxidized product **A1TEGOx** differs from its neutral counterpart by the TEG protons signals as well as by the dihydroanthracenyl proton that is shifted downfield from 7.6 ppm to 8.1 ppm in the oxidized anthracenyl state. As discussed before, this is clear evidence that the structure of the product involves the planar aromatic anthracene backbone. As expected, the calculated hydrodynamic radii of **A1TEG** and **A1TEGOx** show comparable values (ca. 8.5 Å) from the Stokes-Einstein equation.

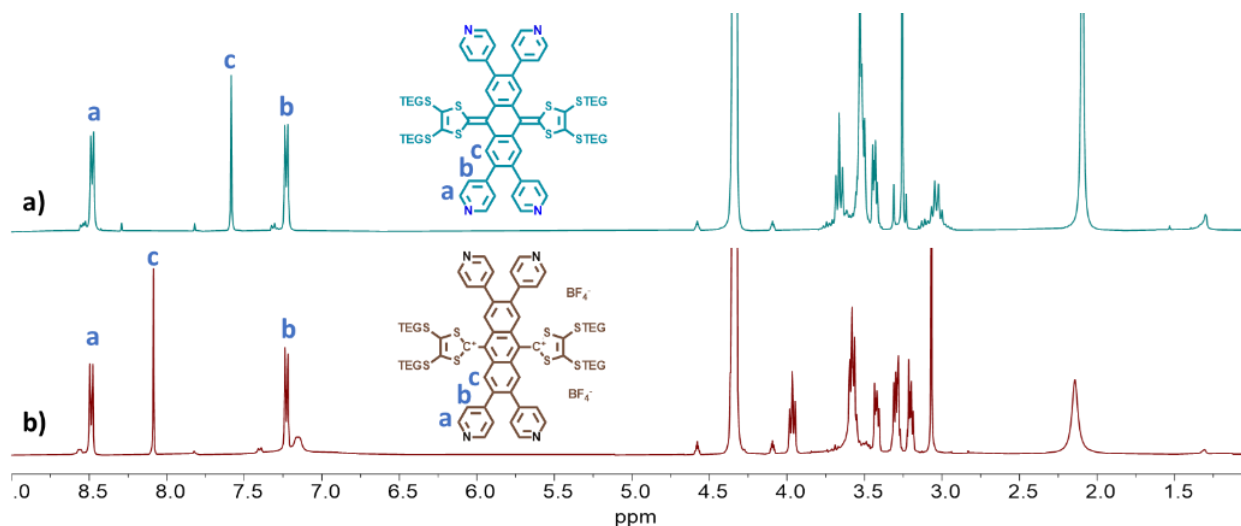


Figure 52. ^1H NMR spectra of a) **A1**, b) **A1TEGOx** in CD_3NO_2 .

Similar conditions were then applied to the most stable self-assembled structure, **Pt(dppf)A1TEG**. Unfortunately, the resulting ^1H NMR was not symmetrical that might suggest the oligomerization in those conditions (Figure 53). Due to lack of time, this study was not pursued, and it is now necessary to explore the self-assembly properties of the oxidized ligand.

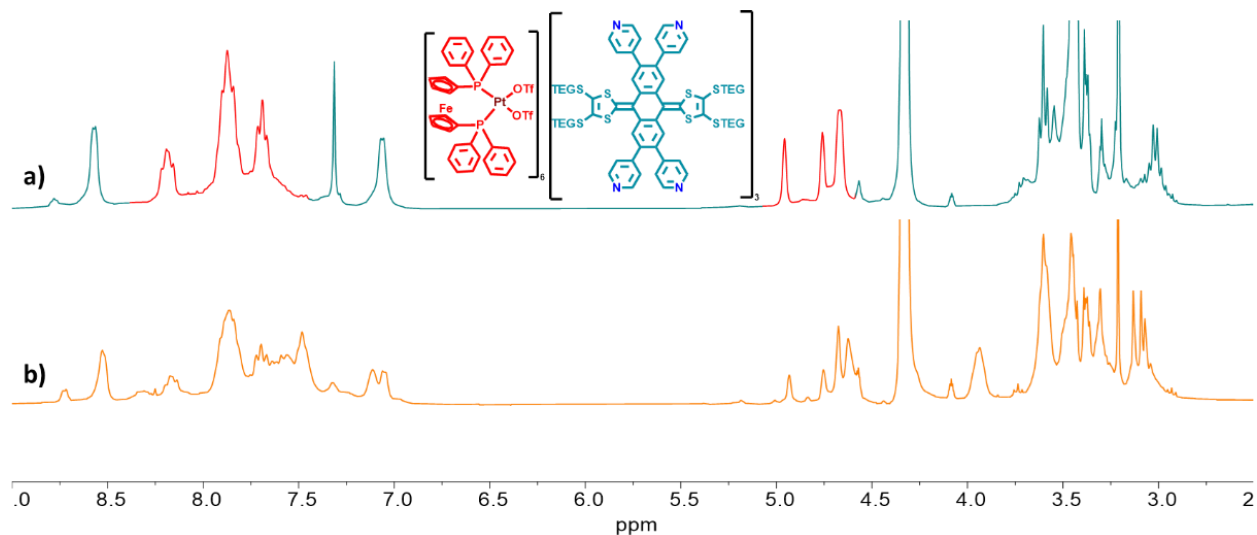


Figure 53. ^1H NMR spectra of a) **Pt(dppf)A1TEG**, b) **Pt(dppf)A1TEG** in presence of 2 equiv. of **PTZ**.

In summary, the synthesis of a new generation of exTTF based ligands (**A1TEG**, **A1Me**) bearing coordinating pyridine units on the dihydroanthracene part of the exTTF skeleton has been carried out. Compared to their previous regio isomer ligands (**exTTFaH**, **exTTFaTEG**) for which the pyridyl units are located on the dithiole units, the new ligands exhibit a much less pronounced curvature around their coordinating face (dihydroanthracenyl platform). This explains why their self-assembly process with **Pd(dppf)OTf₂** leads to a large M_6L_3 hexagonal structure instead of a compact M_4L_2 container as observed in the case of the more curved **exTTFaH** and **exTTFaTEG** ligands. The usual electrochemical properties of the exTTF moiety are retained in the corresponding large self-assembled cavities. Synthesizing such ligands offers a new alternative in the preparation of self-assembled electron-rich receptors involving dihydroanthracenyl walls as the internal cavity. Such a geometry has been successfully used for designing macrocyclic covalent hosts for interacting with fullerene derivatives,¹⁰⁴ taking advantage of the convex-concave geometric complementarity of both constituents. Investigation of the guest binding ability of the large **Pd₆(L2TEG)₃¹²⁺** cavity was nevertheless unsuccessful, due to stability reasons.

2.2. Self-assemblies involving exTTF-based ligands and bis(Ruthenium) complexes

As stated above, exTTF derivatives undergo a drastic conformational change upon a two-electron oxidation, shifting from a bent butterfly dihydroanthracene shape to a fully aromatic dithiolium-anthracene structure (Figure 35). Importantly, this structural modification is reversible upon reduction. On this basis, there is a clear interest to explore this opportunity in self-assembled discrete architectures with the objective to control on-demand, through a redox stimulus, the volume of the corresponding cavity. Such a redox-controlled "breathing" process (Figure 54) would offer a complementary mechanism of guest release to those already described by the group, i.e. guest release through disassembly of a cage¹⁰⁹ or guest exchange.¹¹⁰ One should note that a similar mechanism has been recently depicted by the group of G. Clever from a dithienylethene based cage stimulated by light,⁸³ but that to the best of our knowledge no example involving an electron transfer has been depicted till now.

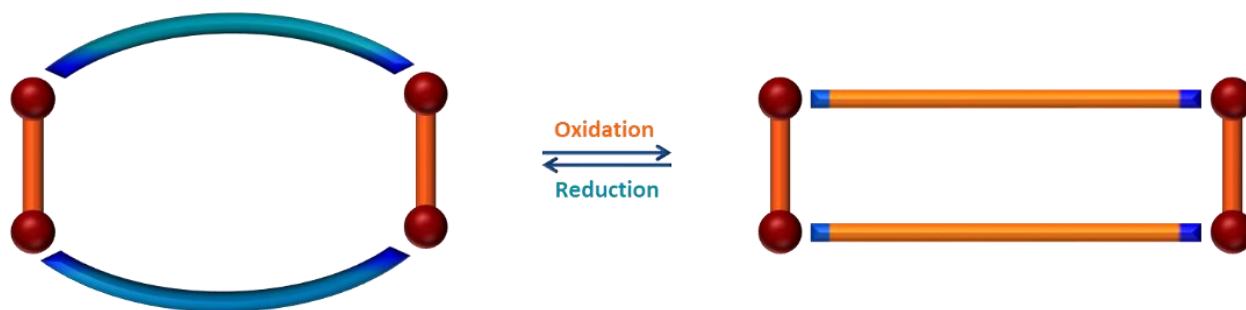
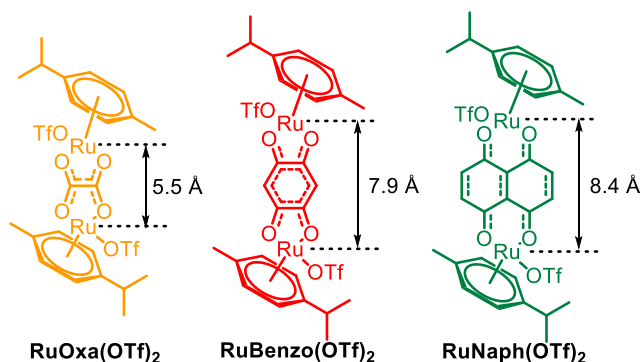


Figure 54. A breathing cavity controlled by a redox stimulus.

The new generation of ligand developed during this thesis is characterized by a much lower curvature of the face carrying the coordinating units, with a dihedral angle between the coordination planes of 145° versus 84° for the first generation. Such a difference opens new synthetic perspectives based on other metal complexes. This is why, we explored the self-assembly process with bis(Ruthenium) complexes already mentioned in chapter 1, **RuOxa(OTf)₂**, **RuBenzo(OTf)₂** and **RuNaph(OTf)₂** (Figure 55), assuming a sufficient flexibility of the exTTF based target ligands to effectively coordinate these acceptors.

Figure 55. The structures of the bis(Ruthenium) acceptors **RuOxa(OTf)₂**, **RuBenzo(OTf)₂** and **RuNaph(OTf)₂**.

For solubility reason, only the self-assembly reactions between **A1TEG** and bis(Ruthenium) acceptors were investigated and carried out in nitromethane at 50°C . After one night, the resulting products were precipitated with Et_2O and characterized by ^1H , COSY, DOSY NMR and mass spectrometry. **RuOxaA1**, **RuBenzoA1** and **RuNaphA1**, respectively obtained from reactions with **RuOxa(OTf)₂**, **RuBenzo(OTf)₂** and **RuNaph(OTf)₂**, showed a symmetrical picture in ^1H NMR (Figure 56). However, the signals corresponding to their pyridine system as well as their Benzo and Naphtho linker signals "d" are split, which indicates a different electronic environment between the two sides of the pyridine rings and a hindered rotation of the aromatic ring in the complex. Their respective D values extracted from DOSY experiments allowed for the determination of hydrodynamic radii of ca. 11 \AA , a value which seems too low for cage structures. A high resolution HRMS mass spectrometry analysis (these measurements were made recently and the detailed spectra will be provided soon by our collaborators) revealed indeed that **RuOxaA1**, **RuBenzoA1** and **RuNaphA1** have a Ru_4L stoichiometry and correspond to panel-like structures with one bis(Ruthenium) complex occupying the two coordinating pyridine units on each side of the dihydroanthracene moiety. No signal corresponding to expected cages could be detected. This result can be easily explained by the good size matching between the Ru-Ru

and N-N distances, similar to a previous example already reported in our group with a TTF-based ligand (Figure 32).

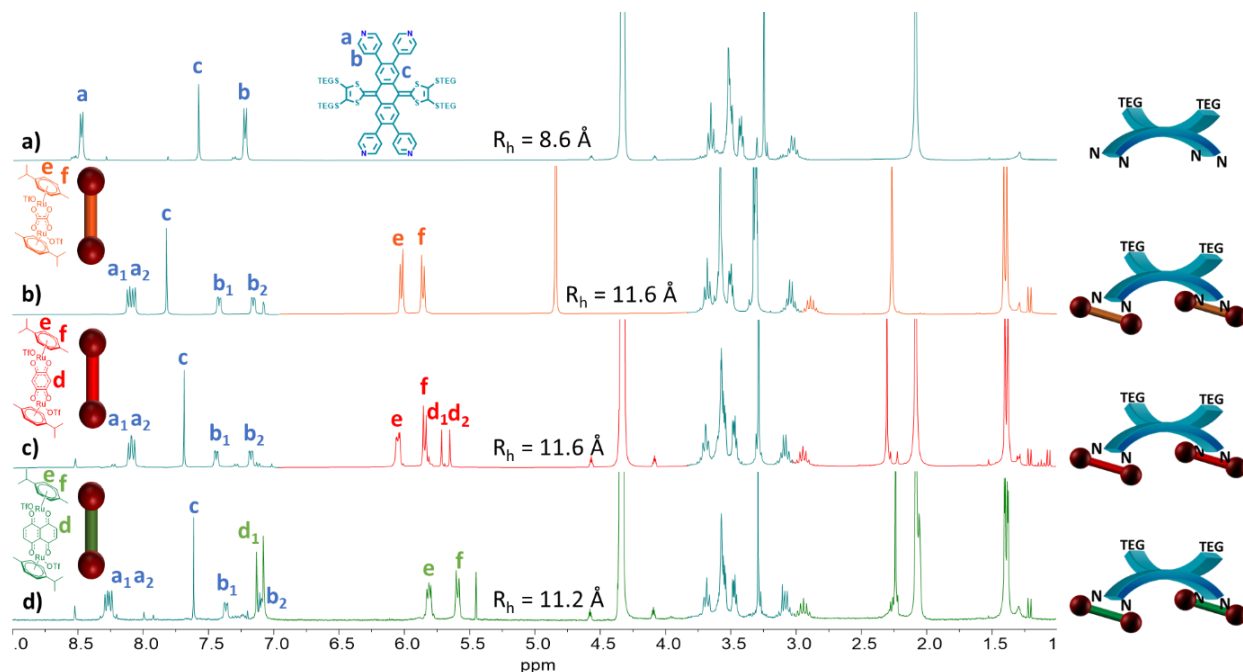


Figure 56. ^1H NMR spectrum ($C = 10^{-3}$ M) of a) **A1** in CD_3NO_2 , b) **RuOxaA1** in CD_3OD , c) **RuBenzoA1** in CD_3NO_2 , d) **RuNaphA1** in CD_3NO_2 .

Since ligand **A1TEG** can be isolated as a solid in its oxidized form, similar reactions were carried out from **A1TEGox** and bis(Ruthenium) acceptors in CD_3NO_2 . In these cases, the pyridine signals were not split, which is expected from the planar geometry of the oxidized form. However, the hydrodynamic radii of ca. 11 Å calculated from DOSY experiments suggest again the formation of panel structures (Figure 57). This has been confirmed unambiguously by a HRMS analysis. Here again, detailed spectra will be provided soon.

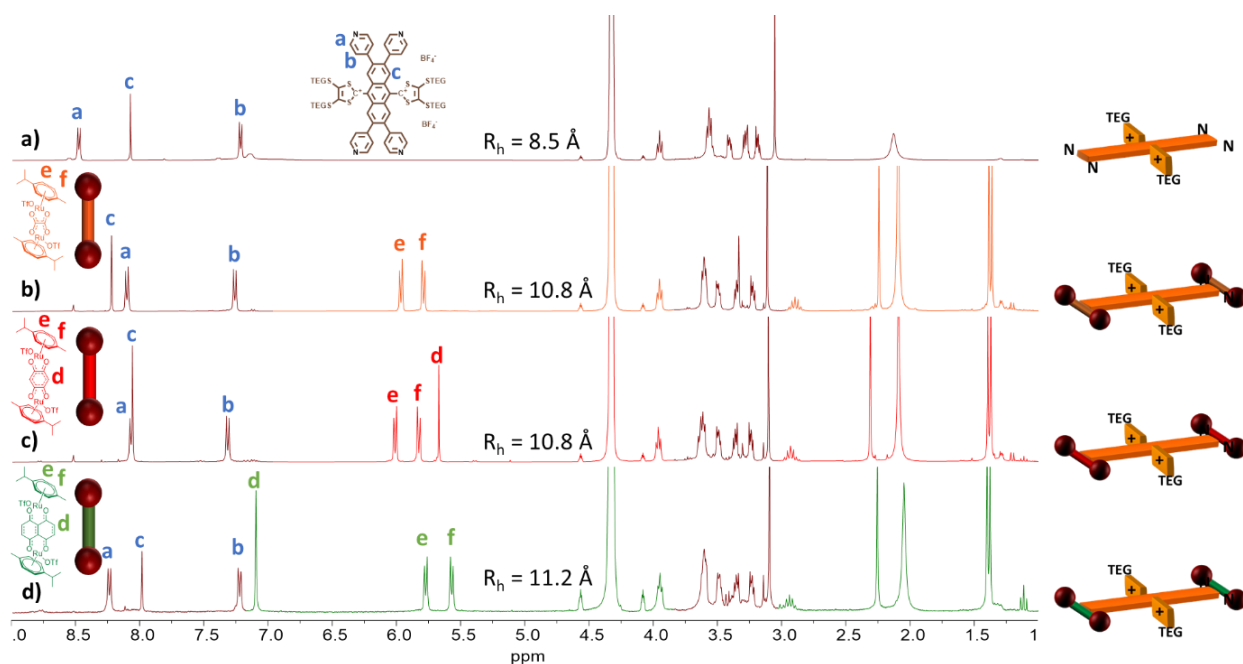


Figure 57. ^1H NMR spectrum ($C = 10^{-3}$ M), of a) **A10x**, b) **RuOxaA10x**, c) **RuBenzoA10x**, d) **RuNaphA10x** in CD_3NO_2 .

While all attempts to grow single crystals from **RuOxaA1**, **RuBenzoA1** and **RuNaphA1** were unsuccessful, a partial crystal structure from the oxidized species **RuBenzoA10x** could be obtained. As expected, the usual shape of dicationic exTTF derivatives is observed, with a planar anthracene moiety bearing two almost perpendicular dithiolium rings. The Ru-Ru distance is similar to that observed in the starting **RuBenzo(OTf)₂** complex (7.8 \AA vs 7.9 \AA) since the benzoquinonato spacer is only slightly curved to bind two adjacent pyridine units.

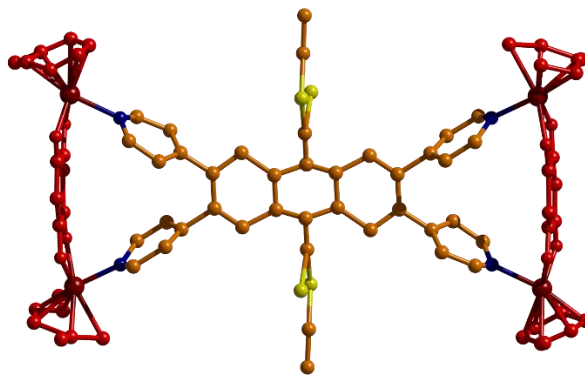


Figure 58. Partial X-Ray crystal structure of **RuBenzoA10x**.

These results show that metalla-panels are more thermodynamically favorable compared to the corresponding cages, due to the highest entropy that compensates the distorted coordination to the Ruthenium metal centers. As all three Ruthenium acceptors led to panel structures, we decided to increase the distance separating the pyridine moieties in the ligand and we therefore designed ligands **A2** and **A3** (Figure 59) which involve a longer linker between exTTF and pyridyl units. Doing so, the formation of a panel should be highly unfavorable due to the distance mismatch between pyridine nitrogen atoms and Ruthenium atoms in a bis(Ruthenium)

complex (Figure 16). As demonstrated in Figure 59, even the larger **RuNaph(OTf)₂** acceptor is too small (Ru-Ru distance of 8.4 Å) to fit between two vicinal pyridine and coordination to these moieties should be highly unfavorable.

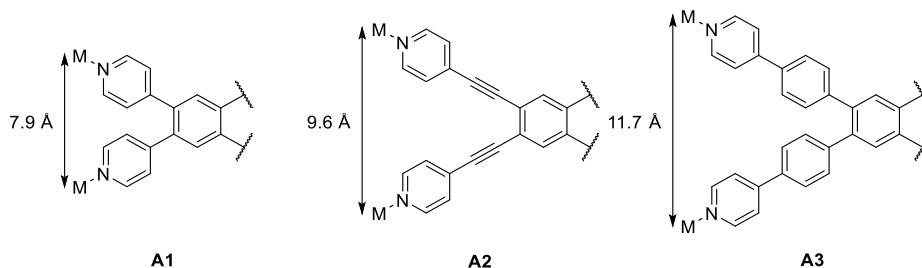
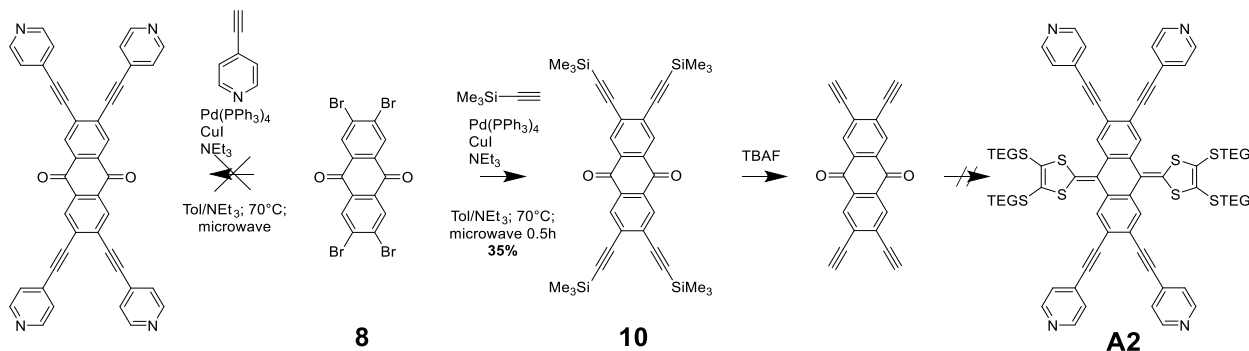


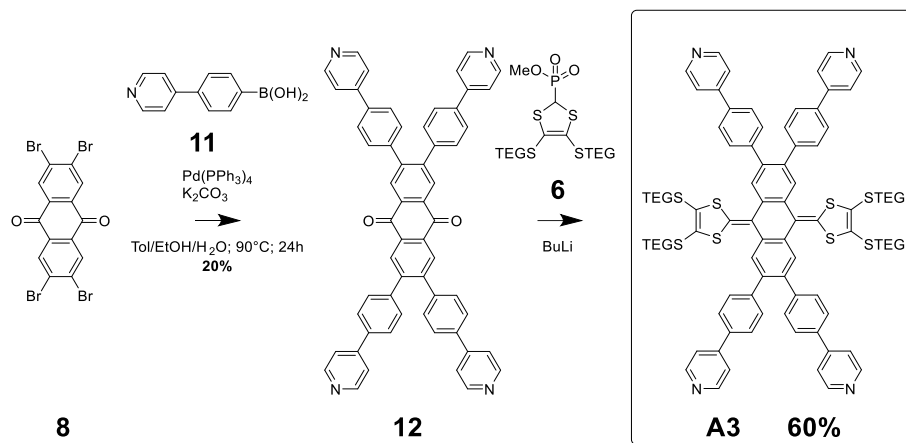
Figure 59. The optimal distances between two metal sites in the ligands **A1**, **A2** and **A3**.

The synthesis of ligand **A2** was first considered using a similar methodology than for the **A1** series, starting from compound **8** (Scheme 4, left). Unfortunately, the Sonogashira coupling with 4-ethynylpyridine did not afford the desired product even under microwave irradiation. We then changed the strategy through using a three steps procedure (Scheme 4, right): 1) Sonogashira coupling reaction with TMS-protected acetylene, 2) deprotection and second Sonogashira coupling with 4-bromopyridine and 3) HWE reaction. We managed to isolate intermediate **10** with a moderate yield of 35%. However, the deprotection led to a black insoluble product that could not be characterized. Since the synthesis of the ligand **A3** that we were carrying out in parallel, gave good results, we decided to give up with the synthesis of ligand **A2**.



Scheme 4. Attempts towards the synthesis of ligand **A2**.

Synthesis of ligand **A3** is depicted in Scheme 5. The latter was prepared following the same procedure as for **A1** but using the commercially available boronic acid **11** in step 1. After a first Suzuki coupling reaction, a HWE reaction afforded ligand **A3** that was isolated by size exclusion chromatography and characterized by ¹H NMR and mass spectrometry.

Scheme 5. Synthesis of ligand **A3**.

The self-assembly behavior of ligand **A3** with complexes **RuOxa(OTf)₂**, **RuBenzo(OTf)₂** and **RuNaph(OTf)₂** was followed by ¹H NMR in CD₃NO₂. While reactions with **RuOxa(OTf)₂** and **RuNaphto(OTf)₂** do not converge to the formation of a discrete species, the NMR obtained with **RuBenzo(OTf)₂** is well resolved (Figure 60b). The corresponding ¹H DOSY NMRs revealed the formation of a single species ($D = 2.2 \times 10^{-10} \text{ m}^2 \cdot \text{s}^{-1}$) with a calculated hydrodynamic radius of 15.9 Å consistent with the expected Ru₈L₂ cage **RuBenzoA3**. Attribution of the signals was achieved on the basis of the ¹H COSY NMR (Figure S32).

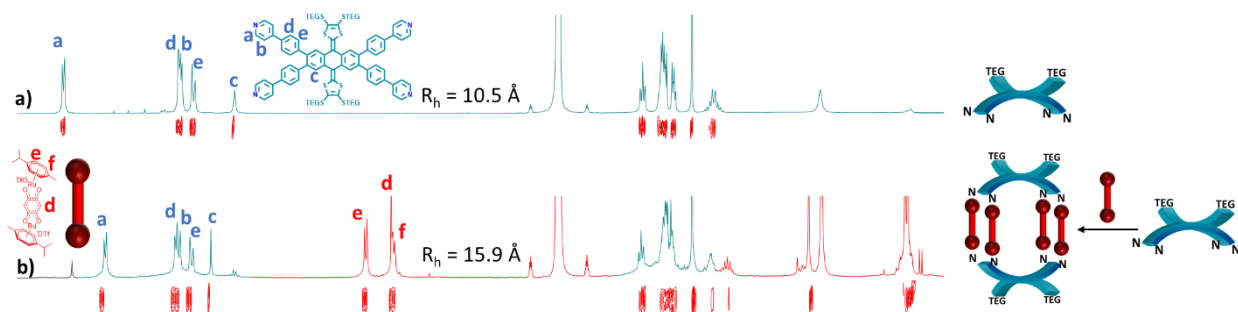


Figure 60. ¹H NMR spectra in CD₃NO₂ ($C = 10^{-3} \text{ M}$), of a) Ligand **A3** and b) **RuBenzoA3** with corresponding ¹H DOSY NMR.

The formation of a L₂M₈ cage instead of panels as observed with the smaller ligand **A1TEG** was unambiguously confirmed by HRMS spectrometry measurements carried out on **RuBenzoA3**. The mass spectrum allows to identify a series of peak arrays located at $m/z = 731.0090, 856.7175, 1024.3290, 1258.9844$ and 1610.9680 that shows very good matching with theoretical values and isotopic patterns corresponding to the species $[\text{L}_2\text{M}_8]^{8+}$, $[\text{L}_2\text{M}_8 + \text{OTf}]^{7+}$, $[\text{L}_2\text{M}_8 + 2\text{OTf}]^{6+}$, $[\text{L}_2\text{M}_8 + 3\text{OTf}]^{5+}$ and $[\text{L}_2\text{M}_8 + 4\text{OTf}]^{4+}$ respectively, where L represents the **A3** ligand and M is a Ruthenium atom.

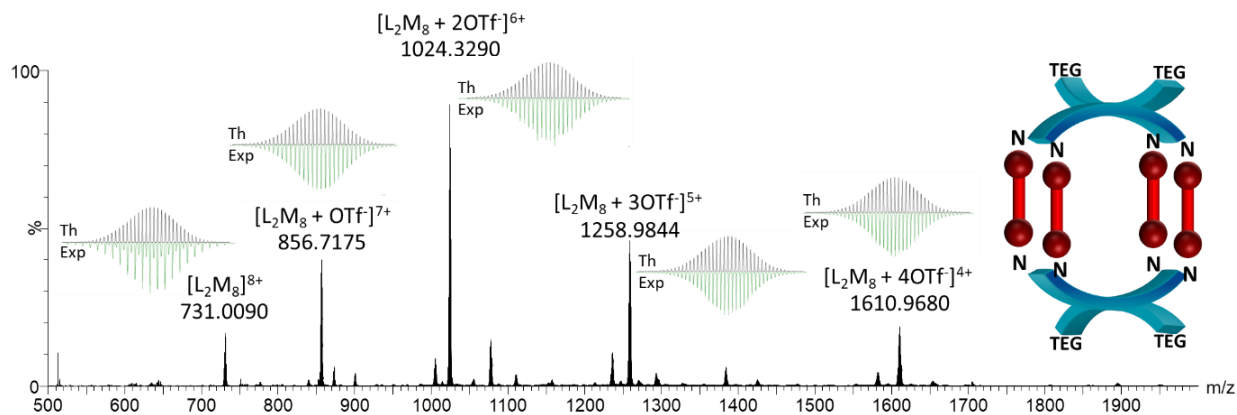


Figure 61. ESI-TOF spectrum of **RuBenzoA3** recorded in CH₃OH/CH₃NO₂ (v/v 10/1) (C = 10⁻⁴ M).

Before studying the redox behavior of the **RuBenzoA3** cage, we first investigated the stability and behavior of ligand **A3** upon a chemical oxidation. This was performed using similar conditions than above for ligand **A1TEG**, in nitromethane with **PTZ** as an oxidant. The oxidized derivative could be isolated by precipitation in Et₂O in 80% yield, and characterized by ¹H and DOSY NMR. The ¹H NMR spectrum of the oxidized product **A30x** also differs from its neutral state by the chemical shifts of the TEG protons, the benzene rings of the phenyl-pyridine linkers (protons c, d) and to a larger extent, by the characteristic downfield shift of the protons from dihydroanthracene (proton e) (Figure 62). The latter can therefore be used as a reliable indicator of the ligand geometry. ¹H DOSY NMR experiments carried out on the neutral and dicationic states show comparable D values (3.3 × 10⁻¹⁰ m².s⁻¹ for **A3** and 3.7 × 10⁻¹⁰ m².s⁻¹ for **A30x**). They correspond to hydrodynamic radii of ca. 10 Å.

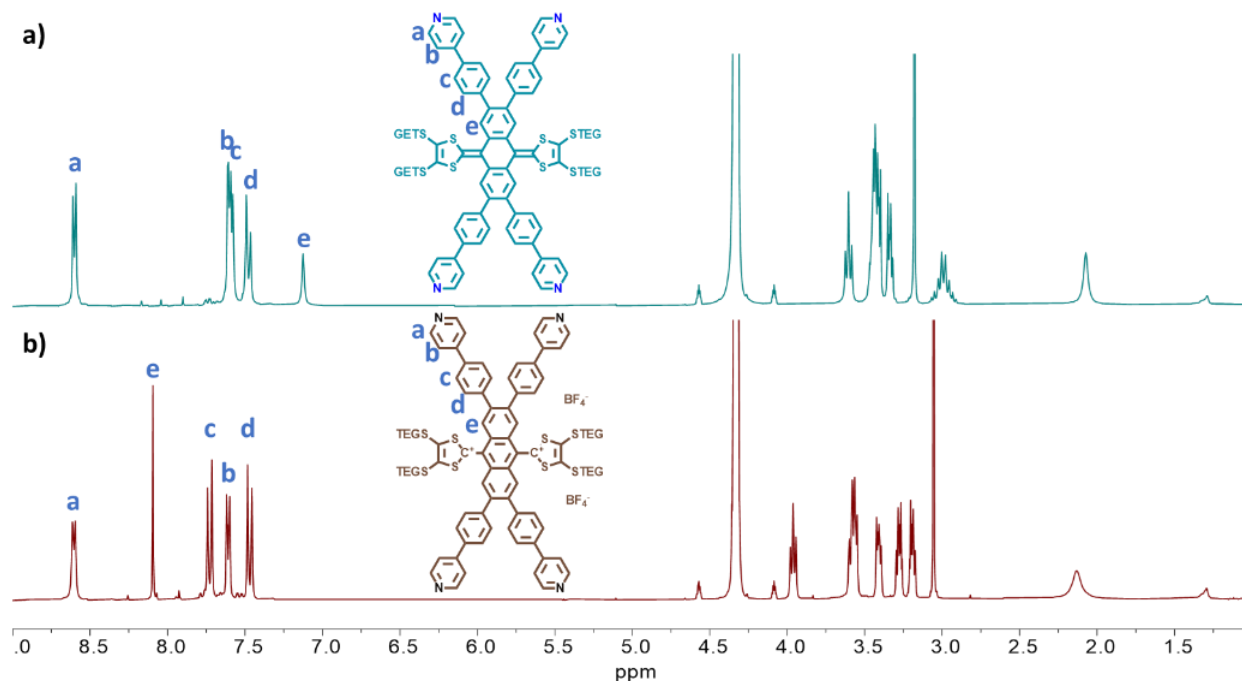


Figure 62. ¹H NMR spectra in CD₃NO₂ of a) **A3** and b) **A30x**.

Based on these results obtained on the ligand alone, the same oxidation process was studied from the preformed self-assembled structures using the same chemical oxidant as for the ligand alone. These

investigations were carried out in the NMR tube (Figure 63). As far as the oxidation path is concerned, the resulting NMR is well resolved and the characteristic shift of the oxidized ligand is present. Moreover, the DOSY NMR shows the presence of only one species in solution with a hydrodynamic radius similar to the one of the starting exTTF cage prior to oxidation (Figure 60) and a calculated radius of 15.7 Å which excludes any disassembly of the system.

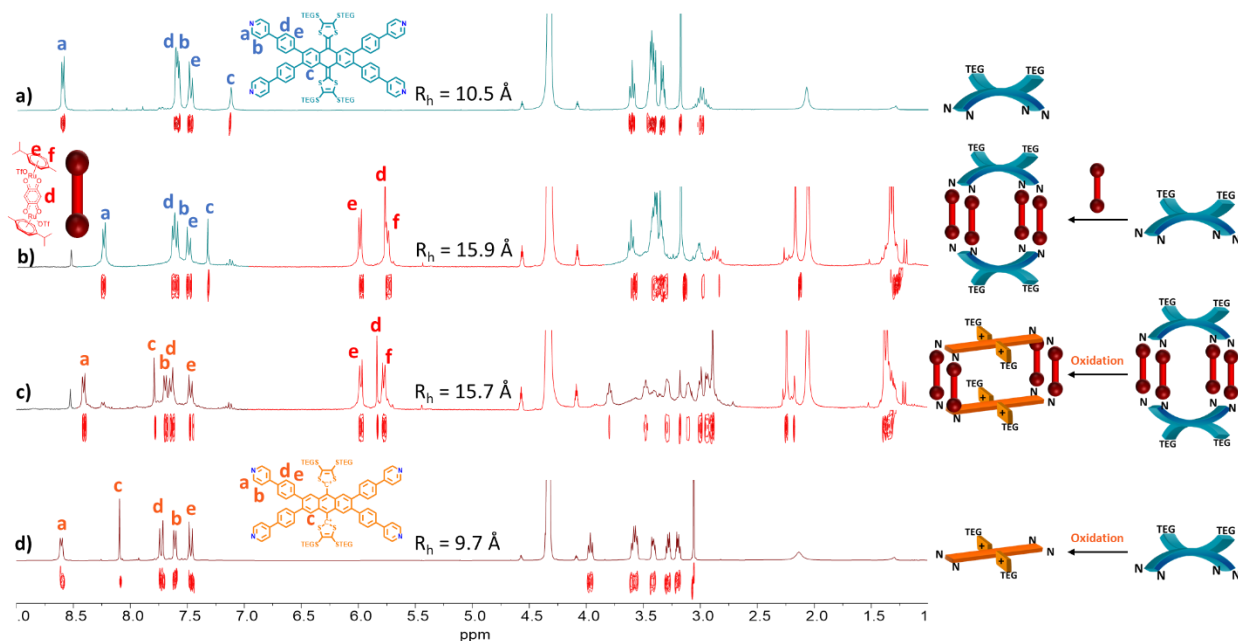


Figure 63. ^1H NMR spectra in CD_3NO_2 ($C = 10^{-3}$ M) of a) Ligand **A3**, b) **RuBenzoA3**, c) **(RuBenzoA3)ox** and d) Ligand **A3Ox** with corresponding ^1H DOSY NMRs.

The formation of the oxidized cage (**RuBenzoA3**)ox has been further confirmed by HRMS analysis carried out in $\text{MeOH}/\text{CH}_3\text{NO}_2$ at $C = 10^{-4}$ M (Figure 64). As expected, each charge state (from 8+ to 4+) presents a series of several peaks because of the presence of BF_4^- and OTf^- anions. Major peaks of each charge state are located at $m/z = 800.8357$, 906.2912, 1082.1693, 1315.9984 and 1328.3864. They show very good matching with theoretical values and isotopic patterns and correspond respectively to $[\text{L}^{2+}_2\text{M}_8 + 4\text{BF}_4^-]^{8+}$, $[\text{L}^{2+}_2\text{M}_8 + 4\text{BF}_4^- + \text{OTf}^-]^{7+}$, $[\text{L}^{2+}_2\text{M}_8 + 4\text{BF}_4^- + 2\text{OTf}^-]^{6+}$, $[\text{L}^{2+}_2\text{M}_8 + 5\text{BF}_4^- + 2\text{OTf}^-]^{5+}$ and $[\text{L}^{2+}_2\text{M}_8 + 4\text{BF}_4^- + 4\text{OTf}^-]^{4+}$.

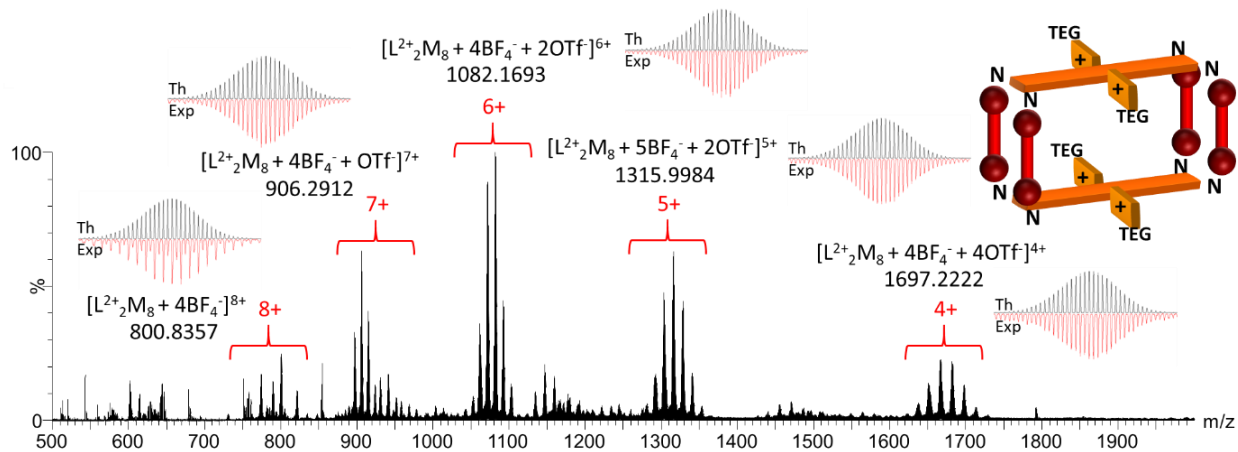


Figure 64. ESI-TOF spectrum of **(RuBenzoA3)Ox** recorded in $\text{CH}_3\text{OH}/\text{CH}_3\text{NO}_2$ (v/v 10/1) ($C = 10^{-4}$ M).

We were also interested in studying the reversibility of this oxidation process. Reduction experiments were followed by ^1H NMR upon addition of 5 equivalents of TDAE (Figure 65). Remarkably, the resulting spectrum is similar to the one of the starting cage prior to oxidation and does not show any sign of degradation, indicating the reversibility of the process. As expected, signals corresponding to the Phenothiazine appear between 6.95 and 7.30 ppm.

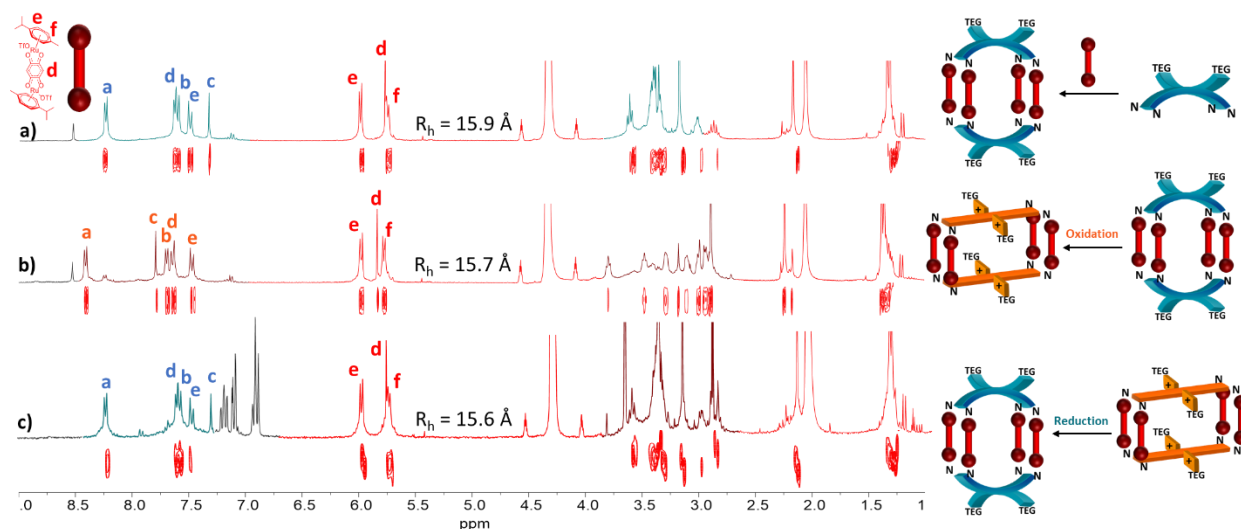


Figure 65. ^1H NMR spectra in CD_3NO_2 ($C = 10^{-3}$ M) of a) **RuBenzoA3**, b) **(RuBenzoA3)ox** and c) **(RuBenzoA3)ox** + TDAE with corresponding ^1H DOSY NMRs (NB. Signals between 6.95 and 7.30 ppm in (c) correspond to Phenothiazine).

These data indicate that the cage structure is stable upon a whole oxidation/reduction cycle. To the best of your knowledge, **RuBenzoA3** is the first example of metalla-cage able to change its size/shape upon a redox process, which can be qualified of a breathing mode.

Regarding the stability of the isolated oxidized ligand, we were interested in producing the oxidized cages through a second pathway, directly from ligand **A3Ox**. Using this strategy, we could avoid the presence of Phenothiazine as observed upon **RuBenzoA3** oxidation. We followed the complexation of **A3Ox** with precursors **RuBenzo(OTf) $_2$** and **RuNaph(OTf) $_2$** by ^1H NMR and DOSY NMR (Figure 66c and d). The spectra are well resolved, with signals which are shifted related to the ligand alone (Figure 66a), indicating that the withdrawal character of the oxidized exTTF moiety does not prevent the pyridine to metal coordination. Interestingly, the NMR corresponding to **RubenzoA3Ox** is very different to the one of the oxidized cage **(RuBenzoA3)ox** (Figure 66b) and the reaction with **RuNaph(OTf) $_2$** converged to a symmetric discrete structure. The corresponding diffusion values extracted from ^1H NMR DOSY experiments ($D = 2.7 \times 10^{-10} \text{ m}^2 \cdot \text{s}^{-1}$ and $D = 2.9 \times 10^{-10} \text{ m}^2 \cdot \text{s}^{-1}$ for **RubenzoA3Ox** and **RuNaphA3Ox** respectively) are higher than the one observed for cage **RubenzoA3** with calculated hydrodynamic radii of 13.2 and 12.3 Å. These oxidized species are therefore smaller than the oxidized cage **(RuBenzoA3)ox** ($R = 15.6$ Å).

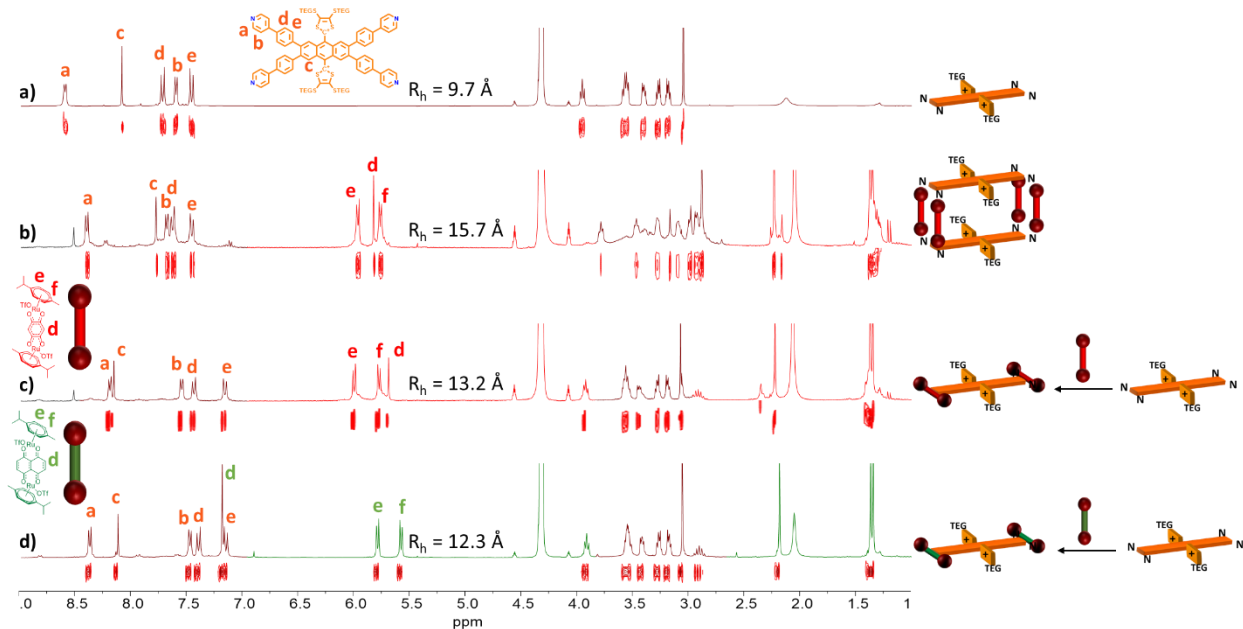


Figure 66. ^1H NMR spectra in CD_3NO_2 ($C = 10^{-3}$ M) of a) Ligand **A3Ox**, b) **(RuBenzoA3)ox**, c) **RuBenzoA3Ox** and d) **RuNaphA3Ox** with corresponding ^1H DOSY NMRs.

We hypothesized that cage formation was disadvantaged using the oxidized ligand because of intramolecular electrostatic repulsions in favor of the panel-like compounds. Their formation was unambiguously confirmed by a HRMS analysis showing the exclusive panel structures with **RuBenzo(OTf) $_2$** as well as **RuNaph(OTf) $_2$** precursors. Only the spectrum measured with the RuBenzo spacer is described since both are very similar (Figure 67). The corresponding **RuBenzoA3Ox** structure shows a series of peak arrays located at $m/z = 602.1086$, 614.7007 , 774.3871 , 789.8717 , 805.6141 , 1082.1626 , 1103.1499 , 1123.7963 that shows very good matching with theoretical values and isotopic patterns corresponding respectively to species $[\text{L}^{2+}\text{M}_4 + \text{BF}_4^-]^{5+}$, $[\text{L}^{2+}\text{M}_4 + \text{OTf}^-]^{5+}$, $[\text{L}^{2+}\text{M}_4 + 2\text{BF}_4^-]^{4+}$, $[\text{L}^{2+}\text{M}_4 + \text{BF}_4^- + \text{OTf}^-]^{4+}$, $[\text{L}^{2+}\text{M}_4 + 2\text{OTf}^-]^{4+}$, $[\text{L}^{2+}\text{M}_4 + 2\text{BF}_4^- + \text{OTf}^-]^{3+}$, $[\text{L}^{2+}\text{M}_4 + \text{BF}_4^- + 2\text{OTf}^-]^{3+}$ and $[\text{L}^{2+}\text{M}_4 + 3\text{OTf}^-]^{3+}$ where L^{2+} represents the **A3Ox** ligand and M a Ruthenium atom (Figure 67). One should note that the presence of BF_4^- anions was expected and comes from the oxidant (**PTZ**) used to prepare **A3Ox**.

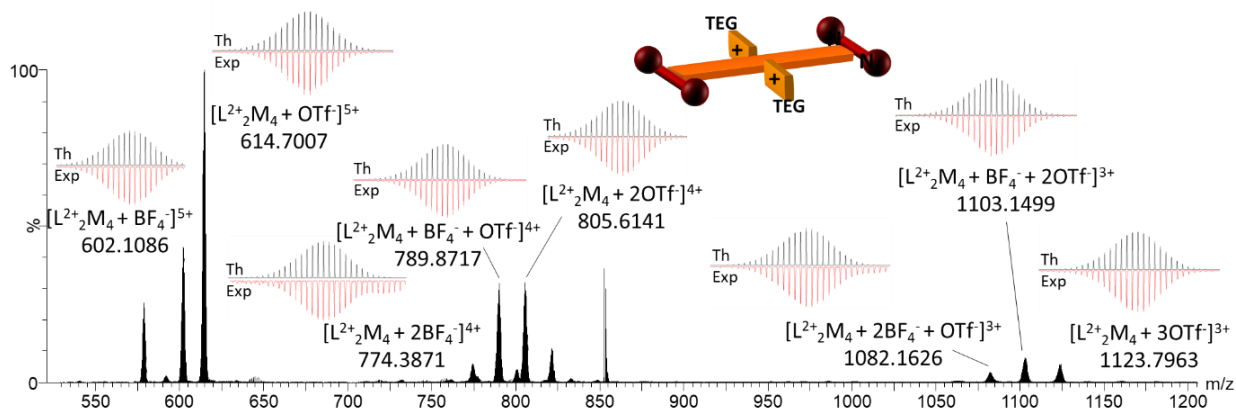


Figure 67. ESI-TOF spectrum of **RuBenzoA3Ox** recorded in $\text{CH}_3\text{OH}/\text{CH}_3\text{NO}_2$ (v/v 10/1) ($C = 10^{-4}$ M).

We then studied the behavior of these L^{2+}M_2 structures upon reduction with TDAE (Figure 68). We expected, after reduction, a reorganization of the neutral panel structures toward the neutral cages. The resulting species

(RuBenzoA3Ox)Red and **(RuNaphtoA3Ox)Red** (Figure 68c and d) show nicely resolved NMR spectra and the presence of only one compound was determined by ^1H DOSY NMR. The corresponding hydrodynamic radii of 13.2 Å and 12.3 Å are smaller than the one observed for cage **RuBenzoA3** ($R_h = 15.9$ Å) suggesting that after reduction, the LM_2 structure remains.

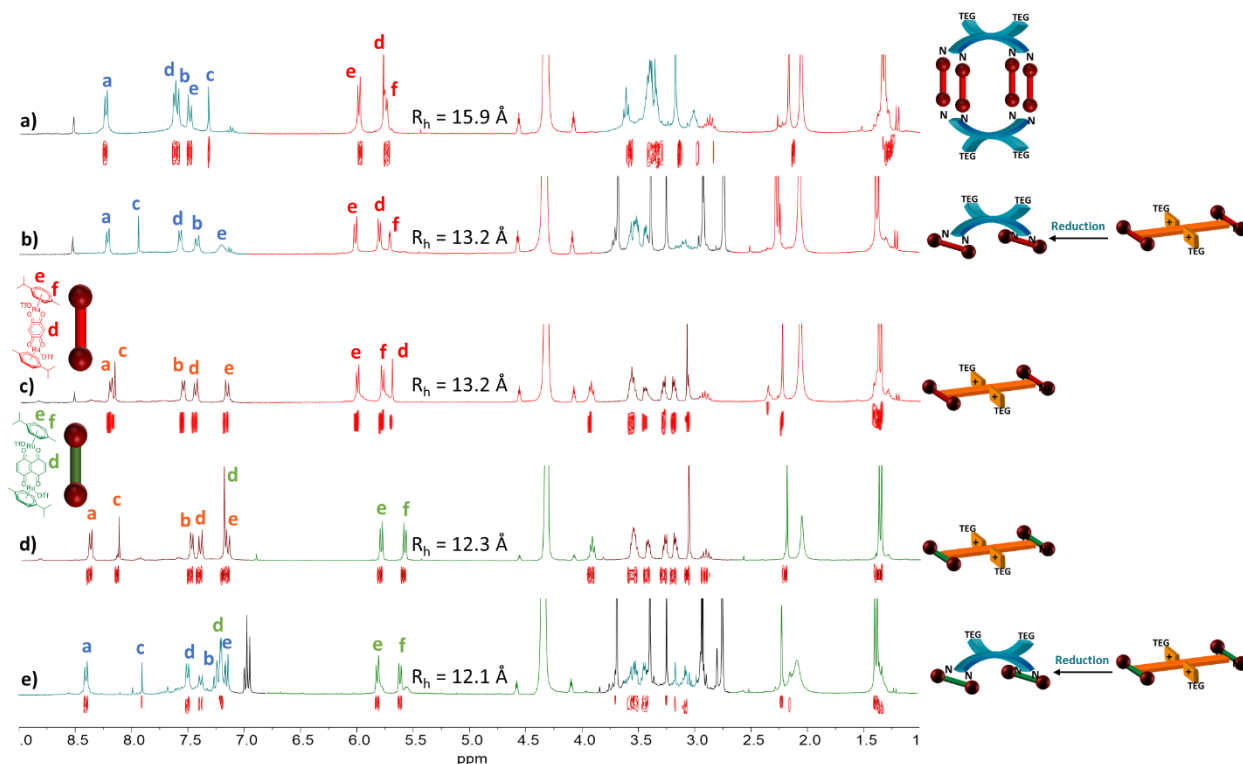


Figure 68. ^1H NMR spectra in CD_3NO_2 ($C = 10^{-3}$ M) of a) **RuBenzoA3**, b) **(RuBenzoA3Ox)Red**, c) **RuBenzoA3Ox**, d) **RuNaphtoA3Ox** and e) **(RuNaphtoA3Ox)Red** with corresponding ^1H DOSY NMRs.

This was further confirmed by HRMS analysis (Figure 69). Once again, we will discuss only the case of **(RuBenzoA3Ox)Red**. The mass spectrum shows only peak arrays corresponding to the LM_4 structure with characteristic signatures located at $m/z = 730.8817$, 1003.5125 and 1024.4993 that shows very good matching with theoretical values and isotopic patterns corresponding respectively to the species $[\text{LM}_4]^{4+}$, $[\text{LM}_4 + \text{BF}_4]^{3+}$ and $[\text{LM}_4 + \text{OTf}]^{3+}$ where L represents the **A3** ligand and M a Ruthenium atom (Figure 69).

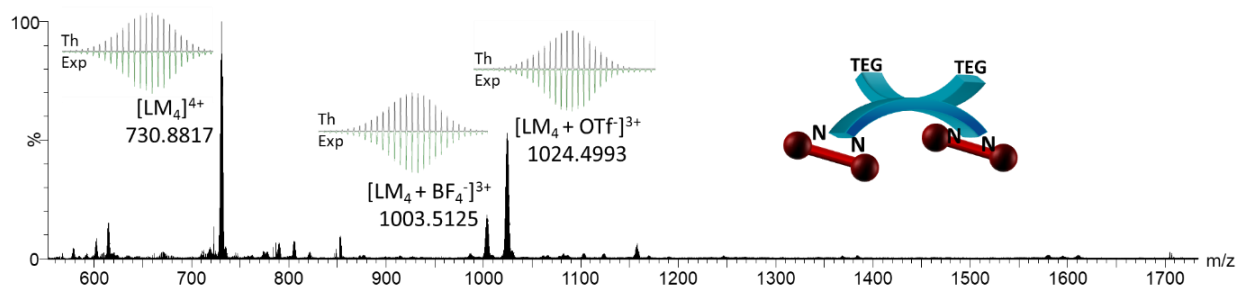


Figure 69. ESI-TOF spectrum of **(RuBenzoA3Ox)Red** recorded in $\text{CH}_3\text{OH}/\text{CH}_3\text{NO}_2$ (v/v 10/1) ($C = 10^{-4}$ M).

Given the difference in self-assembly behavior observed between the neutral ligand and oxidized ligand, a total of 4 species from **RuBenzo(OTf)₂** complex can be obtained from these two ligands (Figure 70). Precisely, the neutral ligand reacts with the **RuBenzo(OTf)₂** complex to form the expected cage. This species

is robust enough to be engaged in an oxidation/reduction process without disassembly. On the other hand, the oxidized ligand reacts with the **RuBenzo(OTf)₂** complex to form a panel, which also can be reduced and then oxidized in a clean manner.

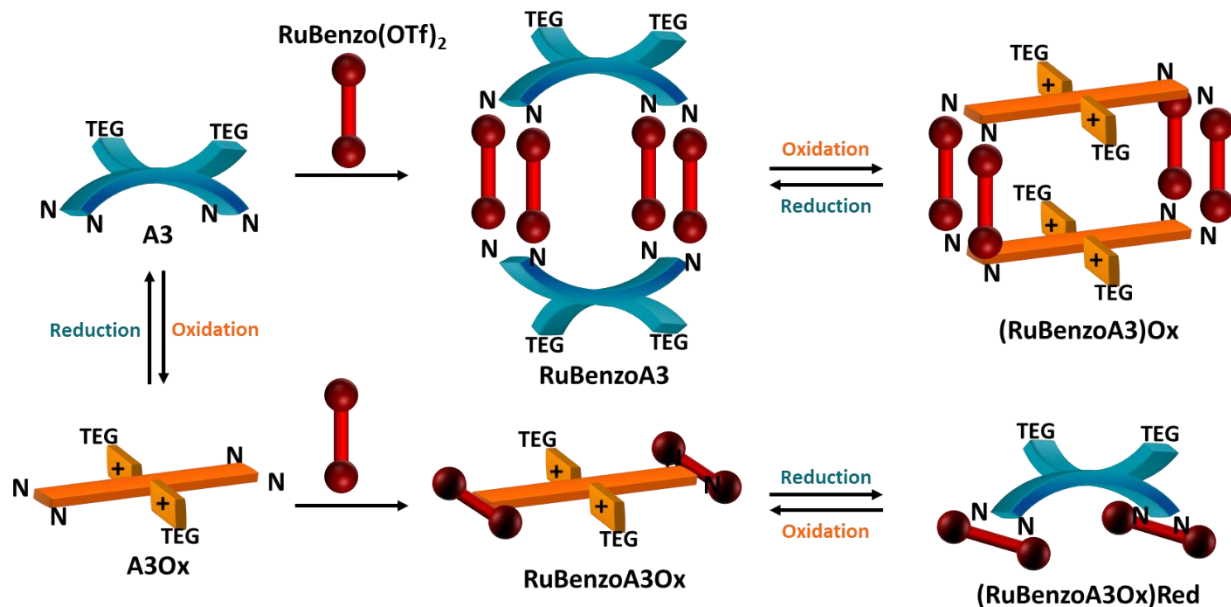


Figure 70. General behavior of metalla-structures obtained from **RuBenzo(OTf)₂** depicted in this section.

Regarding the importance of characterizing self-assembled structures at the solid state, we throw ourselves into the preparation of single crystals. Interestingly, we observed that the oxidized species are much easier to crystalize than the neutral ones. Single crystals of **RuBenzoA3Ox** and **RuNaphA3Ox** could be obtained by vapor diffusion of methyl *tert*-butyl ether into a methanol solution of the corresponding complexes, and the X-ray structures could be solved. These results confirm that these compounds are metalla-panels composed of an oxidized ligand (dicationic) coordinated by two complexes (Figure 71). The central core is therefore constituted by an anthracene unit substituted by two aromatic 1,3-dithiolium rings which are nearly perpendicular to the anthracene platform. The ligand part is highly distorted in these complexes compared to the free ligand. In **RuNaphA3Ox** two PhPy linkers located on the opposite positions are linear while the other pair is bent with an angle of 19° to accommodate two Ruthenium atoms. **RuBenzoA3Ox** is even more distorted as the Ru-Ru distance in **RuBenzo** is shorter. All four PhPy branches were distorted with angles 15-20°. It means that the distortion energy is smaller than the combination of electrostatic repulsion between charged ligands and the entropy benefit of smaller M₄L compounds.

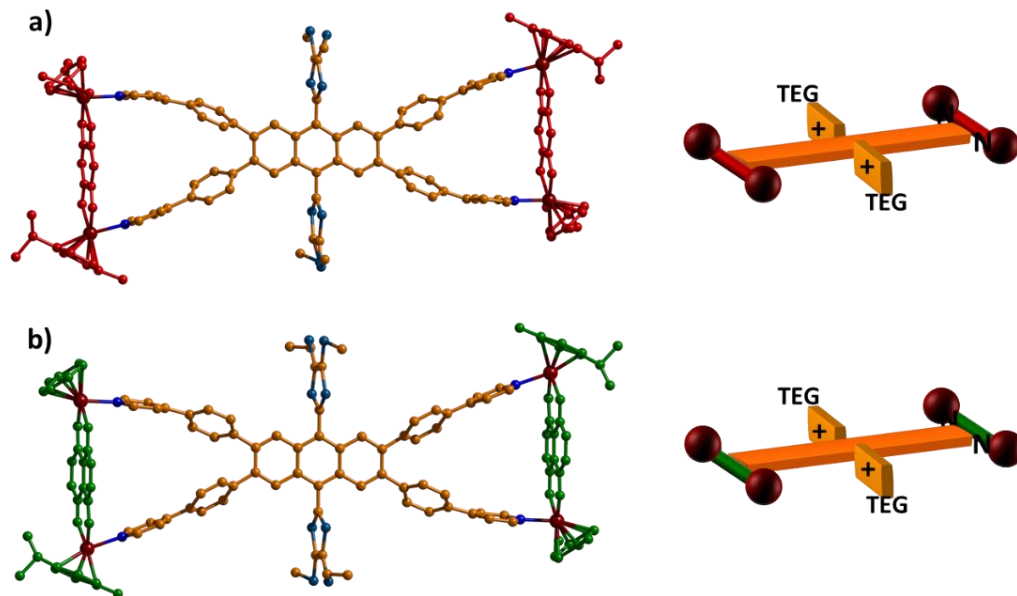


Figure 71. X-ray structures of oxidized panel complexes a) **RuBenzoA3Ox** and b) **RuNaphA3Ox**. TEG chains are omitted for clarity.

Although promising crystals of **RuBenzoA3** were obtained by vapor diffusion of MTBE into a MeOH solution of the cage, they did not diffract strongly enough to determine a structure. The latter was therefore simulated by MM+ modeling (Figure 72a). The dihedral angle measured between the coordination planes is very similar to the one observed for ligand **A1** (Figure 45a), with respective values of 140° and 145° indicating that the constraint on the ligand is low to incorporate the cage structure. A maximal distance of 15.1 \AA is calculated between both ligands, which offer promising perspectives in terms of host recognition, in particular when considering fullerene derivatives.

Remarkably, single crystals of the oxidized molecular cage (**RuBenzoA3**)**Ox** could be obtained by vapor diffusion of MTBE over a solution of (**RuBenzoA3**)**Ox** in $\text{CH}_3\text{NO}_2/\text{CH}_3\text{CN}$ and were analyzed by X-ray diffraction. As expected, both ligands show the typical structural characteristics of the oxidized exTTF^{2+} framework. Their anthracene fragments are separated by a distance of 7.2 \AA , a value which is close to the Ru-Ru one (7.9 \AA) indicating that electrostatic repulsions are not sufficient to distort the oxidized ligand even though the dithiole fragments are tilted by 71° in contrast to 90° in case of a free ligand.

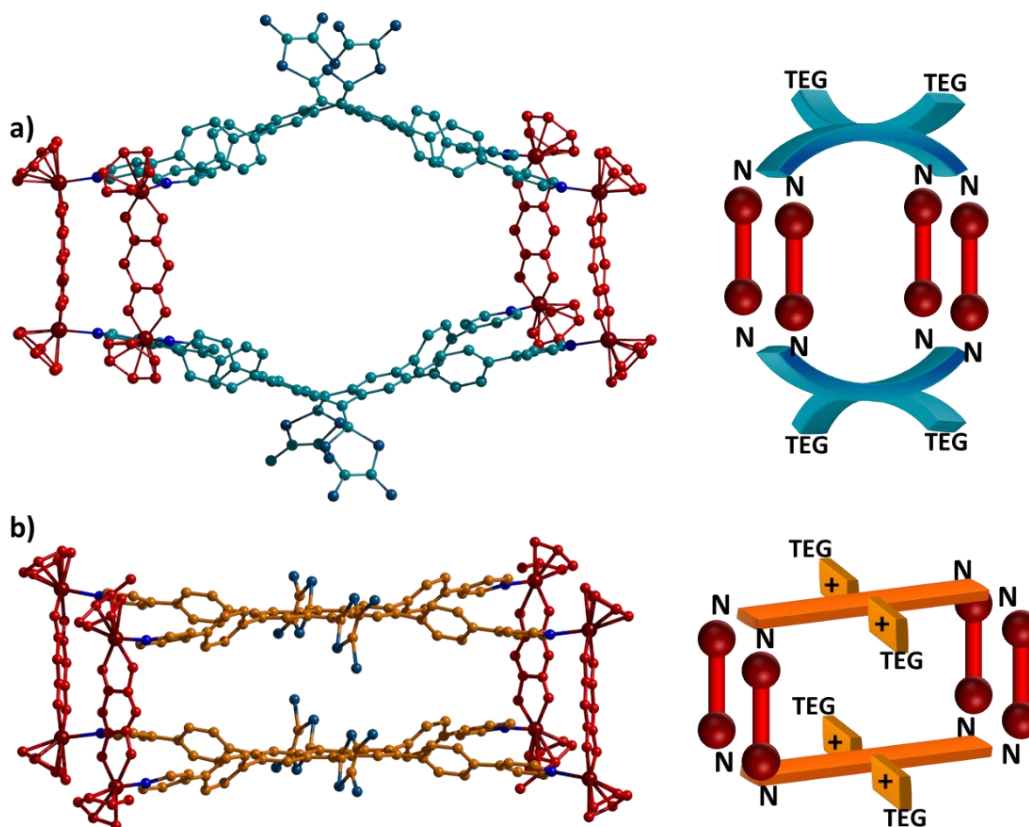


Figure 72. a) MM+ simulation of the neutral cage complex **RuBenzoA3**, b) crystalline structure of the oxidized cage complex (**RuBenzoA3**)Ox. TEG chains are omitted for clarity.

Those characterizations clearly highlight the capacity of this new system to modulate its cavity shape thanks to a redox stimulation.

Cyclic voltammetry experiments were performed on ligand **A3** as well as on the corresponding metalla-structures **RuBenzoA3** and **RuBenzoA3Ox**. As the compound **RuBenzoA3Ox** is already in its oxidized exTTF^{2+} state, the scanning was performed starting from higher to lower potentials. All systems show the characteristic electrochemical behavior of the exTTF framework. (Figure 73). Ligand **A3** is easier to oxidize than ligand **A1TEG** ($E = 0.17 \text{ V}$ vs $E = 0.29 \text{ V}$) as expected from the presence of the intermediate phenyl ring between the exTTF framework and the withdrawing pyridile units. Both metalla-structures are oxidized at higher potential than the ligand **A3**, as expected from coordination to the metal. The cage **RuBenzoA3** shows an oxidation potential of $E = +0.5 \text{ V}$, which is 0.10 V higher than the oxidation potential of **RuBenzoA3Ox** (observed after reduction). This may happen

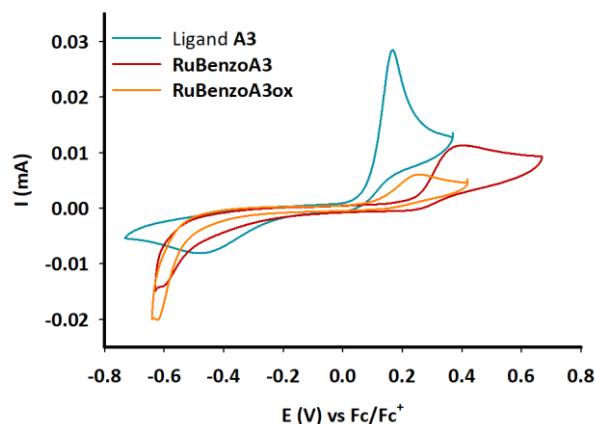


Figure 73. Cyclic voltammetry of **A3** and **RuBenzoA3** cages, CH₃CN (C = 0.2 mM, n-Bu₄NPF₆ (0.1 M)), 100 mV.s⁻¹, Pt, vs Fc/Fc⁺.

because oxidation requires additional energy to overcome the electrostatic repulsion between the two oxidized ligands in **RuBenzoA3**. On the other hand, their reduction waves are at the same potential of $E = -0.5$ V. During this step, there is no energy gain upon exTTF reduction and conformational change to the butterfly-shaped form, since the moieties are not charged anymore (Figure 74).

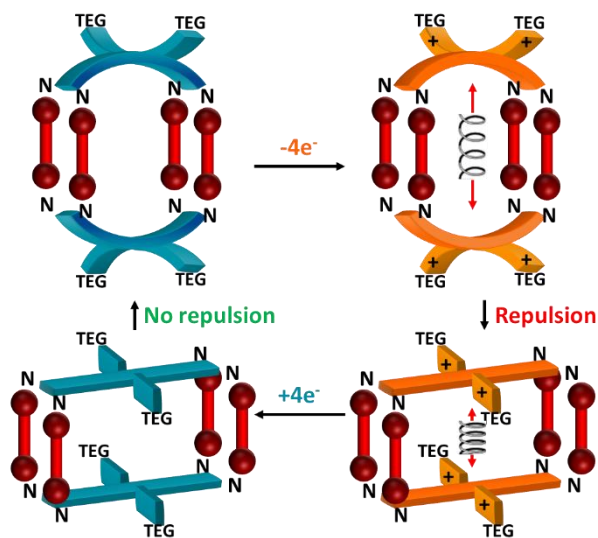


Figure 74. Possible **RuBenzoA3** oxidation/reduction mechanism.

In conclusion, we have described the preparation of a new ligand that is able to react with two bis(Ruthenium) complexes either in its neutral exTTF state or its dicationic exTTF²⁺ oxidized state. While the oxidized form produces L²⁺M₂ panel-type structures, the neutral one provides the expected cage structure with complex **RuBenzo(OTf)₂**. The resulting electro-active cage can be redox-stimulated through a change of the cavity size; this can be illustrated as a breathing movement, with potential applications in terms of controlled guest release. Considering the shape of the cage, spherical guests such as big anions or derivatives of Fullerenes could be considered. Due to time constraints, unfortunately, I could not carry out this study which will be done very soon in the laboratory.

3. Self-assemblies of 2,6 difunctionalized extended TTF ligand

3.1. Toward redox-active Banana-shaped cages

Many examples of M_2L_4 ($M = Pd(II)$) self-assembled cages have been described recently (Figure 75).³⁰ The ligands used to construct these assemblies are then said to be "banana-shaped". A major difference with the Pd-based structures previously discussed in this manuscript, is that these M_2L_4 assemblies are obtained from metal complexes for which all coordination sites are available and from bidentate ligands.

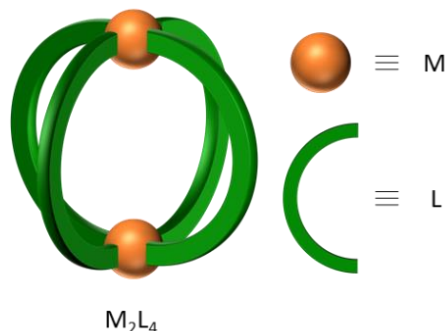
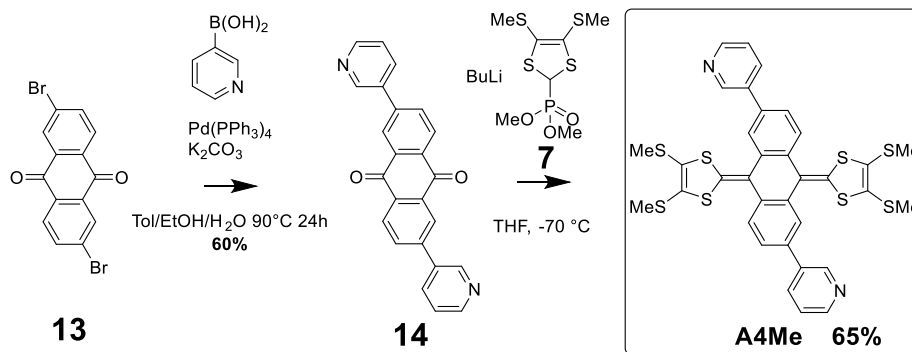


Figure 75. Banana-type cage structure.

On this basis we designed ligand **A4Me**. Its synthesis (Scheme 6) was considered from dibromo anthraquinone **13** (commercially available) in two steps through a Palladium catalyzed Suzuki coupling reaction, followed by an HWE reaction with the appropriate phosphonate anion (generated from the corresponding phosphonate esters **6** or **7**).



Scheme 6. Synthesis of ligands **A4Me**.

The electrochemical properties of the ligands **A1Me** and **A4Me** were compared by cyclic voltammetry in a mixture of DCM and acetonitrile (2:1). Both ligands show one quasi-reversible two-electron oxidation waves at $E_{ox} = -0.18$ V vs Fc/Fc^+ (**A1Me**) and at $E_{ox} = 0.23$ V (**A4Me**). The latter is oxidized at a slightly lower potential due to the presence of only two electrowithdrawing fragments in the molecule, vs four in the case of **A1Me**.

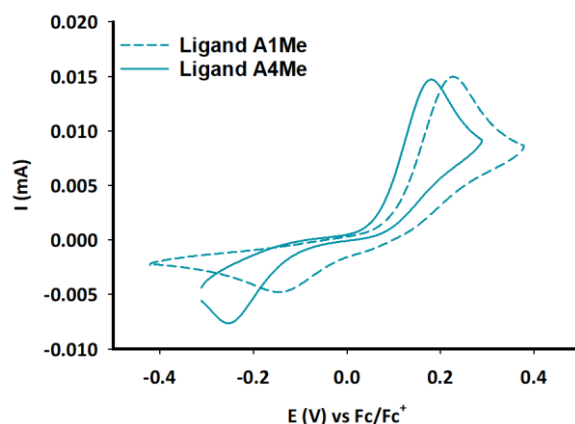


Figure 76. Cyclic voltammetry of **A1Me** and **A4Me**: CH₃CN/CH₂Cl₂ (C = 1 mM, n-Bu₄NPF₆ (0.1 M)), 100 mV.s⁻¹, Pt, vs Fc/Fc⁺.

Following an alternative approach, we mixed the ligand **A4Me** with two linear metal acceptors (PdCl₂(CH₃CN)₂ or AgBF₄) and a square planar one (Pd(CH₃CN)₄(BF₄)₂) in order to synthesize the banana-shaped target assemblies. The reactions were performed in DMSO to accommodate complex solubility. The three corresponding DOSY NMR studies resulted in hydrodynamic radii that are by far too small to correspond to supramolecular assemblies (5.8-7.8 Å). One explanation lies on the formation of coordination polymers that are disassembled by the competitive DMSO solvent. All attempts to grow crystals were unsuccessful.

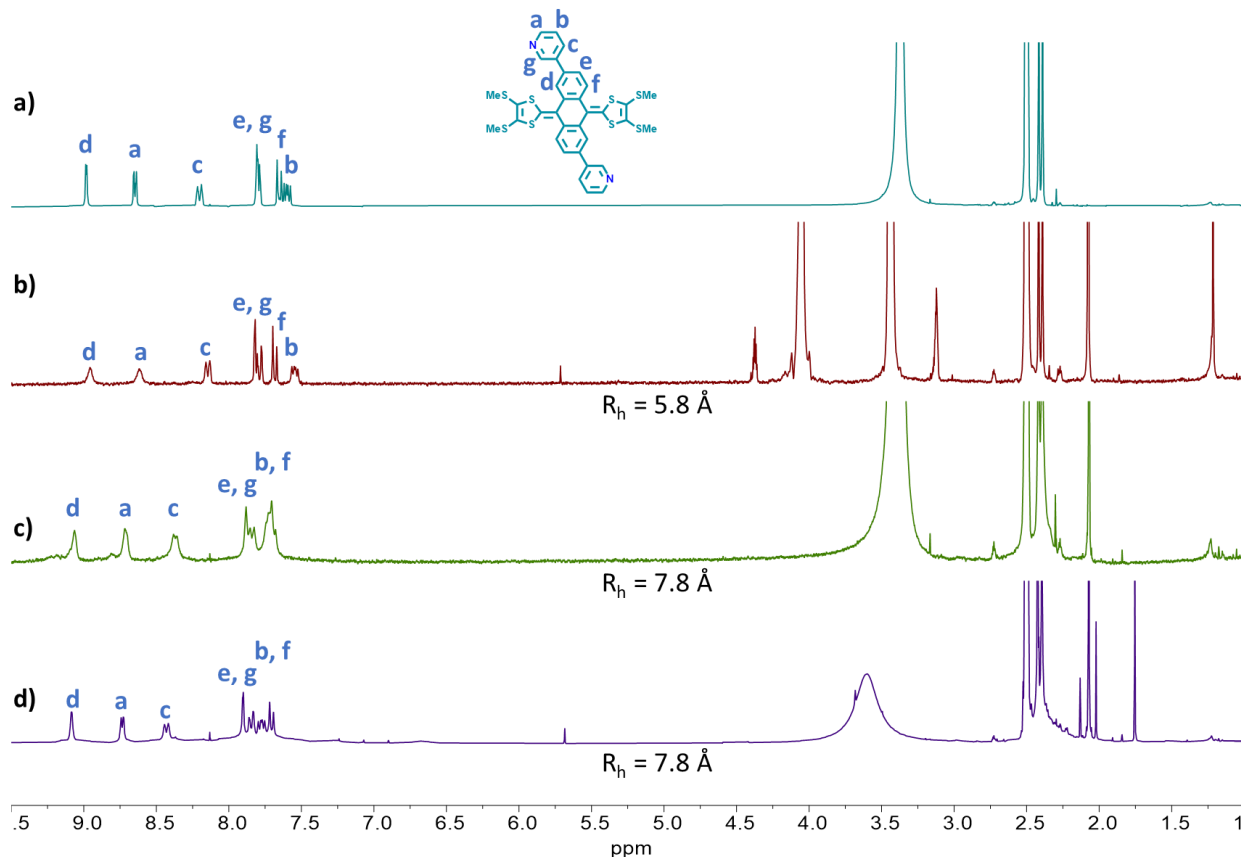


Figure 77. ¹H NMR spectra of a) **A4Me**, b) **A4Me** + AgBF₄, c) **A4Me** + PdCl₂(CH₃CN)₂, d) **A4Me** + Pd(CH₃CN)₄(BF₄)₂.

Quite unexpected results were observed upon the reaction of **A4Me** with AgBF_4 in nitromethane. Instead of the Lewis acid role, the silver salt acted as an oxidizing agent and a grey precipitate was observed. The resulting compound crystallized quite readily, and the crystal structure was obtained (Figure 78). The molecules of the oxidized ligand were arranged in a way that the nitrogen atoms in the pyridine groups of neighboring molecules were facing one another and the distance between them was 2.68 Å. The amount of BF_4^- counteranions suggested the stoichiometry of the compound $\text{A4Me}^{2+}\text{H}^+(\text{BF}_4^-)_3$ wherein the proton was shared by two pyridine fragments of the neighboring molecules.

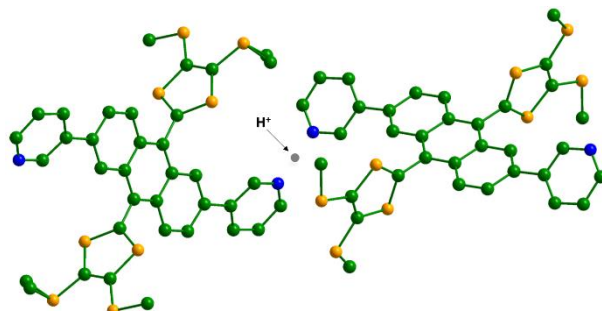


Figure 78. X-ray structure of the oxidized $\text{A4Me}^{2+}\text{H}^+(\text{BF}_4^-)_3$.

3.2. Toward redox-active tetrahedral cages

Another opportunity is to employ the 2,6-disubstituted exTTF in the synthesis of a tetrahedral cage using the strategy recently developed by J. Nitschke (Figure 79), with in mind a change of its internal cavity size with an electrochemical stimulus.

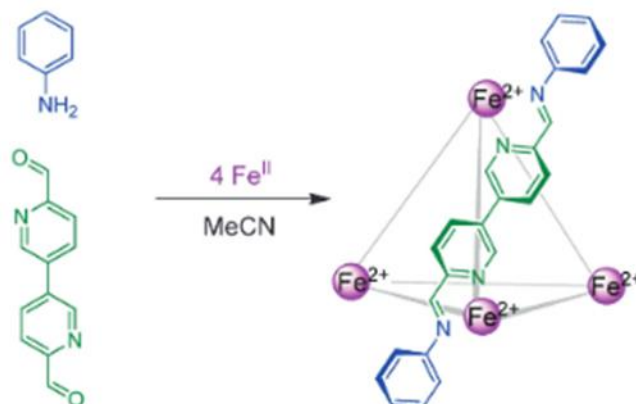
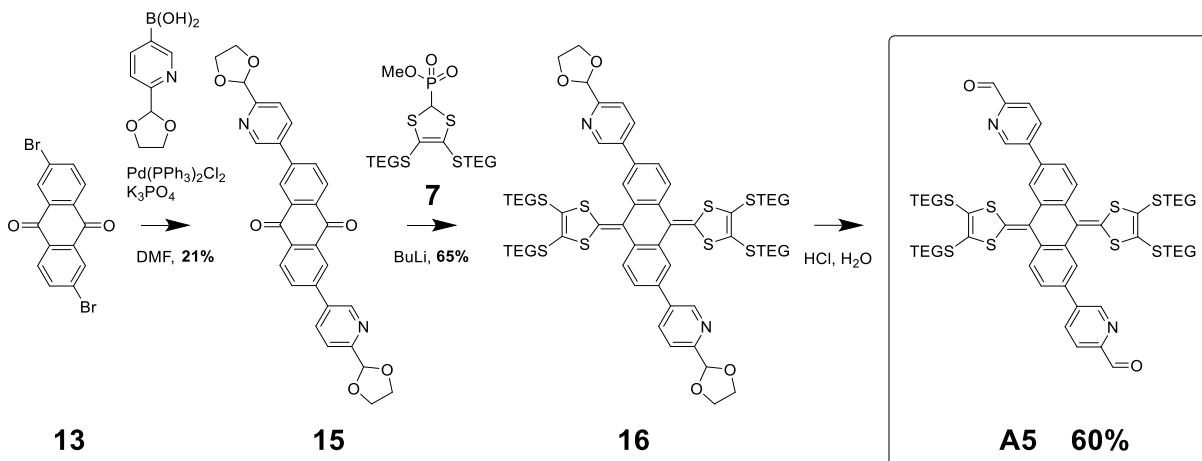


Figure 79. General strategy developed by J. Nitschke for the preparation of tetrahedra cage from aldehydes.¹²⁰

The precursor **A5** was designed in collaboration with Jonathan Nitschke (Univ. Cambridge) and prepared in 3 steps from anthraquinone **13** (Scheme 7). The synthesis starts with a Palladium catalyzed Suzuki coupling reaction to compound **15**, then a HWE reaction with phosphonate **7** produces the protected compound **16** and finally an acid catalyzed hydrolysis of the acetal with a 5% HCl solution leads to the target ligand **A5**.

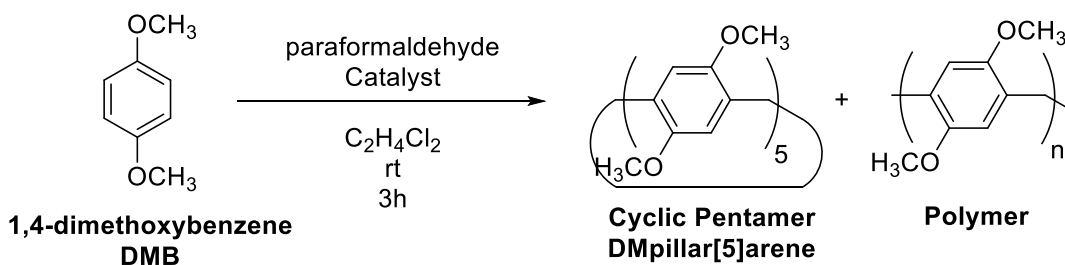
Compound **A5** was sent to Nitschke group, and the work is underway; preliminary results show the ability of the obtained assembly to encapsulate fluoroadamantane.



Scheme 7. Synthesis of ligand **A5**.

4. A pillar[5]arene scaffold modified with electroactive moieties.

Macrocyclic molecules, such as crown ethers, calixarenes, cyclodextrins, and cucurbiturils have been widely used as macrocyclic hosts and continue to play a prominent role in host-guest chemistry. In 2008, a new macrocycle was reported by Ogoshi et al.¹²¹ which was named pillar[*n*]arene (Scheme 8). Pillar[*n*]arenes and its derivatives are cyclic derivatives, consisting of hydroquinone units (*n* units) linked by methylene bridges on *para*-positions. Composition of pillar[*n*]arenes is almost analogous to typical calix[*n*]arenes and the most common representative of the series is the pillar[5]arene. However, because its repeating units are connected by methylene bridges at the *para*-position, pillar[*n*]arenes form a unique symmetrical pillar architecture, which is different from the basket structure (cone) observed for the meta-bridged calixarenes (e.g. case of the calix[4]arene derivative). They are usually prepared from 1,4-dialkoxybenzene derivatives and paraformaldehyde in the presence of a Lewis acid catalyst.¹²²



Scheme 8. Condensation of 1,4-Dimethoxybenzene with Lewis Acids to afford pillar[5]arene.

The cavity size of pillar[5]arenes is approximately 5.5 Å, and it is more rigid and *n*-rich than the traditional calixarenes, which may afford highly efficient binding affinities to specially designed guests, with a particular affinity for linear alkanes containing electron-poor systems such as amine, ammonium, cyano, and halogen groups, as well as simple aromatic compounds such as pyridinium and viologen derivatives.^{122, 123} The pillar[5]arene scaffold can be easily functionalized, with up to 10 substituents. Because of their intrinsic

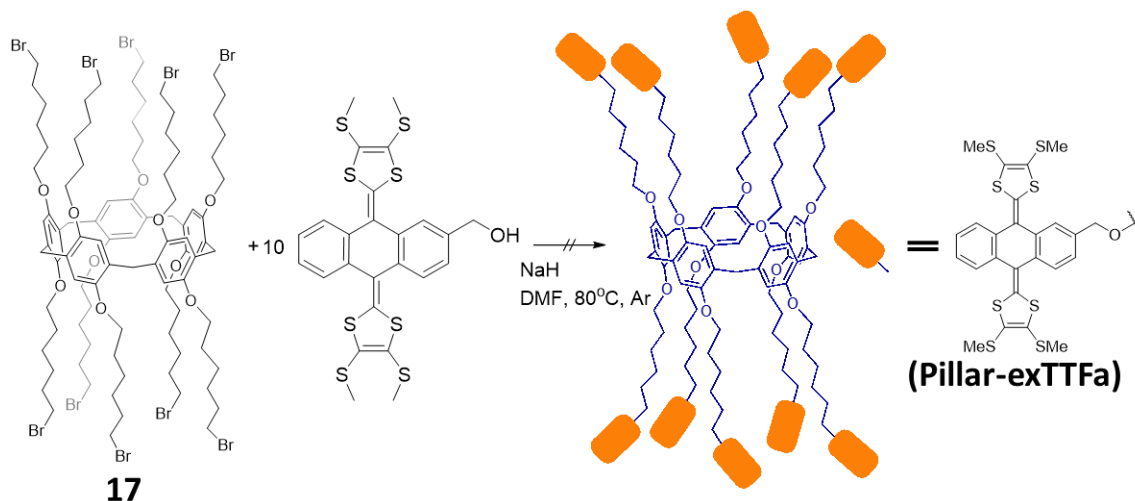


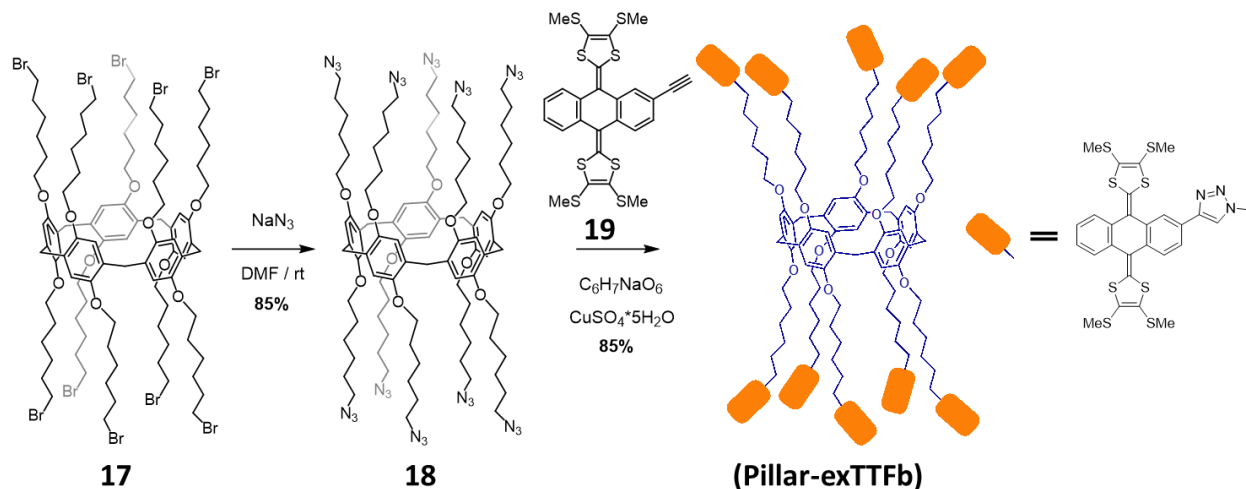
Figure 81. Synthetic scheme towards exTTF grafted pillar[5]arene, initial target of a pillar[5]arene persubstituted with exTTF moieties **pillar-exTTFa**.¹²⁵

Following these results, G. Mengheres also tried to synthesize a pillar[5]arene substituted with 10 exTTF units **pillar-exTTFa** (Figure 81). Indeed, the concave surface of *n*-extended tetrathiafulvalene derivatives is known to efficiently recognize the convex surface of C₆₀.¹⁰⁴ This geometrical characteristic was notably exploited in the case of poly-exTTF rings,¹²⁷ for which the different exTTF units contribute in a concerted manner to the C₆₀ binding, through wrapping the spherical guest. The fullerene recognition is thermodynamically driven by a concave-convex complementarity and charge transfer.

Nevertheless, presumably because of the higher steric demand of exTTF compared to TTF, the targeted 10-fold substituted system could not be reached, and a maximum of six exTTF units were introduced, as identified by mass spectrometry.

One solution that was considered to overcome this failure consisted in using a pillar[5]arene scaffold bearing longer bromo-alkyl substituents (C₆ instead of C₂), in order to allow more space and flexibility on the periphery of the persubstituted system. Nevertheless, this option led to the same negative result.

On this basis, we decided in the course of my PhD thesis project, to explore an alternative synthetic strategy based on click chemistry, well-known for high yields and mild conditions, and already applied to pillar[5]arene derivatives in the group of Strasbourg.¹²⁸

Figure 82. Synthesis of **Pillar-exTTFb**.

The target pillararene **Pillar-exTTFb** was obtained in two steps from precursor **17** (provided by J.-F. Nierengarten group). The first step corresponds to the preparation of azide¹²⁹ **18** from **17** by the reaction with sodium azide in DMF. The reaction went to completeness and was quenched by water. After extraction with diethyl ether the product did not require any additional purification. The organic azide **18** was characterized by IR and ¹H NMR spectrometry. The IR has demonstrated a characteristic absorption peak of azide at 2085 cm⁻¹. The completeness of the reaction was verified by the symmetry of ¹H NMR spectrum. Interestingly, the presence of dichloromethane has an impact on the chemical shift of these protons (Figure 83). In presence of dichloromethane, the signal of the CH₂ bridge protons (protons a) is upfield shifted from 3.74 ppm to 3.70 ppm, and the terminal CH₂N₃ signal (c) is downfield shifted to from 3.10 ppm to 3.27 ppm. Also, the signal of the O-CH₂ protons (b) is doubled. This suggests that one CH₂Cl₂ guest molecule is present in the core, which breaks the symmetry of the molecule, and leads to discriminate O-CH atoms that are situated next to, and laterally to the chlorine atoms. The competitive strong binding of one dichloromethane molecule within the pillar arene cavity is well-established and could be overcome by using chloroform as the solvent during host-guest binding studies.¹³⁰

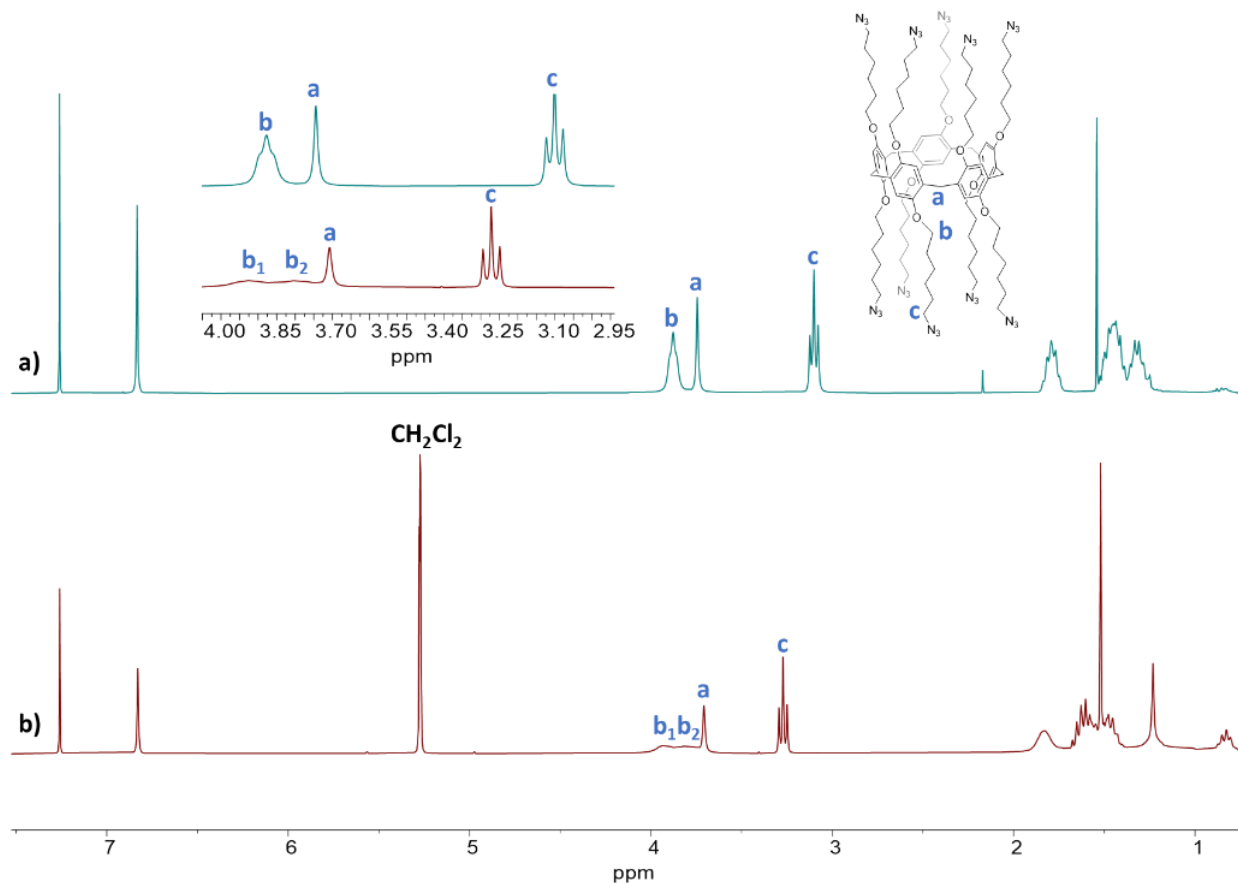


Figure 83. ^1H NMR spectra of **18** a) in absence and b) in presence of dichloromethane.

Compound **18** was functionalized with exTTF by CuAAC click reaction in $\text{CHCl}_3/\text{H}_2\text{O}$ with the exTTF **19** derivative¹³¹ bearing an alkyne moiety. The latter was synthesized following the synthetic scheme described in Figure 82.¹³¹ The completeness of the 10-fold substitution towards **Pillar-exTTFb** was confirmed by mass-spectrometry. The absence of oxygen was required for a complete substitution. The target product was characterized by NMR spectrometry, including a DOSY study (Figure 84). The signals related to the exTTF unit are broad in contrast to the sharp peaks observed for precursor **19**, which results from the oligomeric nature of **Pillar-exTTFb**. DOSY NMR data are consistent with the structure of the targeted system since all the signals are attributed to a single diffusion coefficient which corresponds to hydrodynamic radius ca. 13.5 \AA , a value which is consistent with the expected molecules of this size.

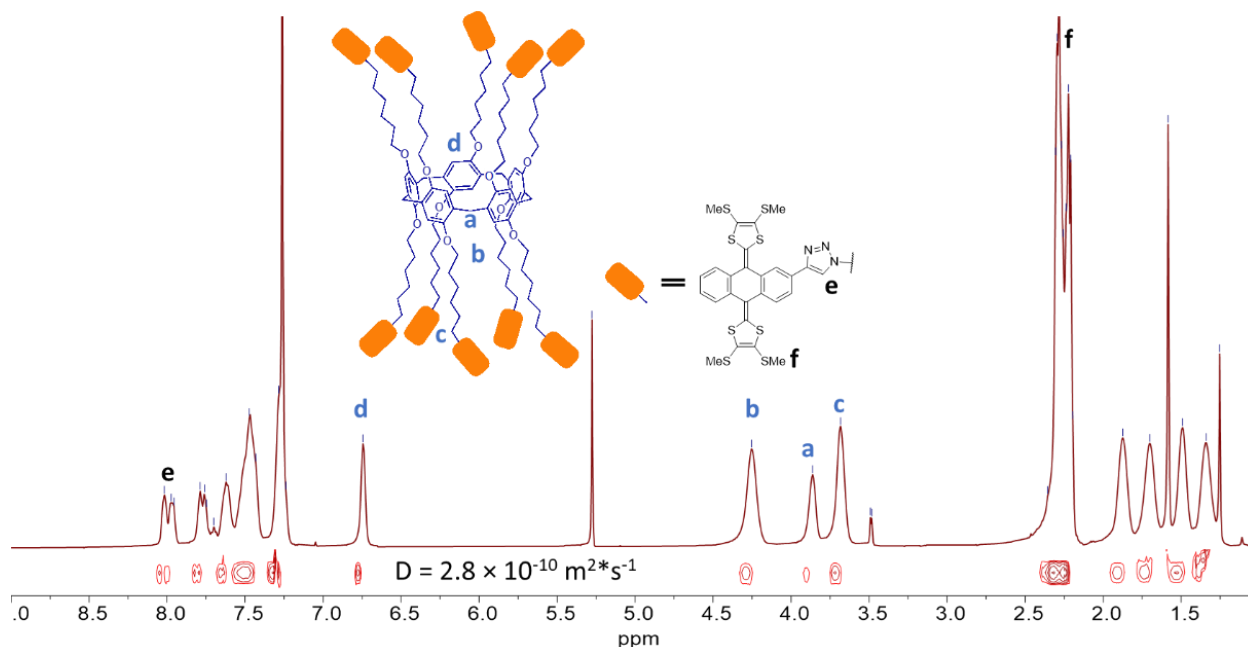


Figure 84. ^1H and Diffusion coefficient value (DOSY NMR) of **Pillar-exTTFb** in CDCl_3 .

The redox properties of **Pillar-exTTFb** were studied by Thin Layer Cyclic Voltammetry¹²⁶ (Figure 85). A single redox wave is observed. Its shape and $E_{1/2}$ value correspond to the usual electrochemical behavior of exTTF derivatives (an electrochemically irreversible (chemically reversible) two-electron oxidation process), which is accompanied by a severe conformational change. A coulometric internal reference was used (2,3-dichloronaphthoquinone) for evaluating the total number of electrons exchanged upon oxidation of **Pillar-exTTFb**.^{125, 126} The oxidation is not completely chemically reversible in pure CH_2Cl_2 and solubility issues prevent the use of a $\text{CH}_2\text{Cl}_2/\text{CH}_3\text{CN}$ mixture. Moreover, in presence of the electrochemical reference (2,3-dichloronaphthoquinone), the reduction wave becomes even wider and the voltammogram appears irreproducible. This suggests that the area under curve contains a contribution from chemical kinetics, which prevents to quantify the total amount of electrons transferred to the electrode.

$$i_p = 2.69 \times 10^5 n^{\frac{3}{2}} A D^{\frac{1}{2}} C v^{\frac{1}{2}}$$

Equation 2. Randles-Sevcik equation for 25 °C

We also tried to determine the number of electrons via the Randles-Sevcik equation (Equation 2), using the diffusion coefficient obtained by DOSY NMR (Figure 84). Yet the results proved to be inconclusive as well, due to the lack of reversibility of the electrochemical process. The obtained results show that **Pillar-exTTFb** is not optimal for thorough investigation of electrochemical properties as its electrochemical processes involve complex kinetics that cannot be accounted for by standard electrochemical analytical methods.

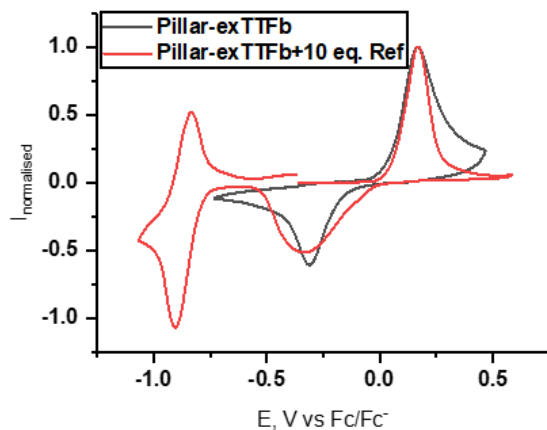


Figure 85. Thin Layer Cyclic voltammetry of 2.5×10^{-5} M **Pillar-exTTFb** (black line), 2.5×10^{-5} M **Pillar-exTTFb** + 2.5×10^{-4} M of 2,3-dichloronaphthoquinone¹²⁵ (red line) in CH_2Cl_2 ($E_{\text{ref}} = -0.87$ V), 0.1 M TBAPF₆, scan rate: $2 \text{ mV}\cdot\text{s}^{-1}$.

An evident objective guiding the design of such electron-rich pillararene receptors lies on their potential for hosting electron-poor fullerenes, which are complementary in terms of shape (concave/convex complementarity) and in terms of electronic character (pi-donor/pi-acceptor). A preliminary titration experiment led on **Pillar-exTTFb** with C_{60} was followed by UV-vis. No isosbestic point was observed (Figure 86a), meaning that no interaction between C_{60} and **Pillar-exTTFb** was developed. The only observable effect was the photoactivation of ExTTF moieties¹³² by C_{60} leading to the photodecomposition of the **Pillar-exTTFb** host (Figure 86b).

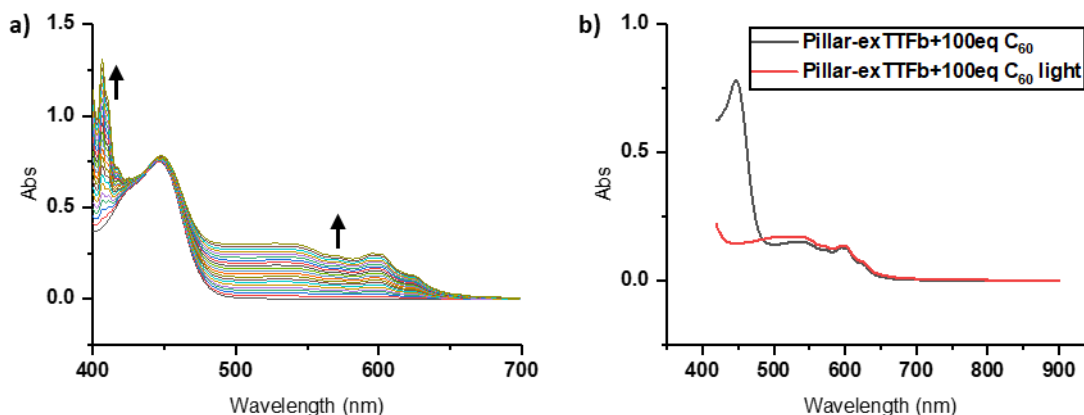
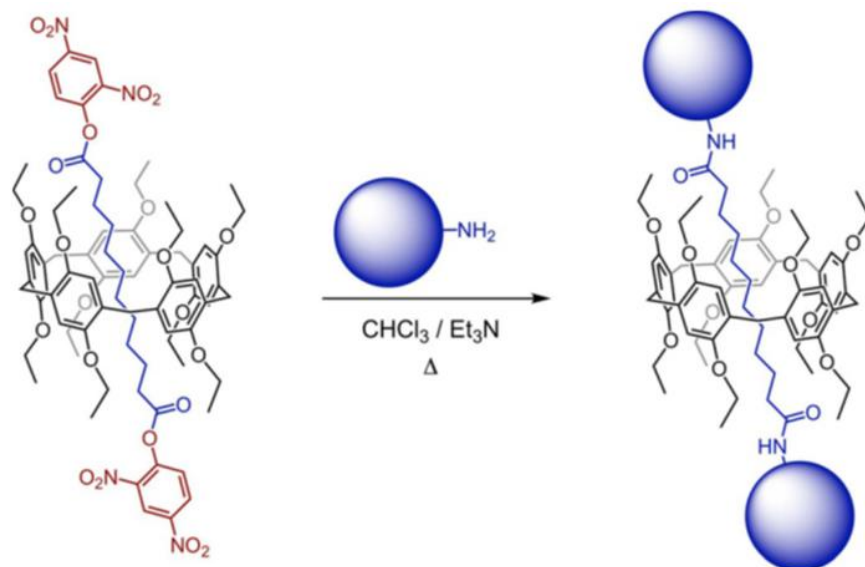


Figure 86. UV-Vis absorption studies of **Pillar-exTTFb** a) titration of 3×10^{-6} M **Pillar-exTTFb** with C_{60} , b) the solution of 3×10^{-6} M **Pillar-exTTFb** and 1.5×10^{-4} M C_{60} before (black line) and after (red line) 2h of daylight exposition.

Another approach which was considered from this new **Pillar-exTTFb** derivative, consisted in exploring the capacity of pillar arene derivatives to generate rotaxanes. For instance, Nierengarten *et al.* have obtained pillar-arene rotaxanes with a stopper-exchange strategy where a long alkyl chain was used as internal moiety (Figure 87).¹³³ Using this strategy, C_{60} appeared as a good candidate as a wide stopper.

Figure 87. Stopper exchange rotaxane preparation.¹³³

On this basis, the **Pillar-exTTFb** compound was sent to Strasbourg where Iwona Nierengarten performed the titration experiments with two axes, **C₆₀CN** (disymmetrical) and **diCN** (symmetrical) (Table 2). All obtained association constants with **C₆₀CN** are lower than the values corresponding to **diCN**. Therefore, there is no synergetic effect of C₆₀ moiety complexation with exTTF units. This demonstrates that the alkyl chain capped with cyano group is responsible for the interaction between the pillararene cavity and the guest. Remarkably, the association constant in CDCl₃ appears significantly higher in the case of **Pillar-exTTFb** than with **Pillar-TTF** or **Pillar-OEt**. Taking into account that **Pillar-TTF** and **Pillar-OEt** have only short ethyl chain linkers, there is a positive binding effect between long hexyl chain linkers and dodecyl nitrile chain of **C₆₀CN**. Contrariwise, **Pillar-TTF** presents the lowest affinity, be that with **C₆₀CN** or **diCN**. This is assigned to the shorter linker between the Pillar-arene rim and the TTF units, which presumably leads to a strong hindrance blocking the access of the guest to the rim cavity. Though the exTTF unit is more spatially extended than TTF, such behavior is not observed in the case of **Pillar-exTTFb**, thanks to the longer alkyl linkers (C₆) which allow a higher degree of conformational freedom. Finally, one will note that the binding constant is systematically higher with the **diCN** axle in front of **C₆₀CN**, whatever the pillararene derivative.

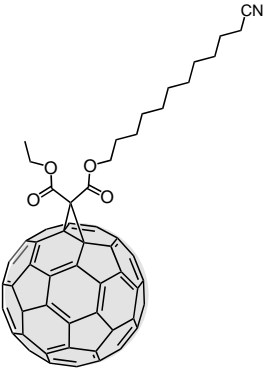
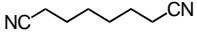
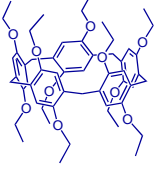
Host / Guest	C, mM	 (C ₆₀ CN)	C, mM	 (diCN)
 (Pillar-OEt)	3.8	1.62(5)	2.1	2.9(1)
(Pillar-TTF)	4.0	0.7(2)	3.4	1.5(1)
(Pillar-exTTFb)	2.9	2.2(1)	2.2	3.35(9)

Table 2. Values of the association constants ($\log K_a$) calculated for the 1:1 host-guest complexes in CDCl₃.

In conclusion, the new **Pillar-exTTF** exhibits electrochemical properties which are typical for exTTF derivatives, with no evidence of any interaction occurring between the redox-active units. Therefore, the stability of such systems and the possibility they offer to control reversibly the charge (from the neutral state to polycationic species (20 positive charges)), open promising perspectives in terms of guest binding and transport. Though these pillararenes do not show any remarkable encapsulation properties of C₆₀, they do complex **C₆₀CN** and **diCN** axes. For a thorough investigation of the electrochemical properties of these substituted polyaromatic scaffolds bearing 10 redox units, the introduction of electrochemically reversible redox systems and long enough linkers to avoid intramolecular interactions is required.

Chapter 3.

Self-assemblies incorporating the “DTF” scaffold

1. Dithiafulvene-based self-assembled tweezers

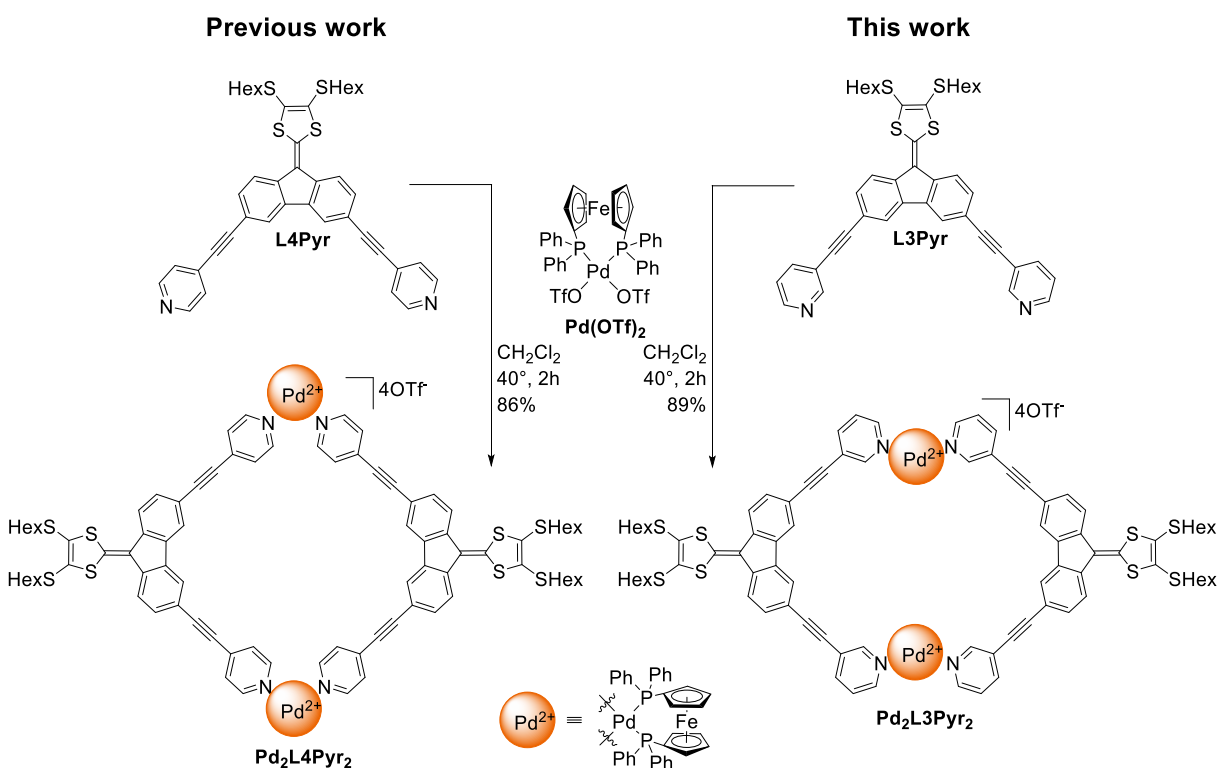
This paragraph has been mainly published in reference "Tuning the structure and the properties of dithiafulvene metalla-assembled tweezers" (Org. Chem. Front. 2020).¹³⁴ Some additional data are provided below.

In the course of the studies led in the laboratory on redox active systems, the efficiency of the 9-(1,3-dithiol-2-ylidene)fluorene (DTF)-based ligands in generating self-assembled discrete structures, has been illustrated with the preparation of rings,¹⁰³ tweezers¹³⁵ or cages.¹⁰² The DTF moiety can be oxidized reversibly at low potential to the corresponding radical cation,^{101, 136} a species which is prone to form mixed valence or n-dimer species under specific conditions. This driving force can be exploited to control, reversibly, the release of a guest compound thanks to a redox driven dimerization process.¹³⁵

We report herein that the shape, the redox and the binding properties of coordination-driven self-assembled metalla-cycles constructed from ditopic DTF-based ligands and the *cis*-Pd(dppf)(OTf)₂ complex (dppf = 1,1'-bis(diphenylphosphino)ferrocene; OTf = trifluoromethanesulfonate), can be efficiently and readily tuned by a simple change from a 4-pyridyl coordinating unit to a 3-pyridyl one.

As previously reported by our group, the self-assembly of the **L4Pyr** ligand with *cis*-Pd(dppf)(OTf)₂ in dichloromethane at 40 °C converges to a single symmetrical M₂L₂ discrete species (Scheme 9 left).¹⁰³

In this work, we applied a similar synthetic protocol to ligand **L3Pyr** which is a position isomer of **L4Pyr** (Scheme 9 right) and which was already available in the laboratory,¹⁰² and compared their properties.



Scheme 9. Synthesis of metalla-cycles **Pd₂L₄Pyr₂**¹⁰³ (left) and **Pd₂L₃Pyr₂**¹³⁴ (right).

The presence of the 3-pyridyl unit leads to a more complex ^1H NMR spectrum due to the symmetry loss (Figure 88a). Nevertheless, all aromatic signals could be attributed using a COSY experiment (Figure S59). In particular, all signals of pyridyl proton in **Pd₂L3Pyr₂** are upfield shifted compared to the free **L3Pyr** ligand, except H₆ (Figure 88b). This global observation is assigned to the shielding effect promoted by the phenyl rings from the *dppf* coligand, which is compensated in the case of H₆ by coordination to the metal. The presence of only one discrete species is confirmed by ^1H DOSY NMR experiment (Figure 88c and Figure S60). The latter shows a single set of signals with a diffusion coefficient of $D = 4.96 \times 10^{-10} \text{ m}^2 \cdot \text{s}^{-1}$, a value which is very similar to the one measured for the **Pd₂L4Pyr₂** metalla-cycle (Figure 88c'). This observation suggests that the self-assembled structure obtained from **L3Pyr** is similar in size to the one of **Pd₂L4Pyr₂**. The corresponding estimated hydrodynamic radius is of *ca* 10 Å, as extracted from the Stokes-Einstein equation ($T = 298 \text{ K}$),^{72, 137} a value which is consistent with the formation of a M_2L_2 architectures as in the case of **Pd₂L4Pyr₂**.¹⁰³

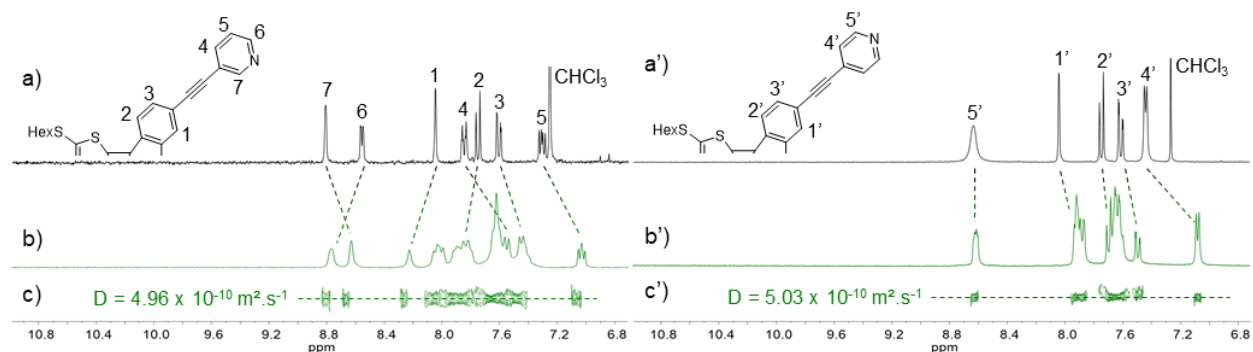


Figure 88. ^1H NMR spectra (aromatic region) of ligands **L3Pyr** (a) and **L4Pyr** (a') in CDCl_3 , metalla-cycles **Pd₂L3Pyr₂** (b) and **Pd₂L4Pyr₂** (b') in CD_2Cl_2 and corresponding ^1H NMR DOSY spectra (c and c') related to (b) and (b').

The stoichiometry of the self-assembly **Pd₂L3Pyr₂** was confirmed by high-resolution ESI-FTICR-MS spectrometry (Figure 89). In addition to signals of the expected M_2L_2 molecular clip [**Pd₂L3Pyr₂** - 2OTf]²⁺; $m/z = 1510.667$), peaks corresponding to higher molecular masses were observed despite variations carried out on the instrumental conditions, the concentration ($10^{-5} \text{ M} < C < 10^{-3} \text{ M}$) and the solvent. Taken into account the above DOSY NMR data, these experiments suggest aggregation of the starting M_2L_2 metalla-cycle upon ESI. Such behavior is known in the literature with soft ionization conditions¹³⁸ and was also observed in the case of the **Pd₂L4Pyr₂** analogue.¹⁰³

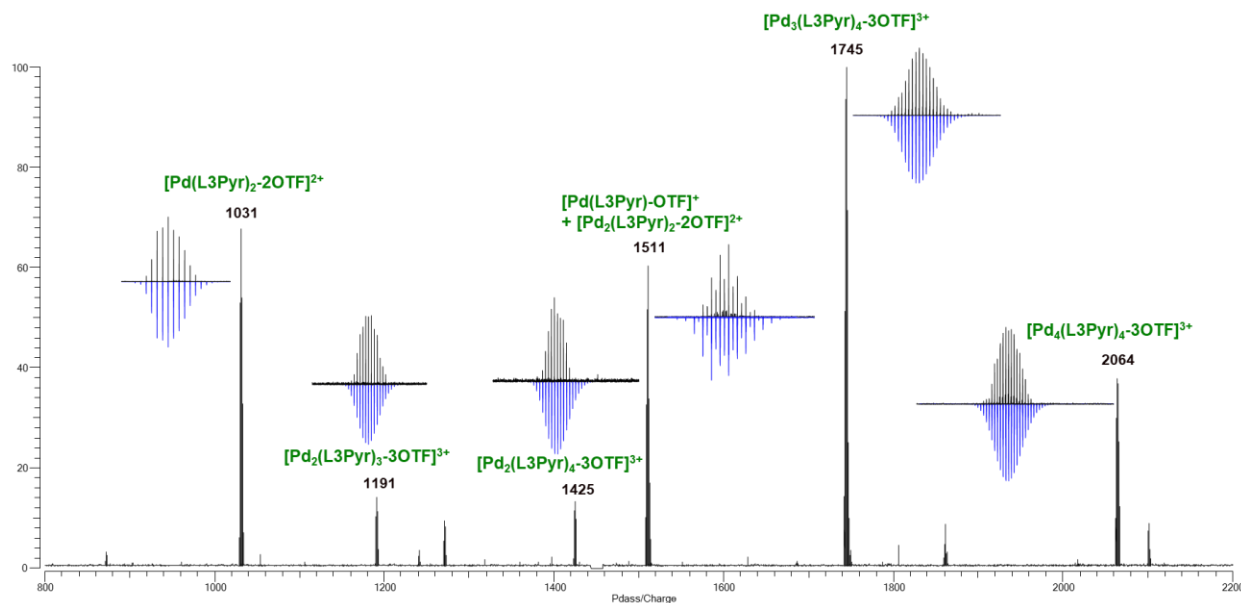


Figure 89. ESI-FTICR spectrum of **Pd₂L₃Pyr₂** recorded in CH₂Cl₂/CH₃NO₂ (v/v 1/1) (C = 10⁻³ M).

Unfortunately, attempts to grow single crystals of **Pd₂L₃Pyr₂** suitable for X-ray analysis were unsuccessful. Theoretical calculations using the MM+ model were undertaken and the results compared to similar experiments carried out for **Pd₂L₄Pyr₂** (Figure 90). Molecular modeling was performed by using the molecular mechanics force field MM+ method from the HyperChem Professional 8.0.3 program (Hypercube, Inc., Waterloo, ON, Canada,) configured *in vacuo*, with an RMS of 10⁻⁵ kcal/mole, a number of maximum cycles of 32500, and a Polak-Ribiere algorithm. Counter anions were omitted to simplify the calculation. The calculated **Pd₂L₄Pyr₂** structure (Figure 90a) is fully consistent with the one observed in the corresponding X-ray crystallography structure (Figure 94c). In particular, a dihedral angle of ca. 80° between both fluorenyl mean planes, and an intramolecular S⋯S distance between facing dithiole rings of ca. 15 Å, were found, and these values are very close to those observed in the crystal. Importantly, switching from a 4-pyridyl coordinating unit to a 3-pyridyl one, drastically modifies the shape of the metalla-clip. The metal coordination in the meta position of the pyridyl groups in **Pd₂L₃Pyr**, results in a significant conformational change with much closer electroactive units. In particular, **Pd₂L₃Pyr** shows a dihedral angle between both fluorenyl units of ca. 27° and a S⋯S distance of ca. 8.5 Å.

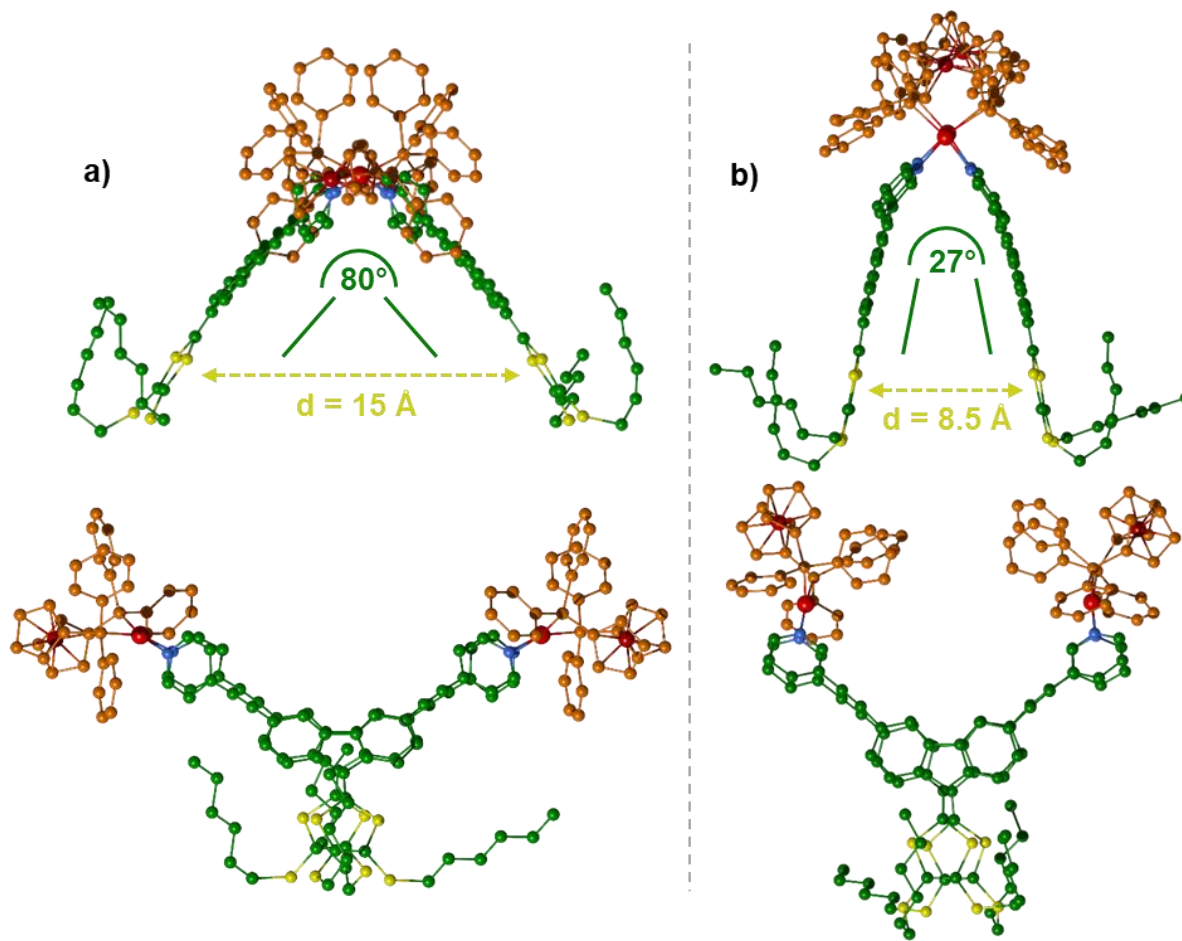


Figure 90. Molecular force field (MM+) model of tweezers **Pd₂L₄Pyr₂** (a) and **Pd₂L₃Pyr₂** (b).

The electrochemical properties of the metalla-clip **Pd₂L₃Pyr₂** were studied by cyclic voltammetry (CV) in CH₃CN/CH₂Cl₂ and compared to the previously described **Pd₂L₄Pyr₂** homolog¹⁰³(Figure 91a). Both **L₄Pyr** and **L₃Pyr** ligands exhibit one reversible redox wave, centered on the DTF moiety at $E^{\text{ox}} = 0.56$ and 0.46 V vs Fc/Fc⁺ respectively. One reversible oxidation is also observed for the DTF moieties in **Pd₂L₄Pyr₂** ($E_1^{\text{ox}} = 0.59$ V vs Fc/Fc⁺) which is followed by oxidation of the ferrocene moieties at $E_2^{\text{ox}} = 0.82$ V vs Fc/Fc⁺. This observation indicates that both DTF ligands are electronically equivalent and independent in **Pd₂L₄Pyr₂**. A striking different behavior is observed for tweezer **Pd₂L₃Pyr₂**. The CV of the latter exhibits a splitting of the redox wave corresponding to the DTF units, with 2 reversible oxidations occurring at $E_1^{\text{ox}} = 0.49$ V and $E_2^{\text{ox}} = 0.63$ V vs Fc/Fc⁺, suggesting that both tips of the tweezer do not behave independently. Such splitting has already been reported in the case of molecular tweezers bearing TTF¹³⁹ and more recently with DTF tips,¹³⁵ and was ascribed to the formation of mixed-valence and π -dimer species upon oxidation. The above-mentioned estimated distance of 8.5 \AA between both panels in **Pd₂L₃Pyr₂** should in principle allow the sandwiching of a planar aromatic species between both tips,^{140, 141} including a self-intercalation of two molecular tweezers if no other species is present in solution. This was confirmed by a concentration-dependent CV study of **Pd₂L₃Pyr₂**, which shows the disappearance of the splitting phenomenon upon diluting the solution from $C = 10^{-3}$ M to $C = 6.25 \times 10^{-5}$ M (Figure 91c,d). Such behavior is similar to the one reported by E. Levillain and P. Hudhomme for TTF-based molecular clips.¹³⁹

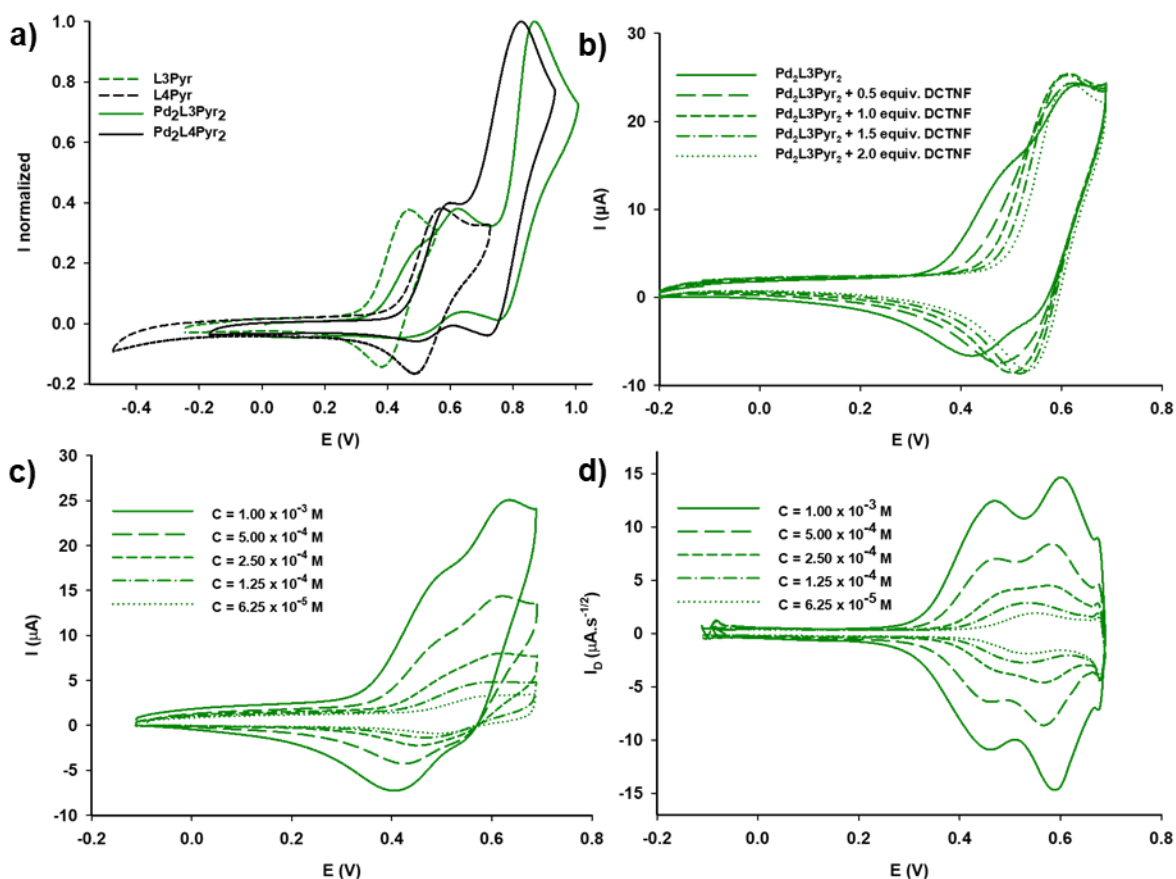


Figure 91. Cyclic voltammograms (CH₃CN/CH₂Cl₂ (v/v 1/1), 0.1 M nBu₄NPF₆, 100 mV·s⁻¹, CG, V vs Fc/Fc⁺) of a) **L3Pyr**, **L4Pyr**, **Pd₂L4Pyr₂** and **Pd₂L3Pyr₂** at C = 10⁻³ M, b) **Pd₂L3Pyr₂** at C = 10⁻³ M in presence of DCTNF, c) **Pd₂L3Pyr₂** at different concentrations and d) the deconvoluted CV corresponding to (c).

Thanks to the modelling of cyclic voltammetry experiments, these authors could demonstrate that the stepwise oxidation process follows a square scheme involving both neutral and radical cation species, which interact either inside or outside the cavity (Figure 92a). This difference of the CV behavior between **Pd₂L3Pyr₂** and **Pd₂L4Pyr₂**, is therefore correlated to the distance separating both tips of the tweezer: whereas **Pd₂L3Pyr₂** can bind a planar guest in the cavity through the simultaneous contribution of both tips (S...S distance 8.5 Å) (Figure 92b), **Pd₂L4Pyr₂** (S...S distance 15 Å) cannot.

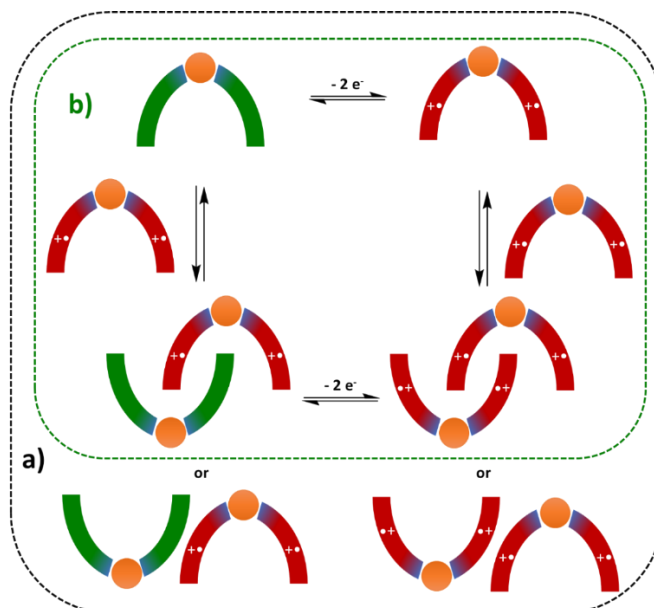


Figure 92. Schematic representation of the stepwise oxidations mechanism proposed by P. Hudhomme and E. Levillain in case of TTF based molecular clips (a),¹³⁹ and the square scheme involved in the oxidation of $\text{Pd}_2\text{L3Pyr}_2$ (b).

Based on those electrochemical experiments and geometrical optimizations, it appears that metalla-clip $\text{Pd}_2\text{L3Pyr}_2$ provides a cavity suitable for guest encapsulation. Additional cyclic voltammetry experiments were therefore carried out to monitor the host-guest interaction process, in presence of 9-dicyanomethylene-2,4,7-trinitrofluorene (DCTNF), an electro-deficient planar aromatic compound (Figure 91b). Interestingly, the addition of an increasing amount of DCTNF into a solution of $\text{Pd}_2\text{L3Pyr}_2$ shifts the first oxidation process to higher potential with the disappearance of the wave splitting. This suggests the intercalation of the DCTNF unit between both electron-rich DTF tips, which prevents therefore the above-mentioned self-intercalation process of two oxidized metalla-clips to occur. Moreover, the splitting observed during the reduction process of the oxidized molecular tweezer also disappears in the host-guest system (Figure 91b), ruling out a guest release phenomenon upon oxidation. As expected, similar studies carried out with $\text{Pd}_2\text{L4Pyr}_2$ did not show any significant changes of the cyclic voltammogram, except a very weak anodic shift (Figure 93).

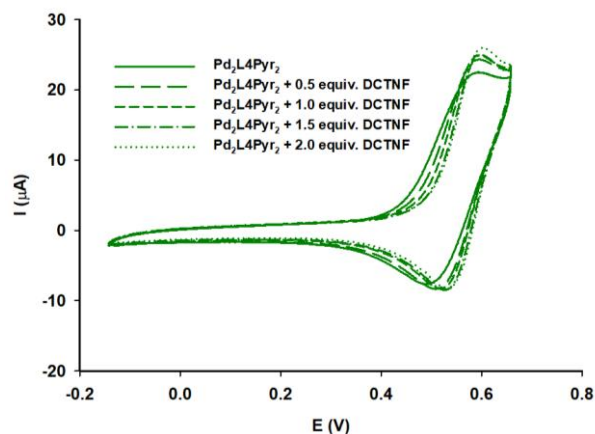


Figure 93. Cyclic voltammograms ($\text{CH}_3\text{CN}/\text{CH}_2\text{Cl}_2$ (v/v 1/1), $0.1 \text{ M nBu}_4\text{NPF}_6$, $100 \text{ mV}\cdot\text{s}^{-1}$, CG, V vs Fc/Fc^+) of $\text{Pd}_2\text{L4Pyr}_2$ at $C = 10^{-3} \text{ M}$ in presence of DCTNF.

To get a better understanding of those interactions we tried to grow single crystals from solutions containing **Pd₂L4Pyr₂** or **Pd₂L3Pyr₂** and DCTNF (2 equiv.). Even though all attempts to get cocrystallized structures were unsuccessful, vapor diffusion of MeOtBu into a mixture of **Pd₂L4Pyr₂** and DCTNF has led to single crystals that does not show presence of DCTNF in the structure.¹⁴²⁻¹⁴⁴ The latter exhibits a packing mode that differs from the one obtained in absence of DCNTF¹⁰³ (Figure 94c) and shows some specific features (Figure 95). It includes three independent M₂L₂ metalla-clip units interacting through head-to-tail n-n stacking between their respective DTF units, with interplanar distances of *ca.* 3.5 Å. As a result, they form an original discrete architecture constructed from two distinctive supramolecular interactions, *i.e.* coordination bonds and parallel displaced aromatic-aromatic interactions.

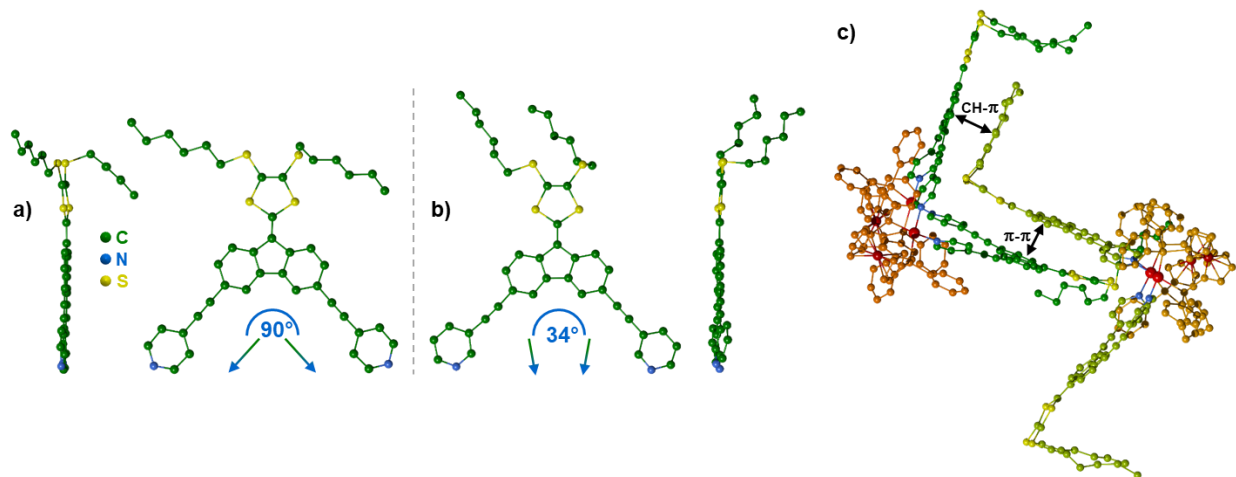


Figure 94. X-Ray crystal structures of ligands **L4Pyr¹⁰³** (a) and **L3Pyr¹⁰²** (b), crystal packing of **Pd₂L4Pyr₂¹⁰³** crystallized by slow diffusion of MeOtBu in a solution of CH₂Cl₂ (c). **Pd₂L4Pyr₂** solution in CHCl₃ containing 2 equiv. of DCTNF

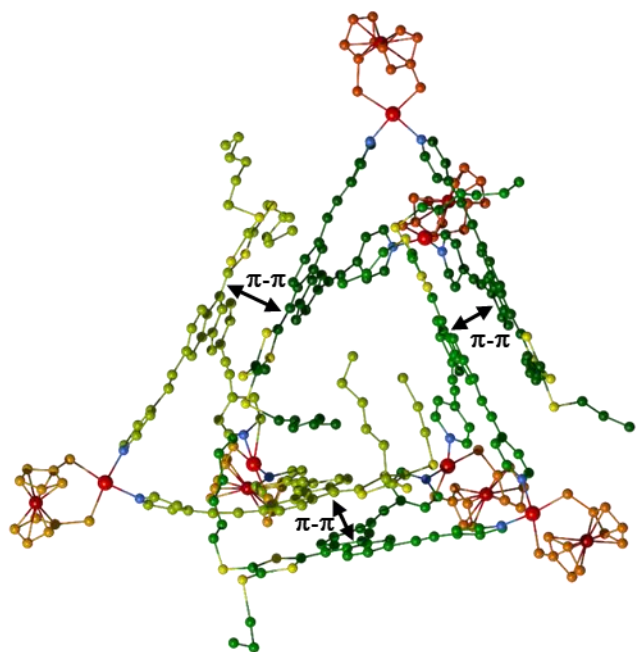
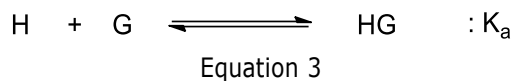


Figure 95. Crystal packing of **Pd₂L4Pyr₂** crystallized by slow diffusion of MeOtBu in a solution of CHCl₃ containing 2 equiv. of **DCTNF** (dppf phenyl rings omitted for clarity).

The attempts to follow the interaction between **Pd₂L3Pyr₂** and DCTNF by NMR were compromised by generation of paramagnetic mixed-valence species that have broadened the signals. The attempt to add an acid to the NMR tube to quench the radicals were unsuccessful. The required concentration of trifluoroacetic acid to sharpen the signals has led to complete disassembly of **Pd₂L3Pyr₂** that was observed by DOSY NMR. Deeper insights related to the interactions mode occurring between DCTNF and **Pd₂L4Pyr₂** or **Pd₂L3Pyr₂** were provided by UV-Vis experiments carried out in CH₂Cl₂ (Figure 96). In order to determine the binding constant, UV-Vis titration experiment was led in DCM by adding a solution of **DCTNF** ($C = 5 \times 10^{-4}$ M) and **Pd₂L3Pyr₂** ($C = 10^{-5}$ M) onto a solution of pure **Pd₂L3Pyr₂** ($C = 10^{-5}$ M). In this way, the host concentration was maintained constant during the titration.¹¹⁴ In the case of a 1:1 complex, the equilibrium under consideration can be described by Equation 3:



The evolution of the absorbance A at a given wavelength can be expressed according to Equation 4:

$$\Delta A = (\epsilon_{\text{HG}} - \epsilon_{\text{H}} - \epsilon_{\text{G}})l \frac{[\text{H}]_0 + [\text{G}]_0 + 1/K_a \pm \sqrt{([\text{H}]_0 + [\text{G}]_0 + 1/K_a)^2 - 4[\text{H}]_0[\text{G}]_0}}{2}$$

Equation 4

Where ϵ_{H} , ϵ_{G} and ϵ_{HG} are the molar extinction coefficients of the host, the guest and the host-guest association respectively, l is the optical path of the quartz cell and K_a the binding constant. Concentrations $[\text{H}]_0$ and $[\text{G}]_0$ correspond to the introduced concentrations of host and guest within the quartz cell. This theoretical equation was fitted to the corresponding experimental data with the least-squares method, affording an evaluation of the desired binding constant.

Both metalla-clips show absorption spectra close to those of their constitutive ligands (**L4Pyr** and **L3Pyr**) with, as expected, molar extinction coefficients which are twice higher. They are characterized by two absorption bands at high energy localized around 300 nm which are ascribed to π - π^* transitions located on the pyridine and fluorene units as well as an intense ICT band around 480 nm coming from the HOMO_{DTF} – LUMO_{pyridine} transition.¹⁴⁵ Job Plot experiments were carried out at $\lambda_{\text{max}} = 465$ nm (**Pd₂L3Pyr₂**, Figure 96b) and 480 nm (**Pd₂L4Pyr₂**, Figure 96d), at $C = 10^{-5}$ M in CH₂Cl₂, upon addition of aliquots of DCTNF ($C = 5 \times 10^{-4}$ M in CH₂Cl₂). As expected from CV experiments, both metalla-tweezers exhibit highly distinctive behaviors. As clearly seen from Figure 96b, a maximum is observed for a molar fraction of 0.5 in the Job plot titration of **Pd₂L3Pyr₂** with DCTNF. This value is assigned to the formation of a 1:1 host-guest complex, for which both DTF units cooperatively contribute to the guest binding, according to a sandwich-mode. A binding constant of $K_a = 7.8 (\pm 0.9) \times 10^5$ was calculated¹¹⁴, a value which illustrates the remarkable ability of this tweezer to complex the electro-deficient DCTNF unit. On the other hand, the Job plot titration in the case of **Pd₂L4Pyr₂** (Figure 96d) exhibits a maximum for *ca.* 0.6-0.7. This value correlates with a 1:2 stoichiometry, meaning that even though the metalla-assembly **Pd₂L4Pyr₂** does not possess a cavity suitable for recognition of planar guests, it is able to interact with two DCTNF units.

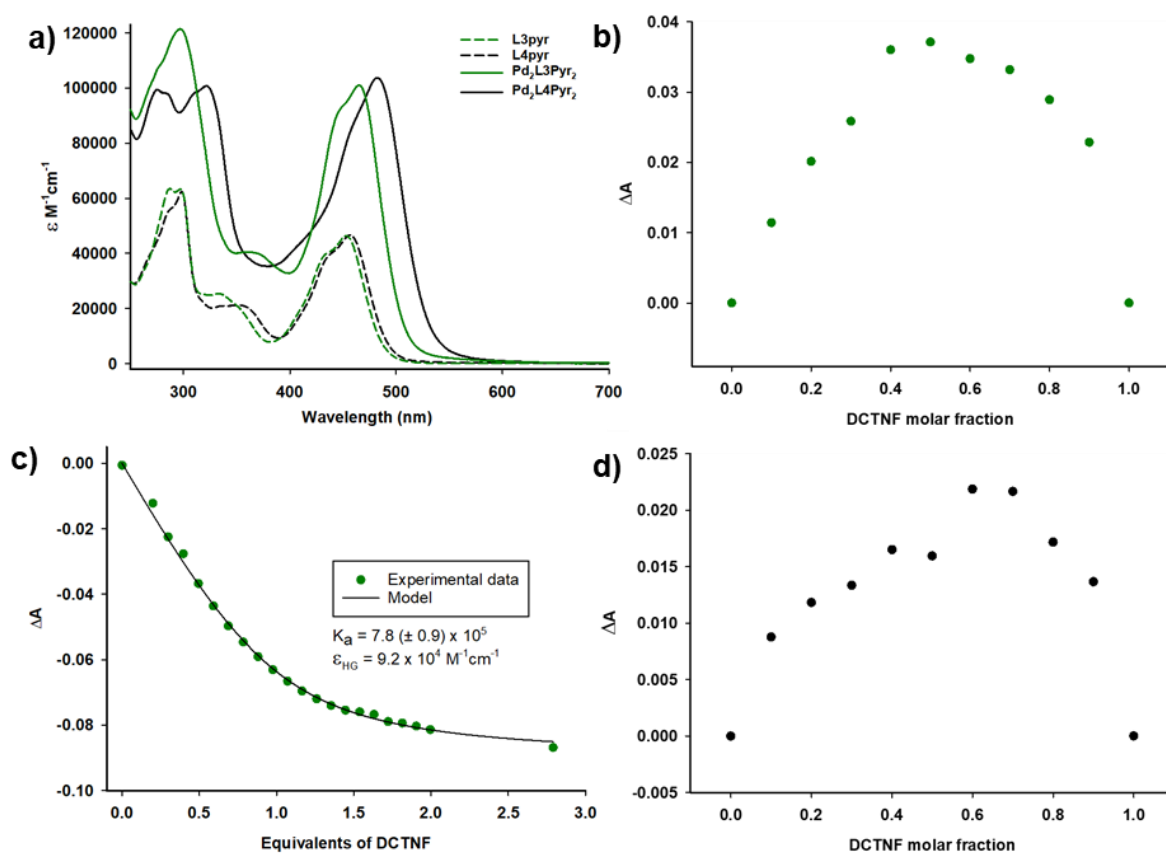


Figure 96. UV-Vis spectra of ligands **L3Pyr**, **L4Pyr** and metalla-tweezers **Pd₂L3Pyr₂** and **Pd₂L4Pyr₂** recorded in CH₂Cl₂ (a), Job plots for complexation of receptor **Pd₂L3Pyr₂** (b) and **Pd₂L4Pyr₂** (d) with DCNTF determined by UV-Vis spectroscopy at respectively 465 and 480 nm (CH₂Cl₂, C = 10⁻⁵ M), and plots of absorbance of a UV-vis titration for complexation of receptor **Pd₂L3Pyr₂** (CH₂Cl₂, C = 10⁻⁵ M) with DCNTF (CH₂Cl₂, 5 × 10⁻⁴ M) at 465 nm (c).

On this basis, we assume that each DTF fragment can interact independently with one DCTNF unit. This is corroborated by a ¹H NMR experiment, which shows that signals of a mixture of a DTF ligand and DCTNF, are shifted related to the species recorded alone (Figure 97).

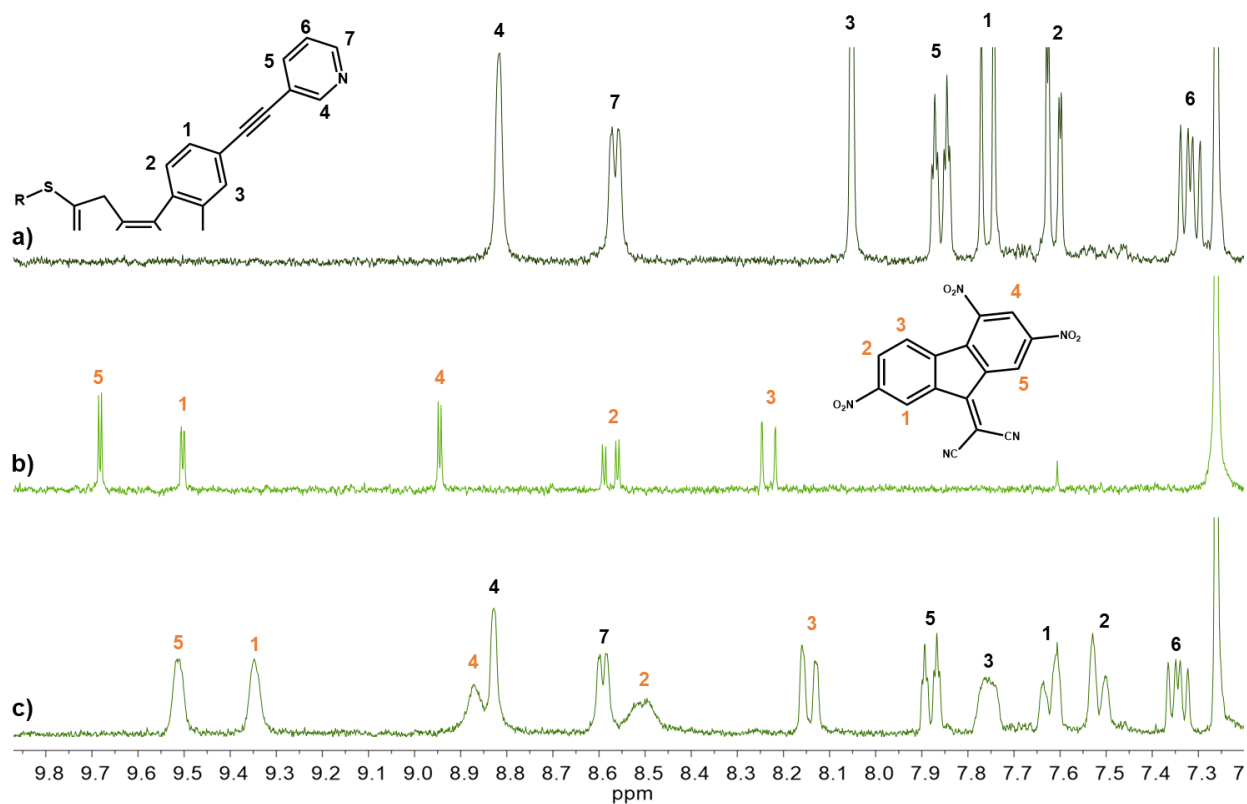


Figure 97. ^1H NMR of ligand **L3Pyr** (a), DCTNF (b) and their 1/1 mixture (c) in CDCl_3 at $C = 10^{-3}$ M.

To conclude, the properties of both M_2L_2 metalla-clips, **Pd₂L4Pyr₂** and **Pd₂L3Pyr₂**, constructed from the same *cis*-blocked $\text{Pd}(\text{dppf})(\text{OTf})_2$ complex and two isomeric DTF-based ligands differing by the position of the nitrogen atom on the pyridyl coordinating units, have been compared. While the molecular tweezer built from **L4Pyr** shows an intramolecular distance of ca. 15 Å between both redox-active tips, the one obtained from ligand **L3Pyr** features a cavity in which both DTF units are separated by 8.5 Å. The latter structural organization is favorable for promoting *i*) a tweezer dimerization upon oxidation, through formation of intercalated cationic dimeric species *ii*) formation of a host-guest complex with an electro-deficient DCTNF unit, with an association constant of 7.8×10^5 in methylene chloride. These results illustrate to which extent minor structural changes led on the starting ligand, may drastically impact the geometry and hosting properties of the resulting metalla-species prepared through a coordination-driven self-assembled processes.

2. Interlocking of DTF-based molecular clips

This study has been mainly developed in reference "Metalla-Assembled Electron-Rich Tweezers: Redox-Controlled Guest Release Through Supramolecular Dimerization" (Angew. Chem. Int. Ed. 2020).¹³⁵ Some additional data are provided below.

Aside from the widely described family of coordination rings and cages that feature a closed cavity, molecular tweezers constitute a class of acyclic host molecules prone to bind various guest systems. As seen in § 1 of this Chapter, the cavity is in this case geometrically defined by two panels facing each other and maintained in an approximately parallel conformation by a linker. Their guest-binding capacities depend on the inherent

properties (for example, electronic) of their panels and on the distance separating them. For instance, a distance of about 7 Angstrom is likely to facilitate the binding of a planar aromatic molecule.

The following paragraph depicts a new family of a coordination-driven self-assembled tweezers based on the DTF electroactive moiety, as an additional example beside the example described above in § 1,. They associate the **L4Pyr** DTF-based ligand (see §1) to bis(Ruthenium) complexes (**RuOxa(OTf)₂** and **RuNaph(OTf)₂**) varying by the length of the linker separating both metal atoms (Figure 79). The self-assembly of **Oxa₂L4Pyr₂** and **Naph₂L4Pyr₂** was performed in dichloromethane. Whereas the smaller tweezer **Oxa₂L4Pyr₂** is observed as an individual unit, the larger one spontaneously forms the interpenetrated supramolecular dimer (**Naph₂L4Pyr₂**)₂ in solution and in the solid state. This dimer can be dissociated either upon dilution to $C < 10^{-3}$ M, or upon addition of an electron-poor aromatic guest (i.e. 9-dicyanomethylene-2,4,7-trinitrofluorene (DCTNF)), affording the **Naph₂L4Pyr₂** monomer or the DCTNF⊂**Naph₂L4Pyr₂** host guest complex respectively. Remarkably, the latter can be reversibly shifted to a tweezer dimer upon oxidation, with concomitant guest release (Figure 98).

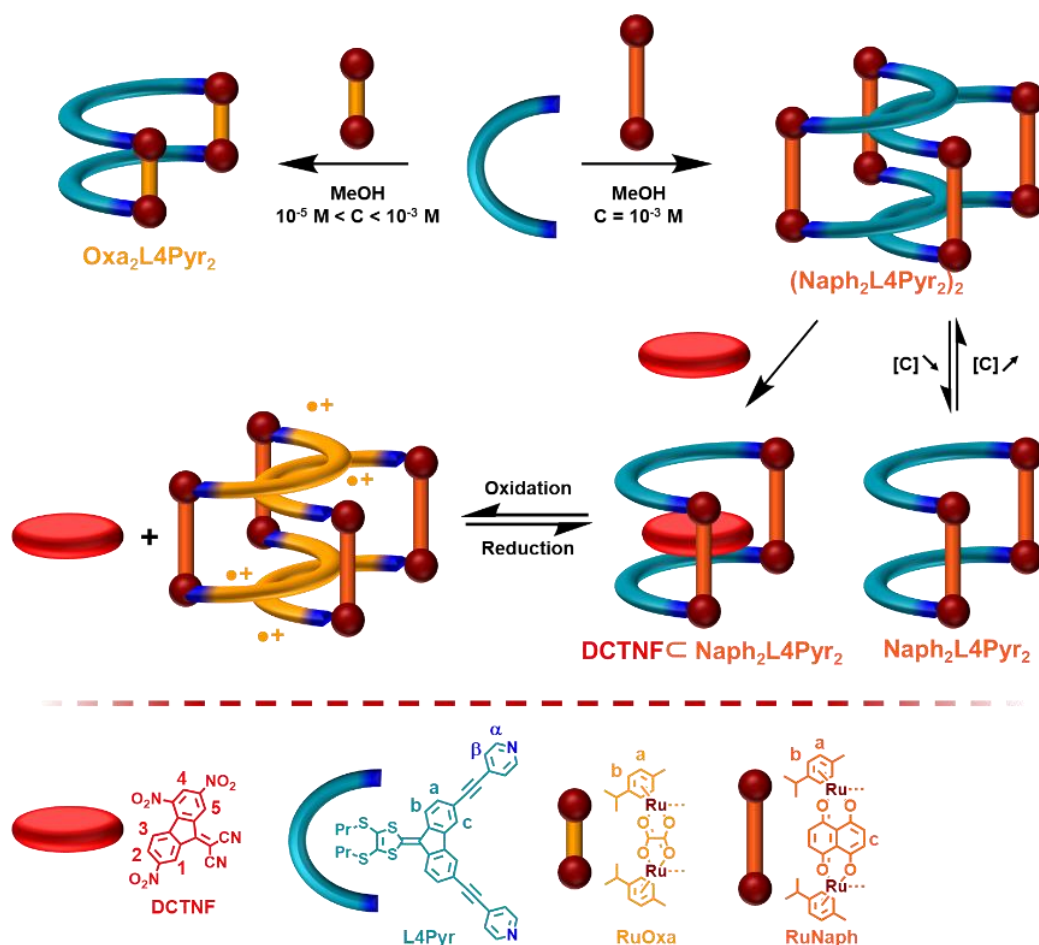


Figure 98. Synthesis of self-assembled tweezers **Oxa₂L4Pyr₂** and **(Naph₂L4Pyr₂)₂** from ligand **L4Pyr** and complexes **RuOxa(OTf)₂** and **RuNaph(OTf)₂** respectively, and supramolecular transformations occurring from **(Naph₂L4Pyr₂)₂**.

The synthesis of tweezer **Oxa₂L4Pyr₂** was achieved in one-step from a stoichiometric mixture of redox active ligand **L4Pyr**¹⁰³ and arene Ruthenium acceptor **RuOxa(OTf)₂**¹⁴⁶ in MeOH at $C = 10^{-3}$ M (15 h, 50°C). After

precipitation with Et₂O, the resulting solid exhibits a ¹H NMR spectrum (MeOD) with α/β pyridyl and fluorenyl signals upfield shifted in comparison with starting **L4Pyr**, as a result of the metal-ligand coordination (Figure 99a-b). A ¹H NMR DOSY experiment (Figure S63) revealed the presence of only one discrete species in solution with a diffusion coefficient (D) of 3.31 × 10⁻¹⁰ m² s⁻¹ in MeOD at C = 10⁻³ M. The corresponding calculated Stokes radius of 12 Å, is in good agreement with the formation of the expected M₄L₂ species.^{72, 137} Interestingly, the ¹H NMR spectrum (MeOD) obtained from the reaction of **L4Pyr** with the **RuNaph(OTf)₂**¹⁴⁷ acceptor (Figure 99c), shows a splitting of each signal, indicating the possible formation of a dimer structure. In particular, the large upfield shifts of fluorenyl aromatic protons (a-c) in the 5.5–7.0 ppm region suggests an association driven by π-π interactions. The formation of a dimeric structure is further confirmed by the Stokes radius of 19 Å calculated from a ¹H DOSY NMR experiment (Figure S66), a value which is significantly larger than the one observed with **RuOxa(OTf)₂**. One will note that no discrete structure could be reached from the larger **RuTetra** acceptor.¹⁴⁷

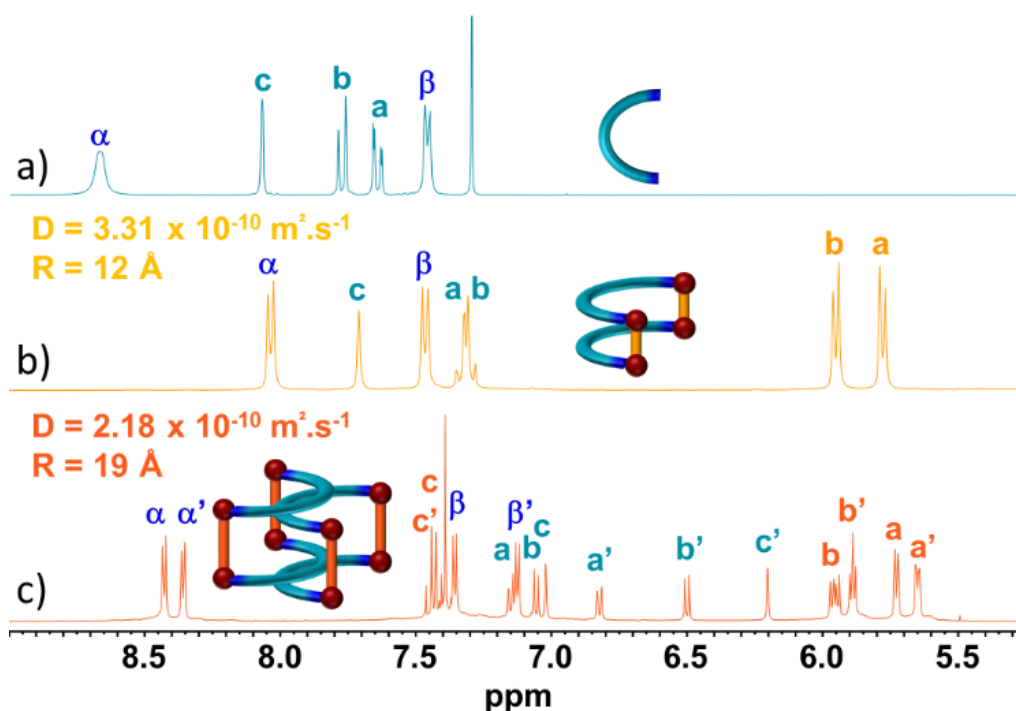


Figure 99. ¹H NMR (298 K, C = 10⁻³ M, downfield region) of a) ligand **L4Pyr** in CDCl₃, b) **Oxa2L4Pyr2** in MeOD and c) **(Naph2L4Pyr2)₂** in MeOD. See Figure 98 for ¹H NMR assignments. D corresponds to the diffusion coefficient extracted from a ¹H DOSY NMR experiment and R to the corresponding hydrodynamic radii calculated from the Stokes-Einstein equation.

High-resolution ESI-FTICR-MS spectrometry experiments were carried out on the isolated **Oxa2L4Pyr2** and **(Naph2L4Pyr2)₂** self-assembled complexes in CH₃CN at C = 10⁻³ M (Figure 100, Figure S73 and Figure S74). While the metalla-tweezer obtained from **RuOxa(OTf)₂** exhibits only signals resulting from the monomeric **Oxa2L4Pyr2** species at m/z = 1325.0751 and 833.3996 (main contributions, Figure 100a), the self-assembly isolated from the reaction between **L4Pyr** and the larger **RuNaph(OTf)₂** acceptor shows one isotopic pattern at m/z = 1949.4623 corresponding to the dimeric **(Naph2L4Pyr2)₂** species (main contribution, Figure 100b). It is worth noting that no signal corresponding to the monomeric tweezer is observed, highlighting the

stability of the supramolecular dimer, even in the gas phase. Eventually, all experimental isotopic distributions are in good agreement with calculated theoretical ones (Figure S73 and Figure S74).

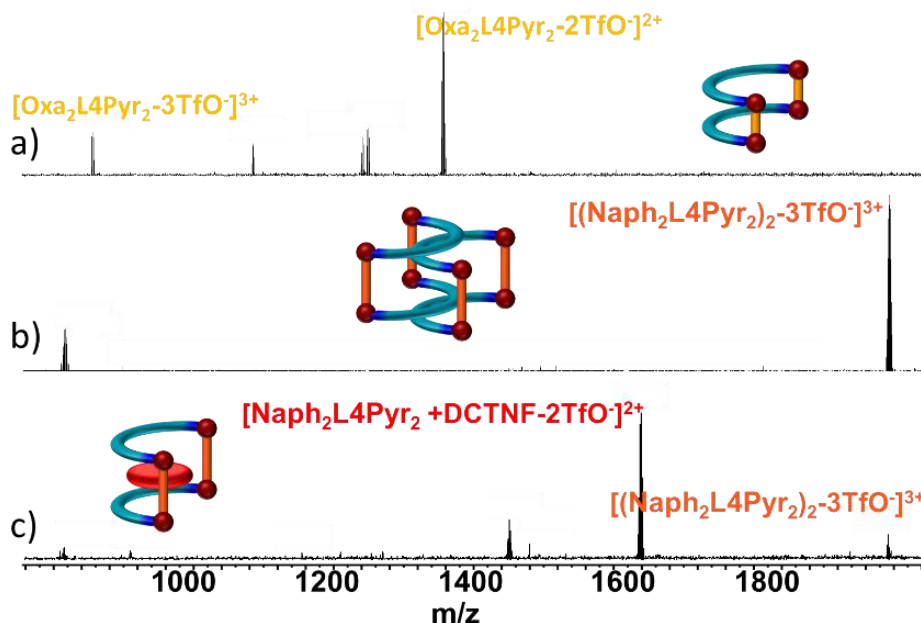


Figure 100. ESI-FTICR mass spectra recorded in CH_3CN at $C = 10^{-3}$ M of a) **Oxa₂L4Pyr₂**, b) **(Naph₂L4Pyr₂)₂** and c) **(Naph₂L4Pyr₂)₂** with 2 equiv. of DCTNF.

Single crystals suitable for X-ray diffraction analyses were obtained for both Ruthenium-based tweezers, by liquid diffusion of methyl *tert*-butyl ether into a solution of the self-assembled structures in methanol at room temperature (Figure 101). The monomeric structure of **Oxa₂L4Pyr₂** consists in two DTF electro-active units facing each other thanks to π - π interactions, with a distance of 3.47(1) Å (Figure 101a). Consequently, both **RuOxa** spacers, in which the Ruthenium atoms are separated by 5.49(1) Å, are twisted by 19.55 and 32.65° respectively from the ideal perpendicular conformation with the dithiafulvenyl fragments (Figure 101a). The X-ray crystal structure of **(Naph₂L4Pyr₂)₂** reveals that two metalla-tweezers are partially stacked and stabilized by intermolecular π - π interactions with distances in the range of 3.44-3.56(1) Å (Figure 101b). No additional stabilization forces such as CH- π interactions between the DTF ligands and the hydroxy-naphthoquinonato units are observed, while these have been described as the main driving forces for interlocking carbazole-based ligands.⁵⁶

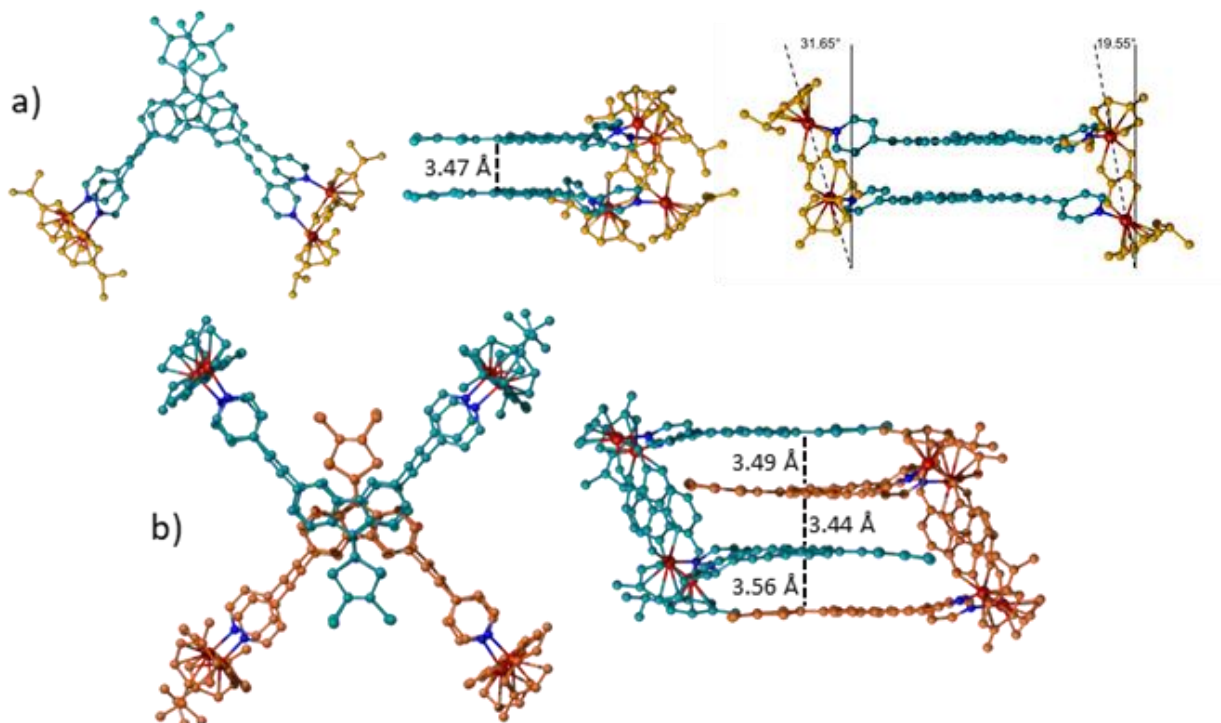
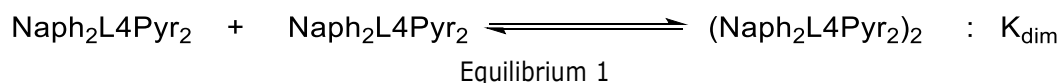


Figure 101. X-Ray crystal structures of a) **Oxa₂L4Pyr₂** and b) **(Naph₂L4Pyr₂)₂**. Propyl chains have been omitted for clarity.

The stability of the dimer arrangement has been investigated by performing variable-concentration NMR experiments in deuterated methanol at 298 K (Figure 103a-c and Figure S68). Diluting the solution from $C = 10^{-3}$ M to $C = 3 \times 10^{-5}$ M results in a drastic simplification of the NMR spectrum and to the disappearance of all signals in the 6–7 ppm region. Dissociation of the dimer is further supported by a ^1H DOSY NMR experiment recorded at $C = 3 \times 10^{-5}$ M from which a diffusion coefficient $D = 3.63 \times 10^{-10} \text{ m}^2 \cdot \text{s}^{-1}$ has been extracted (Figure S69), a value similar to that observed for the monomer **Oxa₂L4Pyr₂** tweezer ($D = 3.31 \times 10^{-10} \text{ m}^2 \cdot \text{s}^{-1}$, Figure 99 and Figure S63). The slow equilibrium between the monomer and the dimer species at the NMR timescale, allowed a straightforward determination of the dimerization constant. Considering Equilibrium 1, which involves monomer **Naph₂L4Pyr₂** and dimer **(Naph₂L4Pyr₂)₂**, one can express the concentration $[\text{Naph}_2\text{L4Pyr}_2]$ as a function of the total concentration $C_0 = [\text{Naph}_2\text{L4Pyr}_2] + 2[(\text{Naph}_2\text{L4Pyr}_2)_2]$ according to Equation 5.



$$[\text{Naph}_2\text{L4Pyr}_2] = \frac{-1 + \sqrt{1 + 8K_{\text{dim}}C_0}}{4K_{\text{dim}}}$$

Equation 5

Variable concentration NMR experiments allowed determining the concentrations of dimer and monomer at different total concentrations C_0 . Fitting these experimental data to Equation 1 affords the dimerization constant and the corresponding standard deviation $K_{\text{dim}}(\text{MeOD}) = 4416 \pm 246$ (Figure 102).¹⁴⁸

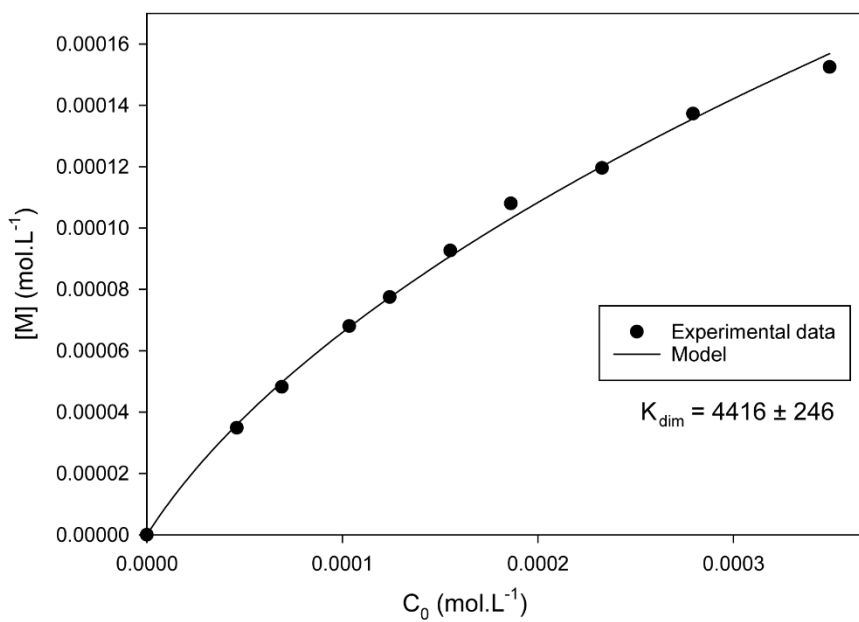


Figure 102. Evolution of the monomer concentration [**Naph₂L4Pyr₂**] as a function of the total concentration C_0 in MeOD (T = 298 K).

In order to study further the stability of the dimeric (**Naph₂L4Pyr₂**)₂ species, we investigated its behavior in presence of 9-dicyanomethylene-2,4,7-trinitrofluorene (DCTNF), such electron-poor unit being known to interact strongly with electron-rich derivatives.¹⁴⁹ Interestingly, upon addition of 4 equivalents of DCTNF into a solution of (**Naph₂L4Pyr₂**)₂ ($C = 10^{-3}$ M, MeOD), the ¹H NMR spectrum appeared significantly simplified (Figure 103d), illustrating the dissociation of the dimeric species. Moreover, the resulting α and β protons show chemical shifts similar to those of the **Naph₂L4Pyr₂** monomer (Figure 103c), while signals corresponding to the DTF core are upfield shifted. Such observation suggests the intercalation of the electron-poor DCTNF plan between both DTF tips of the **Naph₂L4Pyr₂** monomer. A ¹H NMR DOSY experiment from which diffusion coefficients of 3.07×10^{-10} m².s⁻¹ and 3.73×10^{-10} m².s⁻¹ could be extracted for the host and the guest respectively (Figure 103d and Figure S72) confirms *i*) the drastic decreasing of the self-assembly radius size, which is now comparable to the one of **Naph₂L4Pyr₂** monomer and *ii*) the strong host-guest interaction.

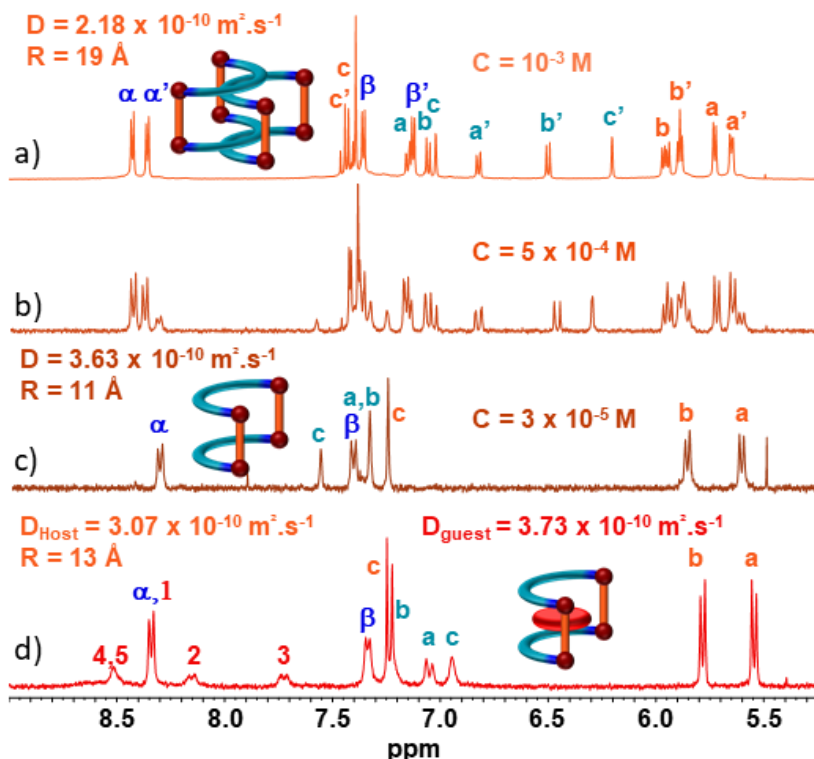


Figure 103. a-c) ^1H NMR spectra evolution in MeOD of $(\text{Naph}_2\text{L4Pyr}_2)_2$ from $C = 10^{-3}$ M to $C = 3 \times 10^{-5}$ M and d) ^1H NMR spectrum recorded from a solution at $C = 10^{-3}$ M of $(\text{Naph}_2\text{L4Pyr}_2)_2$ containing 4 equiv. of DCTNF.

Finally, the formation of the $\text{DCTNF} \subset \text{Naph}_2\text{L4Pyr}_2$ complex is unambiguously demonstrated by an ESI-FTICR mass analysis of a mixture of $(\text{Naph}_2\text{L4Pyr}_2)_2$ and 2 equivalents of DCTNF in acetonitrile, for which a characteristic signal of the doubly charged species is found at $m/z = 1606.6168$ (Figure 100c and Figure S75).

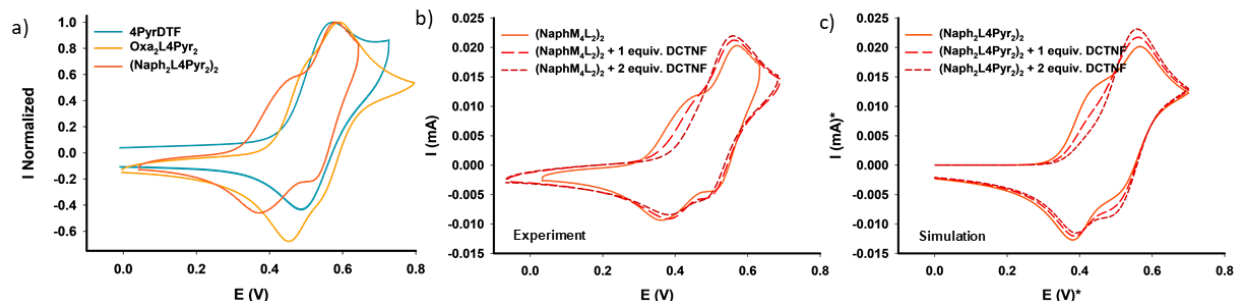


Figure 104. Cyclic voltammogram at $C = 10^{-3}$ M in 0.1 M TBAPF₆ (CH_3CN , $100 \text{ mV}\cdot\text{s}^{-1}$, vs Fc/Fc^+) of a) **L4Pyr**, **Oxa₂L4Pyr₂** and $(\text{Naph}_2\text{L4Pyr}_2)_2$, b) $(\text{Naph}_2\text{L4Pyr}_2)_2$ in presence of **DCTNF**, c) Simulated Cyclic voltammogram of $(\text{Naph}_2\text{L4Pyr}_2)_2$ in presence of **DCTNF**.

The electrochemical properties of both **Oxa₂L4Pyr₂** monomer and $(\text{Naph}_2\text{L4Pyr}_2)_2$ dimer were studied by cyclic voltammetry in CH_3CN at $C = 10^{-3}$ M and compared to those of ligand **L4Pyr** (Figure 104a). The latter exhibits one reversible oxidation wave at $E_{1^{\text{ox}}} = 0.56 \text{ V}$ vs Fc/Fc^+ that is ascribed to the formation of a radical cation.^{101, 136} This value is in good accordance with the one reported for the analogous SHexyl functionalized ligand.¹⁰³ Interestingly, both self-assembled structures **Oxa₂L4Pyr₂** and $(\text{Naph}_2\text{L4Pyr}_2)_2$ show a significant

splitting of the oxidation wave, providing evidence of electronic interactions between DTF units. A similar splitting was already reported in the case of TTF-based molecular tweezers and was ascribed to the formation of mixed valence and π -dimer species.¹³⁹

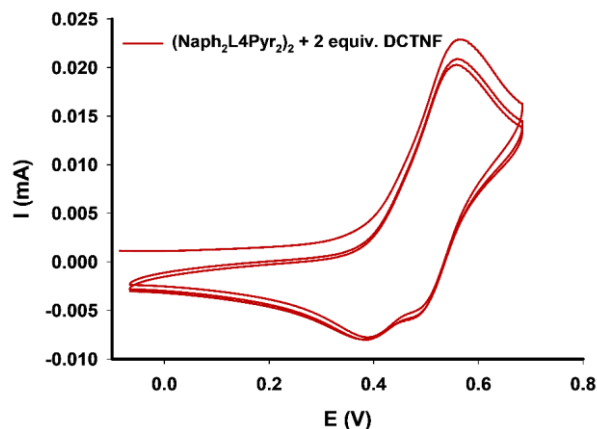


Figure 105. Cyclic voltammogram at $C = 10^{-3}$ M in 0.1 M TBAPF₆ (CH₃CN, 100 mV.s⁻¹) of **(Naph₂L4Pyr₂)₂** in the presence of 2 equiv. of DCTNF.

From a mechanistic point of view the electrochemical process observed for the **(Naph₂L4Pyr₂)₂** dimer consists of two successive oxidations, each involving two electrons (Figure 106a). Cyclic voltammetry was also considered in order to monitor the recognition process of DCTNF by **(Naph₂L4Pyr₂)₂** (Figure 104b). Addition of increasing amount of DCTNF leads to a shift of the binding equilibrium toward the host-guest complex formation, resulting in the disappearance of the oxidation process splitting according to the square scheme shown in Figure 106b. The DCTNF \subset **Naph₂L4Pyr₂** host-guest complex exhibits a unique oxidation process at $E_{1^{ox}} = 0.58$ V vs Fc/Fc⁺ (Figure 104b). Interestingly, two reduction waves remain during the reduction scan, which occur at potentials very similar to those of the dimeric **(Naph₂L4Pyr₂)₂** self-assembly (Figure 104a). The reduction event may therefore be ascribed to the **(Naph₂L4Pyr₂)₂⁴⁺** species that is recovered while releasing the encapsulated DCTNF (Figure 98 and Figure 106). One will note that the release process is reversible since the voltammogram remains identical after several cycles (Figure 105). In order to get a deeper understanding of the release/uptake mechanism, theoretical voltammograms were simulated both in absence and presence of the guest, taking into account equilibria illustrated in Figure 106c. Those electrochemical simulations fit nicely with the experimental CVs (Figure 104c) and confirm that this redox-triggered release process is driven by the highly favorable dimerization process of oxidized **Naph₂L4Pyr₂²⁺** tweezers.

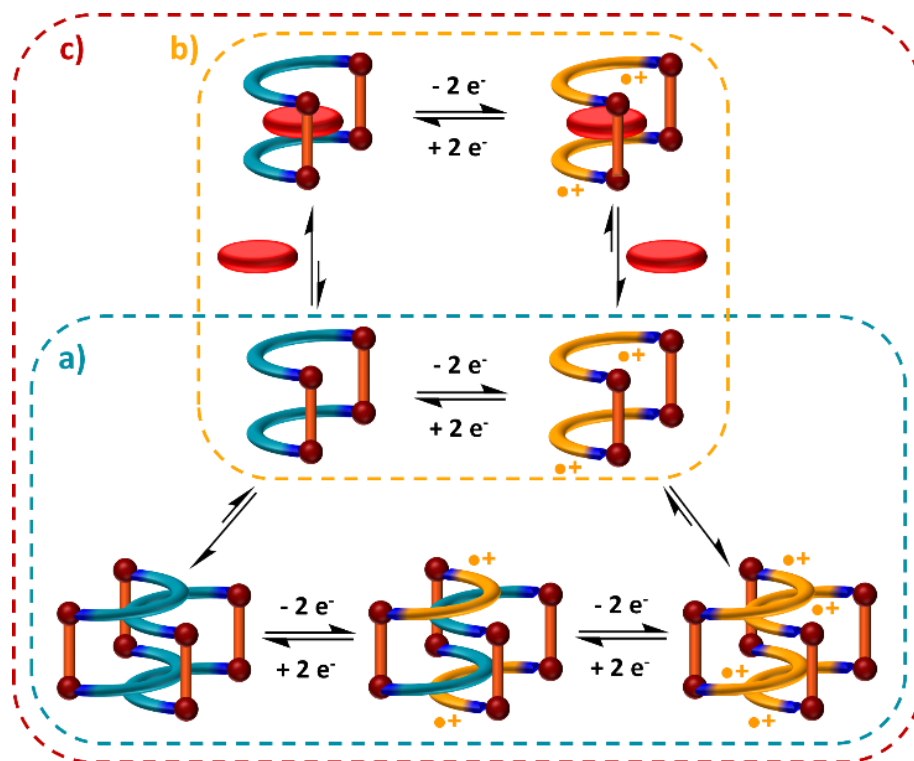


Figure 106. Scheme illustrating equilibria occurring during a) the redox process involving the **(Naph₂L4Pyr₂)₂** dimer, b) the redox-triggered guest release process involving the **Naph₂L4Pyr₂** monomer and c) the complete redox mechanism involved in the guest release process.

To conclude this paragraph, two novel self-assembled metalla-tweezers were designed from an electron-rich DTF-based ligand and bis(Ruthenium) complexes. The larger **Naph₂L4Pyr₂** tweezer shows a distance of about 7 Angstrom between both redox-active tips. This geometry proves to be favorable for a spontaneous dimerization into **(Naph₂L4Pyr₂)₂**, which could be characterized in solution, the gas phase, and the solid state. Remarkably, this interpenetrated arrangement can dissociate in the presence of an electron-poor DCTNF unit, leading to a 1:1 host-guest complex (DCTNF **Naph₂L4Pyr₂**). Finally, electrochemical oxidation of this complex allows to regenerate the dimeric structure due to favorable interactions between the oxidized tweezer-like molecules, resulting in a concomitant redox-controlled delivery of the DCTNF guest molecule, illustrating the potential of tweezer-like molecules in this field.

**Chapter 4. Catenane-type
interlocking of benzobisimidazole
/ bis(Ruthenium) molecular
rectangle. Effects of pH, guests
and concentration**

The last part of my work was dedicated to the preparation of a series of stimuli responsive metalla-rectangle bearing the benzobisimidazole moiety. This work was done in collaboration with Dr. Olivier Siri (Marseille) and Dr. Mourad Elhabiri (Strasbourg) and has been published in *Chemistry a European Journal*.¹⁵⁰

1. Concept of the project

Discrete rings and cages constructed through the coordination driven self-assembly generally feature a cavity. This feature has been largely exploited in host-guest chemistry but allows also for reaching intricate interlocked systems. While several synthetic methodologies towards metalla-macrocycles and cages have been described, the reasoned preparation of interlocked architectures, *i.e.* molecular links¹⁵¹⁻¹⁵³ (*e.g.* catenanes,⁴³⁻⁴⁷ ring-in-ring complexes,^{52, 53} Solomon links,⁵⁴⁻⁵⁹ Trefoil Knots^{55, 60-63} or Borromean rings⁶⁴⁻⁷⁰ to cite a few) or interpenetrated cage structures,^{13, 154} remains a challenge since decreasing the number of independent species is entropically unfavorable. Several parameters can help in achieving the locking process by providing an extra enthalpic energy such as for example π - π stacking, electrostatic or hydrogen-bonding interactions, as well as solvophobic effects.¹⁵⁵ See § 1.5 Chapter 1 for more details.

On the other hand, controlling reversibly the supramolecular transformation of coordination-driven architectures focuses much attention.¹⁵⁶ This could be achieved upon *i)* changing solvent or concentration,⁶⁵ *ii)* adding a chemical, *i.e.* a competitive component⁵⁵ or a guest template,¹⁵² or *iii)* using a light¹⁵⁷ or redox^{111, 135} physicochemical stimulation. Scarce examples of pH-sensitive architectures that do not depend on competitive coordination of metal acceptors have been depicted to monitor the supramolecular transformation between metalla-structures. They explore the Lewis-base character of the binding pyridine units and the resulting competing metal coordination/protonation processes, allowing to drive for host's disassembly^{80, 82, 158-163} in a context of guest release^{9, 74, 109, 110, 135} or switching between metalla-structures.¹⁶⁴ To the best of our knowledge, no pH-driven supramolecular transformation has been depicted yet, through assistance of alternative pH-sensitive groups. So, we selected the benzobisimidazole (**BBI**) active moiety that is currently an object of research in Olivier Siri group. We prepared and characterized two self-assembled metalla-rectangles **Oxa₂BBI₂** and **Naph₂BBI₂** featuring this pH sensitive benzobisimidazole unit and studied their properties.

These structures differ essentially by the distances separating both benzobisimidazole ligands (**BBI**), a parameter which is controlled depending on the size of the bis(Ruthenium) complex spacer (**RuOxa** or **RuNaph**) (Figure 107). On this basis, it is worth mentioning that whilst the smaller rectangle (**Oxa₂BBI₂**) exists only as a monomer discrete species, the larger **Naph₂BBI₂** can dimerize to form the catenated (**Naph₂BBI₂**)₂ structure. Remarkably, the latter responsive interlocked species can dissociate in response to three different types of chemical and physical stimuli: *i)* dilution, *ii)* addition of pyrene and *iii)* protonation of the benzobisimidazole side walls (Figure 107).

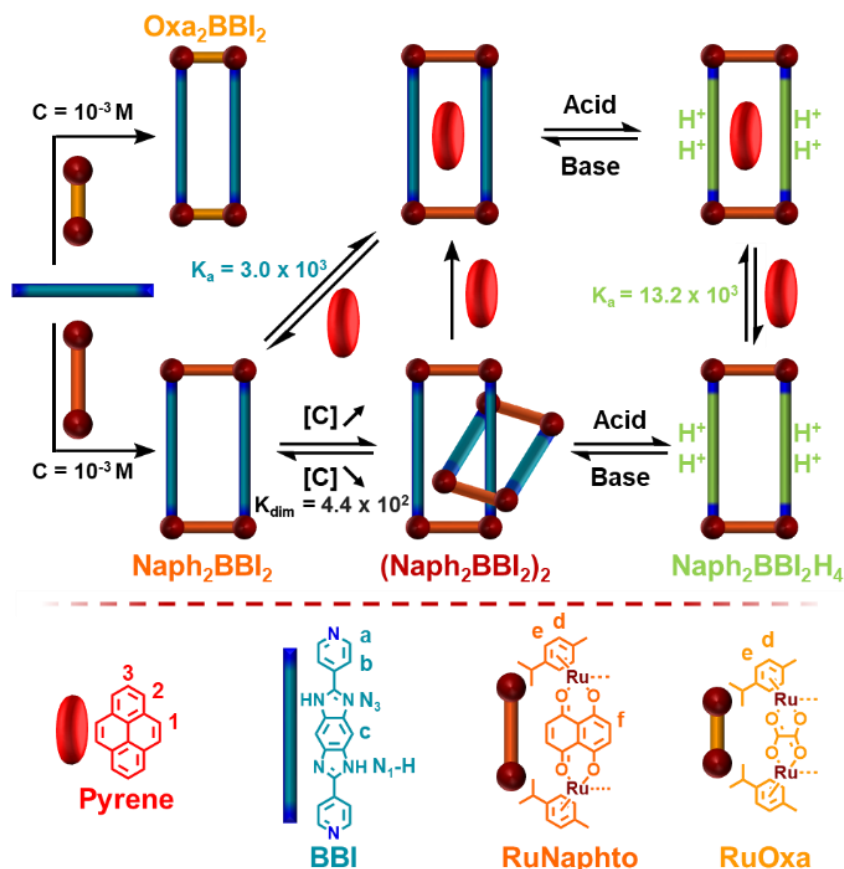
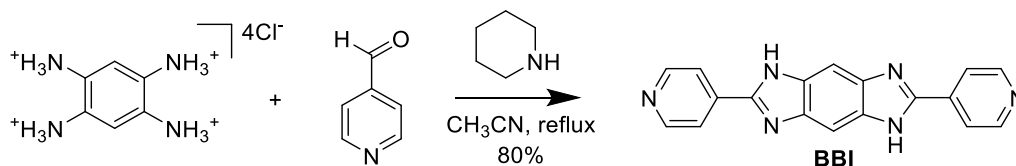


Figure 107. Synthesis of the self-assembled metalla-rectangles **Oxa₂BBI₂** and **Naph₂BBI₂** from the benzobisimidazole ligand (**BBI**) and the bis(Ruthenium) complexes **RuOxa(OTf)₂** or **RuNaph(OTf)₂**, and subsequent supramolecular transformations occurring in MeOD from **Naph₂BBI₂**.

2. Synthesis of the ligand BBI

The synthesis of ligand **BBI** was achieved by the condensation of two equivalents of 4-pyridinecarboxaldehyde with tetraaminobenzene tetrahydrochloride in presence of piperidine and under aerobic conditions. After 16 h in refluxing acetonitrile, the ligand was isolated as a yellow-orange powder in a 80% yield (Scheme 10).



Scheme 10. Synthesis of ligand **BBI**.

3. Synthesis of metalla-structures Oxa₂BBI₂ and Naph₂BBI₂

Reaction between the **RuOxa(OTf)₂**¹⁴⁶ complex and the **BBI** ligand was carried out in MeOD at $C = 10^{-3}$ M ($T = 50$ °C) and followed by ¹H NMR. After 2 h, the reaction converged to a single species that could be isolated upon precipitation with *tert*-butyl methyl ether (MeOtBu). The resulting set of ¹H NMR signals illustrates the symmetry of the resulting self-assembled structure (Figure 108b). A ¹H DOSY NMR experiment revealed the presence of only one species in solution with a diffusion coefficient of $D = 3.9 \times 10^{-10}$ m² s⁻¹ ($T = 298$ K) in

MeOD at $C = 10^{-3}$ M. A hydrodynamic radius of ca. 10 \AA was estimated from the Stokes-Einstein equation^{72, 137}, a value which is compatible with the formation of the expected Ru_4L_2 complex **Oxa₂BBI₂**. Similarly, the reaction carried out between the **RuNaph(OTf)₂**¹⁴⁷ complex and ligand **BBI** in MeOD afforded the metalla-rectangle **Naph₂BBI₂** characterized by a symmetric ¹H NMR spectrum (Figure 108c). As expected, a slightly larger Stokes radius of ca. 11 \AA was extracted from the ¹H DOSY NMR experiment carried out in MeOD at $C = 10^{-3}$ M. Corresponding DOSY and COSY spectra are reported in annexes (Figure S78, Figure S80 and Figure S81).

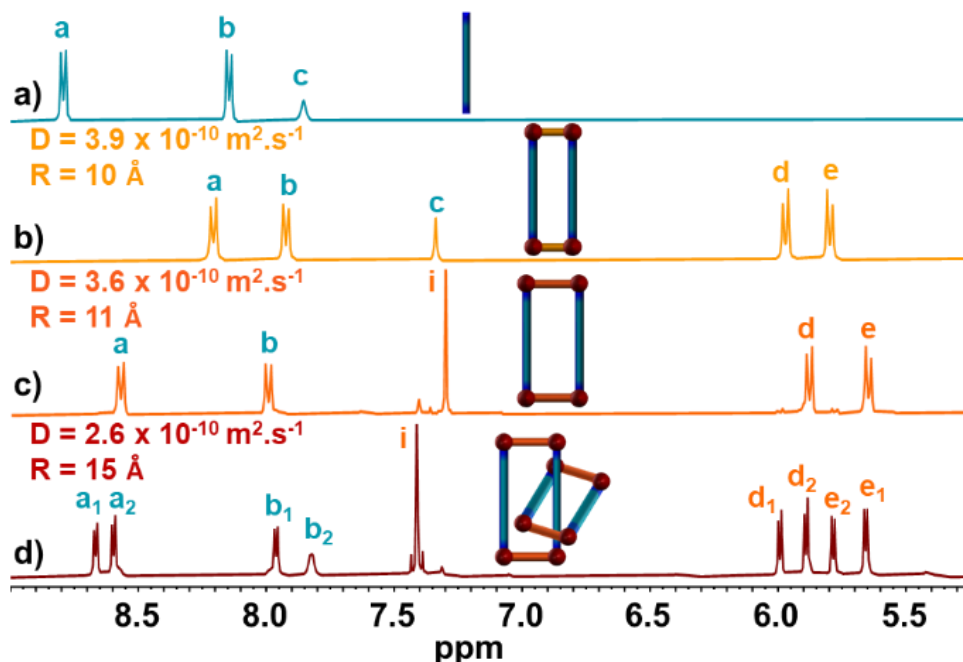


Figure 108. ¹H NMR (298 K, downfield region) of a) ligand **BBI** in DMSO-*d*₆, b) **Oxa₂BBI₂** in MeOD-*d*₄ ($C = 10^{-3}$ M), c) **Naph₂BBI₂** in MeOD-*d*₄ ($C = 10^{-3}$ M) and d) **(Naph₂BBI₂)₂** in MeOD-*d*₄ ($C = 4 \times 10^{-2}$ M). See Figure 107 for ¹H NMR assignments. D corresponds to the diffusion coefficient extracted from the ¹H DOSY NMR experiment and R to the corresponding hydrodynamic radius calculated from the Stokes-Einstein equation.

4. Characterization of metalla-structures Oxa₂BBI₂ and Naph₂BBI₂

Single crystals of both metalla-rectangles were obtained by liquid diffusion of MeOtBu into MeOH solutions ($C = 10^{-3}$ M) containing **Oxa₂BBI₂** and **Naph₂BBI₂** respectively. X-ray crystallography confirmed unambiguously their Ru_4L_2 stoichiometry (Figure 109). While both Ru atoms from a **RuOxa(OTf)₂** complex are separated by 5.5 \AA , π - π interactions occurring between facing benzodiimidazole moieties lead to an interplanar distance of only 3.4 \AA between the central BBI units. Consequently, a significant bending occurs around the peripheral pyridine units, with a torsion of ca. 12° of the BBI-Pyridine junction. In contrast, **Naph₂BBI₂** shows a quasi-rectangular solid structure. Here, the larger distance which separates both **BBI** ligands does not allow π - π interactions to occur between facing π -systems and is compensated by the accommodation of two Et₂O molecules in the central pocket.

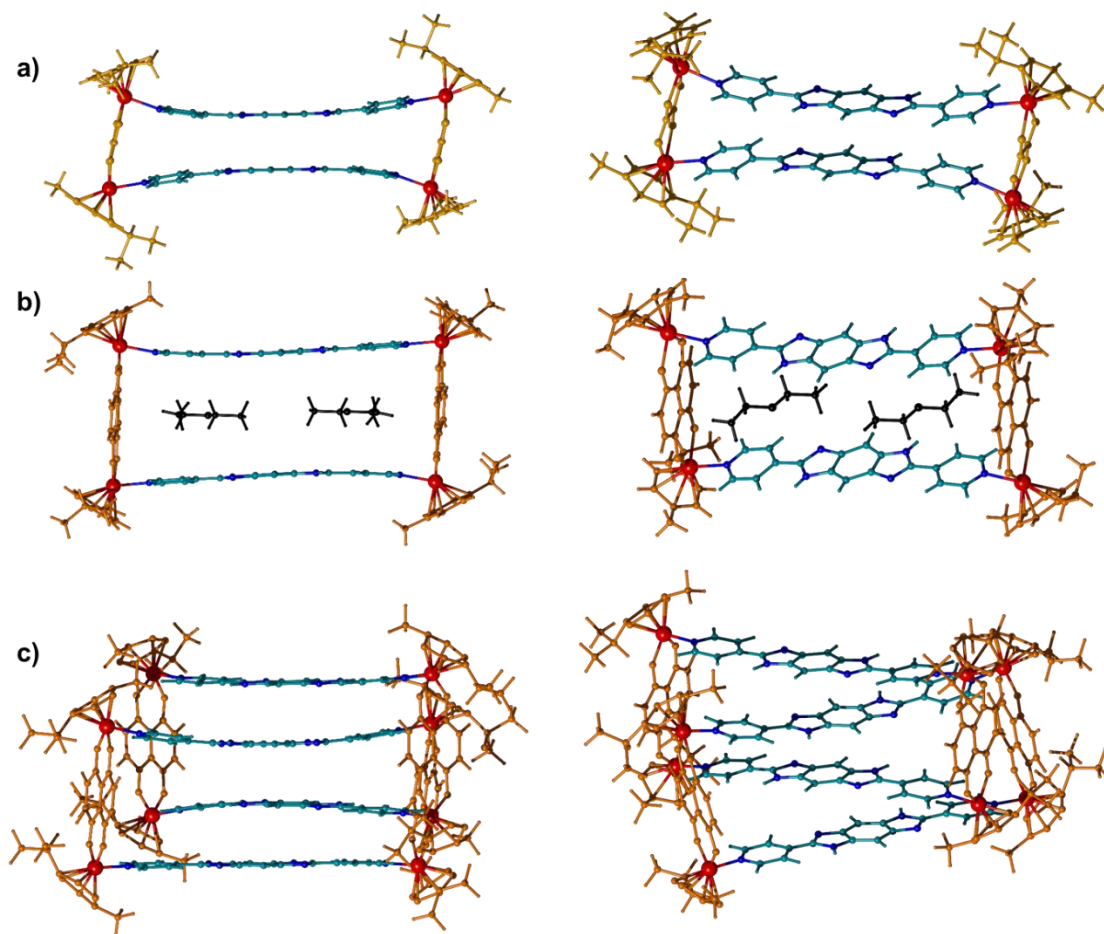


Figure 109. Single crystal X-ray diffraction structures of a) **Oxa₂BBI₂**, b) **Naph₂BBI₂** (including two solvent molecules, Et₂O) and c) MM+ simulation of **(Naph₂BBI₂)₂**. For a) and b) anions are omitted for clarity.

High resolution ESI-FTICR-HRMS spectrometry experiments were also carried out on **Oxa₂BBI₂** and **Naph₂BBI₂** in MeOH at $C = 2 \times 10^{-3}$ M. The reaction with **RuOxa(OTf)₂** shows only signals corresponding to the monomer system **Oxa₂BBI₂** at $m/z = 630.7315$ (3+) and 1020.5756 (2+) (Figure 110).

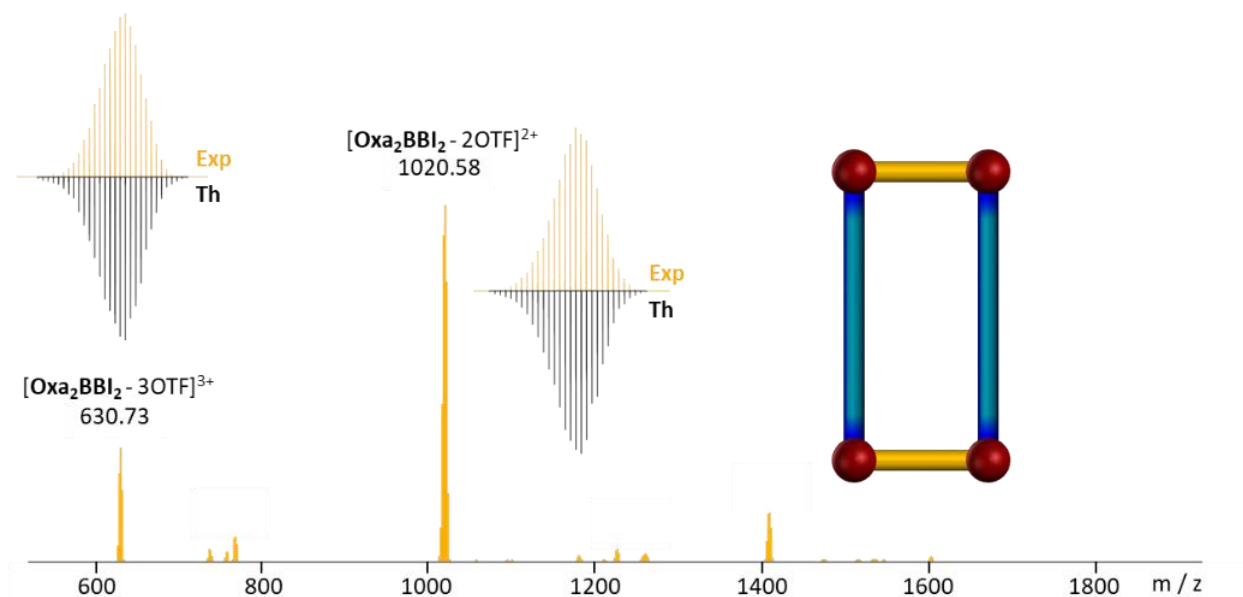


Figure 110. ESI-FTICR spectrum of **Oxa₂BBI₂** recorded in MeOH ($C = 2 \times 10^{-3}$ M).

The species isolated from the reaction with the larger **RuNaph(OTf)₂** acceptor exhibits, under the same conditions, two sets of signals (Figure 111). The latter correspond respectively to the monomeric metalla-rectangle **Naph₂BBI₂** with characteristic isotopic patterns at $m/z = 697.4194$ (3+) and 1120.6059 (2+) (main contributions), and a dimeric (**Naph₂BBI₂)₂** structure with signals recorded at $m/z = 1543.4649$ (3+) and 1120.6059 (4+) (main contribution). In all cases experimental isotopic distribution are in good agreement with theoretical ones.

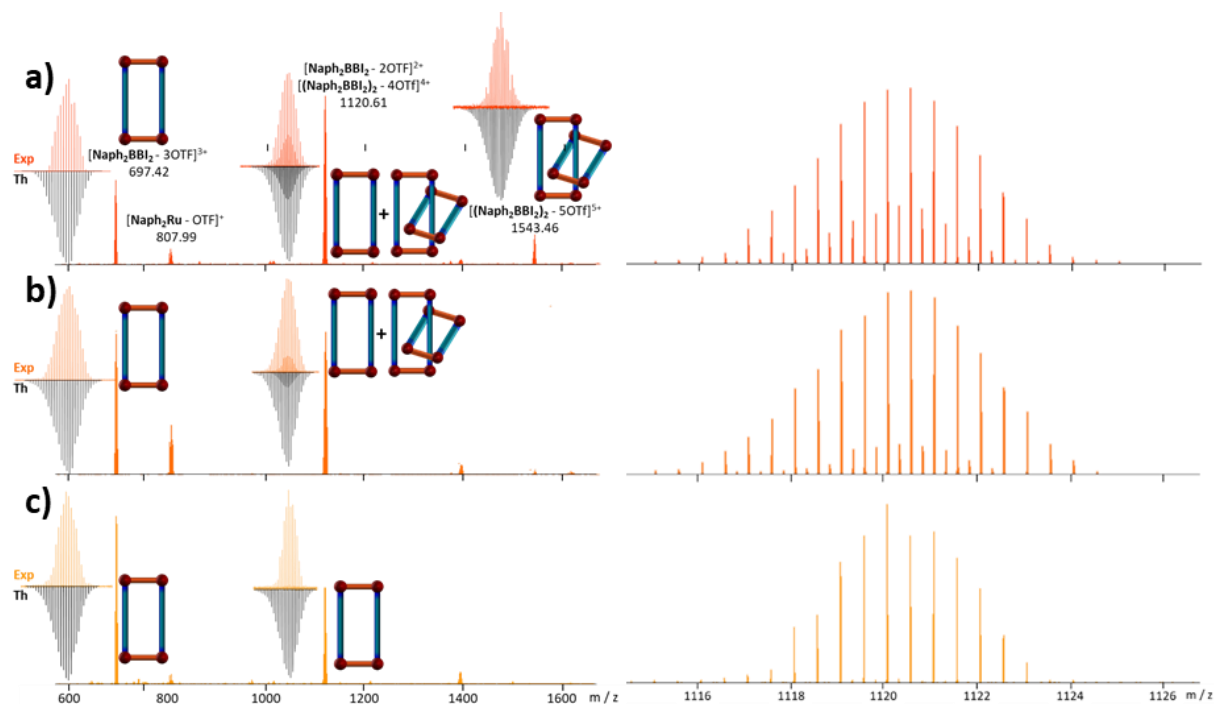
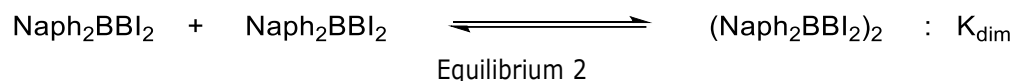


Figure 111. ESI-FTICR spectra of **Naph₂BBI₂** recorded in MeOH at a) $C = 2 \times 10^{-3}$ M, b) $C = 10^{-4}$ M and c) $C = 10^{-5}$ M (full spectra and $m/z = 1120$ region).

4.1. Interlocking properties of metalla-rectangle $\text{Naph}_2\text{BBI}_2$

On this basis, the ability of metalla-rectangle $\text{Naph}_2\text{BBI}_2$ to dimerize was further investigated by concentration dependent ^1H NMR. Following the Le Chatelier's principle, changing the concentration promotes the reversible conversion between the interlocked structure and the monomeric constitutive unit, thanks to the labile nature of the metal-ligand bonds and through-space interactions between the subunits.⁶⁵ While only one set of ^1H -NMR signals is observed at $C = 10^{-3}$ M (Figure 108c), the spectrum recorded at $C = 4 \times 10^{-2}$ M (Figure 108d) shows the splitting of the pyridines units (*a* and *b* protons), paracymene moieties (*d* and *e* protons) and Naphtoquinonato group (*i* protons) signals, in accordance with the quantitative formation of the dimeric interlocked species $(\text{Naph}_2\text{BBI}_2)_2$. The corresponding ^1H DOSY NMR (Figure S83 and Figure S84) measurement confirmed the larger size of the resulting structure with a calculated hydrodynamic radius of ca. 15 Å ($T = 298$ K). Formation of Borromean rings can be ruled out because of the non-symmetrical character of the ^1H -NMR spectra,⁶⁴ as well as by the distances ratio between the long and the short side of the metalla-rectangle, that does not match with the rules proposed by G.-X Jin.⁶⁵

The slow equilibrium between the monomer and the dimer species at the NMR timescale, allowed for a straightforward determination of the dimerization constant. Considering Equilibrium 2, which involves monomer $\text{Naph}_2\text{BBI}_2$ and dimer $(\text{Naph}_2\text{BBI}_2)_2$, one can express the concentration $[\text{Naph}_2\text{BBI}_2]$ as a function of the total concentration $C_0 = [\text{Naph}_2\text{BBI}_2] + 2 [(\text{Naph}_2\text{BBI}_2)_2]$ according to Equation 6.



$$[\text{Naph}_2\text{BBI}_2] = \frac{-1 + \sqrt{1 + 8K_{\text{dim}}C_0}}{4K_{\text{dim}}}$$

Equation 6

Variable concentration NMR experiments allowed determining the concentrations of dimer and monomer at different total concentrations C_0 (Figure 112a). Fitting these experimental data to Equation 6 affords the dimerization constant and the corresponding standard deviation $K_{\text{dim}} (\text{MeOD}) = 4.4 (\pm 0.2) \times 10^2$ (Figure 112b).^{135, 148}

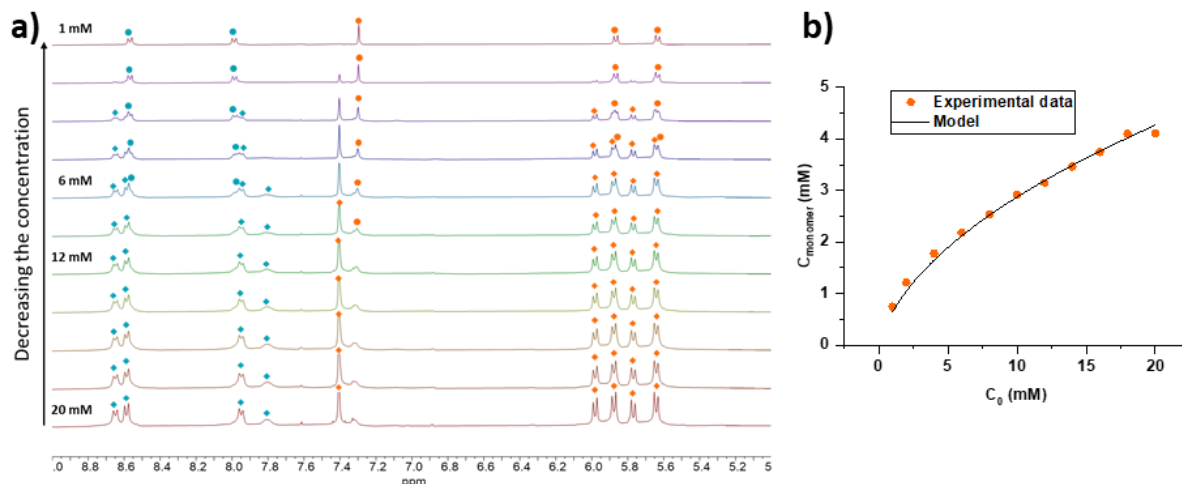


Figure 112. a) ^1H NMR spectra of a sequential dilution experiment of **(Naph₂BBI₂)₂** in MeOD- d_4 (Rhombuses and rounds correspond to **(Naph₂BBI₂)₂** and **Naph₂BBI₂** species respectively) b) Monomer **(Naph₂BBI₂)** concentration plot of a sequential dilution experiment of **(Naph₂BBI₂)₂** in MeOD- d_4 .

Despite numerous attempts, no crystal of **(Naph₂BBI₂)₂** of sufficient quality to be analyzed by X-ray diffraction has been obtained. Molecular force field (MM+) studies were therefore undertaken to determinate the structure of this interlocked species (Figure 109c). This modeling shows that the two metallacycles interlock without distortion with inter-ligand distances of about 3.4 Å as expected for such π - π stacking interactions.^{64, 135}

4.2. Complexation properties of Naph₂BBI₂ and (Naph₂BBI₂)₂ dissociation

The stability of the dimeric **(Naph₂BBI₂)₂** assembly was further investigated upon pyrene complexation. Such an electron rich planar species is expected to fill the cavity of the metalla-rectangle while interacting with both facing electron deficient benzobisimidazole units which are separated by a distance of 7.3 Å, to afford a more thermodynamically stable hot-guest complex. The progressive addition of pyrene to a solution of **(Naph₂BBI₂)₂** at 10^{-2} M in MeOD (Figure 113a) was followed by ^1H -NMR. Remarkably, addition of one equivalent of pyrene per metalla-rectangle unit, was sufficient to drastically simplify the NMR spectrum, a consequence of the dissociation of the dimeric structure. This is attributed to the intercalation of pyrene between both **BBI** panels of **Naph₂BBI₂** (Figure 124a). This was confirmed by a ^1H DOSY NMR measurement (Figure 113b) which demonstrate a higher diffusion value of the resulting species ($3.55 \times 10^{-10} \text{ m}^2 \cdot \text{s}^{-1}$) when compared with **(Naph₂BBI₂)₂**, a value which now corresponds to the one reported for isolated **Naph₂BBI₂** ring (Figure 108c).

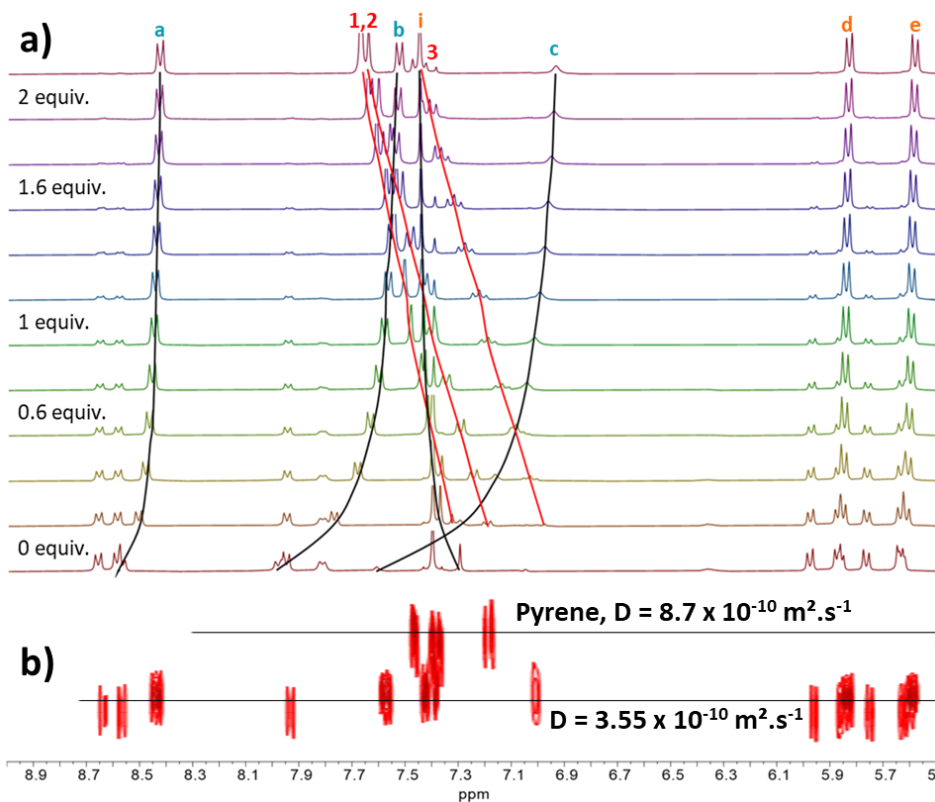


Figure 113. a) ^1H NMR spectra recorded upon progressive addition of a solution of pyrene ($C = 4 \times 10^{-2}$ M in MeOD- d_4) onto a solution of **Naph₂BBI₂** ($C = 10^{-2}$ M in MeOD- d_4), b) ^1H DOSY NMR spectrum of **Naph₂BBI₂** in MeOD- d_4 ($C = 10^{-2}$ M) in the presence of 1 equivalent of pyrene

The complexation capability of **Naph₂BBI₂** for pyrene was evaluated by a ^1H NMR Job Plot experiment (Figure 114a). The chemical shift of the proton "b" (see Figure 107) was plotted against the molar fraction of pyrene. The resulting graph has shown 1:1 stoichiometry of the resulting host-guest complex (Figure 114b).

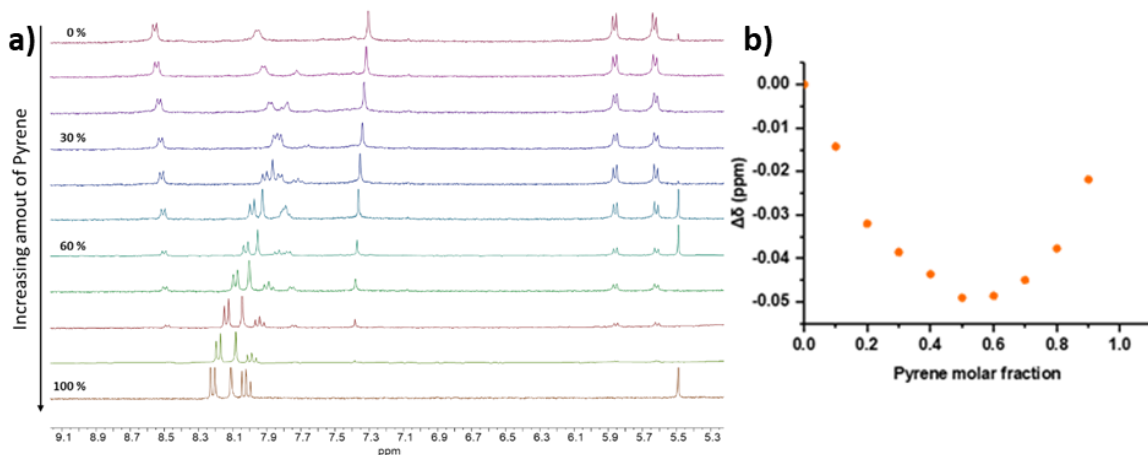


Figure 114. a) ^1H NMR spectra corresponding to the Job Plot analysis of pyrene with **Naph₂BBI₂** recorded at 298K in MeOD- d_4 ($C = 10^{-3}$ M) b) Job plot for complexation of receptor **Naph₂BBI₂** with pyrene determined by ^1H NMR in MeOD at $C = 10^{-3}$ M

To determine the association constant a titration experiment at $C = 10^{-3}$ M in MeOD was performed (Figure 115a).^{114, 131} To keep the host concentration constant the solution of **Naph₂BBI₂** was titrated with the solution of the same concentration of **Naph₂BBI₂** (10^{-3} M) and 10 times higher concentration of pyrene (10^{-2} M).

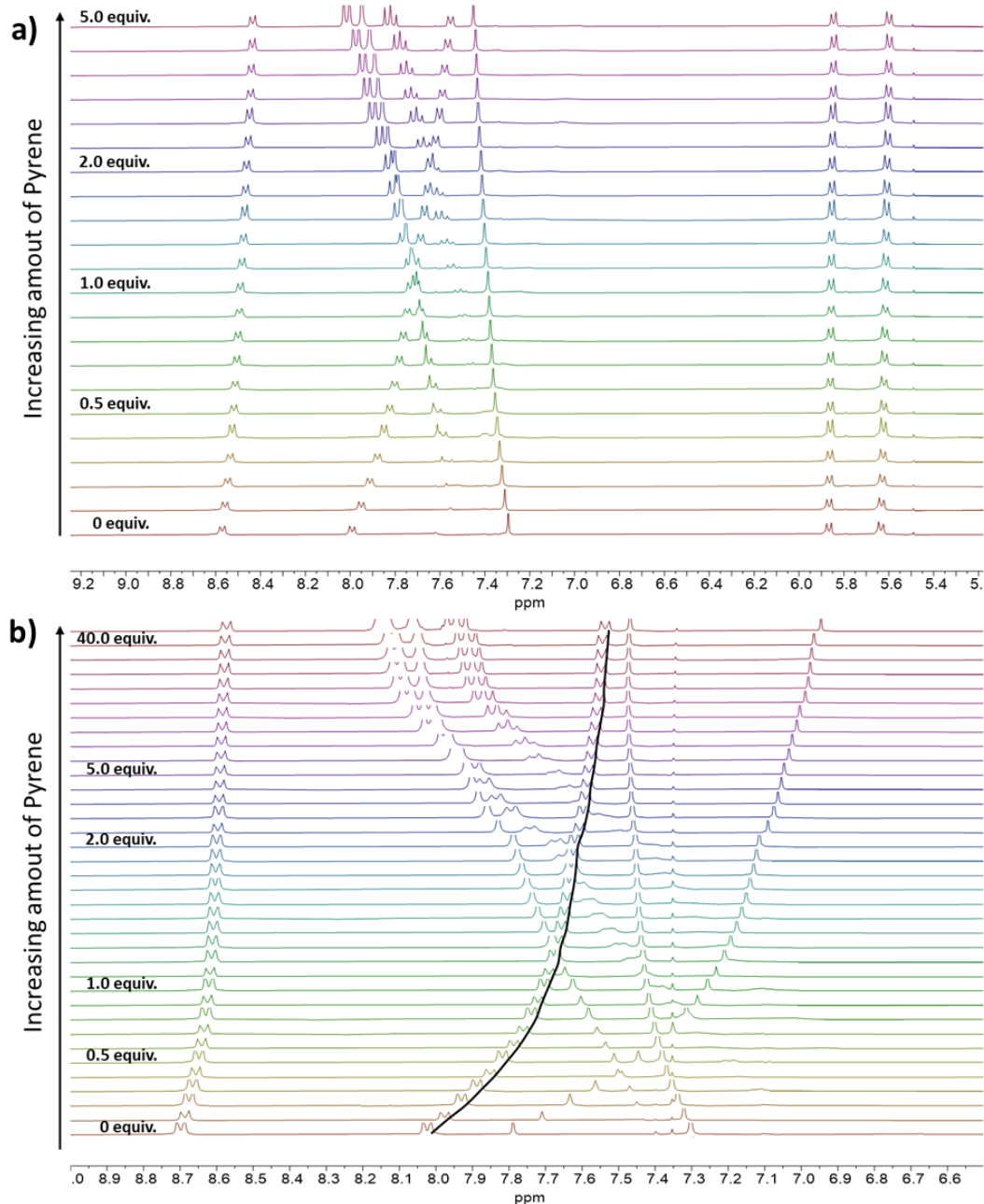
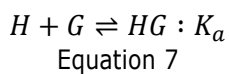


Figure 115. a) ¹H NMR titration experiment recorded in MeOD-*d*₄ by adding a solution of pyrene ($C = 10^{-2}$ M) and **Naph₂BBI₂** ($C = 10^{-3}$ M) onto a solution of **Naph₂BBI₂** ($C = 10^{-3}$ M), b) ¹H NMR titration experiment recorded in MeOD-*d*₄ by adding a solution of pyrene ($C = 10^{-2}$ M) and **Naph₂BBI₂H₄** ($C = 10^{-3}$ M) onto a solution of **Naph₂BBI₂H₄** ($C = 10^{-3}$ M).

In this way, the host concentration was maintained constant during the titration. In the case of a 1:1 complex, the equilibrium under consideration can be described by Equation 7:



The evolution of the chemical shift δ can be expressed according to Equation 8:

$$\delta = \delta_0 + (\delta_{inf} - \delta_0) * \frac{\left(1 + x + \frac{1}{C * K_a}\right) - \sqrt{\left(1 + x + \frac{1}{C * K_a}\right)^2 - 4 * x}}{2}$$

Equation 8

where δ_0 and δ_{inf} are the chemical shifts of host signal and the host-guest association signal, respectively, x is the number of equivalents of guest (pyrene) in solution, K_a is the binding constant and C the constant concentration of host. This theoretical equation was fitted to the corresponding experimental data with the least squares method, affording an evaluation of the desired binding constant. These measurements revealed the complexation of one pyrene unit in the cavity of **Naph₂BBI₂** with an association constant $K_a = 3.0 \pm 0.2 \times 10^3$ (Figure 116).

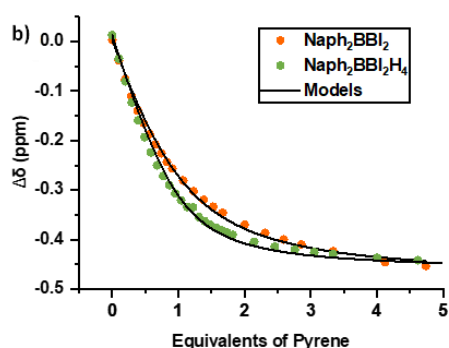


Figure 116. plots of chemical shifts of a ¹H NMR titration for complexation of receptors **Naph₂BBI₂** and **Naph₂BBI₂H₄** in MeOD at $C = 10^{-3}$ M with pyrene. Chemical shifts related to protons b.

4.3. Optical properties of ligand BBI, metalla-structures Oxa₂BBI₂ and Naph₂BBI₂

The optical properties of the ligand and both metalla-macrocycles were then investigated in methanol solutions. While **BBI** shows an absorption maximum at 358 nm (Figure 5a), the corresponding ligand-centered transitions are found at 393 and 386 nm for **Oxa₂BBI₂** and **Naph₂BBI₂**, respectively. These bands show more than doubled molar extinction coefficients ($89\,000 < \epsilon < 101\,000 \text{ M}^{-1} \text{ cm}^{-1}$) compared to the free ligand ($\epsilon = 38\,000 \text{ M}^{-1} \text{ cm}^{-1}$). The red shift triggered by the coordination of the terminal pyridine units to Ruthenium atoms is consistent with the one measured upon protonation of the **BBI** ligand in acidic medium ($\lambda_{\text{max}} = 386 \text{ nm}$, Figure 117a). To gain information into the stability of the complexes, their electronic absorption spectra were monitored over time at different concentrations (Figure 117b,c). At $C = 2 \times 10^{-4}$ M, both **Oxa₂BBI₂** and **Naph₂BBI₂** complexes show unaltered absorptions after several days in solution. In contrast, for $C \leq 2 \times 10^{-5}$ M, an hypsochromic shift is observed after 24 h, corresponding to the release of uncomplexed ligand in solution.

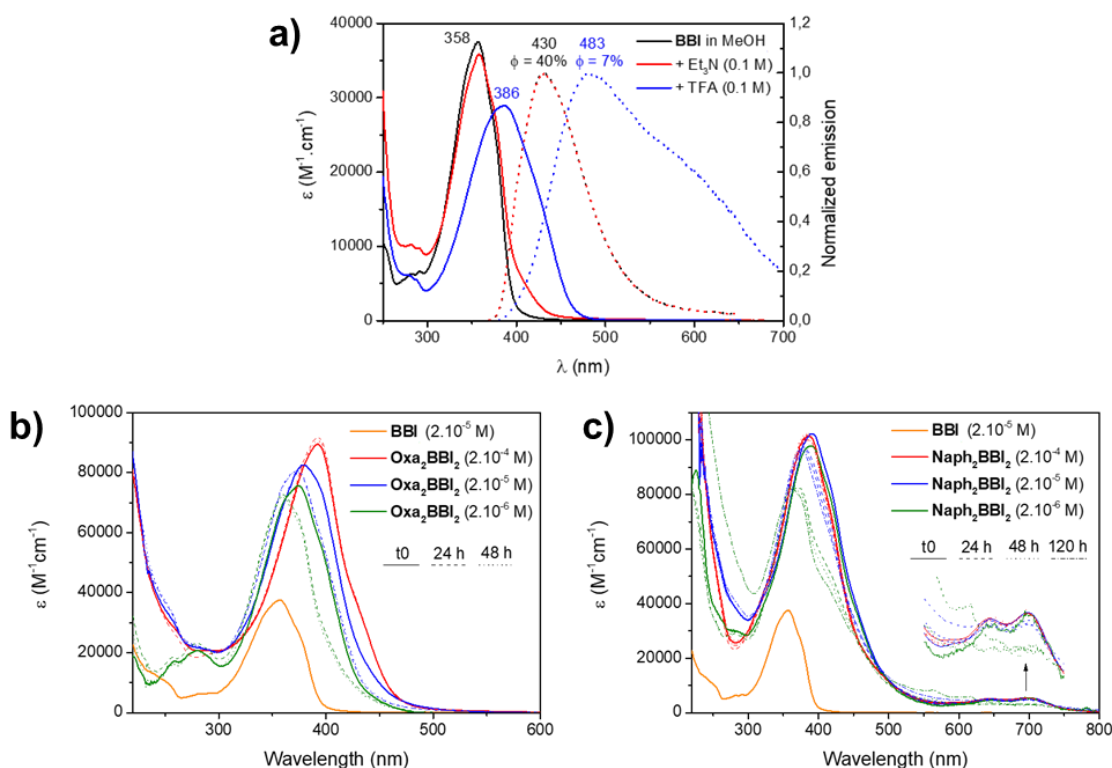


Figure 117. a) Electronic absorption (plain lines) and fluorescence (dotted lines) spectra of **BBI** in basic (0.1 M triethylamine), neutral or acidic (0.1 M trifluoroacetic acid) methanol solutions, Evolution of the electronic absorption of **Oxa₂BBI₂** (b) and **Naph₂BBI₂** (c) in methanol solutions at different concentrations.

A strong emission of the **BBI** ligand was measured in the UV-blue region (Figure 118), with a maximum centered at 430 nm and a fluorescence quantum yield of 40%. For both metalla-macrocycles recorded in fresh solutions at $C = 2 \times 10^{-5}$ M, weaker emissions are observed at around 460 nm, which is consistent with the fluorescence of recently reported tetranuclear Zn-benzobisimidazoles grid complexes.¹⁶⁵

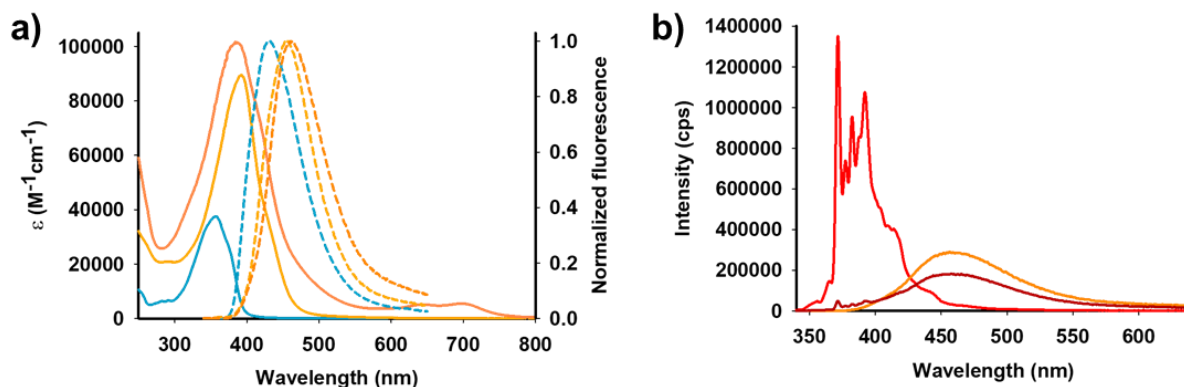


Figure 118. a) Electronic absorption (solid line) and emission (dashed line) spectra of **BBI** ($C = 2 \times 10^{-5}$ M), **Oxa₂BBI₂** and **Naph₂BBI₂** ($C = 2 \times 10^{-4}$ M for absorption and $C = 2 \times 10^{-5}$ M for emission) in methanol and b) fluorescence spectra recorded under the same experimental conditions of pyrene, **Naph₂BBI₂** and 1:1 mixture of both compounds in methanol ($C = 2 \times 10^{-5}$ M and $\lambda_{ex} = 330$ nm).

However, when decreasing the concentration to $C = 10^{-6}$ M, the emission is blue-shifted to 430 nm and most likely corresponds to the free ligand in solution (Figure 119) as already observed by absorption spectrophotometry. No quantum yield could be accurately determined due to the poor stability of the complexes at the concentration requested for the measurements.

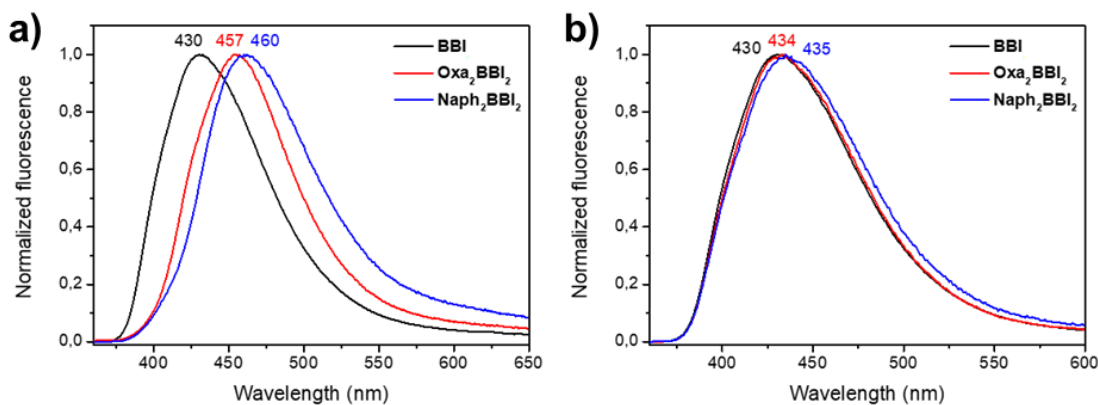


Figure 119. Normalized fluorescence spectra of **BBI**, **Oxa₂BBI₂** and **Naph₂BBI₂** at concentrations of 2×10^{-5} M (a) and 10^{-6} M (b) in methanol solutions.

Complexation properties of **Naph₂BBI₂** were further investigated by UV-vis and fluorescence spectroscopy. The absorption and emission spectra of 1:1 mixture solutions of **BBI**, **Oxa₂BBI₂** or **Naph₂BBI₂** with pyrene were compared at $C = 2 \times 10^{-5}$ M (Figure 118b, Figure 120). As expected, all absorption spectra show an additive effect between the two constituents. On the other hand, while the emission spectra corresponding to the mixture of **Naph₂BBI₂** and pyrene reveal a quasi-complete quenching of the pyrene emission (85 % decrease in the total fluorescence), a much weaker decrease of 21% and 33% is observed in the presence of **Oxa₂BBI₂** or **BBI** ligand respectively (Figure 118b and Figure 120) illustrating the interaction of pyrene with the cavity of **Naph₂BBI₂**. Decrease in emission was evaluated by comparing the emission area of a 1:1 mixture of pyrene and **BBI**, **Oxa₂BBI₂** or **Naph₂BBI₂**, with the addition of emission areas of pyrene and **BBI**, **Oxa₂BBI₂** and **Naph₂BBI₂**, respectively, recorded in the same conditions.

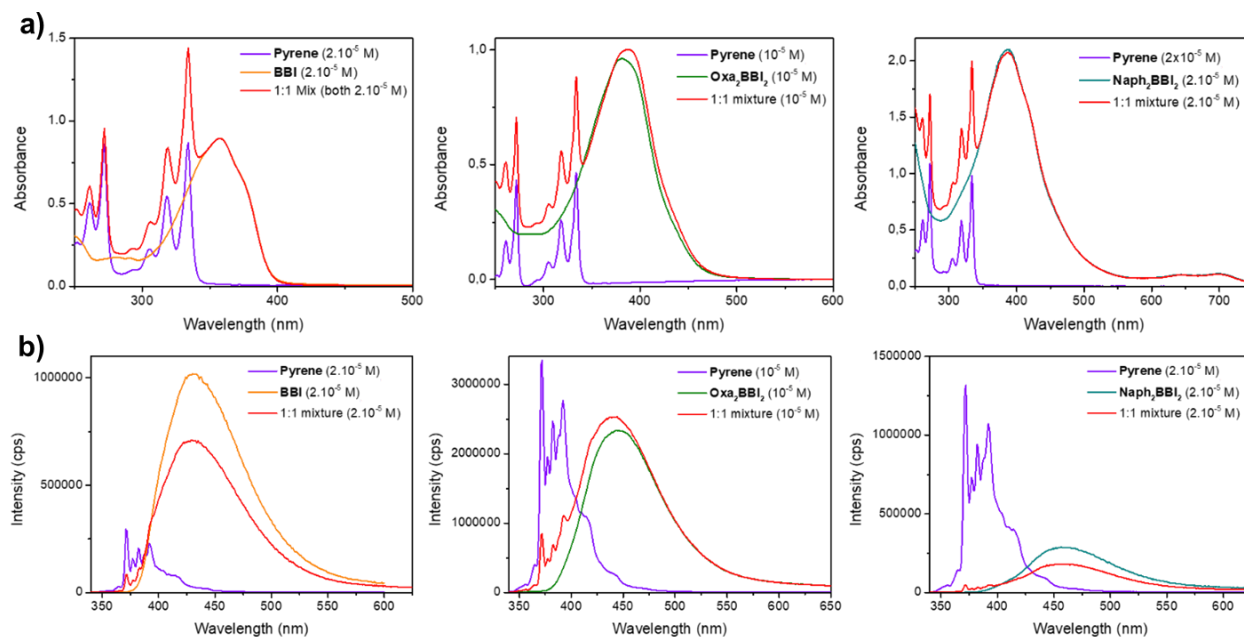


Figure 120. a) Electronic absorption spectra of **pyrene** compared to **BBI** (left), metalla-macrocycles (center: **Oxa₂BBI₂**, right: **Naph₂BBI₂**) and 1:1 mixtures of the compounds and pyrene in methanol, b) Fluorescence spectra of **pyrene** compared to **BBI** (right), **Oxa₂BBI₂** (center) or **Naph₂BBI₂** (right) and 1:1 mixtures of the compounds and pyrene in methanol solutions, upon the same recording conditions ($\lambda_{\text{ex}} = 330 \text{ nm}$).

4.4. Acid-base properties of the BBI ligand and the Naph₂BBI₂ metalla-rectangle

4.4.1. BBI ligand

The acid-base properties of the **BBI** ligand and the **Naph₂BBI₂** metalla-rectangle were then investigated using UV-visible absorption titrations as a function of pH (Figure 121 - Figure 123). This work has been done by Mourad Elhabiri and Valerie Mazan (ECPM Strasbourg). The **BBI** ligand is characterized by 6 pH sensitive reactive sites, i.e. two on each imidazole units and one per pyridyl fragment (Scheme 11).

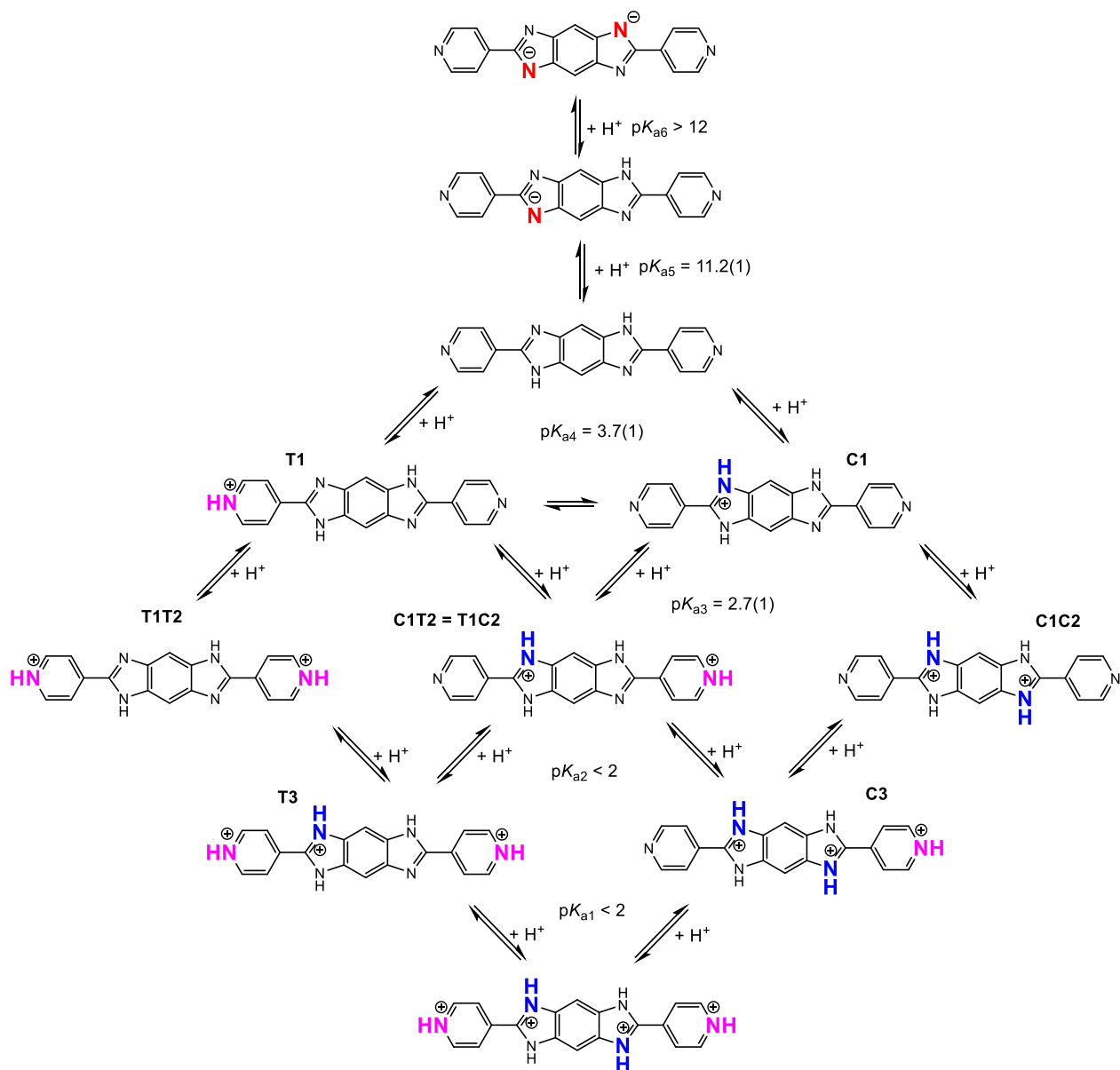


Figure 121 illustrates the spectral variations recorded during absorption spectrophotometric titration of **BBI** as a function of pH, which are in agreement with reported results on 4-pyridylbenzimidazole (4PBI).¹⁶⁶⁻¹⁶⁹ Under neutral pH conditions (MeOH/H₂O 80/20 w/w, Figure 121), **BBI** is characterized by an intense absorption band in the UV region centered at 357 nm ($\epsilon^{357} = 3.50 \times 10^4 \text{ M}^{-1} \text{ cm}^{-1}$) in agreement with the data recorded in methanol. Increasing the pH from ~6.5 to ~11.9 induces a bathochromic shift of 23 nm of the n-n* transitions. The statistical processing of these data led to the determination of a pKa value of 11.2 ± 0.1 that is ascribed to the deprotonation of one of the two N1-imidazole sites (i.e., the pKa value for the deprotonation of the second N1-H function was estimated to be > 12 and could not be determined under our experimental conditions). On the other hand, the decrease in pH from ~6 to ~2.3 also leads to a bathochromic shift. Two pKa values of 3.7 ± 0.1 and 2.7 ± 0.1 were calculated (Figure S38). The two other pKa values were estimated to be < 2 in agreement with repulsive interactions between the various positively charged species.

The neutral **BBI** ligand thus predominates over a broad range of pH (from ~4.5 to ~10.2) and can lead to **BBI**⁴⁺ and **BBI**²⁻ under strongly acidic and basic conditions, respectively.

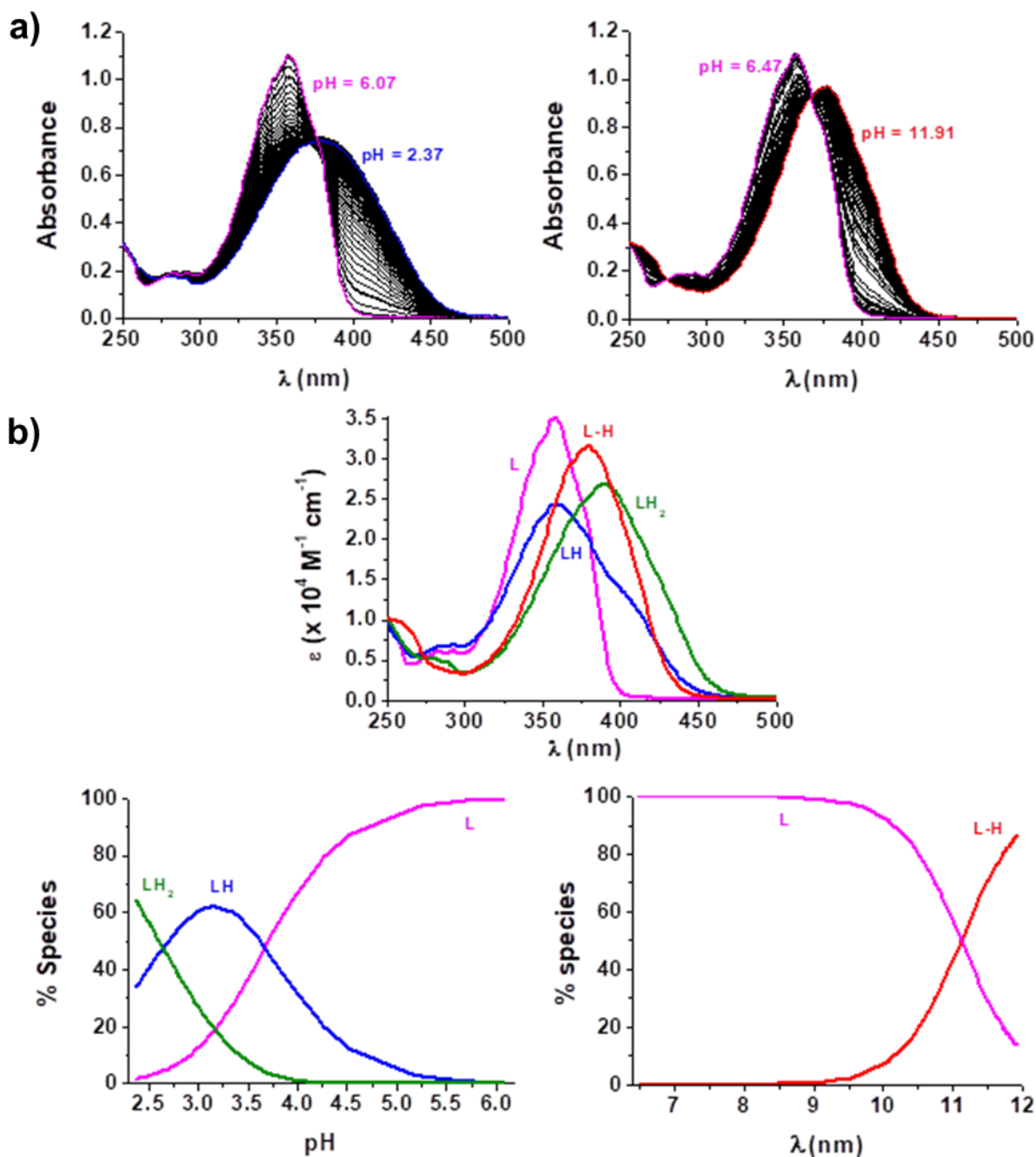


Figure 121. a) UV-visible absorption spectrophotometric titrations of **BBI** as a function of pH. Solvent: MeOH/H₂O (80/20 w/w), I = 0.1 M (NBu₄ClO₄), T = 25.0°C, (left) [**BBI**] = 3.13 × 10⁻⁵ M, (right) [**BBI**] = 3.26 × 10⁻⁵ M. The absorption spectra have not been corrected from dilution effects, b) (top) UV-visible electronic absorption spectra of the protonated species derived from **BBI** and (bottom) distribution diagrams of the protonated species of **BBI** as a function of pH. Solvent: MeOH/H₂O (80/20 w/w), I = 0.1 M (NBu₄ClO₄), T = 25.0°C. **L** stands for **BBI**. The charges have been omitted for the sake of clarity.

4.4.2. Naph₂BBI₂ metalla-rectangle

Since protons can compete for Lewis base pyridine sites in coordination self-assembled structures, acidic conditions often lead to a disassembly process.^{80, 158-163} We therefore investigated the pH-responsive behavior of the **Naph₂BBI₂** metalla-rectangle with the hypothesis that the presence of the imidazole moieties would allow for a selective protonation of the ligands without disassembly. Under neutral pH conditions (MeOH/H₂O 80/20 w/w), **Naph₂BBI₂** is characterized by an intense absorption in the UV region centered at 386 nm ($\epsilon^{386} = 8.88 \times 10^4 \text{ M}^{-1} \text{ cm}^{-1}$) assigned to π - π^* ligand-localized transitions as well as a set of much weaker absorptions at 643 and 693 nm that correspond to LMCT transitions (i.e., signature of the metalla-rectangle).¹⁴⁷ Upon complexation to **RuNaph₂**, the n - π^* transitions of the two **BBI** ligands undergo significant bathochromic and hyperchromic shifts ($\Delta\lambda \sim 29 \text{ nm}$; **BBI**: $\epsilon^{357} = 3.50 \times 10^4 \text{ M}^{-1} \text{ cm}^{-1}$; **Naph₂BBI₂**: $\epsilon^{386} = 8.88 \times 10^4 \text{ M}^{-1} \text{ cm}^{-1}$). Similarly to the observations in MeOH, the effect of complexation to the Ru centers by the terminal pyridines is comparable to that of their protonation (Figure 122, $\lambda = 389 \text{ nm}$ and $\epsilon^{389} = 2.68 \times 10^4 \text{ M}^{-1} \text{ cm}^{-1}$).

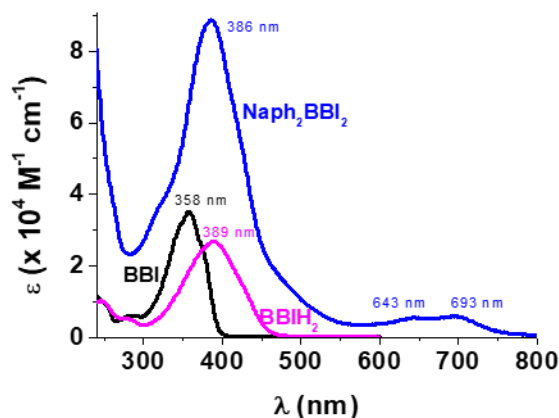


Figure 122. Comparison of the electronic absorption spectra of **BBI** and **Naph₂BBI₂** recorded under neutral pH conditions. Solvent: MeOH/H₂O (80/20 w/w), I = 0.1 M (NBu₄ClO₄), T = 25.0°C.

The absorption *versus* pH titrations demonstrate that no decomposition of **Naph₂BBI₂** occurs over a large range of pH (2.20 – 12.05) as assessed by the ongoing presence of the LMCT signature. The statistical analysis of the data allowed evidencing two pH regions of interest (Figure 123). Under strongly acidic conditions, the **Naph₂BBI₂** metalla-rectangle can undergo four protonation equilibria at its four equivalent N3-imidazole sites and three protonation constants could be accurately determined ($pK_{a4} = 2.7 \pm 0.2$ and $pK_{a3} + pK_{a2} = 4.5 \pm 0.2$). The protonation of these units results in only small spectral variations both of the n - π^* and LMCT transitions. In addition, the calculated pK_a values are lowered compared to those of the free **BBI** ligand ($pK_{a3} = 2.7 \pm 0.1$ and $pK_{a4} = 3.7 \pm 0.1$) due to the coordination of the pyridine units to the **RuNaph₂** metal centers.

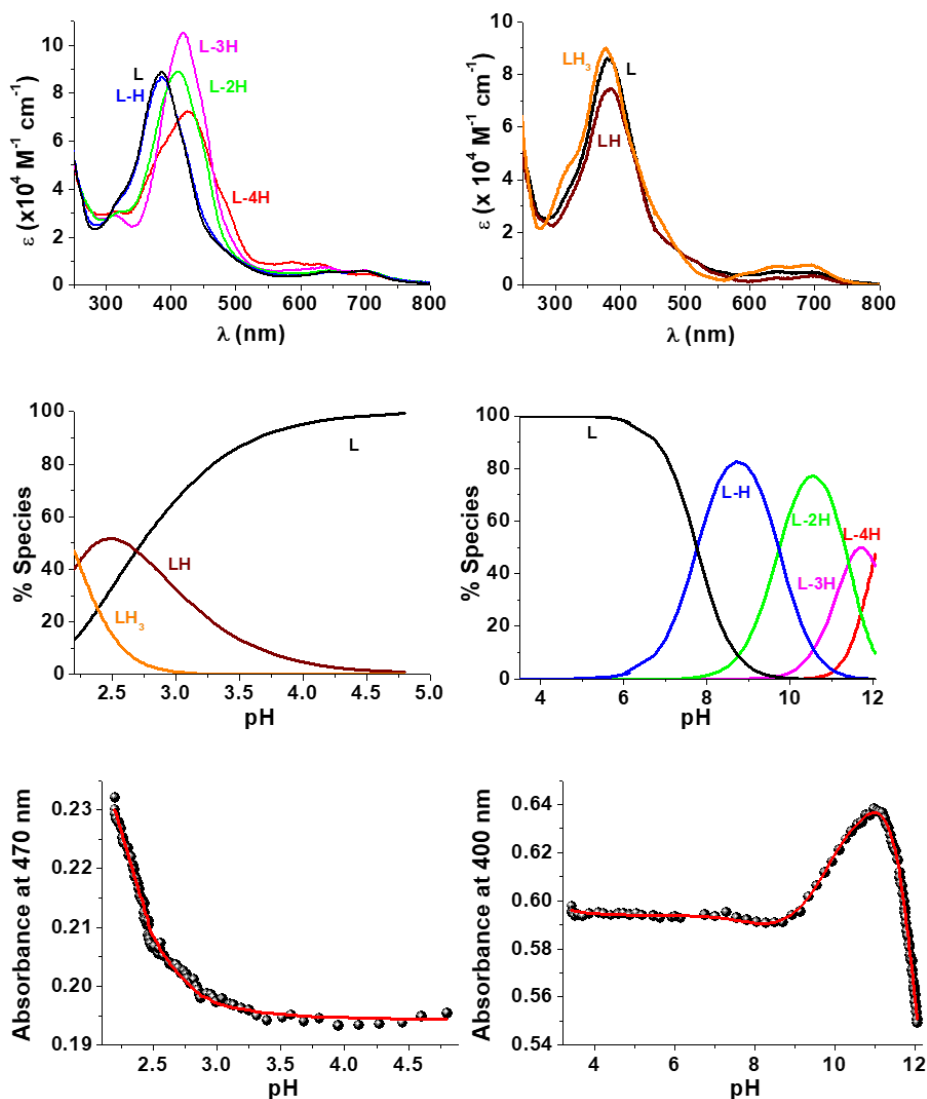
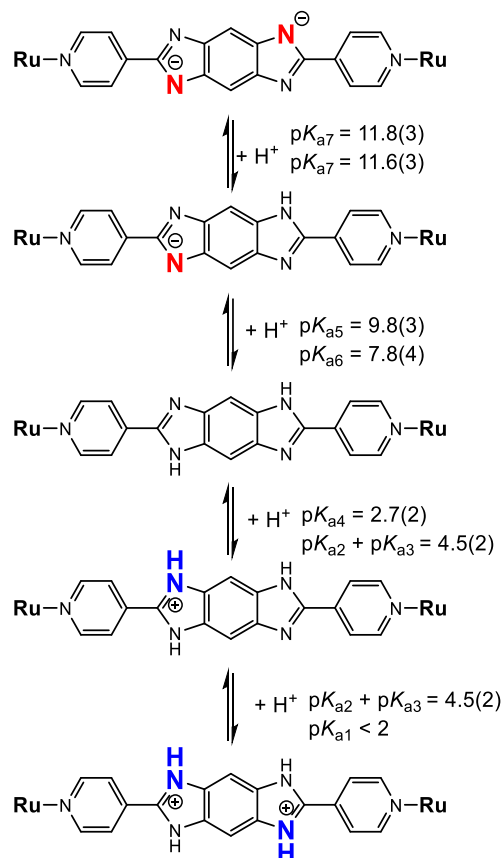


Figure 123. (top) UV-visible electronic absorption spectra of the protonated species derived from **Naph₂BBI₂**, (middle) distribution diagrams of the protonated species of **BBI** as a function of pH and (bottom) variation of the absorbances at 470 and 400 nm as a function of pH. Solvent: MeOH/H₂O (80/20 w/w), I = 0.1 M (NBu₄ClO₄), T = 25.0°C. **L** stands for **Naph₂BBI₂**. The charges have been omitted for the sake of clarity.

These data therefore demonstrate that the **Naph₂BBI₂** meta-rectangle can undergo stepwise protonation on each of its N₃-imidazole units without any apparent signs of structural disassembly. Likewise, each of the N₁-imidazole units can undergo a deprotonation reaction without also affecting the architecture of the metallo-rectangle itself. Four deprotonation constants were determined under basic conditions (Scheme 12). In contrast to acidic conditions, deprotonation of N₁-imidazole units is accompanied by strong spectral variations in both intra-ligand π - π^* transitions ($\lambda = 426$ nm and $\epsilon^{426} = 7.22 \times 10^4$ M⁻¹ cm⁻¹ for **Naph₂BBI₂-4H**) and LMCT transitions (hypsochromic shifts of ~60 nm; Figure 123).



Scheme 12. Possible protonation equilibria that can take place within the **Naph₂BBI₂** metalla-rectangle. Errors on the pK_a values = 3σ with σ = standard deviation. Only one **BBI** ligand is depicted and the two pK_a values correspond to the two face-to-face **BBI** ligands within the **Naph₂BBI₂** assembly.

4.5. pH-controlled dissociation of catenane (**Naph₂BBI₂**)₂

On the basis of this in-depth investigation and considering the stability of cage **Naph₂BBI₂** in acidic media, we investigated by ¹H NMR and DOSY NMR the behavior of interlocked (**Naph₂BBI₂**)₂ in presence of trifluoromethanesulfonic acid (HOTf). We hypothesized that protonation of the **BBI** moieties may lead to intermolecular electrostatic repulsions that could strongly affect the stability of the interlocked structure. Remarkably, addition of HOTf (6 equiv.) into a solution of (**Naph₂BBI₂**)₂ in MeOD at C = 2 × 10⁻² M produces quantitatively a new species (Figure 124c). The latter shows a higher D value and non-splitting NMR signals that are downfield shifted in comparison to those of the dimeric structure (Figure 124b). These NMR characteristics support the dissociation of the protonated (**Naph₂BBI₂**)₂ interlocked dimer and formation of the **Naph₂BBI₂H₄** monomer.

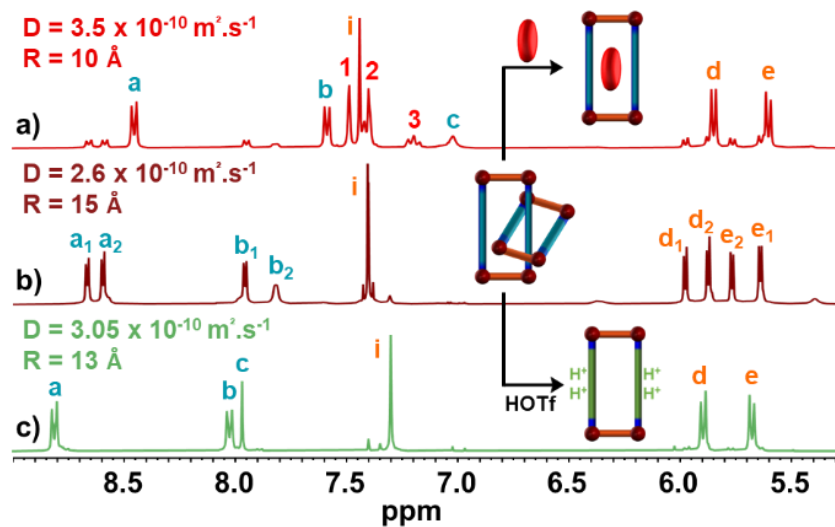


Figure 124. ^1H NMR spectra recorded in MeOD at $C = 2 \times 10^{-2}$ M of a) $(\text{Naph}_2\text{BBI}_2)_2$ in presence of 1 equiv. of pyrene, b) $(\text{Naph}_2\text{BBI}_2)_2$ and c) $(\text{Naph}_2\text{BBI}_2)_2$ in presence of 6 equiv. of HOTf.

This was unambiguously demonstrated through a comparative NMR study with $\text{Naph}_2\text{BBI}_2$ recorded in a 0.12 M solution of HOTf in MeOD at $C = 10^{-3}$ M (Figure 125.e) and $C = 0.02$ M (Figure 125.f). As can be seen from the experimental data, the chemical shifts of the self-assembly at different concentrations are the same in the equal media.

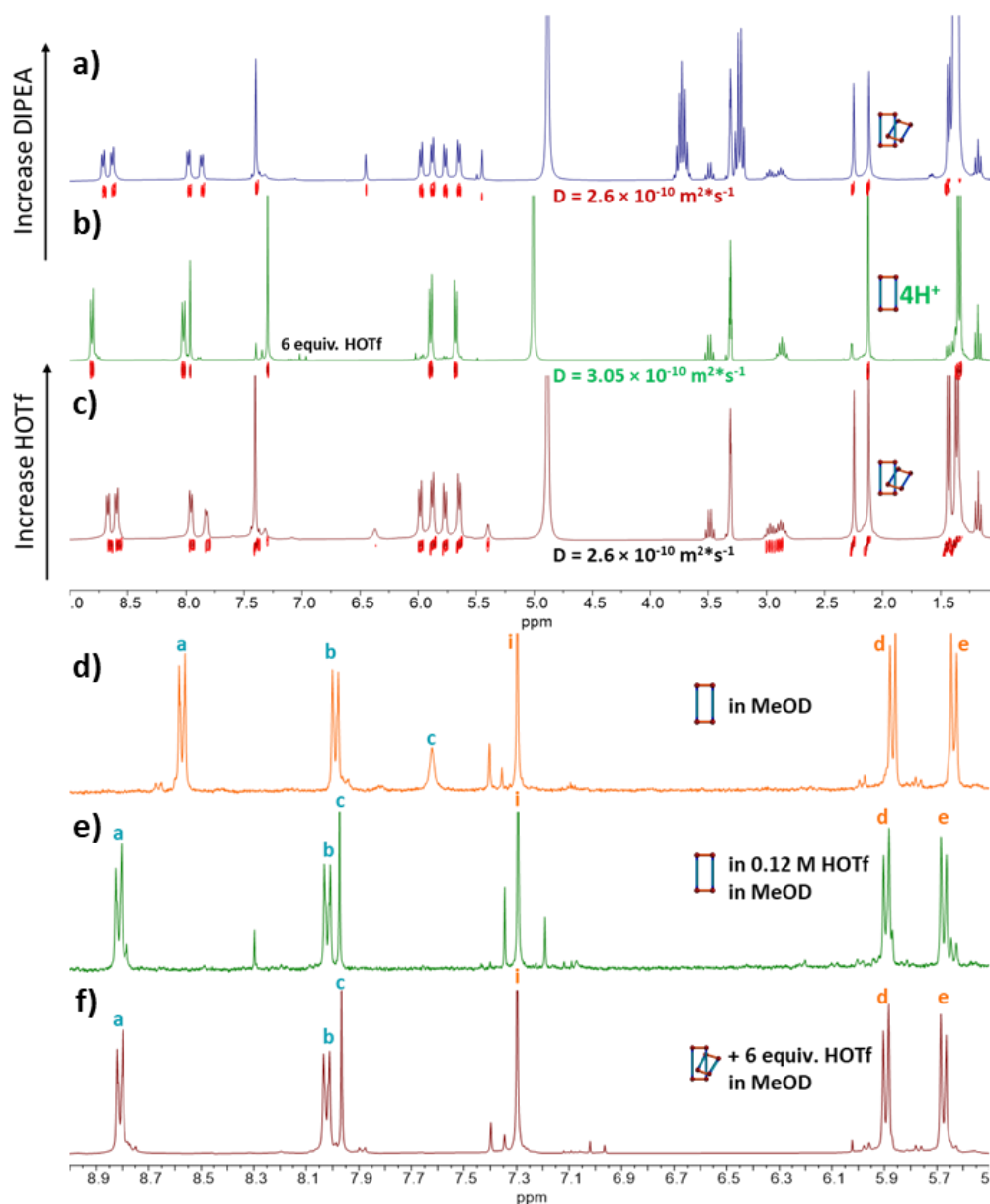


Figure 125. ^1H NMR spectra of a) **Naph₂BBI₂** ($C = 0.02$ M in MeOD- d_4), b) solution (a) after addition of a solution of HOTf ($C = 0.5$ M in MeOD- d_4 , 6 equiv.), c) solution (b) after addition of a solution of diisopropylethylamine ($C = 0.5$ M in MeOD- d_4 , 6 equiv.), d) **Naph₂BBI₂** ($C = 10^{-3}$ M in MeOD- d_4), e) **Naph₂BBI₂** ($C = 10^{-3}$ M in a 0.12 M solution of HOTf in MeOD- d_4) and f) **(Naph₂BBI₂)₂** ($C = 0.02$ M in a 0.12 M solution of HOTf in MeOD- d_4).

The ESI FTICR HRMS measurements have shown the characteristic peaks of monoprotonated species at $m/z = 1345.5436$ (2+) and diprotonated one at $m/z = 960.0010$ (3+) and 1420.4247 (2+) (Figure 126.). Finally, it is worth noting that this original dissociation phenomenon is reversible, since addition of 6 equivalents of diisopropylethylamine (DIPEA) reforms quantitatively the starting interlocked species (Figure 125.a).

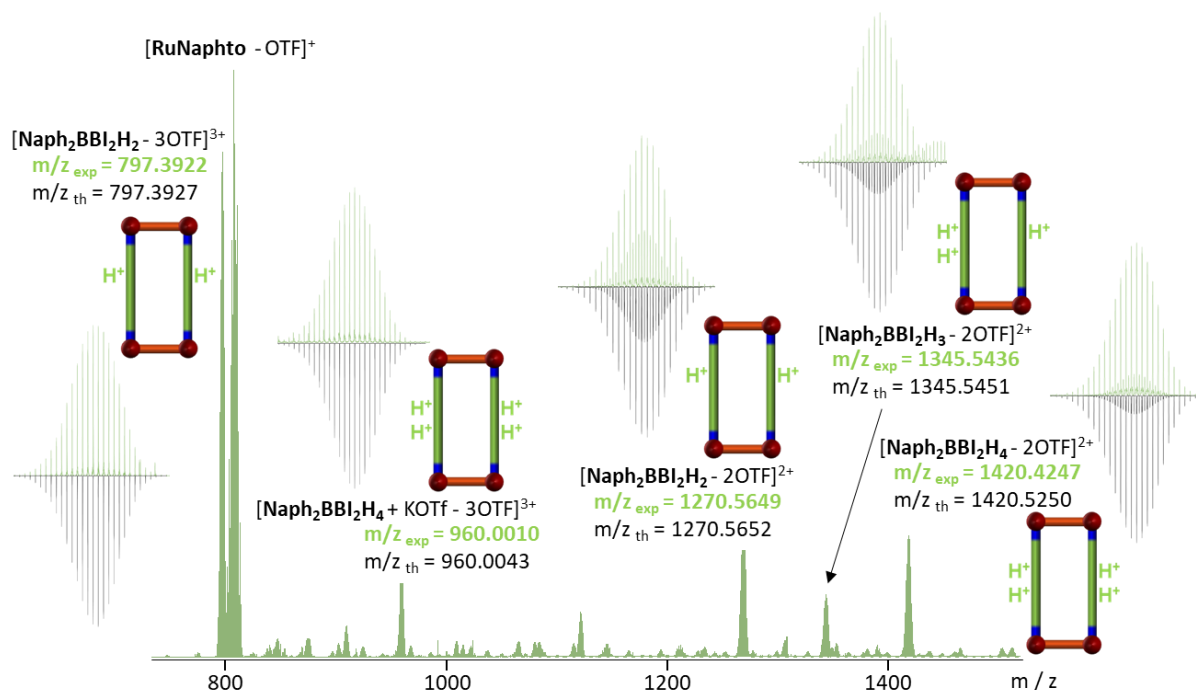


Figure 126. ESI-FTICR spectra of **Naph₂BBI₂** recorded in MeOH at $C = 2 \times 10^{-3}$ M in presence of 6 equivalents of HOTf per metallacycle (full spectra).

4.6. Complexation properties of **Naph₂BBI₂H₄**

Finally, we investigated the complexation ability of **Naph₂BBI₂H₄** toward the electron rich pyrene unit. In order to determine the binding constants, NMR titration experiments were led in methanol-*d*₄ by adding a solution of pyrene (10^{-2} M) and the desired complex (10^{-3} M) onto a solution of pure complex (10^{-3} M). Since protonation of the BBI units increases their electron deficient character, we expected **Naph₂BBI₂H₄** to be a better host for pyrene than **Naph₂BBI₂**. This was confirmed by an NMR titration recorded at $C = 10^{-3}$ M in a solution of HOTf ($C = 6 \times 10^{-3}$ M) in MeOD (Figure 116b). An association constant $K_a = 1.32 \pm 0.09 \times 10^4$ was measured, a value four times higher than the one calculated with the non-protonated **Naph₂BBI₂** host analog. Interestingly, this tunable binding affinity can be followed by ¹H NMR and DOSY NMR upon successive addition of HOTf and DIPEA (Figure 127.).

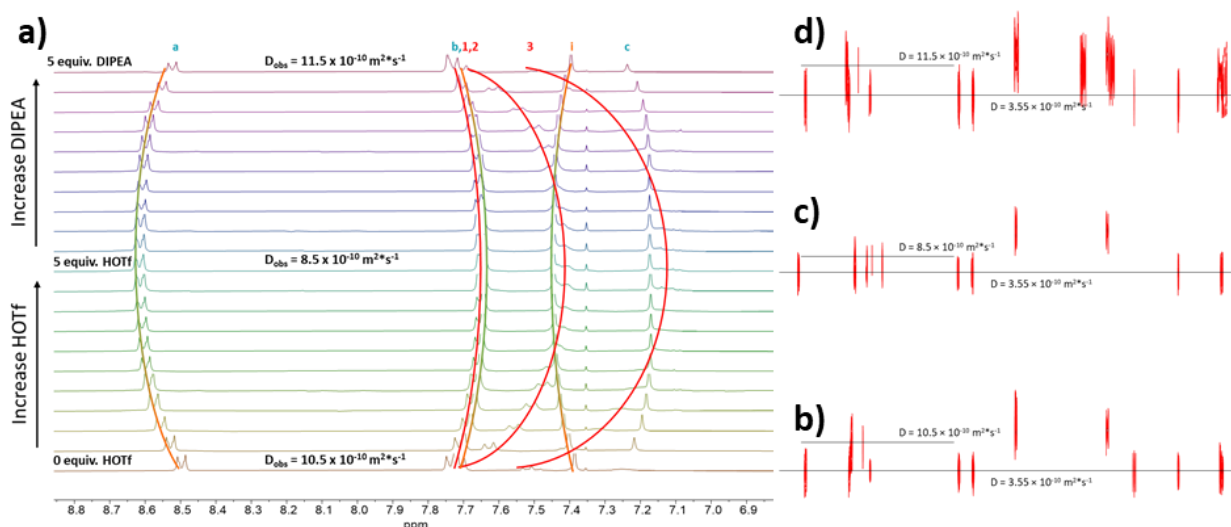


Figure 127. a) Subsequent addition of HOTf ($C = 0.05\text{M}$ in MeOD-d_4 , 5 equiv.) and diisopropylethylamine ($C = 0.05\text{M}$ in MeOD-d_4 , 5 equiv.) onto a solution of **Naph₂BBI₂** ($C = 10^{-3}\text{ M}$ in MeOD-d_4) containing 1 equivalent of pyrene, ^1H DOSY NMR spectrum of **Naph₂BBI₂** in MeOD-d_4 ($C = 10^{-3}\text{ M}$) in the presence of b) 1 equivalent of pyrene, c) 1 equivalent of pyrene and 5 equivalents of HOTf, and d) 1 equivalent of pyrene after subsequent addition of 5 equivalents HOTf and 5 equivalents of DIPEA.

5. Conclusion

Two novel self-assembled metalla-rectangles incorporating a pH sensitive benzobis(imidazole)-based ligand were synthesized. Thanks to the reversible nature of the coordination bonds and favorable electronic interactions, the larger **Naph₂BBI₂** which shows an interplanar distance of 7.3 \AA between both ligand units can be quantitatively transformed to the interlocked molecular structure (**Naph₂BBI₂**)₂ in MeOH at $C = 2 \times 10^{-2}\text{ M}$. Remarkably, this stimuli responsive interpenetrated catenane can be dissociated in three different ways: i) upon dilution to a concentration of $C = 1\text{ mM}$, ii) in the presence of pyrene, leading to the 1:1 host-guest complex $\text{pyrene} \llcorner \text{Naph}_2\text{BBI}_2$ and iii) by selectively protonating the N_3 -imidazole basic sites with HOTf to form the charged **Naph₂BBI₂H₄** metalla-rectangle. Importantly this can be accomplished without any trace of disassembled species as usually observed under acidic conditions and reversibly through addition of DIPEA.

General conclusion

This last part summarizes all the results obtained and proposes some perspectives for future research.

exTTF-based ligands

The development and synthesis of new electroactive ligands has been performed. These compounds were characterized by common spectroscopic methods, such as NMR and mass spectrometry, by cyclic voltammetry, and, for **A1Me**, by X-ray crystallography.

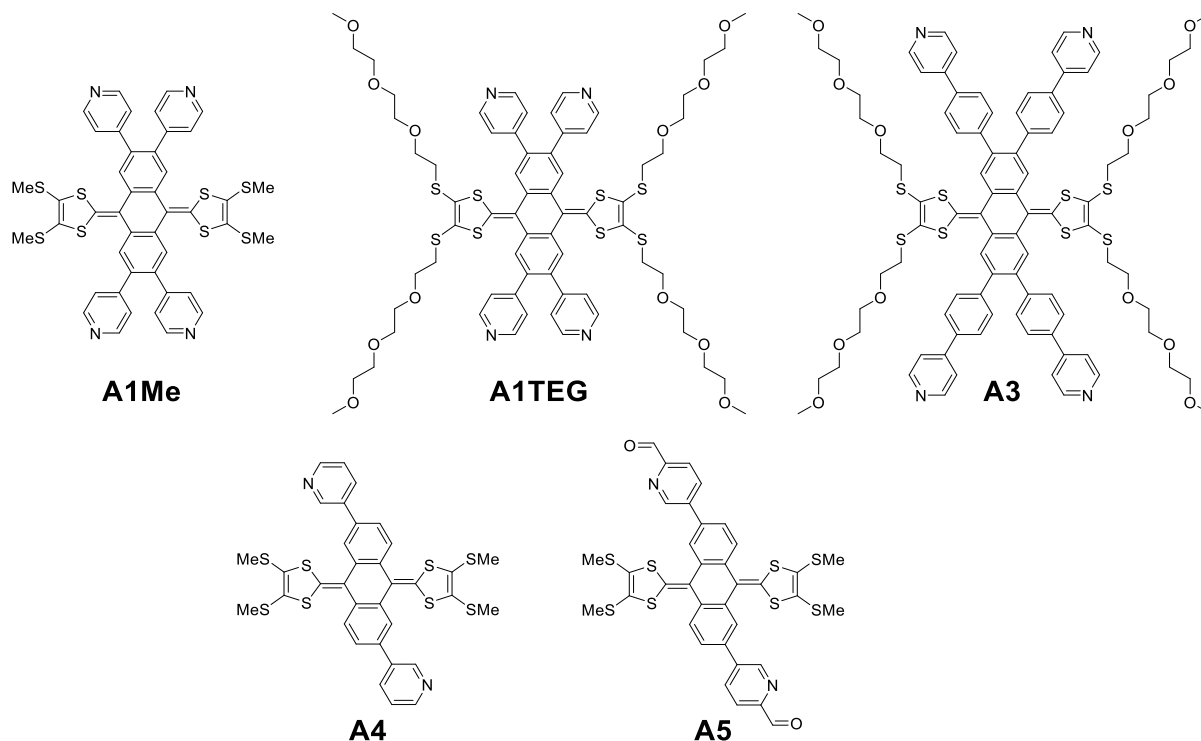
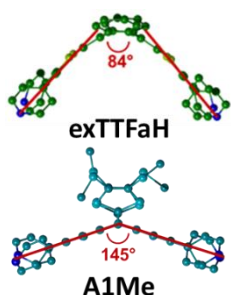


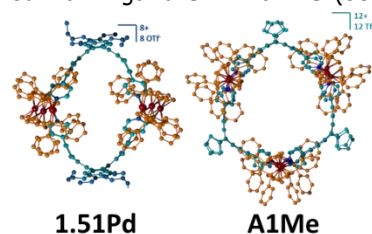
Figure 128. Structures of new exTTF ligands and ligand precursor (**A5**) developed during this thesis and used for the construction of self-assemblies

Tetradentate exTTF ligands with cis-blocked transition metal complexes.

A1Me and **A1TEG** exTTF derivatives (Figure 128), were compared to their regioisomer ligands **exTTFaH** and **exTTFaTEG**, previously obtained and characterized in our group. The X-ray crystal structure of **A1Me** illustrates the geometry difference between both series of regioisomer ligands (see § 1 Chapter 2). The new ligands **A1TEG** was used in the construction of the self-assembled cages **Pd(dppf)A1TEG** and **Pt(dppf)A1TEG**, which were characterized by NMR, mass-spectrometry and cyclic voltammetry. These cages were compared to the previous self-assemblies **1.51Pd** and **1.52Pd**, obtained from ligand **exTTFaTEG** (see



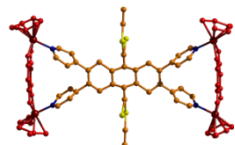
§ 3.1.4 Chapter 1). The ligands developed during this thesis afford large M_6L_3 hexagonal structures, which strongly differs from the previous compact M_4L_2 containers (see § 2.1 Chapter 2). This difference is explained by the fact that the new ligands exhibit a much less pronounced curvature around their face constitutive of the cavity (dihydroanthracenyl part). This cavity is prone to develop a good convex-concave



geometric complementarity with fullerene derivatives as already illustrated in alternative exTTF-based

receptors. Nevertheless, investigation of the guest binding ability of this M_6L_3 cavity has been unsuccessful till now, due to stability reasons.

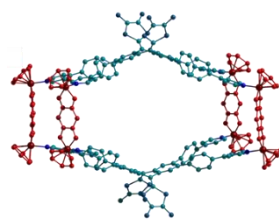
Tetradentate exTTF ligands with bis(Ruthenium) complexes.



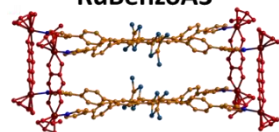
RuBenzoA1

The ligand **A1TEG** (Figure 128) was chemically oxidized to afford **A1TEGOx** which is accompanied by a drastic conformational change. Both (i.e. neutral and oxidized ligands) can react with bidentate bis(Ruthenium) complexes **RuOxa(OTf)₂**, **RuBenzo(OTf)₂** and **RuNaph(OTf)₂**, to afford panel-like Ru_4L self-assemblies (**RuOxaA1**, **RuBenzoA1**, **RuNaphA1** and **RuOxaA1Ox**, **RuBenzoA1Ox**,

RuNaphA1Ox). These structures were established by NMR, mass-spectrometry and confirmed by X-Ray crystallography in the case of **RuBenzoA1Ox**. A ligand **A3** (Figure 128) was designed to limit the formation of panel-like complexes, thanks to the integration of longer phenylpyridyl linkers compared to **A1**. Its oxidized form

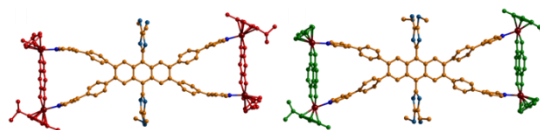


RuBenzoA3



(RuBenzoA3)Ox

A3Ox was also isolated. The reaction of **A3Ox** with



RuBenzoA3Ox

RuNaphA3Ox

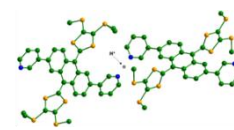
bis(Ruthenium) complexes provided panel-like Ru_4L self-assemblies **RuBenzoA3Ox** and **RuNaphA3Ox**, whose structures were unambiguously determined by NMR, mass-spectrometry and X-Ray crystallography. They can be reduced to afford the neutral corresponding panels (**RuBenzoA3Ox**)Red and (**RuNaphA3Ox**)Red. Interestingly, the reaction between **A3** and **RuBenzo(OTf)₂** provided the sandwich Ru_8L_2 cage **RuBenzoA3**, the composition of which was also confirmed by NMR and mass-spectrometry. The cages **RuBenzoA3** and **RuBenzoA3Ox** did not

interconvert by chemical oxidation. Instead, new species, Ru_8L_2 sandwich (**RuBenzoA3**)Ox was obtained (see § 2.2). Remarkably, the structure of (**RuBenzoA3**)Ox was confirmed by X-Ray crystallography. The cage **RuBenzoA3** provides therefore a "breathing" cavity that is widely open when the exTTF units exist in their neutral state and which is sterically hindered when in their dicationic state. This process, based on a redox control of the cavity geometry, provides an original opportunity to monitor guest encapsulation, an issue of utmost importance.

Bidentate 2,6-difunctionalized exTTF

Bidentate banana-shaped exTTF ligand **A4Me** and ligand precursor **A5** (Figure 128) were obtained and tested in reactions with bidentate linear metal acceptors **AgBF₄** and **Pd(CH₃CN)₂Cl₂** as well as square planar metal acceptor **Pd(CH₃CN)₄(BF₄)₂**.

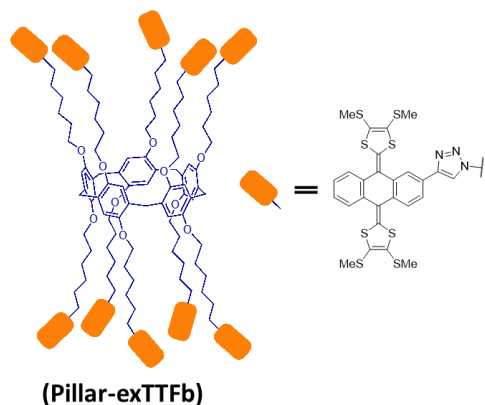
Unfortunately, **A4Me** did not afford any self-assemblies. Only the oxidized compound



A4Me²⁺H⁺(BF₄⁻)₃

A4Me²⁺H⁺(BF₄⁻)₃ was obtained in reaction with **AgBF₄** (see § 3 Chapter 2). Compound **A5** was sent to J. Nitschke group in order to prepare Fe(II)-based self-assemblies capable of binding adamantane-type derivatives; this work is still under progress in their hands.

exTTF moieties, grafted onto a pillar[5]arene scaffold

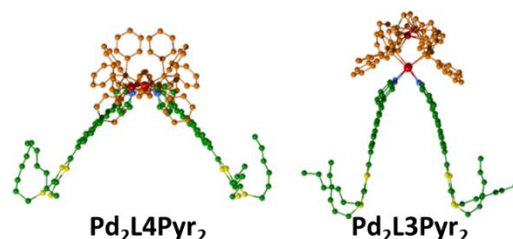


A redox-active pillar[5]arene derivative (**Pillar-exTTFb**), bearing ten exTTF moieties, was synthesized by click reaction. The complete substitution was confirmed by NMR and mass spectrometry. **Pillar-exTTFb** exhibits the usual electrochemical behavior of exTTF and does not show any electronic interactions between exTTF units, which all behave independently. The inherent conformational change kinetics of exTTF electrode process did not allow to determine the number of transferred electrons by common analytical methods. The ability of **Pillar-exTTFb** to form rotaxanes, as well as of **Pillar-OEt** and **Pillar-TTF** (two previously prepared pillararene derivatives), was investigated in the group of J. F. Nierengarten with

the binding study of axles **C₆₀CN** and **DiCN** (control compound). The results confirmed the beneficial effect of a long hexamethylene spacer for the association but did not reveal any synergic help of exTTF-fullerene interaction (see § 4 Chapter 2).

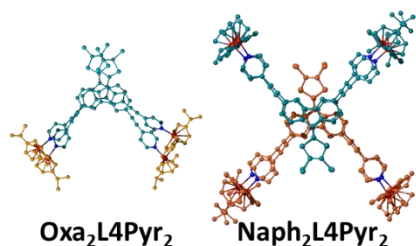
Metalla-clips with cis-blocked Pd(dppf) complexes and dithiafulvene-based ligands

The properties of two M₂L₂ metalla-clips, **Pd₂L4Pyr₂** and **Pd₂L3Pyr₂**, constructed from the same *cis*-blocked Pd(dppf)(OTf)₂ complex and two isomeric DTF-based ligands differing by the position of the nitrogen atom on the pyridyl coordinating units, were compared. While the molecular tweezer **Pd₂L4Pyr₂** is L-shaped with an intramolecular



distance of ca. 15 Å between both redox-active tips, **Pd₂L3Pyr₂** is U-shaped with a cavity in which both DTF units are separated by only 8.5 Å. Cyclic voltammetry experiments on **Pd₂L3Pyr₂** at variable concentrations have revealed an intermolecular process of intercalated mixed-valence species upon electrochemical oxidation. This process can be influenced by formation of a host-guest complex with an electro-deficient **DCTNF** unit. This behavior is not observed with **Pd₂L4Pyr₂**, as this tweezer cannot interact with electron-poor species because of the large distance between both tips.

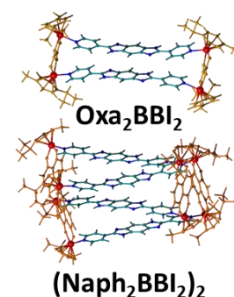
Metalla-tweezers with bis(Ruthenium) complexes



The structure and properties of two self-assembled metalla-tweezers, **Oxa₂L4Pyr₂** and **Naph₂L4Pyr₂** were investigated. X-ray structure data demonstrated that the larger **Naph₂L4Pyr₂** shows a distance of about 7 Å between both tips and spontaneously forms an interpenetrated dimer (**Naph₂L4Pyr₂**)₂ which could be characterized in solution, the gas phase, and the solid state. This arrangement can dissociate in the presence of an electron-poor DCTNF unit, leading to a 1:1 host-guest complex (DCTNF⊂**Naph₂L4Pyr₂**). Finally, electrochemical oxidation of this complex allows to regenerate the dimeric structure due to favorable interactions between the oxidized tweezer-like molecules, resulting in a concomitant redox-controlled delivery of the DCTNF guest molecule, and illustrating the potential of tweezer-like molecules in this field.

pH-responsive cage based on BBI ligand

A final chapter is dedicated to the preparation of stimuli-responsive metalla-cycles incorporating the pH sensitive benzobisimidazole (BBI) moiety. This work was done in collaboration with the group of O. Siri in Marseille. Two novel self-assembled metalla-rectangles **Oxa₂BBI₂** and **Naph₂BBI₂** incorporating a benzobis(imidazole)-based ligand were synthesized and characterized by NMR, mass-spectrometry and X-Ray crystallography. Thanks to the reversible nature of the coordination bonds and favorable electronic interactions, **Naph₂BBI₂**, which shows an interplanar distance of 7.3 Å between both ligand planes, is quantitatively transformed into the interlocked molecular structure **(Naph₂BBI₂)₂** in MeOH at $C = 2 \times 10^{-2}$ M. This stimuli-responsive interpenetrated catenane can be dissociated in three different ways: i) upon dilution to a concentration below $C = 1$ mM, ii) with the presence of pyrene, leading the 1:1 host-guest complex pyrene-**Naph₂BBI₂**, and iii) by selectively protonating the N₃-imidazole basic sites with HOTf to form the charged **Naph₂BBI₂H₄** metalla-rectangle. Importantly this can be accomplished without any trace of disassembled species as usually observed under acidic conditions and can be reversed through addition of DIPEA.



Experimental part

1. Instrumentation

NMR spectra were recorded on Bruker Avance III 300 spectrometer or NMR Bruker Avance III HD 500 spectrometer at room temperature or 298 K (^1H DOSY NMR). NMR chemical shifts are given in ppm (δ) relative to Me_4Si with solvent resonances used as internal standards. IR spectra were recorded on an Agilent Cary 630 FTIR equipped with an attenuated total reflectance (ATR) sampling. High resolution mass measurements were performed either on a FTICR-MS – 7T (Solarix 2xR, Bruker) or a Waters Xevo® G2-XS QT with ESI source in positive ion mode. UV-Vis absorption spectra of the compounds in spectrophotometric grade solvents were recorded in 0.1 or 1 cm length quartz cuvettes on a VARIAN CARY 50 SCAN spectrophotometer at room temperature with a 300 nm/min scan rate.

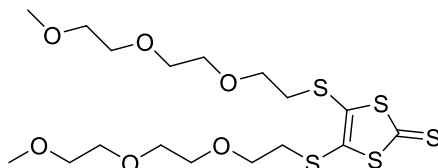
2. Chemicals

All starting reagents were commercial reagent grade and were used without further purification. For synthesis and crystallizations, analytical grade solvents were used.

Bis(tetraethylammonium) bis(1,3-dithiole-2thione-4,5-dithiol)zincate **1**,¹⁷⁰ 2,2'-(2-ethynylanthracene-9,10-diylidene)bis(4,5-bis(methylthio)-1,3-dithiole) **19**,¹³¹ 3,6-bis(pyridin-4-ylethynyl)-9H-fluoren-9-one **22**,¹⁰³ 3,6-bis(pyridin-3-ylethynyl)-9H-fluoren-9-one **23**,¹⁰² dimethyl (4,5-bis(methylsulfanyl)-1,3-dithiol-2-yl)phosphonate **7**, dimethyl (4,5-bis(propylsulfanyl)-1,3-dithiol-2-yl)phosphonate **20** and dimethyl (4,5-bis(hexylsulfanyl)-1,3-dithiol-2-yl)phosphonate **21**¹⁰² were available in the laboratory and synthesized using known procedures. 2,3,6,7-tetrabromoanthracene-9,10-dione **8** was synthesized according to the procedure described in the literature.¹¹⁹ Pillar arene **17** was provided by the group of J. F. Nierengarten. Complexes **Pd(dppf)(OTf)₂**,¹⁷¹ **Pt(dppf)(OTf)₂**,¹⁷¹ **RuOxa(OTf)₂**,¹⁴⁶ **RuBenzo(OTf)₂**,¹⁷² and **RuNaph(OTf)₂**¹⁴⁷ were synthesized using procedures described in the literature.

3. Procedures

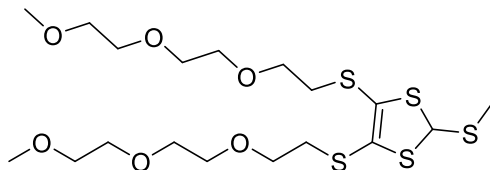
4,5-bis((2-(2-(2-methoxyethoxy)ethoxy)ethyl)thio)-1,3-dithiole-2-thione (2)



In a 100 mL 3-neck flask charged with 5.36 g (7.45 mmol) of bis(tetraethylammonium)bis(1,3-dithiole-2thione-4,5-dithiol)zincate (**1**)¹⁷⁰ was added acetonitrile (40 mL), and the solution was degassed with argon for 10 min. Then 5.45 g (5 mL, 24.01 mmol, 3.2 equiv.) of 1-bromo-2-(2-(2-methoxyethoxy)ethoxy)ethane was added. The reaction was stirred at reflux for 3 h. Then, the solution was concentrated and 50 mL of methylene chloride was added. The resulting white precipitate was filtered through a thin layer of silica. The organic layer was washed with 2 × 100 mL of water, dried over MgSO_4 and concentrated under vacuum. The residue was purified by column chromatography on silica gel with ethyl acetate as eluent to afford compound **2** (7.90 g, 96%) as a red liquid.

^1H NMR (300 MHz, CDCl_3) δ 3.71 (t, J = 6.4 Hz, 4H), 3.64 (s, 8H), 3.67 – 3.60 (m, 4H), 3.56 – 3.53 (m, 4H), 3.38 (s, 6H), 3.07 (t, J = 6.4 Hz, 4H). ^{13}C NMR (76 MHz, CDCl_3) δ 211.06, 136.57, 71.94, 70.64, 70.60, 69.87, 59.06, 36.14. FAB-HRMS: found: 490.0635, calculated: 490.0646.

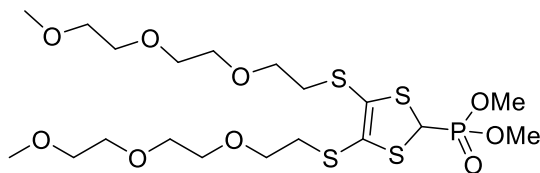
4,5-bis((2-(2-(2-methoxyethoxy)ethoxy)ethyl)thio)-2-(methylthio)-1,3-dithiole (4)



In a 250 mL flask charged with 5.50 g (10.85 mmol) of compound **2**, was added 25 ml of methylene chloride, and the solution was degassed with argon for 5 min. Then, 1.91 g (1.32 mL, 11.66 mmol, 1.07 equiv.) of methyl trifluoromethanesulfonate was added and the reaction was stirred at r.t. overnight. The solution was concentrated and the resulting residue rinsed with 5 ml of diethyl ether and dried under vacuum. To the obtained intermediate compound **3** (7.49 g, red liquid) were added 70 mL of acetonitrile and 30 ml of isopropyl alcohol. The solution was cooled to $-5\text{ }^\circ\text{C}$ and NaBH_4 was added as a solid portion by portion until the bubbling stopped. The solution was stirred for 3 h at r.t.. Then, the mixture was concentrated and the residue was dissolved in ethyl acetate. The organic layer was washed with 2×50 mL of water, dried over MgSO_4 and concentrated to afford compound **4** (5.50 g, 95 %) as a yellow liquid.

^1H NMR (300 MHz, CDCl_3) δ 5.71 (s, 1H), 3.69 – 3.64 (m, 4H), 3.66 (s, 12H), 3.57 – 3.54 (m, 4H), 3.32 (s, 6H), 3.16 – 3.07 (m, 2H), 2.96 – 2.87 (m, 2H), 2.24 (s, 3H). ^{13}C NMR (76 MHz, CDCl_3) δ 125.04, 71.96, 70.58, 70.16, 59.08, 57.38, 35.15, 14.00. FAB-HRMS: found: 506.0952, calculated: 506.0959.

Dimethyl (4,5-bis((2-(2-(2-methoxyethoxy)ethoxy)ethyl)thio)-1,3-dithiol-2-yl)phosphonate (6)

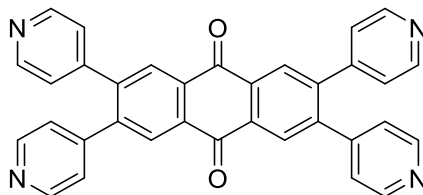


In 250 mL flask charger with 5.60 g (11.05 mmol) of compound **4**, was added 25 ml of acetic anhydride. The solution was degassed with argon for 30 min and 1.97 g (1.67 mL, 12.16 mmol, 1.1 equiv.) of $\text{HBF}_4 \cdot \text{Et}_2\text{O}$ were added. The reaction was stirred for 2 h at r.t.. The solution was then concentrated and the residue rinsed with 25 ml of Et_2O and dried under vacuum to afford intermediate compound **5**. Then, 100 mL of acetonitrile was added and the resulting solution was degassed with argon for 30 min. Then, 2.00 g (13.34 mmol) of NaI and 1.65 g (1.57 mL, 13.33 mmol) of $\text{P}(\text{OMe})_3$ were added, and the reaction was stirred under argon for 3 h. The solution was then concentrated and the resulting solid dissolved in 100 ml of methylene chloride. The organic layer was washed with 3×50 mL of water and 50 mL of brine, dried over MgSO_4 and concentrated. The residue was purified by column chromatography on silica gel with ethyl acetate as eluent to afford compound **6** (2.32 g, 36 %) as a red liquid.

^1H NMR (300 MHz, CDCl_3) δ 4.67 (d, J = 5.8 Hz, 1H), 3.88 (s, 3H), 3.85 (s, 3H), 3.79 – 3.63 (m, 16H), 3.56–3.54 (m, 4H), 3.37 (s, 6H), 3.13 – 3.04 (m, 2H), 2.98 – 2.89 (m, 2H). ^{13}C NMR (76 MHz, CDCl_3) δ 125.63,

71.94, 70.57, 70.46, 70.05, 59.06, 54.79, 41.36 (d, $J(^{13}\text{C}-^{31}\text{P}) = 161$ Hz), 35.30. ^{31}P NMR (121.6 MHz, CDCl_3) δ 18.51. FAB-HRMS: found: 568.1054, calculated: 568.1058.

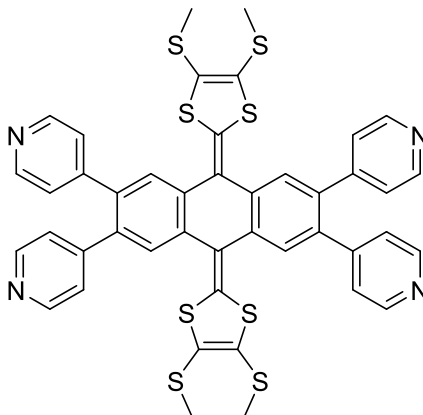
2,3,6,7-tetra(pyridin-4-yl)anthracene-9,10-dione (9)



In a 250 mL Schlenk flask charged with 910 mg (1.08 mmol) of 2,3,6,7-tetrabromoanthracene-9,10-dione **8** and 1.28 g (10.40 mmol, 9.6 equiv.) of 4-pyridylboronic acid was added 140 mL of toluene, 50 mL of ethanol and a solution of K_2CO_3 (4.80 g in 4 mL of water). The mixture was degassed with argon for 1 h. Then, 800 mg (0.69 mmol, 0.64 equiv.) of tetrakis(triphenylphosphine)palladium (0) was added, the mixture was degassed for 15 min and stirred under argon at 90°C for 12 hours. The solution was concentrated and 50 mL of methylene chloride was added. The residue was filtered, concentrated and purified by column chromatography on silica gel with methylene chloride to methylene chloride / methanol (v/v 92/8) as eluent to afford compound **9** (245 mg, 27 %) as a yellow solid.

^1H NMR (300 MHz, CDCl_3) δ 8.61 (d, $J = 6.5$ Hz, 8H), 8.44 (s, 4H), 7.17 (d, $J = 6.5$ Hz, 8H). ^{13}C NMR (76 MHz, CDCl_3) δ 181.62, 150.20, 146.39, 143.82, 133.22, 129.77, 124.06. FAB-HRMS: found: 516.1585, calculated: 516.1586.

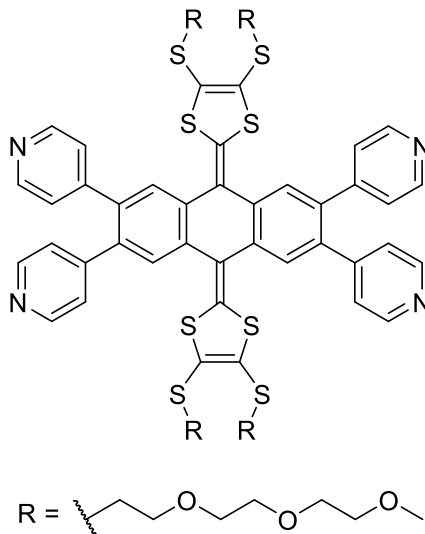
4,4',4'',4'''-(9,10-bis(4,5-bis(methylthio)-1,3-dithiol-2-ylidene)-9,10-dihydroanthracene-2,3,6,7-tetrayl)tetrapyridine (A1Me)



In a 50 mL Schlenk flask charged with 221 mg (0.72 mmol) of phosphonate **7**, was added 4 mL of anhydrous THF and the solution was cooled to -78°C . Then, 280 μL of *n*-Butyllithium (0.70 mmol, 0.97 equiv., 2.5 M) was added and the solution was stirred at -78°C for 1 h. Then, 150 mg of **9** (0.29 mmol, 0.4 equiv.) in 10 mL of anhydrous THF was cannulated into the reaction media and the reaction was warmed up to r.t. overnight. Then, the solution was concentrated and 50 mL of methylene chloride was added. The organic layer was washed with 2×30 mL of water, dried over MgSO_4 and concentrated. The residue was purified by column chromatography on alumina with methylene chloride to methylene chloride / methanol (v/v 99/1) as eluent to afford ligand **A1Me** (151 mg, 60 %) as an orange solid.

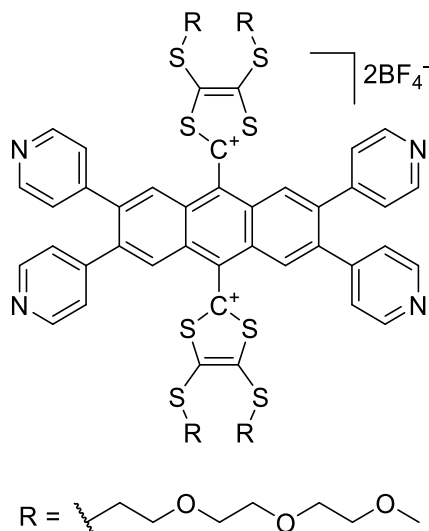
^1H NMR (300 MHz, CDCl_3) δ 8.55 (d, $J = 6.5$ Hz, 8H), 7.65 (s, 4H), 7.11 (d, $J = 6.5$ Hz, 8H), 2.42 (s, 12H).
 ^{13}C NMR (76 MHz, CDCl_3) δ 149.89, 147.92, 135.75, 135.08, 134.70, 127.41, 126.67, 124.51, 120.99, 19.36.
 FAB-HRMS: found: 872.0396, calculated: 872.0393.

4,4',4'',4'''-(9,10-bis(4,5-bis((2-(2-(2-methoxyethoxy)ethoxy)ethyl)thio)-1,3-dithiol-2-ylidene)-9,10-dihydroanthracene-2,3,6,7-tetrayl)tetrapyrindine (A1TEG)



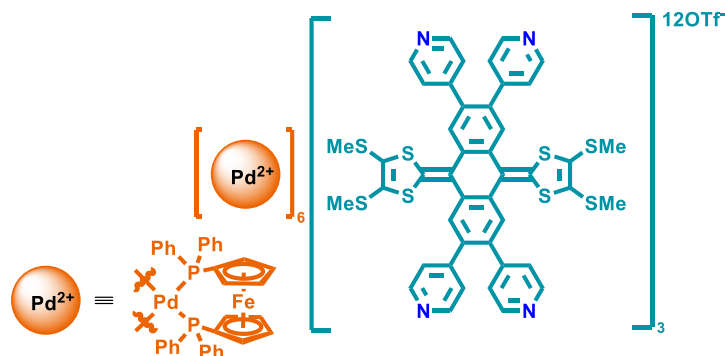
In a 50 mL Schlenk flask charged with 330 mg (0.72 mmol) of phosphonate **6**, was added 4 mL of anhydrous THF and the solution was cooled to -78 °C. Then, 280 μL of *n*-Butyllithium (0.70 mmol, 0.97 equiv., 2.5 M) was added and the solution was stirred at -78 °C for 1 h. Then, 150 mg of **9** (0.29 mmol, 0.4 equiv.) in 10 mL of anhydrous THF was cannulated into the reaction media and the reaction was warmed up to r.t. overnight. Then, the solution was concentrated and 50 ml of methylene chloride was added. The organic layer was washed with 2×30 mL of water, dried over MgSO_4 and concentrated. The residue was purified by column chromatography on alumina with methylene chloride to methylene chloride / methanol (v/v 99/1) as eluent to afford ligand **A1TEG** (176 mg, 65 %) as an orange sticky solid.

^1H NMR (300 MHz, CDCl_3) δ 8.55 (d, $J = 6.5$ Hz, 8H), 7.65 (s, 4H), 7.11 (d, $J = 6.5$ Hz, 8H), 3.74 – 3.64 (m, 12H), 3.71 – 3.61 (m, 32H), 3.54 – 3.50 (m, 8H), 3.35 (s, 12H), 3.03 (td, $J = 6.5$ Hz, 1.3 Hz, 8H). ^{13}C NMR (76 MHz, CDCl_3) δ 150.05, 148.03, 135.92, 135.16, 134.51, 127.45, 127.023, 124.64, 120.75, 72.06, 70.74, 70.68, 70.11, 59.19, 35.81. FAB-HRMS: found: 568.1054, calculated: 568.1058.

A1TEGOx

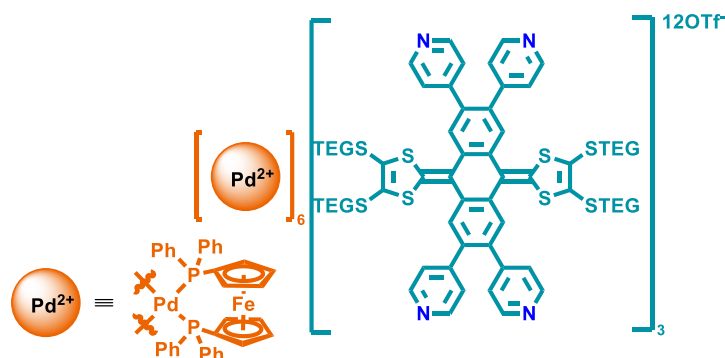
A solution of **PTZ** in CH_3NO_2 (1.14 ml, 0.05 M, 57.07 μmol) was added to a solution of **A1TEG** (40.0 mg, 28.5 μmol) in CH_3NO_2 (2 mL) and the mixture was stirred for 5 minutes. Then, Et_2O was added and the resulting suspension was centrifuged. The solid was rinsed 3 times with Et_2O and dried under vacuum to give **A1TEGOx** (30 mg, 65 %) as an orange powder.

^1H NMR (300 MHz, CD_3NO_2) δ 8.52 – 8.44 (m, 8H), 8.08 (s, 4H), 7.26 – 7.18 (m, 10H), 3.96 (dd, $J = 5.8, 4.7$ Hz, 8H), 3.62 – 3.52 (m, 24H), 3.44 – 3.37 (m, 8H), 3.34 – 3.24 (m, 8H), 3.24 – 3.15 (m, 8H), 3.06 (s, 13H).

Pd(dppf)A1Me

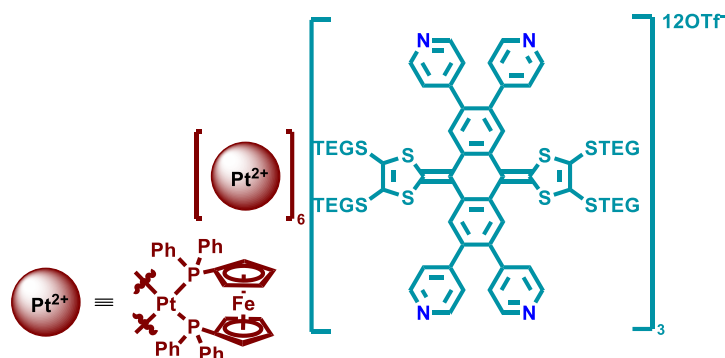
A stoichiometric mixture of ligand **A1Me** (3 mg, 3.44 μmol) and *cis*- $\text{Pd}(\text{dppf})(\text{OTf})_2$ (6.59 mg, 6.88 μmol) in CH_3NO_2 (1 mL) was stirred for 5 min at room temperature. The red solution was analyzed without any purification.

^1H NMR (300 MHz, CD_3NO_2) δ 8.60 – 8.43 (m, 24H), 8.28 – 8.07 (m, 36H), 7.89 (td, $J = 13.1, 10.9, 6.9$ Hz, 108H), 7.70 (d, $J = 9.3$ Hz, 36H), 7.31 (s, 12H), 7.13 – 6.93 (m, 24H), 4.96 (s, 12H), 4.80 (s, 12H), 4.72 (s, 24H), 4.68 (s, 12H), 2.37 (s, 36H). ^{31}P NMR (122 MHz, CD_3NO_2) δ 33.78. DOSY (300 MHz, CD_3NO_2) $D = 2.5 \times 10^{-10} \text{ m}^2 \cdot \text{s}^{-1}$. FTICR-MS: [**Pd(dppf)A1Me-8OTf**] $^{8+}$ found: 1944.1945, calculated: 1944.1937.

Pd(dppf)A1TEG

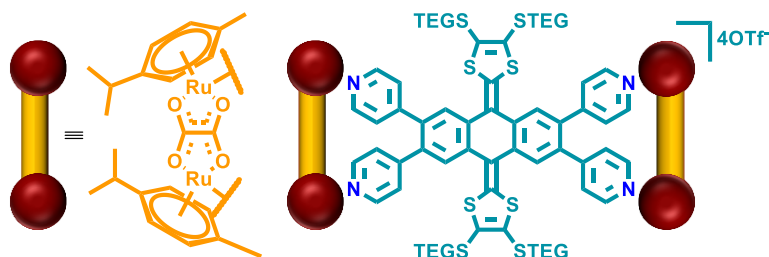
A stoichiometric mixture of ligand **A1TEG** (6.35 mg, 4.53 μmol) and *cis*-Pd(*dppf*)(OTf)₂ (9.06 mg, 6.88 μmol) in CH₃NO₂ (1 mL) was stirred for 5 min at room temperature. The red solution was analyzed without any purification.

¹H NMR (300 MHz, CD₃NO₂) δ 8.53 (s, 24H), 8.18 (dd, *J* = 12.8, 7.3 Hz, 36H), 7.88 (dt, *J* = 13.0, 7.5 Hz, 108H), 7.70 (s, 36H), 7.31 (s, 12H), 7.05 – 6.97 (m, 24H), 4.98 (s, 12H), 4.81 (s, 12H), 4.72 (s, 24H), 4.67 (s, 12H), 3.60 (t, *J* = 6.2 Hz, 24H), 3.49 – 3.41 (m, 72H), 3.42 – 3.34 (m, 24H), 3.21 (s, 36H), 3.02 (td, *J* = 6.9 Hz, 24H). DOSY (300 MHz, CD₃NO₂) *D* = 2.2 × 10⁻¹⁰ m²·s⁻¹. FTICR-MS: [Pd(**dppf**)**A1TEG**-5OTf]⁵⁺ found: 1842.754, calculated: 1842.751, [Pd(**dppf**)**A1TEG**-4OTf]⁴⁺ found: 2340.672, calculated: 2340.680.

Pt(dppf)A1TEG

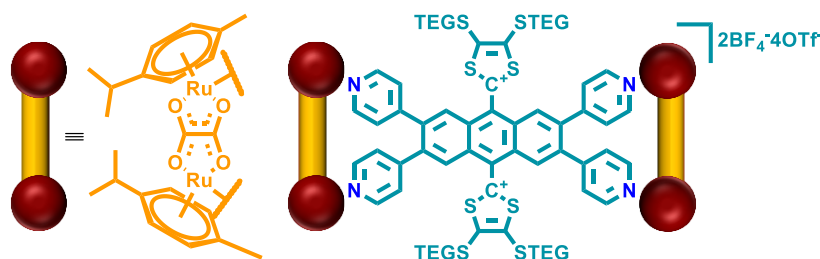
A stoichiometric mixture of ligand **A1TEG** (4.91 mg, 3.50 μmol) and *cis*-Pt(*dppf*)(OTf)₂ (7.34 mg, 7.00 μmol) in CH₃NO₂ (1 mL) was stirred for 2 h at 55 °C. Then, Et₂O was added and the resulting suspension was centrifuged. The solid was rinsed 3 times with Et₂O and dried under vacuum to give **Pt(dppf)A1TEG** as a red powder (7 mg, 56 %).

¹H NMR (300 MHz, CD₃NO₂) δ 8.64 – 8.51 (m, 24H), 8.25 – 8.13 (m, 36H), 7.97 – 7.79 (m, 108H), 7.75 – 7.65 (m, 36H), 7.31 (s, 12H), 7.13 – 7.00 (m, 24H), 4.95 (s, 12H), 4.76 (s, 12H), 4.67 (s, 36H), 3.61 (t, *J* = 6.2 Hz, 24H), 3.51 – 3.41 (m, 72H), 3.41 – 3.34 (m, 24H), 3.21 (s, 36H), 3.06 – 2.97 (m, 21H). ³¹P NMR (122 MHz, CD₃NO₂) δ 3.58. DOSY (300 MHz, CD₃NO₂) *D* = 2.2 × 10⁻¹⁰ m²·s⁻¹. FTICR-MS: [Pt(**dppf**)**A1TEG**-6OTf]⁶⁺ found: 1599.3629, calculated: 1599.3629, [Pt(**dppf**)**A1TEG**-5OTf]⁵⁺ found: 1949.0258, calculated: 1949.0259.

RuOxaA1

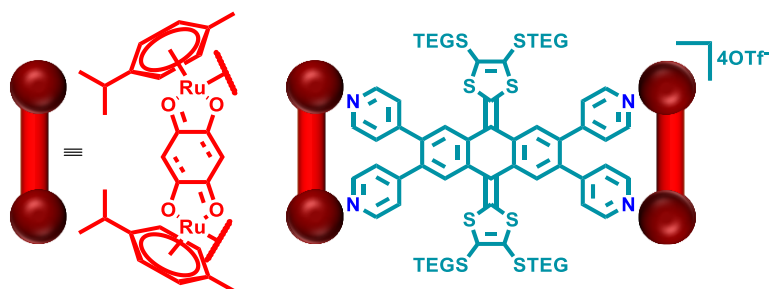
A stoichiometric mixture of ligand **A1TEG** (4.00 mg, 2.85 μmol) and **RuOxa(OTf)₂** (4.89 mg, 5.71 μmol) in CH_3NO_2 (1 mL) was stirred for 2 h at 55 $^\circ\text{C}$. Then, Et_2O was added and the resulting suspension was centrifuged. The solid was rinsed 3 times with Et_2O and dried under vacuum to give **RuOxaA1** as a yellow powder (6 mg, 67 %).

^1H NMR (300 MHz, MeOD) δ 8.09 (dd, $J = 12.4, 5.9$ Hz, 8H), 7.82 (s, 4H), 7.42 (d, $J = 5.8$ Hz, 4H), 7.15 (d, $J = 6.0$ Hz, 4H), 6.02 (d, $J = 6.2$ Hz, 8H), 5.86 (d, $J = 6.1$ Hz, 8H), 3.68 (t, $J = 6.3$ Hz, 8H), 3.61 – 3.55 (m, 24H), 3.53 – 3.47 (m, 8H), 3.33 (s, 12H), 3.09 – 2.99 (m, 8H), 2.97 – 2.80 (m, 4H), 2.27 (s, 12H), 1.40 (d, $J = 6.9$ Hz, 24H). ^1H DOSY NMR (300 MHz, MeOD) $D = 3.5 \times 10^{-10} \text{ m}^2 \cdot \text{s}^{-1}$. HRMS analysis has been carried out recently and confirms the exclusive formation of **RuOxaA1**. The detailed results will be included in the final manuscript version.

RuOxaA1Ox

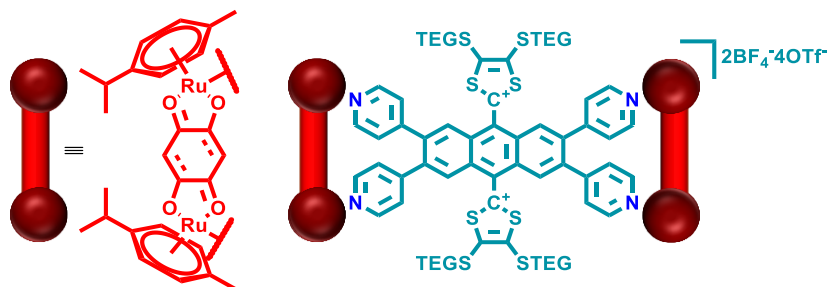
A solution of **PTZ** in CH_3NO_2 (115 μl , 0.05 M, 5.71 μmol) was added to the solution of the ligand **A1TEG** (4.00 mg, 2.85 μmol) in CH_3NO_2 (1 mL). Solid **RuOxa(OTf)₂** (4.89 mg, 5.71 μmol) was added and the resulting solution was stirred for 2 h at 55 $^\circ\text{C}$. The orange solution was used without any purification.

^1H NMR (300 MHz, CD_3NO_2) δ 8.23 (s, 4H), 8.15 – 8.07 (m, 8H), 7.31 – 7.22 (m, 8H), 5.97 (d, $J = 6.2$ Hz, 8H), 5.80 (d, $J = 6.3$ Hz, 8H), 3.96 (t, $J = 5.2$ Hz, 8H), 3.66 – 3.55 (m, 16H), 3.54 – 3.45 (m, 8H), 3.40 – 3.29 (m, 8H), 3.29 – 3.18 (m, 8H), 3.11 (s, 12H), 2.90 (p, $J = 6.9$ Hz, 4H), 2.25 (s, 12H), 1.38 (d, $J = 6.9$ Hz, 24H). ^1H DOSY NMR (300 MHz, CD_3NO_2) $D = 3.3 \times 10^{-10} \text{ m}^2 \cdot \text{s}^{-1}$. HRMS analysis has been carried out recently and confirms the exclusive formation of **RuOxaA1Ox**. The detailed results will be included in the final manuscript version.

RuBenzoA1

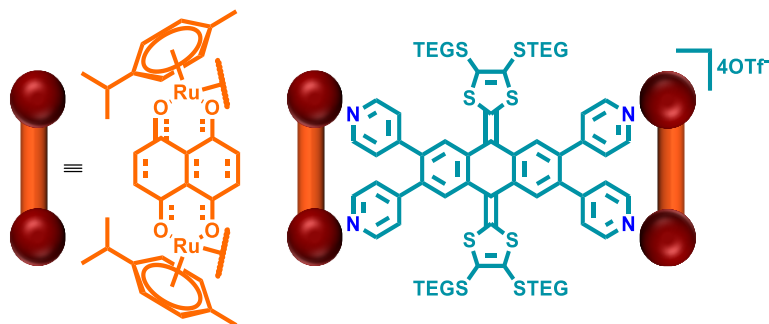
A stoichiometric mixture of ligand **A1TEG** (4.00 mg, 2.85 μmol) and **RuBenzo(OTf)₂** (5.17 mg, 5.71 μmol) in CH_3NO_2 (1 mL) was stirred for 2 h at 55 °C. Then, Et_2O was added and the resulting suspension was centrifuged. The solid was rinsed 3 times with Et_2O and dried under vacuum to give **RuBenzoA1** as a red powder (6.5 mg, 71 %).

^1H NMR (300 MHz, CD_3NO_2) δ 8.09 (dd, $J = 8.1, 5.9$ Hz, 8H), 7.44 (dd, $J = 6.0, 2.1$ Hz, 4H), 7.18 (dd, $J = 6.0, 2.1$ Hz, 4H), 6.10 – 5.98 (m, 8H), 5.84 (dd, $J = 7.3, 5.6$ Hz, 8H), 5.69 (d, $J = 19.0$ Hz, 4H), 3.76 – 3.64 (m, 8H), 3.63 – 3.51 (m, 36H), 3.54 – 3.41 (m, 8H), 3.29 (s, 12H), 3.08 (h, $J = 7.4, 6.7$ Hz, 8H), 2.95 (p, $J = 6.9$ Hz, 4H), 2.30 (s, 12H), 1.43 – 1.33 (m, 24H). ^1H DOSY NMR (300 MHz, CD_3NO_2) $D = 3.2 \times 10^{-10} \text{ m}^2 \cdot \text{s}^{-1}$. HRMS analysis has been carried out recently and confirms the exclusive formation of **RuBenzoA1**. The detailed results will be included in the final manuscript version.

RuBenzoA1Ox

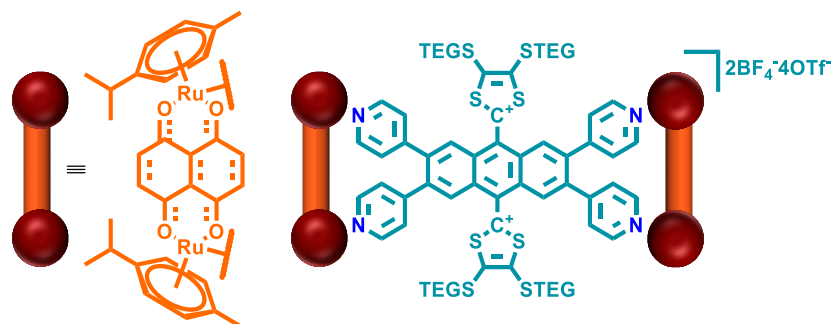
A solution of **PTZ** in CH_3NO_2 (115 μl , 0.05 M, 5.71 μmol) was added to the solution of the ligand **A1TEG** (4.00 mg, 2.85 μmol) in CH_3NO_2 (1 mL). Solid **RuBenzo(OTf)₂** (5.17 mg, 5.71 μmol) was added and the resulting solution was stirred for 2 h at 55 °C. The red solution was used without any purification.

^1H NMR (300 MHz, CD_3NO_2) δ 8.12 (d, $J = 1.6$ Hz, 8H), 8.11 (s, 4H), 7.42 – 7.30 (m, 8H), 6.06 (d, $J = 6.2$ Hz, 8H), 5.87 (d, $J = 6.2$ Hz, 8H), 5.72 (s, 4H), 4.05 – 3.96 (m, 8H), 3.73 – 3.60 (m, 16H), 3.60 – 3.49 (m, 8H), 3.47 – 3.37 (m, 8H), 3.33 – 3.24 (m, 8H), 3.15 (s, 12H), 2.98 (p, $J = 6.9$ Hz, 4H), 2.36 (s, 12H), 1.43 (d, $J = 6.9$ Hz, 24H). ^1H DOSY NMR (300 MHz, CD_3NO_2) $D = 3.3 \times 10^{-10} \text{ m}^2 \cdot \text{s}^{-1}$. HRMS analysis has been carried out recently and confirms the exclusive formation of **RuOxaA1Ox**. The detailed results will be included in the final manuscript version.

RuNaphA1

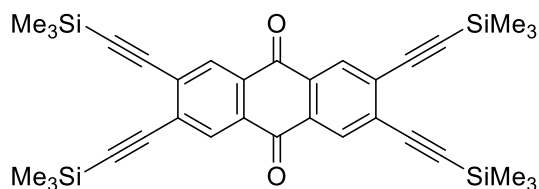
A stoichiometric mixture of ligand **A1TEG** (4.00 mg, 2.85 μmol) and **RuNaph(OTf)₂** (5.46 mg, 5.71 μmol) in CH_3NO_2 (1 mL) was stirred for 2 h at 55 °C. Then, Et_2O was added and the resulting suspension was centrifuged. The solid was rinsed 3 times with Et_2O and dried under vacuum to give **RuNaphA1** as a green powder (6.7 mg, 70 %).

^1H NMR (300 MHz, CD_3NO_2) δ 8.26 (dd, $J = 10.1, 5.8$ Hz, 8H), 7.36 (dd, $J = 5.6, 2.0$ Hz, 4H), 7.10 (d, $J = 17.1$ Hz, 8H), 7.10 (dd, $J = 4.5, 1.9$ Hz, 4H), 5.85 – 5.74 (m, 8H), 5.63 – 5.54 (m, 8H), 3.68 (t, $J = 6.3$ Hz, 8H), 3.61 – 3.52 (m, 24H), 3.50 – 3.42 (m, 8H), 3.28 (s, 12H), 3.07 (dd, $J = 11.8, 5.9$ Hz, 8H), 2.94 (p, $J = 6.9$ Hz, 6H), 2.24 (s, 12H), 1.39 (dd, $J = 6.9, 2.3$ Hz, 24H). ^1H DOSY NMR (300 MHz, CD_3NO_2) $D = 3.3 \times 10^{-10} \text{ m}^2 \cdot \text{s}^{-1}$. HRMS analysis has been carried out recently and confirms the exclusive formation of **RuNaphA1**. The detailed results will be included in the final manuscript version.

RuNaphA1Ox

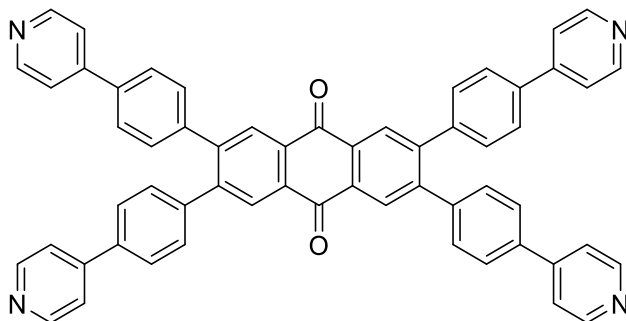
A solution of **PTZ** in CH_3NO_2 (115 μL , 0.05 M, 5.71 μmol) was added to the solution of the ligand **A1TEG** (4.00 mg, 2.85 μmol) in CH_3NO_2 (1 mL). Solid **RuNaph(OTf)₂** (5.46 mg, 5.71 μmol) was added and the resulting solution was stirred for 2 h at 55 °C. Then, Et_2O was added and the resulting suspension was centrifuged. The solid was rinsed 3 times with Et_2O and dried under vacuum to give **RuNaphA1Ox** as a green powder (6 mg, 64 %).

^1H NMR (300 MHz, CD_3NO_2) δ 8.29 – 8.20 (m, 8H), 7.99 (s, 4H), 7.29 – 7.19 (m, 8H), 7.10 (s, 10H), 5.78 (d, $J = 6.0$ Hz, 8H), 5.57 (d, $J = 6.0$ Hz, 8H), 3.95 (t, $J = 5.0$ Hz, 8H), 3.60 (q, $J = 7.8, 6.5$ Hz, 24H), 3.48 (td, $J = 6.8, 6.1, 2.8$ Hz, 8H), 3.36 (dd, $J = 6.2, 3.1$ Hz, 8H), 3.25 (td, $J = 7.3, 6.0, 4.0$ Hz, 8H), 3.10 (d, $J = 2.2$ Hz, 12H), 2.94 (p, $J = 6.9$ Hz, 5H), 2.26 (s, 12H), 1.39 (d, $J = 6.9$ Hz, 25H). ^1H DOSY NMR (300 MHz, CD_3NO_2) $D = 3.3 \times 10^{-10} \text{ m}^2 \cdot \text{s}^{-1}$. HRMS analysis has been carried out recently and confirms the exclusive formation of **RuOxaA1Ox**. The detailed results will be included in the final manuscript version.

2,3,6,7-tetrakis(trimethylsilyl)ethynylanthracene-9,10-dione (10)

In a microwave tube was added 2,3,6,7-tetrabromoanthracene-9,10-dione **8** (100 mg, 191 μ mol), trimethylsilyl acetylene (93.8 mg, 955 μ mol), copper (I) iodide (14.5 mg, 76 μ mol), toluene (2mL) and triethylamine (3 mL). The mixture was degassed for 30 min and tetrakis(triphenylphosphine)palladium (88.3 mg, 76 μ mol) was added. The reaction was carried out under microwave irradiation at 70 $^{\circ}$ C for 30 min. After cooling to room temperature, the solution was concentrated. Then, dichloromethane (10 mL) was added, and the solution was washed with water (3 \times 50 mL). The resulting organic phase was dried with $MgSO_4$ and concentrated under vacuum. The residue was purified by column chromatography on silica gel with a mixture of petroluem ether / dichloromethane as eluant to afford compound **10** (25 mg, 22 %) as a yellow solid.

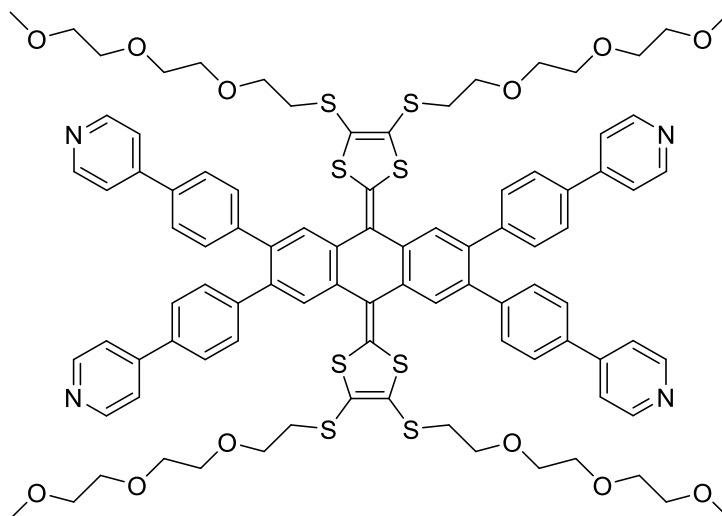
1H NMR (300 MHz, Chloroform-*d*) δ 8.35 (s, 4H), 1.25 (s, 3H), 0.31 (s, 34H). ^{13}C NMR (76 MHz, Chloroform-*d*) δ 181.04, 132.00, 131.43, 104.70, 101.86, -0.05. FAB-HRMS: found: 592.2100, calculated: 592.2105.

2,3,6,7-tetrakis(4-(pyridin-4-yl)phenyl)anthracene-9,10-dione (12)

In a 250 mL Schlenk flask charged with 1.0 g (XXX mmol) of 2,3,6,7-tetrabromoanthracene-9,10-dione **8** and 1.71 g (XX mmol) of (4-(pyridin-4-yl)phenyl)boronic acid was added 140 ml of toluene, 50 ml of ethanol and a solution of K_2CO_3 (4.80 g in 4 ml of water). The mixture was degassed with argon for 1 h. Then, 800 mg (0.69 mmol, 0.64 equiv.) of tetrakis(triphenylphosphine)palladium (0) was added, and the solution was degassed for 15 min. The residue was filtered, concentrated and purified by column chromatography on silica gel with methylene chloride to methylene chloride / methanol (v/v 92/8) as eluent to afford compound **12** (575 mg, 36 %) as a yellow solid.

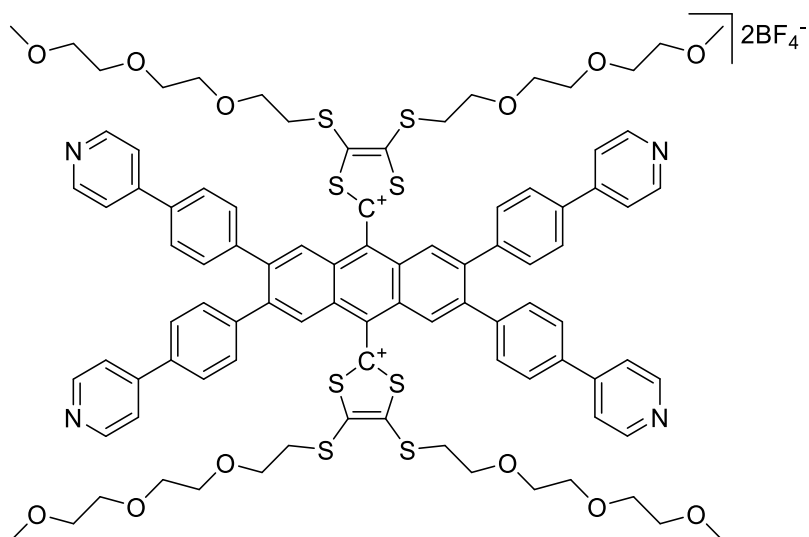
1H NMR (300 MHz, Chloroform-*d*) δ 8.68 (d, J = 5.4 Hz, 8H), 8.49 (s, 4H), 7.63 (d, J = 8.2 Hz, 8H), 7.58 – 7.50 (m, 8H), 7.43 (d, J = 8.2 Hz, 8H). Because of low solubility this compound could not be characterized by ^{13}C NMR. FAB-HRMS: found: 821.2902, calculated: 821.2872.

4,4',4'',4'''-((9,10-bis(4,5-bis((2-(2-(2-methoxyethoxy)ethoxy)ethyl)thio)-1,3-dithiol-2-ylidene)-9,10-dihydroanthracene-2,3,6,7-tetrayl)tetrakis(benzene-4,1-diyl))tetrapyridine (A3)



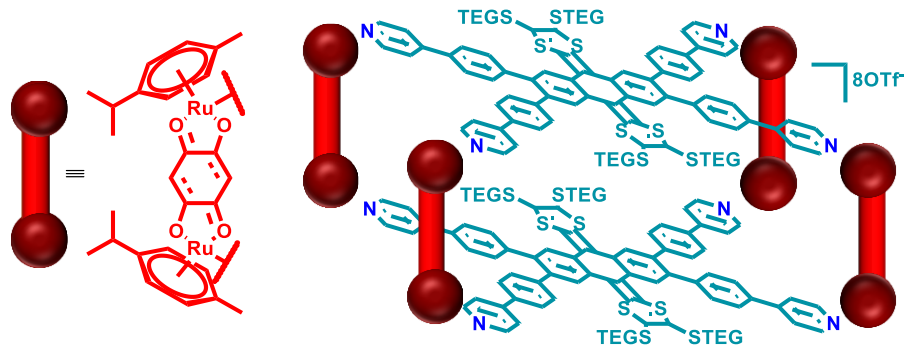
In a 50 mL Schlenk flask charged with 350 mg (0.62 mmol) of phosphonate **6**, was added 4 mL of anhydrous THF and the solution was cooled to -78 °C. Then, 350 μ L of *n*-Butyllithium (0.57 mmol, 0.97 equiv., 2.5 M) was added and the solution was stirred at -78 °C for 1 h. Then, 170 mg of **12** (0.21 mmol, 0.4 equiv.) in 10 mL of anhydrous THF was cannulated into the reaction media and the reaction was warmed up to r.t. overnight. Then, the solution was concentrated and 50 ml of methylene chloride was added. The organic layer was washed with 2 \times 30 mL of water, dried over MgSO₄ and concentrated. The residue was purified by column chromatography on alumina with methylene chloride to methylene chloride / methanol (v/v 99/1) as eluent to afford ligand **A3** (230 mg, 65 %) as an orange sticky solid.

¹H NMR (300 MHz, Chloroform-*d*) δ 8.70 – 8.62 (m, 8H), 7.70 (s, 4H), 7.66 – 7.57 (m, 8H), 7.57 – 7.50 (m, 8H), 7.41 – 7.31 (m, 8H), 3.70 (td, *J* = 6.8, 3.8 Hz, 8H), 3.61 (s, 16H), 3.64 – 3.56 (m, 8H), 3.54 – 3.47 (m, 8H), 3.34 (s, 12H), 3.05 (td, *J* = 6.6, 1.9 Hz, 8H). ¹³C NMR (76 MHz, Chloroform-*d*) δ 150.41, 148.09, 140.20, 138.21, 136.73, 134.74, 130.79, 128.32, 127.87, 126.97, 121.54, 72.06, 70.73, 70.15, 59.18, 35.82. FAB-HRMS: found: 821.2902, calculated: 821.2872.

A30x

A solution of **PTZ** in CH_3NO_2 (0.94 ml, 0.05 M, 46.9 μmol) was added to a solution of ligand **A3** (40.0 mg, 23.4 μmol) in CH_3NO_2 (2 mL). Then, Et_2O was added and the resulting suspension was centrifuged. The resulting solid was rinsed 3 times with Et_2O and dried under vacuum to give **A30x** (35 mg, 80 %) as an orange powder.

^1H NMR (300 MHz, CD_3NO_2) δ 8.64 – 8.56 (m, 8H), 8.09 (s, 4H), 7.82 – 7.69 (m, 8H), 7.69 – 7.57 (m, 8H), 7.52 – 7.42 (m, 8H), 4.01 – 3.91 (m, 8H), 3.63 – 3.52 (m, 16H), 3.45 – 3.36 (m, 8H), 3.33 – 3.24 (m, 8H), 3.24 – 3.14 (m, 8H), 3.06 (s, 12H). ^1H DOSY NMR (300 MHz, CD_3NO_2) $D = 3.7 \times 10^{-10} \text{ m}^2 \cdot \text{s}^{-1}$. HRMS analysis has been carried out recently and confirms the exclusive formation of **A30x**. The detailed results will be included in the final manuscript version.

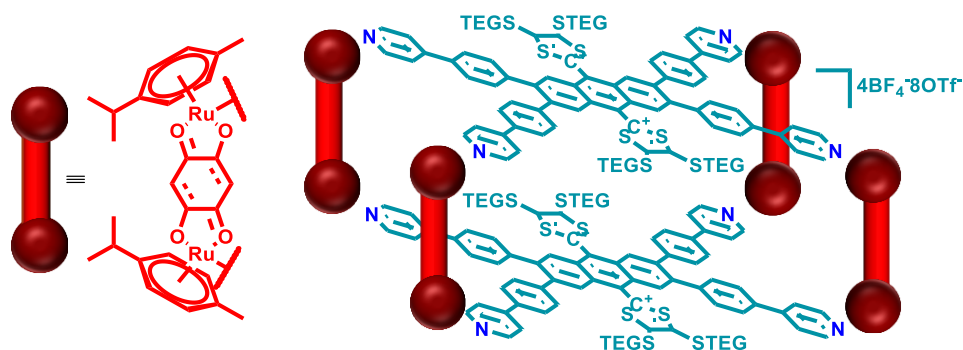
RuBenzoA3

A mixture of ligand **A3** (4.00 mg, 2.34 μmol) and **RuBenzo(OTf)₂** (4.25 mg, 4.69 μmol) in CH_3NO_2 (1 mL) was stirred for 2 h at 55 °C. Then, Et_2O was added and the resulting suspension was centrifuged. The solid was rinsed 3 times with Et_2O and dried under vacuum to give **RuBenzoA3** as a red powder (6 mg, 72 %).

^1H NMR (300 MHz, CD_3NO_2) δ 8.24 (d, $J = 6.3$ Hz, 16H), 7.63 (d, $J = 6.6$ Hz, 16H), 7.61 (d, $J = 8.6$ Hz, 16H), 7.49 (d, $J = 8.2$ Hz, 16H), 7.33 (s, 6H), 5.99 (d, $J = 6.3$ Hz, 16H), 5.77 (s, 8H), 5.75 (d, $J = 6.2$ Hz, 16H), 3.62 (t, $J = 6.2$ Hz, 16H), 3.47 – 3.38 (m, 48H), 3.37 – 3.32 (m, 16H), 3.18 (s, 24H), 3.08 – 2.98 (m, 16H), 2.95 – 2.81 (m, 8H), 2.18 (s, 24H), 1.33 (dd, $J = 6.9, 1.4$ Hz, 48H). DOSY (300 MHz, CD_3NO_2) $D = 2.2 \times 10^{-10} \text{ m}^2 \cdot \text{s}^{-1}$. HRMS: $[\text{L}_2\text{M}_8]^{8+}$ found: 731.0090, calculated: 731.0075, $[\text{L}_2\text{M}_8 + \text{OTf}]^{7+}$ found: 856.7175,

calculated: 856.7161, $[\text{L}_2\text{M}_8 + 2\text{OTf}]^{6+}$ found: 1024.3290, calculated: 1024.3275, $[\text{L}_2\text{M}_8 + 3\text{OTf}]^{5+}$ found: 1258.9844, calculated: 1258.9844, $[\text{L}_2\text{M}_8 + 4\text{OTf}]^{4+}$ found: 1610.9680, calculated: 1610.9674.

(RuBenzoA3)Ox



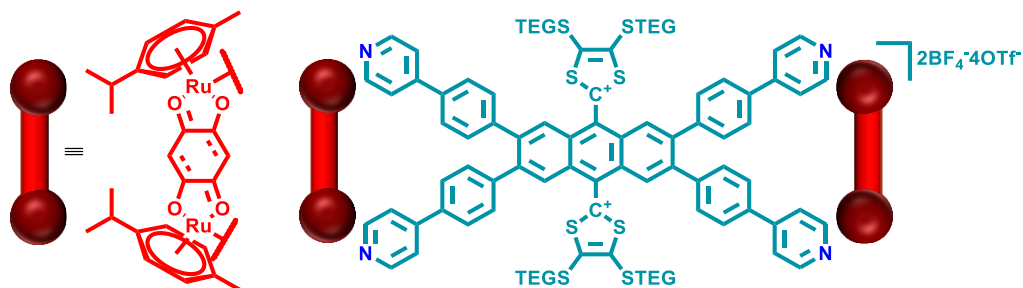
A solution of **PTZ** in CH_3NO_2 (66 μl , 0.05 M, 3.3 μmol) was added to the solution of **RuBenzoA3** (6 mg, 0.81 μmol) in CH_3NO_2 (1 mL). The red solution was used without any purification.

^1H NMR (300 MHz, CD_3NO_2) δ 8.41 (d, $J = 6.4$ Hz, 16H), 7.79 (s, 8H), 7.69 (d, $J = 6.2$ Hz, 16H), 7.64 (d, $J = 8.1$ Hz, 16H), 7.47 (d, $J = 8.1$ Hz, 16H), 5.98 (d, $J = 6.6$ Hz, 16H), 5.84 (s, 8H), 5.78 (d, $J = 6.6$ Hz, 16H), 3.80 (t, $J = 5.3$ Hz, 16H), 3.48 (t, $J = 5.0$ Hz, 16H), 3.32 – 3.25 (m, 16H), 3.15 – 3.07 (m, 16H), 3.04 – 2.98 (m, 16H), 2.98 – 2.83 (m, 24H), 2.89 (s, 24H), 2.25 (s, 24H), 1.37 (dd, $J = 6.9, 1.9$ Hz, 48H). DOSY (300 MHz, CD_3NO_2) $D = 2.0 \times 10^{-10} \text{ m}^2 \cdot \text{s}^{-1}$. HRMS: $[\text{L}^{2+}_2\text{M}_8 + 4\text{BF}_4^- + \text{OTf}]^{7+}$ found: 906.2912, calculated: 906.2895, $[\text{L}^{2+}_2\text{M}_8 + 4\text{BF}_4^- + 2\text{OTf}]^{6+}$ found: 1082.1693, calculated: 1082.1632, $[\text{L}^{2+}_2\text{M}_8 + 4\text{BF}_4^- + 3\text{OTf}]^{5+}$ found: 1328.3864, calculated: 1328.3864, $[\text{L}^{2+}_2\text{M}_8 + 4\text{BF}_4^- + 4\text{OTf}]^{4+}$ found: 1697.7222, calculated: 1697.7211.

((RuBenzoA3)Ox)Red

A solution of **TDAE⁻** in CH_3NO_2 (66 μl , 0.05 M, 3.3 μmol , 4 equiv.) was added to the solution of **(RuBenzoA3)Ox** (6.3 mg, 0.81 μmol) in CH_3NO_2 (1 mL). The red solution was used without any purification. HRMS: $[\text{L}_2\text{M}_8 + \text{BF}_4^-]^{7+}$ found: 847.7277, calculated: 847.7235, $[\text{L}_2\text{M}_8 + \text{BF}_4^- + \text{OTf}]^{6+}$ found: 1013.8386, calculated: 1013.8361, $[\text{L}_2\text{M}_8 + \text{BF}_4^- + 2\text{OTf}]^{5+}$ found: 1246.6001, calculated: 1246.5938, $[\text{L}_2\text{M}_8 + \text{BF}_4^- + 3\text{OTf}]^{4+}$ found: 1595.4836, calculated: 1595.4804.

RuBenzoA3Ox

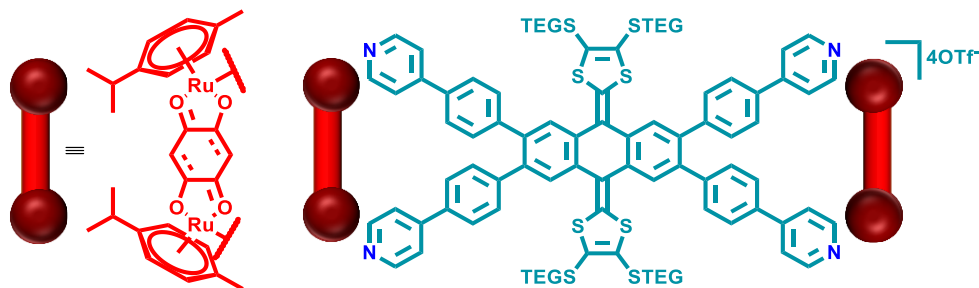


A solution of **PTZ** in CH_3NO_2 (94 μl , 0.05 M, 4.69 μmol) was added to a solution of ligand **A3** (4.00 mg, 2.34 μmol) in CH_3NO_2 (1 mL). Solid **RuBenzo(OTf)₂** (4.25 mg, 4.69 μmol) was added and the solution was stirred for 2 h at 55 °C. Then, Et_2O was added and the resulting suspension was centrifuged. The solid was rinsed 3 times with Et_2O and dried under vacuum to give **RuBenzoA3Ox** as a red powder (7 mg, 85 %).

^1H NMR (300 MHz, CD_3NO_2) δ 8.20 (d, $J = 6.2$ Hz, 8H), 8.17 (s, 4H), 7.56 (d, $J = 6.5$ Hz, 8H), 7.44 (d, $J = 8.1$ Hz, 8H), 7.17 (d, $J = 8.1$ Hz, 8H), 6.01 (d, $J = 6.3$ Hz, 8H), 5.79 (d, $J = 6.3$ Hz, 8H), 5.70 (s, 4H), 3.93 (t,

$J = 5.3$ Hz, 8H), 3.63 – 3.50 (m, 24H), 3.49 – 3.41 (m, 8H), 3.33 – 3.24 (m, 8H), 3.23 – 3.17 (m, 8H), 3.08 (s, 12H), 2.99 – 2.86 (m, 4H), 2.23 (s, 12H), 1.37 (d, $J = 6.9$ Hz, 24H). DOSY (300 MHz, CD_3NO_2) $D = 2.8 \times 10^{-10} \text{ m}^2 \cdot \text{s}^{-1}$. HRMS: $[\text{RuBenzoA3Ox}^{6+} + \text{BF}_4^-]^{5+}$ found: 602.1086, calculated: 602.1066, $[\text{L}^{2+}_2\text{M}_4 + \text{OTf}]^{5+}$ found: 614.7007, calculated: 614.6962, $[\text{L}^{2+}_2\text{M}_4 + 2\text{BF}_4^-]^{4+}$ found: 774.3871, calculated: 774.3842, $[\text{L}^{2+}_2\text{M}_4 + \text{BF}_4^- + \text{OTf}]^{4+}$ found: 789.8717, calculated: 789.8713, $[\text{L}^{2+}_2\text{M}_4 + 2\text{OTf}]^{4+}$ found: 805.6141, calculated: 805.6084, $[\text{L}^{2+}_2\text{M}_4 + 2\text{BF}_4^- + \text{OTf}]^{3+}$ found: 1082.1626, calculated: 1082.1632, $[\text{L}^{2+}_2\text{M}_4 + \text{BF}_4^- + 2\text{OTf}]^{3+}$ found: 1103.1499, calculated: 1103.1459, $[\text{L}^{2+}_2\text{M}_4 + 3 \text{OTf}]^{3+}$ found: 1123.7969, calculated: 1123.7953.

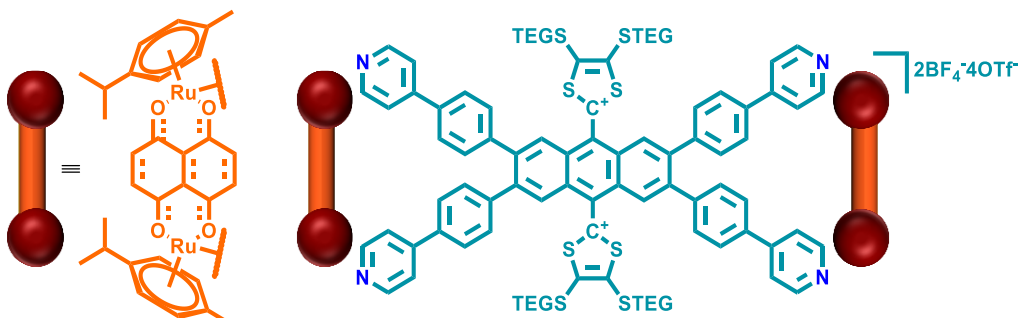
(RuBenzoA3Ox)Red



A solution of **TDAE** in CH_3NO_2 (42 μl , 0.05 M, 2.1 μmol) was added to the solution of **RuBenzoA3Ox** (3.93 mg, 0.5 μmol) in CH_3NO_2 (1 mL). The red solution was used without any purification.

^1H NMR (300 MHz, CD_3NO_2) δ 8.21 (d, $J = 6.2$ Hz, 8H), 7.94 (s, 4H), 7.57 (d, $J = 6.0$ Hz, 8H), 7.42 (d, $J = 8.2$ Hz, 8H), 7.20 (s, 8H), 6.01 (d, $J = 6.2$ Hz, 8H), 5.80 (d, $J = 6.2$ Hz, 8H), 5.71 (d, $J = 2.2$ Hz, 4H), 3.72 (d, $J = 6.3$ Hz, 8H), 3.62 – 3.53 (m, 8H), 3.57 – 3.46 (m, 16H), 3.48 – 3.38 (m, 8H), 3.25 (s, 12H), 3.18 – 2.98 (m, 8H), 2.26 (s, 12H), 1.38 (d, $J = 6.9$ Hz, 24H). DOSY (300 MHz, CD_3NO_2) $D = 2.8 \times 10^{-10} \text{ m}^2 \cdot \text{s}^{-1}$. HRMS: $[\text{L}_2\text{M}_4]^{4+}$ found: 730.8817, calculated: 730.8824, $[\text{L}^{2+}_2\text{M}_4 + \text{BF}_4^-]^{3+}$ found: 1003.5125, calculated: 1003.5113, $[\text{L}^{2+}_2\text{M}_4 + \text{OTf}]^{3+}$ found: 1024.4993, calculated: 1024.1941.

RuNaphA3Ox

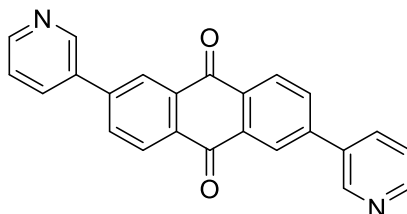


A solution of **PTZ** in CH_3NO_2 (94 μl , 0.05 M, 4.69 μmol) was added to the solution of the ligand **A3** (4.00 mg, 2.34 μmol) in CH_3NO_2 (1 mL). Solid **RuNaph(OTf)₂** (4.49 mg, 4.69 μmol) was added and the resulting solution was stirred for 2 h at 55 $^\circ\text{C}$. Then, Et_2O was added and the resulting suspension was centrifuged. The solid was rinsed 3 times with Et_2O and dried under vacuum to give **RuNaphA3Ox** as a yellow powder (6 mg, 71 %).

^1H NMR (300 MHz, CD_3NO_2) δ 8.42 – 8.36 (m, 8H), 8.13 (s, 4H), 7.52 – 7.45 (m, 8H), 7.41 (d, $J = 8.3$ Hz, 8H), 7.19 (s, 8H), 7.16 (d, $J = 8.3$ Hz, 8H), 5.80 (d, $J = 6.2$ Hz, 8H), 5.59 (d, $J = 6.1$ Hz, 8H), 3.92 (t, $J = 5.3$ Hz, 8H), 3.61 – 3.50 (m, 16H), 3.48 – 3.41 (m, 8H), 3.33 – 3.23 (m, 8H), 3.23 – 3.14 (m, 8H), 3.07 (s, 12H),

2.92 (p, $J = 6.9$ Hz, 4H), 2.20 (s, 12H), 1.36 (d, $J = 6.9$ Hz, 25H). DOSY (300 MHz, CD_3NO_2) $D = 2.8 \times 10^{-10} \text{ m}^2 \cdot \text{s}^{-1}$. HRMS analysis has been carried out recently and confirms the exclusive formation of **RuNaphA30x**. The detailed results will be included in the final manuscript version.

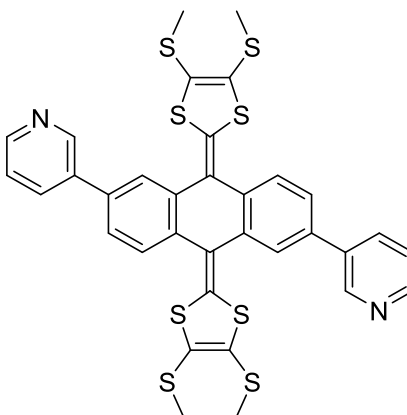
2,6-di(pyridin-3-yl)anthracene-9,10-dione (14)



In a 250 mL Schlenk flask charged with 500 mg (1.37 mmol) of 2,6-dibromoanthracene-9,10-dione **13** and 504 mg (4.1 mmol, 3 equiv.) of 3-pyridylboronic acid was added 80 mL of toluene, 20 mL of ethanol and a solution of K_2CO_3 (3.80 g in 3 ml of water). The mixture was degassed with argon for 1 h. Then, 315 mg (0.27 mmol, 0.2 equiv.) of tetrakis(triphenylphosphine)palladium (0) was added, the mixture was degassed for 15 min and stirred under argon at 90°C for 12 hours. The solution was concentrated and 50 ml of methylene chloride was added. The residue was filtered and concentrated and purified by column chromatography on silica gel with methylene chloride to methylene chloride / methanol (v/v 95/5) as eluent to afford compound **14** (150 mg, 30 %) as a yellow solid.

^1H NMR (300 MHz, Chloroform-*d*) δ 9.00 (d, $J = 2.4$ Hz, 2H), 8.72 (dd, $J = 4.8, 1.6$ Hz, 2H), 8.57 (d, $J = 1.9$ Hz, 2H), 8.47 (d, $J = 8.1$ Hz, 2H), 8.10 – 8.00 (m, 4H), 7.47 (ddd, $J = 8.0, 4.8, 0.9$ Hz, 2H). ^{13}C NMR (76 MHz, CDCl_3) δ 182.65, 150.16, 148.50, 143.95, 134.77, 134.29, 132.88, 132.58, 128.62, 125.92, 124.00, 77.58, 77.36, 77.16, 76.74, 29.84. FAB-HRMS: found: 362.1049, calculated: 362.1055.

3,3'-(9,10-bis(4,5-bis(methylthio)-1,3-dithiol-2-ylidene)-9,10-dihydroanthracene-2,6-diyl)dipyridine (A4Me)

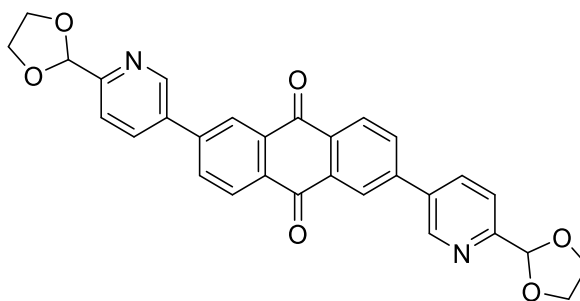


In a 50 mL Schlenk flask charged with 315 mg (0.41 mmol) of dimethyl (4,5-bis(methylthio)-1,3-dithiol-2-yl)phosphonate **7**, was added 4 mL of anhydrous THF and the solution was cooled to -78°C . Then, 400 μL of *n*-Butyllithium (1 mmol, 2.4 equiv., 2.5 M) was added and the solution was stirred at -78°C for 1 h. Then, 150 mg of 2,6-di(pyridin-3-yl)anthracene-9,10-dione **14** (0.29 mmol, 0.4 equiv.) in 10 mL of anhydrous THF was cannulated into the reaction media and the reaction was warmed up to r.t. overnight. Then, the solution was concentrated, and 50 ml of methylene chloride was added. The organic layer was washed with 2×30 mL of water, dried over MgSO_4 and concentrated. The residue was purified by column chromatography on alumina

with methylene chloride to methylene chloride / methanol (v/v 99/1) as eluent to afford ligand **A4Me** (190 mg, 64 %) as an orange sticky solid.

^1H NMR (300 MHz, Chloroform-*d*) δ 8.94 (dd, $J = 2.4, 0.9$ Hz, 2H), 8.63 (dd, $J = 4.8, 1.6$ Hz, 2H), 7.94 (ddd, $J = 7.9, 2.4, 1.6$ Hz, 2H), 7.75 (d, $J = 1.8$ Hz, 2H), 7.66 (d, $J = 8.0$ Hz, 2H), 7.55 (dd, $J = 8.0, 1.9$ Hz, 2H), 7.42 (ddd, $J = 7.9, 4.8, 0.8$ Hz, 2H), 2.40 (d, $J = 5.1$ Hz, 12H). ^{13}C NMR (76 MHz, CDCl_3) δ 148.72, 148.33, 136.13, 135.81, 135.47, 134.45, 134.37, 132.77, 126.73, 126.31, 125.69, 125.06, 124.06, 123.89, 122.79, 77.58, 77.37, 77.16, 76.74, 19.39, 19.26. FAB-HRMS: found: 717.9854, calculated: 717.9862.

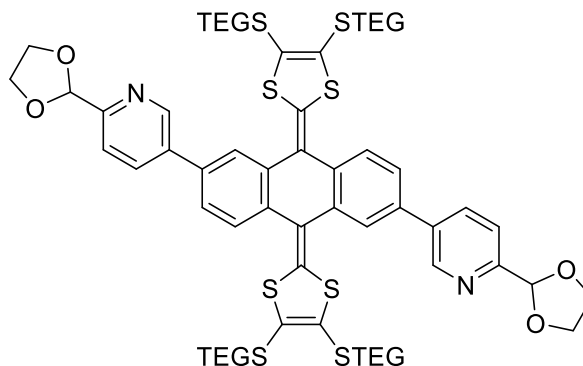
2,6-bis(6-(1,3-dioxolan-2-yl)pyridin-3-yl)anthracene-9,10-dione (15)



In a 20 ml microwave tube containing 782 mg (2.14 mmol) of 2,6-dibromoanthracene-9,10-dione **13**, 75 mg (0.1 mmol, 5 %) of $\text{Pd}(\text{PPh}_3)_2\text{Cl}_2$, 2.7 g (12.8 mmol) of K_3PO_4 , and 1.00 g (5.13 mmol) of 6-(1,3-dioxolan-2-yl)pyridin-3-yl)boronic acid were added 80 ml of anhydrous DMF. The mixture was degassed for 10 min and heated under microwave irradiation at 120°C for 2 h. Then, water (1 L) was added to the resulting green mixture. The red precipitate was filtered, solubilized in DCM (50 mL) and washed 3 times with water. The organic extracts were concentrated and purified by column chromatography on silica gel, with methylene chloride to methylene chloride / methanol (v/v 99/1) as eluent to afford 2,6-bis(6-(1,3-dioxolan-2-yl)pyridin-3-yl)anthracene-9,10-dione **15** (420 mg, 38 %) as an orange solid.

^1H NMR (300 MHz, Chloroform-*d*) δ 9.00 (dd, $J = 2.3, 0.8$ Hz, 2H), 8.57 (d, $J = 1.9$ Hz, 2H), 8.47 (d, $J = 8.1$ Hz, 2H), 8.08 (ddd, $J = 15.1, 8.1, 2.2$ Hz, 4H), 7.72 (d, $J = 8.1$ Hz, 2H), 5.97 (s, 2H), 4.31 – 4.07 (m, 8H). ^{13}C NMR (76 MHz, CDCl_3) δ 182.59, 157.59, 147.99, 143.59, 135.71, 135.11, 134.32, 132.99, 132.68, 128.67, 126.00, 121.12, 103.45, 77.58, 77.36, 77.16, 76.74, 65.87, 29.87. FAB-HRMS: found: 507.1566, calculated: 507.1511.

5,5'-(9,10-bis(4,5-bis((2-(2-methoxyethoxy)ethoxy)ethyl)thio)-1,3-dithiol-2-ylidene)-9,10-dihydroanthracene-2,6-diyl)bis(2-(1,3-dioxolan-2-yl)pyridine) (16)

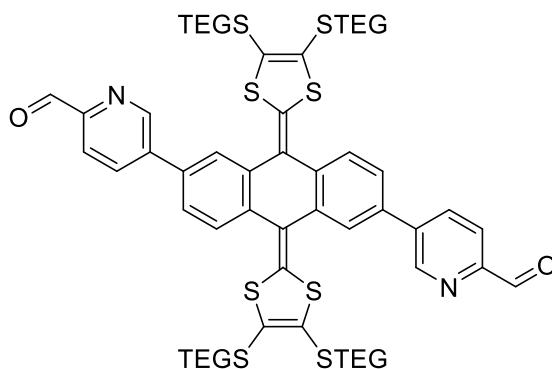


In a 25 mL Schlenk flask charged with 292 mg (0.51 mmol, 3 equiv.) of phosphonate **6**, was added 6 mL of anhydrous THF and the solution was cooled to -78 °C. Then, 295 μL of *n*-Butyllithium (0.47 mmol, 2.75 equiv.,

1.6 M) was added and the solution was stirred at $-78\text{ }^{\circ}\text{C}$ for 1 h. Then, 87 mg of **15** (0.17 mmol, 1 equiv.) in 10 mL of anhydrous THF was cannulated into the reaction media and the reaction was warmed up to r.t. overnight. Then, the solution was concentrated, and 30 ml of methylene chloride was added. The organic layer was washed with $2 \times 30\text{ mL}$ of water, dried over MgSO_4 and concentrated. The residue was purified by column chromatography on alumina with methylene chloride to methylene chloride / methanol (v/v 99/1) as eluent to afford compound **16** (210 mg, 88 %) as a red viscous liquid.

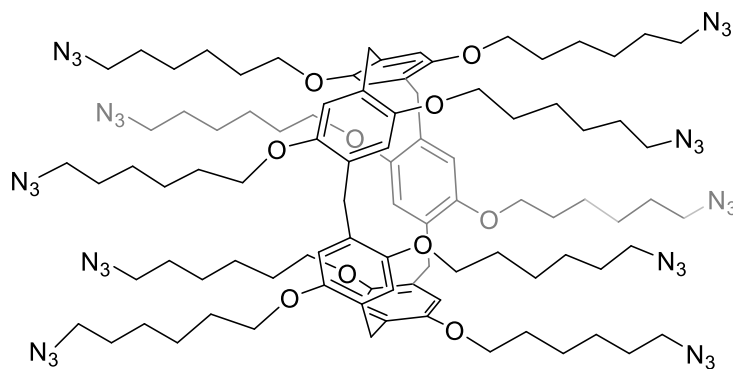
Butyllithium ^1H NMR (300 MHz, Chloroform-*d*) δ 8.93 (d, $J = 2.2\text{ Hz}$, 2H), 7.99 (dd, $J = 8.1, 2.3\text{ Hz}$, 2H), 7.78 (d, $J = 1.8\text{ Hz}$, 2H), 7.70 (d, $J = 8.0\text{ Hz}$, 2H), 7.65 (d, $J = 8.1\text{ Hz}$, 2H), 7.55 (dd, $J = 8.0, 1.9\text{ Hz}$, 2H), 5.94 (s, 2H), 4.30 – 4.05 (m, 8H), 3.76 – 3.59 (m, 32H), 3.53 (pd, $J = 4.9, 1.6\text{ Hz}$, 8H), 3.35 (d, $J = 2.4\text{ Hz}$, 12H), 3.02 (q, $J = 6.7\text{ Hz}$, 8H). ^{13}C NMR (76 MHz, CDCl_3) δ 156.11, 148.04, 136.49, 135.61, 135.51, 135.19, 134.51, 132.69, 127.06, 126.30, 126.19, 125.24, 124.07, 122.27, 120.97, 103.68, 77.58, 77.36, 77.16, 76.74, 72.09, 70.72, 70.68, 70.20, 70.14, 65.80, 59.18, 53.56, 35.78, 35.61. FAB-HRMS: found: 1390.3456, calculated: 1390.3430.

5,5'-(9,10-bis(4,5-bis((2-(2-methoxyethoxy)ethoxy)ethyl)thio)-1,3-dithiol-2-ylidene)-9,10-dihydroanthracene-2,6-diyl)dipicolinaldehyde (A5)



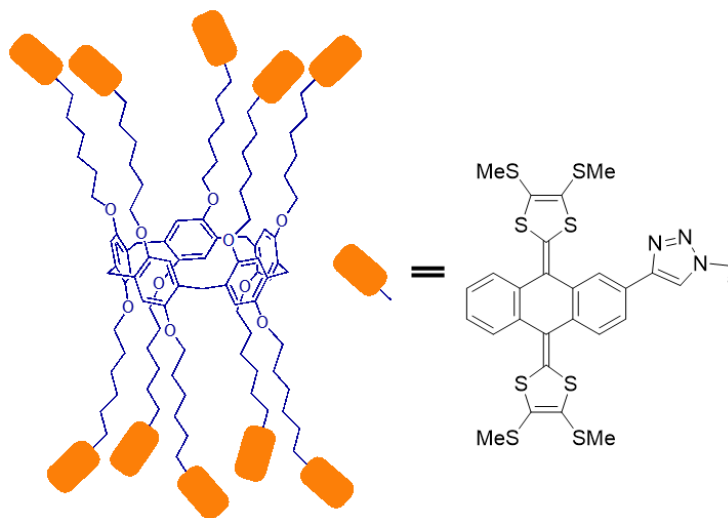
In a 20 ml flask containing **16** (105 mg, 75.4 μmol) was added a 5% solution of HCl (15 mL). The mixture was stirred at $70\text{ }^{\circ}\text{C}$ for 2 h. The reaction was quenched with a saturated solution of NaHCO_3 (200 mL), extracted with DCM (200 mL) and concentrated under vacuum. The residue was purified by column chromatography on alumina with methylene chloride as eluent to afford compound **A5** (84 mg, 85 %) as a red viscous liquid.

^1H NMR (300 MHz, Chloroform-*d*) δ 10.14 (s, 2H), 9.09 (dd, $J = 2.1, 1.0\text{ Hz}$, 2H), 8.12 (dd, $J = 8.1, 2.1\text{ Hz}$, 2H), 8.08 (dd, $J = 8.1, 1.0\text{ Hz}$, 2H), 7.84 (d, $J = 1.8\text{ Hz}$, 2H), 7.73 (d, $J = 8.1\text{ Hz}$, 2H), 7.62 (dd, $J = 8.1, 1.9\text{ Hz}$, 2H), 3.74 – 3.58 (m, 32H), 3.57 – 3.48 (m, 8H), 3.34 (d, $J = 3.4\text{ Hz}$, 12H), 3.09 – 2.93 (m, 8H). ^{13}C NMR (76 MHz, CDCl_3) δ 193.05, 151.80, 148.75, 140.09, 135.67, 135.30, 135.17, 134.65, 133.77, 127.39, 126.49, 126.13, 125.56, 124.27, 122.19, 121.83, 77.58, 77.36, 77.16, 76.74, 72.08, 70.73, 70.69, 70.14, 59.18, 35.81, 35.63, 29.84. FAB-HRMS: found: 1302.2923, calculated: 1302.2906.

Pillar arene (18)¹²⁹

In a 50 ml Schlenk pillar arene **17** (151 mg, 67 μ mol) was dissolved in 3 ml of anhydrous DMF. Then solid NaN₃ (48 mg, 741 μ mol) was added, and the reaction mixture was stirred at room temperature overnight. The reaction was quenched with 5 ml of H₂O and the product was extracted with diethyl ether (3 \times 5 ml). The organic layer was washed with water (3 \times 10 ml), dried on MgSO₄ and carefully concentrated under vacuum. The resulting white crystalline product did not require any further purification.

¹H NMR (300 MHz, Chloroform-*d*) δ 6.84 (s, 10H), 3.88 (t, *J* = 6.3 Hz, 20H), 3.75 (s, 10H), 3.10 (t, *J* = 6.7 Hz, 20H), 1.87 – 1.72 (m, 20H), 1.55 – 1.36 (m, 40H), 1.36 – 1.20 (m, 20H). ¹³C NMR (76 MHz, CDCl₃) δ 149.79, 128.35, 114.89, 77.58, 77.16, 76.74, 68.14, 51.43, 29.80, 29.61, 28.73, 26.69, 25.93. IR, cm⁻¹ 852.42, 877.25, 1038.96, 1204.42, 1254.75, 1405.69, 1472.71, 1497.09, 2084.56, 2859.19, 2933.29.

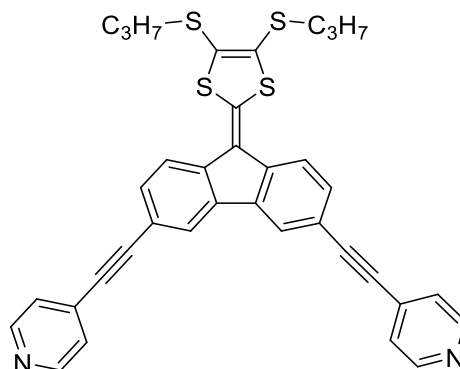
Pillar-exTTF

In a 50 ml Schlenk flask charged with exTTF derivative **19**¹³¹ (87 mg, 147.6 μ mol) was added a solution of pillar arene **18** (25 mg, 13.4 μ mol) in DCM (5 ml) and 3.5 ml of H₂O. The mixture was degassed for 10 minutes. Then CuSO₄·5H₂O (3.3 mg, 13.4 μ mol) and sodium ascorbate (10.6 mg, 54 μ mol) were added, and the reaction mixture was stirred vigorously at room temperature overnight. The organic layer was washed with water (2 \times 20 ml), dried on MgSO₄ and concentrated under vacuum. The residue was purified by column chromatography on silica gel with methylene chloride as eluent to afford compound **Pillar-exTTF** (90 mg, 85 %) as a yellow solid.

¹H NMR (499 MHz, Chloroform-*d*) δ 8.05 – 7.93 (m, 10H), 7.82 – 7.73 (m, 10H), 7.62 (s, 10H), 7.57 – 7.39 (m, 30H), 7.28 (s, 20H), 6.74 (s, 10H), 4.25 (s, 20H), 3.86 (s, 10H), 3.68 (s, 20H), 2.38 – 2.16 (m, 120H),

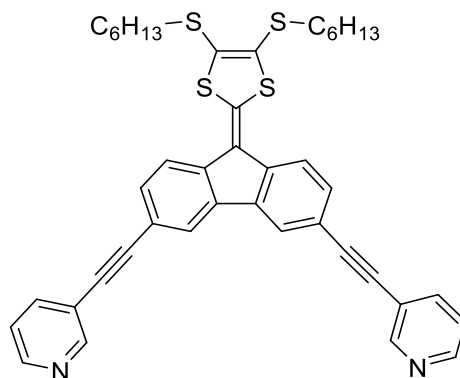
1.87 (s, 20H), 1.70 (s, 20H), 1.49 (s, 20H), 1.34 (s, 20H). ^{13}C NMR (126 MHz, CDCl_3) δ 149.80, 146.97, 135.05, 134.36, 134.02, 131.80, 131.55, 128.73, 128.18, 126.82, 126.46, 126.04, 125.85, 125.48, 123.42, 123.28, 122.33, 120.19, 114.92, 77.30, 77.25, 77.24, 77.05, 76.79, 68.24, 53.46, 50.40, 31.95, 30.41, 29.73, 29.40, 26.58, 25.97, 22.73, 19.31, 19.27, 19.17, 19.07. MALDI-MS: found: 7757, calculated: 7735.

Ligand L4Pyr



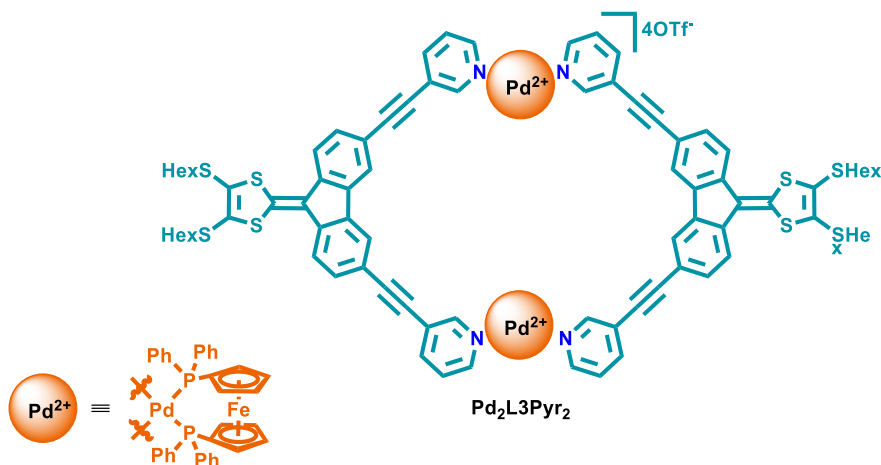
This compound was prepared following a procedure described in the literature.¹⁰³ To a solution of dimethyl (4,5-bis(propylsulfanyl)-1,3-dithiol-2-yl)phosphonate **20**¹⁰² (135 mg, 0.37 mmol, 1.5 equiv.) in anhydrous THF (10 mL) at $-78\text{ }^\circ\text{C}$, was slowly added *n*-butyllithium (0.235 mL, 0.37 mmol, 1.6 M, 1.5 equiv.). The mixture was stirred 1 h at $-78\text{ }^\circ\text{C}$ and a suspension of 3,6-bis(pyridin-4-ylethynyl)-9H-fluoren-9-one **22**¹⁰³ (95 mg, 0.25 mmol, 1 equiv.) in anhydrous THF (10 mL) at $-78\text{ }^\circ\text{C}$ was added *via* cannula. The mixture was stirred 1 h at $-78\text{ }^\circ\text{C}$ and overnight at room temperature. The solvent was removed under vacuum. The residue was treated with water and extracted with dichloromethane. The organic extracts were washed with water and dried over magnesium sulfate. The solvent was removed under vacuum. The residue was purified by chromatography on silica gel using a gradient of eluent from petroleum ether/dichloromethane (1/1) to dichloromethane/methanol (98/2) with constant 1% of trimethylamine followed by recrystallization using a dichloromethane/methanol mixture to give **L4Pyr** (105 mg, 68%) as an orange powder.

^1H NMR (300 MHz, Chloroform-*d*) δ 8.63 (bs, 4H), 8.03 (dd, $J = 1.6\text{ Hz}, 0.7\text{ Hz}$, 2H), 7.74 (dd, $J = 8.2, 0.7\text{ Hz}$, 2H), 7.61 (dd, $J = 8.2\text{ Hz}, 1.6\text{ Hz}$, 2H), 7.42 (d, $J = 6.1\text{ Hz}$, 4H), 2.97 (t, $J = 7.2\text{ Hz}$, 4H), 1.75 (q, $J = 7.3\text{ Hz}$, 4H), 1.09 (t, $J = 7.3\text{ Hz}$, 6H). ^{13}C NMR (76 MHz, CDCl_3) δ 149.84, 142.51, 137.50, 136.85, 131.65, 130.91, 129.68, 125.56, 123.39, 122.72, 119.56, 118.73, 94.87, 87.22, 38.73, 23.19, 13.24. FAB-HRMS: found: 616.1129, calculated: 616.1135.

Ligand L3Pyr

This compound was prepared following a procedure described in the literature.¹⁰² To a solution of dimethyl (4,5-bis(hexylsulfanyl)-1,3-dithiol-2-yl)phosphonate **21**¹⁰² (167 mg, 0.37 mmol) in anhydrous THF (10 mL) at -78 °C, was slowly added *n*-butyl lithium (0.235 mL, 0.37 mmol, 1.6 M). The mixture was stirred one hour at -78 °C and a suspension of 3,6-bis(pyridin-3-ylethynyl)-9H-fluorene-9-one **23** respectively (95 mg, 0.25 mmol) in anhydrous THF (10 mL) at -78 °C was added *via* cannula. The mixture was stirred 1 h at -78 °C and overnight at room temperature. The solvent was removed under vacuum. The residue was treated with water and extracted with dichloromethane. The organic extracts were washed with water and dried over magnesium sulfate. The solvent was removed under vacuum and the residue was purified by chromatography on silica gel using a gradient of eluent: petroleum ether/dichloromethane (1/1) to dichloromethane/methanol (98/2) with constant 1% of trimethylamine followed by recrystallization using a dichloromethane/methanol mixture to give **L3Pyr** (94 mg, 54 %) as red crystals.

¹H NMR (300 MHz, Chloroform-*d*) δ 8.82 (d, *J* = 1.8 Hz, 2H), 8.57 (dd, *J* = 4.9, *J* = 1.8 Hz, 2H), 8.06 (d, *J* = 1.6 Hz, 2H), 7.86 (ddd, *J* = 7.9, *J* = 1.8, *J* = 1.8 Hz, 2H), 7.76 (d, *J* = 8.2 Hz, 2H), 7.62 (dd, *J* = 8.2, *J* = 1.6 Hz, 2H), 7.31 (dd, *J* = 7.9, 4.9 Hz, 2H), 2.99 (m, 4H), 1.71 (m, 4H), 1.48 (m, 4H), 1.33 (m, 8H), 0.90 (t, *J* = 6.8 Hz, 6H). ¹³C NMR (76 MHz, CDCl₃) δ 152.27, 148.43, 141.61, 138.38, 137.04, 136.80, 130.49, 129.22, 123.08, 123.04, 122.57, 120.70, 119.55, 119.04, 93.64, 86.37, 36.67, 31.37, 29.74, 28.29, 22.57, 14.08. FAB-HRMS: found: 700.2067, calculated: 700.2074.

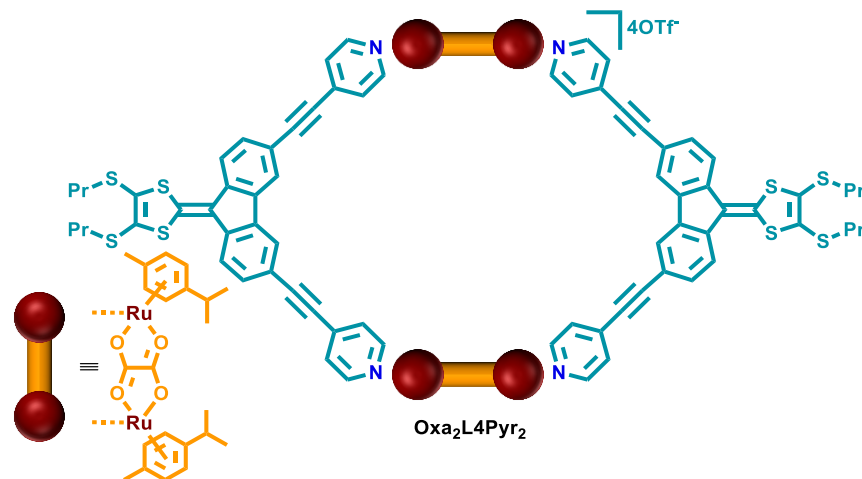
Metalla-structure Pd₂L3Pyr₂

A stoichiometric mixture of ligand **L3Pyr** (7.01 mg, 0.01 mol) and *cis*-Pd(*dppf*)(OTf)₂ (9.57 mg, 0.01 mol) in CH₂Cl₂ (1 mL) was stirred for 2 h at room temperature. Then, Et₂O was added and the resulting suspension

was centrifuged. The solid was rinsed 3 times with Et₂O and dried under vacuum to give **Pd₂L₃Pyr₂** (15.10 mg, 89%) as a red powder.

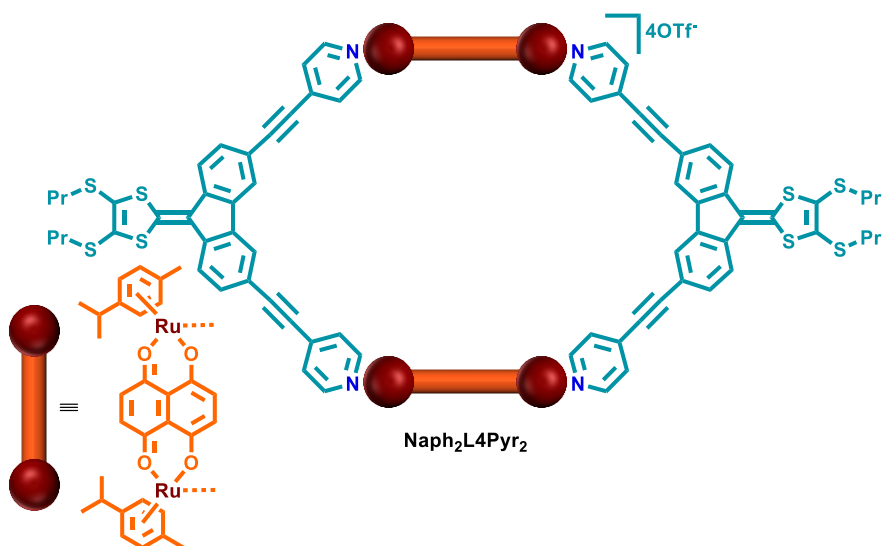
¹H NMR (300 MHz, CD₂Cl₂) δ 8.85 (s, 4H), 8.72 (s, 4H), 8.31 (s, 4H), 8.11 – 8.08 (m, 8H), 7.98 – 7.91 (m, 12H), 7.71 – 7.62 (m, 24H), 7.54 (d, *J* = 7.7 Hz, 8H), 7.12 (t, *J* = 7.5 Hz, 4H), 4.93 (s, 4H), 4.78 (s, 4H), 4.57 (s, 4H), 4.33 (s, 4H), 2.97 (t, *J* = 7.3 Hz, 8H), 1.73 – 1.69 (m, 16H), 1.48 – 1.39 (m, 8H), 1.31 – 1.29 (m, 8H), 0.86 (t, *J* = 7.8, 7.0 Hz, 12H). ¹H DOSY NMR (300 MHz, CD₂Cl₂, C = 10⁻³ M) D = 4.96 × 10⁻¹⁰ m².s⁻¹. ESI-FTICR-HRMS (*m/z*), [[**Pd₂L₃Pyr₂**]⁴⁺ - 2TfO⁻]²⁺: found: 1510.667, calculated 1510.667.

Metalla-tweezer Oxa₂L₄Pyr₂



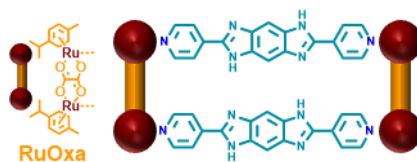
A mixture of **L₄Pyr** (4.40 mg, 7 mmol) and **RuOxa(OTf)₂** (6.11 mg, 7 mmol) in MeOH (1 mL) was stirred overnight at 50 °C. Then, the solution was cooled to room temperature and Et₂O was added. The resulting mixture was centrifuged, the precipitate rinsed 3 times with Et₂O and dried under vacuum to give **Oxa₂L₄Pyr₂** (9.20 mg, 82 %) as a red powder.

¹H NMR (300 MHz, MeOD) δ 8.04 (d, *J* = 6.7 Hz, 8H), 7.71 (d, *J* = 1.5 Hz, 4H), 7.47 (d, *J* = 6.7 Hz, 8H), 7.36 – 7.26 (m, 8H), 5.95 (d, *J* = 6.2 Hz, 8H), 5.78 (d, *J* = 6.2 Hz, 8H), 3.31 – 2.95 (m, 8H), 2.86 (q, *J* = 6.9 Hz, 4H), 2.24 (s, 12H), 1.77 (m, 8H), 1.39 (d, *J* = 6.9 Hz, 24H), 1.12 (t, *J* = 7.3 Hz, 12H). ¹H DOSY NMR (300 MHz, MeOD) D = 3.31 × 10⁻¹⁰ m².s⁻¹. ESI-FTICR-HRMS (CH₃CN) *m/z* calculated: [**Oxa₂L₄Pyr₂** - 3TfO⁻]³⁺ 833.3992, [**Oxa₂L₄Pyr₂** - 2TfO⁻]²⁺ 1325.0747; found: [**Oxa₂L₄Pyr₂** - 3TfO⁻]³⁺ 833.3992, [**Oxa₂L₄Pyr₂** - 2TfO⁻]²⁺ 1325.0747.

Metalla-tweezer ($\text{Naph}_2\text{L4Pyr}_2$)₂

A mixture of **L4Pyr** (4.40 mg, 7 mmol) and **RuNaph(OTf)₂** (6.82 mg, 7 mmol) in MeOH (1 mL) was stirred overnight at 50 °C resulting in a dark-green suspension. Then, the solution was cooled to room temperature, Et₂O was added and the resulting suspension was centrifuged. The solid was rinsed 3 times with Et₂O and dried under vacuum to give **(Naph₂L4Pyr₂)₂** (9.53 mg, 76%) as a dark-green powder.

¹H NMR (500 MHz, MeOD) δ 8.44 – 8.41 (m, 8H), 8.37 – 8.34 (m, 8H), 7.47 – 7.40 (m, 8H), 7.39 (s, 8H), 7.37 – 7.34 (m, 8H), 7.15 (dd, $J = 8.0, 1.5$ Hz, 4H), 7.14 – 7.11 (m, 8H), 7.06 (d, $J = 8.0$ Hz, 4H), 7.02 (d, $J = 1.6$ Hz, 4H), 6.82 (dd, $J = 8.0$ Hz, 1.5 Hz, 4H), 6.50 (d, $J = 7.9$ Hz, 4H), 6.20 (d, $J = 1.7$ Hz, 4H), 5.97 – 5.94 (m, 8H), 5.90 – 5.88 (m, 8H), 5.76 – 5.70 (m, 8H), 5.67 – 5.63 (m, 8H), 3.03 – 2.92 (m, 9H), 2.90 – 2.84 (m, 8H), 2.52 – 2.48 (m, 8H), 2.24 (s, 12H), 2.12 (s, 12H), 1.71 – 1.60 (m, 8H), 1.43 (dd, $J = 7.0, 4.9$ Hz, 24H), 1.36 (dd, $J = 7.0, 5.2$ Hz, 24H), 1.17 – 1.13 (m, 8H), 1.04 (t, $J = 7.3$ Hz, 12H), 0.86 (t, $J = 7.3$ Hz, 12H). ¹H DOSY NMR (500 MHz, MeOD) $D = 2.18 \times 10^{-10} \text{ m}^2 \cdot \text{s}^{-1}$. ESI-FTICR-HRMS (CH₃CN) m/z calculated: **[(Naph₂L4Pyr₂)₂ - 3TfO]³⁺** 1949.45989; found: **[(Naph₂L4Pyr₂)₂ - 3TfO]³⁺** 1949.46229.

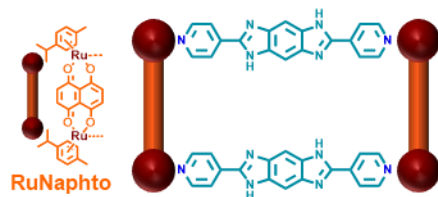
Metalla-rectangle Oxa₂BBI₂

A mixture of **BBI** (11.0 mg, 35.2 μmol) and **RuOxa(OTf)₂** (30.2 mg, 35.2 μmol) in MeOH (2.5 mL) was stirred at 50 °C for 2 h. Then, the solution was cooled to room temperature and Et₂O was added. The resulting mixture was centrifuged, the precipitate rinsed 3 times with Et₂O and dried under vacuum to give **Oxa₂BBI₂** as a yellow powder (24 mg, 58%).

¹H NMR (300 MHz, MeOD-*d*₄) δ 8.20 (d, $J = 6.8$ Hz, 8H), 7.92 (d, $J = 6.8$ Hz, 8H), 7.33 (s, 4H), 5.96 (d, $J = 6.2$ Hz, 8H), 5.78 (d, $J = 6.2$ Hz, 8H), 2.86 (hept, $J = 6.9$ Hz, 4H), 2.23 (s, 12H), 1.38 (d, $J = 6.9$ Hz, 24H). ¹H DOSY NMR (300 MHz, MeOD-*d*₄) $D = 3.9 \times 10^{-10} \text{ m}^2 \cdot \text{s}^{-1}$. UV-Vis (MeOH, $C = 2 \times 10^{-4} \text{ M}$) $\lambda_{\text{max}} = 393 \text{ nm}$ ($\epsilon = 89\,500 \text{ M}^{-1} \text{ cm}^{-1}$). ESI-FTICR-HRMS (MeOH, $C = 10^{-3} \text{ M}$) m/z calculated: **[Oxa₂BBI₂ - 2OTf]²⁺**

1020.57385, [**Oxa₂BBI₂ - 3OTf**]³⁺ 630.73176 ; found: [**Oxa₂BBI₂ - 3OTf**]³⁺ 630.73155; [**Oxa₂BBI₂ - 2OTf**]²⁺ 1020.57562

Metalla-rectangle Naph₂BBI₂



A mixture of **BBI** (10.0 mg, 32,02 μmol) and **RuNaph(OTf)₂** (30.6 mg, 32,02 μmol) in MeOH (2.5 mL) was stirred at 50 °C for 2 h. Then, the solution was cooled to room temperature and Et₂O was added. The resulting mixture was centrifuged, and the green precipitate was rinsed 3 times with Et₂O and dried under vacuum (32 mg, 79%). Species **Naph₂BBI₂** or **(Naph₂BBI₂)₂** are observed in solution according to the solvent and concentration.

Naph₂BBI₂. ¹H NMR (300 MHz, CD₃NO₂, C = 10⁻³ M) δ 8.62 – 8.48 (m, 8H), 8.03 – 7.84 (m, 8H), 7.29 (s, 8H), 5.79 (d, J = 6.1 Hz, 8H), 5.58 (d, J = 6.1 Hz, 8H), 2.92 (hept, J = 6.8 Hz, 4H), 2.17 (s, 12H), 1.37 (d, J = 6.9 Hz, 24H). ¹H DOSY NMR (300 MHz, CD₃NO₂, C = 10⁻³ M) D = 3.3 \times 10⁻¹⁰ m².s⁻¹; ¹H DOSY NMR (300 MHz, MeOD-*d*₄, C = 10⁻⁴ M) D = 3.6 \times 10⁻¹⁰ m².s⁻¹. UV-Vis (MeOH, C = 2.10⁻⁴ M) λ_{max} = 386 (ϵ = 101 500 M⁻¹ cm⁻¹), 642 (ϵ = 5 090 M⁻¹ cm⁻¹), 696 nm (ϵ = 5 440 M⁻¹ cm⁻¹). ESI-FTICR-HRMS (MeOH, C = 10⁻⁵ M) *m/z* calculated: [**Naph₂BBI₂ - 3OTf**]³⁺ 697.41938, [**Naph₂BBI₂ - 2OTf**]²⁺ 1120.60544; found: [**Naph₂BBI₂ - 3OTf**]³⁺ 697.41938, [**Naph₂BBI₂ - 2OTf**]²⁺ 1120.60594.

(Naph₂BBI₂)₂. ¹H NMR (499 MHz, MeOD-*d*₄, C = 4 \times 10⁻² M) δ 8.67 (d, J = 6.6 Hz, 8H), 8.60 (d, J = 6.5 Hz, 8H), 7.96 (d, J = 6.6 Hz, 8H), 7.84 – 7.80 (m, 8H), 7.44 – 7.37 (m, 16H), 5.98 (d, J = 6.0 Hz, 8H), 5.88 (d, J = 6.0 Hz, 8H), 5.77 (d, J = 6.1 Hz, 8H), 5.64 (d, J = 6.0 Hz, 8H), 2.97 (hept, J = 7.0 Hz, 4H), 2.88 (hept, J = 7.1 Hz, 4H), 2.24 (s, 12H), 2.12 (s, 12H), 1.43 (d, J = 6.9 Hz, 24H), 1.36 (d, J = 6.9 Hz, 24H). ¹H DOSY NMR (300 MHz, MeOD-*d*₄, C = 4 \times 10⁻² M) D = 2.6 \times 10⁻¹⁰ m².s⁻¹. ESI-FTICR-HRMS (MeOH, C = 10⁻³ M) *m/z* calculated: [(Naph₂BBI₂)₂ - 3OTf]³⁺ 1543.45832; [(Naph₂BBI₂)₂ - 4OTf]⁴⁺ 1120.60544; found: [(Naph₂BBI₂)₂ - 3OTf]³⁺ 1543.46492; [(Naph₂BBI₂)₂ - 4OTf]⁴⁺ 1120.60594.

4. Supporting materials

4.1. Additional analyses related to Chapter 2

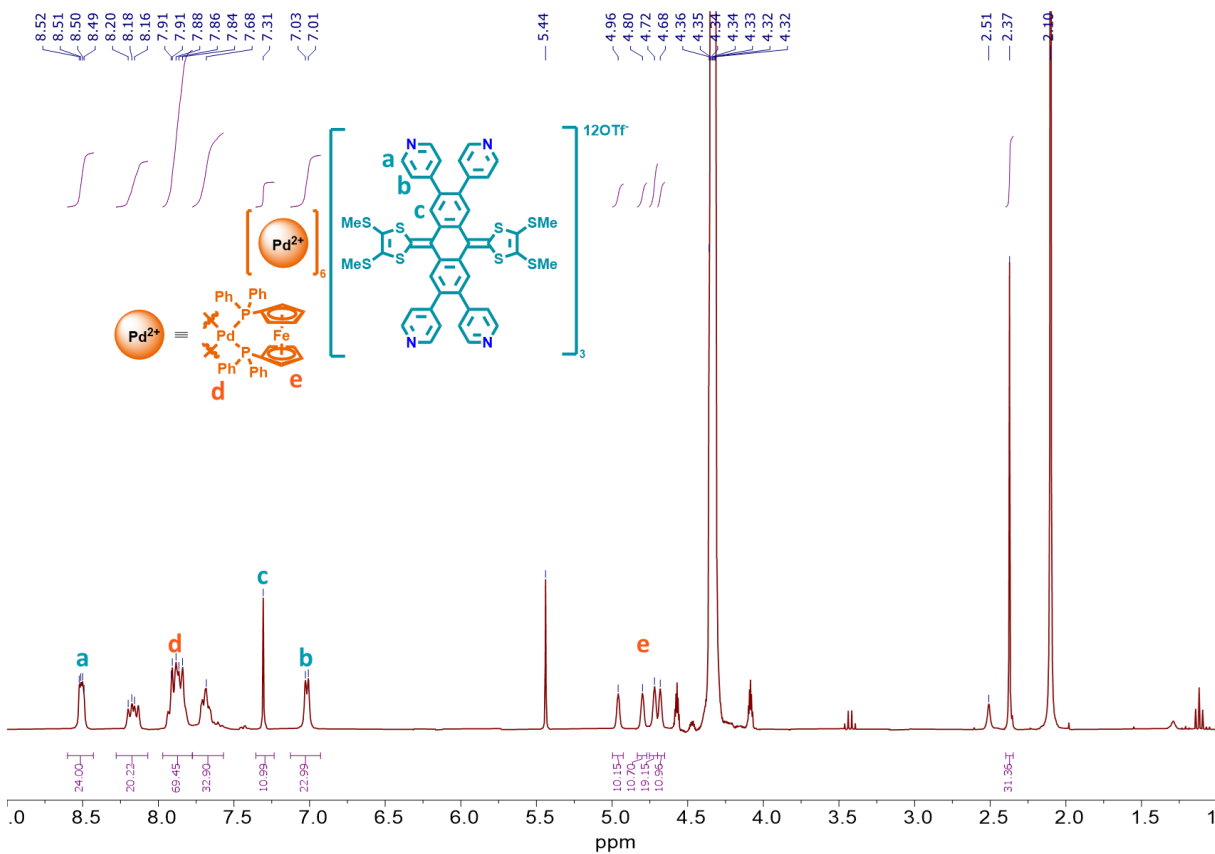
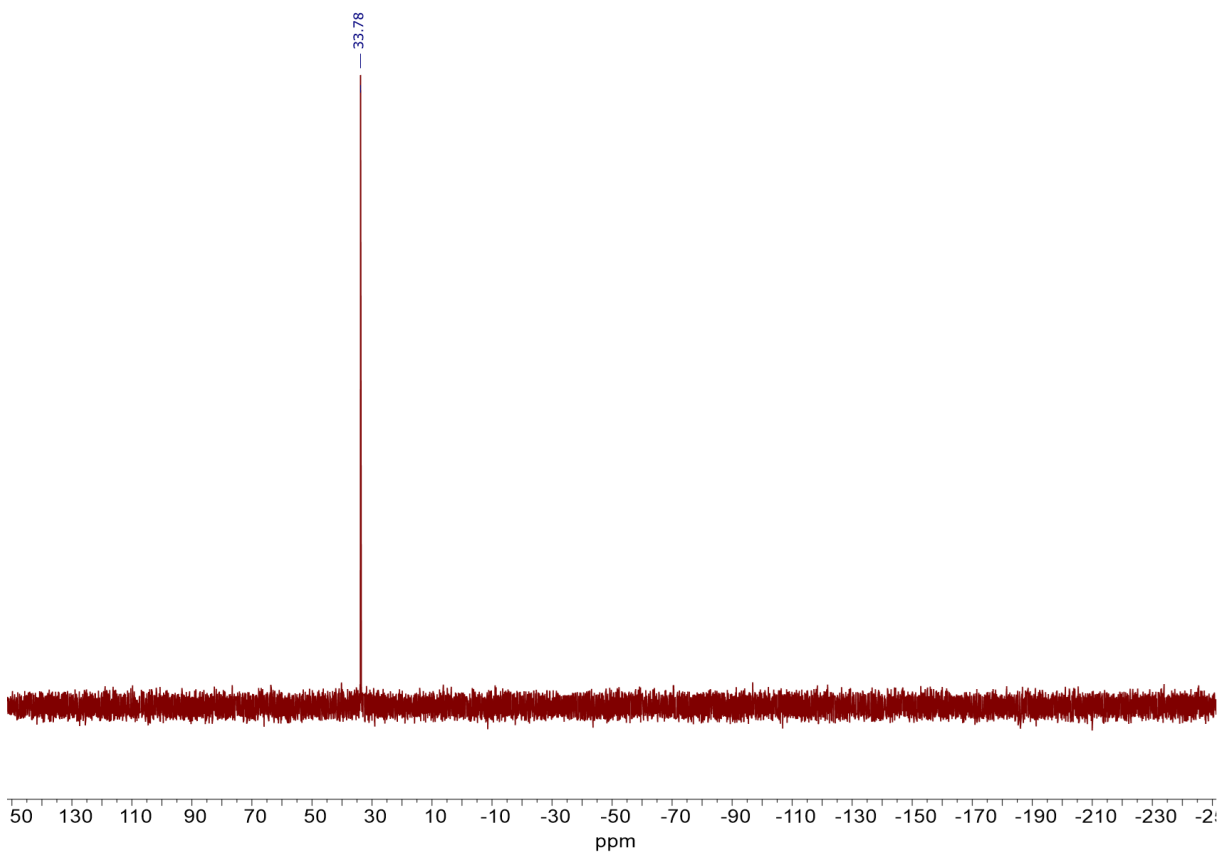
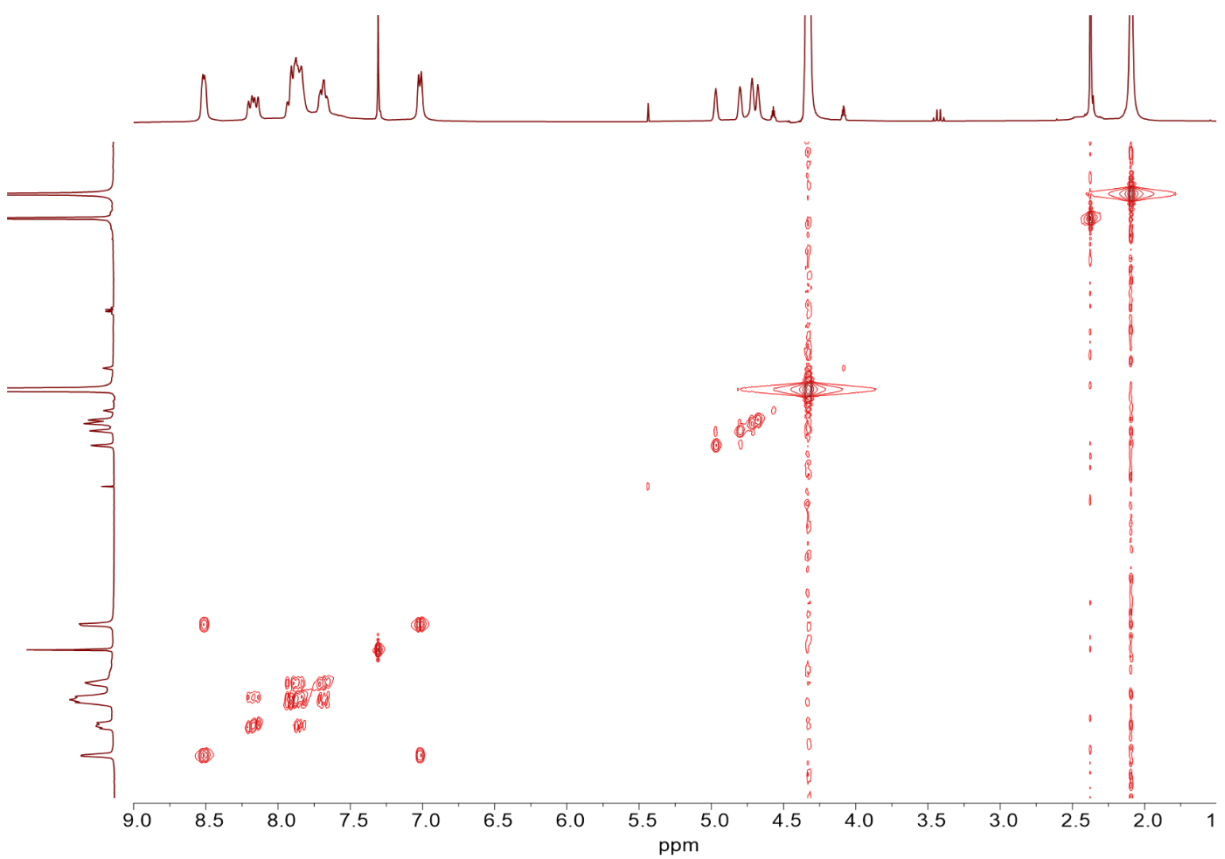


Figure S1. ^1H NMR spectrum of $\text{Pd}(\text{dppf})\text{A1Me}$ in CD_3NO_2 .

Figure S2. ^{31}P NMR spectrum of **Pd(dppf)A1Me** in CD_3NO_2 .Figure S3. COSY NMR spectrum of **Pt(dppf)A1Me** in CD_3NO_2 .

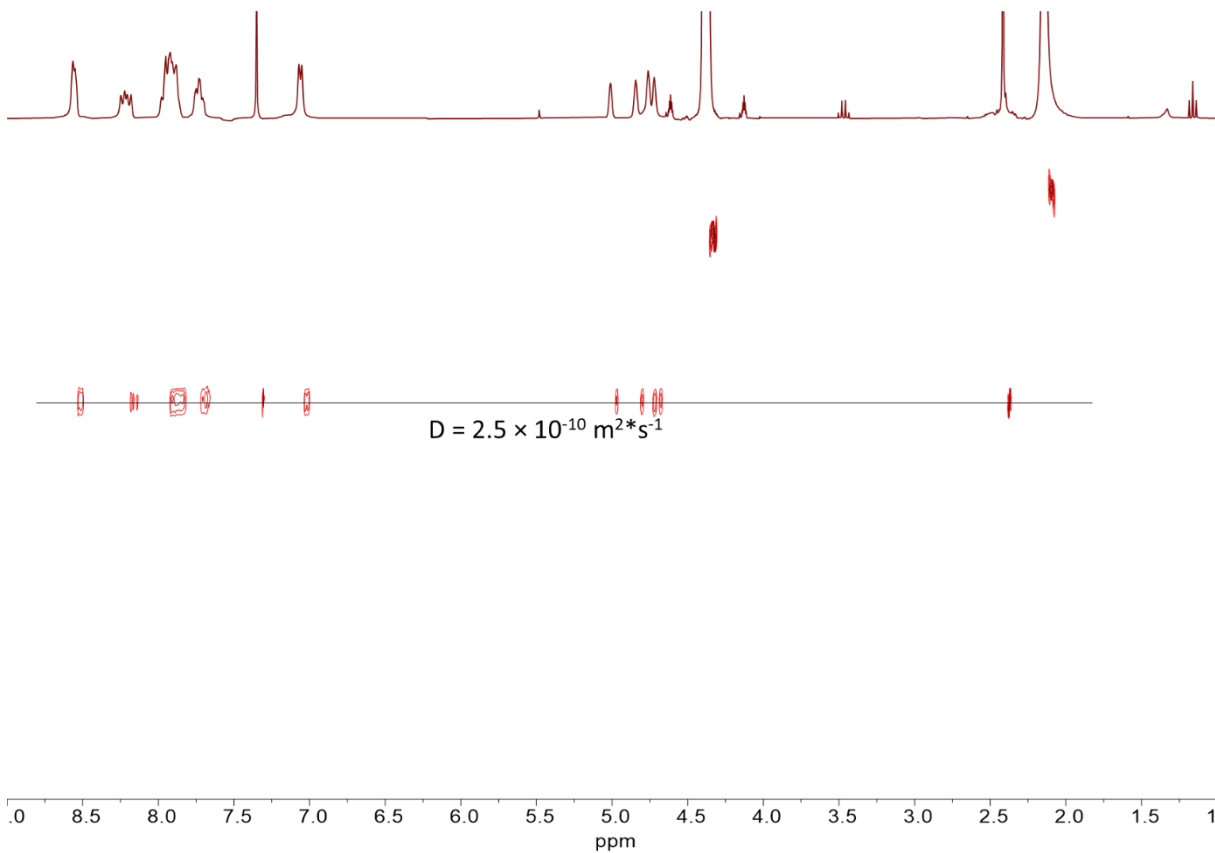


Figure S4. DOSY NMR spectrum of **Pd(dppf)A1Me** in CD_3NO_2 .

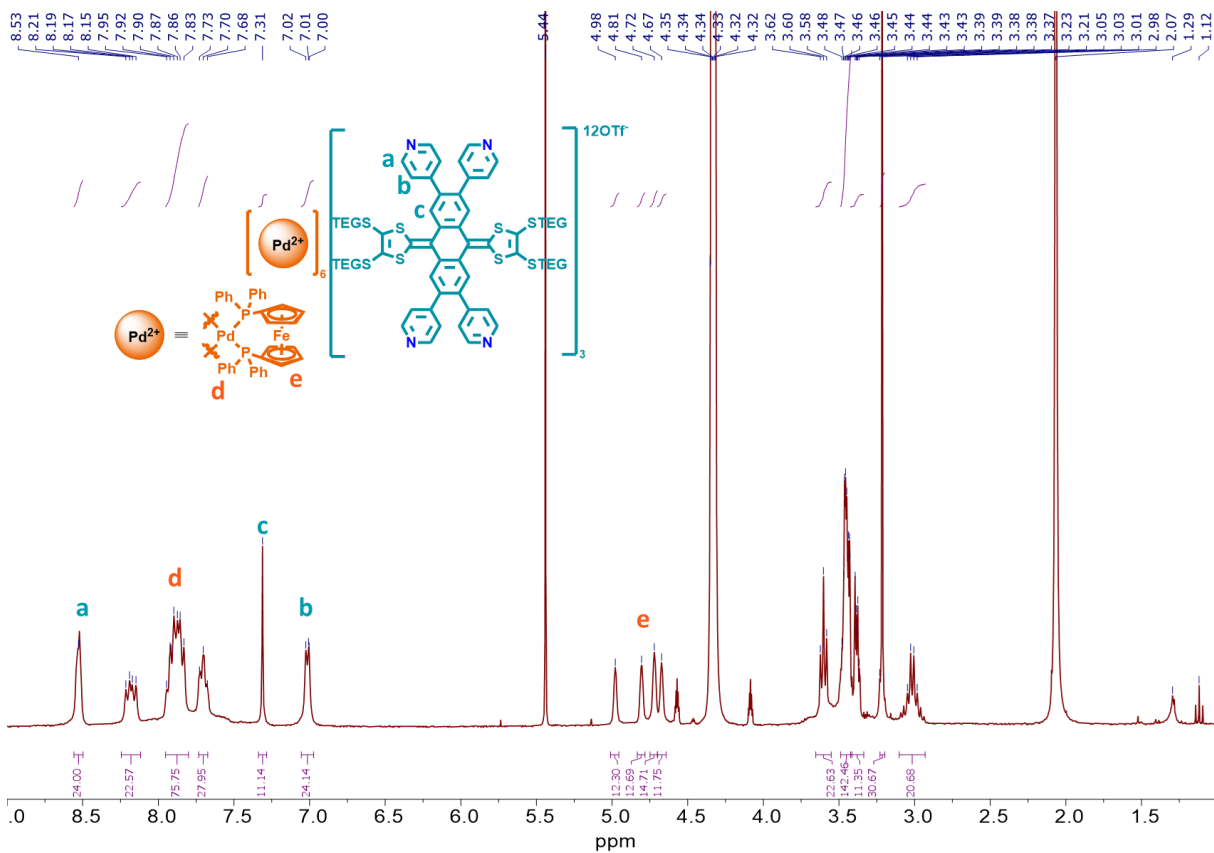
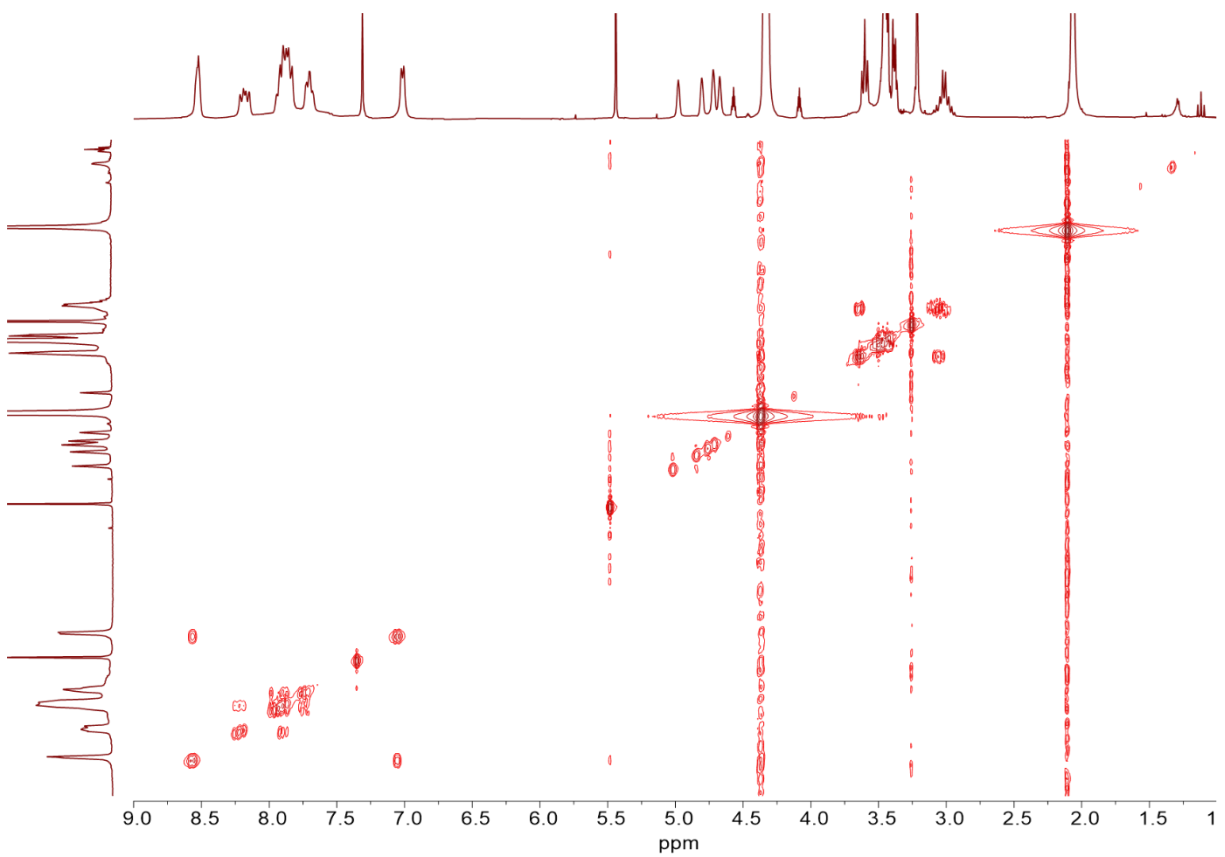
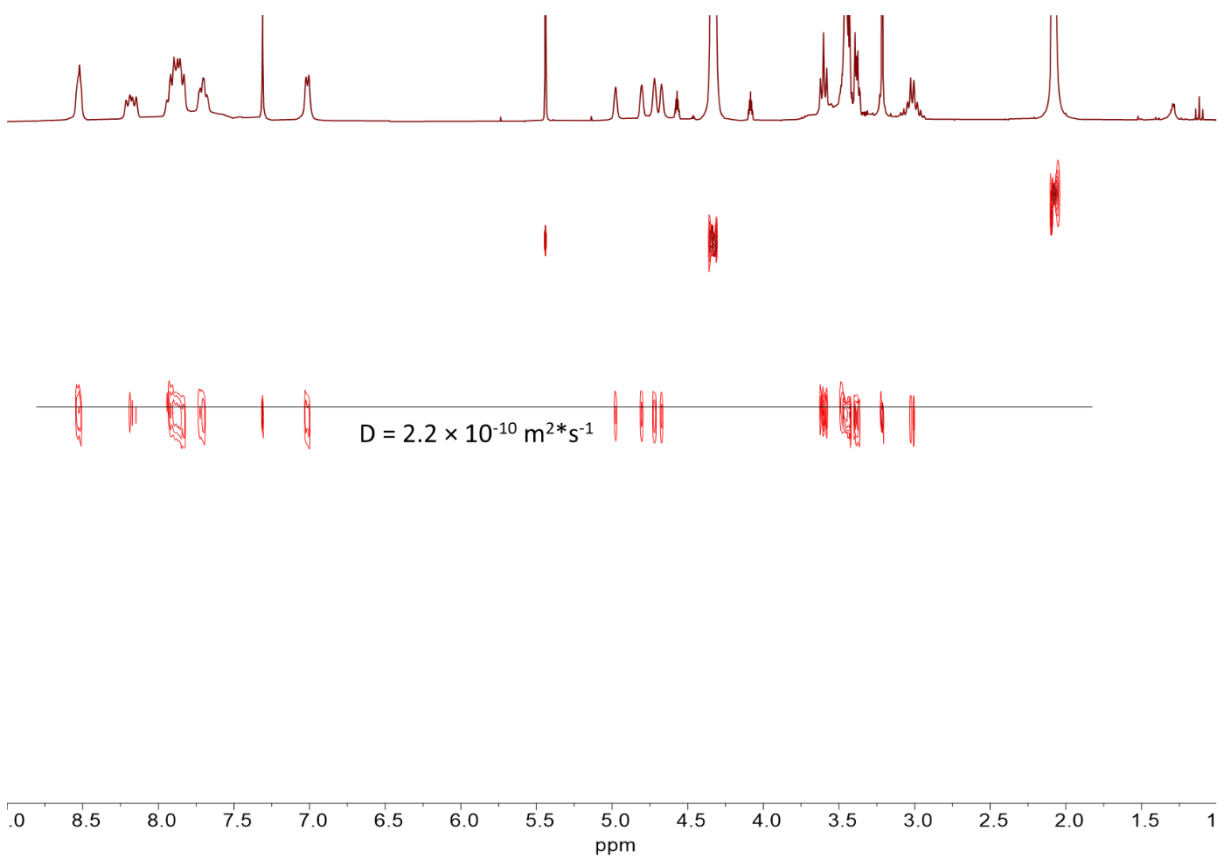


Figure S5. ^1H NMR spectrum of **Pd(dppf)A1TEG** in CD_3NO_2 .

Figure S6. COSY NMR spectrum of **Pd(dppf)A1TEG** in CD₃NO₂.Figure S7. DOSY NMR spectrum of **Pd(dppf)A1TEG** in CD₃NO₂.

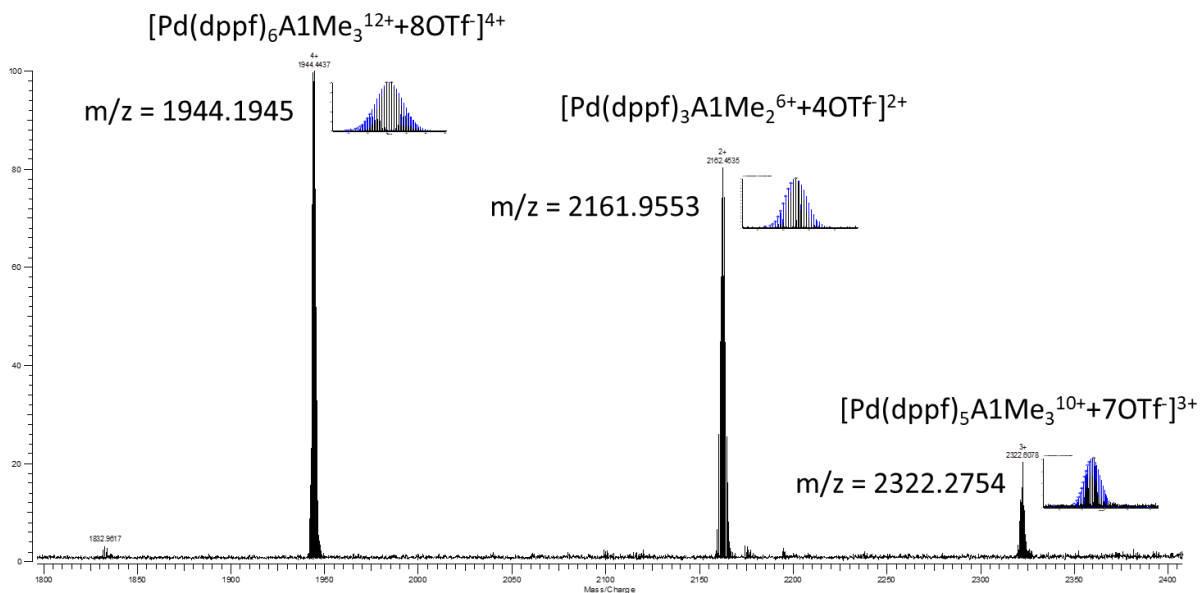


Figure S8. FTICR mass spectrum of **Pd(dppf)A1Me**

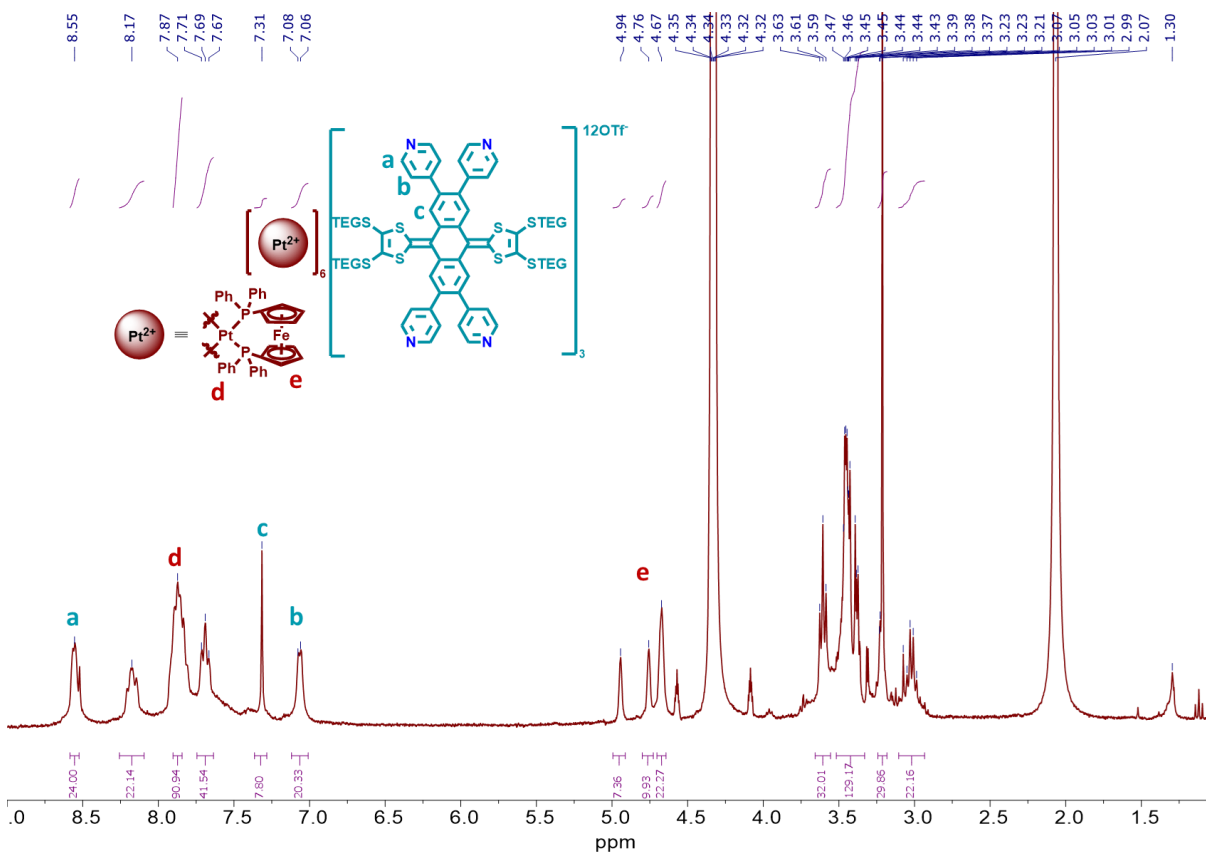
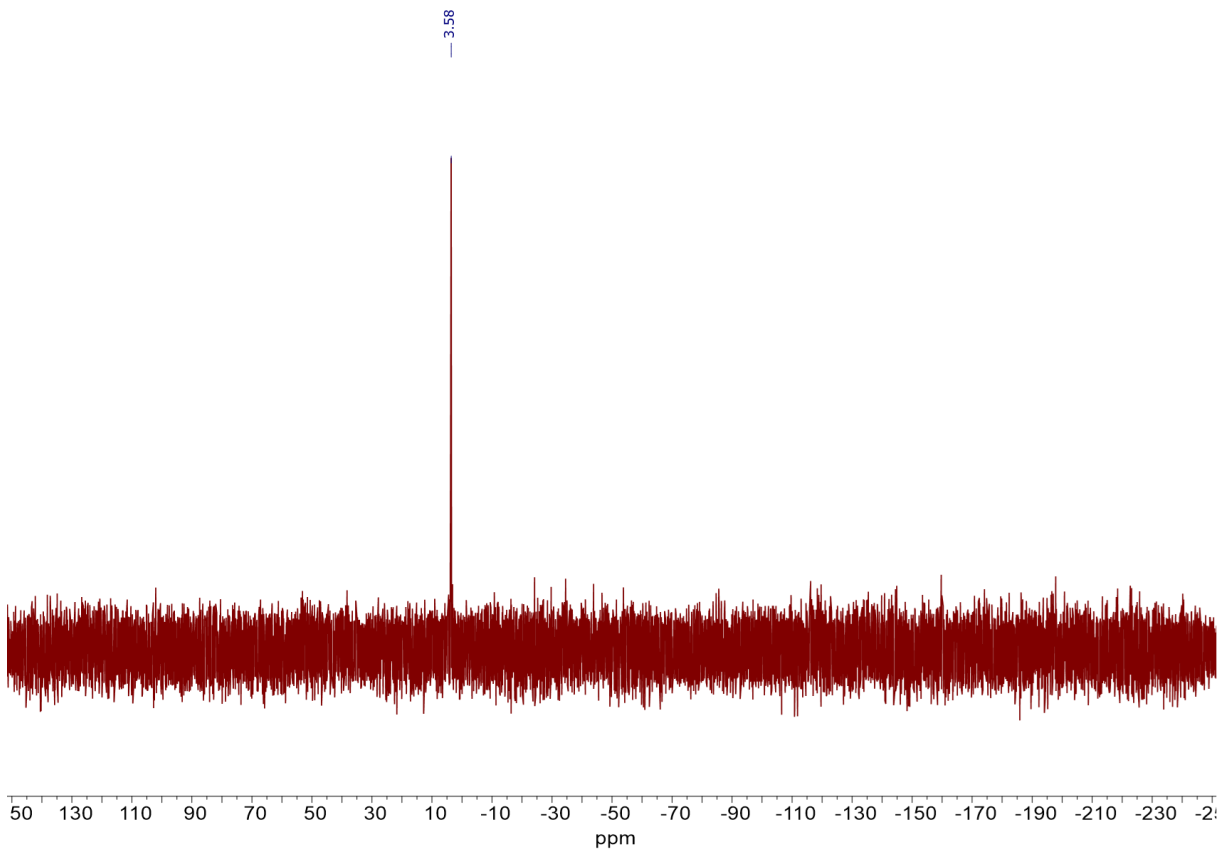
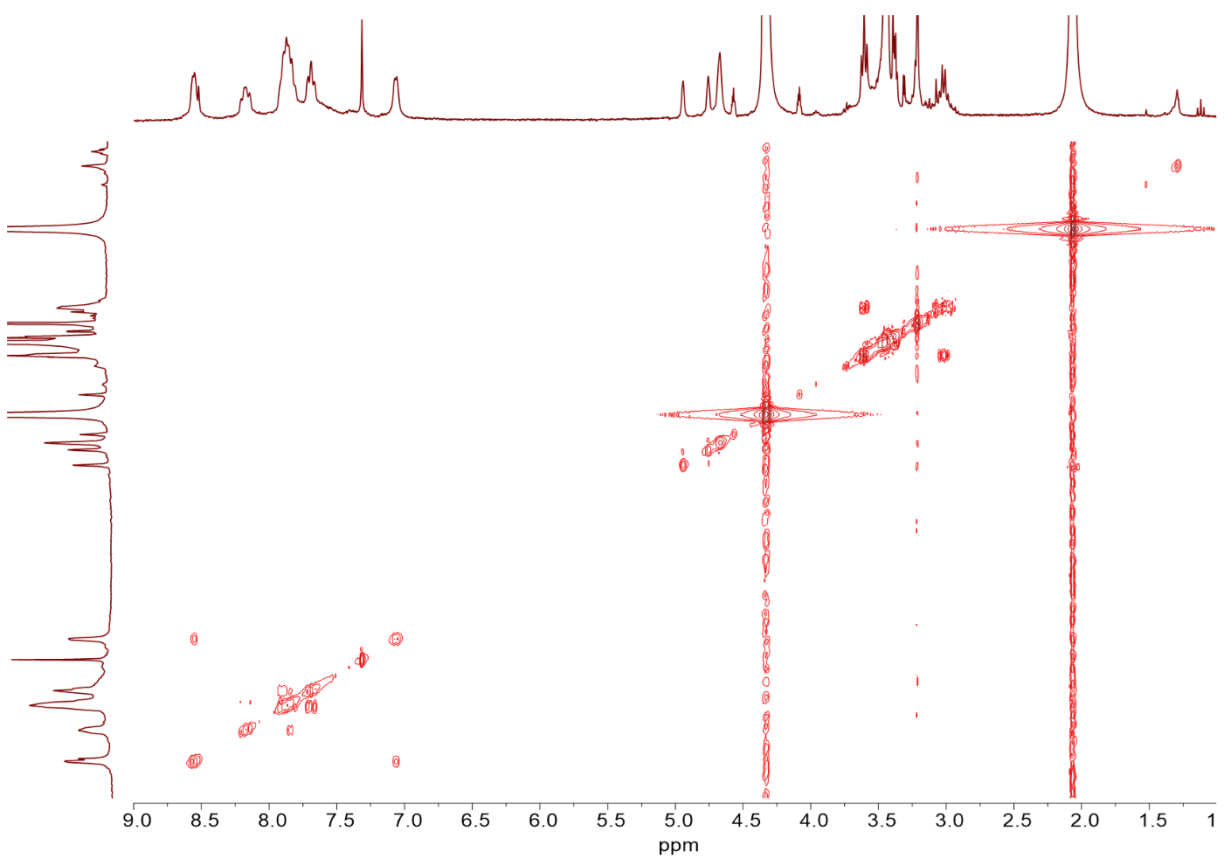


Figure S9. ^1H NMR spectrum of **Pt(dppf)A1TEG** in CD_3NO_2 .

Figure S10. ^{31}P NMR spectrum of **Pt(dppf)A1TEG** in CD_3NO_2 .Figure S11. COSY NMR spectrum of **Pt(dppf)A1TEG** in CD_3NO_2 .

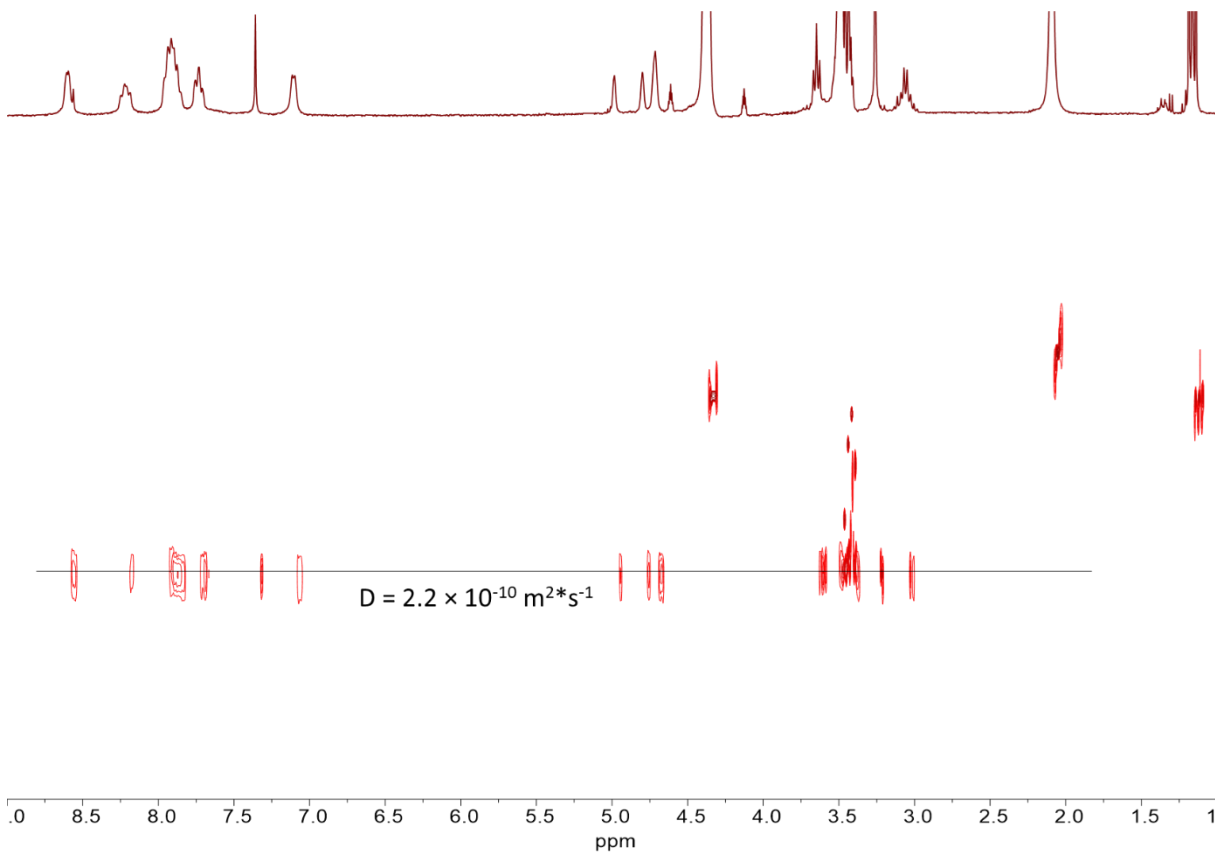


Figure S12. DOSY NMR spectrum of **Pt(dppf)A1TEG** in CD_3NO_2 .

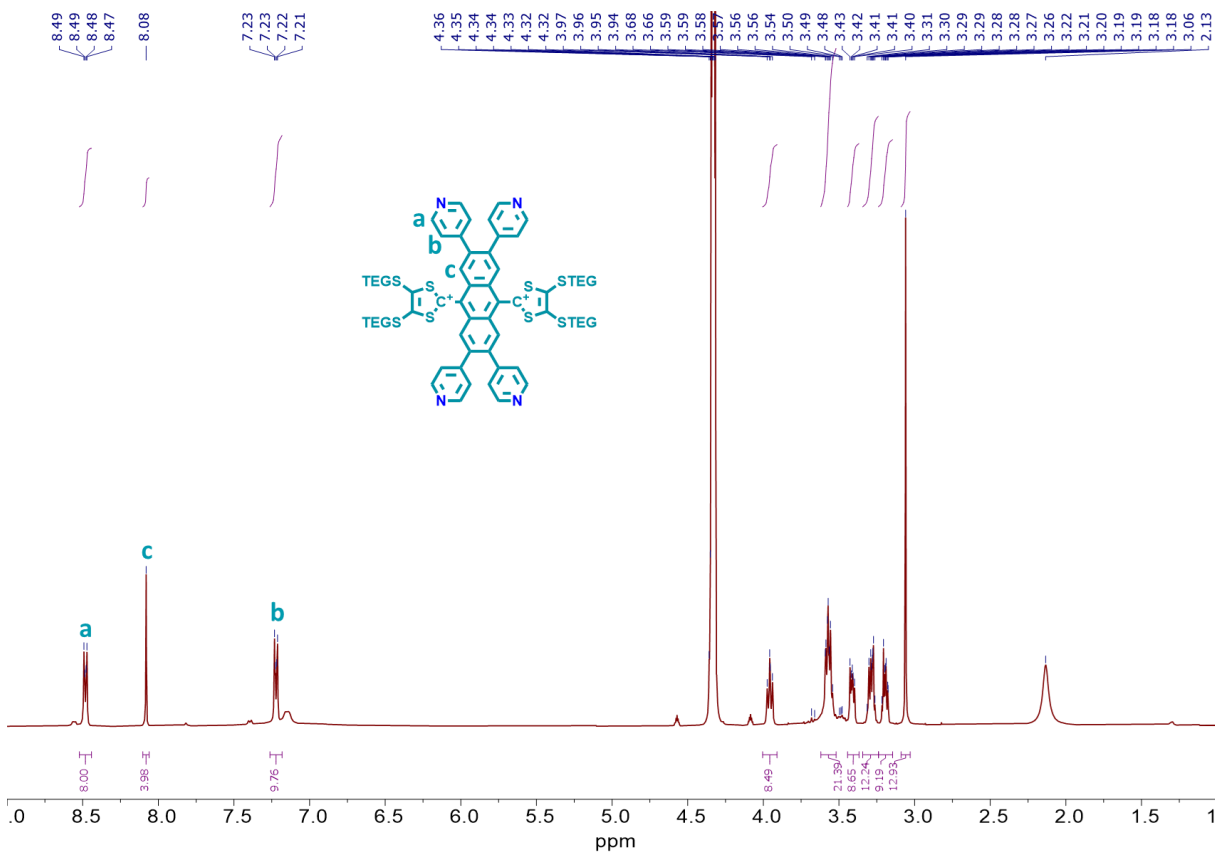


Figure S13. ^1H NMR spectrum of **A10x** in CD_3NO_2 .

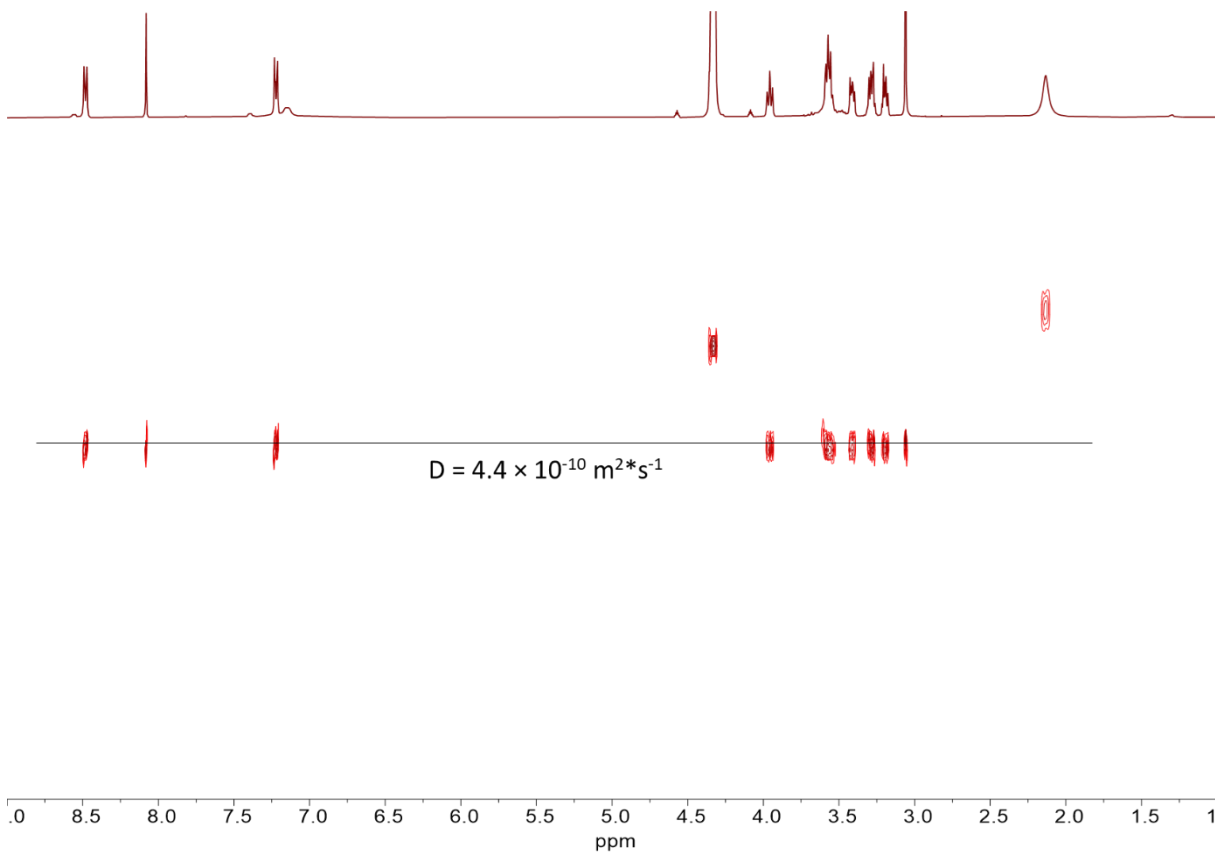


Figure S14. DOSY NMR spectrum of **A10x** in CD_3NO_2 .

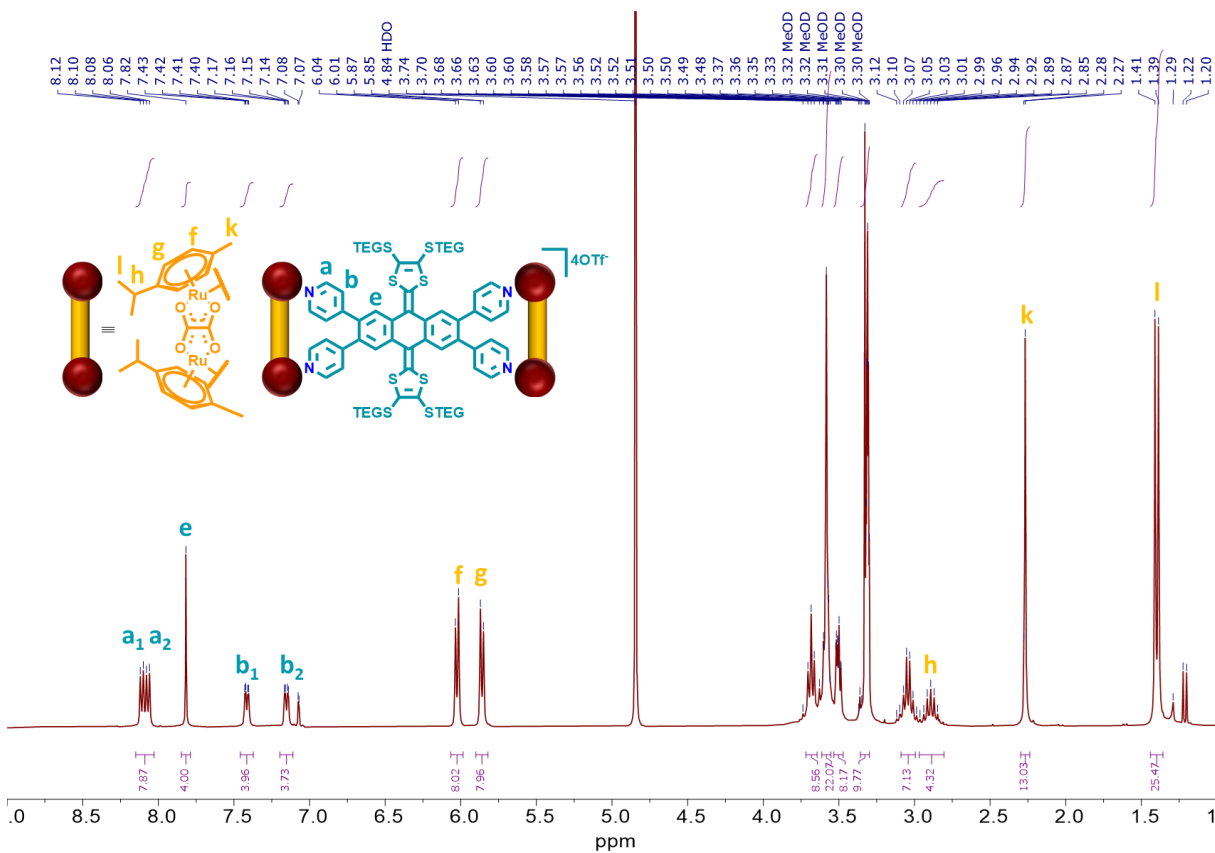
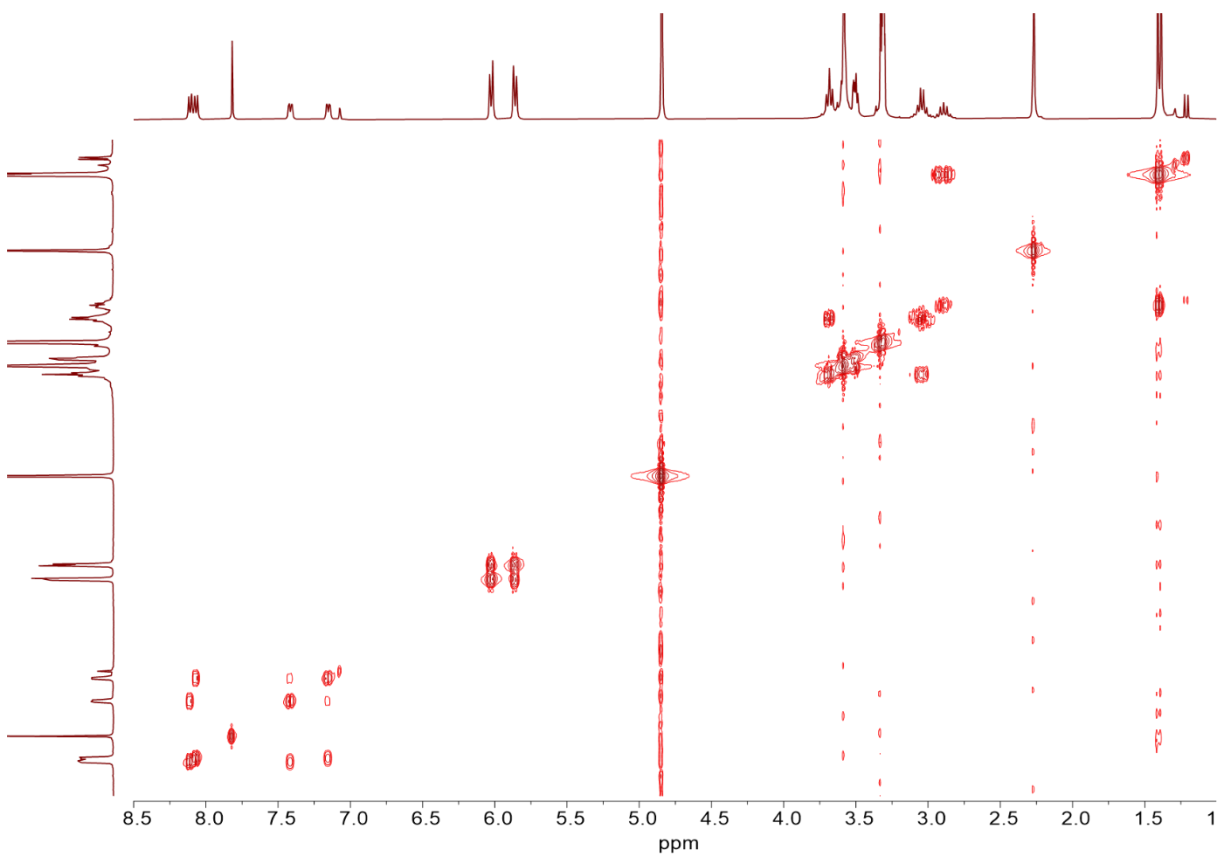
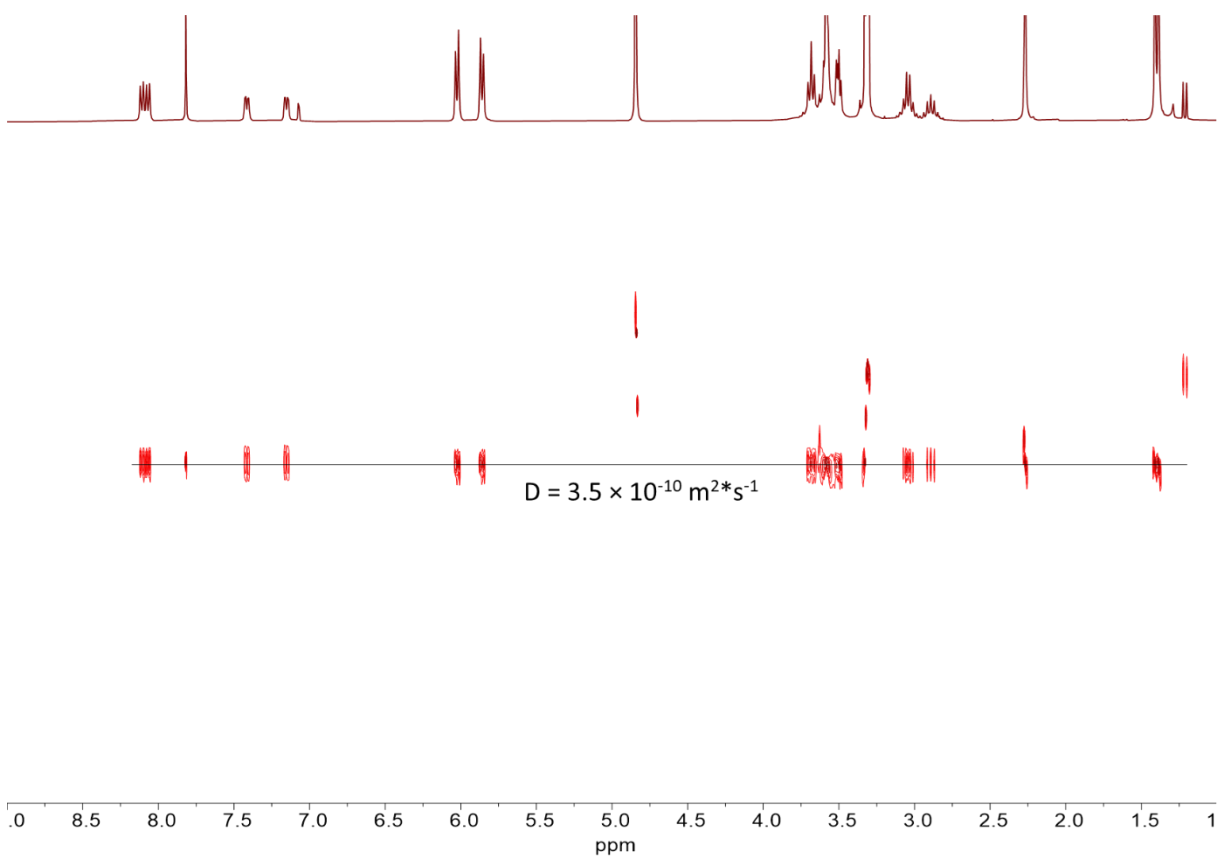


Figure S15. 1H NMR spectrum of **RuOxaA1TEG** in CD_3NO_2 .

Figure S16. COSY NMR spectrum of **RuOxaA1TEG** in CD_3NO_2 .Figure S17. DOSY NMR spectrum of **RuOxaA1TEG** in CD_3NO_2 .

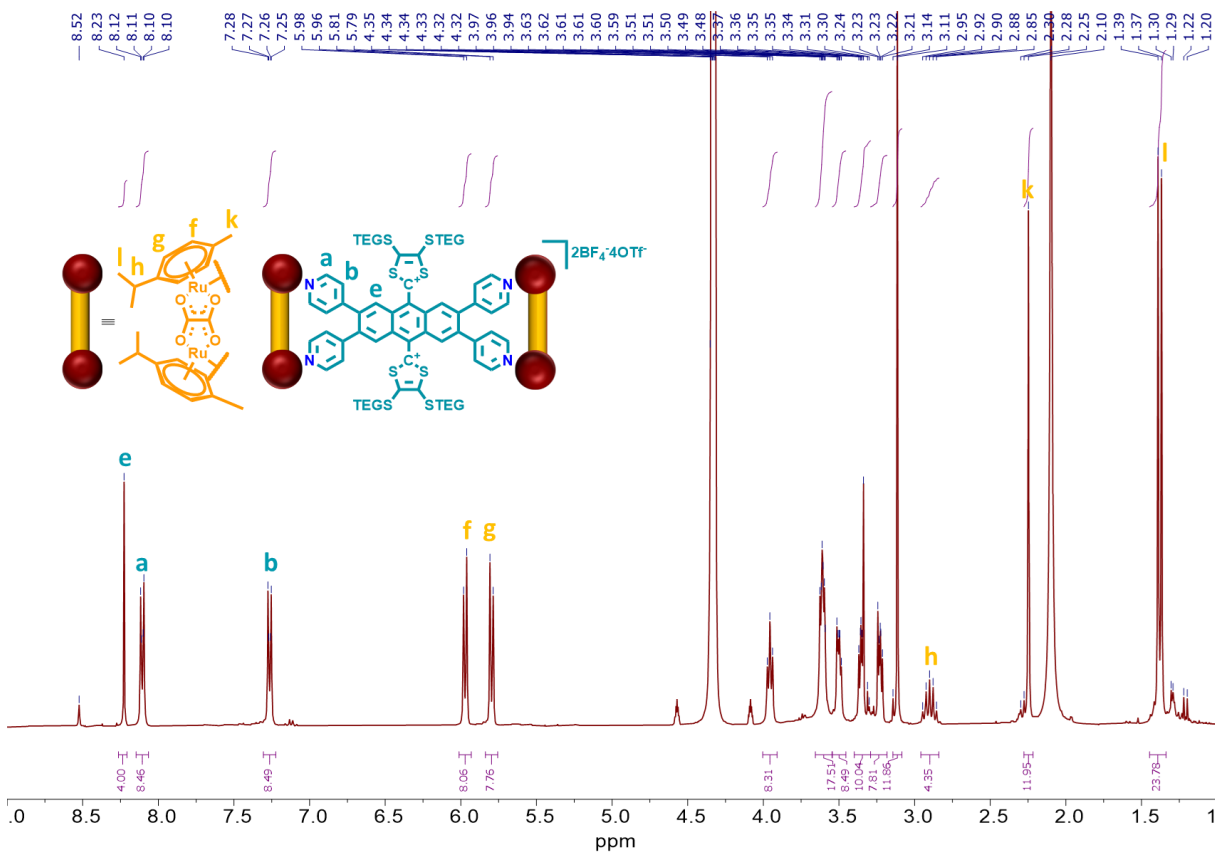


Figure S18. ¹H NMR spectrum of RuOxaA10x in CD₃NO₂.

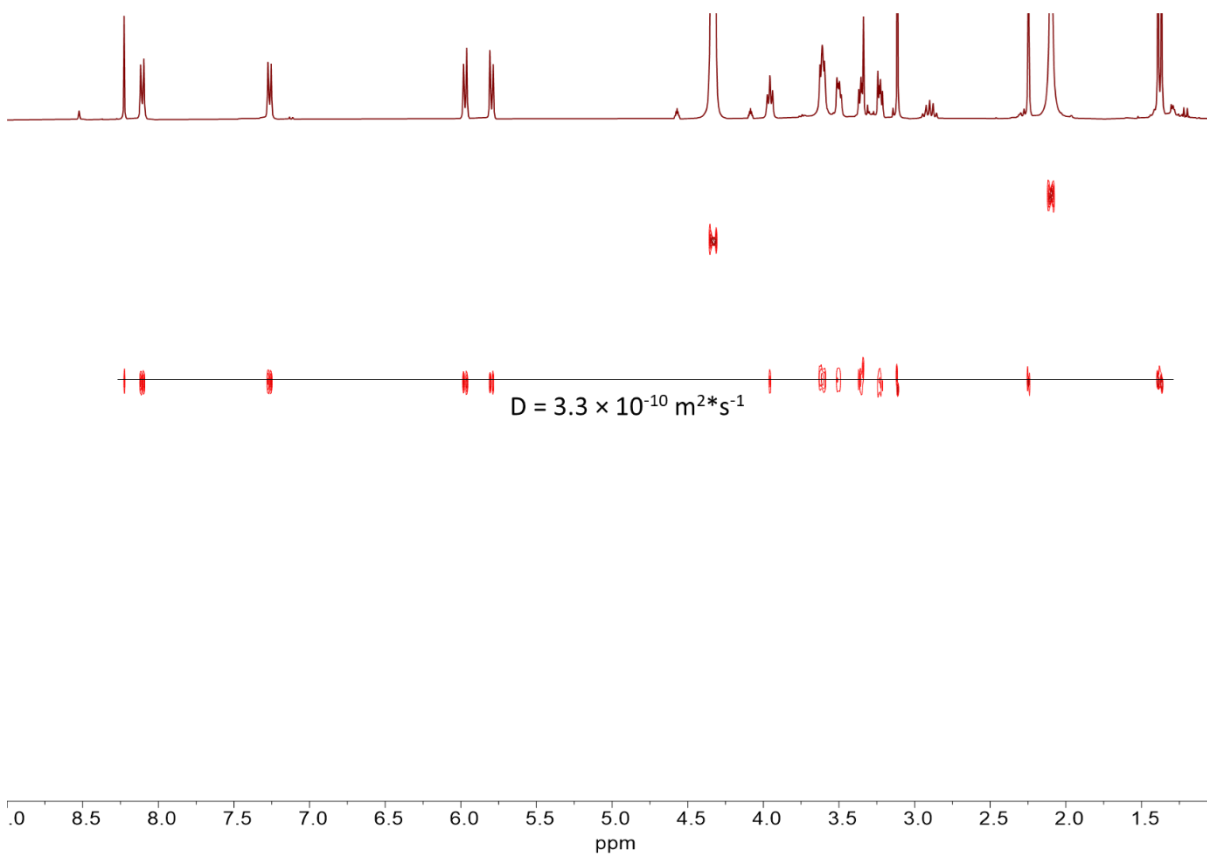
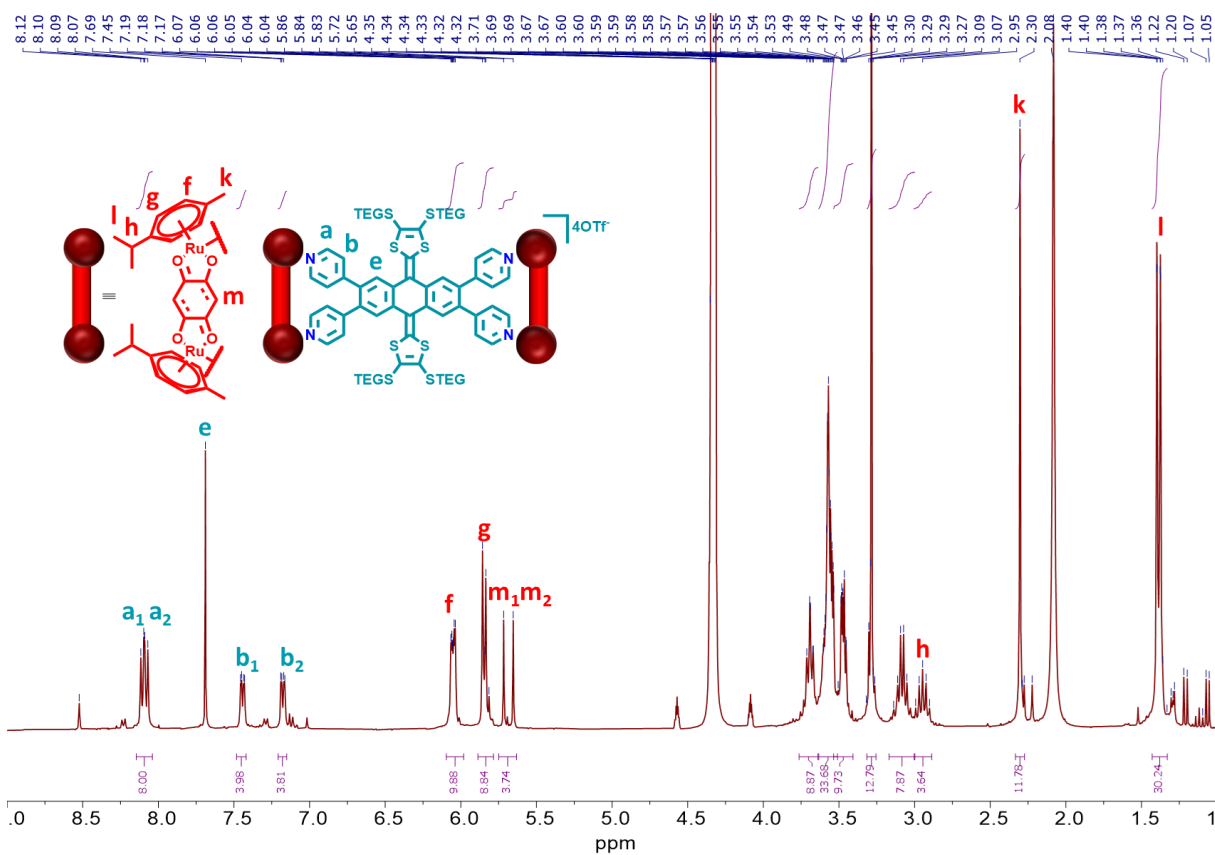
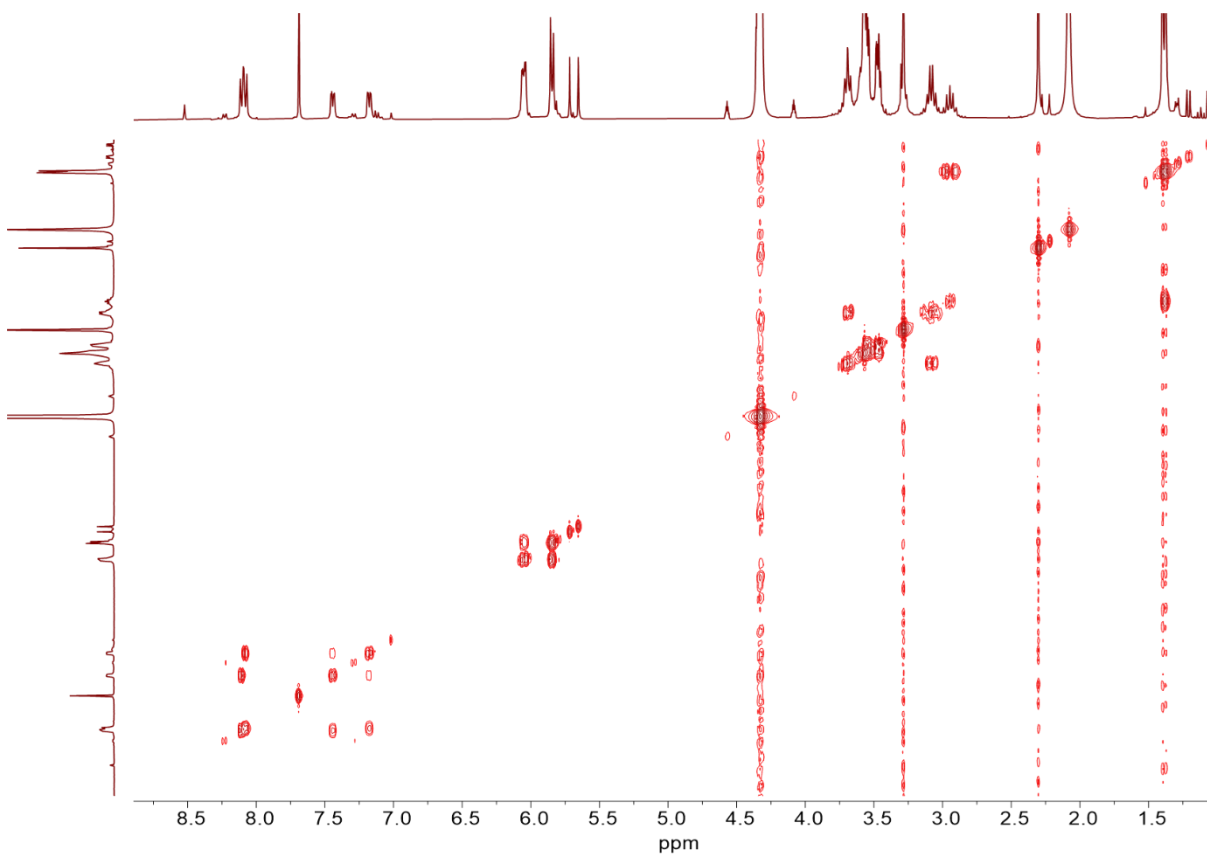


Figure S19. DOSY NMR spectrum of RuOxaA10x in CD₃NO₂.

Figure S20. ^1H NMR spectrum of **RuBenzoA1TEG** in CD_3NO_2 .Figure S21. COSY NMR spectrum of **RuBenzoA1TEG** in CD_3NO_2 .

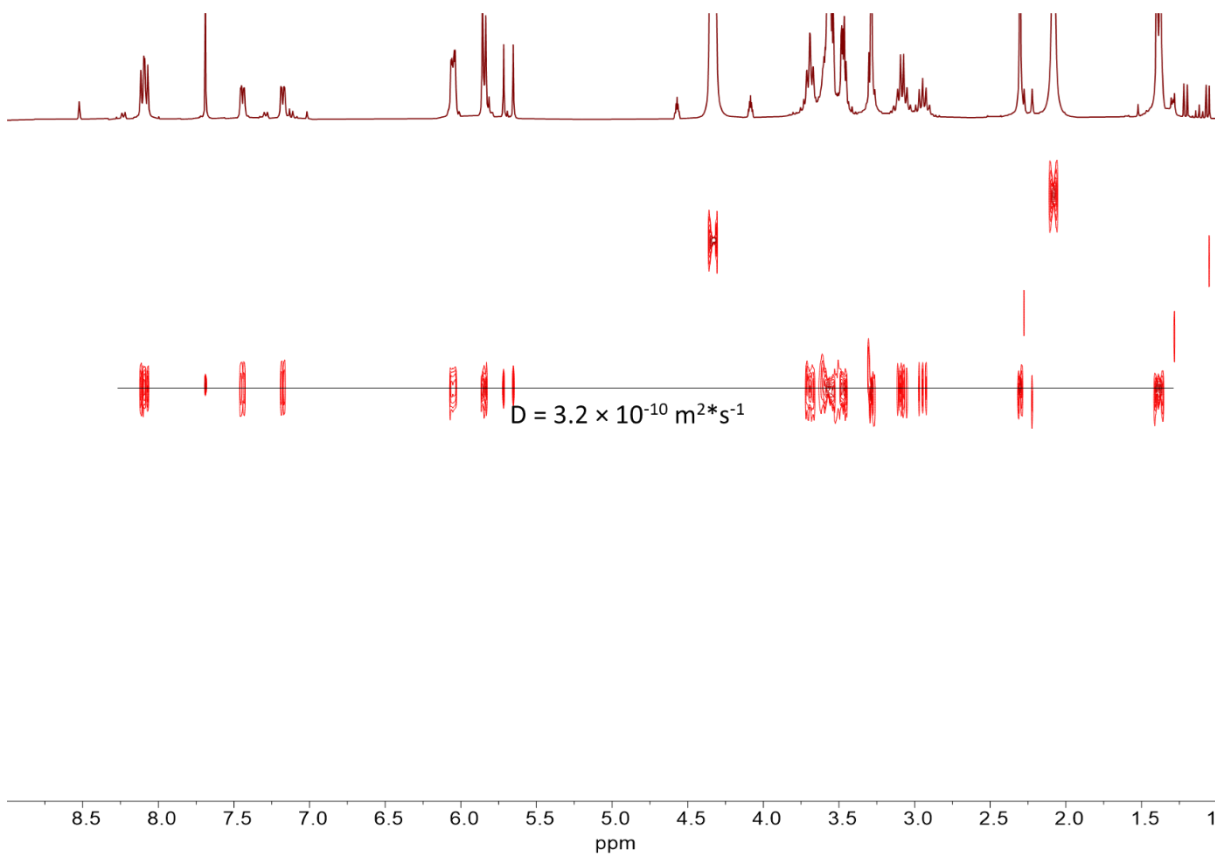


Figure S22. DOSY NMR spectrum of **RuBenzoA1TEG** in CD_3NO_2 .

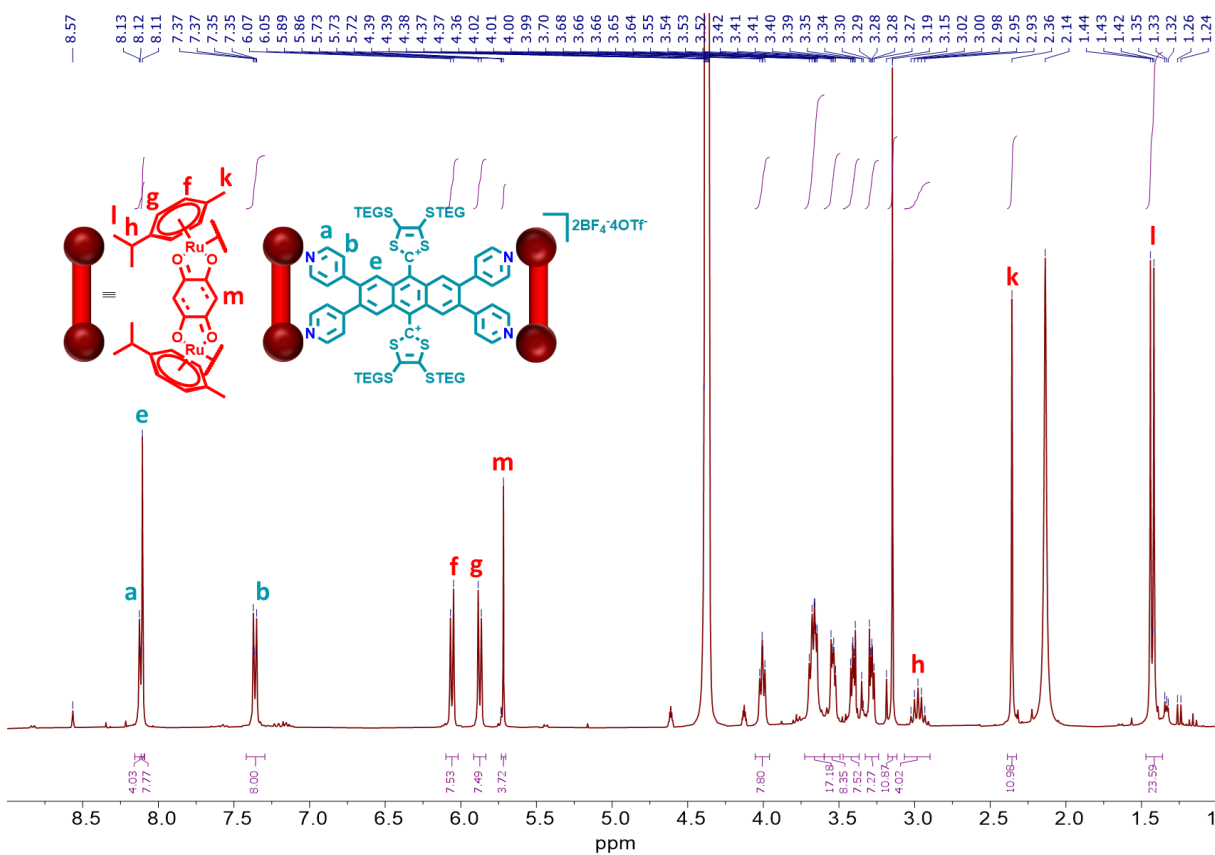


Figure S23. 1H NMR spectrum of **RuBenzoA1Ox** in CD_3NO_2 .

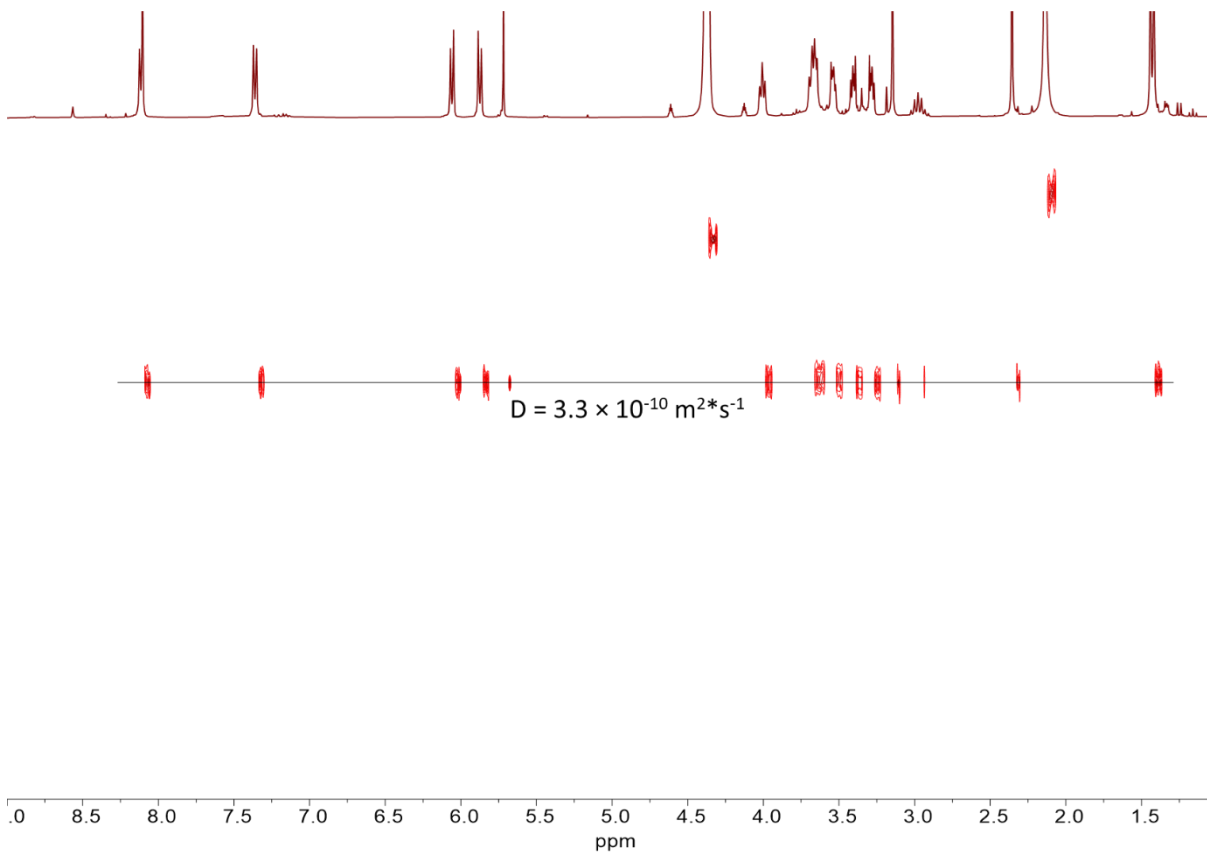


Figure S24. DOSY NMR spectrum of **RuBenzoA10x** in CD_3NO_2 .

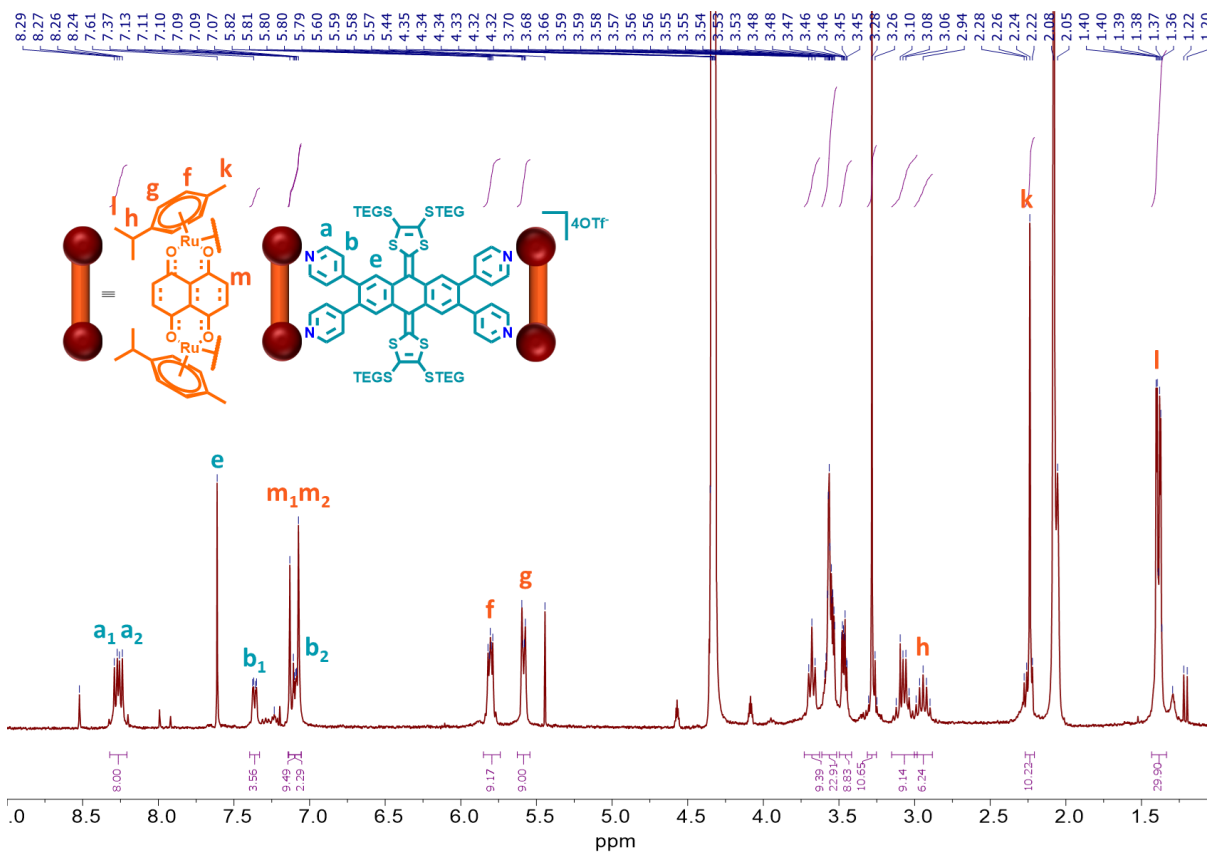
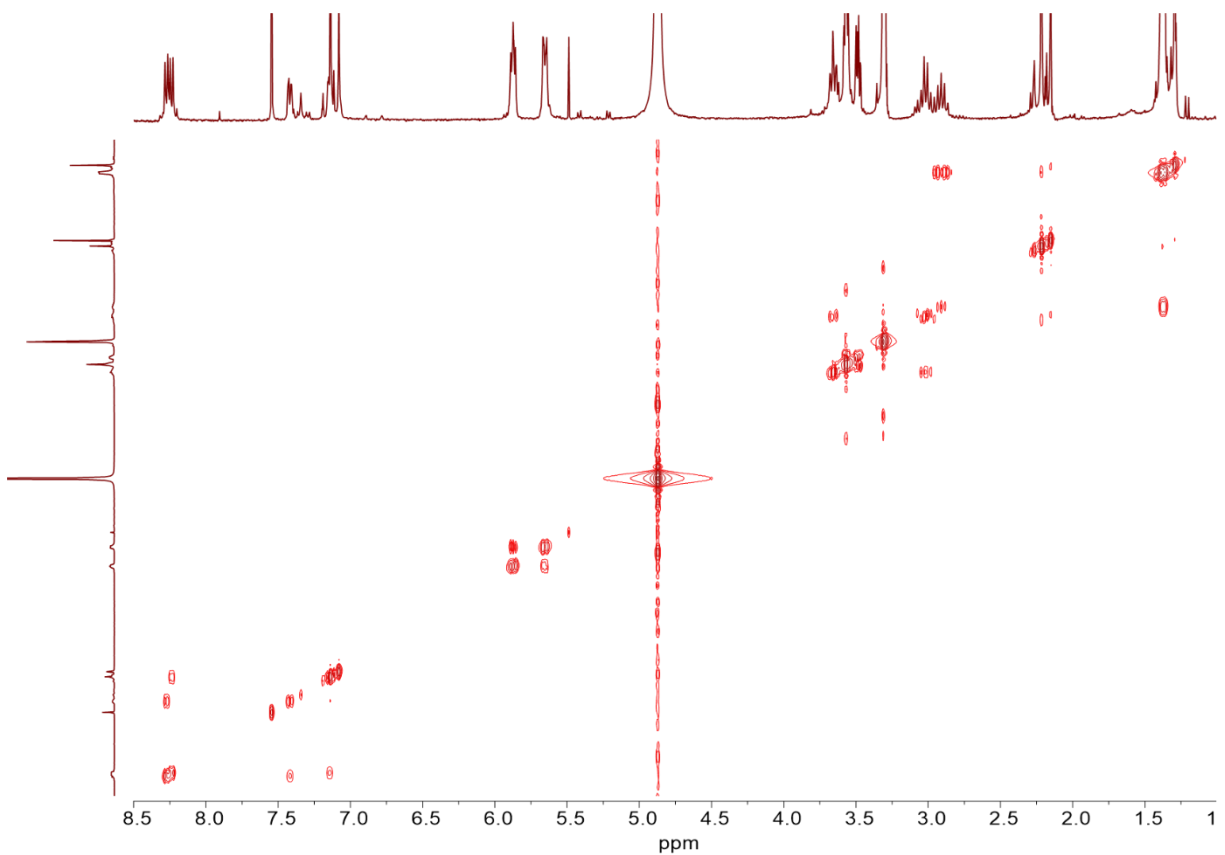
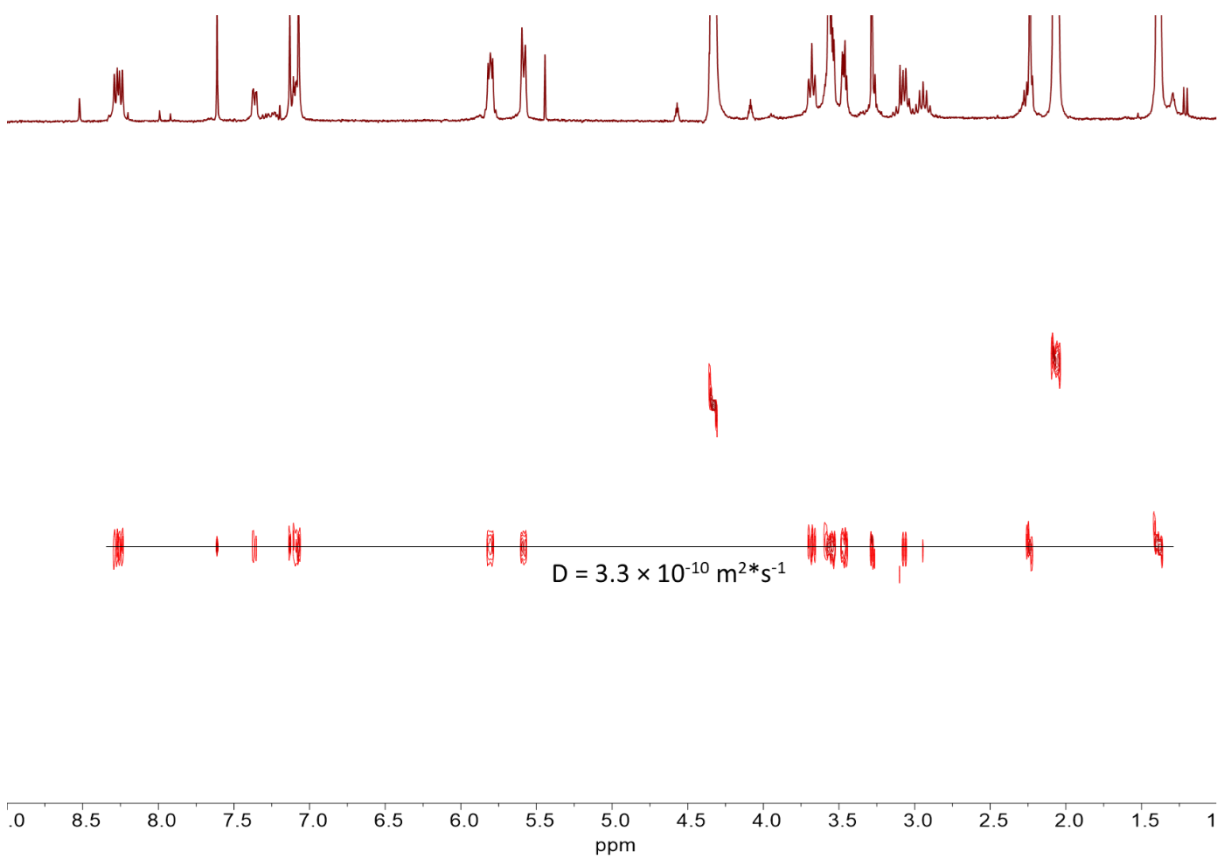


Figure S25. ^1H NMR spectrum of **RuNaphA1TEG** in CD_3NO_2 .

Figure S26. COSY NMR spectrum of **RuNaphA1TEG** in CD_3NO_2 .Figure S27. DOSY NMR spectrum of **RuNaphA1TEG** in CD_3NO_2 .

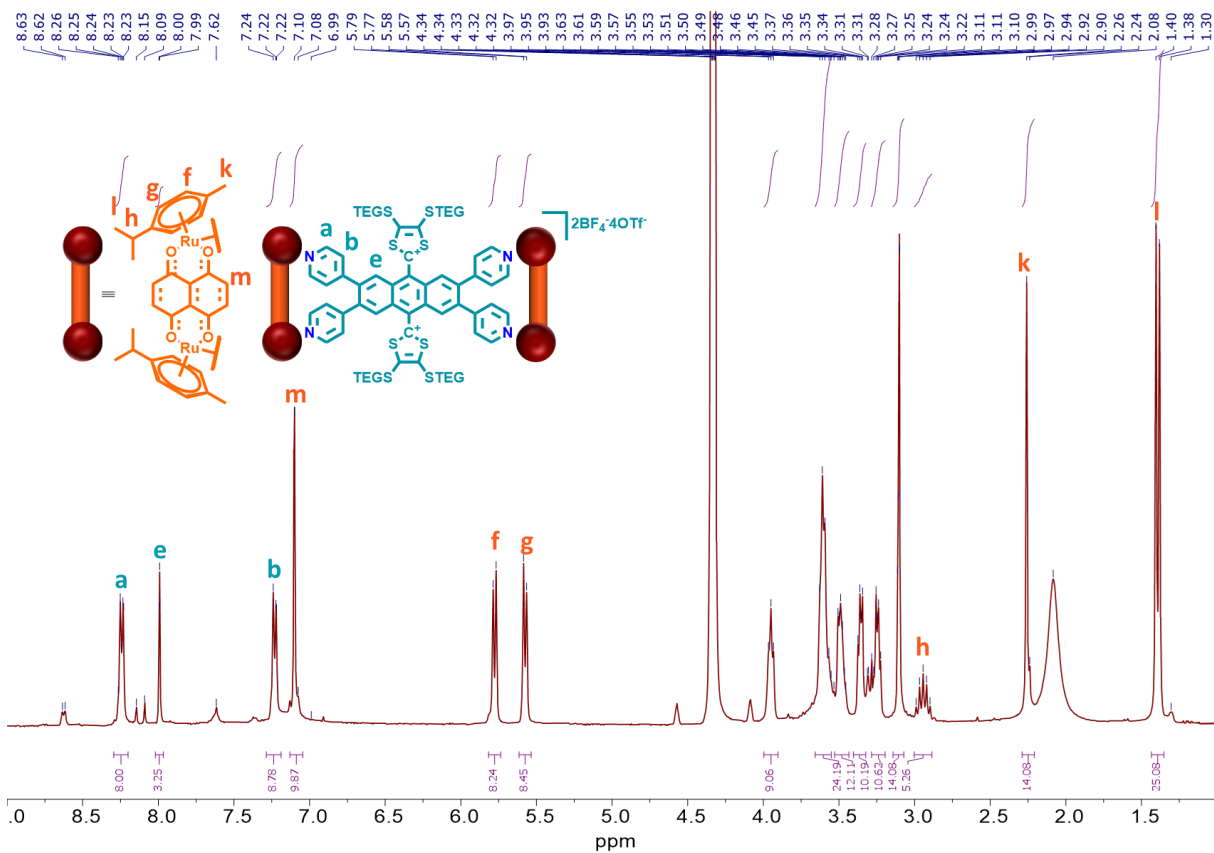


Figure S28. ^1H NMR spectrum of **RuNaphA10x** in CD_3NO_2 .

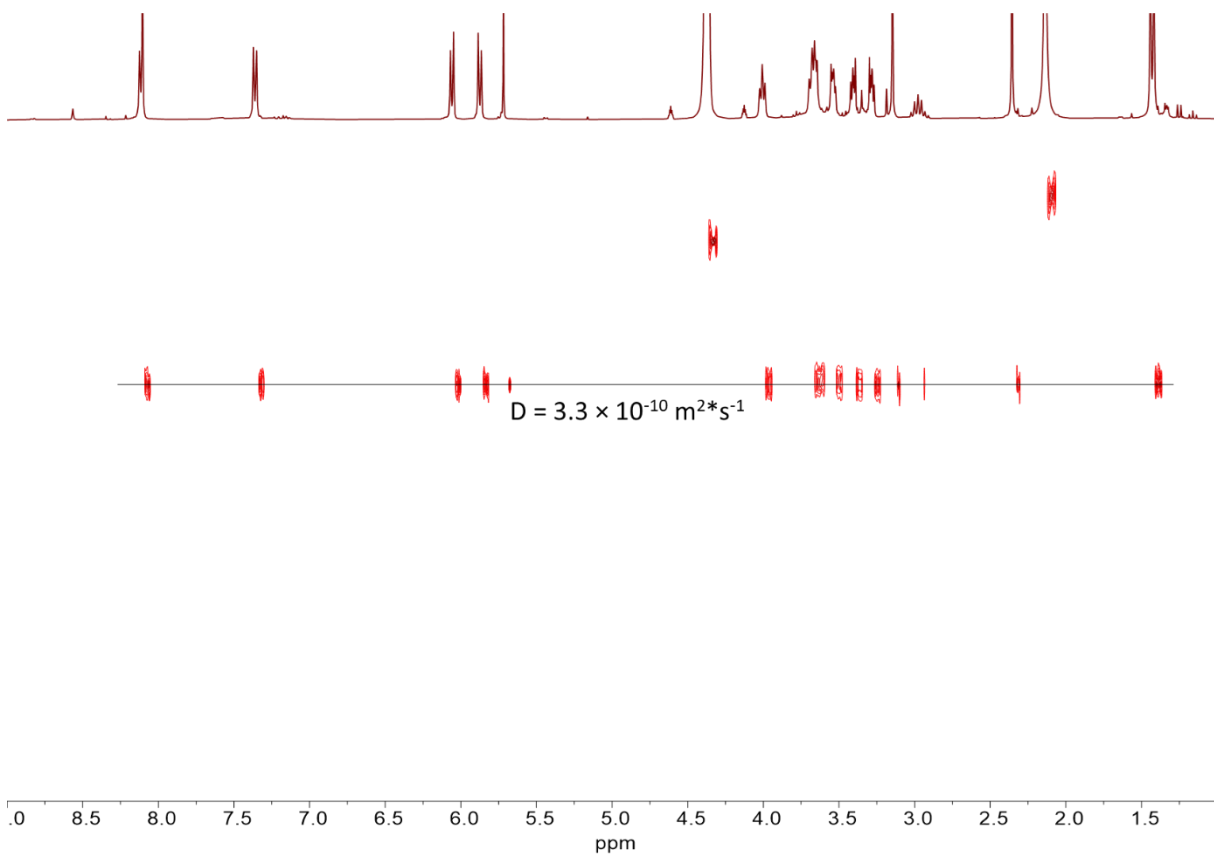
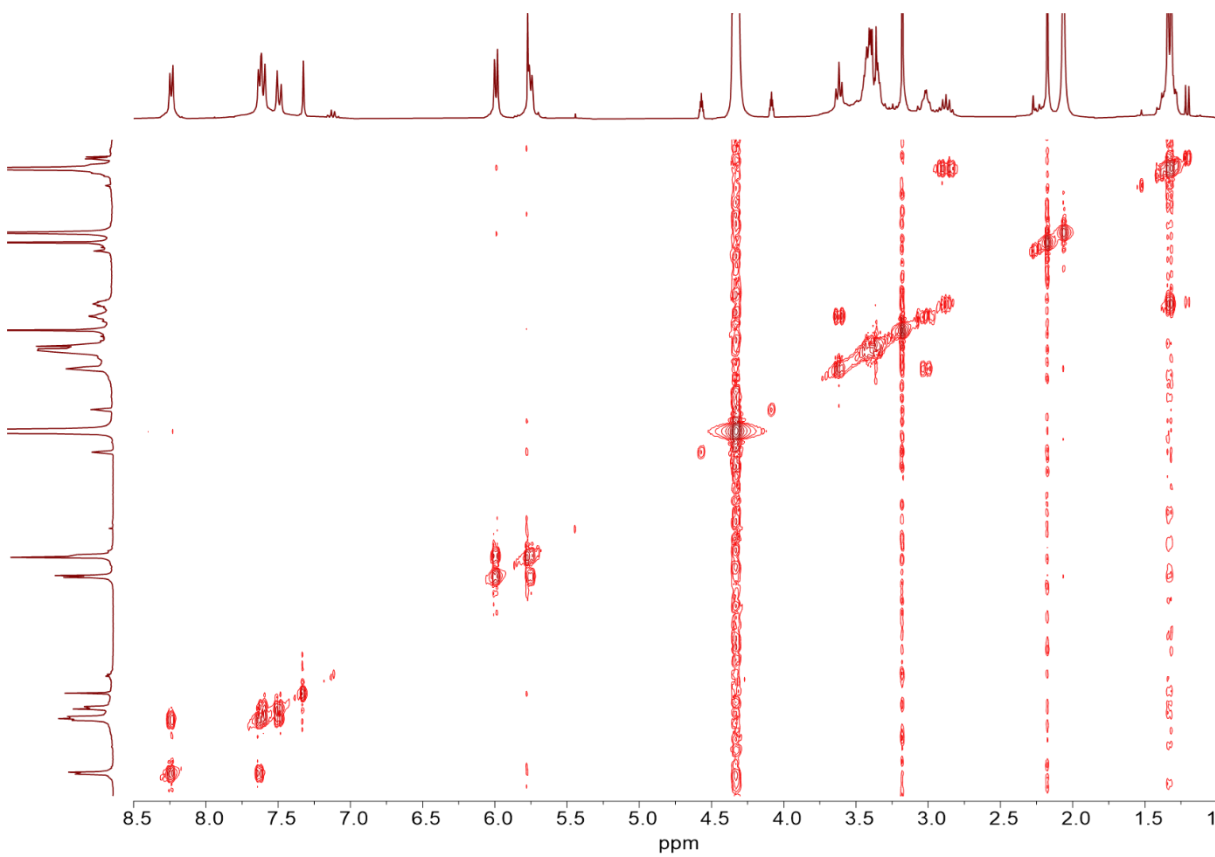
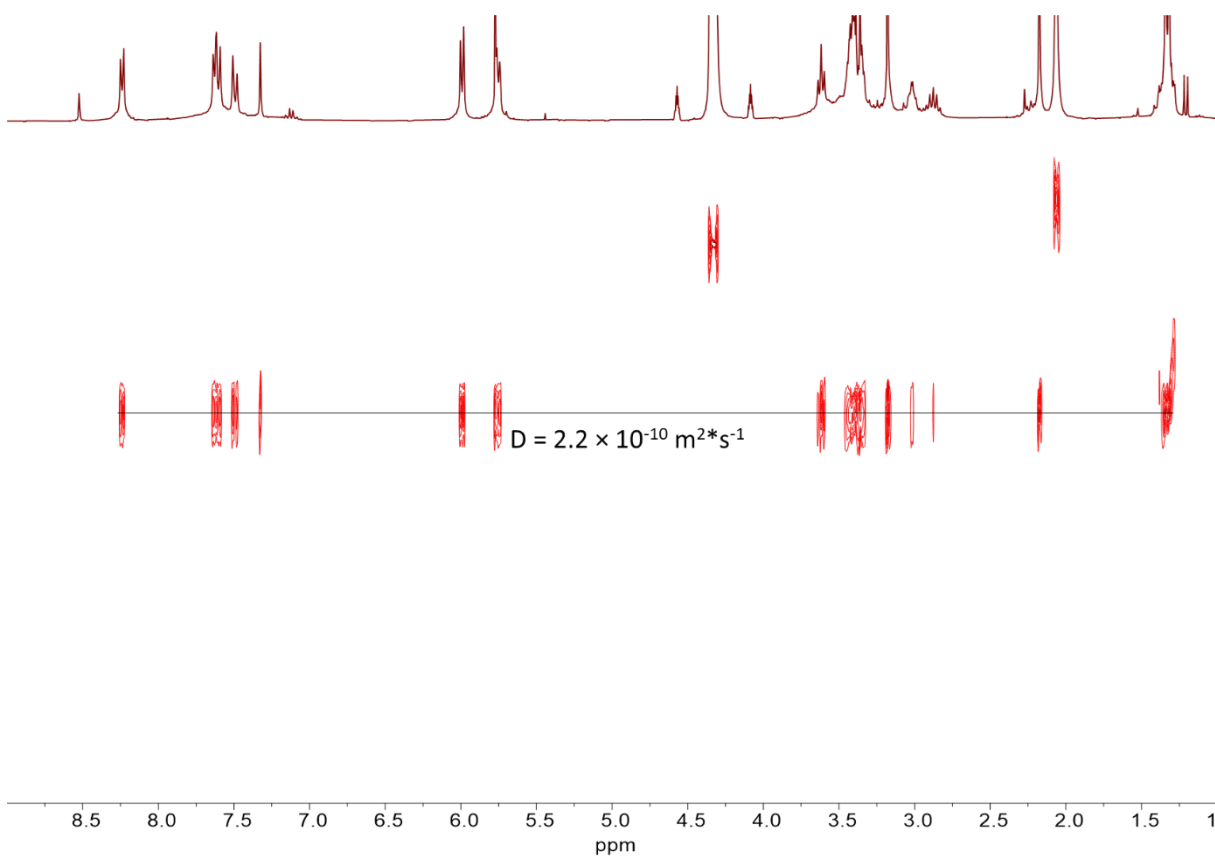


Figure S29. DOSY NMR spectrum of **RuNaphA10x** in CD_3NO_2 .

Figure S32. COSY NMR spectrum of **RuBenzoA3** in CD_3NO_2 .Figure S33. DOSY NMR spectrum of **RuBenzoA3** in CD_3NO_2 .

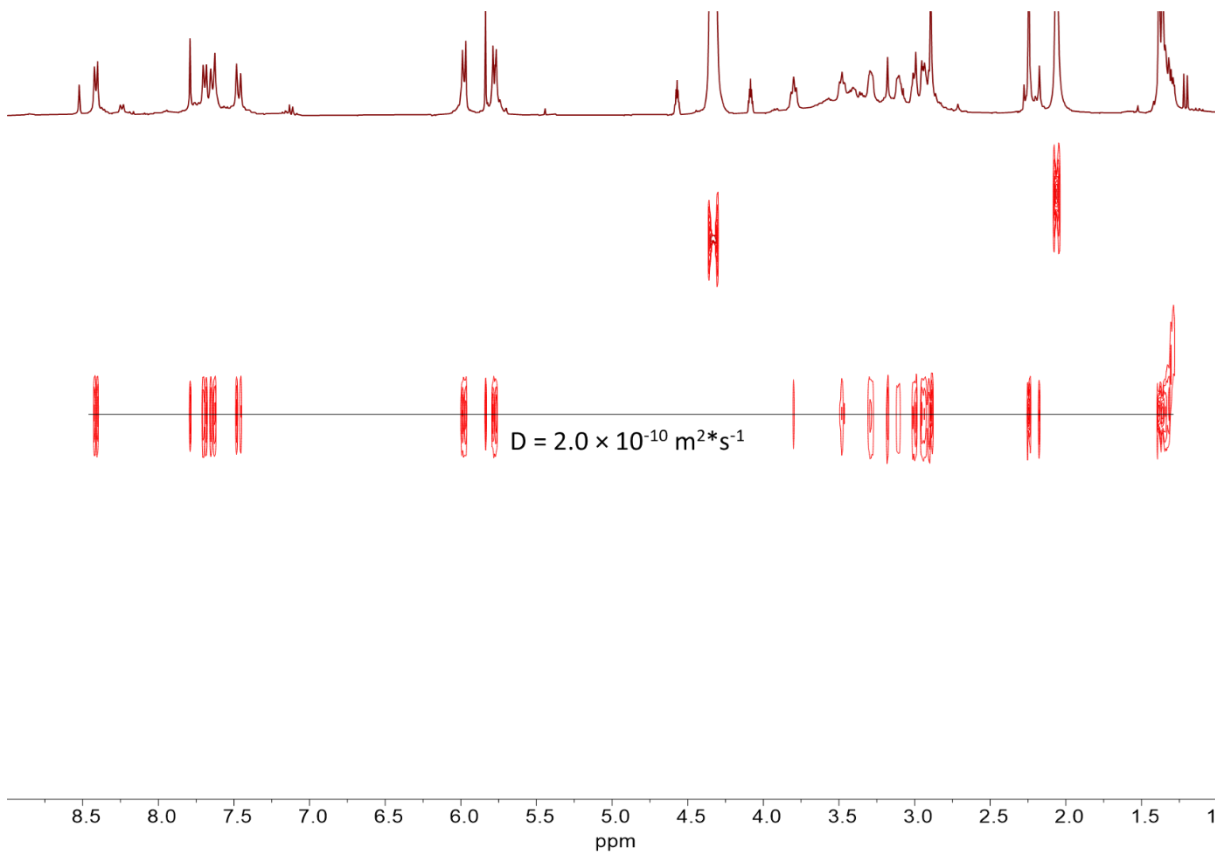


Figure S36. DOSY NMR spectrum of **(RuBenzoA3)Ox** in CD_3NO_2 .

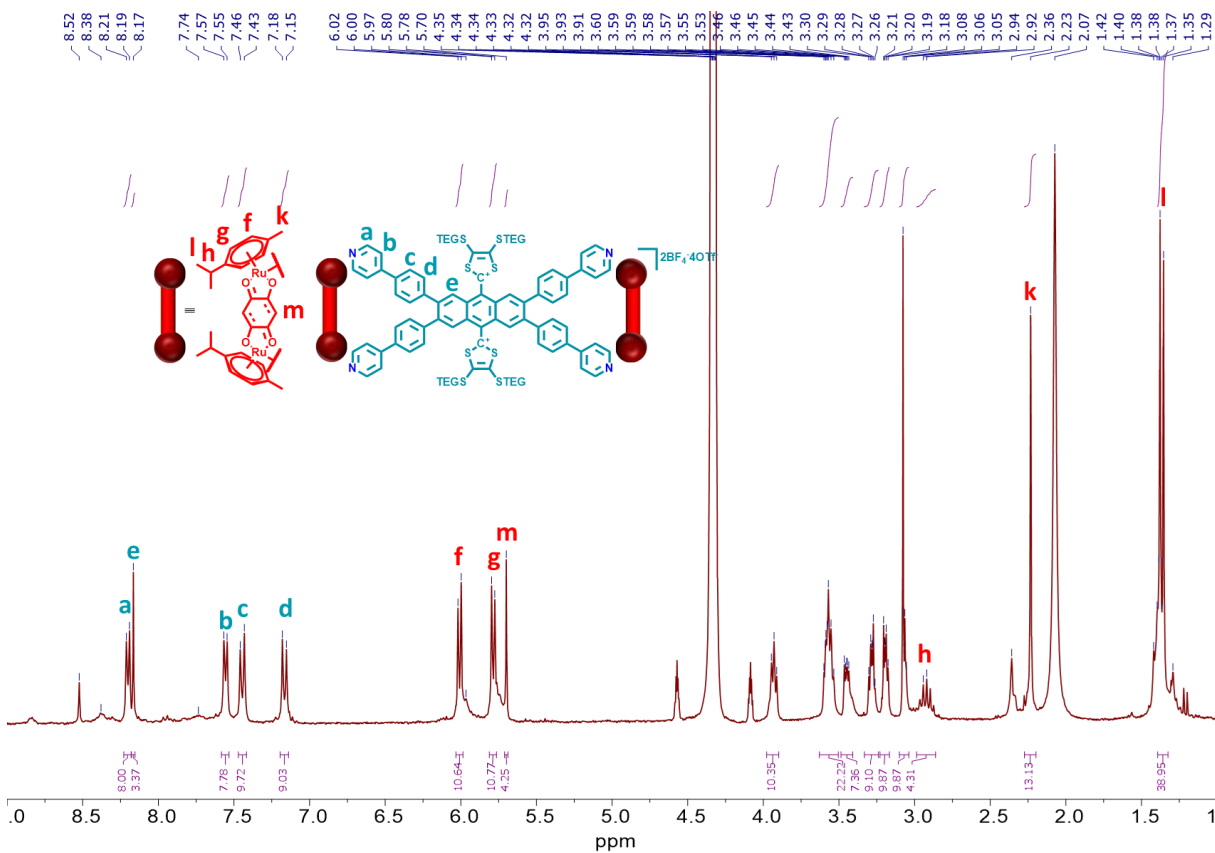
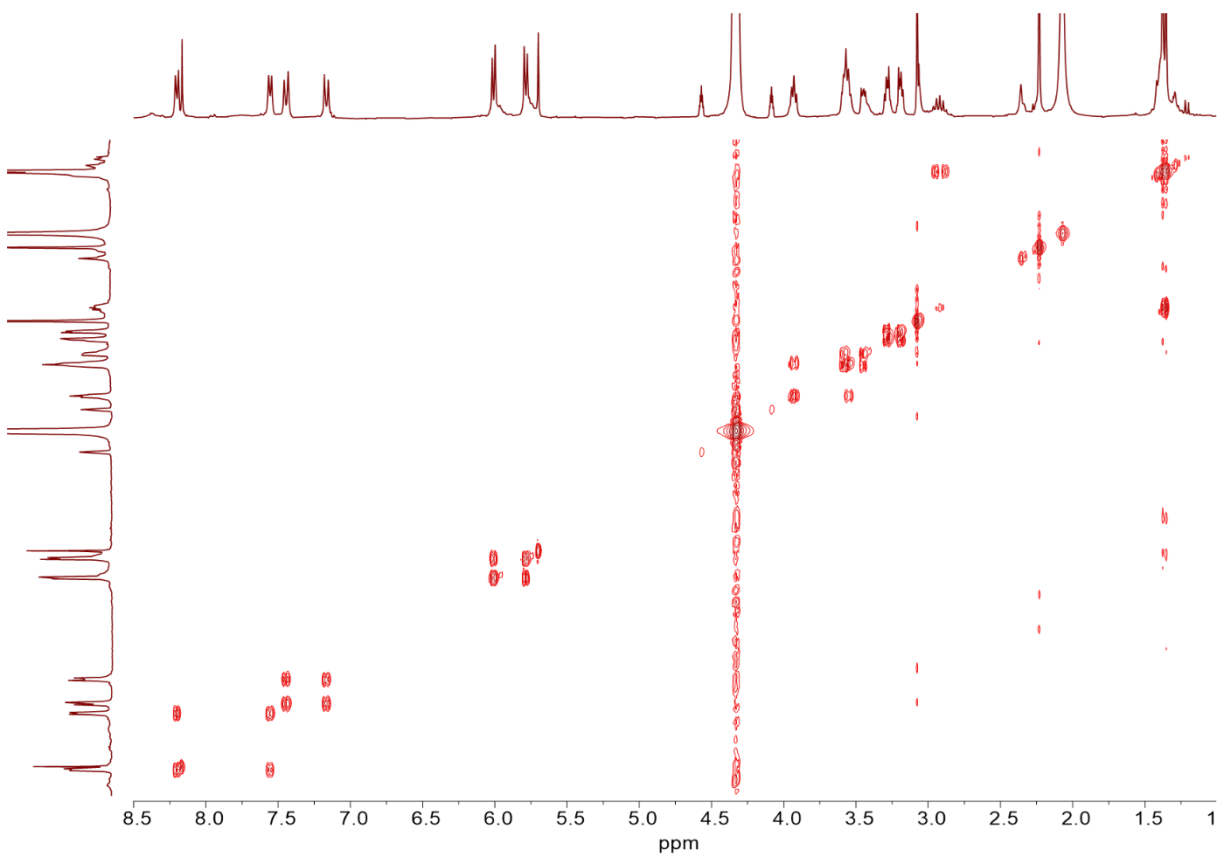
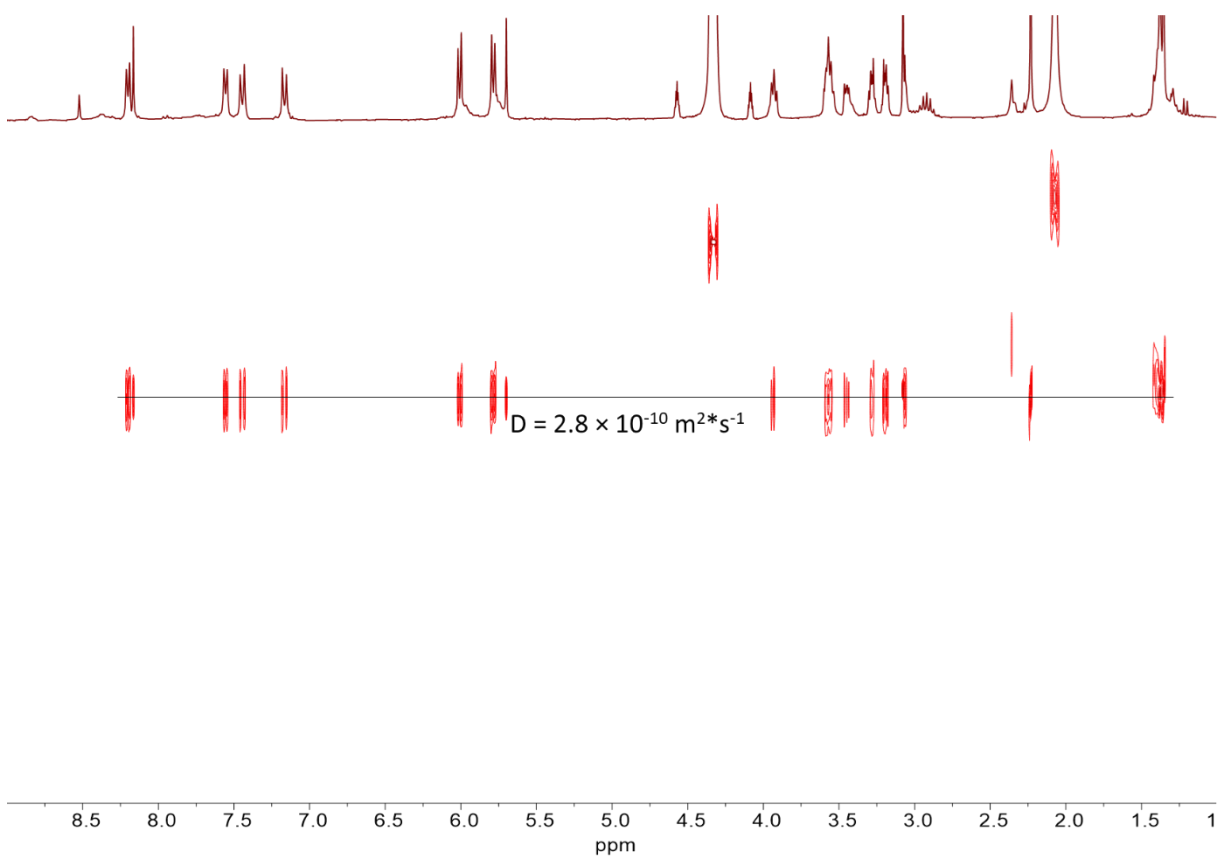


Figure S37. ^1H NMR spectrum of **RuBenzoA3Ox** in CD_3NO_2 .

Figure S38. COSY NMR spectrum of **RuBenzoA3Ox** in CD₃NO₂.Figure S39. DOSY NMR spectrum of **RuBenzoA3Ox** in CD₃NO₂.

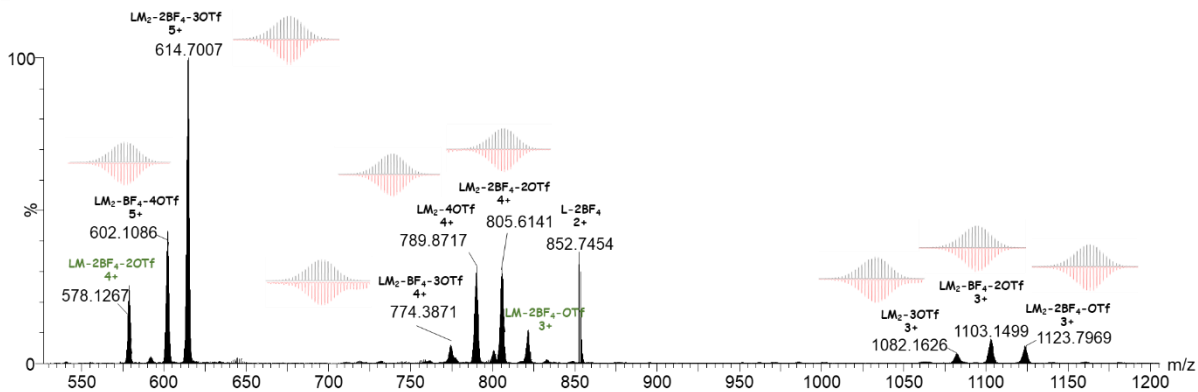


Figure S40. ESI-TOF spectrum of **RuBenzoA3Ox** recorded in CH₃OH/CH₃NO₂ (v/v 10/1) (C = 10⁻⁴ M).

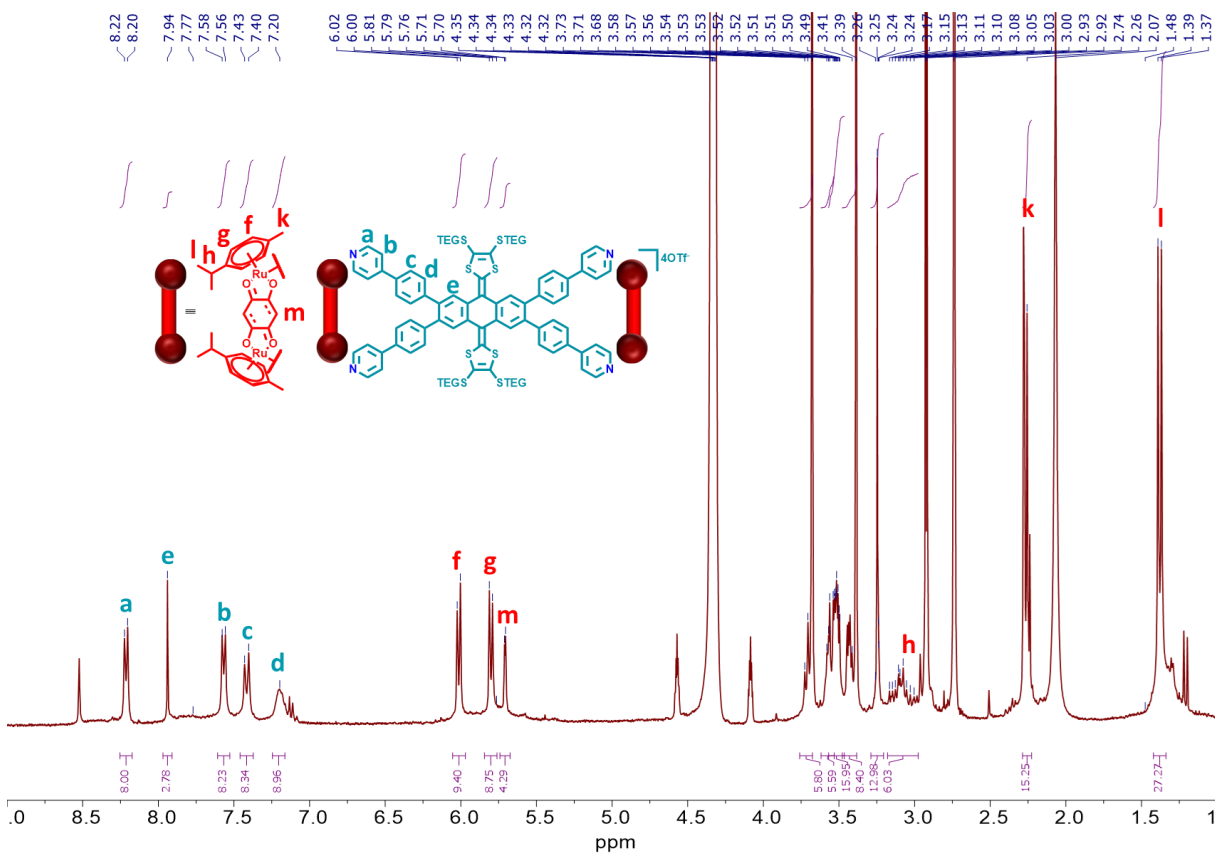
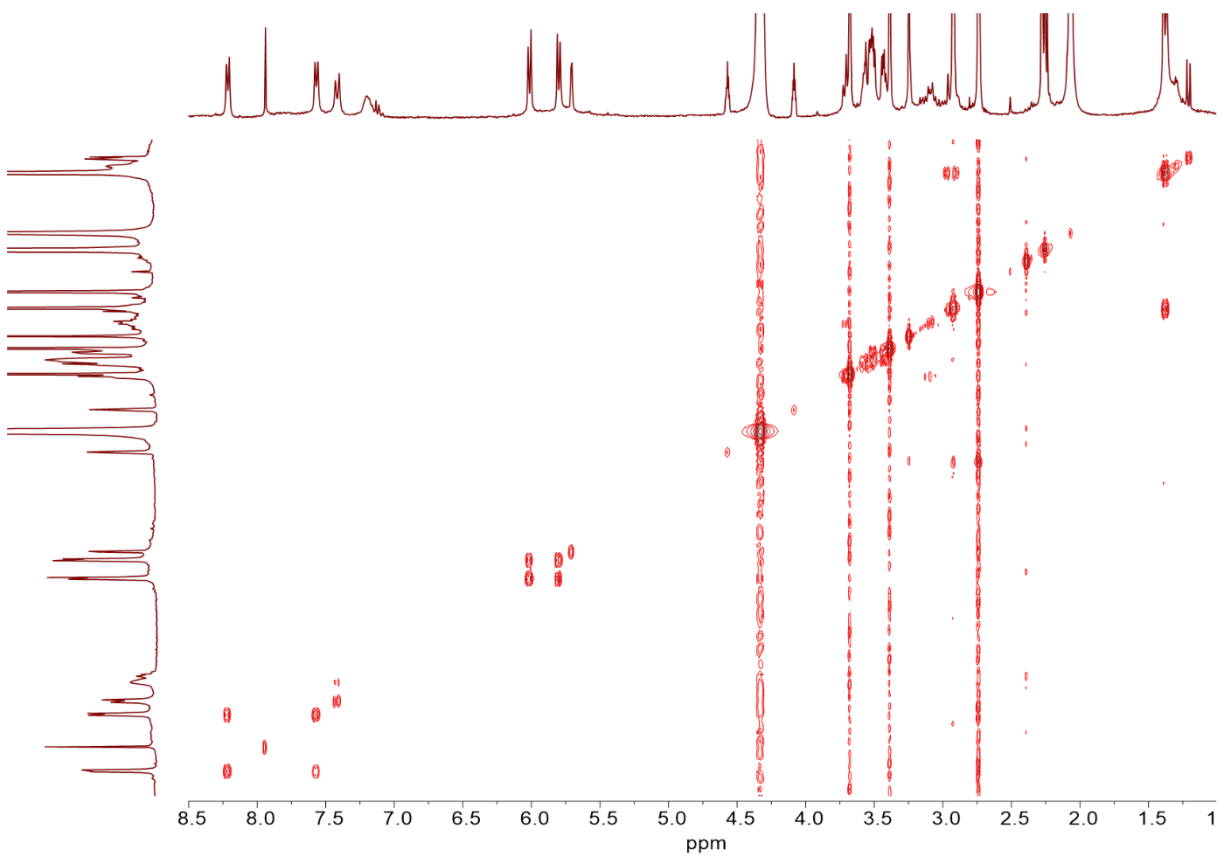
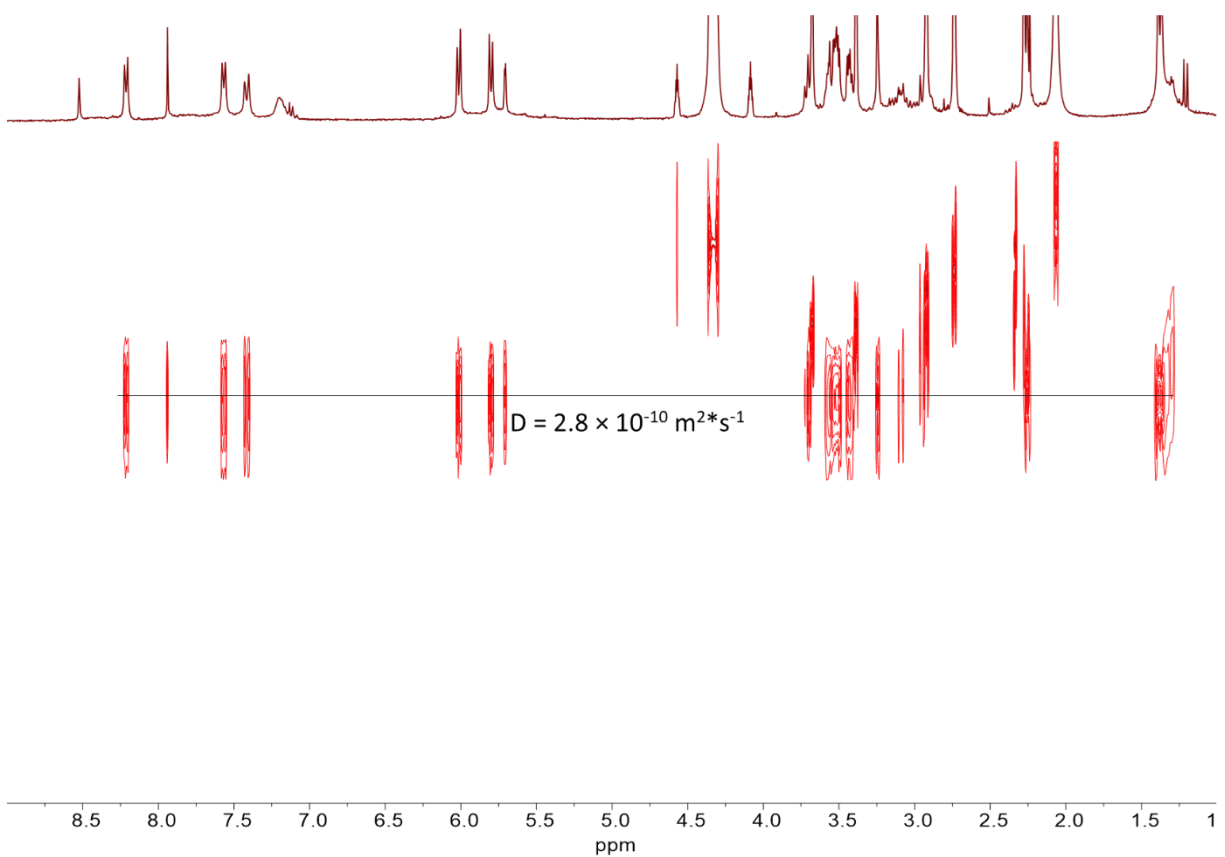


Figure S41. ¹H NMR spectrum of **(RuBenzoA3Ox)Red** in CD₃NO₂.

Figure S42. COSY NMR spectrum of **(RuBenzoA3Ox)Red** in CD₃NO₂.Figure S43. DOSY NMR spectrum of **(RuBenzoA3Ox)Red** in CD₃NO₂.

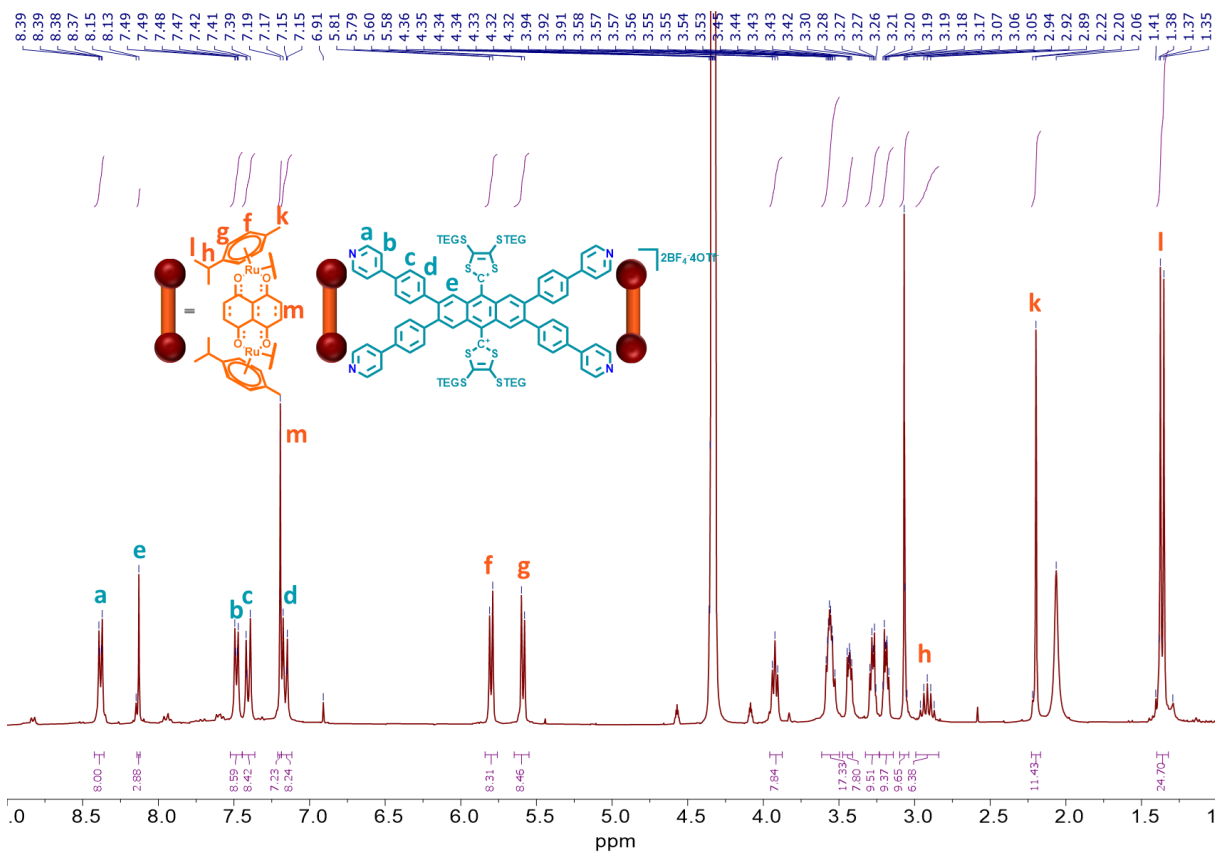


Figure S44. ¹H NMR spectrum of **RuNaphA3Ox** in CD₃NO₂.

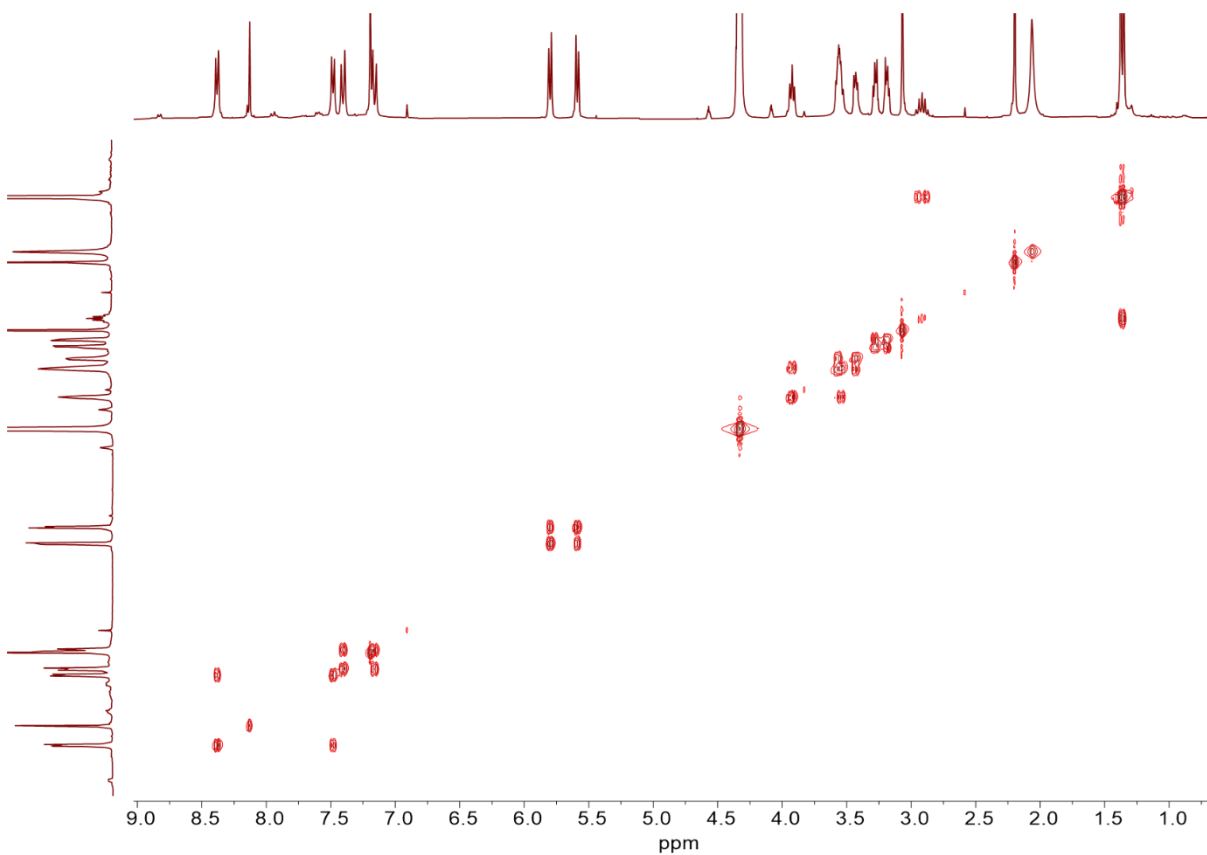
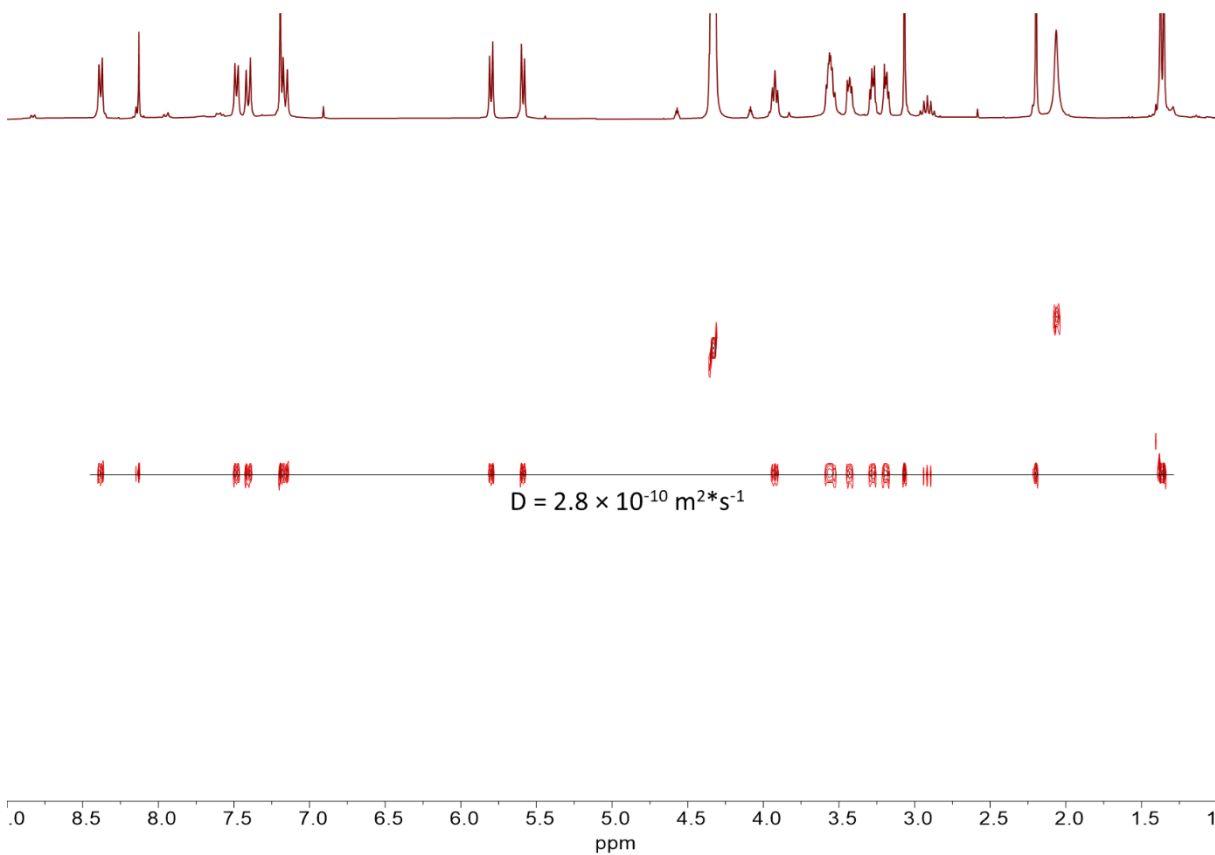
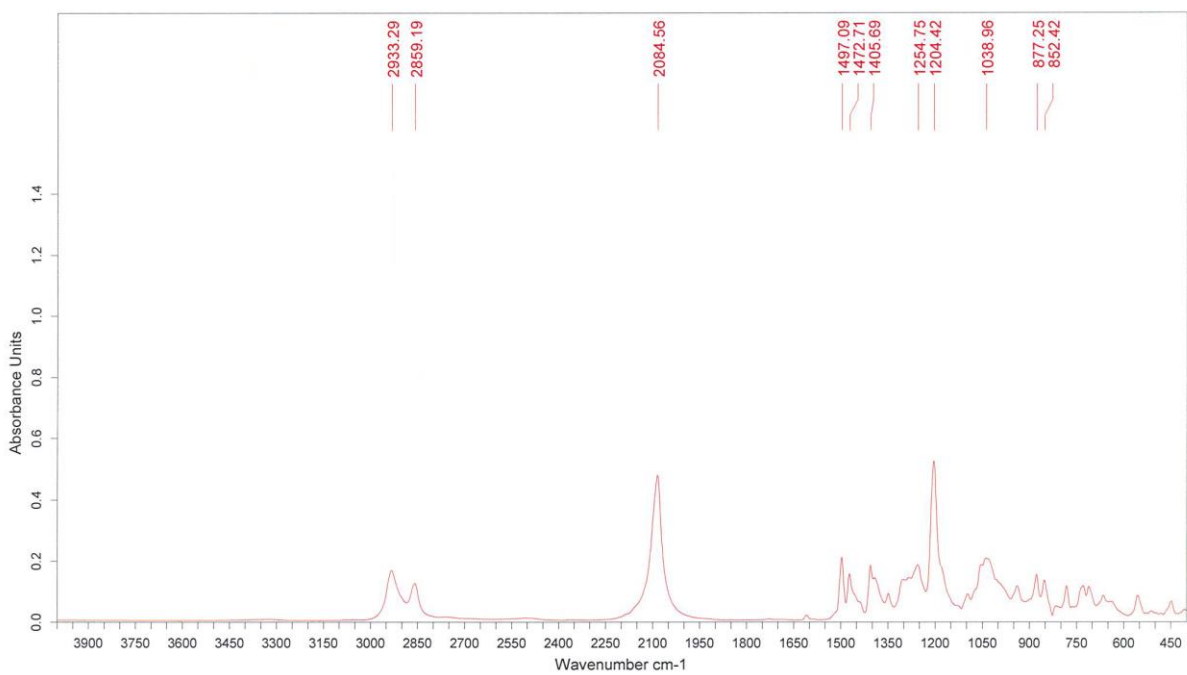


Figure S45. COSY NMR spectrum of **RuNaphA3Ox** in CD₃NO₂.

Figure S46. DOSY NMR spectrum of **RuNaphA30x** in CD_3NO_2 .Figure S47. IR spectrum of **18** in CDCl_3 .

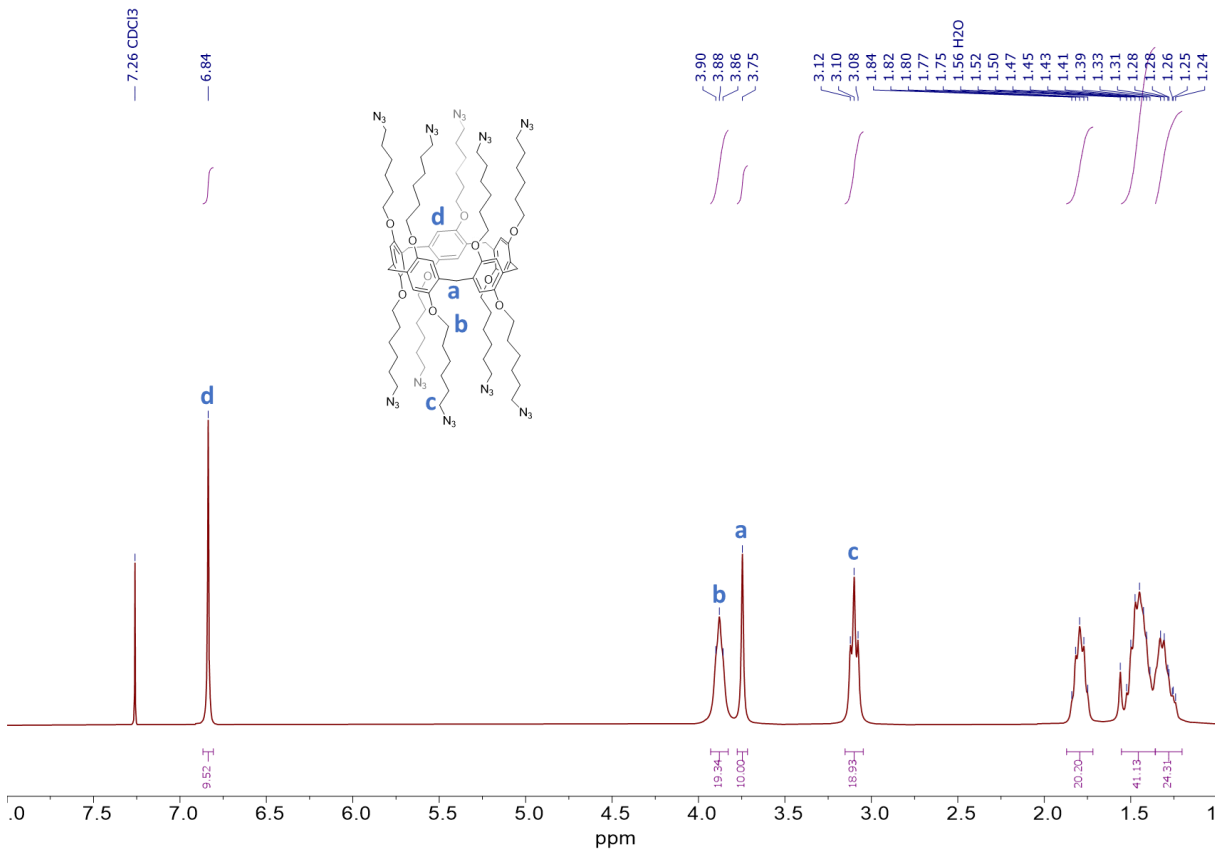


Figure S48. ¹H NMR spectrum of **18** in CDCl₃.

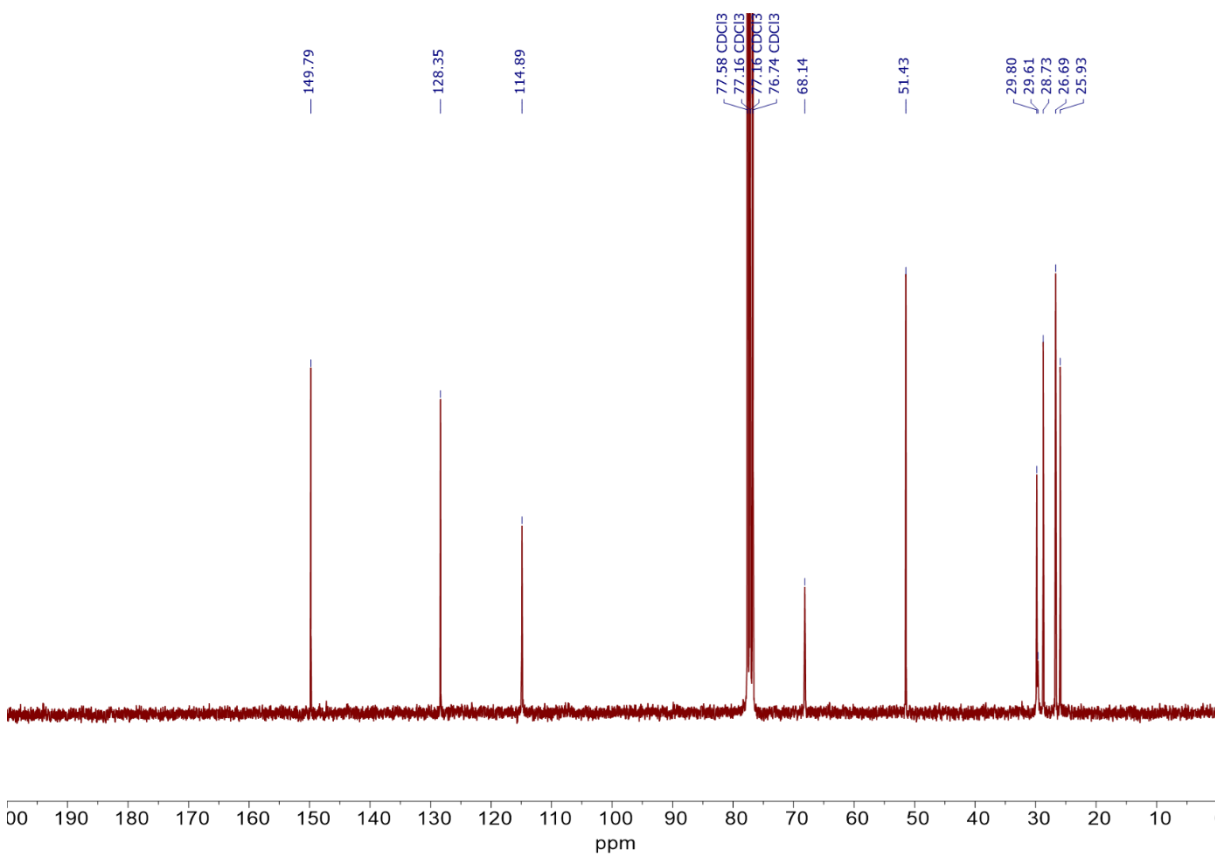
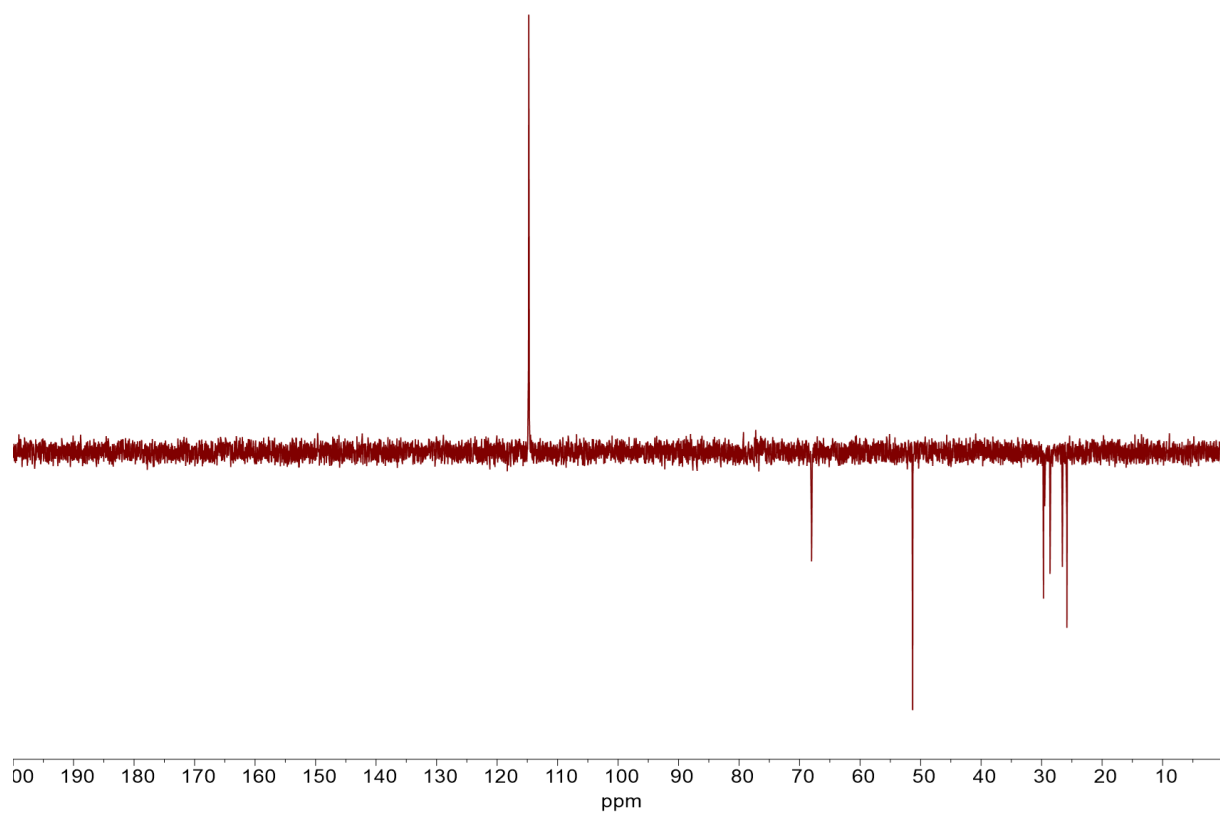
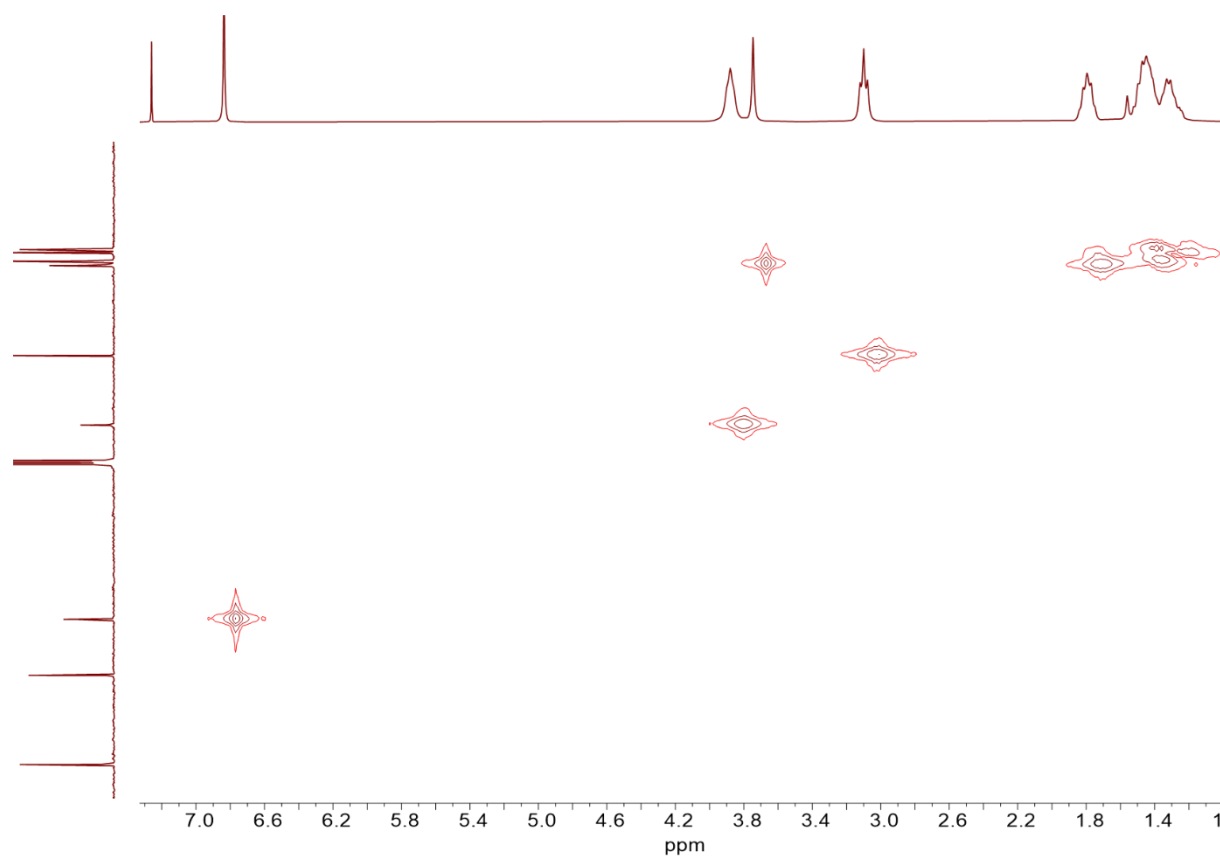


Figure S49. ¹³C NMR spectrum of **18** in CDCl₃.

Figure S50. DEPT NMR spectrum of **18** in CDCl₃.Figure S51. HMQC NMR spectrum of **18** in CDCl₃.

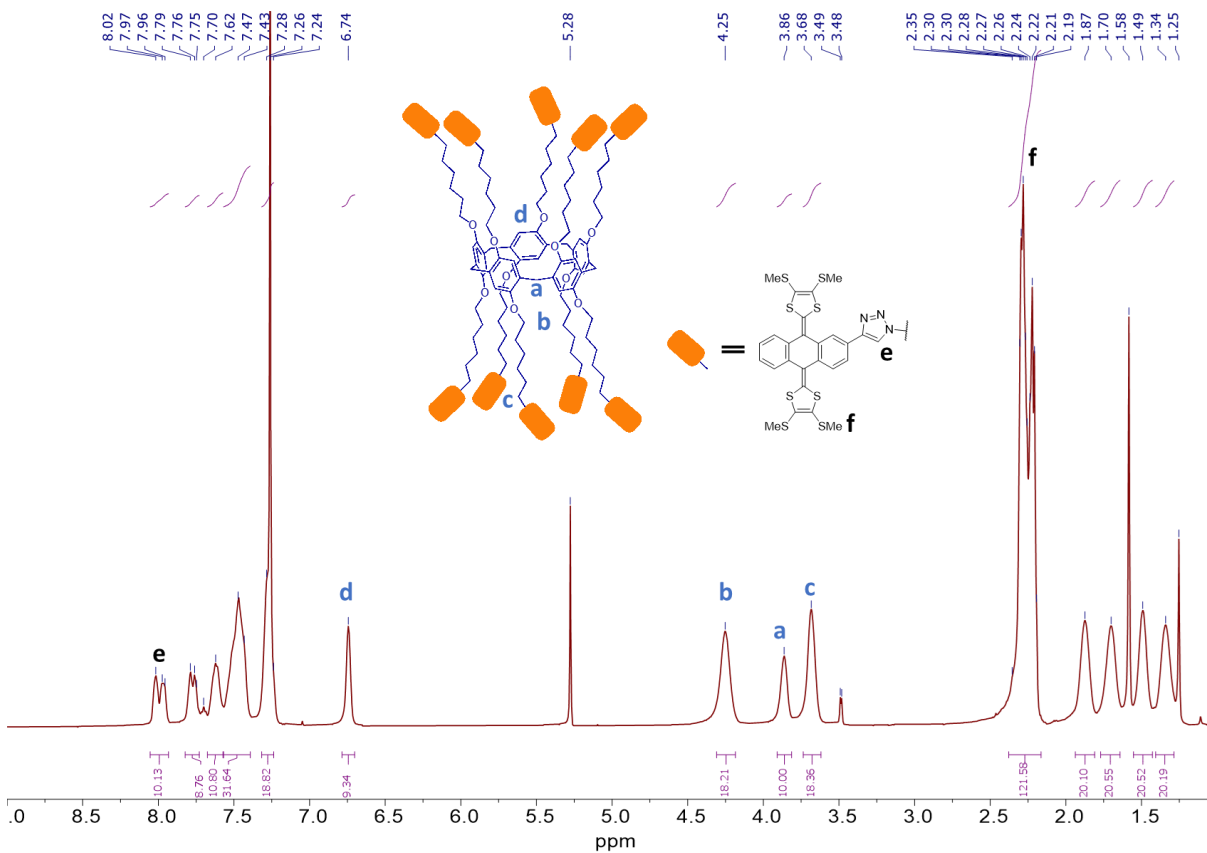


Figure S52. ^1H NMR spectrum of **Pillar-exTTF** in CDCl_3 .

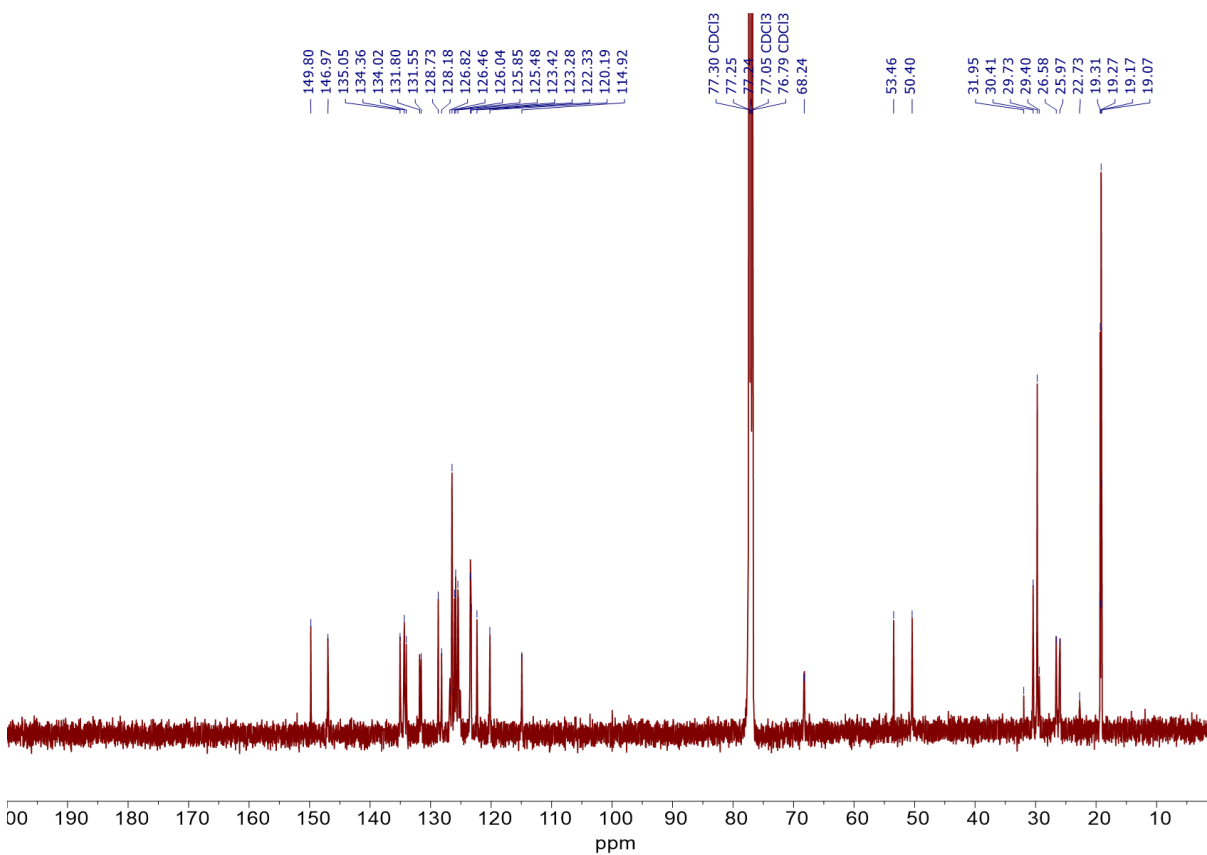
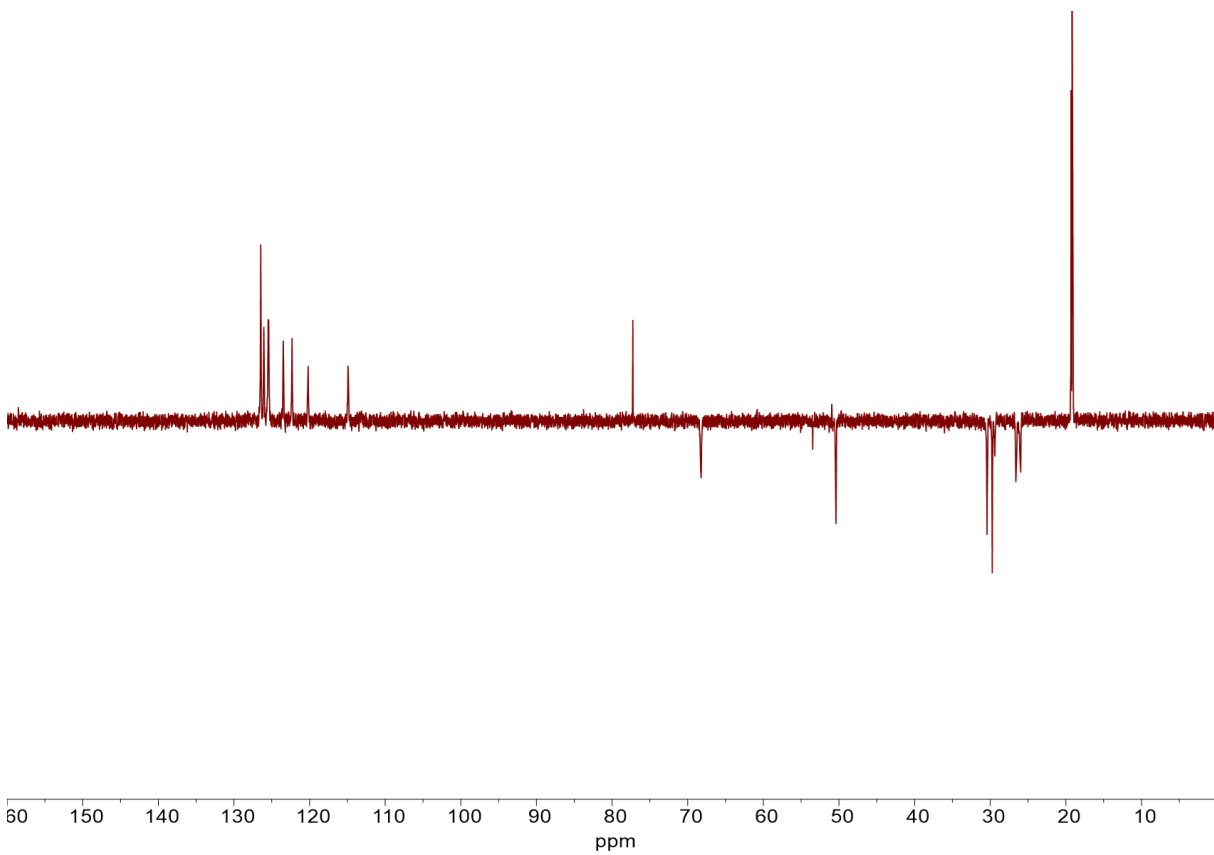
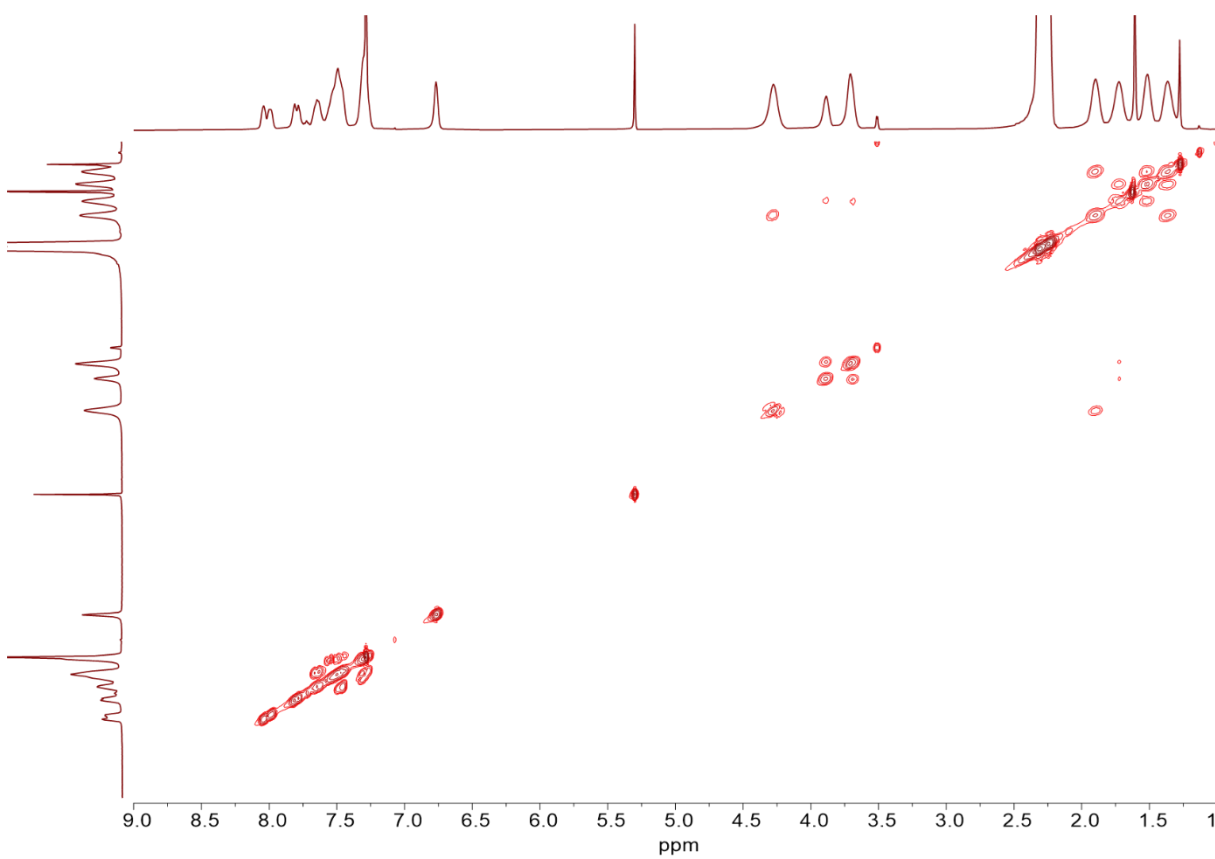
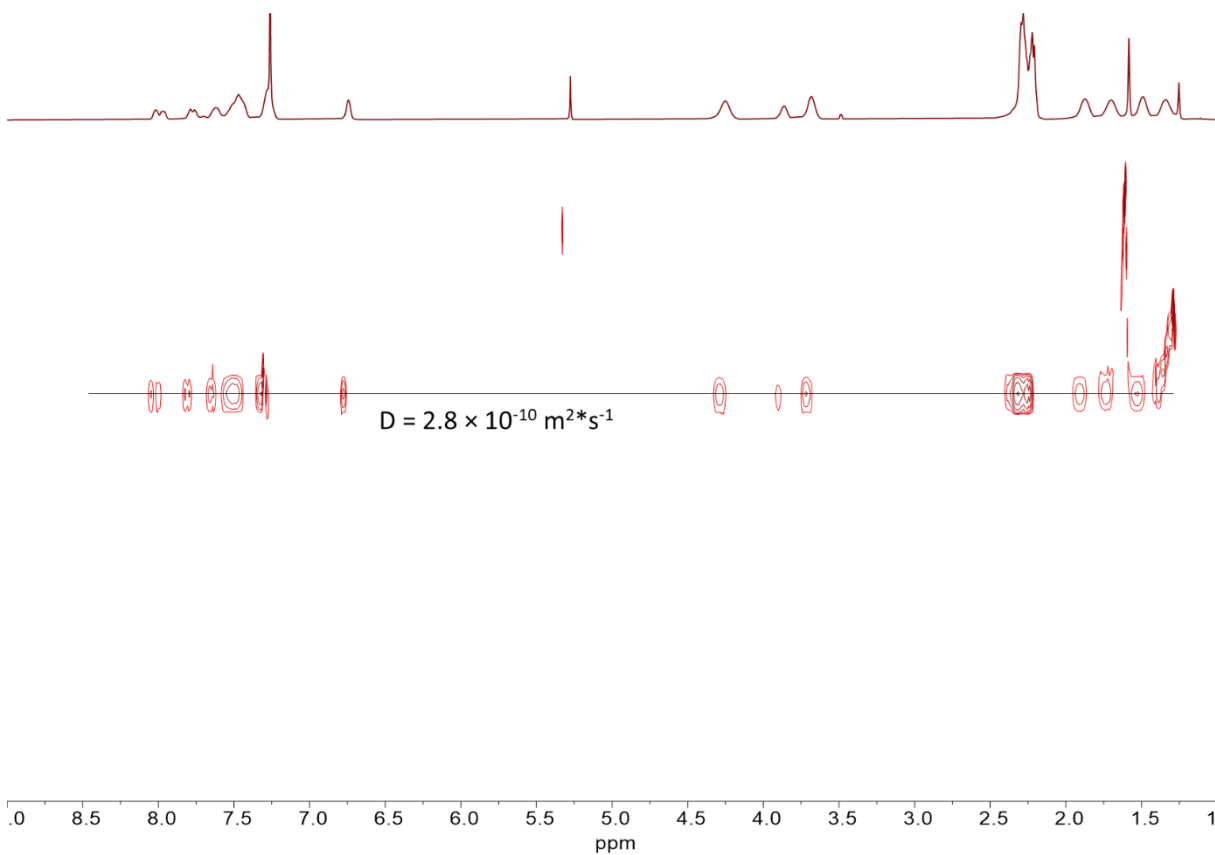
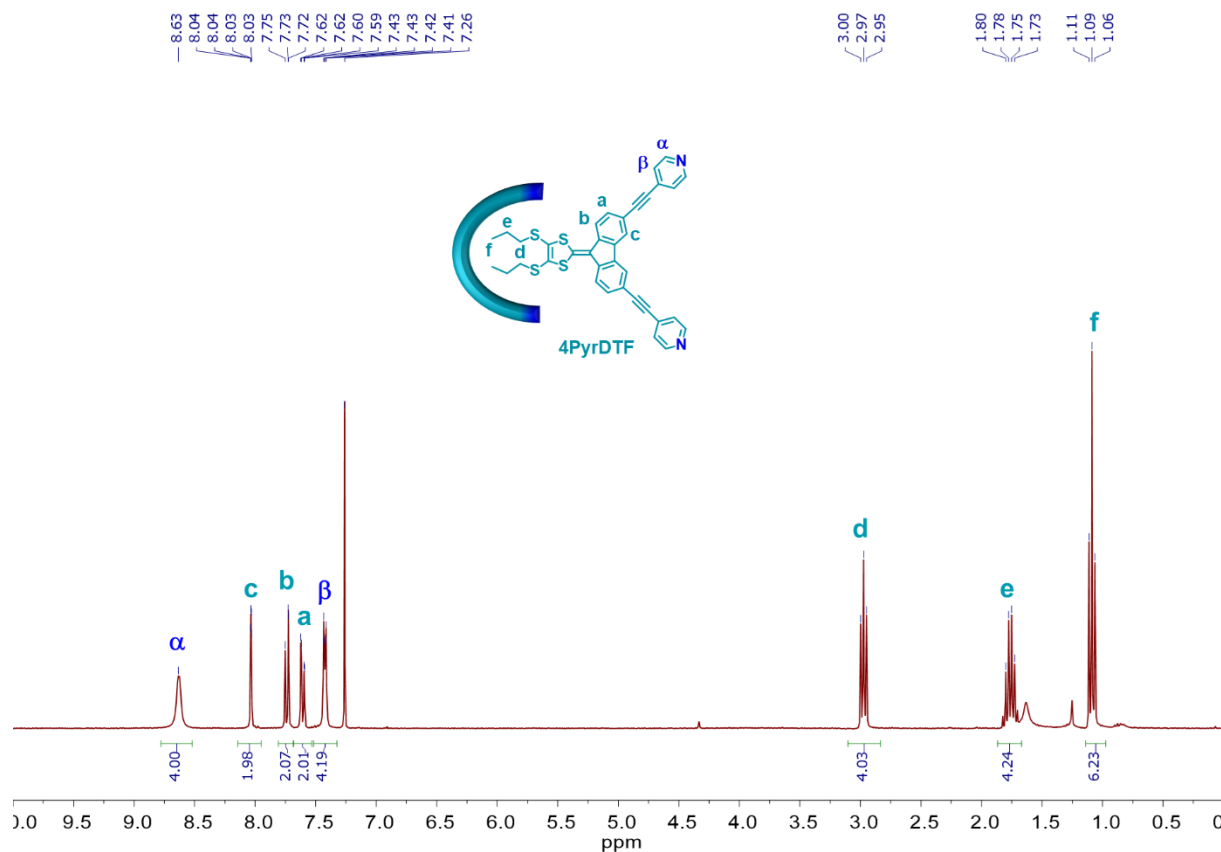


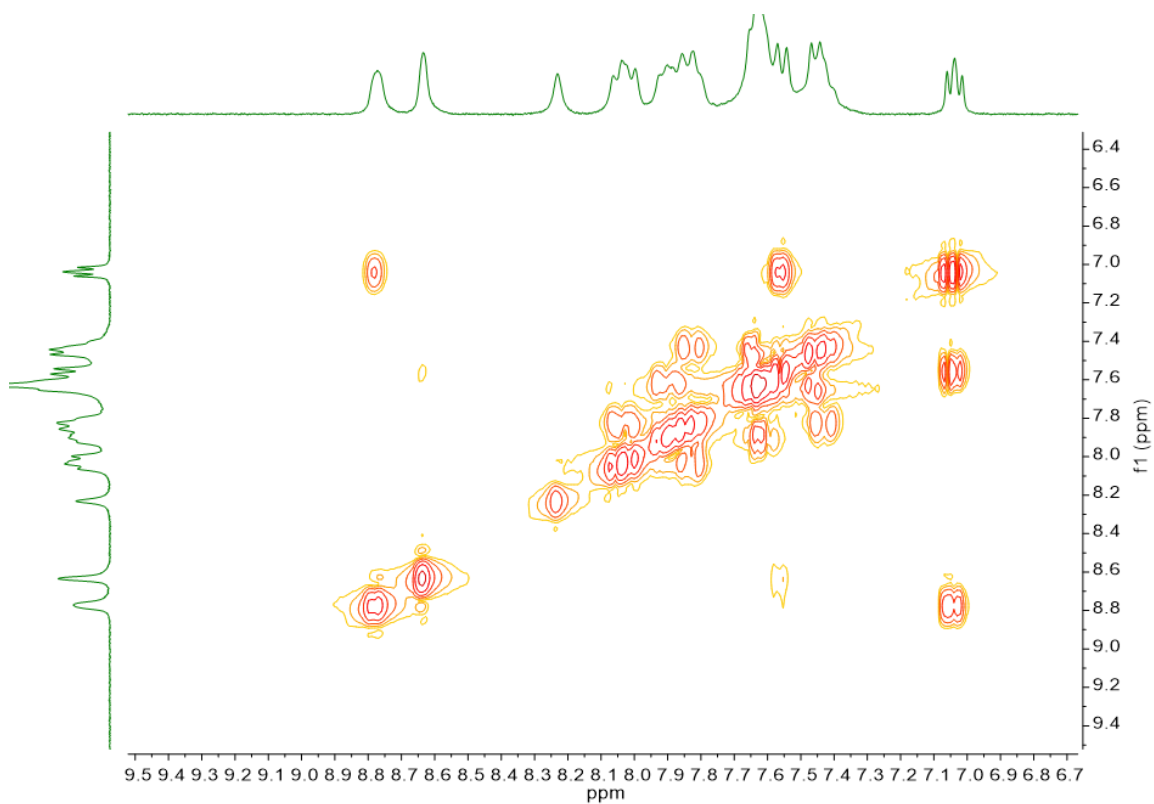
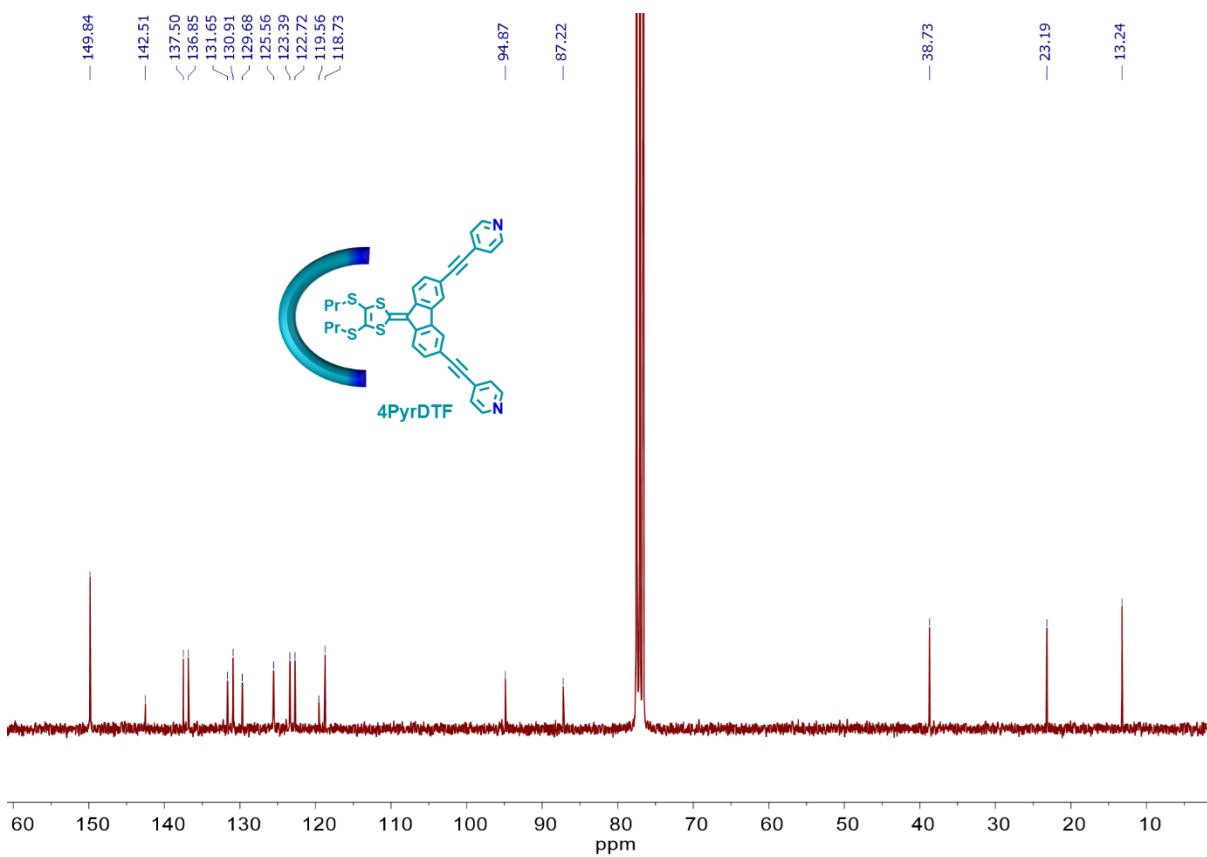
Figure S53. ^{13}C NMR spectrum of **Pillar-exTTF** in CDCl_3 .

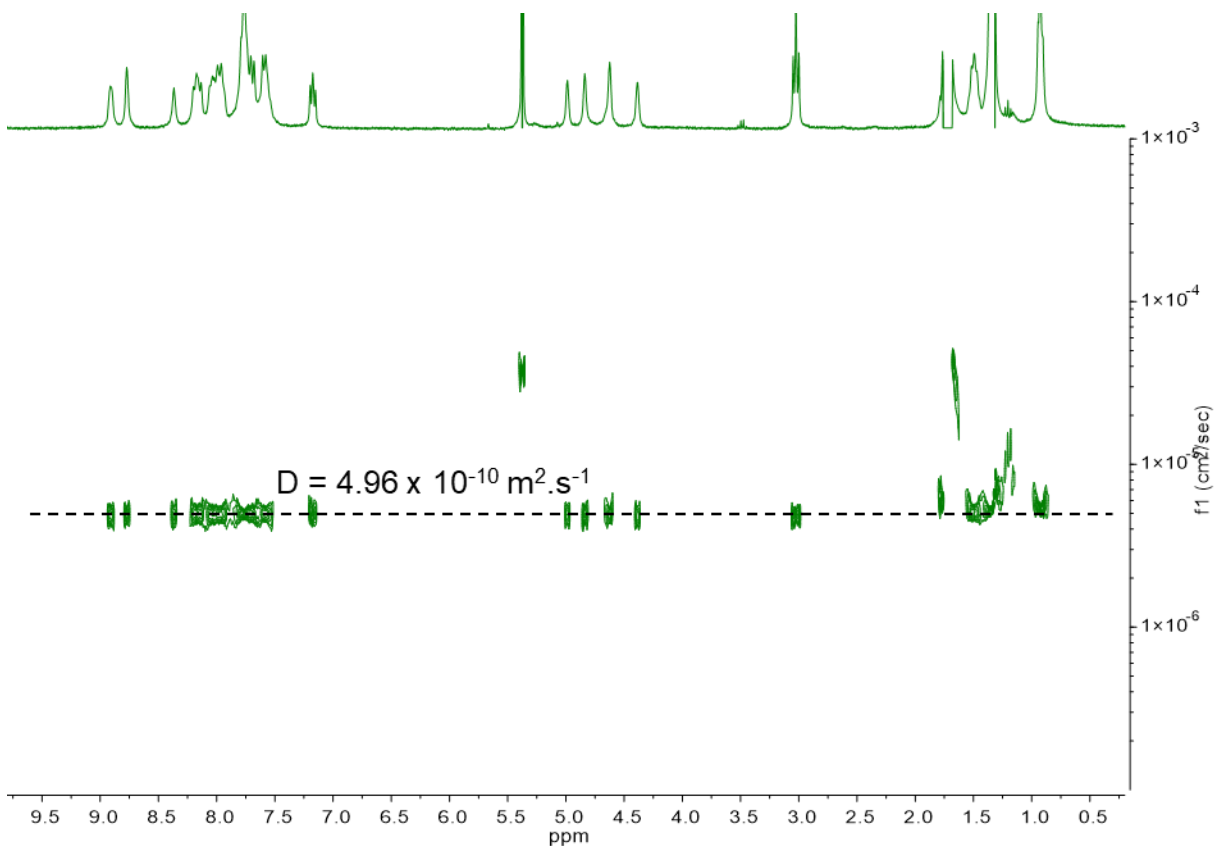
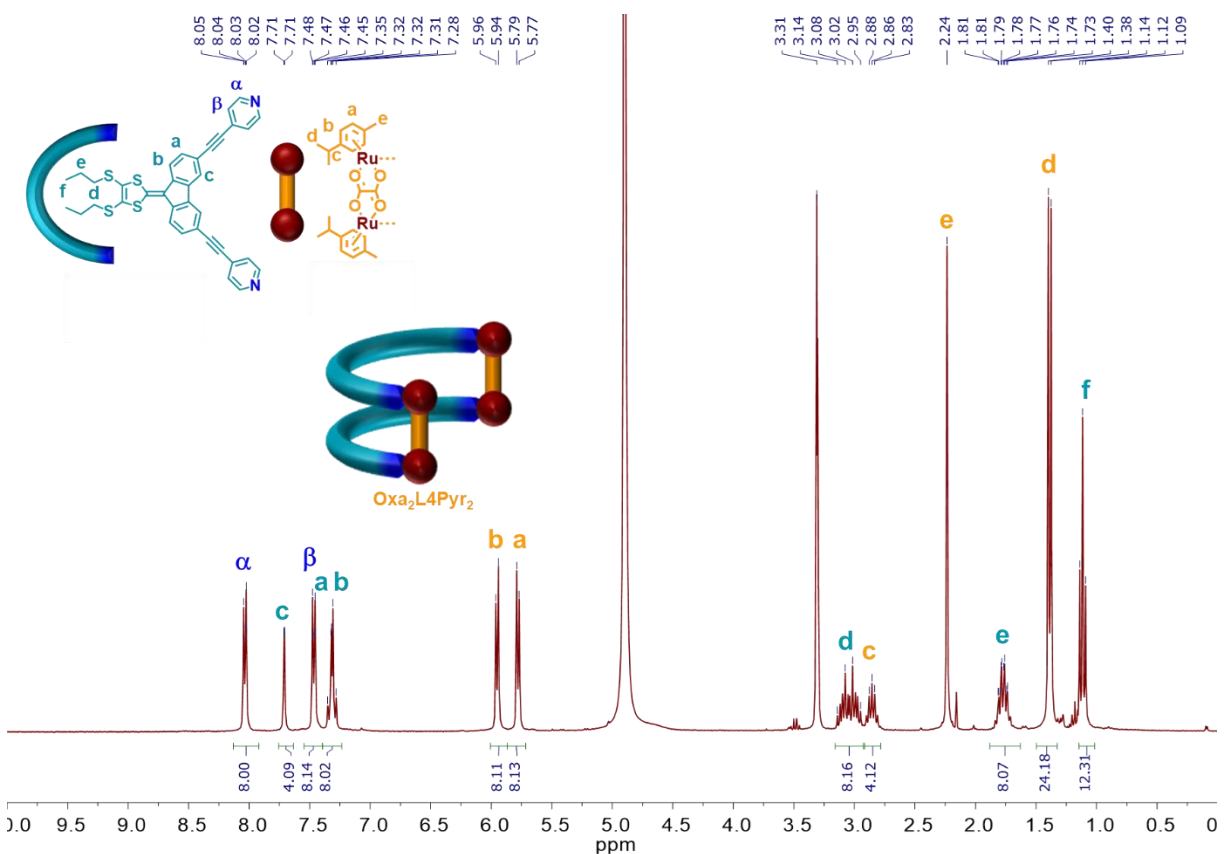
Figure S54. DEPT NMR spectrum of **Pillar-exTTF** in CDCl₃.Figure S55. COSY NMR spectrum of **Pillar-exTTF** in CDCl₃.

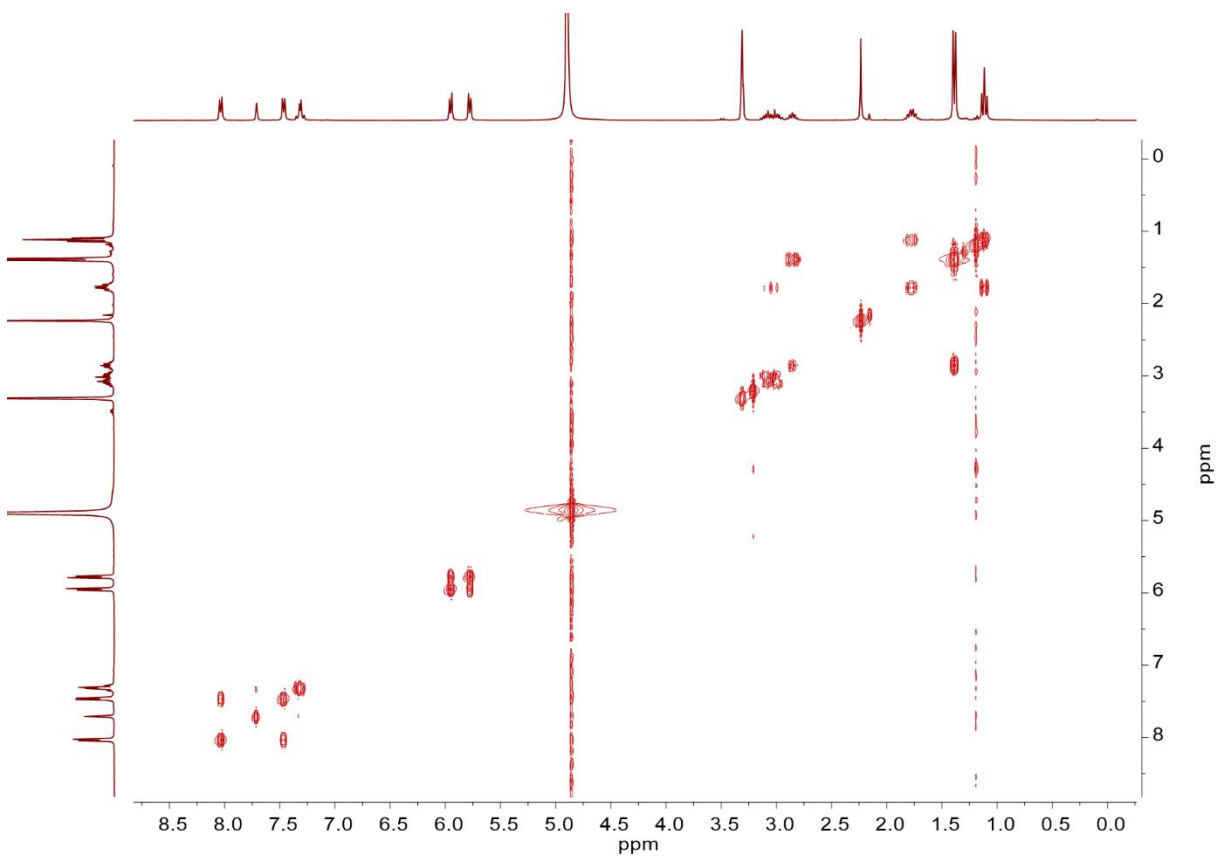
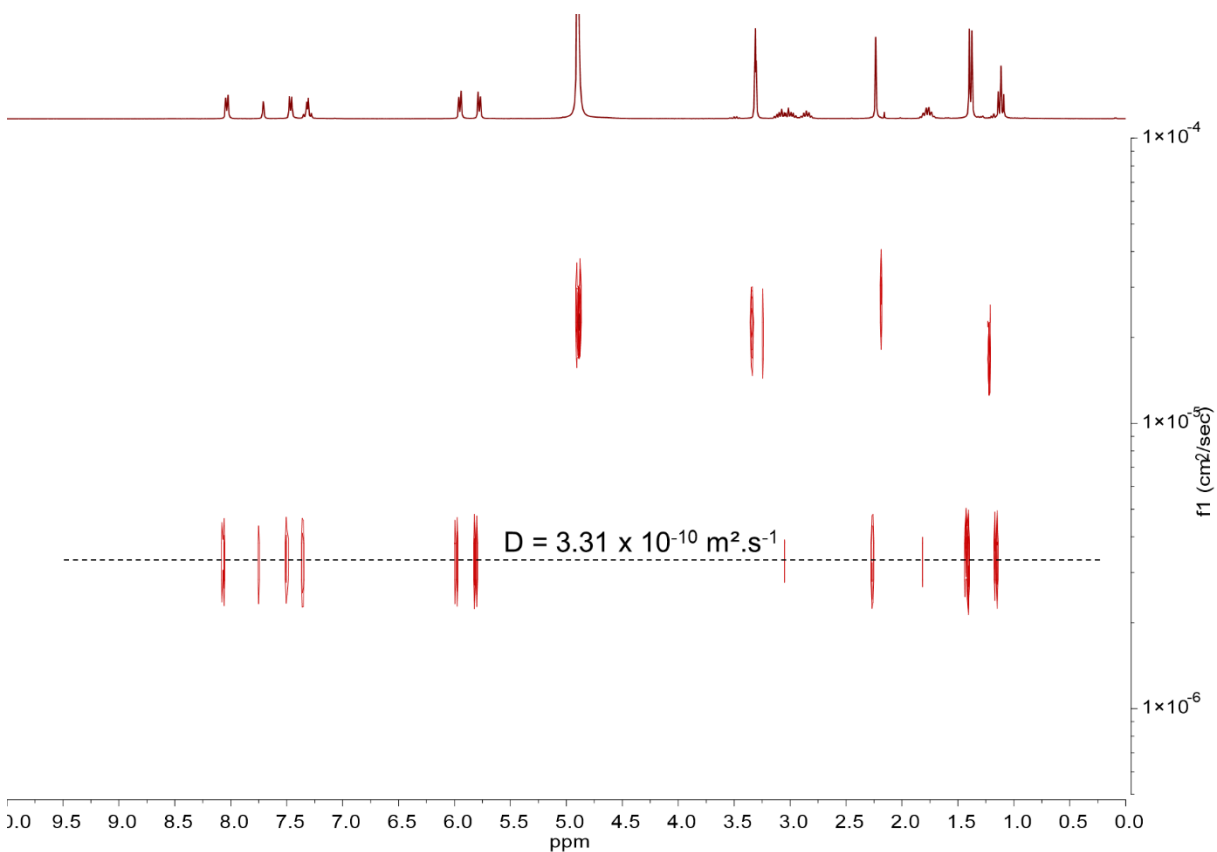
Figure S56. DOSY NMR spectrum of **Pillar-exTTF** in CDCl_3 .

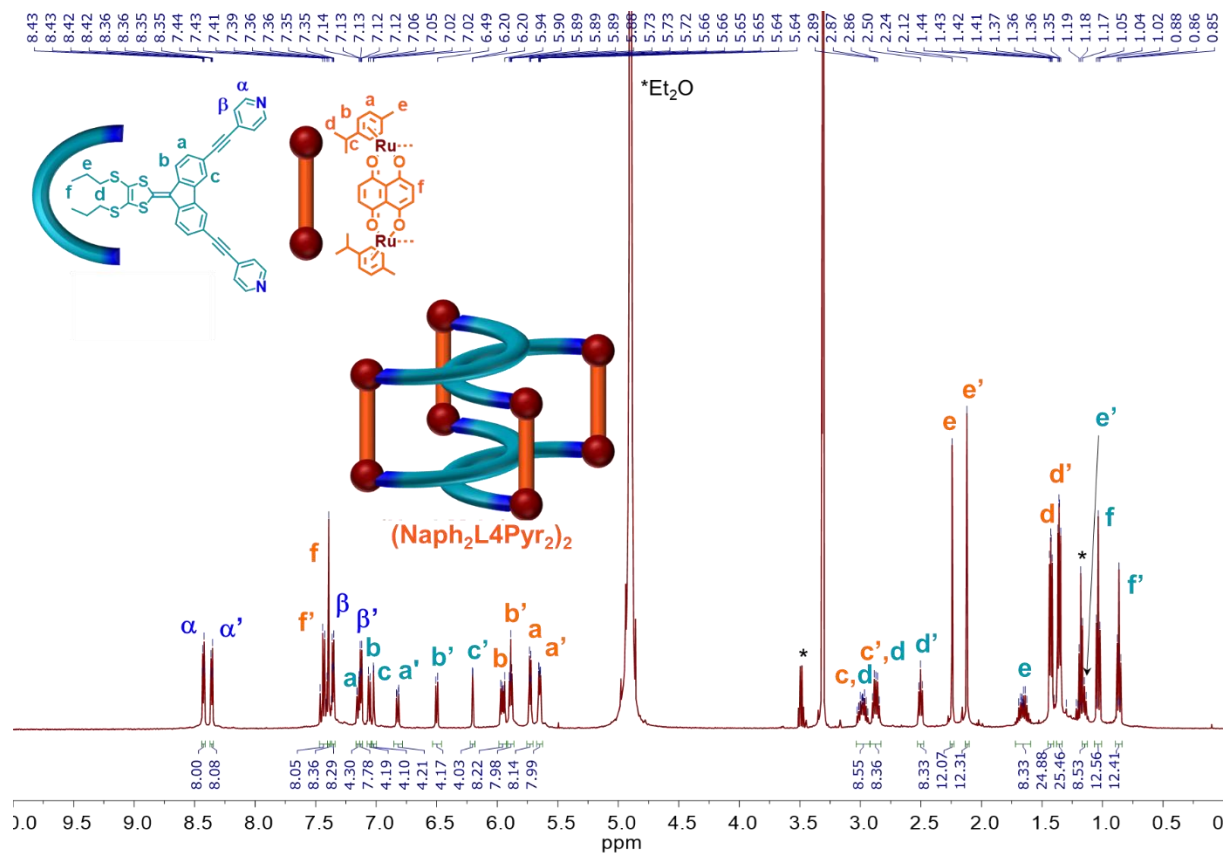
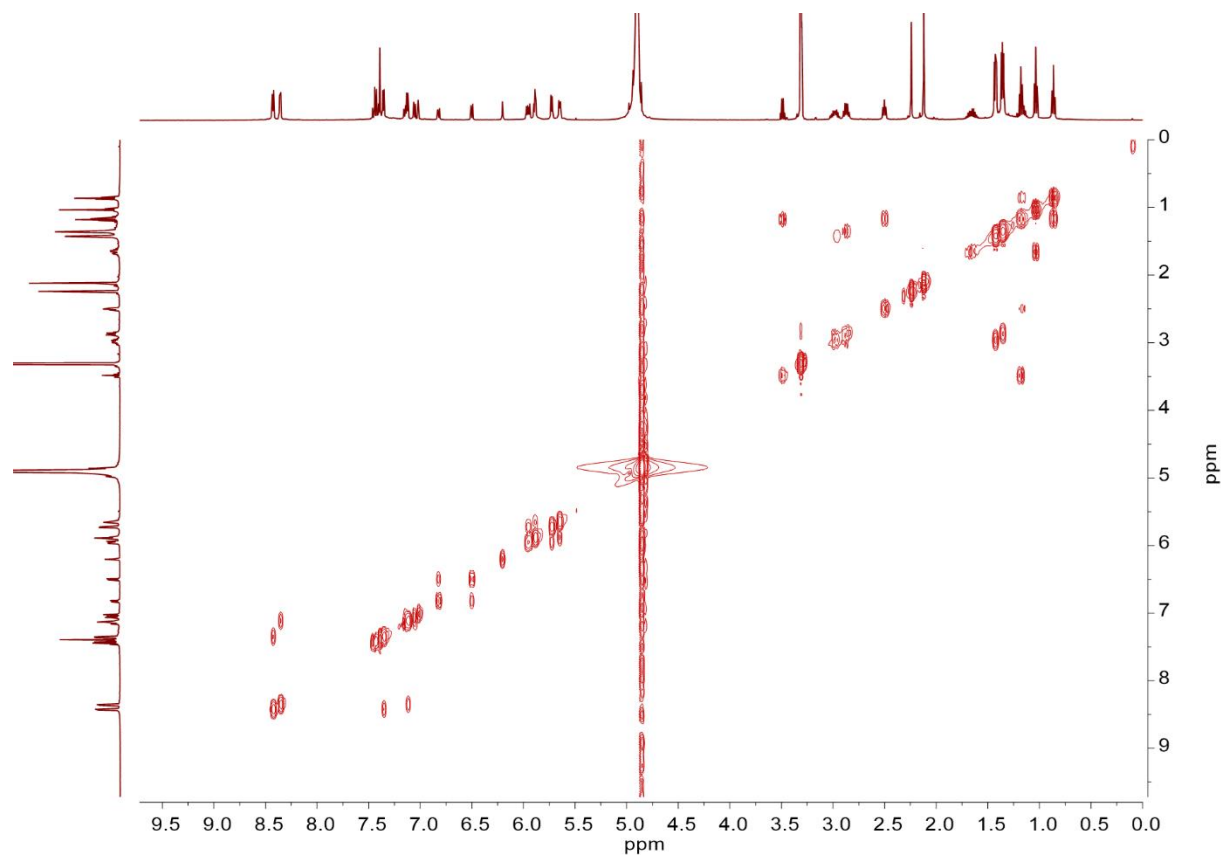
4.2. Additional analyses related to Chapter 3

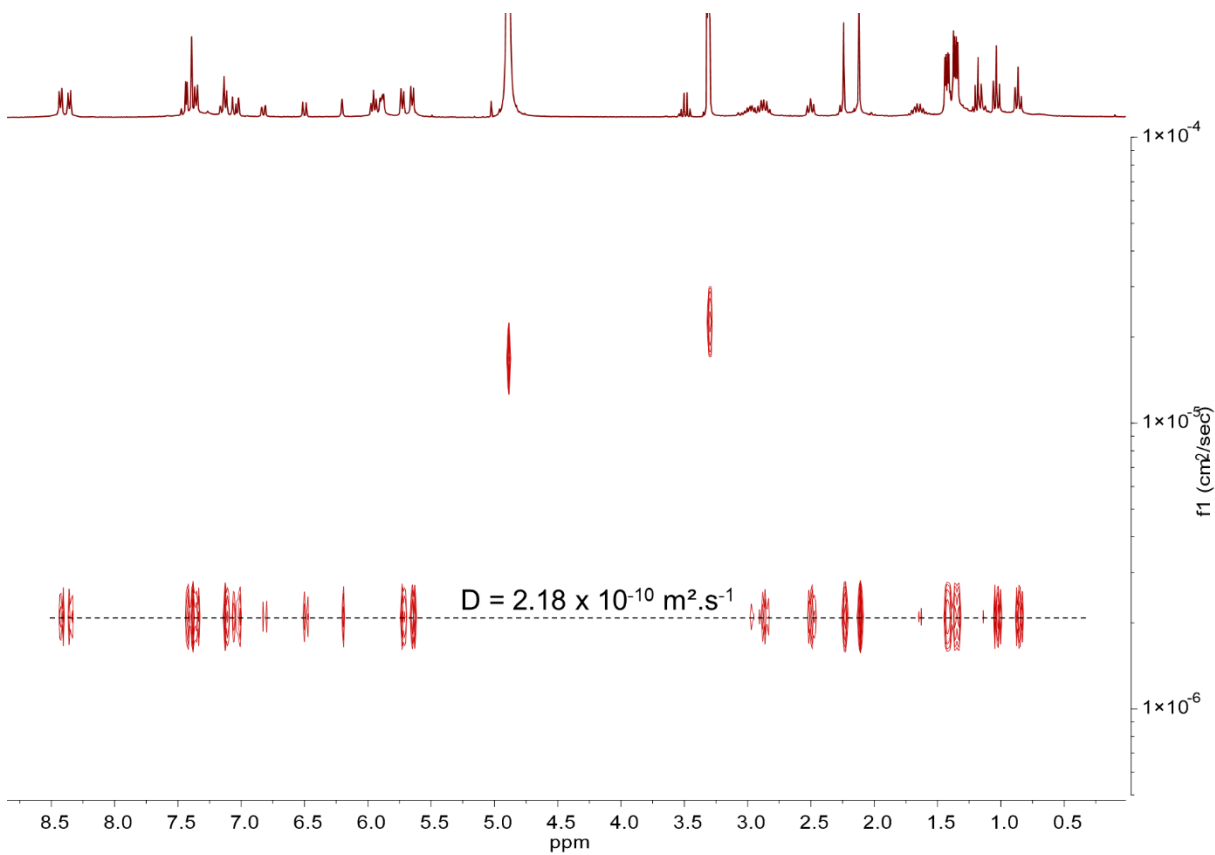
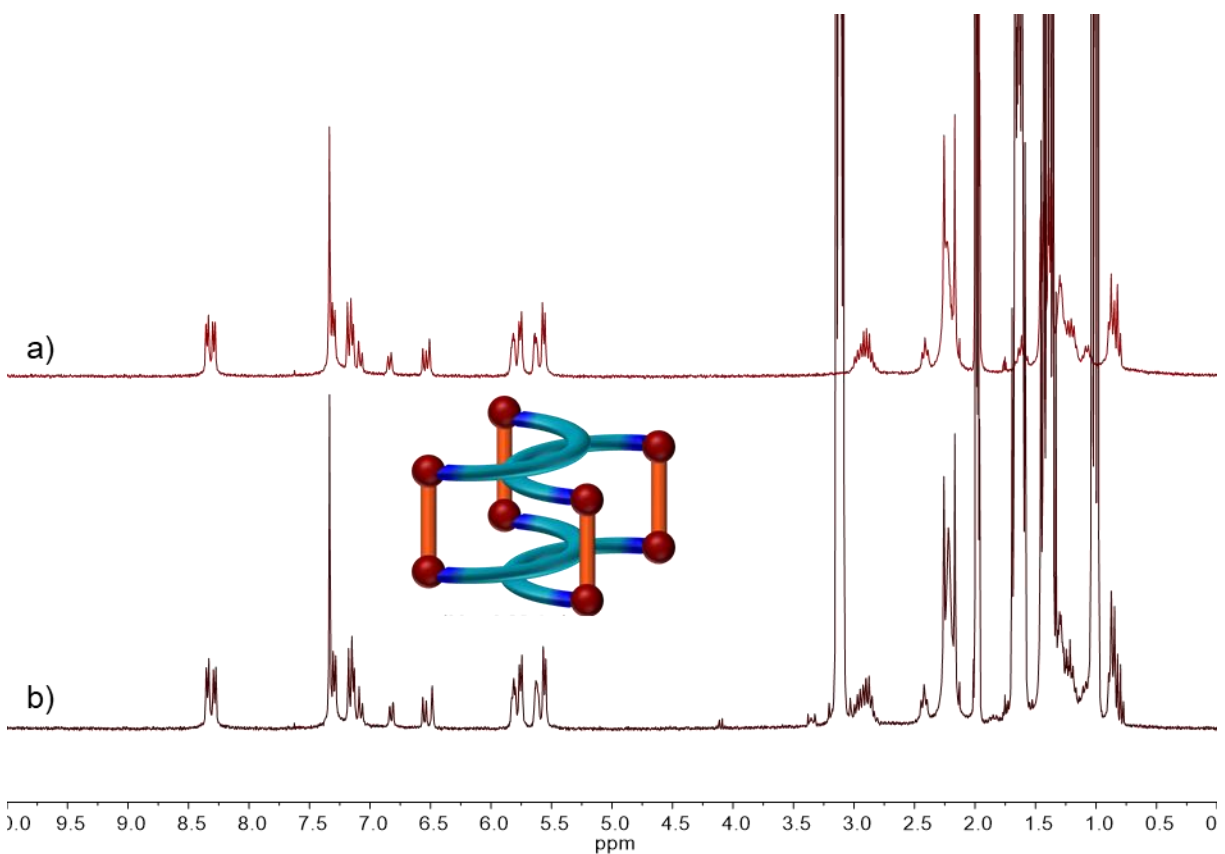
Figure S57. ^1H NMR spectrum of **L4Pyr** in CDCl_3 .



Figure S60. ^1H DOSY NMR spectrum of $\text{Pd}_2\text{L3Pyr}_2$ in CD_2Cl_2 .Figure S61. ^1H NMR spectrum of $\text{Oxa}_2\text{L4Pyr}_2$ in MeOD.

Figure S62. ¹H COSY NMR spectrum of **OxazL4Pyr₂** in MeOD.Figure S63. ¹H DOSY NMR spectrum of **OxazL4Pyr₂** in MeOD.

Figure S64. ^1H NMR spectrum of $(\text{Naph}_2\text{L4Pyr}_2)_2$ in MeOD.Figure S65. ^1H COSY NMR spectrum of $(\text{Naph}_2\text{L4Pyr}_2)_2$ in MeOD.

Figure S66. ^1H DOSY NMR spectrum of $(\text{Naph}_2\text{L4Pyr}_2)_2$ in MeOD.Figure S67. ^1H NMR spectra of $(\text{Naph}_2\text{L4Pyr}_2)_2$ in a) CD_3CN and b) a solution of tetrabutylammonium hexafluorophosphate in CD_3CN ($C = 0.1 \text{ M}$).

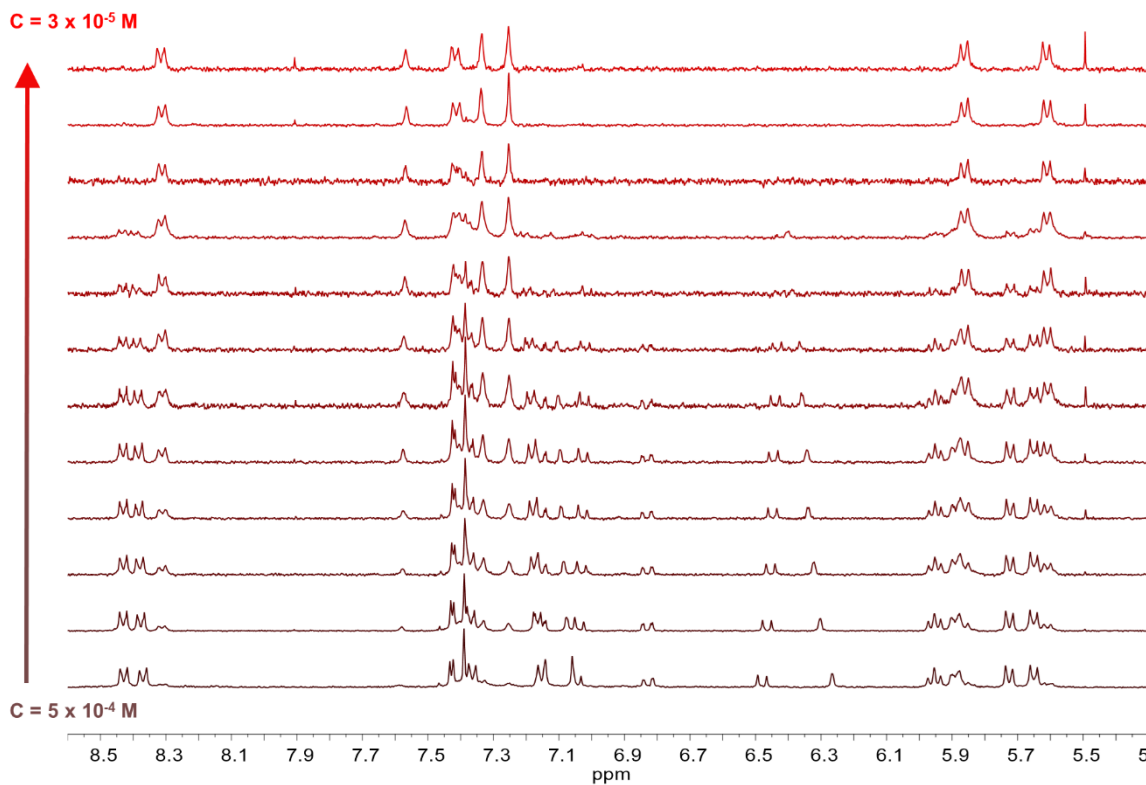


Figure S68. ^1H NMR spectra of **Naph₂L4Pyr₂** in MeOD at concentrations ranging from $C = 5 \times 10^{-4} \text{ M}$ to $C = 3 \times 10^{-5} \text{ M}$.

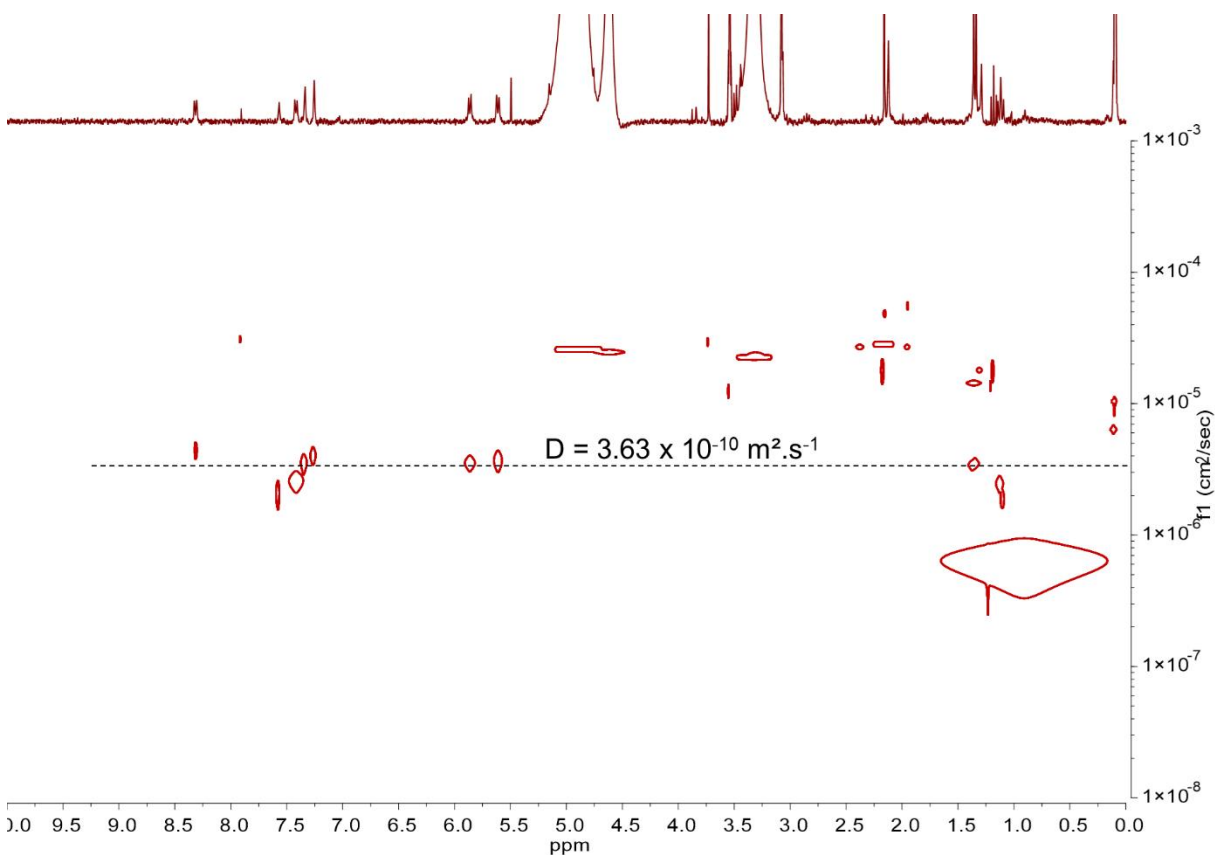


Figure S69. ^1H DOSY NMR spectrum recorded after dilution of **(Naph₂L4Pyr₂)₂** in MeOD to $C = 3 \times 10^{-5} \text{ M}$.

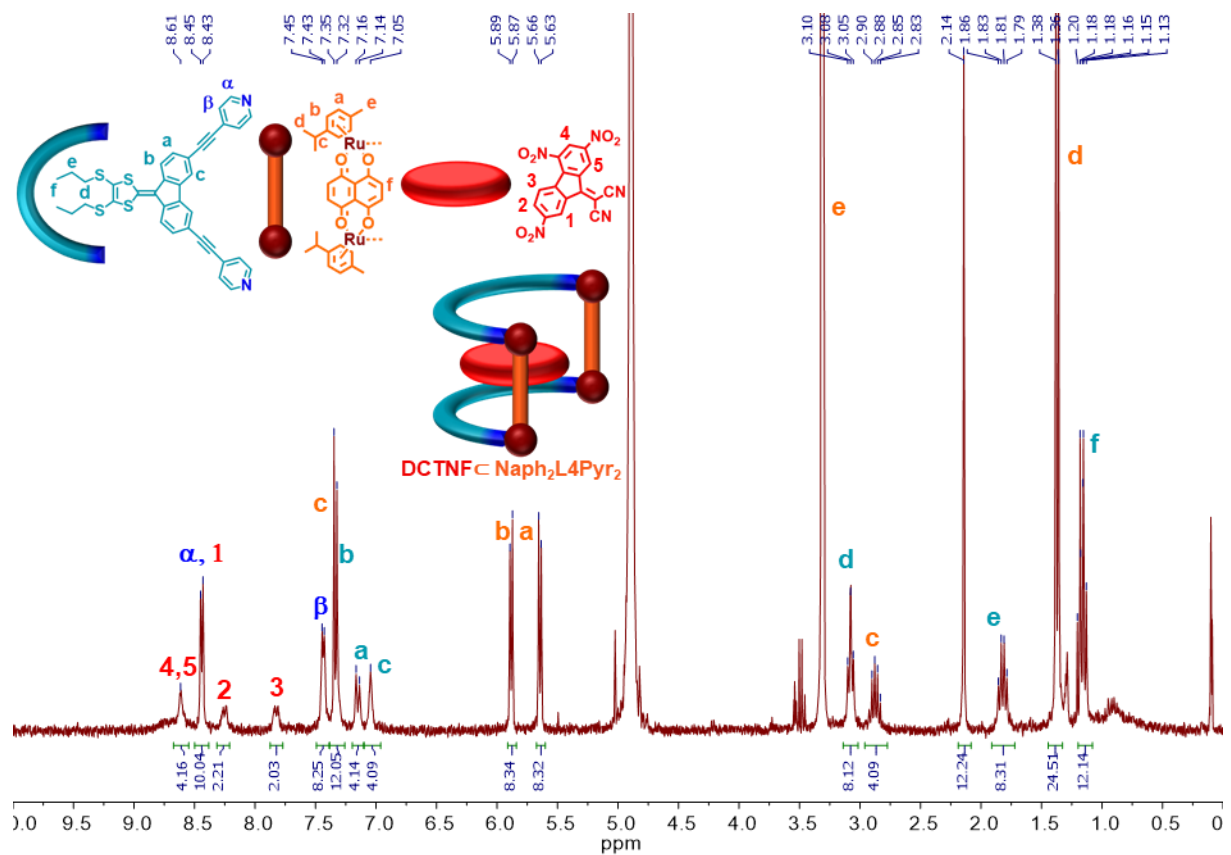


Figure S70. ^1H NMR spectrum of $(\text{Naph}_2\text{L4Pyr}_2)_2$ in MeOD ($C = 10^{-3}$ M) in presence of 4 equiv. of DCTNF.

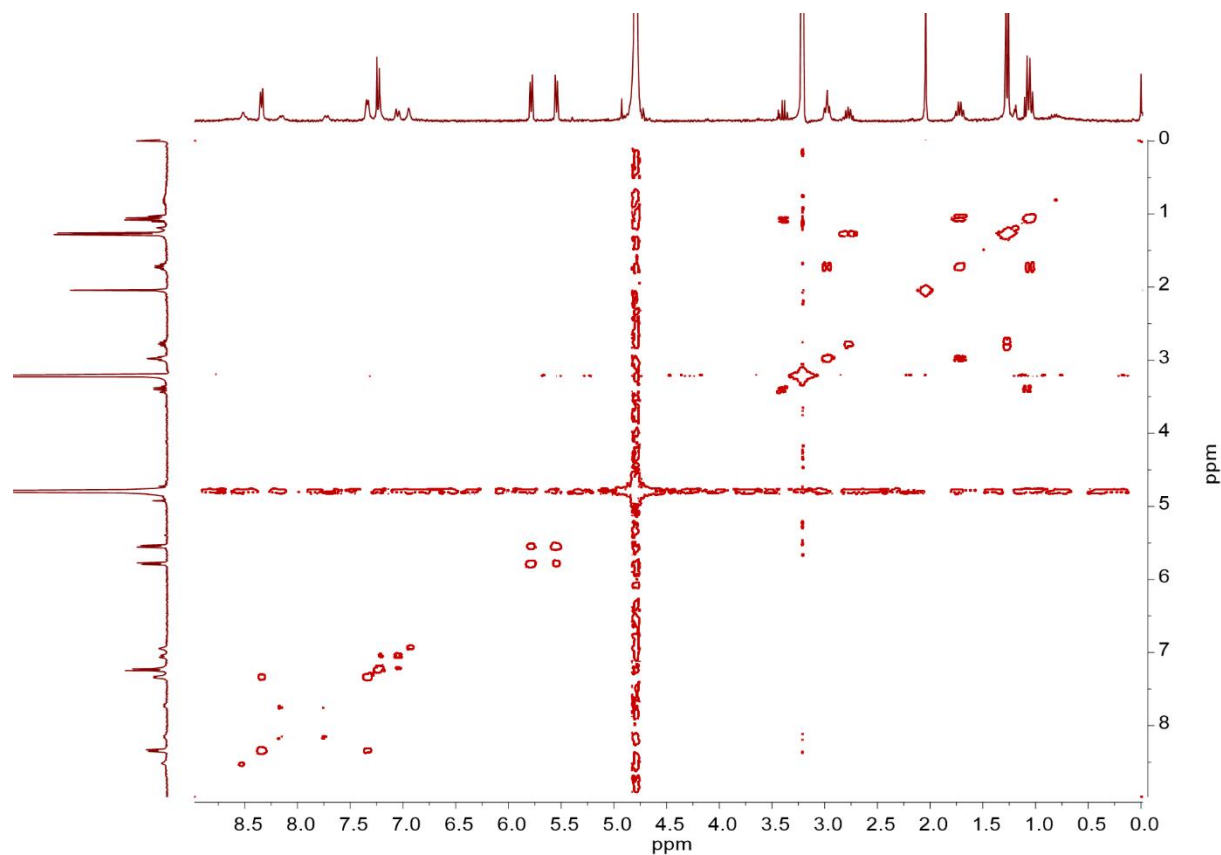


Figure S71. ^1H COSY NMR spectrum of $(\text{Naph}_2\text{L4Pyr}_2)_2$ in MeOD ($C = 10^{-3}$ M) in the presence of 4 equiv. of DCTNF.

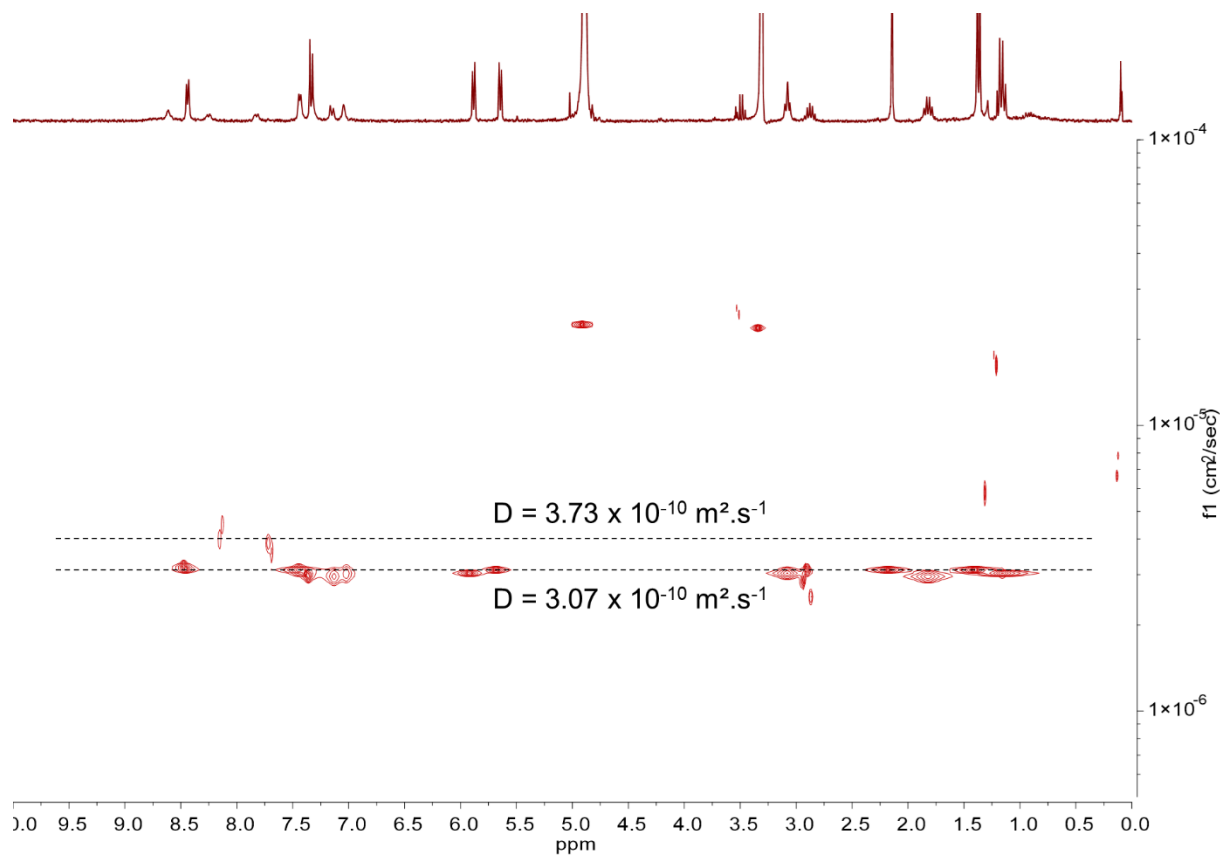


Figure S72. ^1H DOSY NMR spectrum of $(\text{Naph}_2\text{L4Pyr}_2)_2$ in MeOD ($C = 10^{-3}$ M) in the presence of 4 equiv. of DCTNF.

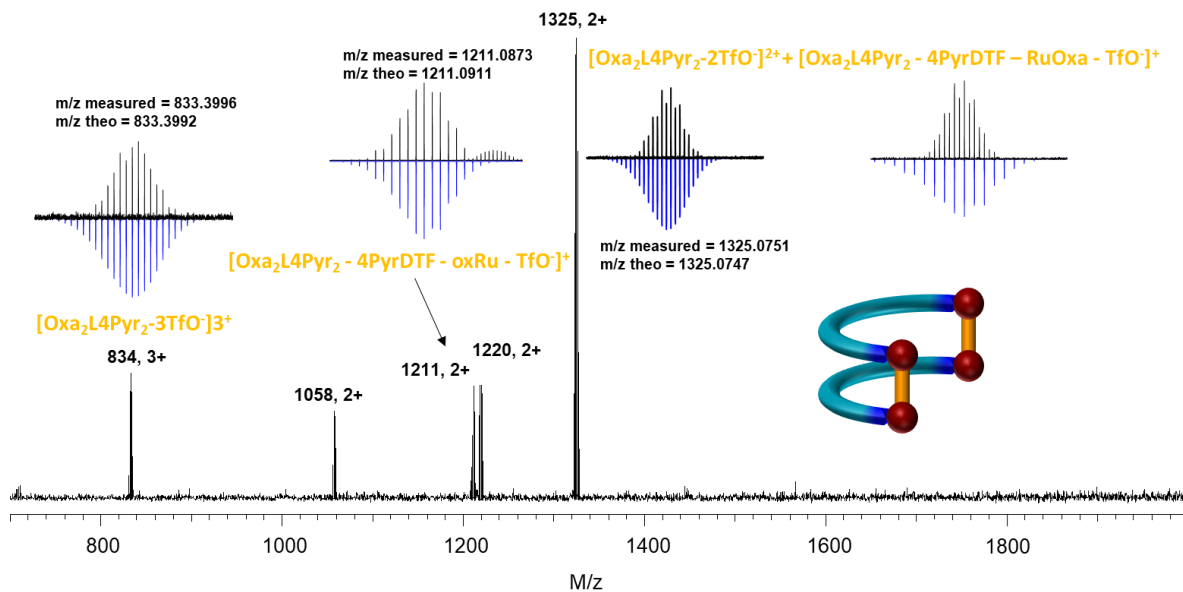


Figure S73. ESI-FTICR spectrum of $\text{Oxa}_2\text{L4Pyr}_2$ recorded in CH_3CN ($C = 10^{-3}$ M).

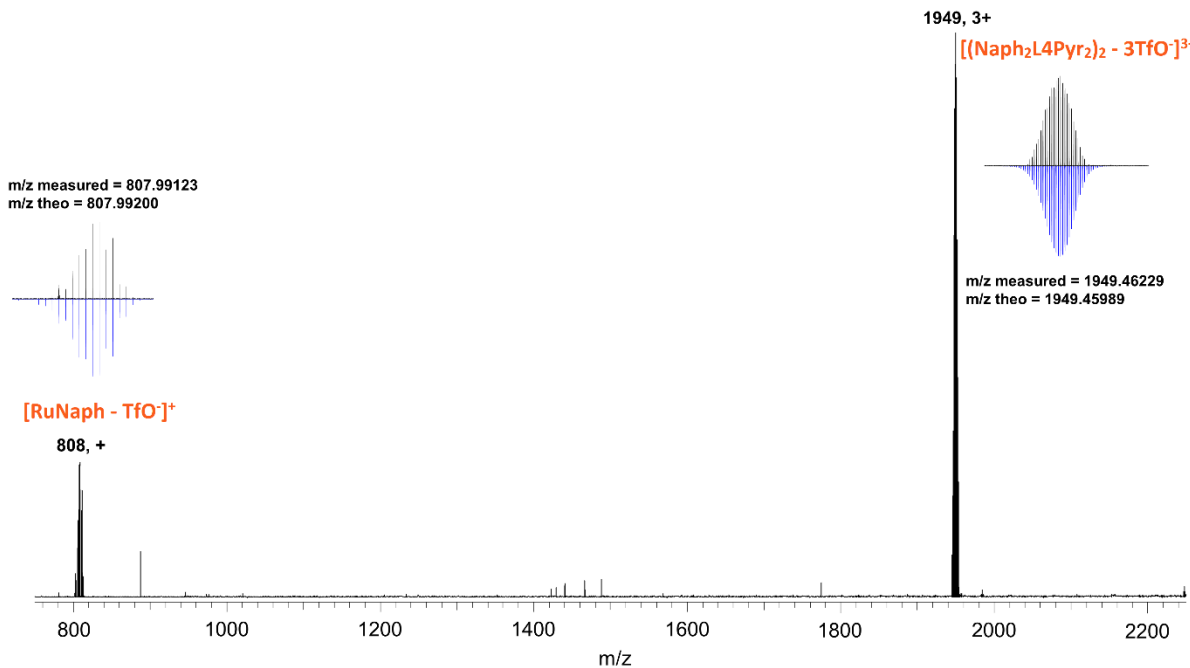


Figure S74. ESI-FTICR spectrum of $(\text{Naph}_2\text{L4Pyr}_2)_2$ recorded in CH_3CN ($C = 10^{-3} \text{ M}$).

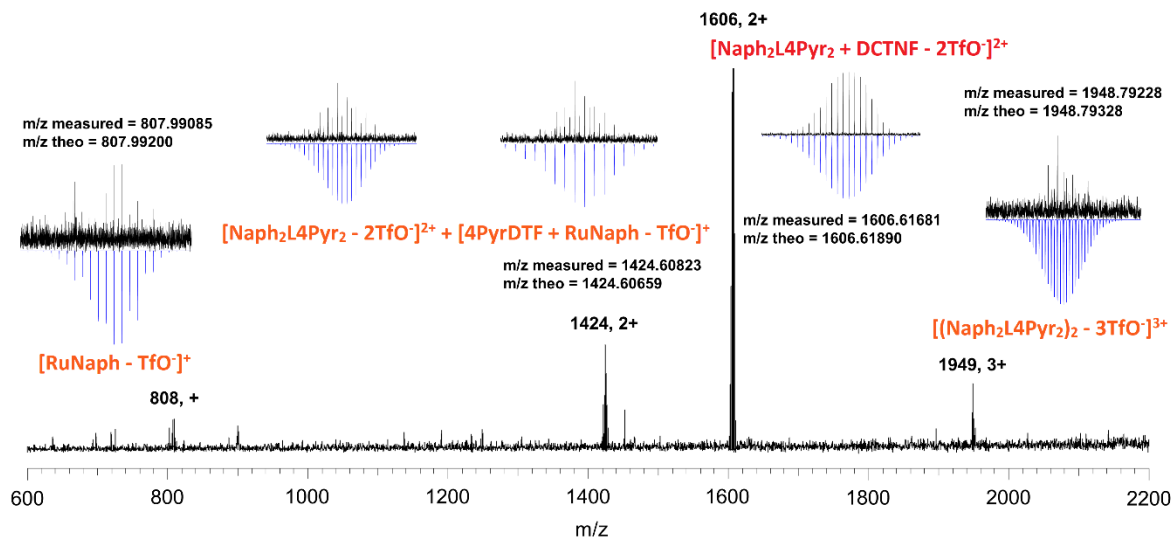
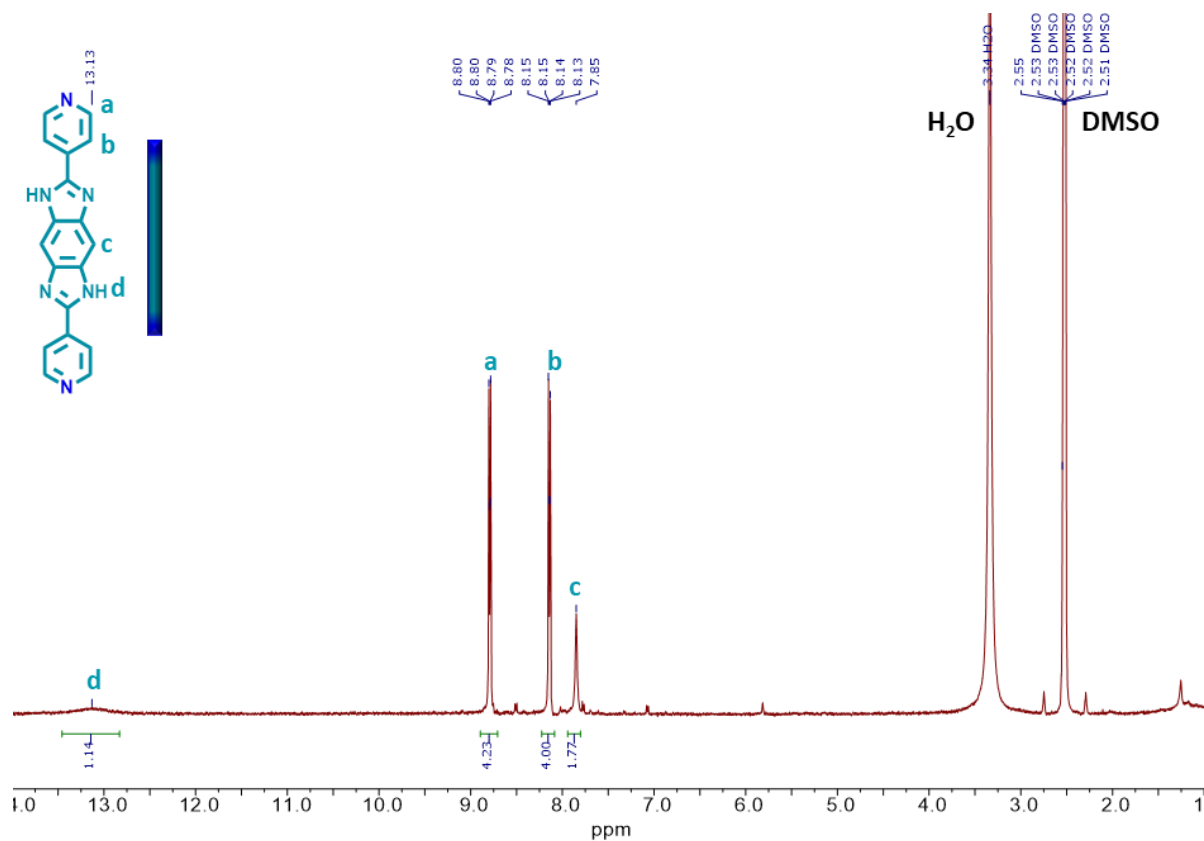
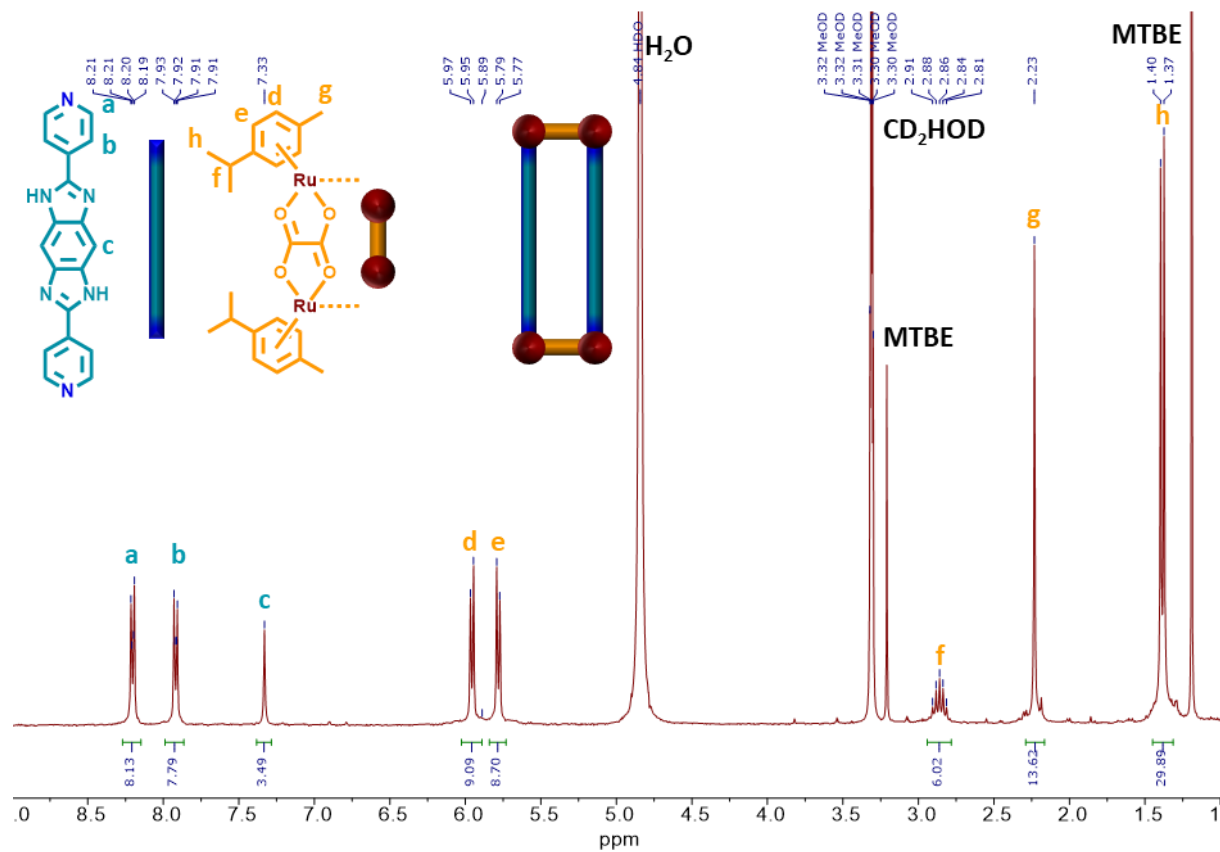


Figure S75. ESI-FTICR spectrum of $(\text{Naph}_2\text{L4Pyr}_2)_2$ recorded in CH_3CN ($C = 10^{-3} \text{ M}$) in the presence of 2 equiv. of DCTNF.

4.3. Additional analyses related to Chapter 4

Figure S76. ^1H NMR spectrum of ligand **BBI** in DMSO.Figure S77. ^1H NMR spectrum of **Oxa₂BBI₂** in MeOD- d_4 ($C = 10^{-3}$ M).

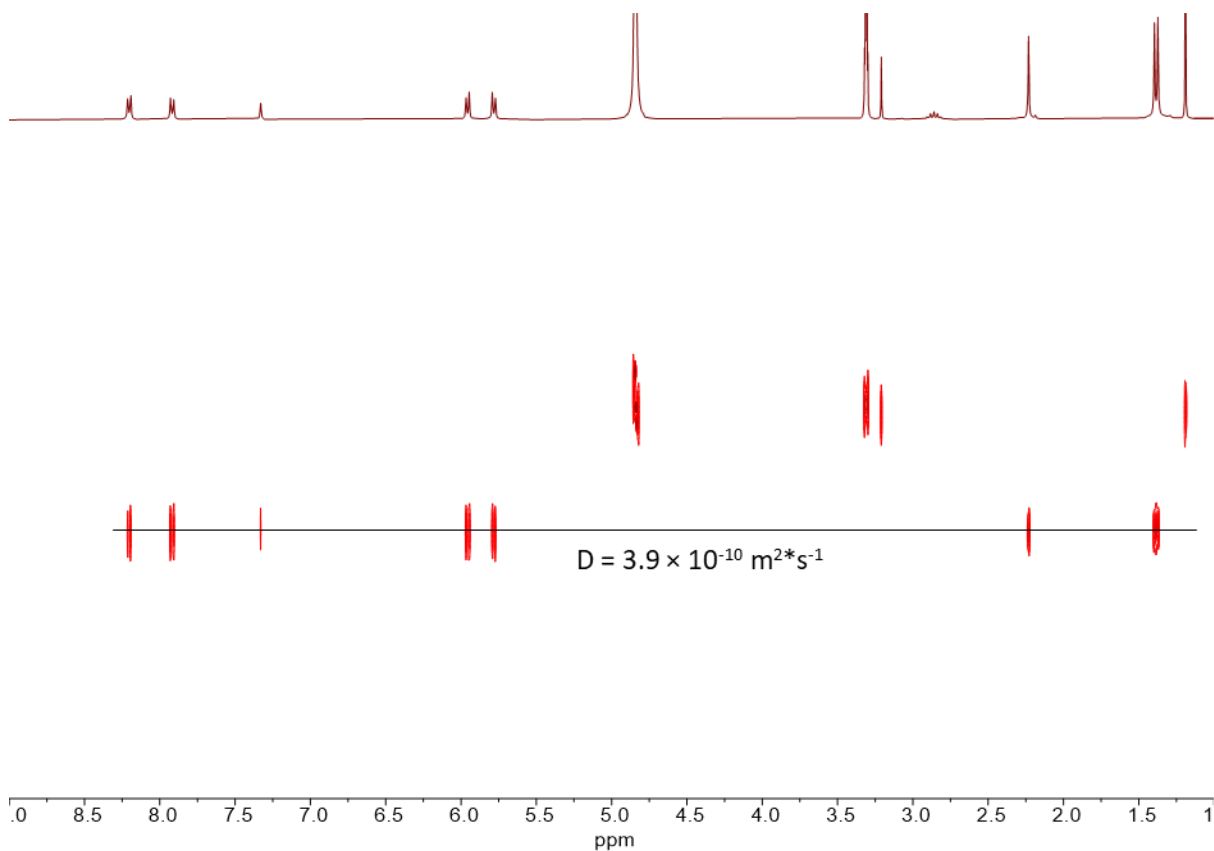


Figure S78. ^1H DOSY NMR spectrum of **Oxa₂BBI₂** in MeOD- d_4 ($C = 10^{-3}$ M, $T = 298$ K).

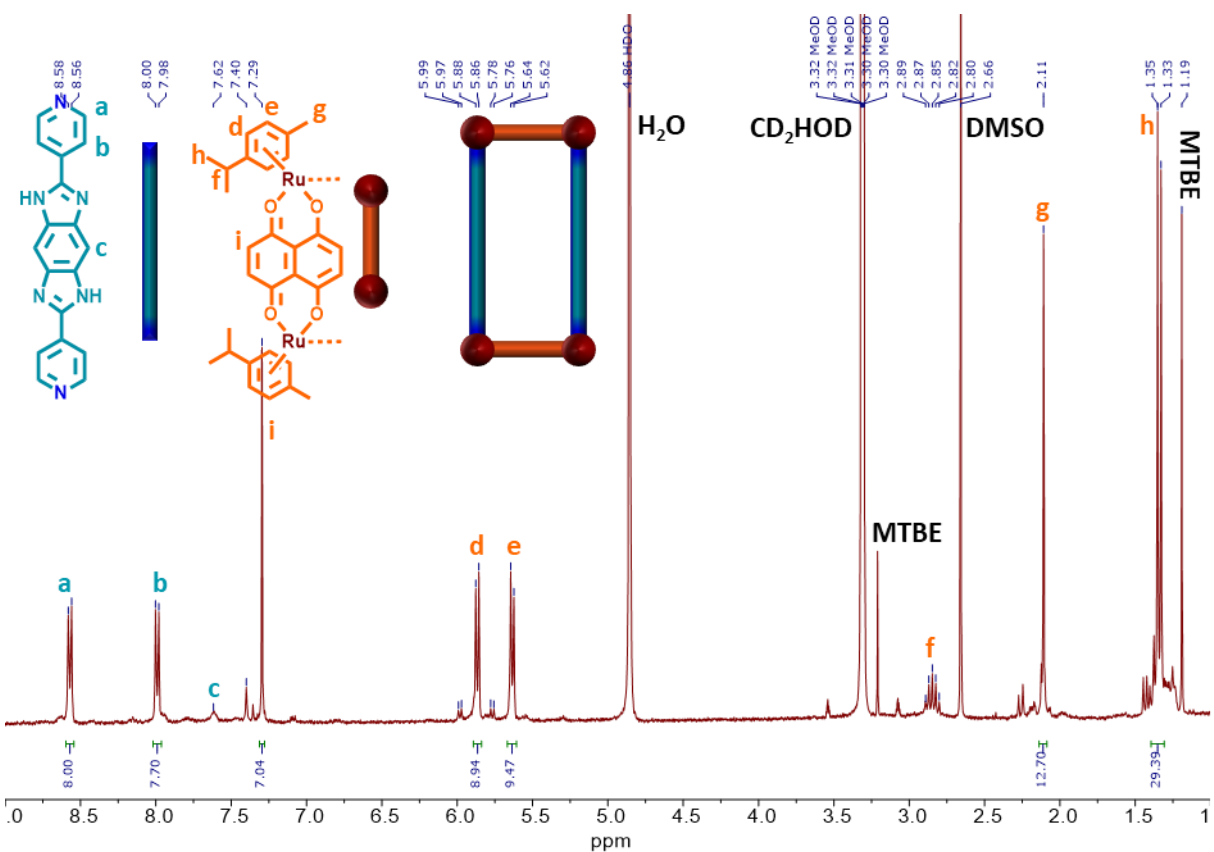
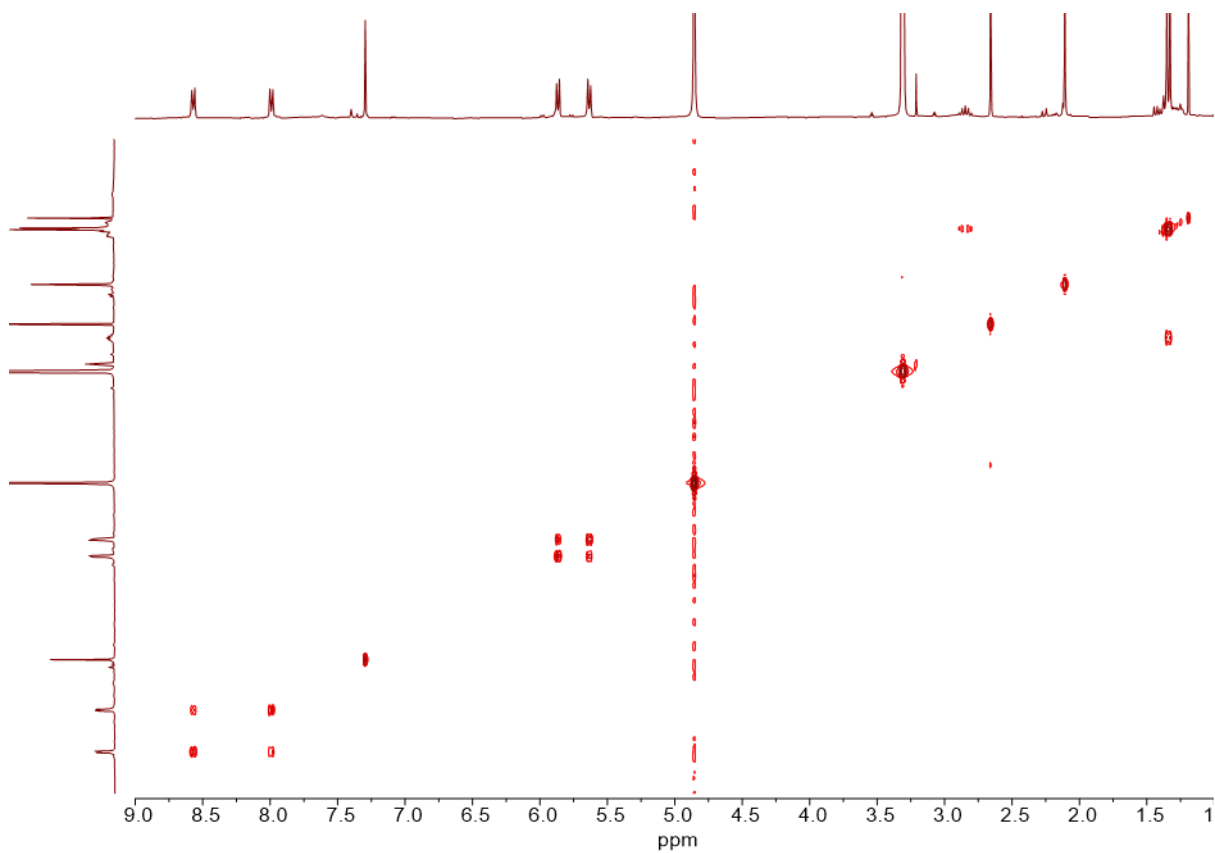
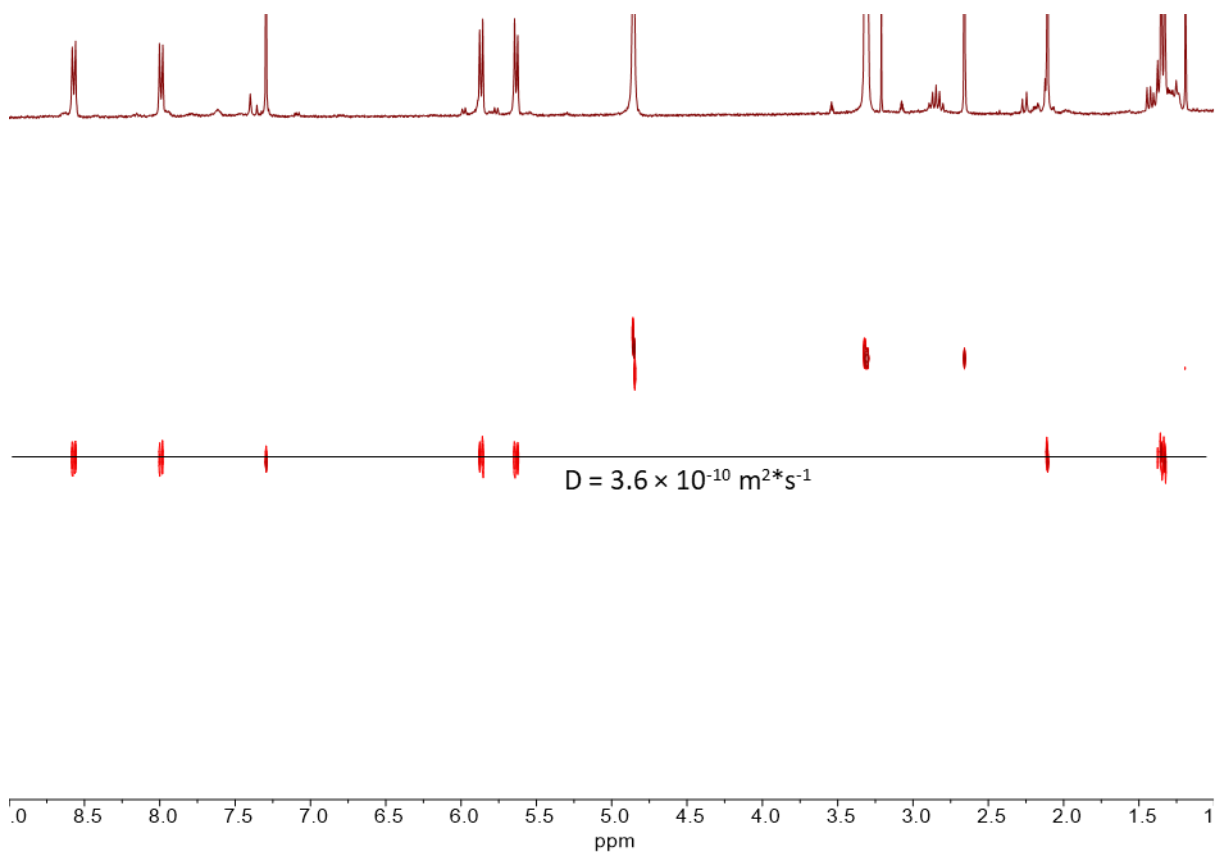


Figure S79. ^1H NMR spectrum of **Naph₂BBI₂** in MeOD- d_4 ($C = 10^{-3}$ M).

Figure S80. ^1H COSY NMR spectrum of **Naph₂BBI₂** in MeOD- d_4 ($C = 10^{-3}$ M).Figure S81. ^1H DOSY NMR spectrum of **Naph₂BBI₂** in MeOD- d_4 ($C = 10^{-3}$ M, $T = 298$ K).

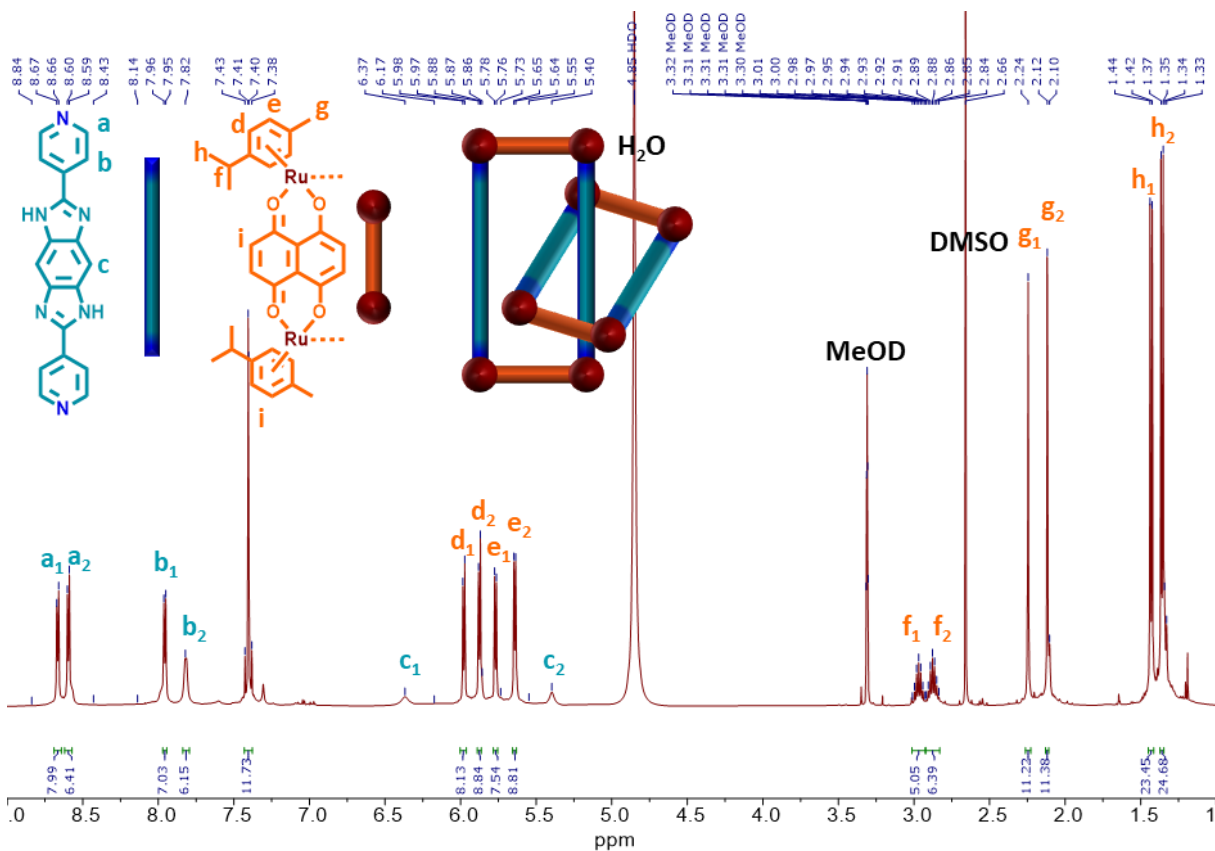


Figure S82. ^1H NMR spectrum of $(\text{Naph}_2\text{BBI}_2)_2$ in MeOD-d_4 ($C = 4 \times 10^{-2}$ M).

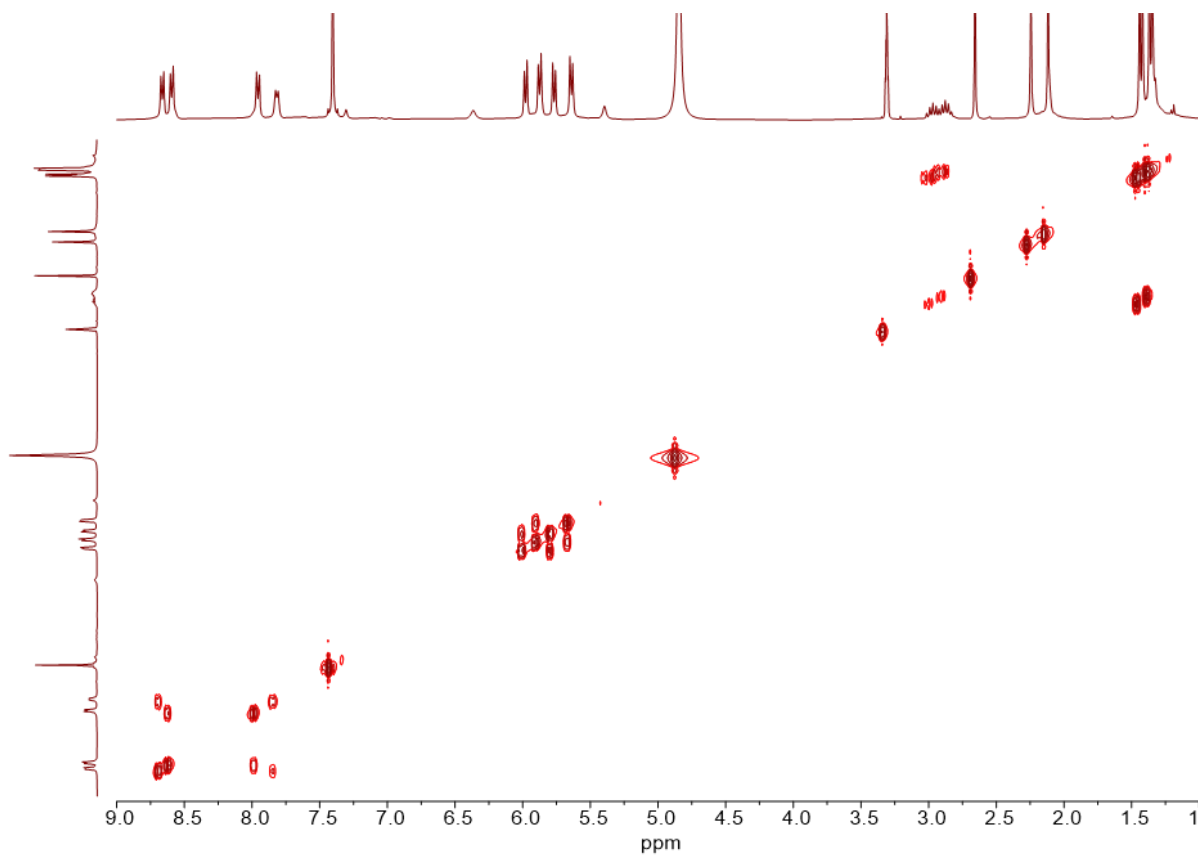


Figure S83. ^1H COSY NMR spectrum of $(\text{Naph}_2\text{BBI}_2)_2$ in MeOD-d_4 ($C = 4 \times 10^{-2}$ M).

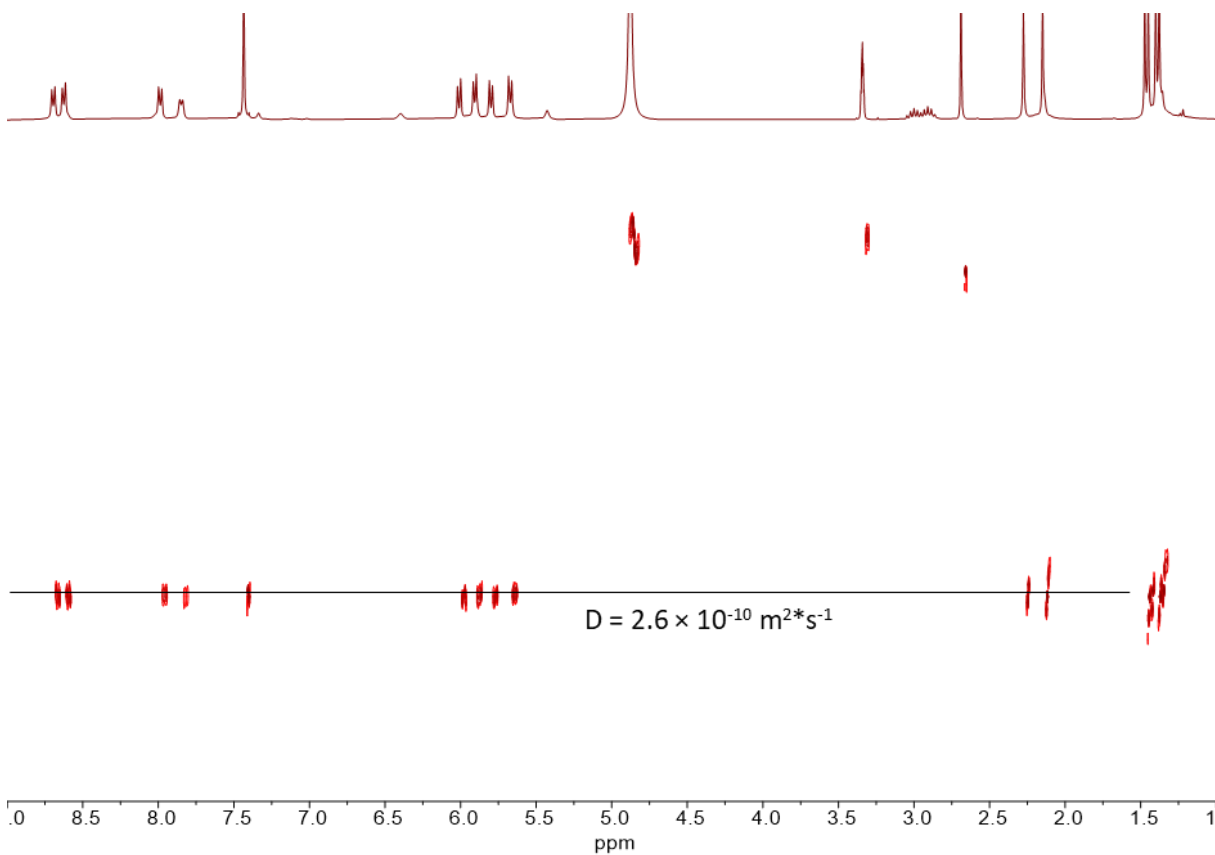


Figure S84. ^1H DOSY NMR spectrum of **(Naph₂BBI₂)₂** in MeOD- d_4 ($C = 4 \times 10^{-2}$ M).

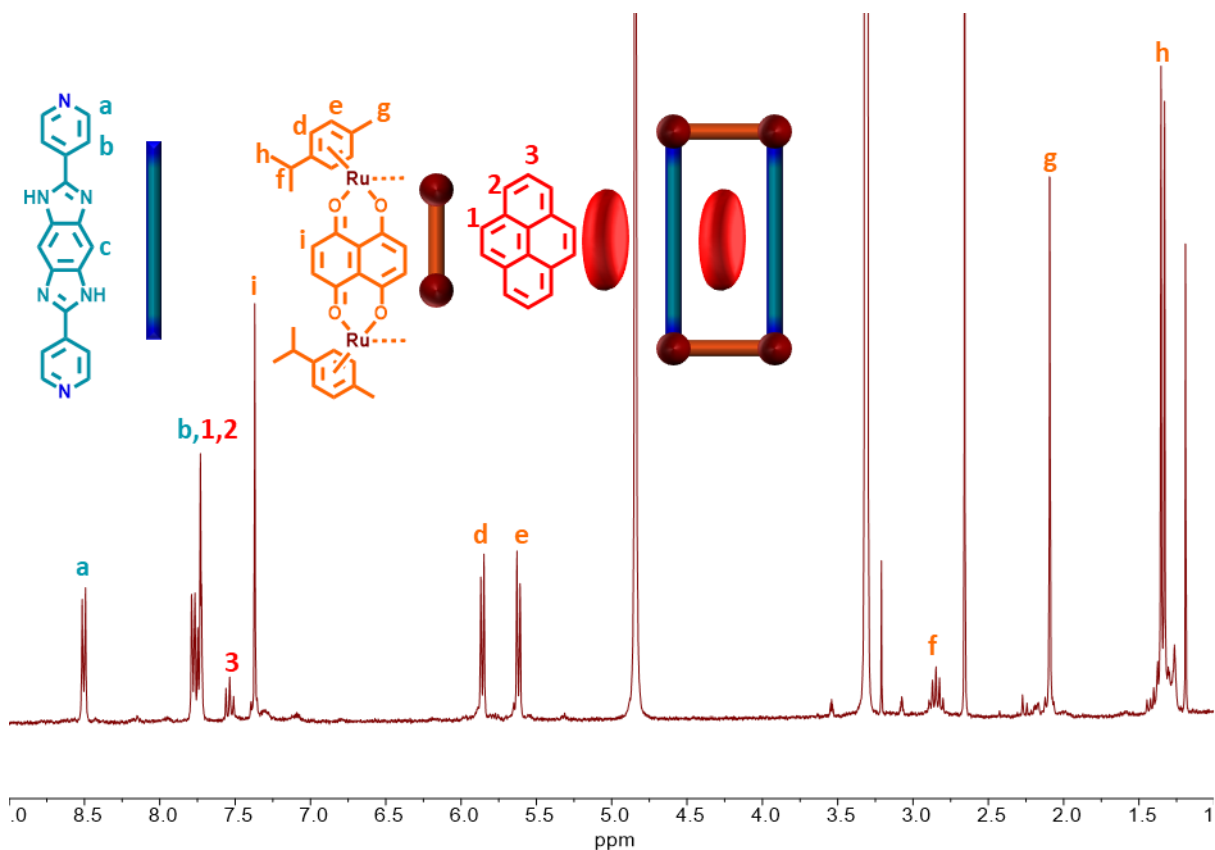


Figure S85. ^1H NMR spectrum of **Naph₂BBI₂** in MeOD- d_4 ($C = 10^{-3}$ M) in the presence of 1 equivalent of pyrene.

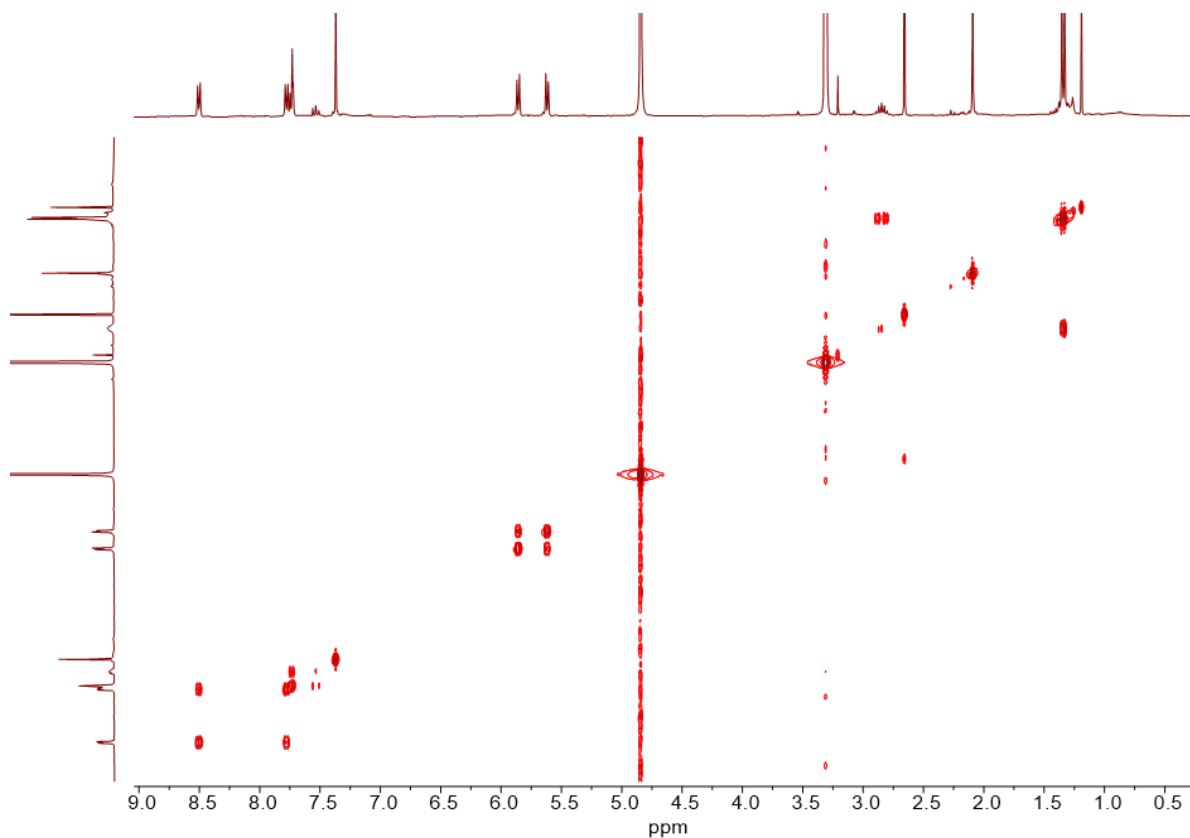


Figure S86. ¹H COSY NMR spectrum of **Naph₂BBI₂** in MeOD-d₄ (C = 10⁻³ M) in the presence of 1 equivalent of pyrene.

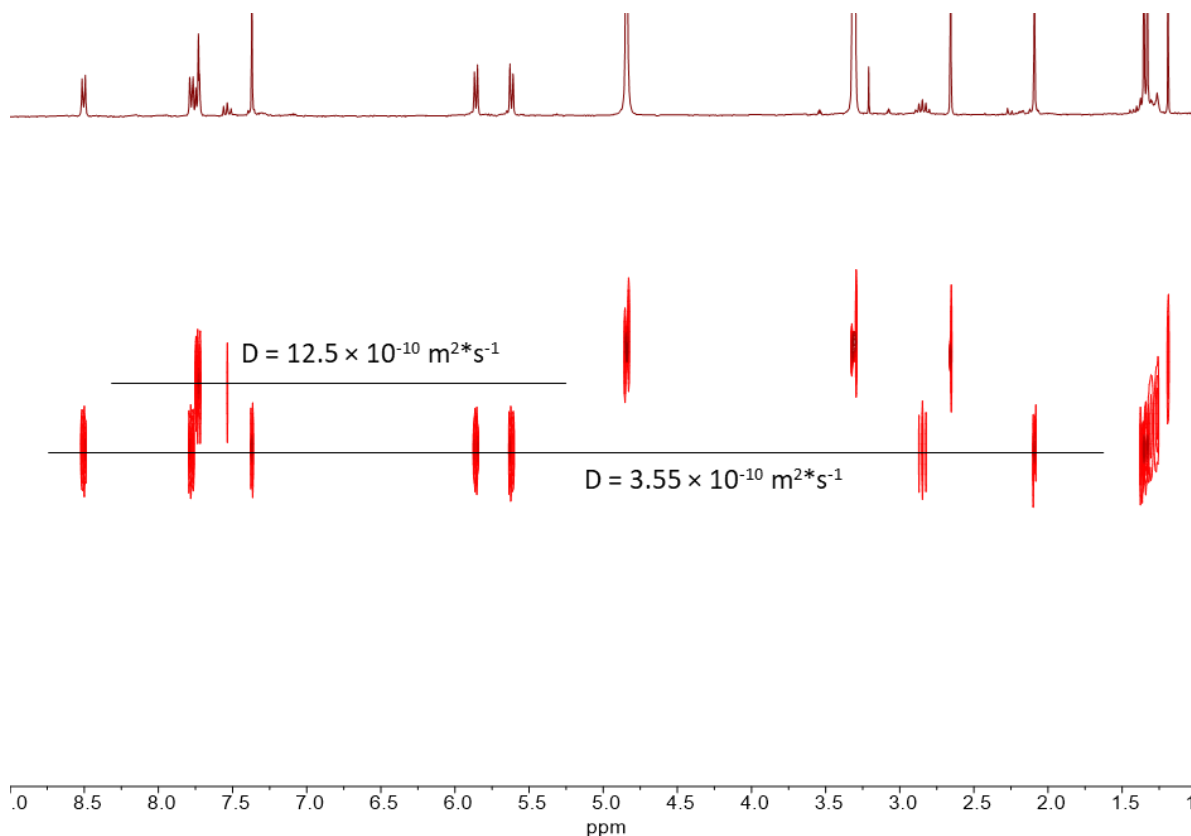


Figure S87. ¹H DOSY NMR spectrum of **Naph₂BBI₂** in MeOD-d₄ (C = 10⁻³ M) in presence of 1 equiv. of Pyrene.

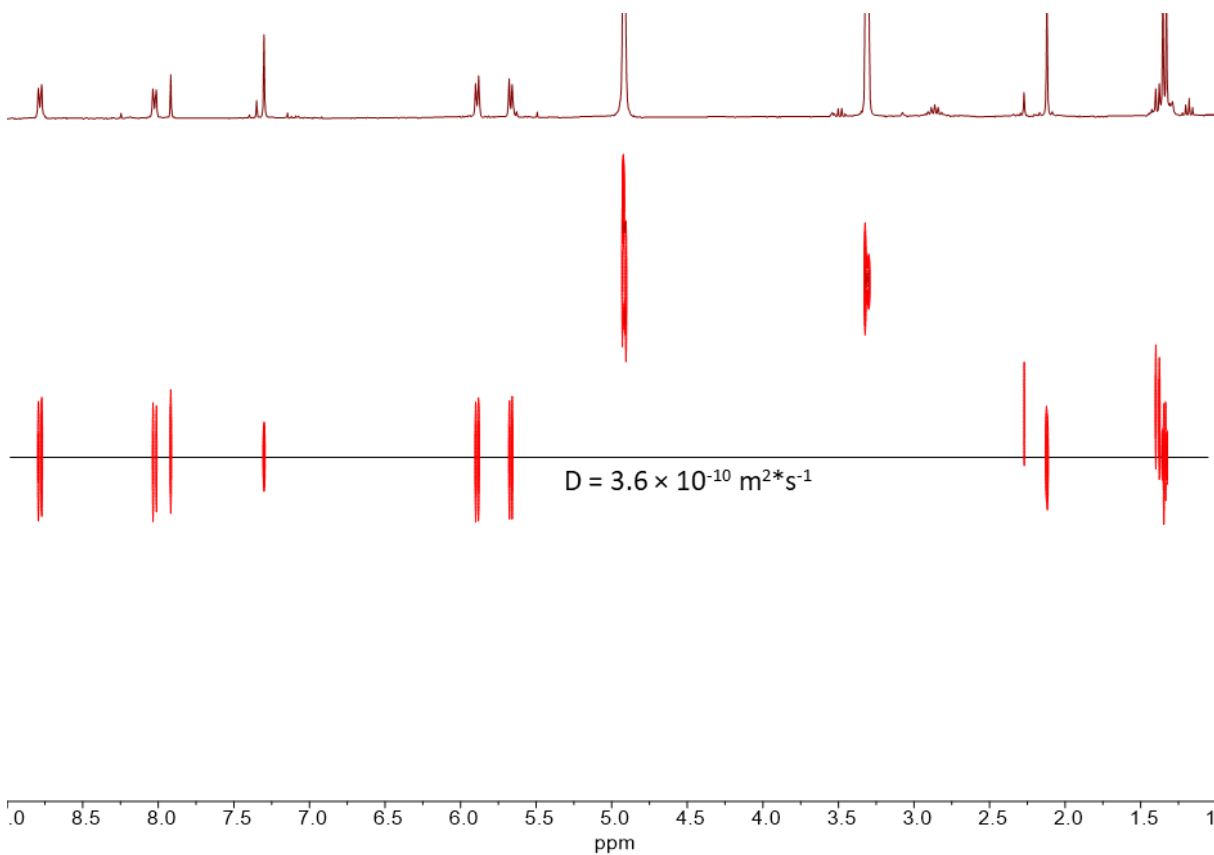
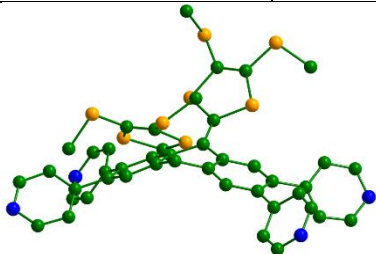
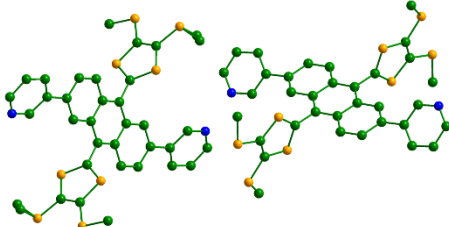


Figure S88. ^1H DOSY NMR spectrum of **Naph₂BBI₂** in MeOD- d_4 ($C = 10^{-3}$ M) in presence of 0.12 M of HOTf.

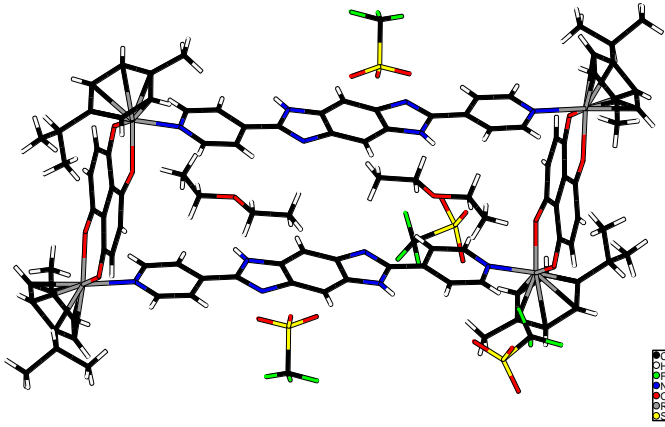
X-ray data for ligand A1Me

Empirical formula	C ₄₄ H ₃₂ N ₄ S ₈
Formula weight, <i>mr</i>	873.21
Temperature	150.0(1) K
Wavelength	1.54184 Å
Crystal system, space group	Monoclinic, P 21/c
Unit cell dimensions	a = 13.6654(2) Å α = 90° b = 14.8503(2) Å β = 92.850(1)° c = 20.1186(3) Å γ = 90°
Volume, <i>V</i>	4077.7(1) Å ³
Number of molecules, <i>z</i>	4
Calculated density, <i>ρ</i>	1.422 mg/m ³
Absorption coefficient	4.358 mm ⁻¹
F(000)	1808
Crystal size	0.371 x 0.223 x 0.201 mm
θ range for data collection	3.238° - 76.421°
Limiting indices	-16 ≤ h ≤ 17, -18 ≤ k ≤ 18, -25 ≤ l ≤ 19
Reflections collected / unique	17395 / 8328 [R(int) = 0.0236]
Completeness to θ = 25.00	98.5 %
Absorption correction	Semi-empirical from equivalents
Max. and min. transmission	1.00000 and 0.49440
Refinement method	Full-matrix least-squares on F ²
Data / restraints / parameters	8328 / 0 / 509
Goodness-of-fit on, F2	1.035
Final R indices [<i>I</i> > 2σ(<i>I</i>)]	R1 = 0.0490, wR2 = 0.1314 [7702 Fo]
R indices (all data)	R1 = 0.0538, wR2 = 0.1359
Largest diff. peak and hole	0.789 and -0.702 e.Å ⁻³
	

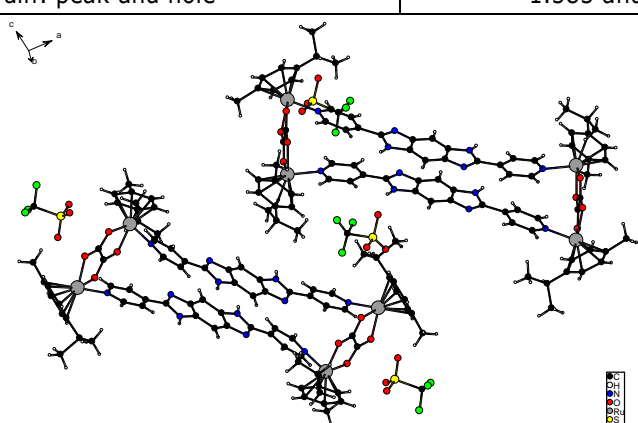
X-ray data for A4Me²⁺H⁺(BF₄⁻)₃

Empirical formula	C ₇₀ H ₆₀ B ₆ F ₂₄ N ₆ O ₄ S ₁₆ or C ₃₄ H ₂₈ N ₂ S ₈ , C ₃₄ H ₂₆ N ₂ S ₈ , 6(BF ₄), 2(CH ₃ NO ₂)
Formula weight, <i>Mr</i>	2083.06
Temperature	150.0(1) K
Wavelength	1.54184 Å
Crystal system, space group	Triclinic, P -1
Unit cell dimensions	a = 11.8930(4) Å α = 103.063(3)° b = 13.6825(5) Å β = 107.748(3)° c = 15.7713(4) Å γ = 110.358(4)°
Volume, <i>V</i>	2127.22(14) Å ³
Number of molecules, <i>z</i>	1
Calculated density, <i>ρ</i>	1.626 mg/m ³
Absorption coefficient	4.715 mm ⁻¹
F(000)	1056
Crystal size	0.301 x 0.219 x 0.065 mm
θ range for data collection	3.169° - 71.858°
Limiting indices	-14 ≤ h ≤ 13, -16 ≤ k ≤ 16, - 17 ≤ l ≤ 19
Reflections collected / unique	16795 / 8005 [R(int) = 0.0268]
Completeness to θ = 25.00	98.3 %
Absorption correction	Semi-empirical from equivalents
Max. and min. transmission	1.00000 and 0.65996
Refinement method	Full-matrix least-squares on F ²
Data / restraints / parameters	8005 / 56 / 679
Goodness-of-fit on, F2	1.035
Final R indices [<i>I</i> > 2σ(<i>I</i>)]	R1 = 0.0692, wR2 = 0.1875 [7207 Fo]
R indices (all data)	R1 = 0.0742, wR2 = 0.1931
Largest diff. peak and hole	1.017 and -1.093 e.Å ⁻³
	

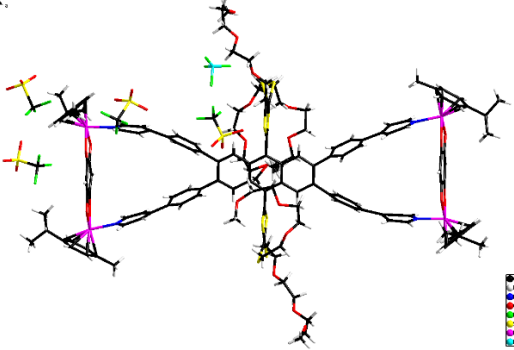
X-ray data for self-assembly RuNaph₂BBI₂

Empirical formula	C ₁₁₀ H ₁₁₆ F ₁₂ N ₁₄ O ₂₇ Ru ₄ S ₄ or 2(C ₁₈ H ₁₂ N ₆), 2(C ₃₀ H ₃₂ O ₄ Ru ₂), 4(CF ₃ O ₃ S), 2(C ₄ H ₁₀ O), 2(CH ₃ NO ₂), (H ₂ O)
Formula weight, <i>Mr</i>	2826.68
Temperature	150.0(1) K
Wavelength	1.54184 Å
Crystal system, space group	Monoclinic, P 21/c
Unit cell dimensions	a = 17.5506(14) Å α = 90° b = 18.9218(15) Å β = 110.323(9)° c = 18.9567(14) Å γ = 90°
Volume, <i>V</i>	5903.4(9) Å ³
Number of molecules, <i>z</i>	2
Calculated density, <i>ρ</i>	1.590 mg/m ³
Absorption coefficient	5.571 mm ⁻¹
F(000)	2876
Crystal size	0.078 x 0.045 x 0.031 mm
Θ range for data collection	2.958° - 72.262°
Limiting indices	-18<=h<=21, -21<=k<=23, - 22<=l<=23
Reflections collected / unique	24501 / 11272 [R(int) = 0.0766]
Completeness to θ = 25.00	98.5 %
Absorption correction	Semi-empirical from equivalents
Max. and min. transmission	1.00000 and 0.85134
Refinement method	Full-matrix least-squares on F ²
Data / restraints / parameters	11272 / 22 / 738
Goodness-of-fit on, F2	1.057
Final R indices [<i>I</i> >2σ(<i>I</i>)]	R1 = 0.0979, wR2 = 0.2437 [6117 Fo]
R indices (all data)	R1 = 0.1567, wR2 = 0.2944
Largest diff. peak and hole	1.133 and -1.411 e.Å ⁻³
	

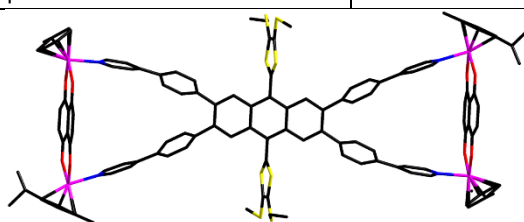
X-ray data for self-assembly RuOxa₂BBI₂

Empirical formula	C ₁₇₄ H ₁₇₆ F ₂₄ N ₂₄ O ₄₂ Ru ₈ S ₈ or 4(C ₁₈ H ₁₂ N ₆), 4(C ₂₂ H ₂₈ O ₄ Ru ₂), 8(CF ₃ SO ₃), C ₅ H ₁₂ O, CH ₄ O
Formula weight, <i>Mr</i>	4796.42
Temperature	150.0(1) K
Wavelength	1.54184 Å
Crystal system, space group	Monoclinic, P 21/c
Unit cell dimensions	a = 29.738(3) Å α = 90° b = 10.4996(10) Å β = 96.847(8)° c = 30.390(3) Å γ = 90°
Volume, <i>V</i>	9421.2(15) Å ³
Number of molecules, <i>z</i>	2
Calculated density, <i>ρ</i>	1.691 mg/m ³
Absorption coefficient	6.801 mm ⁻¹
F(000)	4840
Crystal size	0.153 x 0.070 x 0.046 mm
θ range for data collection	2.929° - 73.051°
Limiting indices	-34 ≤ h ≤ 36, -11 ≤ k ≤ 12, - 37 ≤ l ≤ 36
Reflections collected / unique	39607 / 17986 [R(int) = 0.1189]
Completeness to θ = 25.00	99.3 %
Absorption correction	Semi-empirical from equivalents
Max. and min. transmission	1.00000 and 0.79937
Refinement method	Full-matrix least-squares on F ²
Data / restraints / parameters	17986 / 85 / 1053
Goodness-of-fit on, F ²	1.019
Final R indices [<i>I</i> > 2σ(<i>I</i>)]	R1 = 0.1558, wR2 = 0.3667 [8171 Fo]
R indices (all data)	R1 = 0.2285, wR2 = 0.4179
Largest diff. peak and hole	1.585 and -1.032 e.Å ⁻³
	

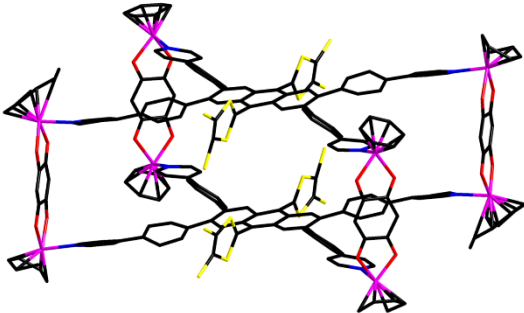
X-ray data for self-assembly RuBenzoA3Ox

Empirical formula	$C_{158}H_{180}B_2F_{20}N_4O_{34}Ru_4S_{12}$ or $C_{92}H_{96}N_4O_{12}S_8$, $2(C_{26}H_{30}O_4Ru_2)$, $4(CF_3O_3S)$, $2(BF_4)$, $2(C_5H_{12}O)$
Formula weight, Mr	3869.67
Temperature	150.0(1) K
Wavelength	1.54184 Å
Crystal system, space group	Triclinic, P -1
Unit cell dimensions	$a = 12.3916(4)$ Å $\alpha = 89.857(3)^\circ$ $b = 14.8190(5)$ Å $\beta = 84.579(3)^\circ$ $c = 23.2471(8)$ Å $\gamma = 84.102(3)^\circ$
Volume, V	$4227.2(2)$ Å ³
Number of molecules, z	1
Calculated density, ρ	1.520 mg/m ³
Absorption coefficient	5.040 mm ⁻¹
F(000)	1986
Crystal size	0.242 x 0.077 x 0.028 mm
Θ range for data collection	2.998° - 76.341°
Limiting indices	-15 ≤ h ≤ 15, -18 ≤ k ≤ 18, - 28 ≤ l ≤ 29
Reflections collected / unique	36842 / 22403 [R(int) = 0.0393]
Completeness to $\theta = 25.00$	98.5 %
Absorption correction	Gaussian
Max. and min. transmission	0.986 and 0.354
Refinement method	Full-matrix least-squares on F^2
Data / restraints / parameters	22403 / 440 / 2043
Goodness-of-fit on, F_2	1.025
Final R indices [$I > 2\sigma(I)$]	R1 = 0.0654, wR2 = 0.1790 [16981 F_o]
R indices (all data)	R1 = 0.0829, wR2 = 0.1995
Largest diff. peak and hole	1.431 and -1.180 e.Å ⁻³
	

X-ray data for self-assembly RuNaphA30x

Empirical formula	$C_{156}H_{160}F_{12}N_4O_{32}Ru_4S_{12}$
Formula weight, <i>mr</i>	3619.87
Temperature	293(2) K
Wavelength	1.54184 Å
Crystal system, space group	Triclinic, P -1
Unit cell dimensions	a = 15.0510(3) Å α = 108.256(3)° b = 17.9606(5) Å β = 97.104(3)° c = 20.7657(8) Å γ = 114.561(2)°
Volume, <i>V</i>	4634.4(3) Å ³
Number of molecules, <i>z</i>	1
Calculated density, <i>ρ</i>	1.297 mg/m ³
Absorption coefficient	4.492 mm ⁻¹
F(000)	1856
Θ range for data collection	2.939° - 76.354°
Limiting indices	-18<= <i>h</i> <=14, -21<= <i>k</i> <=22, -26<= <i>l</i> <=25
Reflections collected / unique	44218 / 19029 [R(int) = 0.0357]
Completeness to θ = 67.684	99.9 %
Refinement method	Full-matrix least-squares on F ²
Data / restraints / parameters	19029 / 0 / 993
Goodness-of-fit on, F2	1.224
Final R indices [<i>I</i> >2σ(<i>I</i>)]	R1 = 0.1043, wR2 = 0.2970
R indices (all data)	R1 = 0.1270, wR2 = 0.3369
Largest diff. peak and hole	1.097 and -1.000 e.Å ⁻³
	

X-ray data for self-assembly (RuBenzoA3)Ox

Empirical formula	C ₂₉₆ H ₃₁₂ F ₂₄ N ₈ O ₆₄ Ru ₈ S ₂₄
Formula weight, <i>mr</i>	7039.52
Temperature	293(2) K
Wavelength	0.67093 Å
Crystal system, space group	Monoclinic, P 21/c
Unit cell dimensions	a = 22.2837(7) Å α = 90° b = 16.9440(4) Å β = 91.897(3)° c = 48.5473(13) Å γ = 90°
Volume, <i>V</i>	18320.2(9) Å ³
Number of molecules, <i>z</i>	2
Calculated density, <i>ρ</i>	1.276 mg/m ³
Absorption coefficient	0.534 mm ⁻¹
F(000)	7216
Θ range for data collection	1.472° - 24.678°
Limiting indices	-27 <= h <= 26, -20 <= k <= 20, -59 <= l <= 59
Reflections collected / unique	288332 / 34848 [R(int) = 0.2013]
Completeness to θ = 25.00	99.7 %
Refinement method	Full-matrix least-squares on F ²
Data / restraints / parameters	34848 / 0 / 1198
Goodness-of-fit on, F ²	1.728
Final R indices [<i>I</i> > 2σ(<i>I</i>)]	R1 = 0.2522, wR2 = 0.5624
R indices (all data)	R1 = 0.3823, wR2 = 0.6077
Largest diff. peak and hole	2.919 and -1.048 e.Å ⁻³
	

References

1. Lehn J.-M., Perspectives in Supramolecular Chemistry—From Molecular Recognition towards Molecular Information Processing and Self-Organization. *Angewandte Chemie International Edition in English* **1990**, *29* (11), 1304-1319.
2. Watson J. D., Crick F. H. C., Molecular Structure of Nucleic Acids: A Structure for Deoxyribose Nucleic Acid. *Nature* **1953**, *171* (4356), 737-738.
3. Mateos-Timoneda M. A., Kerckhoffs J. M. C. A., Crego-Calama M., Reinhoudt D. N., Ditopic Complexation and Release of Neutral Guest Molecules by a Hydrogen-Bonded "Endo-Exo" Receptor. *Angewandte Chemie International Edition* **2005**, *44* (21), 3248-3253.
4. Huerta E., Serapian S. A., Santos E., Cequier E., Bo C., de Mendoza J., Molecular Basis for the Recognition of Higher Fullerenes into Ureidopyrimidinone–Cyclotrimeratrylene Self-Assembled Capsules. *Chemistry – A European Journal* **2016**, *22* (38), 13496-13505.
5. Appavoo D., Carnevale D., Deschenaux R., Therrien B., Combining coordination and hydrogen-bonds to form arene ruthenium metalla-assemblies. *Journal of Organometallic Chemistry* **2016**, *824*, 80-87.
6. Hasell T., Cooper A. I., Porous organic cages: soluble, modular and molecular pores. *Nature Reviews Materials* **2016**, *1*, 16053.
7. Fujita M., Yazaki J., Ogura K., Preparation of a macrocyclic polynuclear complex, [(en)Pd(4,4'-bpy)]₄(NO₃)₈ (en = ethylenediamine, bpy = bipyridine), which recognizes an organic molecule in aqueous media. *Journal of the American Chemical Society* **1990**, *112* (14), 5645-5647.
8. Saha S., Regeni I., Clever G. H., Structure relationships between bis-monodentate ligands and coordination driven self-assemblies. *Coordination Chemistry Reviews* **2018**, *374*, 1-14.
9. Kim T. Y., Vasdev R. A. S., Preston D., Crowley J. D., Strategies for Reversible Guest Uptake and Release from Metallosupramolecular Architectures. *Chemistry – A European Journal* **2018**, *24* (56), 14878-14890.
10. Zhang Y.-Y., Gao W.-X., Lin L., Jin G.-X., Recent advances in the construction and applications of heterometallic macrocycles and cages. *Coordination Chemistry Reviews* **2017**, *344*, 323-344.
11. Yoshizawa M., Yamashina M., Coordination-driven Nanostructures with Polyaromatic Shells. *Chemistry Letters* **2017**, *46* (2), 163-171.
12. Pan M., Wu K., Zhang J.-H., Su C.-Y., Chiral metal–organic cages/containers (MOCs): From structural and stereochemical design to applications. *Coordination Chemistry Reviews* **2017**.
13. Huang S.-L., Hor T. S. A., Jin G.-X., Metallacyclic assembly of interlocked superstructures. *Coordination Chemistry Reviews* **2017**, *333*, 1-26.
14. Bloch W. M., Clever G. H., Integrative self-sorting of coordination cages based on 'naked' metal ions. *Chemical Communications* **2017**, *53* (61), 8506-8516.
15. Chakrabarty R., Mukherjee P. S., Stang P. J., Supramolecular Coordination: Self-Assembly of Finite Two- and Three-Dimensional Ensembles. *Chemical Reviews* **2011**, *111* (11), 6810-6918.
16. Stang P. J., Cao D. H., Transition Metal Based Cationic Molecular Boxes. Self-Assembly of Macrocyclic Platinum(II) and Palladium(II) Tetranuclear Complexes. *Journal of the American Chemical Society* **1994**, *116* (11), 4981-4982.
17. L. Caulder D., N. Raymond K., The rational design of high symmetry coordination clusters. *Journal of the Chemical Society, Dalton Transactions* **1999**, (8), 1185-1200.
18. Caulder D. L., Brückner C., Powers R. E., König S., Parac T. N., Leary J. A., Raymond K. N., Design, Formation and Properties of Tetrahedral M₄L₄ and M₄L₆ Supramolecular Clusters. *Journal of the American Chemical Society* **2001**, *123* (37), 8923-8938.
19. Fujita M., Metal-directed self-assembly of two- and three-dimensional synthetic receptors. *Chemical Society Reviews* **1998**, *27* (6), 417-425.
20. Fujita M., Tominaga M., Hori A., Therrien B., Coordination Assemblies from a Pd(II)-Cornered Square Complex. *Accounts of Chemical Research* **2005**, *38* (4), 369-378.
21. Fujita M., Umemoto K., Yoshizawa M., Fujita N., Kusukawa T., Biradha K., Molecular paneling via coordination. *Chemical Communications* **2001**, (6), 509-518.
22. Holliday B. J., Mirkin C. A., Strategies for the Construction of Supramolecular Compounds through Coordination Chemistry. *Angewandte Chemie International Edition* **2001**, *40* (11), 2022-2043.
23. Gianneschi N. C., Masar M. S., Mirkin C. A., Development of a Coordination Chemistry-Based Approach for Functional Supramolecular Structures. *Accounts of Chemical Research* **2005**, *38* (11), 825-837.
24. Oliveri C. G., Ulmann P. A., Wiester M. J., Mirkin C. A., Heteroligated Supramolecular Coordination Complexes Formed via the Halide-Induced Ligand Rearrangement Reaction. *Accounts of Chemical Research* **2008**, *41* (12), 1618-1629.

25. Kyba E. P., Helgeson R. C., Madan K., Gokel G. W., Tarnowski T. L., Moore S. S., Cram D. J., Host-guest complexation. 1. Concept and illustration. *Journal of the American Chemical Society* **1977**, *99* (8), 2564-2571.
26. Thanasekaran P., Lee C.-H., Lu K.-L., Neutral discrete metal-organic cyclic architectures: Opportunities for structural features and properties in confined spaces. *Coordination Chemistry Reviews* **2014**, *280*, 96-175.
27. Mann S., Huttner G., Zsolnai L., Heinze K., Supramolecular Host-Guest Compounds with Tripod-Metal Templates as Building Blocks at the Corners. *Angewandte Chemie International Edition in English* **1996**, *35* (23-24), 2808-2809.
28. Tidmarsh I. S., Taylor B. F., Hardie M. J., Russo L., Clegg W., Ward M. D., Further investigations into tetrahedral M4L6 cage complexes containing guest anions: new structures and NMR spectroscopic studies. *New Journal of Chemistry* **2009**, *33* (2), 366-375.
29. Kuehl C. J., Kryschenko Y. K., Radhakrishnan U., Seidel S. R., Huang S. D., Stang P. J., Self-assembly of nanoscopic coordination cages of D_{3h} symmetry. *Proceedings of the National Academy of Sciences* **2002**, *99* (8), 4932-4936.
30. Han M., Engelhard D. M., Clever G. H., Self-assembled coordination cages based on banana-shaped ligands. *Chemical Society Reviews* **2014**, *43* (6), 1848-1860.
31. McMorran D. A., Steel P. J., The First Coordinatively Saturated, Quadruply Stranded Helicate and Its Encapsulation of a Hexafluorophosphate Anion. *Angewandte Chemie International Edition* **1998**, *37* (23), 3295-3297.
32. Amouri H., Mimassi L., Rager M. N., Mann B. E., Guyard-Duhayon C., Raehm L., Host-Guest Interactions: Design Strategy and Structure of an Unusual Cobalt Cage That Encapsulates a Tetrafluoroborate Anion. *Angewandte Chemie International Edition* **2005**, *44* (29), 4543-4546.
33. Howlader P., Das P., Zangrando E., Mukherjee P. S., Urea-Functionalized Self-Assembled Molecular Prism for Heterogeneous Catalysis in Water. *Journal of the American Chemical Society* **2016**, *138* (5), 1668-1676.
34. Vilar R., Mingos D. M. P., White A. J. P., Williams D. J., Anion Control in the Self-Assembly of a Cage Coordination Complex. *Angewandte Chemie International Edition* **1998**, *37* (9), 1258-1261.
35. Caulder D. L., Powers R. E., Parac T. N., Raymond K. N., The Self-Assembly of a Predesigned Tetrahedral M4L6 Supramolecular Cluster. *Angewandte Chemie International Edition* **1998**, *37* (13-14), 1840-1843.
36. Kusukawa T., Fujita M., Encapsulation of Large, Neutral Molecules in a Self-Assembled Nanocage Incorporating Six Palladium(II) Ions. *Angewandte Chemie International Edition* **1998**, *37* (22), 3142-3144.
37. Kusukawa T., Fujita M., Self-Assembled M6L4-Type Coordination Nanocage with 2,2'-Bipyridine Ancillary Ligands. Facile Crystallization and X-ray Analysis of Shape-Selective Enclathration of Neutral Guests in the Cage. *Journal of the American Chemical Society* **2002**, *124* (45), 13576-13582.
38. Kishi N., Li Z., Sei Y., Akita M., Yoza K., Siegel J. S., Yoshizawa M., Wide-Ranging Host Capability of a PdII-Linked M2L4Molecular Capsule with an Anthracene Shell. *Chemistry - A European Journal* **2013**, *19* (20), 6313-6320.
39. Kroto H. W., C60: Buckminsterfullerene, The Celestial Sphere that Fell to Earth. *Angewandte Chemie International Edition in English* **1992**, *31* (2), 111-129.
40. Kishi N., Li Z., Yoza K., Akita M., Yoshizawa M., An M2L4 Molecular Capsule with an Anthracene Shell: Encapsulation of Large Guests up to 1 nm. *Journal of the American Chemical Society* **2011**, *133* (30), 11438-11441.
41. Yamashina M., Yuki T., Sei Y., Akita M., Yoshizawa M., Anisotropic Expansion of an M2L4Coordination Capsule: Host Capability and Frame Rearrangement. *Chemistry - A European Journal* **2015**, *21* (11), 4200-4204.
42. Fujita M., Ibukuro F., Hagihara H., Ogura K., Quantitative self-assembly of a [2]catenane from two preformed molecular rings. *Nature* **1994**, *367* (6465), 720-723.
43. Siddiqui M., Saha R., Mukherjee P. S., Ruthenium(II) Metalla[2]catenanes and Macrocycles via Donor-Dependent Self-Assembly. *Inorg. Chem.* **2019**, *58* (7), 4491-4499.
44. Singh J., Kim D. H., Kim E.-H., Singh N., Kim H., Hadiputra R., Jung J., Chi K.-W., Selective and quantitative synthesis of a linear [3]catenane by two component coordination-driven self-assembly. *Chemical Communications* **2019**, *55* (48), 6866-6869.

45. Jo J.-H., Singh N., Kim D., Cho S. M., Mishra A., Kim H., Kang S. C., Chi K.-W., Coordination-Driven Self-Assembly Using Ditopic Pyridyl–Pyrazolyl Donor and p-Cymene Ru(II) Acceptors: [2]Catenane Synthesis and Anticancer Activities. *Inorganic Chemistry* **2017**, *56* (14), 8430-8438.
46. Lee H., Elumalai P., Singh N., Kim H., Lee S. U., Chi K.-W., Selective Synthesis of Ruthenium(II) Metalla[2]Catenane via Solvent and Guest-Dependent Self-Assembly. *Journal of the American Chemical Society* **2015**, *137* (14), 4674-4677.
47. Mishra A., Dubey A., Min J. W., Kim H., Stang P. J., Chi K.-W., Molecular self-assembly of arene-Ru based interlocked catenane metalla-cages. *Chem. Commun.* **2014**, *50* (56), 7542-7544.
48. Lu J., Turner D. R., Harding L. P., Byrne L. T., Baker M. V., Batten S. R., Octapi Interactions: Self-Assembly of a Pd-Based [2]Catenane Driven by Eightfold π Interactions. *Journal of the American Chemical Society* **2009**, *131* (30), 10372-10373.
49. Hovorka R., Meyer-Eppler G., Piehler T., Hytteballe S., Engeser M., Topić F., Rissanen K., Lützen A., Unexpected Self-Assembly of a Homochiral Metallosupramolecular M4L4 Catenane. *Chemistry – A European Journal* **2014**, *20* (41), 13253-13258.
50. Xue H., Jiang F., Chen Q., Yuan D., Pang J., Lv G., Wan X., Liang L., Hong M., Conformation driven in situ interlock: from discrete metallocycles to infinite polycatenanes. *Chemical Communications* **2015**, *51* (71), 13706-13709.
51. Chen Q., Jiang F., Yuan D., Chen L., Lyu G., Hong M., Anion-driven self-assembly: from discrete cages to infinite polycatenanes step by step. *Chem. Commun.* **2013**, *49* (7), 719-721.
52. Singh N., Kim D., Kim D. H., Kim E.-H., Kim H., Lah M. S., Chi K.-W., Selective synthesis of iridium(iii)-derived molecular Borromean rings, [2]catenane and ring-in-ring macrocycles via coordination-driven self-assembly. *Dalton Trans.* **2017**, *46* (2), 571-577.
53. Vajpayee V., Song Y. H., Cook T. R., Kim H., Lee Y., Stang P. J., Chi K.-W., A Unique Non-catenane Interlocked Self-Assembled Supramolecular Architecture and Its Photophysical Properties. *Journal of the American Chemical Society* **2011**, *133* (49), 19646-19649.
54. Cui Z., Lu Y., Gao X., Feng H.-J., Jin G.-X., Stereoselective Synthesis of a Topologically Chiral Solomon Link. *J. Am. Chem. Soc.* **2020**, *142* (32), 13667-13671.
55. Zhang H.-N., Gao W.-X., Lin Y.-J., Jin G.-X., Reversible Structural Transformation between a Molecular Solomon Link and an Unusual Unsymmetrical Trefoil Knot. *J. Am. Chem. Soc.* **2019**, *141* (40), 16057-16063.
56. Song Y. H., Singh N., Jung J., Kim H., Kim E.-H., Cheong H.-K., Kim Y., Chi K.-W., Template-Free Synthesis of a Molecular Solomon Link by Two-Component Self-Assembly. *Angewandte Chemie International Edition* **2016**, *55* (6), 2007-2011.
57. Beves J. E., Danon J. J., Leigh D. A., Lemonnier J.-F., Vitorica-Yrezabal I. J., A Solomon Link through an Interwoven Molecular Grid. *Angew. Chem. Int. Ed.* **2015**, *54* (26), 7555-7559.
58. Schouwey C., Holstein J. J., Scopelliti R., Zhurov K. O., Nagornov K. O., Tsybin Y. O., Smart O. S., Bricogne G., Severin K., Self-assembly of a giant molecular Solomon link from 30 subcomponents. *Angew. Chem. Int. Ed.* **2014**, *53* (42), 11261-11265.
59. Pentecost C. D., Chichak K. S., Peters A. J., Cave G. W. V., Cantrill S. J., Stoddart J. F., A Molecular Solomon Link. *Angew. Chem. Int. Ed.* **2007**, *46* (1-2), 218-222.
60. Dang L.-L., Gao X., Lin Y.-J., Jin G.-X., s-Block metal ions induce structural transformations between figure-eight and double trefoil knots. *Chem. Sci.* **2020**, *11* (5), 1226-1232.
61. Fielden S. D. P., Leigh D. A., Woltering S. L., Molecular Knots. *Angew. Chem. Int. Ed.* **2017**, *56* (37), 11166-11194.
62. Dang L.-L., Sun Z.-B., Shan W.-L., Lin Y.-J., Li Z.-H., Jin G.-X., Coordination-driven self-assembly of a molecular figure-eight knot and other topologically complex architectures - Nature Communications. *Nat. Commun.* **2019**, *10* (2057), 1-9.
63. Guo B.-B., Lin Y.-J., Jin G.-X., Design of and Stability Studies on Trefoil Knots Featuring RhCp* Building Blocks. *Chem. Eur. J.* **2019**, *25* (41), 9721-9727.
64. Feng H.-J., Gao W.-X., Lin Y.-J., Jin G.-X., Selective Synthesis of Discrete Mono-, Interlocked-, and Borromean Ring Ensembles Based on a n -Electron-Deficient Ligand. *Chem. Asian J.* **2019**, *14* (15), 2712-2718.
65. Lu Y., Zhang H.-N., Jin G.-X., Molecular Borromean Rings Based on Half-Sandwich Organometallic Rectangles. *Accounts of Chemical Research* **2018**, *51* (9), 2148-2158.
66. Lu Y., Lin Y., Li Z., Jin G., Highly Stable Molecular Borromean Rings. *Chinese Journal of Chemistry* **2018**, *36* (2), 106-111.

67. Zhang H.-N., Gao W.-X., Deng Y.-X., Lin Y.-J., Jin G.-X., Stacking-interaction-induced host-guest chemistry and Borromean rings based on a polypyridyl ligand. *Chemical Communications* **2018**, 54 (13), 1559-1562.
68. Lu Y., Deng Y.-X., Lin Y.-J., Han Y.-F., Weng L.-H., Li Z.-H., Jin G.-X., Molecular Borromean Rings Based on Dihalogenated Ligands. *Chem* **2017**, 3 (1), 110-121.
69. Kim T., Singh N., Oh J., Kim E.-H., Jung J., Kim H., Chi K.-W., Selective Synthesis of Molecular Borromean Rings: Engineering of Supramolecular Topology via Coordination-Driven Self-Assembly. *Journal of the American Chemical Society* **2016**, 138 (27), 8368-8371.
70. Huang S.-L., Lin Y.-J., Hor T. S. A., Jin G.-X., Cp*Rh-Based Heterometallic Metallarectangles: Size-Dependent Borromean Link Structures and Catalytic Acyl Transfer. *Journal of the American Chemical Society* **2013**, 135 (22), 8125-8128.
71. Alvarino C., Platas-Iglesias C., Blanco V., García M. D., Peinador C., Quintela J. M., Stimuli-responsive metal-directed self-assembly of a ring-in-ring complex. *Dalton Transactions* **2016**, 45 (29), 11611-11615.
72. Avram L., Cohen Y., Diffusion NMR of molecular cages and capsules. *Chemical Society Reviews* **2015**, 44 (2), 586-602.
73. Chichak K. S., Cantrill S. J., Pease A. R., Chiu S.-H., Cave G. W. V., Atwood J. L., Stoddart J. F., Molecular Borromean Rings. *Science* **2004**, 304 (5675), 1308-1312.
74. Goeb S., Sallé M., Electron-rich Coordination Receptors Based on Tetrathiafulvalene Derivatives: Controlling the Host-Guest Binding. *Accounts of Chemical Research* **2021**, 54 (4), 1043-1055.
75. Cullen W., Turega S., Hunter C. A., Ward M. D., pH-dependent binding of guests in the cavity of a polyhedral coordination cage: reversible uptake and release of drug molecules. *Chemical Science* **2015**, 6 (1), 625-631.
76. Clever G. H., Tashiro S., Shionoya M., Light-Triggered Crystallization of a Molecular Host-Guest Complex. *Journal of the American Chemical Society* **2010**, 132 (29), 9973-9975.
77. Sun W.-Y., Kusukawa T., Fujita M., Electrochemically Driven Clathration/Declathration of Ferrocene and Its Derivatives by a Nanometer-Sized Coordination Cage. *Journal of the American Chemical Society* **2002**, 124 (39), 11570-11571.
78. Zheng Y.-R., Suntharalingam K., Johnstone T. C., Lippard S. J., Encapsulation of Pt(IV) prodrugs within a Pt(II) cage for drug delivery. *Chemical Science* **2015**, 6 (2), 1189-1193.
79. Mal P., Breiner B., Rissanen K., Nitschke J. R., White Phosphorus Is Air-Stable Within a Self-Assembled Tetrahedral Capsule. *Science* **2009**, 324 (5935), 1697-1699.
80. Lewis J. E. M., Gavey E. L., Cameron S. A., Crowley J. D., Stimuli-responsive Pd2L4 metallocage: towards targeted cisplatin drug delivery. *Chemical Science* **2012**, 3 (3), 778-784.
81. Preston D., Fox-Charles A., Lo W. K. C., Crowley J. D., Chloride triggered reversible switching from a metallocage [Pd2L4]4+ cage to a [Pd2L2Cl4] metallo-macrocycle with release of endo- and exo-hedrally bound guests. *Chemical Communications* **2015**, 51 (43), 9042-9045.
82. Chan A. K.-W., Lam W. H., Tanaka Y., Wong K. M.-C., Yam V. W.-W., Multiaddressable molecular rectangles with reversible host-guest interactions: Modulation of pH-controlled guest release and capture. *Proceedings of the National Academy of Sciences* **2015**, 112 (3), 690-695.
83. Han M., Michel R., He B., Chen Y.-S., Stalke D., John M., Clever G. H., Light-Triggered Guest Uptake and Release by a Photochromic Coordination Cage. *Angewandte Chemie International Edition* **2013**, 52 (4), 1319-1323.
84. Schoepff L., Kocher L., Durot S., Heitz V., Chemically Induced Breathing of Flexible Porphyrinic Covalent Cages. *The Journal of Organic Chemistry* **2017**, 82 (11), 5845-5851.
85. Nilsson J. R., O'Sullivan M. C., Li S., Anderson H. L., Andréasson J., A photoswitchable supramolecular complex with release-and-report capabilities. *Chemical Communications* **2015**, 51 (5), 847-850.
86. Guo J., Xu Y.-W., Li K., Xiao L.-M., Chen S., Wu K., Chen X.-D., Fan Y.-Z., Liu J.-M., Su C.-Y., Regio- and Enantioselective Photodimerization within the Confined Space of a Homochiral Ruthenium/Palladium Heterometallic Coordination Cage. *Angewandte Chemie International Edition* **2017**, 56 (14), 3852-3856.
87. Croué V., Goeb S., Sallé M., Metal-driven self-assembly: the case of redox-active discrete architectures. *Chem. Commun.* **2015**, 51 (34), 7275-7289.
88. Furutani Y., Kandori H., Kawano M., Nakabayashi K., Yoshizawa M., Fujita M., In Situ Spectroscopic, Electrochemical, and Theoretical Studies of the Photoinduced Host-Guest Electron Transfer that Precedes Unusual Host-Mediated Alkane Photooxidation. *Journal of the American Chemical Society* **2009**, 131 (13), 4764-4768.

89. Mahata K., Frischmann P. D., Würthner F., Giant Electroactive M4L6 Tetrahedral Host Self-Assembled with Fe(II) Vertices and Perylene Bisimide Dye Edges. *Journal of the American Chemical Society* **2013**, *135* (41), 15656-15661.
90. Frank M., Hey J., Balcioglu I., Chen Y.-S., Stalke D., Suenobu T., Fukuzumi S., Frauendorf H., Clever G. H., Assembly and Stepwise Oxidation of Interpenetrated Coordination Cages Based on Phenothiazine. *Angewandte Chemie International Edition* **2013**, *52* (38), 10102-10106.
91. Jana A., Bähring S., Ishida M., Goeb S., Canevet D., Sallé M., Jeppesen J. O., Sessler J. L., Functionalised tetrathiafulvalene- (TTF-) macrocycles: recent trends in applied supramolecular chemistry. *Chemical Society Reviews* **2018**, *47* (15), 5614-5645.
92. Canevet D., Salle M., Zhang G., Zhang D., Zhu D., Tetrathiafulvalene (TTF) derivatives: key building-blocks for switchable processes. *Chemical Communications* **2009**, (17), 2245-2269.
93. Martín N., Tetrathiafulvalene: the advent of organic metals. *Chemical Communications* **2013**, *49* (63), 7025-7027.
94. Balandier J.-Y., Chas M., Goeb S., Dron P. I., Rondeau D., Belyasmine A., Gallego N., Salle M., A self-assembled bis(pyrrolo)tetrathiafulvalene-based redox active square. *New Journal of Chemistry* **2011**, *35* (1), 165-168.
95. Goeb S., Bivaud S., Dron P. I., Balandier J.-Y., Chas M., Sallé M., A BPTTF-based self-assembled electron-donating triangle capable of C60 binding. *Chemical Communications* **2012**, *48* (25), 3106.
96. Bivaud S., Goeb S., Balandier J.-Y., Chas M., Allain M., Sallé M., Self-Assembled Cages from the Electroactive Bis(pyrrolo)tetrathiafulvalene (BPTTF) Building Block. *European Journal of Inorganic Chemistry* **2014**, *2014* (14), 2440-2448.
97. Bivaud S., Balandier J.-Y., Chas M., Allain M., Goeb S., Sallé M., A Metal-Directed Self-Assembled Electroactive Cage with Bis(pyrrolo)tetrathiafulvalene (BPTTF) Side Walls. *Journal of the American Chemical Society* **2012**, *134* (29), 11968-11970.
98. Goeb S., Bivaud S., Croué V., Vajpayee V., Allain M., Sallé M., A Self-Assembled Electro-Active M8L4 Cage Based on Tetrathiafulvalene Ligands. *Materials* **2014**, *7* (1), 611-622.
99. Vajpayee V., Bivaud S., Goeb S., Croué V., Allain M., Popp B. V., Garci A., Therrien B., Sallé M., Electron-Rich Arene-Ruthenium Metalla-architectures Incorporating Tetrapyrrolyl-Tetrathiafulvalene Donor Moieties. *Organometallics* **2014**, *33* (7), 1651-1658.
100. Krykun S., Croué V., Alévêque O., Levillain E., Allain M., Mézière C., Carré V., Aubriet F., Voïtenko Z., Goeb S., Sallé M., A self-assembled tetrathiafulvalene box. *Organic Chemistry Frontiers* **2021**, *8* (5), 883-890.
101. Amriou S., Wang C., Batsanov A. S., Bryce M. R., Perepichka D. F., Ortí E., Viruela R., Vidal-Gancedo J., Rovira C., The Interplay of Inverted Redox Potentials and Aromaticity in the Oxidized States of New π -Electron Donors: 9-(1,3-Dithiol-2-ylidene)fluorene and 9-(1,3-Dithiol-2-ylidene)thioxanthene Derivatives. *Chemistry - A European Journal* **2006**, *12* (12), 3389-3400.
102. Croué V., Krykun S., Allain M., Morille Y., Aubriet F., Carre V., Voitenko Z., Goeb S., Salle M., A Self-Assembled M2L4 Cage incorporating Electron-rich 9-(1,3-dithiol-2-ylidene)Fluorene Units. *New Journal of Chemistry* **2017**, *41* (9), 3238-3241.
103. Krykun S., Allain M., Carré V., Aubriet F., Voitenko Z., Goeb S., Sallé M., A M2L2 Redox-Active Metalla-Macrocyclic Based on Electron-Rich 9-(1,3-Dithiol-2-ylidene)Fluorene. *Inorganics* **2018**, *6* (2), 44.
104. Brunetti F. G., López J. L., Atienza C., Martín N., π -Extended TTF: a versatile molecule for organic electronics. *Journal of Materials Chemistry* **2012**, *22* (10), 4188.
105. Bryce M. R., Moore A. J., Hasan M., Ashwell G. J., Fraser A. T., Clegg W., Hursthouse M. B., Karaulov A. I., Electrical and Magnetic Properties and X-Ray Structure of a Highly Conductive 4:1 Complex of Tetracyanoquinodimethane and a Tetrathiafulvalene Derivative. *Angew. Chem. Int. Ed.* **1990**, *29* (12), 1450-1452.
106. Moore A. J., Bryce M. R., Highly conjugated [p]-electron donors for organic metals: synthesis and redox chemistry of new 1,3-dithiole and 1,3-selenathiole derivatives. *Journal of the Chemical Society, Perkin Transactions 1* **1991**, *0* (1), 157-168.
107. Bivaud S., Goeb S., Croué V., Dron P. I., Allain M., Sallé M., Self-Assembled Containers Based on Extended Tetrathiafulvalene. *Journal of the American Chemical Society* **2013**, *135* (27), 10018-10021.
108. Szalóki G., Croué V., Allain M., Goeb S., Sallé M., Neutral versus polycationic coordination cages: a comparison regarding neutral guest inclusion. *Chem. Commun.* **2016**, *52* (65), 10012-10015.
109. Croué V., Goeb S., Szaloki G., Allain M., Salle M., Reversible Guest Uptake/Release by Redox-Controlled Assembly/Disassembly of a Coordination Cage. *Angew Chem Int Ed Engl* **2016**, *55* (5), 1746-50.

110. Szaloki G., Croue V., Carre V., Aubriet F., Aleveque O., Levillain E., Allain M., Arago J., Orti E., Goeb S., Salle M., Controlling the Host-Guest Interaction Mode through a Redox Stimulus. *Angew Chem Int Ed Engl* **2017**, 56 (51), 16272-16276.
111. Szalóki G., Krykun S., Croué V., Allain M., Morille Y., Aubriet F., Carré V., Voitenko Z., Goeb S., Sallé M., Redox-Driven Transformation of a Discrete Molecular Cage into an Infinite 3D Coordination Polymer. *Chemistry – A European Journal* **2018**, 24 (44), 11273-11277.
112. Dekhtiarenko M., Allain M., Carre V., Aubriet F., Voitenko Z., Salle M., Goeb S., Comparing the self-assembly processes of two redox-active exTTF-based regioisomer ligands. *New Journal of Chemistry* **2021**.
113. Canevet D., Pérez E. M., Martín N., Wraparound Hosts for Fullerenes: Tailored Macrocycles and Cages. *Angewandte Chemie International Edition* **2011**, 50 (40), 9248-9259.
114. Canevet D., Gallego M. a., Isla H., De Juan A., Pérez E. M., Martín N., Macrocyclic Hosts for Fullerenes: Extreme Changes in Binding Abilities with Small Structural Variations. *Journal of the American Chemical Society* **2011**, 133 (9), 3184-3190.
115. Grimm B., Santos J., Illescas B. M., Muñoz A., Guldi D. M., Martín N., A New exTTF-Crown Ether Platform To Associate Fullerenes: Cooperative n–n and n–n Effects. *J. Am. Chem. Soc.* **2010**, 132 (49), 17387–17389.
116. Isla H., Gallego M., Pérez E. M., Viruela R., Ortí E., Martín N., A Bis-exTTF Macrocyclic Receptor That Associates C60 with Micromolar Affinity. *J. Am. Chem. Soc.* **2010**, 132 (6), 1772–1773.
117. Perez E. M., Capodilupo A. L., Fernandez G., Sanchez L., Viruela P. M., Viruela R., Orti E., Bietti M., Martin N., Weighting non-covalent forces in the molecular recognition of C(60). Relevance of concave-convex complementarity. *Chem. Commun.* **2008**, 38 (38), 4567-9.
118. Pérez E. M., Sánchez L., Fernández G., Martín N., exTTF as a Building Block for Fullerene Receptors. Unexpected Solvent-Dependent Positive Homotropic Cooperativity. *J. Am. Chem. Soc.* **2006**, 128 (22), 7172–7173.
119. Bailey D., Williams V. E., An efficient synthesis of substituted anthraquinones and naphthoquinones. *Tetrahedron Letters* **2004**, 45 (12), 2511-2513.
120. Ronson T. K., Zarra S., Black S. P., Nitschke J. R., Metal-organic container molecules through subcomponent self-assembly. *Chemical Communications* **2013**, 49 (25), 2476-2490.
121. Ogoshi T., Kanai S., Fujinami S., Yamagishi T.-a., Nakamoto Y., para-Bridged Symmetrical Pillar[5]arenes: Their Lewis Acid Catalyzed Synthesis and Host-Guest Property. *Journal of the American Chemical Society* **2008**, 130 (15), 5022-5023.
122. Ogoshi T., Yamagishi T.-a., Pillararenes: Versatile Synthetic Receptors for Supramolecular Chemistry. *European Journal of Organic Chemistry* **2013**, 2013 (15), 2961-2975.
123. Li C., Pillararene-based supramolecular polymers: from molecular recognition to polymeric aggregates. *Chemical Communications* **2014**, 50 (83), 12420-12433.
124. Díaz M. C., Illescas B. M., Martín N., Stoddart J. F., Canales M. A., Jiménez-Barbero J., Sarova G., Guldi D. M., Supramolecular pseudo-rotaxane type complexes from n-extended TTF dimer crown ether and C60. *Tetrahedron* **2006**, 62 (9), 1998-2002.
125. Gabriel Mengheres S. G., Marc SALLÉ *Synthesis, electrochemical and host-guest properties of pillar[5]arene substituted with tetrathiafulvalene and n-extended tetrathiafulvalene*; Laboratory MOLTECH – Anjou: 2016.
126. Carrier R., Frère P., Sallé M., Roncali J., Jubault M., Tallec A., Gorgues A., Prediction of the stoichiometry of cation radical salts of organic metals by thin layer cyclic voltammetry. *Advanced Materials* **1993**, 5 (6), 445-447.
127. Calbo J., De Juan A., Aragón J., Villalva J., Martín N., Pérez E. M., Ortí E., Understanding the affinity of bis-exTTF macrocyclic receptors towards fullerene recognition. *Physical Chemistry Chemical Physics* **2019**, 21 (22), 11670-11675.
128. Steffenhagen M., Latus A., Trinh T. M. N., Nierengarten I., Lucas I. T., Joiret S., Landoulsi J., Delavaux-Nicot B., Nierengarten J.-F., Maisonhute E., A Rotaxane Scaffold Bearing Multiple Redox Centers: Synthesis, Surface Modification and Electrochemical Properties. *Chemistry – A European Journal* **2018**, 24 (7), 1701-1708.
129. Nierengarten I., Buffet K., Holler M., Vincent S. P., Nierengarten J.-F., A mannosylated pillar[5]arene derivative: chiral information transfer and antiadhesive properties against uropathogenic bacteria. *Tetrahedron Letters* **2013**, 54 (19), 2398-2402.
130. Ma Y., Chen L., Li C., Müllen K., A fishing rod-like conjugated polymer bearing pillar[5]arenes. *Chemical Communications* **2016**, 52 (40), 6662-6664.
131. Bastien G., Dron P. I., Vincent M., Canevet D., Allain M., Goeb S., Sallé M., C₆₀ Recognition from Extended Tetrathiafulvalene Bis-acetylide Platinum(II) Complexes. *Organic Letters* **2016**, 18 (22), 5856-5859.

132. Guldi D. M., Sánchez L., Martín N., Formation and Characterization of the π -Radical Cation and Dication of π -Extended Tetrathiafulvalene Materials. *The Journal of Physical Chemistry B* **2001**, *105* (29), 7139-7144.
133. Nierengarten I., Meichsner E., Holler M., Pieper P., Deschenaux R., Delavaux-Nicot B., Nierengarten J.-F., Preparation of Pillar[5]arene-Based [2]Rotaxanes by a Stopper-Exchange Strategy. *Chemistry – A European Journal* **2018**, *24* (1), 169-177.
134. Dekhtiarenko M., Krykun S., Carré V., Aubriet F., Canevet D., Allain M., Voitenko Z., Sallé M., Goeb S., Tuning the structure and the properties of dithiafulvene metalla-assembled tweezers. *Organic Chemistry Frontiers* **2020**, *7* (15), 2040-2046.
135. Krykun S., Dekhtiarenko M., Canevet D., Carré V., Aubriet F., Levillain E., Allain M., Voitenko Z., Sallé M., Goeb S., Metalla-Assembled Electron-Rich Tweezers: Redox-Controlled Guest Release Through Supramolecular Dimerization. *Angewandte Chemie International Edition* **2020**, *59* (2), 716-720.
136. Perepichka D. F., Perepichka I. F., Ivasenko O., Moore A. J., Bryce M. R., Kuz'mina L. G., Batsanov A. S., Sokolov N. I., Combining High Electron Affinity and Intramolecular Charge Transfer in 1,3-Dithiole-Nitrofluorene Push-Pull Diads. *Chem. - Eur. J.* **2008**, *14* (9), 2757-2770.
137. Macchioni A., Ciancaleoni G., Zuccaccia C., Zuccaccia D., Determining accurate molecular sizes in solution through NMR diffusion spectroscopy. *Chem. Soc. Rev.* **2008**, *37* (3), 479-489.
138. Ferrer M., Gutiérrez A., Rodríguez L., Rossell O., Ruiz E., Engeser M., Lorenz Y., Schilling R., Gómez-Sal P., Martín A., Self-Assembly of Heterometallic Metallomacrocycles via Ditopic Fluoroaryl Gold(I) Organometallic Metalloligands. *Organometallics* **2012**, *31* (4), 1533-1545.
139. Cotellet Y., Hardouin-Lerouge M., Legoupy S., Alévêque O., Levillain E., Hudhomme P., Glycoluril-tetrathiafulvalene molecular clips: on the influence of electronic and spatial properties for binding neutral accepting guests. *Beilstein Journal of Organic Chemistry* **2015**, *11*, 1023-1036.
140. Leblond J., Petitjean A., Molecular Tweezers: Concepts and Applications. *Chemphyschem* **2011**, *12* (6), 1043-1051.
141. Hardouin-Lerouge M., Hudhomme P., Sallé M., Molecular clips and tweezers hosting neutral guests. *Chem. Soc. Rev.* **2011**, *40* (1), 30-43.
142. Shtukenberg A. G., Ward M. D., Kahr B., Crystal Growth with Macromolecular Additives. *Chem. Rev.* **2017**, *117* (24), 14042-14090.
143. Shtukenberg A. G., Lee S. S., Kahr B., Ward M. D., Manipulating Crystallization with Molecular Additives. *Annu. Rev. Chem. Biomol. Eng.* **2014**, *5* (1), 77-96.
144. Jones F., Ogden M. I., Controlling crystal growth with modifiers. *Crystengcomm* **2010**, *12* (4), 1016-1023.
145. Niu Z., Li D., Liu D., Xia D., Zou Y., Sun W., Li G., Syntheses, electrochemical behaviors, spectral properties and DFT calculations of two 1,3-dithiole derivatives. *Chem. Res. Chin. Univ.* **2014**, *30* (3), 425-430.
146. Yan H., Suss-Fink G., Neels A., Stoeckli-Evans H., Mono-, di- and tetra-nuclear p -cymeneruthenium complexes containing oxalato ligands. *Journal of the Chemical Society, Dalton Transactions* **1997**, (22), 4345-4350.
147. Barry N. P. E., Furrer J., Therrien B., In- and Out-of-Cavity Interactions by Modulating the Size of Ruthenium Metallarectangles. *Helv. Chim. Acta* **2010**, *93* (7), 1313-1328.
148. Faour L., Adam C., Gautier C., Goeb S., Allain M., Levillain E., Canevet D., Sallé M., Redox-controlled hybridization of helical foldamers. *Chem. Commun.* **2019**, *55* (40), 5743-5746.
149. Aparicio F., Faour L., Allain M., Canevet D., Sallé M., A pyrene-functionalized foldamer: structural impact and recognition properties supported by donor-acceptor interactions. *Chem. Commun.* **2017**, *53* (88), 12028-12031.
150. Dekhtiarenko M., Pascal S., Elhabiri M., Mazan V., Canevet D., Allain M., Carré V., Aubriet F., Voitenko Z., Sallé M., Siri O., Goeb S., Reversible pH-Controlled Catenation of a Benzobisimidazole-Based Tetranuclear Rectangle. *Chemistry – A European Journal* *n/a* (n/a).
151. Gao W. X., Feng H. J., Guo B. B., Lu Y., Jin G. X., Coordination-Directed Construction of Molecular Links. *Chem. Rev.* **2020**, *120* (13), 6288-6325.
152. Lu Y., Liu D., Lin Y.-J., Li Z.-H., Jin G.-X., Self-assembly of metalla[3]catenanes, Borromean rings and ring-in-ring complexes using a simple n -donor unit. *Natl. Sci. Rev.* **2020**, *7* (10), 1548-1556.
153. Gil-Ramírez G., Leigh D. A., Stephens A. J., Catenanes: Fifty Years of Molecular Links. *Angew. Chem. Int. Ed.* **2015**, *54* (21), 6110-6150.
154. Frank M., Johnstone M. D., Clever G. H., Interpenetrated Cage Structures. *Chem. Eur. J.* **2016**, *22* (40), 14104-14125.

155. Bruns C. J., Stoddart J. F., *The Nature of the Mechanical Bond: From Molecules to Machines*. Wiley: Hoboken, NJ, USA, 2016.
156. Wang W., Wang Y.-X., Yang H.-B., Supramolecular transformations within discrete coordination-driven supramolecular architectures. *Chemical Society Reviews* **2016**, 45 (9), 2656-2693.
157. Wezenberg S. J., Light-switchable Metal-Organic Cages. *Chem. Lett.* **2020**, 49 (6), 609-615.
158. Mal P., Schultz D., Beyeh K., Rissanen K., Nitschke J. R., An Unlockable-Relockable Iron Cage by Subcomponent Self-Assembly. *Angew. Chem. Int. Ed.* **2008**, 47 (43), 8297-8301.
159. Xu L., Zhang D., Ronson T. K., Nitschke J. R., Improved Acid Resistance of a Metal-Organic Cage Enables Cargo Release and Exchange between Hosts. *Angew. Chem. Int. Ed.* **2020**, 59 (19), 7435-7438.
160. Riddell I. A., Smulders M. M. J., Clegg J. K., Nitschke J. R., Encapsulation, storage and controlled release of sulfur hexafluoride from a metal-organic capsule. *Chem. Commun.* **2010**, 47 (1), 457-459.
161. Henkelis J. J., Fisher J., Warriner S. L., Hardie M. J., Solvent-Dependent Self-Assembly Behaviour and Speciation Control of Pd₆L₈ Metallo-supramolecular Cages. *Chem. Eur. J.* **2014**, 20 (14), 4117-4125.
162. Ganta S., Chand D. K., Multi-Stimuli-Responsive Metallogel Molded from a Pd₂L₄-Type Coordination Cage: Selective Removal of Anionic Dyes. *Inorg. Chem.* **2018**, 57 (7), 3634-3645.
163. Lisboa L. S., Findlay J. A., Wright L. J., Hartinger C. G., Crowley J. D., A Reduced-Symmetry Heterobimetallic [PdPtL₄]₂(4+) Cage: Assembly, Guest Binding, and Stimulus-Induced Switching. *Angew. Chem. Int. Ed.* **2020**, 59 (27), 11101-11107.
164. Jansze S., Severin K., Palladium-Based Metal-Ligand Assemblies: The Contrasting Behavior upon Addition of Pyridine or Acid. *J. Am. Chem. Soc.* **2019**, 141 (2), 815-819.
165. Schäfer B., Suryadevara N., Greisch J.-F., Fuhr O., Kappes M. M., Ruben M., Ditopic Hexadentate Ligands with a Central Dihydrobenzo-diimidazole Unit Forming a [2x2] Zn₄ Grid Complex. *Eur. J. Org. Chem.* **2021**, 2021 (16), 2301-2310.
166. Singhal N., Mishra A., Datta A., Excited-State Proton Transfer and Conformational Relaxation of 2-(4'-Pyridyl)benzimidazole in Nafion Films. *Chemphyschem* **2016**, 17 (19), 3004-3009.
167. Khorwal V., Datta A., Ground and excited state prototropism of 2-(4'-pyridyl)benzimidazole in micelles. *J. Photochem. Photobiol., A* **2012**, 250, 99-102.
168. Novo M., Mosquera M., Rodriguez Prieto F., Excited-State Behavior of 2-(4'-Pyridyl)benzimidazole in Aqueous Solution: Proton-Transfer Processes and Dual Fluorescence. *J. Phys. Chem.* **1995**, 99 (40), 14726-14732.
169. Novo M., Mosquera M., Prieto F. R., Prototropic equilibria of 2-pyridylbenzimidazoles in aqueous solution. *Can. J. Chem.* **1992**, 70 (3), 823-827.
170. Wang C., Batsanov A. S., Bryce M. R., Howard J. A. K., An Improved Large-Scale (90 g) Synthesis of Bis(tetraethylammonium)bis(1,3-dithiole-2-thione-4,5-dithiol)zincate: Synthesis and X-ray Crystal Structures of Bicyclic and Tricyclic 1,4-Dithiocines Derived from 1,3-Dithiole-2-thione-4,5-dithiolate (DMIT). *Synthesis* **1998**, 11 (11), 1615-1618.
171. Bar A. K., Chakrabarty R., Chi K.-W., Batten S. R., Mukherjee P. S., Synthesis and characterisation of heterometallic molecular triangles using ambidentate linker: self-selection of a single linkage isomer. *Dalton Transactions* **2009**, (17), 3222-3229.
172. Therrien B., Süß-Fink G., Govindaswamy P., Renfrew A. K., Dyson P. J., The "Complex-in-a-Complex" Cations [(acac)₂M=Cu₆(p-iPrC₆H₄Me)₆(tpt)₂(dmbq)₃]₆⁺: A Trojan Horse for Cancer Cells. *Angewandte Chemie International Edition* **2008**, 47 (20), 3773-3776.

Titre : Construction d'architectures moléculaires auto-assemblées par des métaux, capables de répondre à un stimulus

Mots clés : Redox, Complexe hôte-invité, Relargage contrôlé

Résumé : Ce travail est lié à la synthèse et la caractérisation de cages auto-assemblées redox-actives ou sensibles au pH, ainsi qu'à l'étude de leur capacité à opérer des changements conformationnels ou supramoléculaires à l'aide de stimuli redox ou acide-base. La première partie concerne le développement et la synthèse de ligands riches en électrons dérivés de l'unité tétrathiafulvalène π -étendu (exTTF). Cette unité présente des propriétés électroniques et géométriques remarquables avec en particulier un important changement structural au cours du processus d'oxydation. Plusieurs ligands bidentes et tétradentes ont été préparés. Les auto-assemblages correspondants présentent des cavités dont la forme et la charge peuvent être modulées par stimulus redox.

De plus, les propriétés électroniques et supramoléculaires d'une plateforme pillar[5]arène originale, greffée par dix unités exTTF, ont été étudiées. La seconde partie décrit la capacité de pinces moléculaires construites à partir de ligands dérivés du 9-(1,3-dithiol-2-ylidène)fluorène (DTF) à se dimériser spontanément grâce à des interactions électroniques spécifiques. Les structures interpénétrées obtenues peuvent être dissociées de façon originale, par reconnaissance d'un invité électro-déficient et régénérées par oxydation avec la libération concomitante de l'invité. Enfin, la caténation d'un rectangle moléculaire, construit à partir d'un ligand benzobisimidazole sensible au pH, est étudié par dilution, modification du pH ou ajout d'une molécule invitée

Title : Construction of stimuli-responsive architectures through coordination-driven self-assembly

Keywords : Supramolecular chemistry, Organic synthesis, Self-assembly, Molecular cage, Tetrathiafulvalene, Redox, Host-guest complex, Controlled delivery

Abstract : This work is related to the synthesis and characterization of redox-active or pH-sensitive self-assembled cages, as well as the study of their ability to effect conformational or supramolecular changes with redox or acid-base stimuli. The first part concerns the development and synthesis of electron-rich ligands derived from the π -extended tetrathiafulvalene unit (exTTF). This unit shows remarkable electronic and geometrical properties with in particular an important structural change during the oxidation process. Several bidentate and tetradent ligands have been prepared. The corresponding self-assemblies present cavities whose shape and charge can be modulated by redox stimulus.

In addition, the electronic and supramolecular properties of an original pillar[5]arene platform, grafted with ten exTTF units, have been studied. The second part describes the ability of molecular clamps constructed from 9-(1,3-dithiol-2-ylidene)fluorene (DTF) derived ligands to spontaneously dimerize through specific electronic interactions. The resulting interpenetrating structures can be dissociated in a novel way, by recognition of an electro-deficient guest and regenerated by oxidation with concomitant release of the guest. Finally, the catenation of a molecular rectangle, built from a pH sensitive benzobisimidazole ligand, is studied by dilution, pH modification or addition of a guest molecule.